Jefferson Lab JLEIC EIC² EIC Center at Jefferson Lab

Jefferson Lab ELECTRON-ION COLLIDER

Pre-Conceptual Design Report

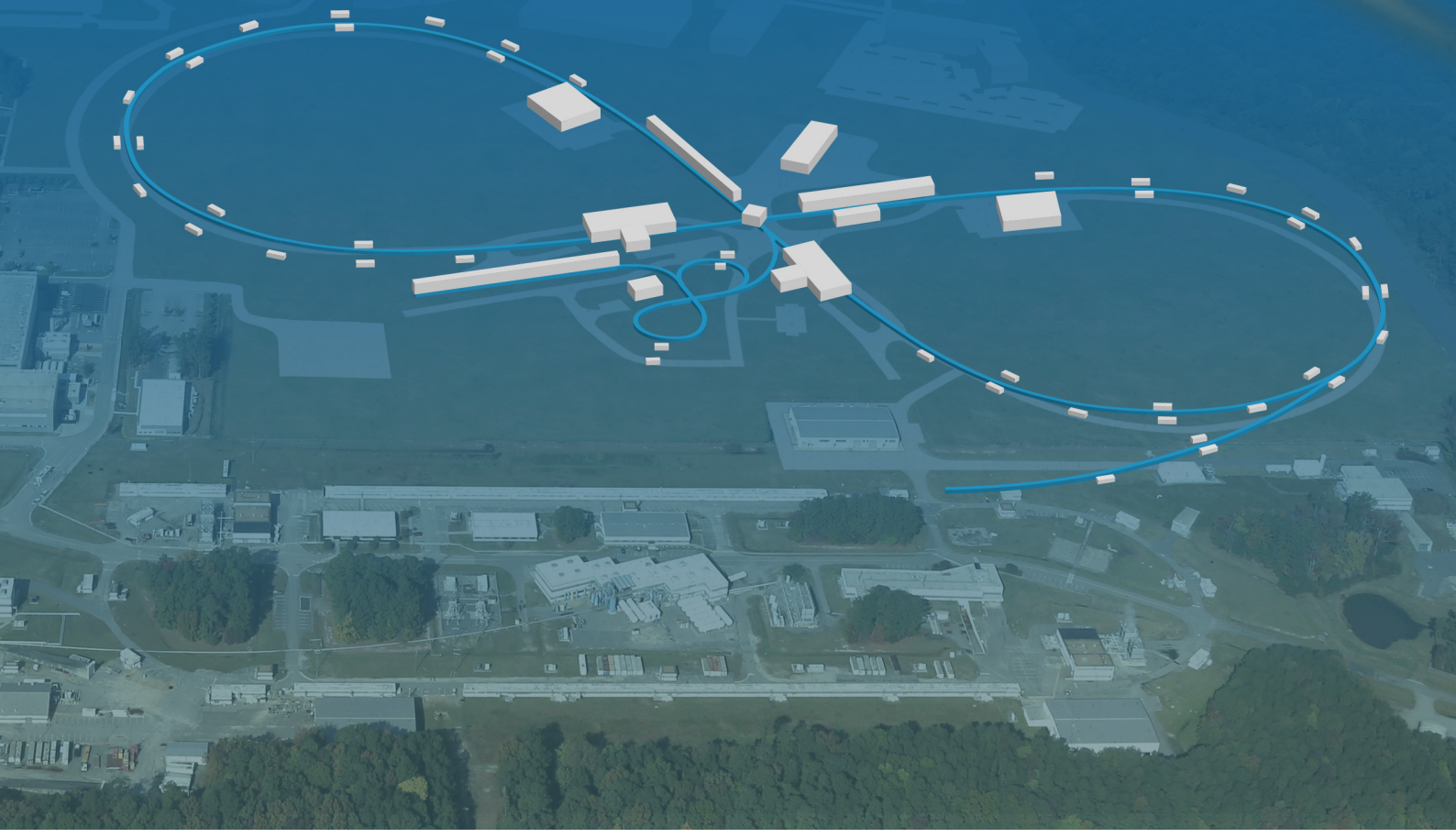

Pre-Conceptual Design Report (pCDR)
for
The Jefferson Lab Electron-Ion Collider JLEIC

Jefferson Lab

February 13, 2019
JLAB-ACC-19-R001

Jefferson Lab is managed and operated by
The Southeastern Universities Research Association (SURA) for
the Office of Science of the U.S. Department of Energy
under Contract DE-AC05-06OR23177

Jefferson Lab
12000 Jefferson Avenue
Newport News, VA 23606
www.jlab.org
(757) 269-7100

Contents

CHAPTER 1

EXECUTIVE SUMMARY

1.1 Introduction

Jefferson Lab proposes to build an electron-ion collider (EIC) facility called the Jefferson Lab Electron-Ion Collider (JLEIC), having a peak luminosity over $10^{34}\,\mathrm{cm}^{-2}\,\mathrm{s}^{-1}$, and a collider center-of-mass (CM) energy range ∼20–∼100 GeV upgradeable to ∼140 GeV. An EIC has been selected as the primary new facility construction priority in the U.S. Department of Energy Nuclear Physics Long Range Plans in 2007 [1] and 2015 [2]. Such a facility must be very flexible over a multi-decade operating lifetime, supporting exploration of nuclear physics over a wide range of CM energies and ion species with highly polarized electrons and light ions. These requirements are spelled out in a white paper [3], the 2015 NSAC Long Range Plan [2] and National Academies of Science Committee recommendations [4].

We have known for fifty years that protons and neutrons that comprise nuclei of the elements are composed of quarks and gluons. We have also understood that properties of nucleons and nuclei, such as their mass, spin, and their interactions are the consequences of the underlying physics of quarks and gluons. This has resulted in the development of a new science of emergent phenomena in nuclear material, and 3D nuclear structure — nuclear femtography. A major part of the science program at the 12 GeV CEBAF facility is aimed at this new science; JLEIC enables a full exploration of nuclear femtography.

Jefferson Lab, in collaboration with Argonne National Laboratory, Brookhaven National Laboratory, Lawrence Berkeley National Laboratory, and Stanford National Accelerator Laboratory, has developed a pre-conceptual design for an electron-ion collider that meets, and in many cases exceeds, these stringent requirements. The design integrates the experience of high-luminosity operations from recent accelerators and the innovations developed by the JLEIC designers to produce

Figure 1.1: JLEIC site plan at Jefferson Lab.

a diverse array of collisions between polarized electrons and polarized nucleons. This capability will open the door to the exploration of the three-dimensional distributions of all the partons in the nucleon over an unprecedented kinematic range. The result will be an unparalleled exploration of the way in which the phenomena of nuclear physics, the mass, and the spin, emerge from the fundamental interactions of the partons using a detector configuration matched to the interaction dynamics.

The JLEIC ion ring is based on an innovative figure-8 synchrotron design (Figure 1.1) that will, for the first time, guarantee high polarization of protons, deuterons, and other light ion beams. This new topology, which has been extensively simulated and positively reviewed, ensures that polarized ions can be accelerated, manipulated and spin-flipped without losing polarization. This includes polarized deuterium ions, which have never been available in any other collider. A new, fully modern ion complex will be assembled that uses this figure-8 topology for polarization control. This complex will use state of the art magnets and ion sources to transport ion beams, including polarized deuterons, to the figure-8 collider ring for high luminosity collisions.

The polarization measurement accuracy in nuclear femtography is proportional to the square of the polarization in each beam. The high polarization in JLEIC (>80% in the electron ring and >85% in the ion ring) compared with the minimum requirement [3] (>70% for both beams) decreases the time needed for a polarized beam experiment by a factor of nearly two. This is equivalent to doubling the effective luminosity from the white paper base requirement.

JLEIC maximally leverages the existing CEBAF capability for production of polarized electron beams. These polarized electrons are transported to a figure-8 electron collider ring in the same

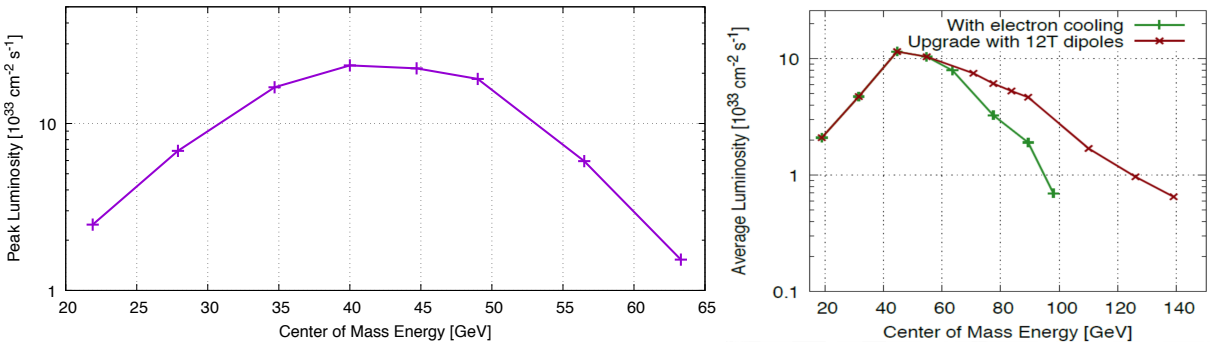

Figure 1.2: JLEIC *e-p* peak luminosity, with CM energy up to 65 GeV as detailed in the main body of this report (left), and *average* luminosity up to 100–140 GeV as described in the high energy option of Appendix A (right).

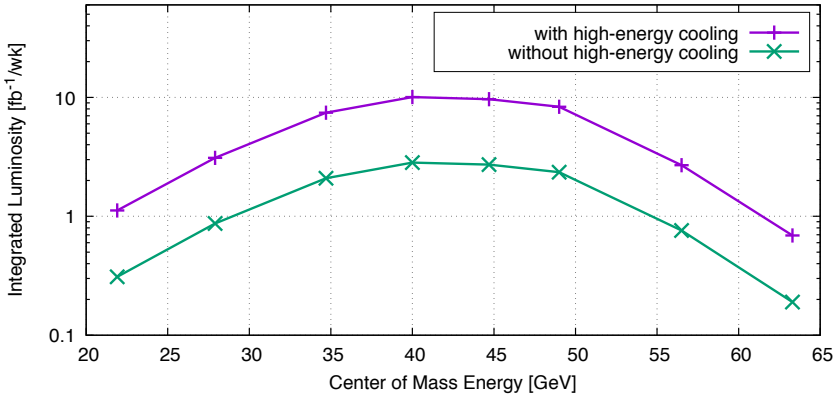

Figure 1.3: JLEIC *e-p* integrated luminosity per week, with and without high energy electron cooling.

tunnel as the ion ring. Polarized electrons can also be injected during collisions ("top-off") to replace electrons that interacted, maintaining both high luminosity and high electron polarization.

HERA [5], the first and only electron-ion collider to date, operated from 1992–2007. HERA was a technological achievement, but the physics output was limited by its low luminosity; the maximum achieved was $\sim 5 \times 10^{31}\,\mathrm{cm}^{-2}\,\mathrm{s}^{-1}$. The JLEIC designers have taken this lesson to heart and focused on maximizing the luminosity, both peak and integrated. The peak luminosity is achieved using DC magnetized electron cooling of the ions at low energy. This is a well-developed technique, pioneered by the Budker Institute in Novosibirsk [6]. The highest energy DC electron cooling was at 4 MeV in the Fermilab Recycler [7]; this is the maximum energy proposed for DC cooling in JLEIC thus far. Following acceleration of the ions, the initial luminosity is determined by this low energy cooling, reaching $2 \times 10^{34}\,\mathrm{cm}^{-2}\,\mathrm{s}^{-1}$, more than 400 times the HERA luminosity as shown in Figure 1.2 (left).

An advantage of designing JLEIC to use electron cooling throughout the ion complex is that ion bunches will be short; they will indeed be similar in length to the electron bunches. This means that the experience of the B-Factories (PEP-II in the USA and KEKB in Japan) can be applied directly to the JLEIC design. This optimization leads to a large number of bunches (>3000), each

Table 1.1: EIC White Paper Luminosity Needs. Units are integrated luminosity in fb^{-1}. High luminosity requirements are bolded. Values in parentheses can be acquired concurrently with other measurements. A blank entry does not mean there is no interest; rather that the White Paper [3] does not discuss these measurements explicitly. A fuller picture of EIC measurements is shown in Figures 2.1 and 2.2 in the next Chapter. Ion and electron polarizations are indicated as unpolarized (U), transverse (T), and longitudinal (L).

Physics	**White Paper Reference**	**eP low** (∼20 GeV)	**eP medium** (∼40 GeV)	**eP high** (∼60–∼100 GeV)	**eP Phase II** (140 GeV)	**eD or e^3He**	**eCa**	**eAu**
Gluon Spin (UL)	Table 2.1	–	–	(10)	–	(10)	–	–
Quark TMD (LL+LT)	Figs. 2.15–2.16	10+10	(10+10)	(10+10)	–	–	–	–
Gluon TMD (LL+LT)	Figs. 2.17	–	–	**100+100**	–	–	–	–
DVCS (LL+LT)	Fig. 2.21, 2.6	–	**100+100**	(100+100)	–	–	–	–
DVCS eD (LL+LT)	Sec. 2.4.6	–	–	–	–	**100+100**	–	–
Saturation (UU)	Figs. 3.16–3.20	–	–	(10)	10	–	10	10

with a relatively small number of particles ($\sim 10^{10}$), reducing many of the problems of collective effects that tend to enlarge the beam size and reduce luminosity.

Intra-beam scattering, residual gas scattering, and beam-beam interactions all increase the ion emittance, so the luminosity decreases during the beam store. The JLEIC design includes high-energy bunched electron cooling to combat this effect, also using magnetized electron beams to improve the cooling rate. This system involves a bunched electron beam, which is accelerated in a superconducting booster and energy-recovery linac, before being injected into a circulator-cooler ring. Each injection replaces every eleventh bunch, so the circulating current that cools the ions is eleven times the current from the gun. The cooling electrons are then decelerated in the energy-recovery linac for energy efficiency, a technique refined in the Jefferson Lab FEL [8] and now used world-wide.

Maintaining small ion emittance with bunched-beam cooling during the store results in a significant improvement in integrated luminosity, as shown in Figure 1.3. After a luminosity upgrade in 2000–2003, HERA reached a steady-state integrated luminosity delivery of $\sim 5 \times 10^{-3}\,\text{fb}^{-1}$/week. As designed, JLEIC will be able to surpass the integrated luminosity of the HERA physics program after only a few days of running, the key to making new discoveries.

The planned experimental program for JLEIC is shown in Table 1.1, divided by energy range. The great majority of the experiments described in the White Paper can be optimally performed in the energy range of 40–60 GeV, with a total integrated luminosity of $640\,\text{pb}^{-1}$, and that even with the luminosities achievable with JLEIC, the program already spans a decade. This underlines the extreme importance of high luminosity in completing the designated physics program. Even a reduction of a factor of two would add a decade to the experimental program.

Electrons and ions in the two rings are brought into collision in the interaction regions. The JLEIC design prioritizes full acceptance for the detector to ensure that all interactions can be fully identified. Construction of a new kind of interaction region also allows integration and optimization of the detector to realize the full range of physics goals detailed in [3]. Collisions occur with a crossing angle, which enables clean separation of the final-state particles and therefore full reconstruction of all events. This detector includes ultra-forward hadron detection for maximum acceptance of the forward scattered collision products.

The superconducting final focusing magnets in the interaction region are within the state of the art and are staggered in the two rings to avoid beams passing through the yoke of the magnets in the other ring. A crossing angle minimizes the complexities of these magnets.

Since the bunches are pencil-shaped, a crossing angle means that most of the particles in a bunch do not interact directly with most of the particles in the other bunch during a collision. This luminosity reduction can be avoided by "twisting" the bunches with so-called "crab cavities" so the bunches collide head-on. Crab cavities were installed successfully at KEKB and used to surpass the world record in luminosity for a collider. The high luminosity upgrade of the LHC at CERN will also have crab cavities. JLEIC is designed with complete crab cavity systems for both electron and ion beams.

The present JLEIC design was developed in close collaboration with the future users and prioritizes high luminosity in the 20–60 GeV CM energy range where high luminosity is paramount and where the detector acceptance is optimally matched to the collision kinematics and physics objectives. Use of 6 T dipoles results in an extension of the JLEIC CM energy reach to 100 GeV. This choice results in a average luminosity of $\sim 10^{33}\,\mathrm{cm}^{-2}\,\mathrm{s}^{-1}$ at a CM energy of ∼100 GeV (about 20 times the HERA luminosity) as shown in Figure 1.2. With a further upgrade to the ion dipole magnets, the maximum CM energy would be 140 GeV, still with a luminosity of $10^{33}\,\mathrm{cm}^{-2}\,\mathrm{s}^{-1}$.

The JLEIC design has matured over the last decade with the fundamental design remaining unchanged. It has been extensively reviewed by experts in the field who have endorsed the design and the luminosity estimates. However, there are still some areas where the technology needs further R&D and opportunities for cost-risk-performance optimization.

1.2 Capabilities

The requirements of an EIC as described in the white paper [3] include:

- Highly polarized (∼70%) electron and nucleon beams
- Ion beams from deuteron to the heaviest nuclei (uranium or lead)
- Variable CM energies from ∼20–∼100 GeV, upgradable to ∼140 GeV
- High collision luminosity of $\sim 10^{34}\,\mathrm{cm}^{-2}\,\mathrm{s}^{-1}$
- Possibilities of having more than one interaction region

JLEIC polarized electron-proton luminosities as a function of CM energy are shown in Figure 1.2. A detailed discussion of the facility physics motivation is provided in Chapter 2, and details of the luminosity concept are provided in Chapter 3.

1.3 JLEIC Facility

The JLEIC facility is comprised of the following elements:

- The existing 12 GeV CEBAF polarized electron accelerator complex.
- A new figure-8 electron collider ring, optimized for electron polarization and collision luminosity over beam energies of 5–12 GeV.
- An electron transport system from CEBAF to the electron collider ring.
- A new ion injector complex, optimized for production of a range of polarized light ions (including deutrons), and unpolarized heavy ions.
- A new figure-8 ion collider ring, optimized for ion polarization and collision luminosity over beam energies of 20–100 GeV.

- A new experimental hall and interaction region, optimized for full acceptance, high luminosity, and particle detection required for nuclear femtography and nuclear imaging.
- Basic infrastructure for a future second experimental hall and interaction region.

The overall facility site plan is illustrated in Figure 1.1.

1.4 Document Overview

This pre-conceptual design report is organized as follows. In Chapter 2, we describe the existing nuclear physics landscape and objectives of EIC in the framework of JLEIC, emphasizing the nuclear physics problems that JLEIC is particularly well-designed to address and demonstrating how JLEIC meets the requirements of the white paper [3] and the NSAC Long Range Plan and National Academies of Science Committee recommendations [2, 4]. In Chapter 3, we describe the overall facility conceptual design, including major design drivers that will deliver the required high luminosity and highly polarized beams for nuclear physics studies.

In Chapters 4 and 5, we include detailed designs of the electron and ion collider complexes, respectively, including sources, injectors, and spin design for beam polarization. Chapter 6 discusses the beam cooling concepts and design necessary to achieve JLEIC luminosity goals. Chapter 7 describes the integrated interaction region (IR) and detector design. Both the IR and detector must be considered together due to physics requirements for nearly full acceptance and the importance of forward tagging.

Chapter 8 includes sections addressing accelerator physics issues related to the collider ring designs, such as beam-beam and dynamic aperture effects, and impedances and instabilities. Chapter 9 discusses engineering details of the facility: magnet requirements and design, power supplies, vacuum requirements, cryogenics, and controls. Chapter 10 presents considerations of conventional facilities, including buildings and civil support infrastructure. Chapter 11 presents cryogenic requirements and equipment for JLEIC. Chapter 12 presents considerations of other safety systems for personnel and machine protection.

Appendix A presents considerations of a high-energy option for JLEIC using 6 T dipoles. Appendix B collects important tables from the overall document for reference.

REFERENCES

1. R. Tribble *et al.*, "The Frontiers of Nuclear Science: A Long Range Plan", `https://science.energy.gov/~/media/np/nsac/pdf/docs/NuclearScienceHighRes.pdf`, December 2007.
2. A. Aprahamian *et al.*, "Reaching for the Horizon: The 2015 Long Range Plan for Nuclear Science", `https://science.energy.gov/~/media/np/nsac/pdf/2015LRP/2015_LRPNS_091815.pdf`, October 2015.
3. A. Accardi *et al.*, "Electron Ion Collider: The Next QCD Frontier - Understanding the Glue that Binds Us All", Eur. Phys. J. **A52**, p. 268 (2016), `https://doi.org/10.1140/epja/i2016-16268-9`
4. National Academies of Sciences, Engineering, and Medicine. 2018. "An Assessment of U.S.-Based Electron-Ion Collider Science". Washington, DC: The National Academies Press. `https://doi.org/10.17226/25171`
5. F. Willeke, "HERA and the Next Generation of Lepton-Ion Colliders", in *Proc. of EPAC'06*, Edinburgh, Scotland, paper FRXBPA01, pp. 3621–5, 2006.
6. G.I. Budker *et al.*, "Experimental Studies of Electron Cooling", *Particle Accelerators* **7**, pp. 197–211, 1976.
7. S. Nagaitsev *et al.*, "Experimental Demonstration of Relativistic Electron Cooling", *Phys. Rev. Lett* **96**, p. 044801, 2006.
8. G.R. Neil *et al.*, "The JLab High Power ERL Light Source", *NIM:A* **557** issue 1, pp. 9–15, Feb. 2006, `https://doi.org/10.1016/j.nima.2005.10.047`

CHAPTER 2

NUCLEAR PHYSICS

2.1 Nuclear Physics at the Electron-Ion Collider

As stated in the National Academy of Sciences Committee recommendations (NAS report) [1], "a central goal of modern nuclear physics is to understand the structure of the proton and neutron directly from the dynamics of their quarks and gluons, governed by the theory of their interactions, quantum chromodynamics (QCD), and how nuclear interactions between protons and neutrons emerge from these dynamics." The scientific program of the Electron-Ion Collider (EIC) is one that is designed to make unprecedented progress towards this goal.

Within this central goal, topics specifically identified in the NAS report as being the main program of research at the EIC are the emergences of 1) mass of the nucleons, 2) spin of the nucleons and 3) properties of dense system of gluons from underlying QCD interactions. The last of these also encompass the question of the emergence of nuclear forces. A credible research program into these profound questions has become conceivable due to advances in both theory and experiment, as well as in accelerator science.

The discussion of a design of the accelerator forms the bulk of this document. Also, there are several existing documents that discuss the science of EIC in some detail [1, 2]. In this chapter, a brief discussion of the origin of the science program at EIC is presented with the main purpose of articulating the requirements placed on the EIC accelerator performance.

2.2 Longitudinal Quark/Gluon Structure of Nucleons and Nuclei

Quarks were discovered in late 1960's in electron-proton (and nuclei) scattering experiments carried out at the SLAC laboratory [3]. The 4-momentium transfer, Q, of the scattering is inversely

proportional to the distance scale at which the proton is probed. If Q is sufficiently high to probe the inner structure of the proton then the scattering process is called Deep Inelastic Scattering (DIS). It was the independence vs Q of the electron-proton cross section divided by the Mott cross-section (i.e. that of a point-like particle scattering) observed at the SLAC experiment that showed that the electrons were scattering from quasi-free point-like particles from within the proton—later identified with quarks. Indeed, DIS remains the process of choice to probe the structure of nucleons and nuclei due to the point-like nature of the electron; the EIC also aims to use the DIS process to explore nucleons and nuclei.

The theoretical issue that needs to be resolved in order to be able to discuss the quark-gluon structure of protons (or indeed of any target) determined via DIS, or any other process, is quantum entanglement. The quantum mechanical cross-sections, in general, cannot be simply decomposed into a part describing the proton structure and a part describing the probe, the virtual-photon coupling the electron and the quark in case of DIS. It was shown in QCD factorization theorems [4] that indeed, in the case of DIS, and in fact in a large set of high Q scattering processes, that the cross-sections "factorize" into the proton structure and the point-like scattering of the quarks with electrons, if, the process is evaluated in the "infinite momentum frame" where the fast moving protons are flattened due to relativistic length-contraction and transverse kinematics of the quarks and gluons can be ignored.

This first QCD factorization led to a very successful set of DIS, and other, measurements, aimed at the determination of the parton distribution functions (PDFs) that quantify the longitudinal structure of quark and gluon in the protons (and also nuclei). The PDFs are determined as a function of "x", the fraction of the longitudinal momentum of the proton carried by the quark or gluon (and Q). These measurements have provided a set of PDFs that have been shown to be a consistent description over many different processes above Q of a few GeV and a reliable predictor of "parton luminosities" at energy frontier colliders such as the LHC.

There have been three main experimental results that connect nucleon and nuclear characteristics with PDFs.

- DIS experiments on polarized targets by the EMC collaboration [5] first showed that the quarks carry only a small portion of the proton spin leading to the so-called "spin crisis"; which is not resolved. The subsequent experiments at CERN, HERA and RHIC show that gluons carry, possibly, a substantial part of the proton spin. There are also indications that orbital angular momentum play a significant role.

- EMC collaboration also conducted DIS experiments off nuclei [6] that showed that the PDFs are modified within nuclei at intermediate to high-x (the "EMC effect"). This may be due to an effective field present in the nucleus. Recently a strong linear relationship between short-range nucleon-nucleon correlation and the EMC effect has been shown experimentally.

- Experiments at HERA as well as those at RHIC and LHC show some indications that a regime in which "gluon recombination" takes place due to the high density of gluons reached at low x has been probed (see for example, Sec 3.2.1 in [2]). Closely related is the discovery of the phenomenon of DIS diffraction where proton remains intact in the final state despite a high 4-momentum transfer (Q) of above a few GeV.

Despite these, and other, tantalizing hints of the relationship of quarks/gluons distributions, and QCD to nucleon and nuclear characteristics, the question of how mass and spin, and nuclear forces arise from the underlying interactions and structure has not been answered in terms of PDFs that provide distributions only as a function of longitudinal momentum fraction x.

2.3 Transverse Quark/Gluon Structure of Nucleons and Nuclei

Theoretical developments (see for example [7]) over the last decades have led to factorization theorems for non-inclusive DIS processes that contain two scales. One scale is the 4-momentum transfer Q as in the first factorization of inclusive DIS. The second is a scale transverse to the direction of motion of the nucleon, either the transverse position or the momentum of the probed parton. The magnitude of these transverse scales are comparable to a fraction of the nucleon mass and in the range 10–100 MeV. There are two types or non-inclusive DIS processes that are factorized.

- Processes sensitive to the impact parameter (or transverse position of the struck quark) b of the collision which is conjugate to the transverse momentum transfer to the final state nucleon. These processes require a final state nucleon that remains intact and whose transverse momentum is measured, and the remaining final state that can be well-defined such as a photon or a vector meson (in addition to the scattered electron). These processes are called exclusive DIS processes. These measurements can be used to extract Generalized Parton Distributions (GPDs) that depend on b in addition to x.
- Processes sensitive to the transverse momentum of the struck (and/or final state) quark (k_T). The processes are called Semi-inclusive DIS (SIDIS) and require the identification of a particle from the final state associated with the struck quark in the DIS process, as well as the measurement of its transverse momentum out of the scattering plane. These measurements can be used to extract Transverse-momentum dependent Distributions (TMDs) that depend on the transverse momentum of the quark (k_T).

The factorization theorems of these types of processes (second factorization) that have been developed over the last decades allow, finally, a full interpretation, in 3D, of the nucleon (and nuclei) in terms of elementary quarks and gluons that appear in QCD calculations.

With these theoretical developments, the central goal of nuclear physics of understanding the nucleon and nuclear characteristics from the quark/gluon structure and QCD has become realistic. The experimental data obtained so far on GPDs and TMDs can be characterized as exploratory in nature; one of the major aims of the current 12 GeV CEBAF program is the first systematic exploration of the 3D structure of nucleon and nuclei in the valence quark region [8]. The full exploration of the 3D structure requires the EIC.

The measurement of second-factorization DIS processes where both the electron and the nucleon/nuclei are polarized allows the exploration of correlations between x and b or k_T, as well as with the nucleon/nuclear spin and the quark/gluon spin. Such data, if of sufficient statistical and systematic significance over a sufficiently wide kinematic region could lead to a new understanding of the emergence of nucleon and nuclear characteristics–mass, spin, and nuclear forces–in terms of quarks/gluons and QCD. How nuclear modifications to these TMD/GPD objects conspire to produce, for example, the EMC effect, will be a fertile ground for exploration. This is one of the major driving ideas behind the EIC and fixes much of the machine parameters in terms of collision energies, luminosity and polarization capabilities as well as species of ions that need to be available for collisions.

2.4 Dense gluons in Nucleons and Nuclei

The collider experiments at HERA has shown that protons at ever lower x, contain more and more gluons due to QCD radiation; such an unchecked growth of gluon density would eventually violate

unitarity. This growth of gluons should be "tamed" with recombination of gluons to balance out the radiatively produced gluons. The x (for a given Q) at which the growth of gluon density stops due the balance between radiation and recombination of gluons is called the "saturation scale". Since QCD systems radiate and are also confined, saturation is a characteristic of QCD. However, since parameters of confinement is not calculable in perturbative QCD, there is currently no first-principle prediction of the saturation scale; models, however, have been proposed. No clear sign of saturation has been observed thus far, and given current data, the saturation point at Q of 2 GeV for protons is speculated to be around x of 10^{-7}. To reach such a small x at Q of 2 GeV, a center-of-mass energy of several TeV is required, which is out of the scope of any US Electron-Ion Collider proposal.

However, heavy ions, in a fast moving frame, has multiple nucleons overlapping transversely and provide an effective target gluon density that grows like $A^{1/3}$, in absence of effects other than simple geometry. In the rest frame of the ion, this is equivalent to saying that a quark-anti-quark dipole formed from the probing virtual photon has a lifetime, at sufficiently low-x, that is much longer than the time for it to traverse the diameter of the nuclei; therefore, the dipole is able to interact with multiple nucleons within the nuclei.

While the gluon density in an ion at a given x, in this picture, is not equivalent to a proton at a lower x, electron-ion collision at a given x may have similar, or even the same, characteristics as electron-proton collisions at a lower x. The system (the ion) being probed, in this case, is not approaching saturation as a basic characteristics of QCD as in case of single proton. Nevertheless, an interesting study of how an electron interacts with a dense gluon system can be made with electron-ion collisions at the EIC, at lower effective x than with the same energy electron-proton collisions.

Perhaps more interesting is the possibility that color (or gluons) is being exchanged between different nucleons within nuclei, or that gluon saturate faster in nuclei than in single protons; there is even speculation that at sufficiently low-x, nucleons ceases to become the correct degree of freedom to understand nuclei. Such a possibility could be determined with relatively small amount of data at the EIC (see, for example Sec 3.3.1 in [2]).

The electron-ion collision at the EIC will also provide complementary information to the ion-ion collisions used to investigate the phenomenon of quark-gluon plasma. The nuclear structure measurements at the EIC will measure the initial condition for ion-ion collisions. In addition, studies of propagation of the DIS final states, such as vector mesons or jets, through the cold QCD matter of the ions will provide a valuable benchmark to studies of propagation of hadronic states in hot QCD matter.

2.5 Requirements of the EIC

The scientific program of the EIC requires a large variety of nuclei to be probed via DIS. Since both protons and neutron structure need to be measured in order to understand flavor structure of nucleons, deuteron (or ^{3}He) beams as well as proton beams are necessary. Both protons and deuterons (as well as the electrons) need to be polarized so that spin structure of the nucleons can be investigated. Both the transverse and longitudinal polarization states need to be available for protons and deuterons. In case of deuterons, tensor polarized states should also be available in order to investigate the relationship between quark/gluon structure and nuclear spin states. While deuteron beams have some advantages in the extraction neutron structure, ^{3}He beam (also polarizable) is also desirable. It is worth noting that the possibility of having a positron beam instead of electron beam also enhances the ability to understand the flavor structure of the nucleon.

Heavier nuclei are needed for investigation of dense system of gluons, with at least one species of ions of intermediate mass, such as carbon, as well as the heaviest ions available, such as Pb or Au.

The aim of measuring multidimensional distributions of quarks and gluons inside protons as well as neutrons and nuclei (in different polarization states) requires a large amount of data. The HERA collider delivered average luminosities of up to $10^{31}\,\mathrm{cm}^{-2}\,\mathrm{s}^{-1}$ and the collider experiments integrated 1 fb^{-1}, combined, of data over their lifetimes for their measurements of PDFs [9]. Given the fact that the measurements at EIC are more exclusive as well as the multidimensional nature of the measurements, the luminosity requirement of the EIC is 100 to 1000 times that the average luminosity of HERA. This leads to average luminosity requirements of 10^{33} to $10^{34}\,\mathrm{cm}^{-2}\,\mathrm{s}^{-1}$ with the goal to accumulate 10 to 100 fb^{-1} per year of operation, when operated for 3D structure measurements. Indeed, the core measurements discussed in the EIC whitepaper[2] corresponds to approximately 650 fb^{-1} of data indicating the need for higher luminosity approaching 100 fb^{-1} per year.

The kinematic range of the EIC is determined by three factors; the first is the reachable range of x available above a Q of several GeV where the DIS process can be analyzed perturbatively. The kinematic range for 3D structure measurements should extend down below x of 0.01, approaching 0.001, where multi-particle region transition to the radiative region, to fully explore the region in which the non-perturbative quark/gluon structures are likely strongly connected to the nucleon and nuclear characteristics. Secondly, the initial proton/ion energies should not be larger than several hundred GeV so that the transverse quantities, which is in the range of 10–100 MeV can be measured well. These requirements fix the energy parameters of the EIC for center of mass energies in the range 20–60 GeV for electron-proton collisions from the DIS kinematic relationship, $sxy = Q^2$, where s is the center of mass energy squared and y is the inelasticity parameter ranging from 0 to 1 (Typically, the maximum y reachable experimentally is 0.8 to 0.9). Thirdly, the investigations of low-x and collective effects of gluon raise the desirable center of mass energy to 100 GeV, and, ultimately with an accelerator upgrade, to 140 GeV. At the higher center of mass energies of 100–140 GeV the luminosity requirements can be relaxed to a few times $10^{32}\,\mathrm{cm}^{-2}\,\mathrm{s}^{-1}$ since the DIS cross sections rise by an order of magnitude at low-x, the measurement are needed only for the proton and Pb or Au without polarization, and the measurements are mainly for inclusive DIS.

Since effective data size for double polarization asymmetry measurements required for determining the correlations of quarks/gluons spin, x, b, k_T, and the nucleon/nuclear spin is proportional to Luminosity $\times$ polarization$^2_{electron}$ $\times$ polarization$^2_{ion}$, high polarization of the beams is of paramount importance. Polarization of 70% as opposed to 85% is equivalent to losing half of the data. The EIC which operates at $0.5 \times 10^{34}\,\mathrm{cm}^{-2}\,\mathrm{s}^{-1}$ at polarization of 70% polarization per beam will accumulate data at the rate a quarter of one that operates at $1 \times 10^{34}\,\mathrm{cm}^{-2}\,\mathrm{s}^{-1}$ and at 85% polarization, increasing the operation cost for the same science by factor of 4.

2.5.1 Experimental Program at the EIC

The center-of-mass energies of the EIC for the measurements discussed in the EIC whitepaper [2] and the estimated requirements of the needed luminosity are shown in Figure 2.1 and Table 1.1.

It is a clear, however, that the whitepaper from 2016 does not contain all of the compelling measurements at EIC known even at that time. The development of subject from the time of the whitepaper to the present time has also added to the list of compelling physics at EIC and also to the number of needed data sets at an EIC (see for example [10]). A version with an extension of the EIC program beyond the whitepaper and their requirements are shown in Figure 2.2.

Table 2.1: A list (for illustration purpose only) of data sets to be acquired in the first phase of operation at an EIC in order to deliver a substantial part of physics outlined in the EIC Whitepaper [2]. For ep and eD, two different polarization configurations are required, each requiring the same amount of integrated luminosity. Average luminosity of $10^{34}\,\mathrm{cm}^{-2}\,\mathrm{s}^{-1}$, corresponds to integrated luminosity per year of 100 fb^{-1}. Polarization of the required beams are denoted in the same way as in Figure 2.1.

Beam Species(pol)	CMS Energy	Integrated Luminosity required	Physics Topics
ep polarized(LL+LT)	20 GeV	10+10 fb^{-1}	Quark TMD
ep polarized(LL+LT)	40 GeV	100+100 fb^{-1}	Quark and Gluon TMD, GPD
ep polarized(LL+LT)	60 GeV	100+100 fb^{-1}	Quark and Gluon TMD, GPD, Gluon Spin
eD polarized(LL+LT)	60 GeV	100+100 fb^{-1}	Deuteron Structure, Neutron Structure
ePb (unpolarized)	60 GeV	10 fb^{-1}	Saturation, Heavy Ion Structure

While detailed experimental program at the EIC is something that will evolve as the plans of the facility as well as various physics studies proceed, the data sets that should be obtained in order to make substantial progress in the whitepaper program is shown in Table 2.1.

From Table 2.1 it is clear that the accumulation rate of data taking needs to be in the 100 fb^{-1}/year range in order to make reasonable progress on the mission of the EIC. This implies a collider capable of delivering $10^{34}\,\mathrm{cm}^{-2}\,\mathrm{s}^{-1}$ luminosity. An order of magnitude reduction in its luminosity performance will mean that acquisition of such a data set would take 50-100 years and make the program unsustainable.

REFERENCES

1. National Academies of Sciences, Engineering, and Medicine. 2018. An Assessment of U.S.-Based Electron-Ion Collider Science. Washington, DC: The National Academies Press. https://doi.org/10.17226/25171
2. A. Accardi *et al.*, "Electron Ion Collider: The Next QCD Frontier - Understanding the glue that binds us all", Eur. Phys. J. **A52**, p. 268 (2016), [arXiv:1212.1701 [nucl-ex]].
3. The Nobel Prize in Physics 1990. NobelPrize.org. Nobel Media AB 2019. Mon. 4 Feb 2019. https://www.nobelprize.org/prizes/physics/1990/summary/
4. J. C. Collins, D. E. Soper and G. F. Sterman, Adv. Ser. Direct. High Energy Phys. **5**, 1 (1989) [hep-ph/0409313].
5. J. Ashman *et al.* [European Muon Collaboration], Phys. Lett. B **206**, 364 (1988).
6. J. J. Aubert *et al.* [European Muon Collaboration], Phys. Lett. **123B**, 275 (1983).
7. J. Collins, Camb. Monogr. Part. Phys. Nucl. Phys. Cosmol. **32**, 1 (2011).
8. R.D. McKeown, "The Jefferson Lab 12 GeV Upgrade", in Proc. of MENU 2010, AIP Conference Proceedings **1374**, 121 (2011); doi: 10.1063/1.3647109. reference for CEBAF 12 GeV physics?'
9. H. Abramowicz *et al.* [H1 and ZEUS Collaborations], Eur. Phys. J. C **75**, no. 12, 580 (2015).

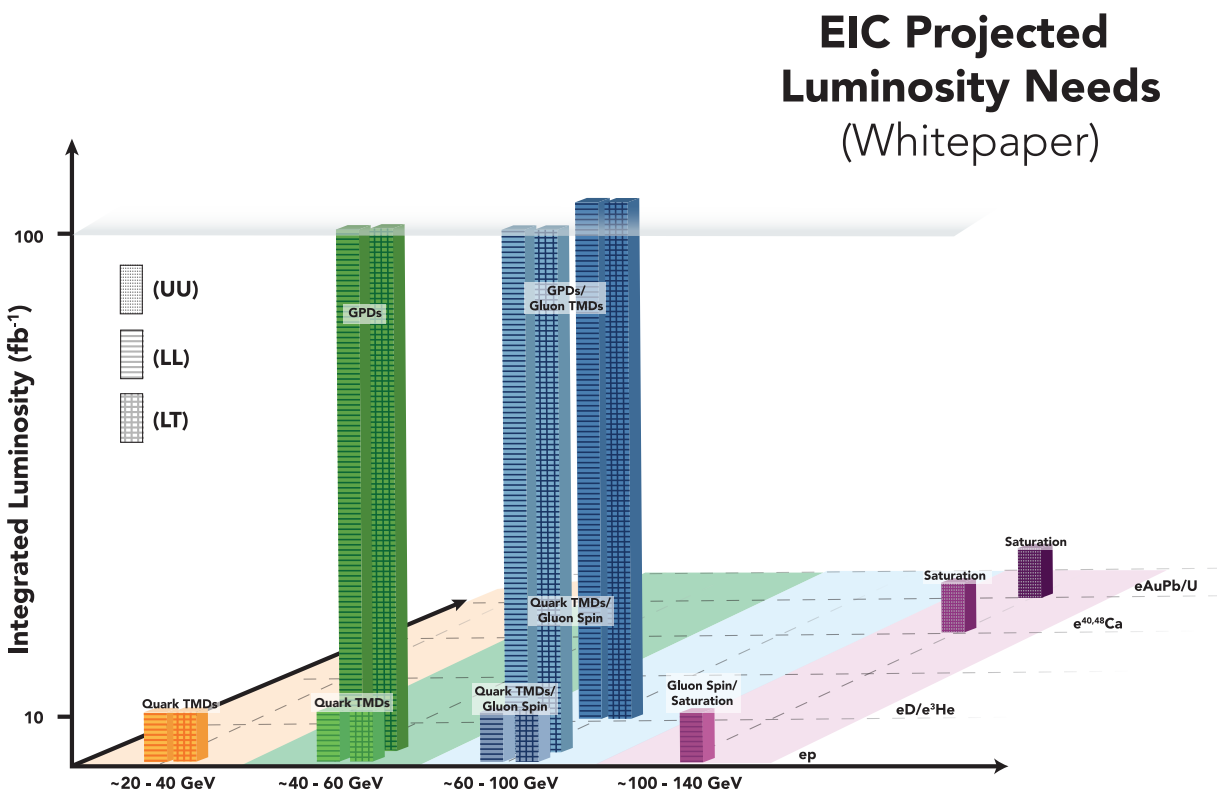

Figure 2.1: Integrated luminosity requirements for various types of nuclear physics measurements corresponding to the physics topics described in the EIC whitepaper [2]. Different beam polarizations are indicated as L: longitudinal, T: transverse, and U: unpolarized. The polarization for the electron beam is indicated first and the ion beam second. For example, (LT) indicates longitudinally polarized electron beam colliding with transversely polarized ion beam.

10. INT Program INT-18-3: Probing Nucleons and Nuclei in High Energy Collisions, `http://www.int.washington.edu/PROGRAMS/18-3/`

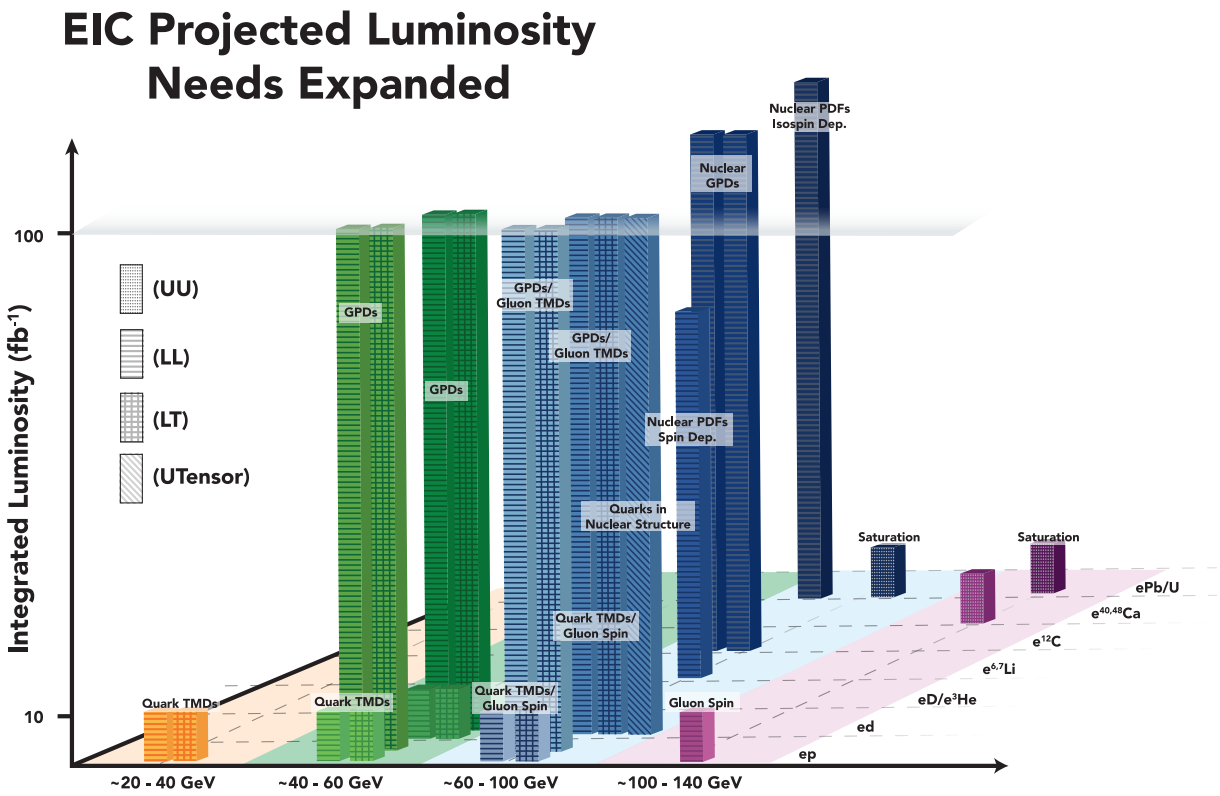

Figure 2.2: Integrated luminosity requirements for various types of nuclear physics measurements, expanded with physics topics beyond the whitepaper [2] at being discussed in the EIC community (see for example [10]). Polarization is noted in the same way as in Figure 2.1, and in addition tensor polarization for Deuteron beam is indicated.

CHAPTER 3

DESIGN, LUMINOSITY, AND POLARIZATION CONCEPTS

This chapter presents an overview of the JLEIC accelerator reference design, and the relevant luminosity and polarization design concepts. Section 3.1 lists a set of high-level accelerator design goals derived from the EIC science program, and it is followed by a brief description of the present reference design of the JLEIC accelerator facility in Section 3.2. A brief discussion of the design concept for JLEIC to deliver high luminosity is presented in Section 3.3. The main design parameters and luminosity performance of e-p collisions are presented in Section 3.4. Section 3.5 presents the polarization requirements and challenges, a discussion of the figure-8 synchrotron polarization preservation concept, and polarized luminosity figure of merit advantages for JLEIC.

3.1 Machine Design Goals

The EIC science program outlined in Chapter 2 and the EIC White Paper [1] provide a set of high-level requirements for JLEIC:

1. *Energy*

   The range of center-of-mass (CM) energy of this collider should be between ∼20–∼70 GeV. JLEIC achieves this with electron beam energies of 3–12 GeV, proton beam energies of 30–100 GeV, and ion beam energies up to 40 GeV/u. A straightforward extension to 200 GeV protons, 80 GeV/u ions, and CM energy to 100 GeV is described in Appendix A.

2. *Ion species*

   Ion species of interest include polarized protons, deuterons, and helium-3. Unpolarized heavier ions up to lead are required. All ions are fully stripped at collisions.

3. *Multiple detectors*

   The JLEIC facility should be able to accommodate up to two detectors; both detectors should support full acceptance of particle detection.

4. *Luminosity*

   The JLEIC luminosity should be in the range of 10^{33} to above $10^{34}\,\mathrm{cm}^{-2}\,\mathrm{s}^{-1}$ per interaction point (IP) for *e-p* and *e-A* collisions. The JLEIC luminosity is optimized around 45 GeV CM energy.

5. *Polarization*

   JLEIC should provide higher than 70% polarization in longitudinal direction at IPs for both electron and light-ion beams, and also in transverse direction at IPs for light ion beams only. Spin-flip of both beams is extremely desirable. High-precision (∼1%) ion polarimetry is required.

6. *Positrons*

   Collision of polarized positrons with protons and ions is desirable, though the luminosity and positron beam polarization may be less than the electron-ion collisions.

7. *Energy upgrade*

   The JLEIC accelerator design should include an option of future energy upgrade for reaching a CM energy of 140 GeV.

3.2 Reference Design

JLEIC is designed to take advantage of the existing CEBAF at Jefferson Lab. This electron SRF recirculating linac accelerator was successfully upgraded recently to 12 GeV for driving a fixed target nuclear science program. It will be used to provide an electron beam for JLEIC.

The JLEIC collider includes figure-8 shaped electron and ion collider rings, as shown in Figure 3.1. The electron ring consists of normal conducting magnets and stores an electron beam of 3–12 GeV energy and up to 3 A average current. The CEBAF accelerator will serve as a full-energy injector into the electron ring, and requires no upgrade for energy, beam current or polarization. The ion collider ring consists of $\cos\theta$ 3 T superconducting magnets (or 6 T, see Appendix A) and stores a proton beam with energy of 30–100 GeV, or fully-stripped ion beam up to 40 GeV per nucleon (or up to 200 GeV protons and 80 GeV per nucleon ion beams for a 6 T ring; see Appendix A). Proton and ion beams are generated and accelerated in a new ion complex that will be described below. The two collider rings are stacked vertically and have nearly identical circumferences of approximately 2.25 km, and therefore are housed in the same underground tunnel next to the CEBAF facility.

The unique figure-8 shape of the JLEIC collider rings optimizes ion spin polarization during acceleration and collisions. There is a complete cancellation of spin precession in the left and right arcs of the figure-8 ring, thus the net spin tune is zero and energy independent. The spin tune will be moved away from zero by spin rotators of very low magnetic field. The figure-8 ring design also provides the only practical solution for acceleration and storage of polarized deuteron beam.

The crossing angle of this figure-8 is 77.4°. The electron and ion collider rings intersect at one point in each of two long straights of the figure-8 and thus will accommodate two detectors. The electrons execute a vertical excursion to the plane of the ion ring to realize electron-ion collisions. The two long straights also accommodate other utility components of the collider rings, including injection/ejection, RF system, electron cooling and polarimetry.

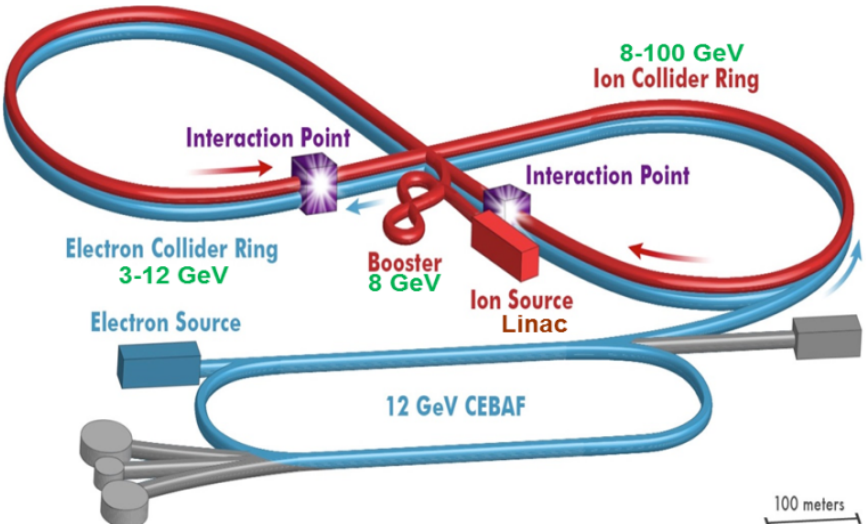

Figure 3.1: A schematic drawing of JLEIC.

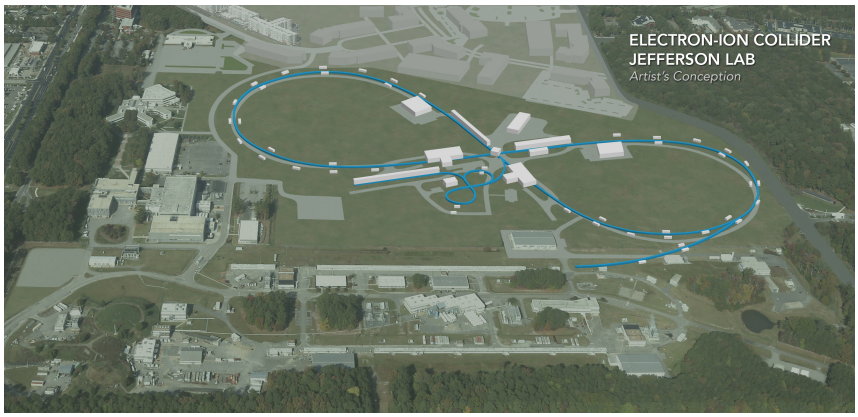

Figure 3.2: JLEIC on the Jefferson Lab site.

JLEIC takes advantage of two design features for delivering high luminosities: an existing highly polarized electron beam with up to 1.5 GHz bunch repetition rate from CEBAF, and a new ion complex. In particular, this new green field ion complex is designed to deliver colliding ion beams that match the phase-space structure and high bunch repetition rate of the colliding electron beam for implementing a novel luminosity scheme (Section 3.3). Figure 3.1 illustrates that the ion injector consists of sources for polarized light ions and non-polarized light to heavy ions; a 285 MeV linac with a RFQ and a warm DTL-type apparatus followed by a SRF linac section; and a figure-8 compact booster ring with an extraction energy of 8 GeV for protons, and corresponding energies for partially stripped heavy ions.

CEBAF will be used as a full-energy injector to the electron collider ring. The filling time of this collider ring is short, on the order of a few seconds. This leads to two consequences. Firstly, the stored beam in the electron ring will be easily replaced or "topped-off" when necessary, such as when the beam emittance or polarization become unsatisfactory.The CEBAF fixed target program may be operated simultaneously along with JLEIC, with only a negligible loss of the duty factor. Secondly, the ring-ring collider design also enables collisions of polarized positrons and ions since

the CEBAF accelerator can accelerate positrons as efficiently as electrons. The luminosity of positron-ion collisions will likely be lower due to low currents available from a projected polarized positron source.

3.3 Luminosity Concept

For many ring-ring colliders involving hadron beams, there are traditionally small numbers of bunches per beam, therefore the bunch collision frequencies are small. For example, the peak LHC collision rate is 40 MHz with 25 ns bunch spacing. With large bunch charges of 10^{11} to maintain a modest beam current, bunch lengths are long (8 cm) mainly due to limits of collective beam physics effects and lack of damping. Long bunches prevent a small beta-star (strong final focusing) due to the hour-glass effect, and combined with large transverse emittance, lead to fairly large beam spots at collision points. As a result, hadron colliders have historically delivered lower luminosities than, e.g., B-factories.

The primary JLEIC luminosity design strategy is to provide high bunch collision frequency colliding beams with modest bunch intensities. This design concept is summarized by the following list of key ingredients:

- High bunch repetition rate for both colliding beams
- Very small bunch charge
- Very short bunch lengths
- Very small transverse emittance
- Very strong final focusing (small beta-star)
- Large attainable beam-beam tune shift
- Crab crossing of colliding beams
- Strong synchrotron radiation damping for electron beam
- Strong cooling of proton and ion beams

The first four items specify the design of colliding beams in terms of their phase space structure (bunch length and emittance) and time structure (bunch frequency). The next three items specify the design of the interaction regions to take advantage of high-bunch-repetition colliding beams; crab crossing is required to eliminate parasitic collisions and associated long-range beam-beam effects. The last two items of the list, electron synchrotron radiation damping and strong cooling of proton and ion beams, are essential to preserve the stored electron beam, and for formation of the ion beams and reducing the ion beam emittance, respectively. This three-tier luminosity concept is illustrated in Figure 3.3.

JLEIC proton and ion beams are designed to have very short bunch length and very small transverse emittance, such that a strong final focusing is applied to reduce the beam spot sizes to a few μm at collision points. This in turn increases the collider luminosity. This is seen from the standard luminosity formula that it is inversely proportional to the product of transverse beam spot sizes at IP. A high bunch repetition rate ensures a very small bunch charge (hence much weaker collective beam effects) while maintaining nominal average current; therefore short bunch length and small transverse emittance will be achieved. A detailed discussion of this novel luminosity concept is found in [2].

This luminosity concept was demonstrated by several lepton-lepton colliders, and has led to the present world record of the highest achieved luminosity at the KEK-B factory [3]. By adopting this

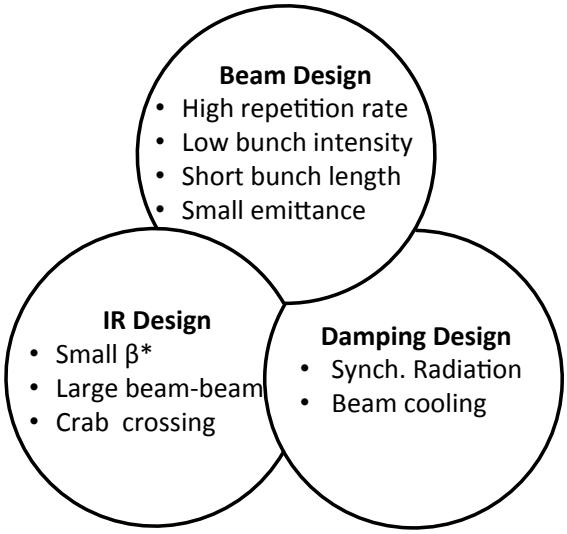

Figure 3.3: Fundamental ingredients of the JLEIC luminosity concept.

luminosity concept, the lepton-hadron collider of JLEIC is designed like a lepton-lepton collider for achieving high luminosities.

JLEIC can exploit this luminosity concept due to two strategic advantages. The first is that CEBAF delivers an electron beam at 1497 MHz bunch repetition rate. The high-frequency recirculating linac of CEBAF is used as a full-energy injector for the JLEIC electron ring. The second is that we need to produce and store high-average-current ion beams, matched to the electron beam in terms of bunch repetition rates, length and emittance. Production of such ion beams is technically feasible given advances in accelerator technologies over the last several decades, notably in ion sources, SRF linacs, and the ion beam cooling. JLEIC takes advantage of a specially designed ion complex designed to produce these unprecedented ion beams. A description of this ion complex and a conceptual scheme of ion beam formation are presented in Chapter 5.

In the energy range of JLEIC, there is no synchrotron radiation damping of the ion beams. A strong and effective damping mechanism must be used to reduce the 3D ion beam emittance, up to an order of magnitude in all three directions. We have adopted a scheme of multi-phased electron cooling of the ion beam for JLEIC. This scheme employs electron cooling first at the injection energy of the ion collider ring by a high current magnetized DC electron beam for initial emittance reduction; then at the top beam energy by a bunched magnetized electron beam from an ERL cooler with a circulator ring for conditioning the beams to the designed state for collisions. We also apply electron cooling continuously during collisions to suppress IBS and other nonlinear collective effects, and maintain the cooled small emittance. Estimates indicate that, with a proper bunched cooling electron beam, cooling efficiency is enough to maintain design luminosities. The electron cooler design concepts for JLEIC are presented in Chapter 6.

3.4 Primary Design Parameters

The JLEIC nominal parameters at representative low, medium and high CM energy design points are summarized in Table 3.1. The luminosity at these design points are all above $10^{33}\,\mathrm{cm}^{-2}\,\mathrm{s}^{-1}$ for a full-acceptance detector described in Chapter 7, with peak luminosity reaching $2.1 \times 10^{34}\,\mathrm{cm}^{-2}\,\mathrm{s}^{-1}$.

Table 3.1: JLEIC *e-p* Design Parameters

CM energy	[GeV]	21.9		44.7		63.3	
		p	e	p	e	p	e
Beam energy	[GeV]	40	3	100	5	100	10
Collision frequency	[MHz]	476		476		476	
Particles per bunch	[10^{10}]	0.98	3.7	0.98	3.7	0.98	0.93
Beam current	[A]	0.75	2.8	0.75	2.8	0.75	0.71
Polarization	[%]	>80	∼80	>80	>80	>80	>80
RMS bunch length	[cm]	1	1	1	1	1	1
Normalized emittance	[µm-rad]	0.3 / 0.3	24 / 24	0.5 / 0.1	54 / 11	0.9 / 0.18	432 / 86
$\beta^\star$, hori. / vert.	[cm]	8 / 8	13.5 / 13.5	6 / 1.2	5.1 / 1	10.5 / 2.1	4 / 0.8
Vertical beam-beam	[–]	0.015	0.092	0.015	0.068	0.002	0.009
Laslett tune-shift	[–]	0.06	Small	0.055	Small	0.03	Small
Detector space, up / dn	[m]	3.6 / 7	3.2 / 2	3.6 / 7	3.2 / 2	3.6 / 7	3.2 / 2
Hour glass		1		0.87		0.86	
Peak Luminosity/IP	[$10^{33}\,\mathrm{cm}^{-2}\,\mathrm{s}^{-1}$]	2.5		21.4		1.7	

To support the large detection acceptance, the distance from an interaction point (IP) to the front face of the first final focusing quadrupole (FFQ), $L^\star$, must be at least 7 m on the downstream side of the ion beam, however, the distance can be shortened to 3.5 m on the upstream side of the ion beam. For the electron beam, the FFQ magnets will be placed much closer to IPs, at 3.2 m and 3 m on the upstream and downstream sides, respectively. The interaction region magnets and layout are described in Section 9.3.

To reduce project costs, we plan to reuse equipment from the decommissioned PEP-II *e+e-* collider including RF cavities and power sources for the JLEIC electron collider ring (Section 9.7), and HER magnets for the transport beamline from CEBAF to the collider ring (Section 4.2). Reuse of PEP-II RF fixes the JLEIC bunch repetition rate (the bunch collision frequency) at 476 MHz. The new RF systems for the ion collider ring will also be at 476 MHz, with a possible future upgrade to 952 MHz for a luminosity upgrade (Section 9.5).

To derive this set of design parameters, certain limits were imposed on several key machine or beam parameters to improve robustness of the design and to reduce the cost and accelerator R&D challenges. These limits are based largely on previous lepton and hadron collider experiences and present state-of-the-art accelerator technologies:

- The stored beam currents do not exceed 0.75 A for protons or ions (SPS [4]), and do not exceed 3 A for electrons (PEP-II LER [5]).
- Electron synchrotron radiation power should not exceed 10 kW m^{-1} in arc
- The direct space-charge tune-shift of ion beams during beam store should not exceed 0.06 (FNAL recycler [6])
- The proton or ion beam-beam tune-shift at each IP should not exceed 0.015 (LHC [7])
- The electron beam-beam tune-shift at each IP could be a factor of 10 higher, namely, as high as 0.15, due to its synchrotron radiation damping (LEP extrapolation [8]).

JLEIC is designed to achieve high luminosities over a broad CM energy region. The luminosity as a function of CM energy is plotted in Figure 3.4. The same limits have been applied to the

key design parameters over the entire energy ranges. The luminosity performance is limited by the space charge effect at low proton energies (low CM energies) and by synchrotron radiation effect (both radiation power and induced emittance enlargement) at high electron energies (high CM energies). At the middle CM energy range, JLEIC luminosity is limited by the beam-beam effect.

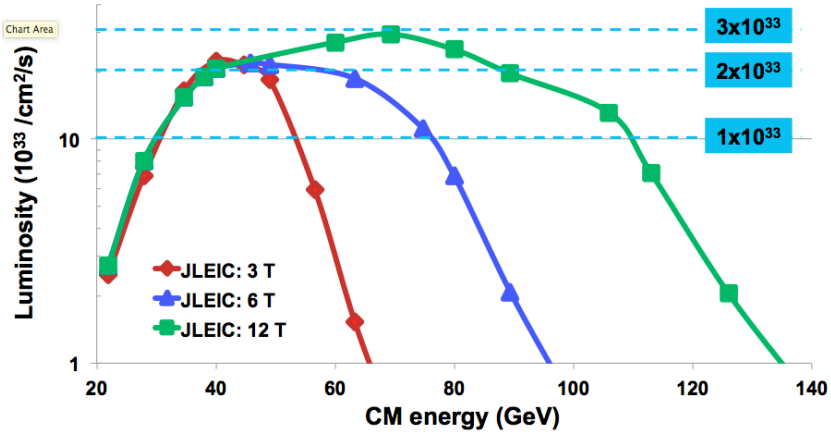

Figure 3.4: JLEIC e-p peak luminosity.

Since the equilibrium emittance of an electron beam in a storage ring depends on synchrotron radiation damping, the normalized emittance can vary by a factor of up to 64 from 3–12 GeV. The ion beam emittance is largely determined by intra-beam scattering, efficiency of beam cooling, and other beam dynamics effects; it is assumed to be relatively stable. As a consequence, the emittances of the two colliding beams of JLEIC are not matched over the entire energy range. To match beam spot sizes at an IP, $\beta^\star$ (the value of betatron function at the IP) values are adjusted accordingly for different energies, as shown in Table 3.1. Matching of spot sizes of colliding beams at an IP is critical in minimizing effects of the highly nonlinear beam-beam forces and maximizing the tolerable beam-beam tune-shift and therefore the luminosity.

In Table 3.1, the proton $\beta^\star$ for the luminosity optimized design point (i.e., 100 GeV $p\times$5 GeV e) is 1.2 cm in the vertical direction. This value is limited by having a sufficient beam-stay-clear at FFQ magnets (which also becomes a requirement of physical aperture of these magnets). On the other hand, at the lower CM energy design point (i.e., 40 GeV $p\times$3 GeV e) in Table 3.1, the proton beam geometry emittance at 40 GeV is 2.5 times large compared to the 100 GeV design point, the $\beta^\star$ is thus relaxed (enlarged) substantially to fit the beam through the same physical aperture of the FFQ magnets. At the same time, the $\beta^\star$ of the electron beam is also enlarged to achieve a match of beam spot sizes at each IP.

Collisions of electrons and ions willbe arranged similarly to electron-proton collisions in JLEIC, and luminosities of e-A collisions should be comparable to e-p collisions.

3.5 Polarization Concept

3.5.1 JLEIC Polarization Requirements and Design Overview

High polarizations of electron, proton or light ion beams are critically important to the EIC science program as it is articulated in the EIC White Paper. The nuclear physics requirements to the JLEIC ion polarization are summarized as:

- High polarization ($\geq$70%) for protons or light ions (d, $^{3}He^{++}$, and possibly $^{6}Li^{+++}$)
- Capability to adjust the polarization to both longitudinal and transverse directions at all collision points
- Sufficiently long lifetime to maintain a high polarization during the store
- Frequent spin flipping

There are a similar requirements of high polarization for the JLEIC electron beam, however, nuclear physics requires only longitudinal polarization at all collision points.

The JLEIC ion polarization design strategy is based state-of-the-art polarized ion sources for generating highly polarized (>90%) proton and light ion beams. The design of the ion booster and collider rings is then focused on maximally preserving the ion beam polarization during acceleration and store. To achieve this goal, we have adopted a figure-8 shape for the ion booster and collider rings for the JLEIC reference design. This is a revolutionary design concept which is based on the fact that the spin tune in a figure-8 ring is always zero since procession of a spin in the left and right half rings are exactly canceled. This feature ensures charged particles of any ion species will never cross any spin resonance in a figure-8 shape ring. Further, an inserted spin rotator with small magnetic field will move the spin tune of a figure-8 ring away from zero to mitigate zero-integer spin resonance. It has been demonstrated by both comprehensive theoretical studies and computer simulations that, with such figure-8 ring design, the JLEIC proton and light ion polarizations could be maintained at approximately 85%, a performance that any of other conventional accelerators has extreme difficulty to match. The figure-8 ring design is the only practical way to accelerate and store a highly polarized deuteron beam in a medium energy region with reasonable polarization lifetime.

The JLEIC electron collider, by following the footprint of the ion collider ring since the two rings are housed in a same tunnel and stacked vertically, also has a figure-8 shape. High polarization of the JLEIC electron beam is guaranteed by two design features, the CEBAF SRF linac as a full-energy injector of a highly polarized beam into the collider ring; and vertical spin orientations alternatively parallel and antiparallel to the dipole fields in the two half rings of a figure-8 to neutralize the quantum radiative self-polarization due to the Sokolov-Ternov effect.

This section will provide a brief explanation why the JLEIC design will provide very high polarized protons and light ions, and electrons as well, for collision. The section is organized in the following way: Section 3.5.2 highlights some limitations of conventional spin control methods and conventional rings; subsection 3.5.3 discusses advantages of a figure-8 shape ring; subsection 3.5.4 provides a brief description of the JLEIC electron polarization design and argues that a figure-8 collider ring also helps to maintain high electron polarization; lastly in subsection 3.5.5 the concept of figure-of-merit of a polarized electron-ion collider is introduced and quantitatively discussed.

3.5.2 Limitations of Conventional Spin Control Methods

In a medium energy range, loss of ion beam polarization in accelerators is caused primarily by spin resonances [9, 10], i.e. periodic spin kicks correlated with the spin precession rate, or the spin tune. Due to the energy dependence of the spin tune in a conventional accelerator, for example, a race-track type accelerator, an ion beam crosses larger number of spin resonances during acceleration to a higher energy, resulting in a partial or complete polarization loss [11].

Several techniques have been proposed to preserve polarization when crossing a spin resonance [12, 13, 14]. Some of them are based on changing the crossing speed or the resonance strength to provide fast or slow resonance crossing [15, 16]. All of these techniques may only

reduce, but not completely eliminate, beam depolarization during resonance crossing. Thus there could be still a significant polarization loss when crossing too many resonances.

One technique, transparent crossing, is based on control of the spin motion directly in the resonance region. In principle, it allows one to eliminate depolarization when crossing resonances [17, 18]. However, its effectiveness depends on the beam momentum spread and the use of quickly changing magnetic fields, which alter the spin dynamics during crossing of the effective resonance region.

The nvention of the Siberian snake [19, 20] is considered to be a major advance in preservation of ion polarization in accelerators. A snake rotates the spin of a charged particle by 180° about an axis lying in the plane of the accelerator, as a result it sets the spin tune of the accelerator to one half for any beam energies, thus avoiding crossing of spin resonances during acceleration. With two snakes located in opposite straight sections of a race-track type storage ring, the spin tune depends on the angle between the two snake axes and equals one half if the angle is 90°, as it was implemented at RHIC [21, 22].

The challenge is how to realize a proper Siberian snake technically and mitigate its beam effects. A Siberian snake is constructed using either longitudinal or transverse fields. The longitudinal field does not change the beam orbit but its spin rotation varies inversely proportionally to the beam momentum [23]. Therefore, application of such type of snakes is limited to relatively very low energies. In helical and dipole snakes, the integral of the transverse field is independent of the beam energy [23]. For example, for one of the helical snakes in RHIC, the transverse field integral for protons is 24 T-m [21, 22]. The limitation on using such snakes is associated with the beam's closed orbit excursion, which becomes satisfactorily small only at relatively high energies. For example, at the RHIC injection energy, the orbit excursion is about 3 cm. Thus, usage of Siberian snakes is problematic in the medium energy range from a few GeV to a few tens of GeV.

Moreover, due to an usually small value of the deuteron anomalous magnetic moment ($G_{\mathrm{d}} \approx -0.143$), use of Siberian snakes with transverse fields for deuterons would require an integrated transverse field in the order of 600 T-m for medium energy range, therefore it demands impractically high field and/or long snake magnets.

Polarization control and spin flip may also be challenging in a conventional accelerators. Adjusting the polarization direction requires large field integrals which will likely affect the beam dynamics. Spin flipping in a conventional ring is usually done by sweeping an RF magnet's frequency through an induced spin resonance [24]. However, this technique causes a finite polarization loss during each spin flip [24]. Therefore, it may introduce a systematic error in an experiment and the polarization cannot be flipped many times.

3.5.3 The Figure-8 Ring Scheme

An elegant solution for acceleration of any polarized ions including deuterons is to use an accelerator with a figure-8 ring configuration [25]. While beam polarization control schemes for conventional accelerators with Siberian snakes remain applicable to figure-8 type accelerators, it offers new opportunities for manipulation of the beam polarization [26, 27, 28, 29, 30, 31, 32, 33, 34, 35] including spin flipping. In such an unconventional accelerator, rotating the spins in one direction in one arc is exactly compensated rotating the spins in the opposite direction in another arc. Such a very desirable feature of energy independence of net spin procession (namely, spin tune) is a topological property of a figure-8 ring, which means it is independent of the dimension and shape of the arcs, nor depending on local bending angles, as long as the accelerator is completely flat. The spin tune of an ideal figure-8 accelerator is zero for any beam energy, i.e. the particles are in the region of the zero-integer spin resonance. To stabilize the polarization direction, instead

of strong snake fields, it is now sufficient to introduce a weak field to overcome the effect of the zero-integer spin resonance strength [26, 27, 28, 29, 30]. As an example, a longitudinal field integral as low as 1 T-m is sufficient to preserve the polarizations of both protons and deuterons during acceleration to 100 GeV in the JLEIC ion collider ring [34]. This is a very substantial advantage of the JLEIC in terms of design simplicity, modest technology specification and cost reduction. To stabilize the spin tune during acceleration, the solenoid field should change proportionally to the beam momentum.

Compensation of the zero-integer spin resonance strength allows one to solve the problem of accelerating polarized beams to energies of the order of 1 TeV and higher.

3.5.4 Electron Polarization in JLEIC

Since 2006 in which year the JLEIC reference design was evolved from an ERL-ring design to a ring-ring design, the JLEIC electron polarization design concept is based on existing 12 GeV CEBAF recirculating SRF linac as a full energy injector of a polarized electron beam into the electron collider ring. It is in a regime of accumulating and stacking highly polarized electron beam with a low current using the strong radiative damping. Actually, lack of a high current polarized electron source at the present time and in foreseeable near future is one of the critical arguments in favor of adopting a ring-ring design for JLEIC while using CEBAF as a full energy polarized electron injector.

The polarized electron current from the CEBAF accelerator is relatively low, being limited by both capability of the polarized electron source and available linac power. However, accumulation and stacking of polarized beam to high circulated current in the electron collider ring will be performed in quite a short time, owing to the fast radiative damping of the injected electrons in the collider ring. Moreover, the CEBAF accelerator offers an opportunity for top-off injection, a quasi-continuous filling regime which is the most adequate to the detector's request of near-constant polarization and luminosity.

Having the CEBAF accelerator as a full energy injector to the JLEIC electron collider ring thus arrives as one of the intrinsic advantages of the Jefferson Lab based electron-ion collider. Two other conceivable design options, namely, 1) relying on the Sokolov-Ternov effect to self-polarize electrons, and 2) employing an injector complex which includes a polarized source, a short linac and a booster synchrotron, are clearly disadvantageous. The first design option is not compatible with the necessity of a fast frequent spin flipping; the second design option is associated with relatively large beating of the beam current in the electron collider ring which may present a significant issue to detector operation.

The JLEIC electron polarization design takes advantages of the figure-8 electron collider ring design for the required spin manipulation and maintenance of the polarization delivered from CEBAF. The collider ring polarization configuration includes the following principal elements:

- Vertical coherent spin of same polarity in two arcs of the figure 8 ring.
- Adjusting electron polarization in longitudinal direction at IRs by using novel Universal Spin Rotators (USR), a special type of energy-tunable, orbital- and optics-independent, spin rotator.
- Dynamical stabilization of electron spin by additional solenoids installed between the two spin rotators, thus, providing a non-zero controllable global spin tune (ultimately equal to one half) required for spin stability.
- Flipping spin is provided by flipping the helicity of laser beam of the photo-gun with frequency 30 Hz as used at CEBAF.

- Continuous injection of extremely small amount of highly polarized electrons fresh from the CEBAF accelerator into the collider ring to maintain high polarization of stored electron beam.

The polarization lifetime of the circulated electrons in the JLEIC electron collider ring is limited by depolarization effects associated mainly with the quantum properties of the synchrotron radiation of electrons. To provide a high polarization of the stored beam, it is necessary to refresh the stored electrons during a time much shorter than the polarization lifetime due to the depolarizing processes. In other words, beam lifetime must be sufficiently short compared to the polarization lifetime. Such replacement of the beam should be executed in a maximally smooth manner to ease the climate for detector operation.

3.5.5 Figure of Merit

In summary, the JLEIC reference design offers a very solid and comprehensive polarization design which is centered on using high polarization electron and ion sources, and a unique figure-8 shape for both collider rings as well as the ion boost ring for maximally preserving beam polarization. It is expected JLEIC will deliver superior polarization for both electron and proton/ion beams. The design studies shows the proton beam will maintain about 85% polarization and the electron beam will achieve 84% to 80% polarization for 3 GeV to 10 GeV beam energy respectively.

In an experiment involving collision of two polarized beams, the Figure of Merit (FOM) is defined as the product of the collider luminosity and squares of the two beam polarizations: FOM$=L\,P_{\mathrm{e}}^2\,P_{\mathrm{p}}^2$, where L is the luminosity, and P_{e} and P_{p} are electron and proton polarizations respectively. This is an important parameter to characterize the overall performance of a polarized collider. This product $P\mathrm{e}^2\,P_{\mathrm{p}}^2$ is 0.24 for 70% polarization for both electron and proton beams, which is the requirement set by the EIC White Paper. For this JLEIC reference design, $P_{\mathrm{e}}^2\,P_{\mathrm{p}}^2$ is approximately 0.46, a factor of two in excess the White Paper FOM polarization requirement. Note that relevant uncertainties also scale as $\sqrt{\mathrm{FOM}}$.

REFERENCES

1. A. Accardi *et al.*, "Electron Ion Collider: The Next QCD Frontier — Understanding the Glue that Binds Us All", Eur. Phys. J. **A52**, p. 268 (2016), https://doi.org/10.1140/epja/i2016-16268-9
2. Y. Zhang *et al.*, "JLEIC Ultimate Luminosity with Strong Electron Cooling", in Proc. IPAC'17, Copenhagen, Denmark, paper TUOCB2, 2017.
3. K. Oide, "KEKB B-Factory, The Luminosity Frontier", Progress of Theoretical Physics, **122**, Issue 1, 1 July 2009, pp. 69–80, https://doi.org/10.1143/PTP.122.69
4. M. Carlà *et al.*, "Studies of a New Optics with Intermediate Transition Energy as Alternative for High Intensity LHC beams in the CERN SPS", Proc. of IPAC'18, Vancouver, BC, Canada, paper TUPAF022, pp. 713–716.
5. M. Zobov, "New Generation Electron-Positron Factories", Physics of Particles and Nuclei, **42** 5, pp. 782–799, 2011.
6. Y. Alexahin, "On the Possibility of Using Nonlinear Elements for Landau Damping in High-Intensity Beams", Proc. of NAPAC'16, Chicago, IL, paper WEPOA17, pp. 729-731,2016.
7. X. Buffat *et al.*, "Limitations Due to Strong Head-On Beam-Beam Interactions", CERN-ACC-NOTE 2017-0044, 23 Jun 2017, http://cds.cern.ch/record/2270590/files/CERN-ACC-NOTE-2017-0044.pdf
8. R. Assmann and K. Cornelis, "The Beam-Beam Interaction in the Presence of Strong Radiation Damping", Proc. of EPAC'00, Vienna, Austria, paper TUP6B01, pp. 1187–1189.
9. E. Courant and R. Ruth, BNL report, BNL-51270 (1980).

10. S.Y. Lee, Spin Dynamics and Snakes in Synchrotrons (World Scientific, Singapore, 1997).
11. F. Khiari *et al.*, Phys. Rev. D 39, 45 (1989).
12. T. Khoe *et al.*, Part. Accel. 6, 213 (1975).
13. J. Laclare *et al.*, Jour. de Phys. 46, C2-499 (1985).
14. H. Sato *et al.*, Nucl. Instrum. Methods A 272, 617 (1988).
15. L.G. Ratner, High Energy Spin Physics-1982, BNL, AIP Conference Proceedings 95, Particles and Fields Subseries 28, p.412 (1982).
16. N.I. Golubeva, A.M. Kondratenko, and Yu.N. Filatov, "A Jump in Spin Precession Frequency as a Method to Pass Spin Resonance" Proc. of the Int. Workshop "Deuteron-93" (1994), p. 374.
17. A.M. Kondratenko, M.A. Kondratenko, and Yu.N. Filatov, "Compensation for particle beam depolarization of spin resonance intersection at accelerators", PEPAN Lett. 1 5 (2004), pp 266-69.
18. V.S. Morozov *et al.*, Phys. Rev. Lett. 102, 244801 (2009).
19. Ya.S. Derbenev and A.M. Kondratenko, Proc.of X Intern. Conf. on High Energy Accel., v. II, p.70, Protvino, 1977.
20. Ya.S. Derbenev and A.M. Kondratenko, Part. Accel. 8, 115 (1978).
21. V. Ptitsin and Y. Shatunov, NIM A398, 126 (1997).
22. H. Huang, in Proc. SPIN 2002, AIP Conf. Proc. 675 (2003), p. 122.
23. T. Roser, Handbook of Accelerator Physics and Engineering, 3rd edition, edited by A.W. Chao and M. Tigner (World Scientific, Singapore, 2006), p. 168.
24. V.S. Morozov *et al.*, Phys. Rev. ST-Accel. Beams 7, 024002 (2004).
25. Ya.S. Derbenev, "The Twisted Spin Synchrotron", University of Michigan report, UM HE 96-05 (1996).
26. Ya.S. Derbenev *et al.*, "Ion Polarization Control in MEIC Rings Using Small Magnetic Field Integrals", PoS (PSTP 2013) 026.
27. Ya.S. Derbenev *et al.*, "Polarization Preservation and Control in a Figure-8 Ring", Int. J. Mod. Phys. Conf. Ser. 40, 1660090 (2016).
28. Ya.S. Derbenev *et al.*, "Polarized Ion Beams in Figure-8 Rings of JLab's MEIC", in Proc. IPAC'14, Dresden, Ger-many, June 2014, paper MOPRO004, pp. 68-70.
29. A.M. Kondratenko *et al.*, "Baseline Scheme for Polarization Preservation and Control in the MEIC Ion Complex", in Proc. IPAC'15, Richmond, VA, USA, May 2015, paper TUPWI029, pp. 2301-2303.
30. A.M. Kondratenko *et al.*, "Numerical Calculation of the Ion Polarization in MEIC", in Proc. IPAC'15, Richmond, VA, USA, May 2015, paper TUPWI030, pp. 2304-2306.
31. A.M. Kondratenko *et al.*, "Ion Polarization Scheme for MEIC", arXiv:1604.05632 [physics.acc-ph] (2016).
32. A.M. Kondratenko *et al.*, "Ion Beam Polarization Dynamics in the 8 GeV Booster of the JLEIC Project at JLab", in Proc. IPAC'16, Busan, Korea, May 2016, paper WEPMW017, pp. 2460-2462.
33. A.M. Kondratenko *et al.*, "Spin Flipping System in the JLEIC Collider Ring", in Proc. NAPAC'16, Chicago, IL, October 2016, paper TUPOB30, pp. 558-560.
34. A.M. Kondratenko *et al.*, "Acceleration of polarized protons and deuterons in the ion collider ring of JLEIC", in Proc. IPAC'17, Copenhagen, Denmark, May 2017, paper WEPIK038, pp. 3014-3017.
35. A.M. Kondratenko *et al.*, "Analysis of spin response function at beam interaction point in JLEIC", in Proc. IPAC'18, Vancouver, BC, Canada, April 2018, paper MOPML007, pp. 400-403.

CHAPTER 4

ELECTRON COMPLEX

The JLEIC electron complex is designed to deliver a high-current highly-polarized electron beam, with long beam lifetime for collisions with an ion beam at the interaction points (IPs). The main design requirements [1, 2] are:

- The collider ring should use warm magnets,
- The collider ring should accommodate electrons in an energy range of 3 to 12 GeV,
- The stored beam current should reach 3 A up to an energy above 6 GeV to maximize the luminosity in the central center-of-mass energy range,
- The stored beam should have a short bunch length (∼1 cm) and small transverse emittances over a wide energy range to support the high luminosity requirement,
- The maximum linear density of synchrotron radiation power should not exceed 10 kW/m and the total power should be less than 10 MW (considering reuse of PEP-II vacuum chambers),
- The stored beam polarization should be 70% or above with a reasonably long lifetime, and
- The polarization should be longitudinal at collision points.

Several successfully-operated and operating lepton storage rings with similar beam energies, currents and bunch repetition rates have demonstrated a high feasibility of designing such an electron complex [3, 4, 5]. Some special design choices are taken to optimize the performance of the complex include:

- Figure-8 shape collider ring
  The figure-8 shape of the collider ring is chosen initially entirely for the benefit of the ion

polarization. The electron ring has the same topology for the purpose of stacking both collider rings in the same tunnel to minimize costs. In addition, the figure-8 shape ring has an advantage of implementing a proper polarization configuration so that two polarization states simultaneously coexisting in the electron collider ring experience the same polarization deterioration.

- Spin manipulation using spin rotators
  The polarization is designed to be vertical in the arcs to minimize spin diffusion (i.e. depolarization), and longitudinal at the collision points for physics experiments, using four universal spin rotators. Such spin rotators, composed of interleaved solenoids and dipole fields, are designed to rotate the electron polarization in the whole desired energy from 3–12 GeV.
- CEBAF full energy injection
  CEBAF (the Continuous Electron Beam Accelerator Facility) at Jefferson Lab serves as a full energy electron injector and polarized electron source (>85%) of the JLEIC electron collider ring. No acceleration is needed in the electron collider ring. No further capability is needed beyond the CEBAF 12 GeV upgrade in terms of beam current and polarization.
- Top-off injection
  One advantage of full energy injection is that top-off injection of electron beam into the collider ring can be performed. Unlike the usual purpose of maintaining a constant beam current to boost the luminosity, top-off injection in JLEIC is crucial to maintain a high equilibrium polarization the electron collider ring.

This chapter is organized as follows. Section 4.1 describes the CEBAF machine and injection scheme of the electron collider ring. It is followed by the optics design of the transport line in Section 4.2. Section 4.3 focuses on the electron collider ring optics design and provides preliminary study results of single particle non-linear beam dynamics, e.g. chromaticity compensation of the collider ring. Section 4.4 describes electron polarization requirements and plans.

4.1 CEBAF and Electron Ring Injection

4.1.1 CEBAF

The JLEIC electron ring uses CEBAF as a full energy injector. CEBAF is a recirculating CW electron linac using superconducting RF (SRF) accelerating structures. The maximum CEBAF extraction energy was recently upgraded from 6 GeV to 12 GeV. This included an increase of the injector energy to to 123 MeV, addition of five C100 cryomodules to each of the north and south linacs, addition of a 10th arc, and a new experimental hall. The CEBAF nominal CW extracted beam power remains unchanged at 1 MW, ultimately limited by the power rating of the high-power beam dumps.

CEBAF is a 1497 MHz CW (every bucket filled) SRF linac. The CEBAF four-hall operation splits the 1497 MHz buckets into 6 groups of buckets each repeating at 249.5 MHz, with a typical pattern of A-(D)-B-D-C-(D). RF separators at the end of the south linac can deliver each of the 249.5 MHz beam to different experiment halls from the desired pass. CEBAF routinely operates with a maximum charge per bunch of approximately 0.2 pC in one of the 249.5 MHz beams, and the beam delivered to other halls has lower charge per bunch, with a total of up to 90 µA.

The JLEIC injection beam will be extracted from the end of CEBAF north linac. With a wide range of beam energies (3–12 GeV) required for JLEIC injection, the beam needs to be extracted on different CEBAF passes. This will be accomplished with DC magnets in periods where there is

no additional CEBAF program. When operating the CEBAF fixed target program simultaneously with JLEIC injection, RF separators at the end of north linac will be used to extract selected bunches to JLEIC, similar to existing CEBAF RF separators.

For each JLEIC electron ring bunch, the injection must be done in multiple injections with intervals of at least twice the transverse damping time. The main limiting factor for the CEBAF pulsed operation is the cavity voltage droop and the resulting energy spread in the beam. If the bunch or the pulsed bunch train is short enough compared to the cavity fill time and the RF feedback delay, and the cavity is operating on-crest on-resonance, the cavity gradient droop under CW RF is

$$\Delta V_c = Q_{\text{train}} \frac{\omega}{2} \frac{R}{Q} \tag{4.1.1}$$

where Q_{train} is the total charge of a bunch train passing through the cavity, and impedance is defined as $R \equiv V^2/P$. The gradient droop will be partially or fully compensated with RF feed-forward. To fully compensate the gradient droop with feed-forward, the maximum pulsed bunch train current is limited by the CEBAF cavities' klystron power and the coupling. With RF feed-forward, maximizing the bunch train length of each injection will help to increase the total charge of each injection [6].

The length of each CEBAF pass ranges between 6545 to 6554 RF wavelengths, or 1310.7–1312.5 m. This is slightly longer than half the circumference of the JLEIC electron ring of ∼2256 m. With gaps for beam abort and/or polarization flipping, the JLEIC electron ring will have two bunch trains of 1047 m each, slightly shorter than the length of one CEBAF pass. We choose the injection bunch train to be the same length of 1047 m or 3.5 µs. The beam current of different passes seen by a CEBAF north linac cavity does not overlap, as shown in Figure 4.1. We will inject one up polarized bunch train into half of the ring, followed by another down polarized train into the other half of the ring, reducing the waiting time between injections to one transverse damping time.

The magnets in CEBAF arcs will be adjusted to the energy of the center of the bunch train. In this case the maximum allowed bunch train head/tail to center gradient droop for one beam

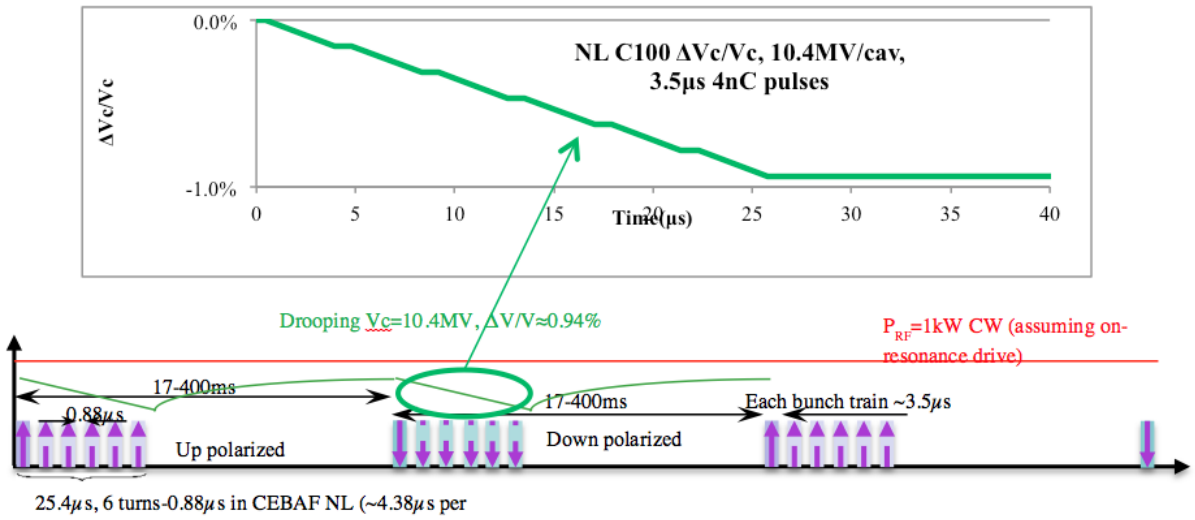

Figure 4.1: Gradient droop in a north linac C100 cavity with typical 10.4 MV voltage and 6 passes of bunch train, CW RF, on-crest on-resonance.

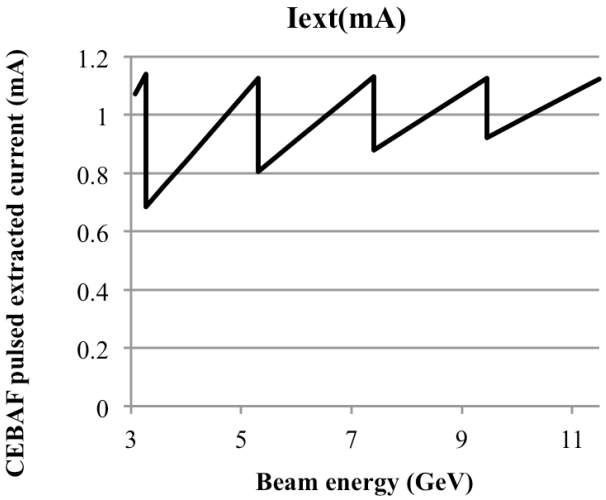

Figure 4.2: Estimated CEBAF extracted 3.5 µs bunch train beam current, assuming CW RF and 0.2% bunch train head to tail energy droop.

pass is the arc momentum acceptance of ±0.2%, or 0.4% head to tail. To allow some room for momentum spread caused by other factors, we limit one pass gradient droop to 0.2% head to tail. Each CEBAF linac has 40 C100 style cavities with R/Q =868.9 Ω and 160 original Cornell (OC) style cavities with R/Q=482.5 Ω. Using Equation 4.1.1, the total voltage droop per linac with CW RF will be

$$\Delta V_{\text{linac}}\ [\text{MV}] = 0.527\, Q_{\text{train}}\ [\text{nC}] \tag{4.1.2}$$

Applying the 0.2% bunch train head to tail energy droop (and total voltage droop) limit, the maximum charge per injection with on-crest, on-resonance CW RF (slow feedback, no feed-forward) will be proportional to the energy gain per linac pass

$$Q_{\text{train}}\ [\text{nC}] = 3.8\, \Delta E_{(\text{linacpass})}\ [\text{GeV}] \tag{4.1.3}$$

As a result, for various JLEIC electron injection energies, we should minimize the number of CEBAF passes to maximize the RF cavity voltage and the energy gain per linac. Figure 4.2 shows the analytically estimated 3.5 µs bunch train current extracted from CEBAF, assuming CW RF on-crest on-resonance operation, and 0.2% bunch train head to tail energy droop. The maximum energy gain per linac is assumed at 1.05 GeV, and as the beam energy increase from 3–11.5 GeV, the number of CEBAF passes increases from 1.5 to 5.5. The maximum charge per injection is about 4 nC when the energy gain per linac reaches the 1.05 GeV, regardless of bunch train length.

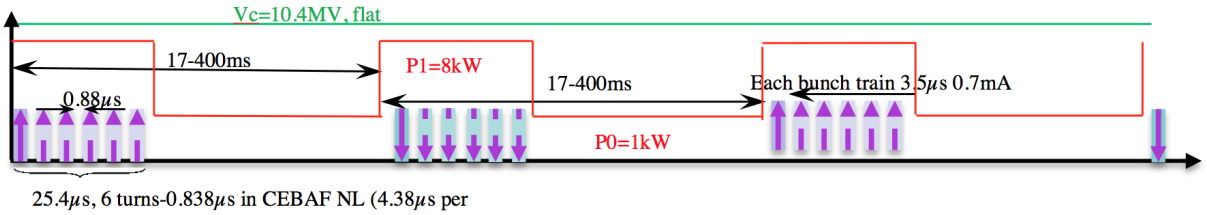

Figure 4.3: Fully correcting transient beam loading in C100 cavities with RF feed-forward.

RF feed-forward could partially or completely compensate the cavity voltage droop [7], as shown in Figure 4.3. We will ramp up the klystron drive signal right before the beam pulse, and ramp down after that, maintaining a near flat cavity voltage. With typical CEBAF cavity coupling and available klystron power (reserving some room for microphonics and RF control), the C100 cavities will be able to fully compensate the voltage droop for up to 0.7 mA beam current; the C50/C20 cavities will handle slightly more current with stronger coupling. Combining all the cavities, CEBAF may be able to fully compensate the energy droop from a bunch train current of 0.8–1.5 mA depending on the energy gain per linac. If we allow 0.2% energy droop, the pulsed extraction current will be 1.9–2 mA, or ∼7 nC total charge per pulse for various energies.

CEBAF's C100 RF modules have digital LLRF systems that support the programming of appropriate feed-forward. C50/C20 LLRF chasses will reuire an upgrade to digital LLRF. A CEBAF LLRF upgrade is planned and scheduled for the period before JLEIC operations.

To match the 1497 MHz RF frequency of CEBAF and the 476 MHz frequency in JLEIC electron ring, the injection bunch train will have a bunch repetition rate of 68.05 MHz, or 1/22 of 1497 MHz. JLEIC electron ring RF frequency will be fine-tuned to 476.3 MHz, 7 times 68.05 MHz. In this case, the maximum charge per bunch will be around 30 pC, two orders of magnitude higher than 12 GeV CEBAF operating conditions, but not beyond the state of the art. JLEIC may also reduce the bunch repetition rate for high energy operation; however the electron ring beam current and injection bunch train waiting time under those energies will be much smaller, so lower injection bunch train current is acceptable, without the need to raise the charge per bunch further.

Beam studies are ongoing to confirm CEBAF's capability to provide the required pulsed beam intensity [8]. Figure 4.4 shows the voltage droop measurement in CEBAF injector's 0L04 cryomodule (R100) cavity 1, which is a C100 style cavity. The cavity was operating at 7.7 MV. The signal shown is AC coupled and proportional to cavity voltage. The common low-frequency 60 Hz mode that appears as drift in this figure is quite stable, and probably caused by the klystron power supply. With 300 µA 10 µs beam, the signal has a drop of 0.5 mV. The DC coupled measurement shows a signal of 0.93 V, implying a cavity voltage drop of 0.05%, which is factor of three smaller than the analytical estimate.

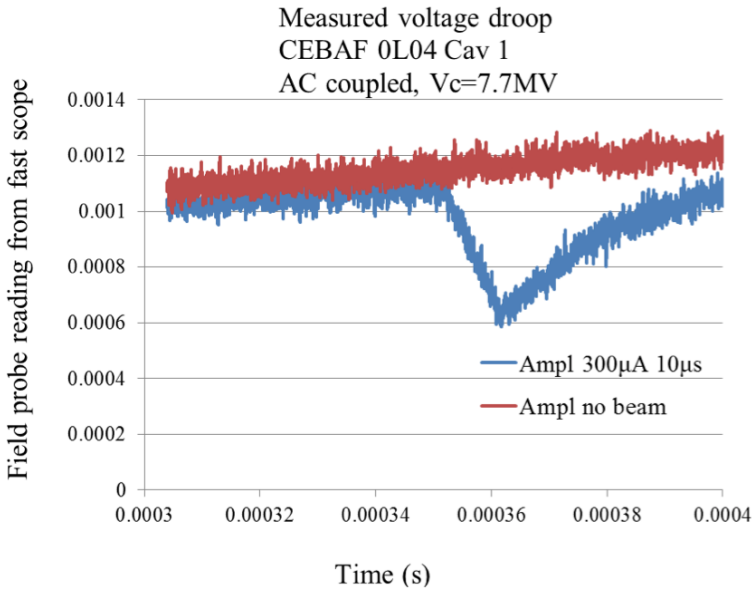

Figure 4.4: Measured voltage droop in CEBAF 0L04 Cav 1 during beam studies.

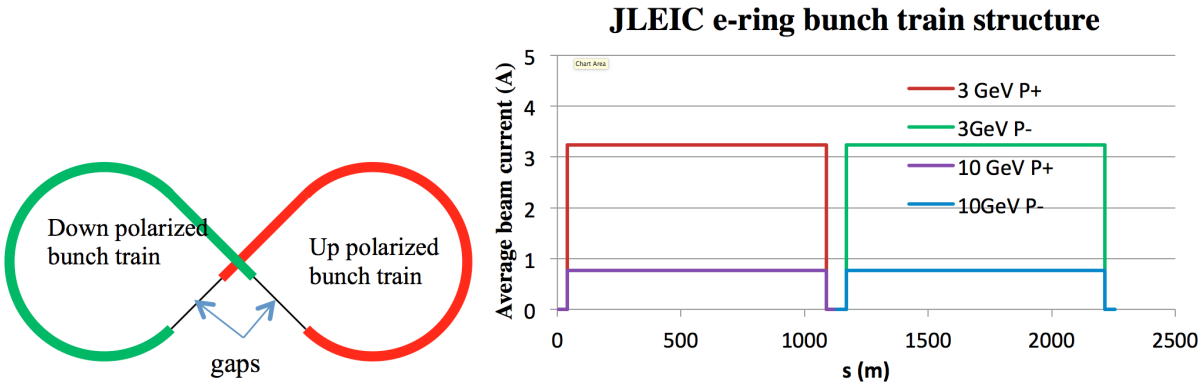

Figure 4.5: Bunch train pattern in the JLEIC electron ring. P+ and P- indicate polarization polarities.

4.1.2 Collider Ring Injection Scheme

Typically an electron collider ring has close to uniform bunches in most part of the ring, with one gap to accommodate the abort kicker rise time, and also serve as ion clearing gap. PEP-II was designed to operate with 1658 bunches at 238 MHz and an abort gap of 370 ns or 5% circumference (88 bunches missing), but the best run in 2008 achieved 1732 filled bunches with a gap of 14 missing bunches (or ∼60 ns) [3].

The circumference of the electron ring design has a harmonic number of 3584, with a circumference of 2256 m and the revolution time of 7.52 µs. A major portion of JLEIC's physics will be colliding polarized electrons with polarized protons and light ions. In these runs, the electron beam will be split into two bunch trains with opposite polarizations, as shown in Figure 4.5. There are two gaps of ∼270 ns each between the two long bunch trains, leaving two long bunch trains of 1047 m each. The gaps will match the ion ring abort gaps, and also serve as injection/abort kicker and ion clearing gaps.

Using an SRF linac as an electron storage ring injector is unconventional. An electron storage ring usually uses a warm pulsed linac or booster to inject single bunches at low repetition rate. The repetition rate of a warm linac is typically tens of Hz, while a typical booster cycle takes seconds. This low repetition rate provides enough intervals to damp the transverse motion of the newly injected particles, and for kickers to recover.

Although CEBAF provides much higher average beam current, the charge per bunch is much lower than a typical warm pulsed linac and orders of magnitude lower than the JLEIC electron ring. Each JLEIC electron bunch must be injected and topped off by multiple injections. The intervals between injections into the same bunch will be at least twice the transverse synchrotron radiation damping time. For each electron collider ring kicker cycle, a long bunch train of ∼1047 m will be injected into the electron collider ring, with alternating polarization. The intervals between injections will be one transverse synchrotron radiation damping time or kicker recovery time (assumed kicker repetition rate 60 Hz maximum), whichever is longer.

The JLEIC electron ring design also attempts to reuse the PEP-II 476 MHz RF systems, including the RF cavities, klystrons, as well as the high power RF distribution components, with the capability to upgrade to 952 MHz SRF systems. To match the frequencies of the two RF systems, CEBAF will operate at a bunch repetition rate of 68.05 MHz (1/22 of 1497 MHz), while the nominal drive frequency of the electron collider ring RF system will adjust slightly to 476.318 MHz

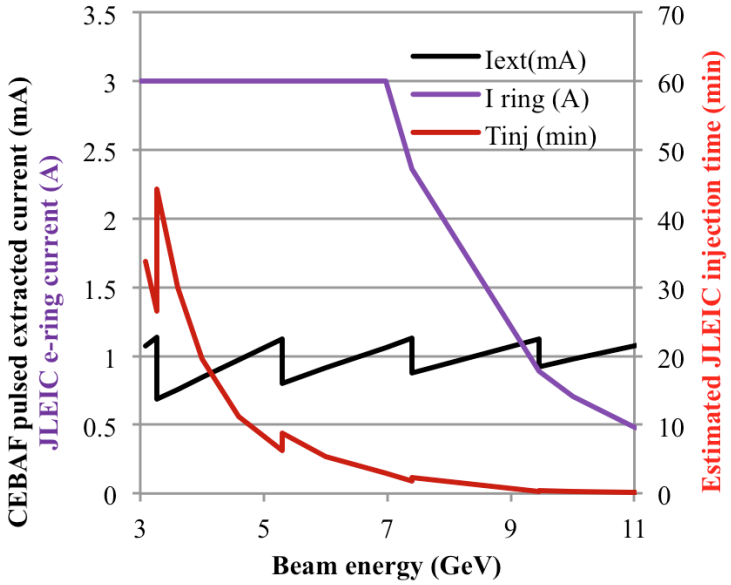

Figure 4.6: Beam current in the JLEIC electron collider ring and estimated injection time, CW RF on crest, on resonance, with no effective RF feed-forward/feedback.

(7×68.05 MHz). CEBAF also must support bunch repetition rates of 34.02 MHz and 17.01 MHz when the collider is operated at reduced collision rate, or 136.09 MHz after a electron collider ring RF upgrade.

The JLEIC electron ring injection time can be estimated by

$$T_{\text{inj}} = \frac{Q_{\text{ring}}}{Q_{\text{inj}}} \text{Max}(16.7\,\text{ms}, \tau_{(\text{d,SR})}) \tag{4.1.4}$$

The CEBAF extraction beam current or Q_{inj} can be estimated from Equation 4.1.1. Synchrotron radiation damping time inversely scales as energy to the third power, assuming no damping wigglers are used. The damping time range is ∼400 ms at 3 GeV to ∼6 ms at 12 GeV. The maximum injection kicker repetition rate is assumed to be 60 Hz. The maximum JLEIC electron ring beam current is 3 A, and is limited by the 10 MW synchrotron radiation power limit. Assuming 0.2% head-to-tail momentum spread limit and CW RF, the JLEIC electron ring injection time is estimated in Figure 4.6. This estimate does not consider the time needed for the electron ring RF system to adapt to the increasing current, such as adjusting the cavity detuning for the increasing beam loading, usually this takes a few minutes. The estimated electron injection time is below 30 minutes for most of the energy range, except for 3.3–3.6 GeV, when the energy gain per linac is as low as 0.63 GeV. The injection time can be further lowered by about factor of 2 with RF feed-forward in CEBAF.

The electron ring RF drive frequency will range from 476.252–476.385 MHz with varying circumference, as required by the electron-ion beam synchronization (Section 8.1). Currently CEBAF's path length adjustment range is only ±1 cm, far below the ±10 cm in each arc required to provide the exactly matching tuning range of ±210 kHz needed to synchronize the full range of the electron collider ring RF frequency change. Use of CEBAF path length chicanes to provide this path length is likely not the best technical solution.

Alternatively, we keep the CEBAF frequency at the nominal value, and inject electron bunch trains with RF phase slip in the electron ring at various energies provided the electron ring has a

large enough longitudinal dynamic aperture. The half-length of the long bunch train from CEBAF is slightly less than 1/4 of the JLEIC circumference, and the RF frequency range of the electron ring is $\Delta f = \pm f_0/(2h) = \pm f_{\rm rev}/2$. Therefore, the maximum phase difference between the head (or tail) and the center of the injected bunch train is

$$\Delta\phi_{\rm max} = 2\pi\frac{\Delta f}{f}\frac{h}{4} = \pm\frac{\pi}{4} \tag{4.1.5}$$

Since the maximum energy spread form the CEBAF is about $\pm 0.2\%$, the longitudinal dynamic aperture in the electron collider ring must tolerate particles with $(\phi, \delta) = (\pm\pi/4, \pm 0.2\%)$. Figure 4.7 shows the separatrix orbit with synchrotron phase $\phi_{\rm s}$ in the JLEIC baseline design at 10 GeV. The red rectangle box shows the maximum required longitudinal dynamic range for the injected electron bunch trains. In principle, all particles within this dynamic range should be stable and will be damped eventually. This will be confirmed by further simulations in the future. The shaded parallelogram shows the longitudinal phase space of the injected beam for the case that the electron ring operates at 476.252 MHz, assuming the energy droop in the bunch train max out the CEBAF arc acceptance.

When the JLEIC electron collider ring upgrades to 952.6 MHz RF with doubled harmonic number $h_1 = 2h_0$, there are some scenarios, such as two IP operation, that need to keep the relative RF frequency range unchanged, and the absolute frequency range doubled to $\Delta f = \pm f_0/(2h_0) = \pm f_0/h_1 = \pm f_{\rm rev}$. In this case, we may need to reduce the injection bunch train length by factor of two to around 2 ns for operations in a certain ion energy range.

Information about beam polarization lifetime and continuous injection is located in Section 4.4.3.

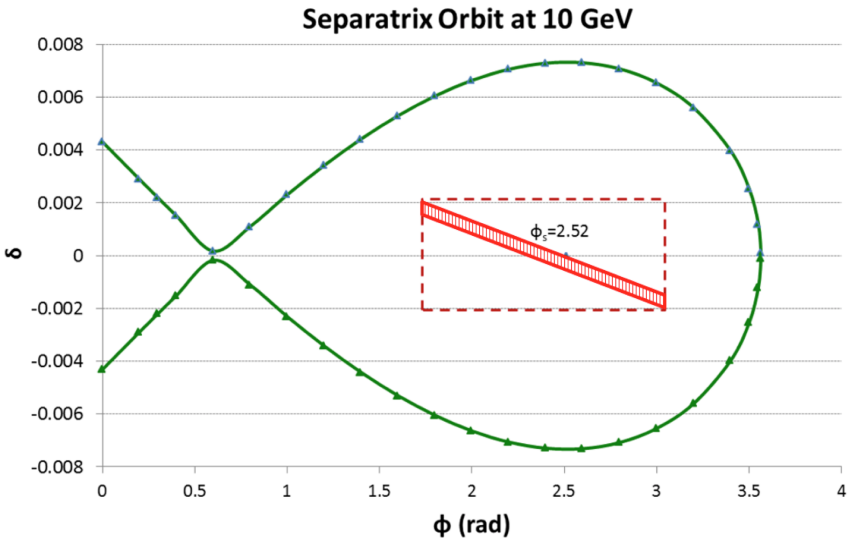

Figure 4.7: Separatrix orbit at 10 GeV JLEIC electron ring with the synchrotron phase $\phi_{\rm s}$. The red rectangle box shows the maximum required longitudinal dynamic range for the injected electron bunch trains, while the shaded parallelogram shows the longitudinal phase space of the injected beam when the electron ring operates at 476.252 MHz.

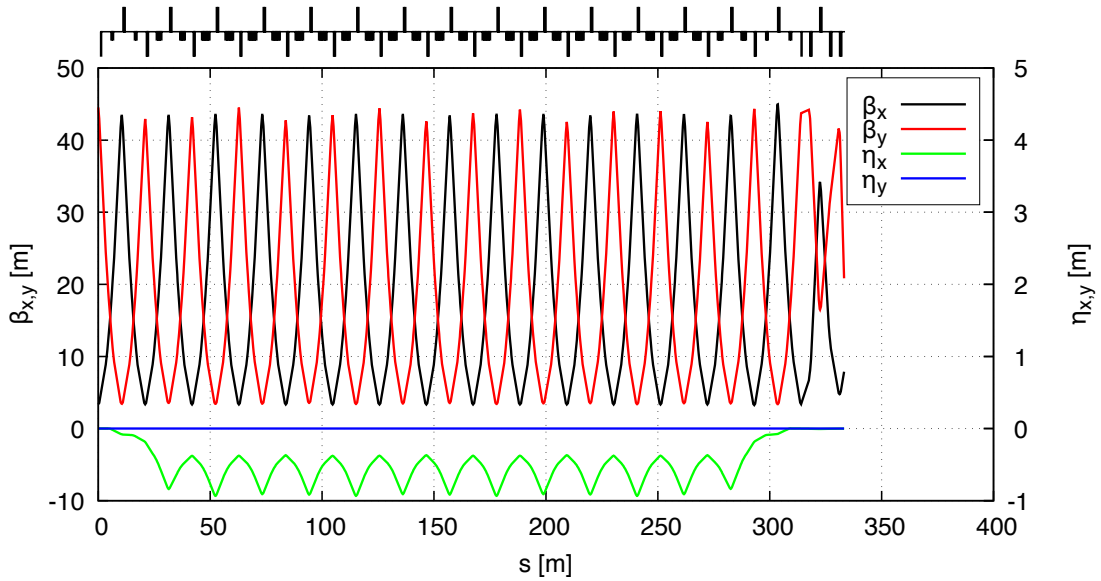

Figure 4.8: Optics for the CEBAF to electron collider ring transfer line. Optics at s =0 m match to the CEBAF AE extraction region. Quadrupoles near s =325 m provide the injection match into the electron collider ring.

4.2 Electron Transport Line

After the last recirculation in the CEBAF accelerator, the beam is sent to a transfer line located upstream of the ramp to the experimental hall after CEBAF's north linac. The transfer line between the linac and the JLEIC electron collider ring is made up of FODO cells with 120° of phase advance per cell. There are fifteen such cells, each of length 20.93 m. We plan to reuse the PEP-II Low Energy Ring (LER) quadrupoles and dipoles to construct the transfer line. We were able to use the LER components (designed for an energy of 3.5 GeV/c) by doubling up the quadrupoles, changing the FODO structure and using dipoles in groups of six. We use a total of 156 dipoles and 68 quadrupoles, which is below the total available count in the PEP-II. Dipoles are combined in two groups of six in each FODO cell. Each dipole is powered at 0.57 T at 10 GeV and bends 0.44°, well within the original specifications of these dipoles. The quadrupoles are used in pairs yielding a maximum individual gradient of 2.8 T/m, also well within their specifications.

We chose a phase advance per cell of 120° for a number of reasons. First, this keeps the quadrupole gradients low enough that we can reuse the PEP-II quads. Secondly, it is compatible with a missing dipole scheme for dispersion suppression. Lastly, this choice for phase advance insures that there is no significant emittance growth due to synchrotron radiation during the transport from CEBAF to the JLEIC electron collider ring.

The whole beamline is rendered achromatic by altering the first two and last two cells to have 8 and 4 missing dipoles, respectively. The optics of the transfer line is shown in Figure 4.8.

The injection into the electron ring occurs at the 90° point from the straight and the optical matching is accomplished by a straight section comprised of five quadrupoles. The length of the entire beamline is about 333 m.

New vacuum chambers are considered for the dipoles to minimize the number of flanges. Each group of six dipoles will be strung on a single curved stainless-steel vacuum chamber terminated by flanges. Pumping ports will be installed after each such section.

The LER powering scheme will be reused, which consists of using a single magnet bending string with the dipole magnets connected in series by water cooled aluminum cables and powered by two 500 V, 640 A power supplies regulated at 0.01%. The quadrupoles, also using aluminum cables, can also be connected in two separate strings (for the focusing and defocusing quadrupoles) and powered likewise. Individual power supplies will be required for the last five quadrupoles which are part of the matching section.

A separate water cooling system for the transfer line is considered because both quads and dipoles are using hollow core aluminum conductors. We expect to be able to reuse the existing LER design (but not the components) which calls for about 1 gpm at 130 psi.

4.3 Electron Collider Ring

4.3.1 Layout

In JLEIC, the electron and ion collider rings follow the same footprint and are vertically stacked in the same tunnel, with the ion ring above the electron ring. A compact design of the two collider rings is favorable as it is most cost effective and guaranteed to fit in the Jefferson Lab site. However, the size and dimension of the two rings should be sufficiently large to accommodate all machine components. The major components or sections of electron collider ring include spin rotators, interaction region (IR), injection, RF system, electron polarimeter, etc. The major components of ion collider ring are reported in Section 5.4.

Figure 4.9 shows the top-view layout of electron collider ring that accommodates all machine components, with main parameters listed in Table 4.1. Figure 4.10 shows the side-view layout of electron collider ring. Vertical doglegs are incorporated in the electron spin rotators to bring the electron beam to the (elevated) ion beam plane for collisions at the interaction point (IP). The separation of two beamlines is 1.2 m.

4.3.2 Linear Optics Design

The linear optics design of the electron collider ring is optimized to minimize the beam emittance while incorporating provisions for chromaticity compensation to obtain sufficient energy acceptance

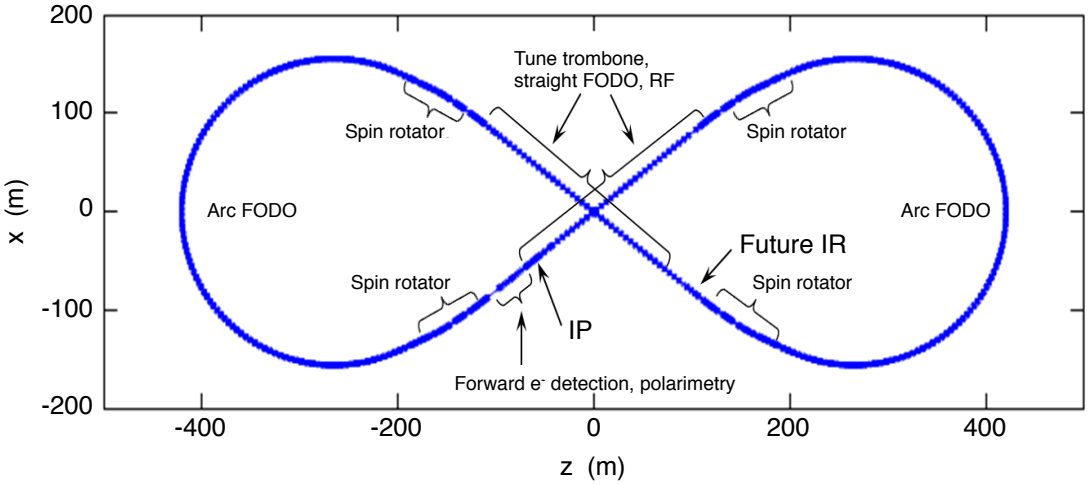

Figure 4.9: The JLEIC electron collider ring top-view layout.

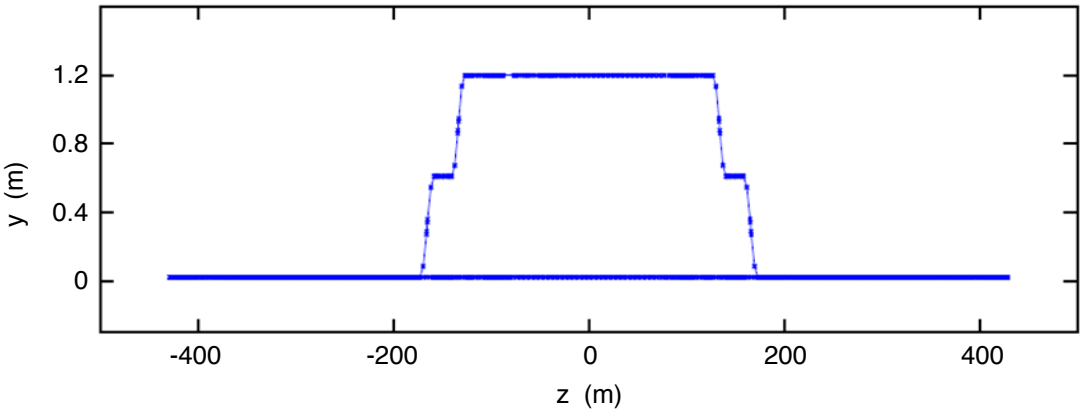

Figure 4.10: JLEIC electron collider ring side-view layout.

Table 4.1: Main Geometric Parameters of the JLEIC Electron Collider Ring

Circumference	[m]	2256.61
Figure-8 crossing angle	[deg]	77.4
Arc length (per arc)	[m]	892.97
Arc bending angle (per arc)	[deg]	257.40
Arc bending radius	[m]	155.52
Straight length (per straight)	[m]	235.33

and dynamic aperture [9, 10], and maintaining reasonable magnet strengths. The lattice is a FODO lattice in both arcs and straights. Optics were designed and optimized using the accelerator design code MAD-X [11]. Machine sections with special functions, such as spin rotator and detector region, are designed as modules and inserted into the lattice with proper optics matching.

The normal arc FODO cell is 11.4 m long, with two 3.6 m long normal conducting dipole magnets. The filling factor is 63%. Each dipole has a maximum field of ∼0.41 T at 12 GeV and bends the beam by 2.1° with a bending radius of ∼98 m (resulting in a sagitta of 1.65 cm). The betatron phase advance per cell is 108° in both transverse planes. This value is fairly close to 137°, the optimal value associated with the minimum equilibrium horizontal emittance of a FODO lattice. By having this phase advance, the third-order geometrical aberrations generated by sextupoles, used for linear chromaticity compensation, are canceled within an achromat which consists of 5 arc cells. Each quadrupole is followed by a focusing-plane corrector and BPM for closed orbit measurement and correction. The optics of the arc FODO is shown in Figure 4.11. Corresponding magnet parameters are listed in Table 4.2.

The spin rotator is designed with interleaved solenoids and dipoles, quadrupoles in between for the optics, to rotate the electron polarization between the vertical (in arcs) and longitudinal (at IP) directions in the whole energy range [12, 13, 14]. Spin rotator is part of the arc optics, providing a horizontal bending angle of 13.2°. In addition to the spin manipulation, the spin rotator is also designed to transport the electron beam, through a vertical-dogleg design, from the electron collider ring plane to the ion collider ring plane for collisions at the IP. The advantages of doing this are twofold. First, the dipole fields used to transport the electron beam are much weaker than those used to transport the ion beam since the electron beam energy is much lower than the ion

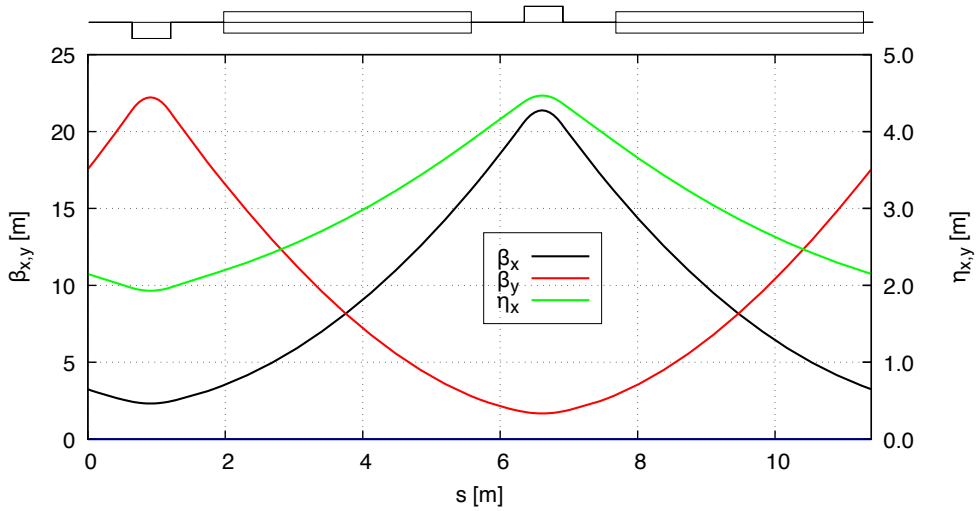

Figure 4.11: Electron collider ring arc FODO optics.

Table 4.2: Electron Ring Arc FODO Magnet Parameters at 12 GeV

Dipole length	[m]	3.6
Dipole bending radius	[m]	98.2
Dipole bending angle	[deg]	2.1
Dipole bending field	[T]	0.41
Quadrupole length	[m]	0.56
Quadrupole strength	[T/m]	21
Sextupole length	[m]	0.44
Sextupole strength	[T/m^2]	692
BPM length	[m]	0.05
Corrector length	[m]	0.3
Corrector strength	[T]	TBD

beam energy. Second, space is tighter in the ion collider ring because more machine elements are required, such as an electron cooling section, accelerating and bunching cavities, dedicated region for far-forward ion detection after collisions, etc. Placing the vertical dogleg into the electron collider ring provides enough space for all required machine components in the ion collider ring.

The radial dipole fields that bend the electron beam vertically in the dogleg are not interleaved with the vertical dipole fields that are required for the spin manipulation. Therefore, the dogleg has zero net effect on the spin rotation in the first order. However, the depolarization caused by the spin-orbit coupling effect might be enhanced due to the radial dipole fields in the dogleg. Spin tracking simulations will be performed to provide a quantitative estimate of how much the polarization lifetime is affected.

The longitudinal fields in the solenoids cause coupling between the horizontal and vertical motions. Although such transverse coupling may be a benefit in the operation of synchrotrons to adjust the vertical emittance and increase the Touschek lifetime, the accompanying coupling reso-

nances may reduce the available dynamic aperture for the particle motion and accordingly decrease the beam lifetime. Therefore, transverse orbital coupling is usually undesirable and should be compensated in a storage ring. Two solutions of coupling compensation have been studied. One is to use normal quadrupoles [15]. In this scheme, a solenoid is divided into two equal parts and an insert composed of normal quadrupoles is placed between them. The quadrupole strengths are chosen so that for the whole combination (half solenoid, quadrupole insert, and half solenoid), the 4×4 transport matrix is block-diagonal. Then the transverse coupling due to the solenoids is neutralized. In this scheme, the quadrupole strengths are independent of the solenoid fields, however, they are relatively strong. A relatively large longitudinal space for the compensating quadrupoles is also needed to create a block-diagonal transport matrix. Another solution that is being applied in the JLEIC spin rotator for the coupling compensation is to use skew quadrupoles. Each solenoid is divided into four equal parts and skew quadrupoles are inserted in between. The coupling effect induced by skew quadrupoles cancels that due to the solenoids, with a block-diagonal 4×4 transport matrix of the whole insertion. Splitting long solenoids into four parts makes the optics straightforward to control. This scheme places no requirements on the strengths and lengths of different solenoids. The skew quadrupole strengths depend on the solenoid strengths, and vary with the beam energy.

The optics of the spin rotator is shown in Figure 4.12. The 1.2 m vertical dogleg is shown in Figure 4.13. However, the spin rotator does not change the design orbit over the entire range of electron beam energy. Each spin rotator has four 1.25 m-long solenoids, four 2.5 m-long solenoids, eight 3.6 m-long vertical bending dipoles, six 2 m-long horizontal bending dipoles, 8 skew quadrupoles (in 4 families) and 30 quadrupoles (in 24 families) to control the optics. The dipoles have a maximum field of ∼0.77 T at 12 GeV, and solenoids have a maximum field of ∼7.6 T at 12 GeV. The dipole bending angles and optics are chosen and designed to control the emittance contribution in both horizontal and vertical planes. Zero dispersion in the solenoids avoids synchrotron sideband spin resonances. Integrals of solenoid field at various energies are listed in Table 4.3. Note that with one IR, two spin rotators are implemented in two ends of the IR straight, i.e., one end of each arc connecting with the IR straight. Space is reserved in another end of each arc, which are connecting with the ends of the second IR straight, for another two spin rotators for a second IR. In each of

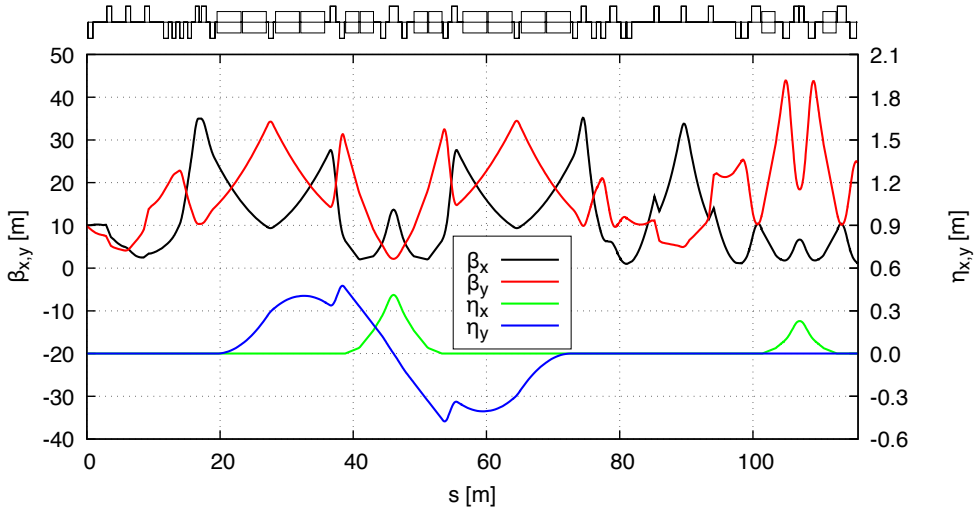

Figure 4.12: Electron collider ring spin rotator optics.

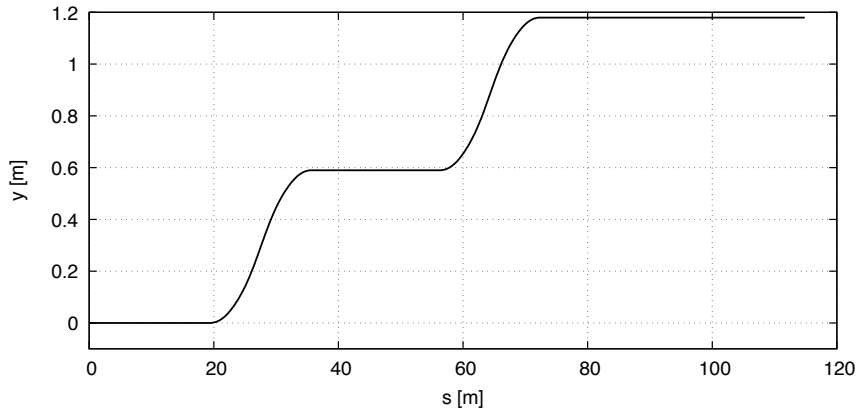

Figure 4.13: Vertical dogleg in the spin rotator transports the electron beam by 1.2 m in the vertical direction.

Table 4.3: Integrals of Solenoid Field in the Spin Rotator

Energy	Solenoid 1 (2.5+2.5 m)	Solenoid 2 (5+5 m)
GeV	T-m	T-m
3	15.7	0
5	11.9	28.7
7	13.1	47.1
9	15.7	62.8
12	24.6	76.4

these two regions, only vertical bends are placed to provide a horizontal bending angle of 13.2°, and solenoids and horizontal bends are replaced by quadrupoles for the optics control.

The interaction region is designed with small $\beta^\star$ to provide a small beam size at the IP for collisions with an ion beam to reach a desired high luminosity. Two triplets are used in both up- and downstream IR to guarantee the desired $\beta^\star$ and control the maximum beta functions. The detector space is made asymmetric to guarantee sufficient space for electron low-Q^2 tagging and minimum chromaticity contribution. Special attention is paid to sizes and positions of machine elements to avoid them interfering with ion detector region elements. In addition, considering engineering fabrication, space is reserved for coil shaping and collars, magnet assembly, bellows, vacuum and cryostat, etc. The downstream optics is designed to focus the beam again to allow closer placement of detectors at those locations, in combination with relatively large dispersion values, which enhances the momentum resolution of the forward detector. The dispersion generated by the spectrometer dipoles is suppressed by a dipole chicane whose parameters are chosen to avoid a significant impact on the equilibrium emittance. Dipoles have a maximum field of ∼0.54 T at 12 GeV. All final focusing quadrupoles (FFQs) have the same length of 0.6 m, with a maximum gradient of ∼54 T/m at 12 GeV. Since skew fields up to ∼10 T/m only is required to compensate the coupling effect induced by the detector solenoid, adding additional skew windings on the FFQs is sufficient to compensate this coupling. The optics of electron ring detector region, with the coupling compensation, is shown in Figure 4.14).

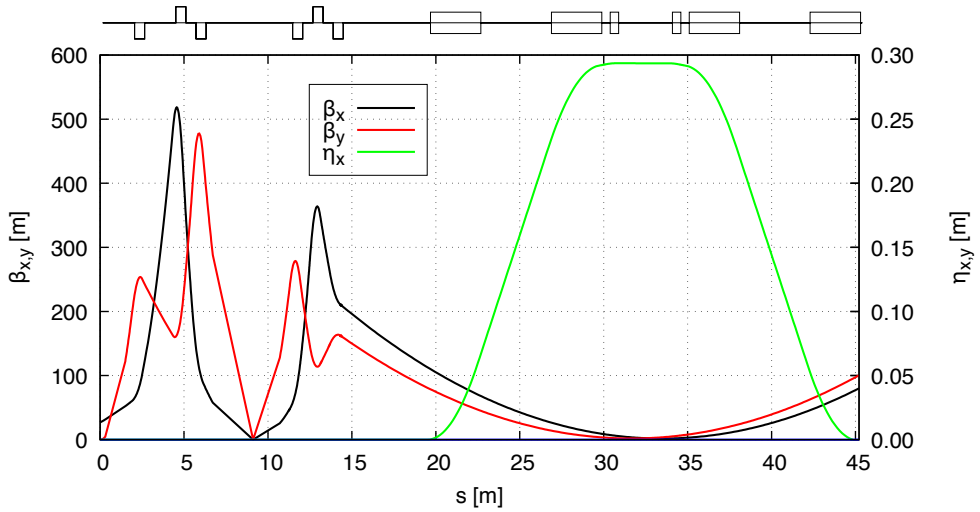

Figure 4.14: Electron collider ring detector region optics.

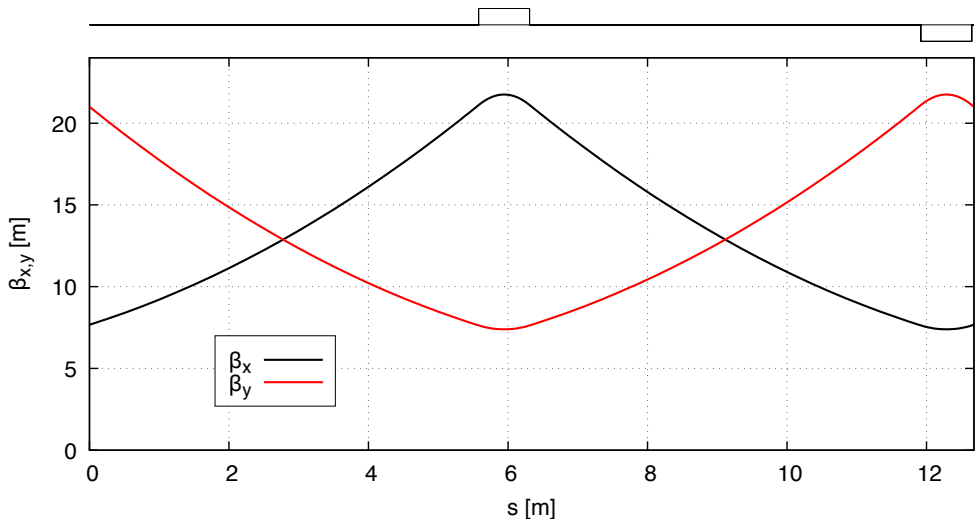

Figure 4.15: Electron collider ring straight FODO optics.

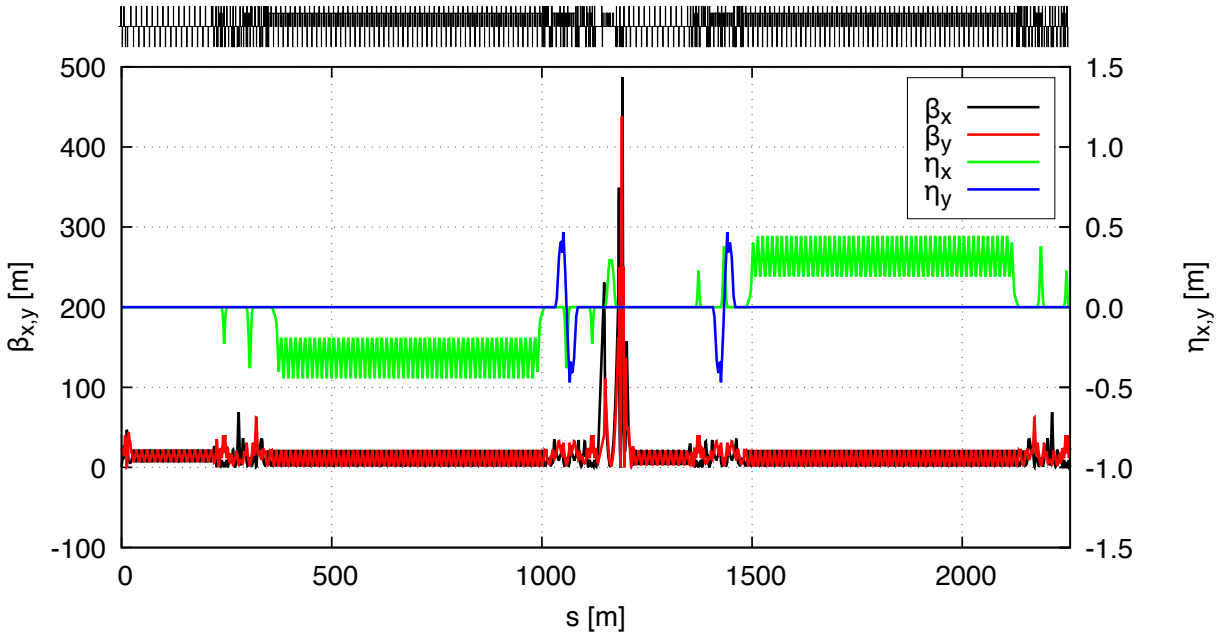

Figure 4.16: Complete electron collider ring optics.

In the JLEIC reference design, only one IR is integrated into the lattice optics. The rest of the IR straight is occupied by FODO cells and necessary matching sections. The second straight is presently filled with FODO cells and space is reserved for a second IR. Some of these FODO cells are used as a tune trombone for the betatron tune adjustment. RF cavities are placed in the straight between quadrupoles in FODO cells. The beta functions in the RF locations are controlled to be relatively small to improve the coupled beam instability thresholds. The straight FODO optics is shown in Figure 4.15. The complete electron collider ring optics is shown in Figure 4.16.

4.3.3 Parameter Tables

More information about the electron collider ring is provided in reference tables here, as a complement to the linear optics design described in the previous section.

Table 4.4 presents high-level optics parameters of the reference design of JLEIC electron collider ring. Note that β^*s at the IP are 10 and 2 cm in the horizontal and vertical planes, respectively. The optics in the IR region will be tuned to reach the desired β^*s at different energies, as shown in Table 3.1.

Table 4.5 lists electron beam parameters at several representative beam energies.

Table 4.6 provides RF system parameters in the electron collider ring.

Table 4.7 lists the magnet inventory of the electron collider ring. Only the maximum strength (at 12 GeV) in each magnet category is presented.

Table 4.8 shows synchrotron radiation density at all dipoles in the electron collider ring.

Table 4.4: JLEIC Electron Collider Ring Lattice Parameters

Parameter	**Units**	**Value**
Circumference	[m]	2256.61
Fig 8 Crossing angle	[deg]	77.4
Total ring bending angle	[deg]	514.8
$\beta_{\mathrm{x}}^{\star}$	[cm]	10
$\beta_{\mathrm{y}}^{\star}$	[cm]	2
$\beta_{\mathrm{x,max}}$	[m]	487
$\beta_{\mathrm{y,max}}$	[m]	438
$D_{\mathrm{x,max}}$	[m]	0.44
$D_{\mathrm{y,max}}$	[m]	0.47
ζ_{x}	[–]	-124
ζ_{y}	[–]	-129
α_{C}	[10^{-4}]	9.97
γ_{T}	[–]	31.67

Table 4.5: JLEIC Electron Beam Parameters

Parameter	**Units**						
Energy	[GeV]	3	5	6.9	9	10	12
Beam current	[A]	3	3	2.6	1	0.673	0.17
Energy loss per turn	[MeV]	0.12	0.93	3.37	9.75	14.86	30.81
Total SR power	[MW]	0.37	2.88	8.76	9.75	10.00	5.24
Energy spread	[10^{-4}]	2.8	4.6	6.4	8.3	9.3	11.1
Transverse damping time	[ms]	375	81	31	14	10	6
Longitudinal damping time	[ms]	187	40	15	7	5	3
Normalized horizontal emittance	[µm]	9.6	44	116	258	354	612
Normalized vertical emittance	[µm]	1.1	5.0	13.1	28.9	39.7	68.6
Bunch length	[cm]	1	1	1	1	1.1	1.5

Table 4.6: RF System Parameters in the Electron Collider Ring.

Parameter	**Units**						
Cavities per klystron	[–]	2	2	2	2	2/4	2/4
Energy	[GeV]	3	5	6.9	9	10	12
V_{peak}	[MeV]	0.534	2.58	7.17	17.09	19.47/3.25	8.18/26
Syn. phase	[deg]	13	21.1	28.0	34.8	46/15	64/65.6
Syn. tune	[$\times 10^{-3}$]	9.93	16.55	22.84	29.79	30.79	26.48
Tuning angle	[deg]	-58	-54.6	-44.4	-44.9	-38.9/-48.2	-6.9/-7.3
Coupling beta	[–]	5	8	10	5	4	4
Total RF power	[MW]	0.57	4.36	12	12	12.9	9.91
Cavity number	[–]	2	10	24	26	28	42
Bucket height/energy spread	[–]	16.6	14.7	13.0	11.5	8.4	3.3

Table 4.7: Electron Collider Ring Magnet Inventory

Magnet category	Length [m]	Number	Maximum strength	Unit
Dipole	3.6	244	0.41	[T]
Dipole	2.0	24	0.77	[T]
Dipole	3.0	4	0.53	[T]
Dipole	0.50	2	0.77	[T]
Quadrupole	0.56	242	21.0	[T/m]
Quadrupole	0.73	174	21.2	[T/m]
Quadrupole	1.00	35	19.3	[T/m]
Quadrupole	1.36	13	19.3	[T/m]
Quadrupole	0.85	8	20.1	[T/m]
Quadrupole	0.60	6	54.6	[T/m]
Sextupole	0.44	160	576	[T/m^2]

Table 4.8: Synchrotron Radiation Density at the dipoles in the electron collider ring

					Energy (GeV)			
					3	5	10	12
Dipole Name	Length	Bending angle	Bending radius	Sagitta	Synchrotron radiation density			
	m	rad	m	cm	kW/m			
Bxarc	3.6	0.037	98.2	1.65	2.74	9.38	9.65	9.70
Bxds1	3.6	0.023	158.9	1.02	1.05	3.58	3.68	3.70
Bxds2	3.6	0.014	257.2	0.63	0.40	1.37	1.41	1.41
Bysr1	3.6	0.034	107.3	1.51	2.30	7.85	8.08	8.12
Bxsr1	2	0.038	52.1	1.00	9.74	33.31	34.28	34.46
Bxsp1	3	0.0375	80	1.41	4.13	14.13	14.54	14.62
Bxsp2	0.5	0.0025	200	0.016	0.66	2.26	2.33	2.34
Bxspl	3	0.04	75	1.50	4.70	16.08	16.54	16.63

4.3.4 Nonlinear Dynamics and Aperture

The design of JLEIC collider rings relies on an ultra-small $\beta^\star$ to achieve a high luminosity of up to $10^{34}\,\mathrm{cm}^{-2}\,\mathrm{s}^{-1}$. Such an approach is associated with a strong focusing of beams resulting in high natural chromaticities and potential beam smear at the IP(s). In addition, the electron collider ring has a significant chromaticity contribution from the arcs, where the FODO cell has a phase advance of up to 108° to achieve a small natural horizontal emittance, and the spin rotators have a relatively strong focusing to save space and control the optics.

Overall, for the horizontal and vertical planes, there are ∼27% and ∼31% chromaticity contributions from the low-beta interaction region, ∼39% and ∼48% from the arcs, and ∼35% and ∼21% from the straights and matching sections. The most straightforward chromatic correction scheme is a global chromaticity compensation using distributed arc sextupoles. The phase advance of 108° per cell provides conditions for cancellation of non-linear resonance effects from the periodic arc sextupoles in every 5 (π phase advance) and 10 (2π phase advance) cells. There are two families of chromaticity sextupoles included in 40 cells of each arc. The maximum sextupole strength is $\sim 576\,\mathrm{T/m}^2$ at 12 GeV. Figure 4.17 shows the variations of momentum dependent tune (left) and $\beta^\star$ (right) after the chromatic correction for a 5 GeV electron beam. The momentum acceptance is $\sim \pm 8\sigma_\mathrm{p}$, where σ_p is the energy spread.

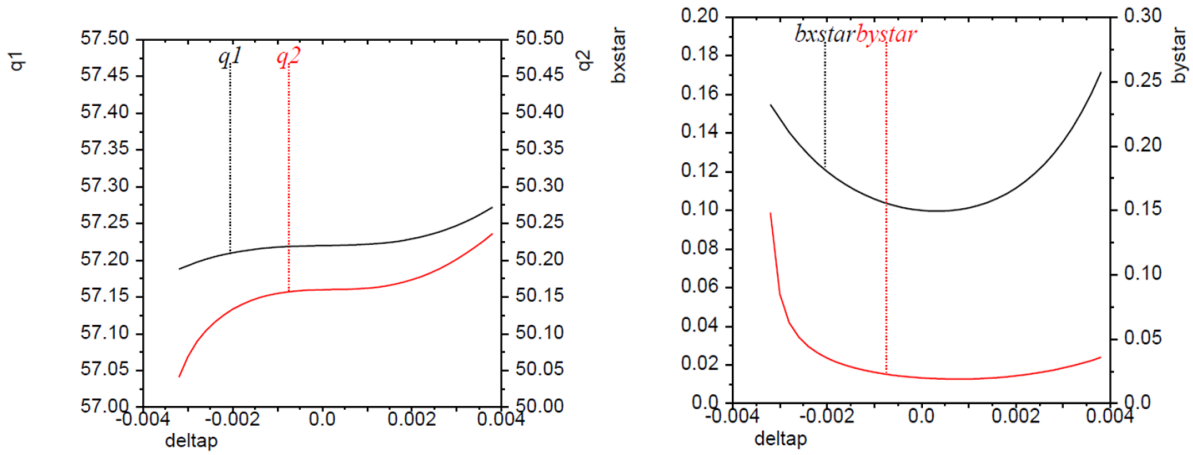

Figure 4.17: Tune as a function of momentum (left) and $\beta^\star$ as a function of momentum (right).

The linear chromaticity (first order chromatic tune shift) is canceled with conventional two-family sextupoles in the arcs, as discussed above. The main concern is the final focusing (FF) non-linear chromaticity causing a large momentum distortion of beta functions and non-linear chromatic tune shift as shown in Figure 4.17. These effects increase the tune spread exposing the beam to more betatron resonances limiting momentum acceptance and dynamic aperture. They also cause chromatic beam smear at the IP, resulting in a larger beam size that limits the luminosity. Compensation of the FF non-linear chromaticity requires a dedicated local correction system. This local chromaticity correction block (CCB), consisting of special optics with sextupoles for the FF correction, can be included at one end of each arc nearest to the IR. The basic principle of the FF non-linear chromaticity correction is that the CCB sextupoles on one side of IR generate a chromatic kick equal to and opposite in phase with the one from the FF on the same side, so they locally cancel the FF first order chromatic beta distortion $d\beta/dp$. An independent correction is

done on the other side of IR. Ideally, this should cancel the $d\beta/dp$ at the IR and in the rest of the ring caused by the FF, as well as the second order term of chromatic tune shift. One additional requirement for such a correction in an electron ring is that it should not significantly increase the beam emittance.

Several CCB-based schemes have been explored using one of the early versions of electron collider ring design, considering both compensation of nonlinear chromaticity and suppression of beam emittance [16, 17]. A CCB-based SuperB-like chromaticity correction scheme with non-interleaved $-I$ sextupole pairs provides a promising solution. The same chromaticity compensation scheme will be considered to be applied in the electron collider ring to study the momentum acceptance and dynamic aperture. The design shown here does not include the CCB and instead only includes global chromaticity correction.

The dynamic aperture (DA) in this design of the electron collider ring with only a global chromaticity compensation is calculated using the code LEGO [18]. The DA is calculated at the IP with a 10000-turn tracking and expressed in units of the rms beam size σ at 5 GeV electron beam energy. The linear chromaticity is always corrected to a positive value of +1 to improve the single and coupled bunch transverse instability thresholds. Figure 4.18 shows dynamic aperture for the bare lattice (without errors) with and without momentum offset$\Delta p/p$, with synchrotron oscillations included. The betatron tunes used in simulations are $\nu_{x,y} = 57.22, 50.16$. The optimal tunes with colliding beams will be determined by both the machine errors and the beam-beam effects.

We also estimate the DA sensitivity to magnet non-linear field errors. Since the Field Quality (FQ) is not yet available for the new electron ring magnets, we have used the measured FQ of PEP-II magnets [19] in all magnets including final focusing quadrupole magnets for DA calculations. The corresponding normal field systematic and random components are listed in Table 4.9. DA with these errors for ten random seeds is shown in Figure 4.19. The minimum DA is 10σ, which has no a significant reduction comparing to the DA of 15σ for on-momentum particles in the bare lattice. However, other types of errors and corrections are not yet included.

Preliminary study of the nonlinear beam dynamics in the electron collider ring with a global chromaticity compensation scheme provides decent momentum range and dynamic aperture. Study of DA sensitivity to magnet non-linear field errors is carried out using the PEP-II measured field

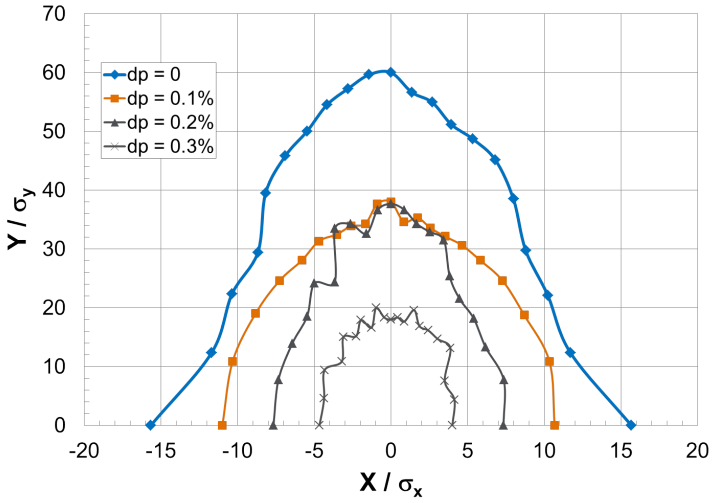

Figure 4.18: Dynamic aperture for the bare lattice with and without momentum offset.

Table 4.9: PEP-II Measured Normal Field Components b_n at the Reference Radius R (in 10^{-3} units) [19]

Dipole	n	Systematic	Random
R=30 mm	3	0.01	0.032
	4		0.032
	5		0.064
	6		0.082
Quadrupole	n	Systematic	Random
R=44.9 mm	3	1.03	0.56
	4	0.56	0.45
	5	0.48	0.19
	6	2.37	0.17
	10	-3.10	0.18
	14	-2.63	0.07
Sextupole	n	Systematic	Random
R=56.52 mm	9	-14.5	2.2
	15	-13.0	1.05

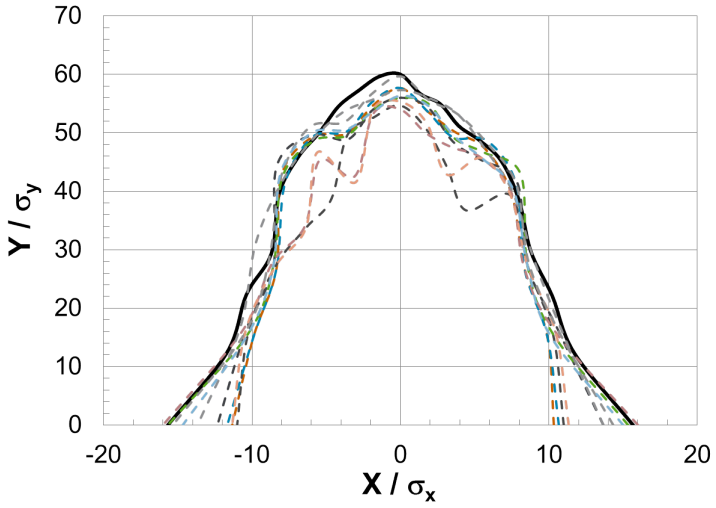

Figure 4.19: Dynamic aperture with PEP-II systematic and random field errors in all magnets for 10 random seeds (dashes). The solid line is the DA without field errors.

quality and shows no significant reduction of DA comparing to the DA in the bare lattice. A more comprehensive tune scan will be performed to determine the optimal tunes with the best DA. Study of nonlinear beam dynamics, considering effects of misalignment and proper machine corrections will be performed in the future.

4.4 Electron Polarization

An essential aspect of the JLEIC design strategy is the requirement to preserve and manipulate a highly polarized electron beam in support of the nuclear physics program. These requirements include:

- polarization of 70% or above,
- longitudinal polarization at collision points,
- polarization flipping at required frequencies.

Various strategies have been carefully considered and investigated to satisfy these requirements [1, 2]. This section describes the design, manipulation, preservation and numerical simulation of electron polarization in the JLEIC electron collider ring. Subsections are included on spin rotators, electron polarization design, polarization lifetime and continuous injection, and spin tracking simulation.

4.4.1 Universal Spin Rotator

CEBAF serves as a full energy electron injector and polarization source of the JLEIC electron ring (Section 4.1). Two Wien filters installed in the photo-injector will be configured to ensure electron beams with a vertical polarization at the injection point of the collider ring. Such an injection has three advantages. First, it accounts for spin decoherence caused by the energy variation during CEBAF acceleration. Second, it simplifies polarization transport between CEBAF and the collider ring. Third, electron beams with vertical polarization are injected in the arc section in the ring. Injection in the arc significantly reduces the background in the detector.

The polarization in the electron collider ring is designed to be vertical in the arcs to minimize spin depolarization and longitudinal at the collision points for the physics experiments. Spin orientation matching between the collision points and arcs is accomplished using spin rotators located at each end of two arcs. A universal spin rotator (USR) has been developed for this purpose [12]. The USR performs over the whole energy range of 3–12 GeV. A schematic drawing of the USR is shown in Figure 4.20.

In the JLEIC electron ring, a 90^o rotation between the vertical and longitudinal direction is required. Implementing this concept requires allocating two arc dipoles (or two sets of arc dipoles) of bending angles $\hat{\alpha}_1$ and $\hat{\alpha}_2$ to the spin rotator (see Figure 4.20). Each of two arc dipoles provides

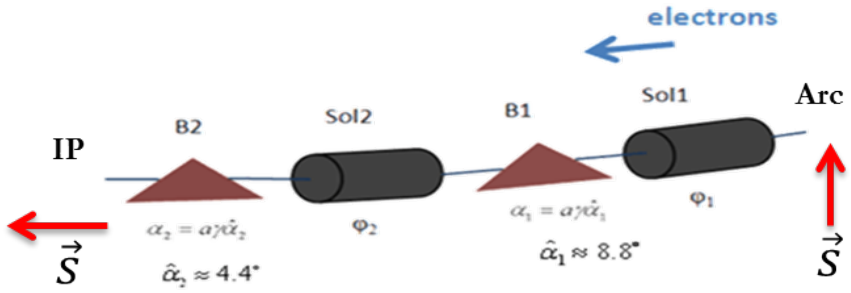

Figure 4.20: Schematic drawing of a USR. B1 and B2 are the two sets of arc dipole bends rotating the spin around the vertical by α_1 and α_2. Sol1 and Sol2 are the solenoids rotating the spins around the longitudinal by ϕ_1 and ϕ_2.

Table 4.10: Parameters of the USR in the JLEIC Electron Collider Ring

Energy	**Solenoid 1**		**B1**	**Solenoid 2**		**B2**
	Spin Rotation	**BDL**	**Spin Rotation**	**Spin Rotation**	**BDL**	**Spin Rotation**
GeV	rad	T-m	rad	rad	T-m	rad
3	$\pi/2$	15.7	$\pi/3$	0	0	$\pi/6$
5	0.23π	11.9	0.56π	0.55π	28.7	0.28π
7	0.18π	13.1	0.78π	0.64π	47.1	0.39π
9	$\pi/6$	15.7	π	$2\pi/3$	62.8	$\pi/2$
12	0.19π	24.6	$4\pi/3$	0.61π	76.4	$2\pi/3$

a spin rotation of $\alpha = G\gamma\hat{\alpha}$,where $G \equiv 0.001159652$ is the gyromagnetic anomaly and γ is the Lorentz factor. The solenoid fields vary to make the net rotation of a spin rotator always equal to a fixed value (90^o for the JLEIC) regardless the beam energy; hence the name "universal". The complete treatment of a USR is given in [12]. The final analytic results are given in the following two equations:

$$\sin\phi_1 \sin\alpha_1 = \cos\alpha_2, \tag{4.4.6}$$

$$\sin\phi_1 \sin\phi_2 \cos\alpha_1 = \cos\phi_1 \cos\phi_2, \tag{4.4.7}$$

where ϕ_1, ϕ_2, α_1 and α_2 are angles of spin rotation in two solenoids and two bending dipoles, respectively, as shown in Figure 4.20. Table 4.10 shows spin rotation angles for two solenoids and two bending dipoles in the USR for several representative electron beam energies, as well as the integrals of solenoid fields. Since the bending angles of the dipoles are fixed, the designed orbit in the spin rotator remains the same in the whole energy range.

Vertical doglegs are inserted in the electron collider ring to bring the electron beam into the ion beam plane for collisions at the IP. The vertical doglegs are implemented as part of a spin rotator, which has no effect on the spin rotation in the first order. Details of such a spin rotator design are given in Section 4.3.2, where transverse coupling induced by the solenoids in the USR is also addressed.

4.4.2 Electron Polarization Design

The Sokolov-Ternov (S-T) effect [20] has been used to support electron and positron polarization in many synchrotrons, such as in HERA [21]. However, this self-polarization becomes impractical at low energy since the time constant for the build-up process scales as the fifth power of the beam energy, and self-polarization occurs over hours to a few tens of hours. The depolarization process caused by the imperfection of magnetic fields in the storage ring is usually much faster than the self-polarization process, resulting in low equilibrium polarization.

Instead of relying on self-polarization, we inject an electron beam with a polarization higher than the equilibrium value P_{dk}; the polarization will then approach equilibrium with a characteristic time τ_{dk} [22, 23]. Injecting a pre-polarized beam is the only practical solution for JLEIC. It also ensures polarized beam availability if the lifetime of the stored beam is small, as full polarization is immediately available while luminosity is still high.

In the JLEIC electron polarization design, CEBAF provides polarization up to ∼90%, much higher than the equilibrium polarization. This is also important at higher JLEIC electron beam

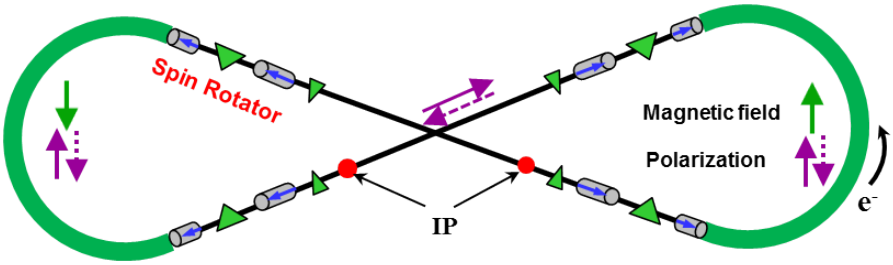

Figure 4.21: Polarization configuration in the JLEIC electron collider ring. Polarization (purple solid and dash arrows) directions remain same in two arcs by having opposite longitudinal solenoid field directions in the same long straight. The blue arrow in the solenoid represents the field direction.

energies since the depolarization rate is high and the spin-orbit coupling function $(\frac{\partial \hat{n}}{\partial \delta})^2$ [22, 23] is large compared to 1. To avoid an immediate loss of polarization in the electron ring, the vertical polarization, lying along the $\hat{n}_0$ vector, is injected at the injection point in the arc. Here $\hat{n}_0$ is the 1-turn periodic solution of the Thomas-BMT equation [24, 25] on the closed orbit.

The polarization configuration in the JLEIC electron collider ring is shown in Figure 4.21. It is determined by the solenoid field directions in the pair of spin rotators in the same long straight [14, 26]. They were chosen to have the opposite solenoid polarities (blue arrows in cylinders shown in Figure 4.21). The polarization is anti-parallel to the vertical guiding field in one arc, and parallel to the guiding field in the other arc, regardless of the choice of two possible opposite longitudinal polarizations (purple solid and dashed arrows in Figure 4.21) at the IPs. The S-T self-polarization process has a net depolarizing effect in the whole collider ring, and both polarization states from the polarized source will be equally affected.

In addition, with such opposite longitudinal solenoid fields in the pair of spin rotators in the same long straight, the net field integral is zero. As a result, the first order spin perturbation in the solenoids for off-momentum particles vanishes. This significantly extends the polarization lifetime and reduces the burden on the spin matching and ring-optics design. Though this polarization configuration has a zero equilibrium polarization, with highly polarized injected beams, the polarization lifetime at low energies ($<$9 GeV) is large enough ($\sim$half an hour to a couple hours) for detectors to collect data.

Such a polarization configuration, combined with a figure-8 geometry of collider ring, produces a net zero spin precession on the designed orbit. Hence the spin tune on the design orbit is zero and independent of beam energy. This significantly reduces the strengths of synchrotron sideband resonances [27]. In addition, since there is no preferred direction of the polarization, the polarization can be easily controlled and stabilized by using relatively small magnetic fields, for example a spin-tuning solenoid in the straights where the polarization is longitudinal. This spin-tuning solenoid introduces additional spin precession only, resulting in a non-zero spin tune that moves spin motion away from the harmful zero spin resonance, but has no effect on $\hat{n}_0$, i.e., the design polarization direction.

Desired spin flipping to reduce systematic uncertainties in the experiments in the JLEIC is implemented by alternating the helicity of the photo-injector driver laser at the source to provide oppositely polarized electron beams. Therefore, two polarization states coexist in the collider ring and have similar polarization degradation in the aforementioned polarization configuration. Figure 4.22 shows two long oppositely polarized bunch trains and polarization pattern in collider ring's arcs, with gaps in between for beam abortion, ion cleaning, etc. The injection time structure of

two polarized electron bunch trains, considering synchronizing different RF frequencies in CEBAF and collider ring, is described in detail in Section 4.1.2.

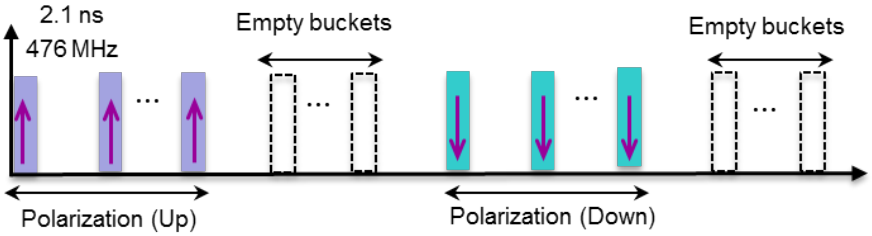

Figure 4.22: Bunch train and polarization pattern in collider ring's arcs.

4.4.3 Polarization Lifetime and Continuous Injection

Analytical estimation of the equilibrium polarization and lifetime, with inclusion of high order resonances, requires evaluating $\hat{n}$ and $(\frac{\partial \hat{n}}{\partial \delta})^2$ [22, 23] all over the orbital phase space and this can require large amounts of computer power. However, valuable first impressions can be obtained easily and quickly by linearizing the spin motion as in the SLIM [28] algorithm. This is implemented in the thick-lens code SLICK. For details of these matters see [29]. The linearization entails assuming that the angle between $\hat{n}$ and $\hat{n}_0$ is small all over phase space. The formalism only exhibits the first order spin-orbit resonances but that suffices in the first step.

Tracking simulations have been performed using the code SLICK/SLICKTRACK [29] to validate the developed spin manipulation scheme and study the spin dynamics. SLICK calculates the polarization lifetime analytically by evaluating the invariant spin field $\hat{n}$ and spin-orbit coupling function $(\frac{\partial \hat{n}}{\partial \delta})^2$ in the Derbenev-Kondratenko formula. SLICKTRACK is an extended version of the analytic code SLICK providing the Monte-Carlo simulation of photo emission and allowing one to numerically track many particles' spins using a full 3D spin motion. Since the full 3D spin motion is considered, SLICKTRACK has the capability of capturing higher-order spin-orbit resonances.

The advantage of the figure-8 shape JLEIC collider rings is removal of the spin-tune energy dependence during the acceleration and storage. Since the designed-orbit spin tune is zero, particles are sitting in the zero-integer spin resonance. To stabilize the spin motion, it is sufficient to use a weak magnet insertion to move the spin tune away from zero. In our electron polarization studies, a spin-tuning solenoid is placed in the straight section as shown in Figure 4.23. Since the polarization is longitudinal in the straight, such a spin-tuning solenoid does not change the polarization direction in the whole ring but causes additional spin precession. Note that the electron beam is injected from the CEBAF to the collider ring at a full energy. Therefore, the spin-tuning solenoid does not need to ramp.

The spin tune at a given energy can be adjusted by varying the strength of the spin-tuning solenoid. Such a procedure is called a spin-tune scan. By doing this, one can find an optimum spin tune that is large enough to avoid the zero-integer spin resonance and give a long polarization lifetime. A spin-tune scan has been performed for electrons at 5 GeV in the JLEIC electron collider ring. Figure 4.24 shows the simulation results where the Sokolov-Ternov time is in red, the spin-orbit coupling depolarization time in the linear approximation (SLICK) is in green and the spin-orbit coupling depolarization time of 500 particles from the Monte-Carlo simulation (SLICKTRACK) is in blue.

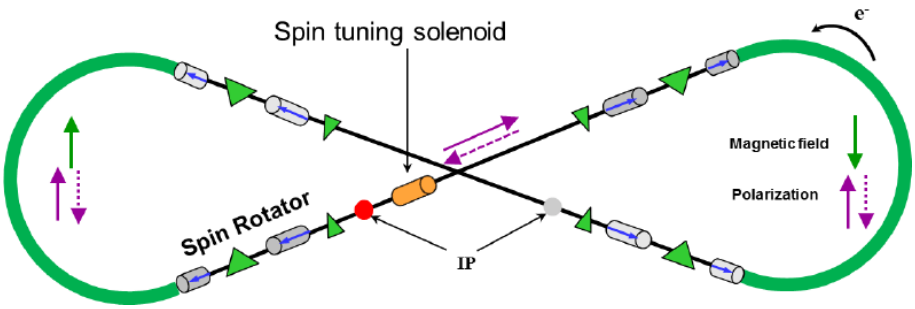

Figure 4.23: Polarization configuration in the electron collider ring, with a spin-tuning solenoid located in the straight where the polarization is longitudinal.

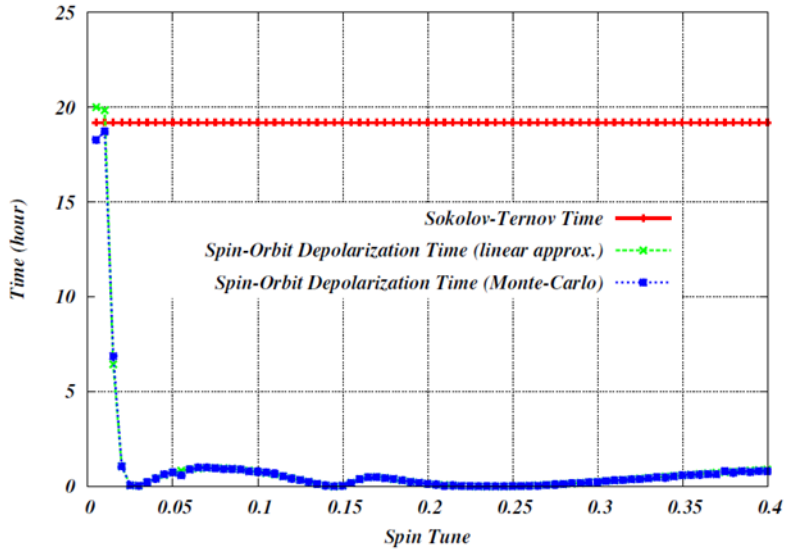

Figure 4.24: Spin-tune scan for a polarized electron beam at 5 GeV in the electron collider ring.

The radial fields due to vertical quadrupole misalignments and dipole rolls tilt the spin from the vertical direction and are the two major contributors to the zero-integer resonance strength. To simplify the simulation and separate different depolarization mechanisms, quadrupoles are randomly shifted in the vertical direction only according to a Gaussian distribution with an rms width of 0.3 mm. The vertical closed orbit excursion shown in Figure 4.25 is corrected with an rms orbit distortion of ∼86 µm at quadrupoles.

As shown in Figure 4.24, a optimum spin-orbit depolarization time $\tau_{\rm dep}$ of ∼19 h can be obtained when the spin tune is moved away from the integer by 0.01. The required field integral of the spin-tuning solenoid is ∼1 T-m only. Then the optimum polarization lifetime τ_{dk} is ∼9 h as calculated with the S-T polarization time of 19 h given in Figure 4.24.

The depolarization time of zero at spin tune 0.027 is due to the first order synchrotron resonance when the spin tune equals the synchrotron tune. It occurs due to breaking of the figure-8 symmetry by the spin-tuning solenoid. The dip depolarization times surrounding 0.15 and 0.24 are due to resonances occurring when the spin tune equals the fraction parts of the horizontal and vertical betatron tunes. Short depolarization times in the spin tune range between 0.03 and 0.33 are due

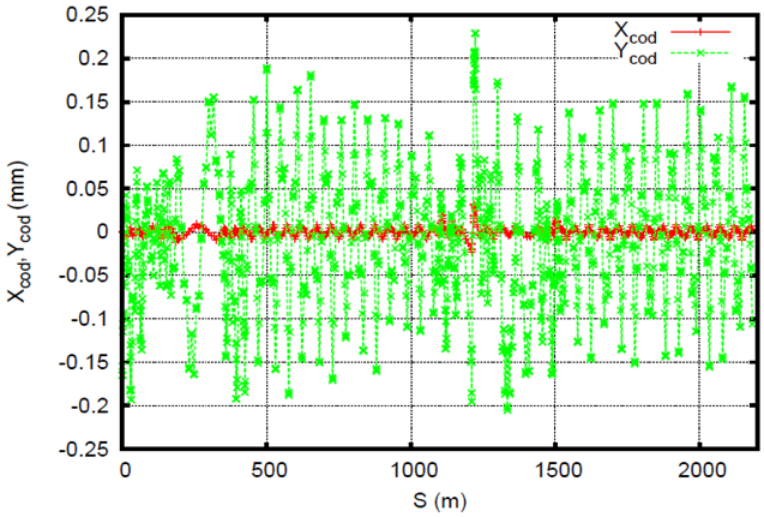

Figure 4.25: Corrected closed orbit distortions with quadrupoles vertically misaligned only.

to stronger breaking of the implemented first-order spin match when increasing the strength of the spin-tuning solenoid to obtain a larger spin tune.

The spin-tune scans obtained through the analytic calculation (the solid green line in Figure 4.24) and the numerical simulation (the dotted blue line in Figure 4.24) completely overlap. This demonstrates, as we predicted, that the figure-8 shaped JLEIC electron collider ring has only weak high-order synchrotron sideband resonances that narrow the range of polarization stability and are difficult to compensate due to the slow synchrotron motion. The wiggles in the Monte-Carlo simulation (the dotted blue line in Figure 4.24) come from the statistical fluctuation and can be suppressed by using more particles in the simulation.

Given the polarization lifetime at 5 GeV beam energy from the tracking simulation, polarization lifetimes listed in Table 4.11 at a few representative electron beam energies are obtained by scaling with the fifth power of the energy. Note that solenoid fields in the spin rotator are not scaled with the beam energy, hence $\hat{n}_0$ in the spin rotator is different at different energies. Polarization lifetimes obtained by simply scaling with the energy may not be very precise. Tracking simulations will be performed for the polarized electron beam at other energies, with proper settings of USR, to obtain accurate polarization lifetimes. In addition, spin matching has been performed to extend the polarization lifetime.

However, there is no doubt that the polarization lifetime decreases with the electron beam energy. In particular, in the JLEIC electron collider ring, the the Sokolov-Ternov self-polarization has a net depolarizing effect. This becomes a challenge at higher energies where the polarization lifetime is mainly determined by the net Sokolov-Ternov depolarization effect and is inversely proportional to the 5^{th} power of the Lorenz factor. Therefore, continuous injection of highly polarized electron beams from the CEBAF is planned to compensate the polarization loss [14, 26], as described in

Table 4.11: Polarization Lifetime in the Electron Collider Ring

Energy	GeV	3	5	7	9	12
Polarization lifetime	Hours	116	9	1.7	0.5	0.1

Section 4.1. Continuous injection, also called top-off injection, has already been successfully applied in the PEP-II at SLAC [30] to increase the integrated luminosity and in the NSLS-II at BNL [31] to maintain the beam current. With the current state of the art, it is not a technical problem. The function of continuous injection in the JLEIC electron collider is two-fold. First, by mixing the partially depolarized stored beam with a fresh highly polarized one through continuous injection, the relative equilibrium polarization at a constant stored beam current is given by

$$\frac{P_{equ}}{P_i} = \frac{\frac{I_{\rm inj}}{I_{ring}} f_{rev}}{\frac{1}{\tau_{dk}} + \frac{I_{\rm inj}}{I_{ring}} f_{rev}}, \tag{4.4.8}$$

where $P_{\rm equ}$ is the attained equilibrium polarization, $P_{\rm i}$ is the injected polarization, $I_{\rm inj}$ is the average injected beam current, $I_{\rm ring}$ is the stored beam current, $f_{\rm rev}$ is the revolution frequency, and $\tau_{\rm dk}$ is the Derbenev-Kondratenko polarization lifetime that can be estimated using the code SLICK. The relative equilibrium polarization as a function of the average injected current at a few of representative energies is shown in Figure 4.26 using the nominal JLEIC design parameters. At a reasonably low average beam current at the nA level, one can achieve a high equilibrium polarization. For example, with a 40 nA average injected beam current, polarization of 80% or above can be reached in all energies below 9 GeV and 75% polarization can be reached at 12 GeV, assuming a 90% injected polarization. Second, the requirement on obtaining large momentum acceptance and dynamic aperture is not strict because the beam lifetime should be comparable to the polarization lifetime. Decent momentum acceptance and dynamic aperture can help particles' extraction. This will significantly reduce the burden of handling the nonlinear beam dynamics.

4.4.4 Analysis of Polarization Control Parameters

Preliminary tracking simulations for a 5 GeV electron beam have also been carried out using the code ZGOUBI [32] to obtain two independent assessments of polarization. Note that ZGOUBI does not have the function to simulate the Sokolov-Ternov self-polarization process. Hence, tracking

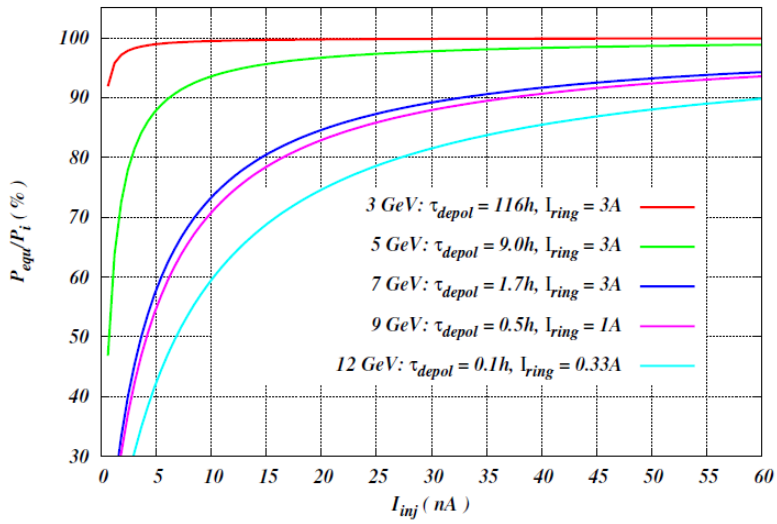

Figure 4.26: Relative equilibrium polarization as a function of average injected beam current at a few of representative energies.

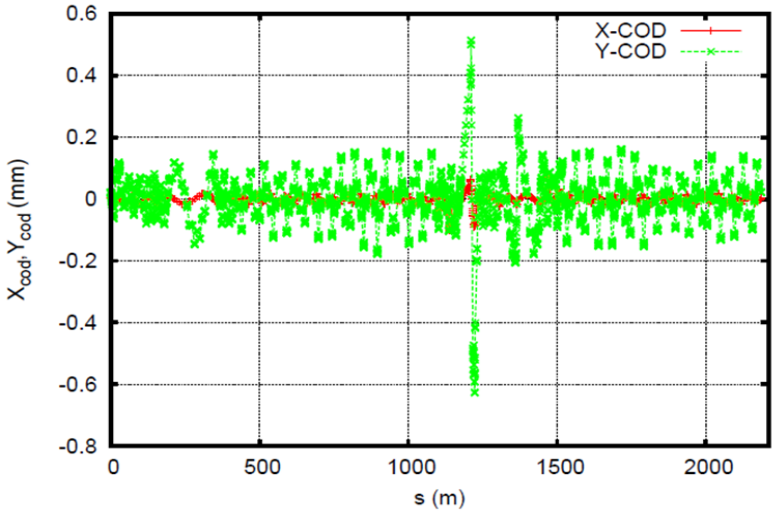

Figure 4.27: Horizontal and vertical closed orbit excursions with random quadrupole misalignments introduced in the vertical plan only.

simulation performed using ZGOUBI only represents the polarization loss due to the imperfection of the magnetic fields and/or particle motions through the spin-orbit coupling effect. To have a fair comparison of simulation results, similar simulation conditions must be established in SLICK/SLICKTRACK and ZGOUBI. For these, only vertical misalignment is introduced to quadrupoles in the electron ring. This results in a rms vertical closed orbit excursion of ∼87 µm at quadrupoles, close to its value in the tracking simulation using SLICK/SLICKTRACK discussed in Section 4.4.3. The closed orbit excursion is shown in Figure 4.27.

Spin tracking simulations are performed using 20 particles to restrict the computing time, with the two characteristic spin tunes, 0.01 and 0.027. According to the simulation results from SLICK/SLICKTRACK, a spin tune of 0.01 produces a long polarization lifetime and a spin tune of 0.027 gives zero polarization lifetime due to the first order synchrotron resonance. To balance the computing time consumption and time needed for electrons damped to the equilibrium condition caused by the synchrotron radiation, tracking simulations are performed for about 3 damping times (∼ 40 k turns) when the electron emittance is approaching to the equilibrium emittance.

Figure 4.28 presents the simulation result of polarization as a function of time with spin tunes of 0.01.

The depolarization time from the ZGOUBI tracking simulation is ∼11 h with a spin tune of 0.01. However, the depolarization time is ∼19 h from the simulation using SLICK/SLICKTRACK. Such a factor of 2 difference in the depolarization time from simulations using two codes is questionable. It might be false because the depolarization time is calculated after 5 damping times in SLICK/SLICKTRACK when the particles are very much damped to the equilibrium emittance, while it is calculated in 3 damping times in ZGOUBI. A long computing time can help obtain more accurate depolarization time in simulations using ZGOUBI. However, this difference might also be real. The orbital motion is linearized in SLICK/SLICKTRACK, while nonlinear particle motion is included in ZGOUBI. More spin resonances may appear in ZGOUBI only because of higher-order harmonics in the orbital motion, this results in more polarization loss comparing to the simulation result from SLICK/SLICKTRACK. Therefore, spin tracking simulations performed by using the code Bmad [33] are being considered to provide an additional assessment of electron polarization in the JLEIC.

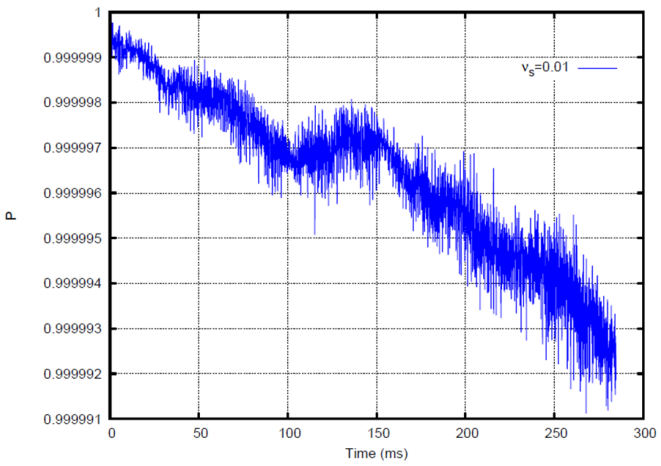

Figure 4.28: Polarization as a function of time with a spin tune of 0.01.

Spin tracking simulation with the spin tune of 0.027 is also performed using ZGOUBI. Figure 4.29 shows the simulation results with spin tunes of 0.01 and 0.027. Just as it is shown in the simulation using the code SLICK/SLICKTRACK, at the optimum spin tune of 0.01, the polarization decays much slower than the one at the spin tune of 0.027 where the first order synchrotron resonance occurs. The polarization lifetime with the spin tune of 0.027 is only about one minute. In a conclusion, tracking simulations using codes of SLICK/SLICKTRACK and ZGOUBI agree that spin tune of 0.01 is the optimum one to maintain a long polarization lifetime.

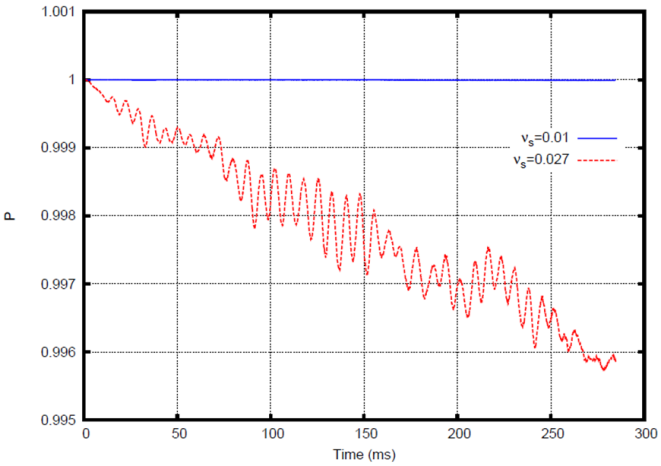

Figure 4.29: Polarization as a function of time with spin tunes of 0.01 and 0.027.

REFERENCES

1. S. Abeyratne *et al.*, "Science Requirements and Conceptual Design for a Polarized Medium Energy Electron-Ion Collider at Jefferson Lab", edited by Y. Zhang and J. Bisognano, arXiv:1209.0757 (2012).
2. S. Abeyratne *et al.*, "MEIC Design Summary", edited by G. Krafft, arXiv:1504.07961 (2015).

3. J.T. Seeman, "Last Year of PEP-II B-Factory Operation", in Proceedings of EPAC'08, Genoa, Italy, TUXG01 (2008).
4. K. Oide, "KEKB B-Factory, The Luminosity Frontier", Progress of Theoretical Physics, Vol. 122, No. 1, July 2009 (2009).
5. Y. Ohnishi *et al.*, "Accelerator Design at SuperKEKB", Prog. Theor. Exp. Phys. 2013, 03A011 (2013).
6. J. Guo *et al.*, "Conceptual MEIC Electron Ring Injection Scheme using CEBAF as a Full Energy Injector", in Proc. IPAC'15, Richmond, VA, paper TUPTY083.
7. H. Wang, J. Guo, R.A. Rimmer, and S.H. Wang, "Transient Beam Loading Effects in RF Systems in JLEIC", in Proc. IPAC'16, Busan, Korea, paper MOPMY003, pp. 518–521.
8. J. Guo *et al.*, "Pulsed Operation of CEBAF for JLEIC Injection", in Proc. Linac'18, Beijing, China, paper THPO004.
9. F. Lin *et al.*, "Towards a Small Emittance Design of the JLEIC Electron Collider Ring", in Proc. of IPAC'16, Busan, Korea, WEPMW016 (2016).
10. Y. Nosochkov *et al.*, "Update on the JLEIC Electron Collider Ring Design", in Proc. of IPAC'17, Copenhagen, Denmark, WEPIK041 (2017).
11. "MADX User's Guide", `http://mad.web.cern.ch/mad/madx.old/madx_manual.pdf`
12. P. Chevtsov, Ya.S. Derbenev, G. Krafft, and Y. Zhang, "Electron-ion Collider Spin Manipulation System and its Mathematics", Jlab-TN-10-026 (2010).
13. H. Sayed, A. Bogacz, and P. Chevtsov, "Spin Rotator Optics for MEIC", in Proc. of IPAC'10, Kyoto, Japan, TUPEB044 (2010).
14. F. Lin, D.P. Barber, Y.S. Derbenev, V.S. Morozov and Y. Zhang, "Polarized Electron Beams in the MEIC Collider Ring at JLab", in proceedings of the 2013 International Workshop on Polarized Sources, Targets and Polarimetry (PSTP'13), PoS(PSTP2013)025 (2013).
15. A. Zholents and V. Litvinenko, "On the Compensation of Solenoid Field Effects by Quadrupole Lenses", BINP (Novosibirsk) Preprint 81-80 (1981). English translation: DESY Report L-Trans 289 (1984).
16. Y. Nosochkov *et al.*, "Compensation of Chromaticity in the JLEIC Electron Collider Ring", in Proc. of NA-PAC'16, Chicago, IL, USA, TUPOB31 (2016).
17. F. Lin *et al.*, "Simulations of Nonlinear Beam Dynamics in the JLEIC Electron Collider Ring", in Proc. of NAPAC'16, Chicago, IL, USA, TUPOB29 (2016).
18. Y. Cai *et al.*, "LEGO: A Modular Accelerator Design Code", SLAC-PUB-7642, August 1997 (1997).
19. Y. Nosochkov *et al.*, "JLEIC Electron Ring Dynamic Aperture with Non-linear Field Errors", in Proc. of IPAC'18, Vancouver, BC, Canada, MOPML008 (2018).
20. A.A. Sokolov and I.M. Ternov, "On Polarization and Spin Effects in Synchrotron Radiation Theory", Sov. Phys. Dokl. **8** N012, p. 1203 (1964).
21. D.P. Barber *et al.*, "The First Achievement of Longitudinal Spin Polarization in a High Energy Electron Storage Ring", Phys. Lett. **343B**, p. 436 (1995).
22. Ya.S. Derbenev and A.M. Kondratenko, "Polarization Kinetics of Particles in Storage Rings", Sov. Phys. JETP **37**, p. 968 (1973).
23. S.R. Mane, "Electron-Spin Polarization in High-Energy Storage Rings. I and II", Phys. Rev., A36, p. 105, p.120 (1987).
24. L.H. Thomas, "The Kinematics of an Electron with an Axis", Phil. Mag. **3**, 1 (1927); V. Bargmann, L. Michel, and V.L. Telegdi, "Precession of the Polarization of Particles Moving in a Homogeneous Electromagnetic Field", Phys. Rev. Lett. **2**, 435 (1956).
25. S.Y. Lee, "Spin Dynamics and Snakes in Synchrotrons", Singapore: World Scientific (1997).
26. F. Lin, D.P. Barber, Y.S. Derbenev, V.S. Morozov and Y. Zhang, "Preservation of Electron Polarization in the MEIC Collider ring", in Proceedings of IPAC'14, Dresden, Hamburg, Germany, MOPRO006 (2014).

27. S.Y. Lee and M. Berglund, "Overlapping Spin Synchrotron Sideband Resonances", Phys. Rev. E 54, 806 (1996).

28. A.W. Chao, "Evaluation of Radiative Spin Polarization in an Electron Storage Ring", Nuc. Ins. and Meth. **180**, pp. 29–36 (1981).

29. D.P. Barber and G. Ripken, "Handbook of Accelerator Physics and Engineering", edited by A.W. Chao and M. Tigner, World Scientific, 1st edition, 3rd printing (2006).

30. J.L. Turner *et al.*, "Trickle-Charge: a New Operational Mode for PEP-II", in proceedings of EPAC'04, Lucerne, Switzerland (2004).

31. T. Shaftan *et al.*, "NSLS-II Injection Concept", in proceedings of PAC'05, Knoxville, Tennessee, USA (2005).

32. F. Meot, "The Ray-Tracking Code ZGOUBI", Nuc. Ins. and Meth. **A427**, p. 353 (1999).

33. D. Sagan, "Bmad: A Relativistic Charged Particle Simulation", Nuc. Ins. and Meth. Phys. Res. A **558**, pp. 356–359 (2016).

CHAPTER 5

ION COMPLEX

The JLEIC ion complex is tailored around the EIC physics needs. It is designed to deliver high-current highly-polarized proton and light ion beams and high-current unpolarized heavy ion beams for collisions with an electron beam at up to two interaction points (IPs). The main design features are:

- The ion complex provides an ion beam for collisions in the center of mass energy range from 20–100 GeV/c. Keeping its size and cost reasonable necessitates use of a 285 MeV SRF linac for initial beam acceleration, an 8 GeV/c superconducting booster, and an 8–100 GeV/c superconducting accelerator/collider ring. The required magnetic fields are modest at about 3 T..
- The ion complex produces, accumulates, accelerates and stores ion beams of up to 0.75 A.
- The ion complex preserves and maintains high polarization of about 80% for light ions including protons and deuterons with an arbitrarily adjustable polarization orientations at the IPs including transverse and longitudinal polarizations. In addition, it offers the capability of frequent spin flips of the ion beam.
- Beam and polarization lifetimes are sufficiently long to maintain a high figure of merit $L \cdot P^2$.
- The interaction regions (IRs) are designed to provide strong beam focusing at their respective IPs while maintaining stable beam dynamics.
- To take full advantage of the strong focusing at the IP, the beam has a high repetition rate of 476 MHz and a short bunch length of the order of 1 cm.

- The beam is cooled in two stages to reach and maintain small transverse emittances and short bunch length while minimizing the required cooling time. This item and the above two items are the basis of the JLEIC high-luminosity concept outlined in Section 3.3.
- The ion collider ring and the primary full-acceptance detector have been designed in close coordination to provide an optimum match to nuclear physics requirements.

The ion complex design relies on conventional technologies as much as possible to minimize technical risk. The design choices taken to optimize the performance of the complex include:

- SRF injector linac
  Our analysis showed that an SRF linac is much more efficient in terms of required RF power than a pulsed warm linac. This outweighs the additional cost of SRF cavities and cryogenics.
- Figure-8 ring design
  A figure-8 ring design is an ultimate solution for preservation and control of ion polarization. In a figure-8 ring, the effect of arcs on the spin is canceled and the spin is controlled by relatively weak lattice imperfections. One then only has to introduce additional weak magnetic fields to overcome or cancel the imperfection fields. This gives full control of the polarization in the ring. A 3D spin rotator, a device described in Section 5.5, provides such control. A 3D spin rotator provides the capability of frequent spin flips of the ion beam. The figure-8 scheme allows one to provide a polarized beam of any particle species including deuterons. It ensures polarization control during storage against higher-order resonances. Moreover, unlike Siberian snakes, the figure-8 design works in the entire energy range of the ion complex with no effect on the beam optics. Solenoidal snakes become inefficient at higher energies while helical Siberian snakes cause large orbit excursions at lower energy and still do not solve the problem of accelerating polarized deuterons to EIC energies.
- Short ion bunch length
  Short ion bunch length is an integral component of the JLEIC high-luminosity strategy. It allows one to take advantage of the strong beam focusing at the IP by reducing the hourglass effect. This has not been common for ion beams in the past, but it is now feasible due to advances in the SRF technology pioneered at Jefferson Lab. A few SRF cryomodules can provide the necessary ion beam strong bunching. Reaching a short bunch length requires a multi-step beam formation scheme. The beam starts out in relatively long bunches and then each bunch is split in half multiple times. The procedure for splitting bunches is well established and requires only warm, low-voltage RF.
- Staged electron cooling
  The JLEIC design relies on electron cooling. The cooling time is proportional to the initial 6D emittance and ion energy squared. Our strategy is to cool the beam in two stages. First, the beam is cooled at a low energy in the booster down to the ion collider space-charge limit using conventional DC cooling technology. The resulting small initial emittance helps cooling at a high energy in the ion collider ring, which only needs to maintain this emittance at a constant level. The high-energy cooler uses an ERL to minimize its power consumption, a circulator ring to relax the electron source requirements, and a magnetized beam in the cooling section for efficient cooling, as described in Chapter 6.
- Integrated full-acceptance interaction region
  Most of the EIC physics program requires detection of forward collision products moving in the ion direction in close proximity to the beam. The challenge of tagging these forward collision products is that nearby machine elements get in the way of detection. Therefore, the JLEIC

full-acceptance detector design has been closely integrated with the machine design of the IR. It relies on a large crossing angle of 50 mrad, a set of spectrometer dipoles, large apertures of the final focusing quadrupoles, and a large dispersion combined with a strong focusing of the beam to a small size at the location of a Roman pot detector located after the downstream ion final focusing quads. To prevent the geometric luminosity loss due to the beam crossing angle, JLEIC employs crab crossing for the electron and ion beams.

This chapter is organized as follows. Section 5.1 describes the ion sources. It is followed by a description of the ion RFQs and linac design in Section 5.2. Section 5.3 presents the design of the ion booster ring. Section 5.4 provides optics design and single-particle non-linear beam dynamics properties of the ion collider ring. Ion polarization design and dynamics studies are presented in Section 5.5. Section 5.6 discusses the ion bunch formation scheme. Transport lines are covered in Section 5.7.

5.1 Ion Sources

Ion source requirements for both polarized light ions and unpolarized heavy ions are listed in Table 5.1. These parameters serve as a reference for the expected ion source performance and drive parameters for the rest of the ion injector complex.

Table 5.1: JLEIC Ion Source Requirements

		Polarized Light Ions	**Unpolarized Heavy Ions**
Parameter	**Units**	**Value**	**Value**
Ion species	[–]	H^-	$^{208}Pb^{30+}$
Pulse current	[mA]	2.0	1.3
Pulse length	[ms]	0.5	0.01
Charge per pulse	[μC]	1.0	0.013
Ions per pulse	[10^{10}]	624	0.27
Repetition rate	[Hz]	5-10	5-10
Emittance (norm.)	[π mm-mrad]	2.0	0.5
Polarization	[%]	90	0

The polarized and unpolarized ion species required for the JLEIC physics program will be provided by dedicated ion sources. Several types of ion sources are being considered. Their attributes are discussed in the following sections.

5.1.1 Polarized Ion Source

5.1.1.1 Atomic Beam Polarized Ion Source (ABPIS) Polarized light ions will be provided by an Atomic Beam Polarized Ion Source (ABPIS) [1, 2, 3, 4]. These sources use resonant charge-exchange reactions between polarized neutral atomic beams and unpolarized atomic ion species to obtain polarized atomic ions. The neutral hydrogen atoms are directly polarized by passage through Stern-Gerlach separating magnets (for electron spin selection) and through RF transition units (for electronic to nuclear polarization transfer via the hyperfine interaction). Ionizing species are

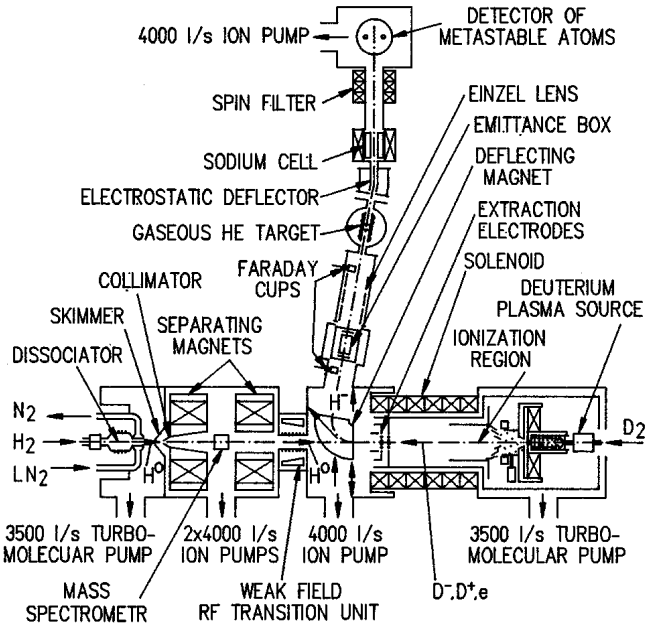

Figure 5.1: Schematic of ABPIS for polarized H^- production [1].

provided by a plasma source. Sources of this type have produced polarized H^+, H^-, D^+ and D^- ions, and may be able to produce polarized ^{3}He and Li ions with additional R&D [5]. An ABPIS producing polarized D^+ ions is currently operating as an injector for the Nuclotron at JINR, and will operate as an injector for the future collider NICA [4].

A schematic of an ABPIS for polarized H^- production is shown in Figure 5.1. Source operation is as follows: an RF gas dissociator provides atomic beam species of the desired polarized ion (i.e. hydrogen atoms when polarized H^- is requested). The atomic hydrogen beam passes through a system of sextupole magnets to focus those atoms with electron spins aligned with the axial magnetic field, defocusing the remaining atoms with antiparallel electron spins. The electron-spin polarized atomic hydrogen beam then passes through a series of RF transition units for the nuclear polarization transfer. The resultant nuclear-spin polarized atomic hydrogen beam is then injected into a solenoid field region for charge-exchange with unpolarized D^- ions. A plasma source provides unpolarized D^+ and D^- ions, as well as electrons, to the charge-exchange region from the opposite end of the solenoid. Use of a plasma source to provide the unpolarized ions allows for densities of slow ions beyond the space charge limit in low energy ion beams. The polarized H^- ions are produced in the charge-exchange reaction:

$$H^0 \uparrow \; + \; D^- \;\; \Rightarrow \;\; H^- \uparrow \; + \; D^0 \tag{5.1.1}$$

The cross-section for reactions of this type, for production of both positive and negative polarized ions, is on the order of $10^{-14}\,\mathrm{cm}^2$ for collision energies on the order of 10 eV. The efficiency of the charge-exchange reaction is calculated as the ratio of the polarized ion current (ions per second) to the intensity of the atomic beam (atoms per second) and is reported to be on the order of 12% for polarized H^- production [2]. Beam currents of milliamps in pulses of hundreds of microseconds have been extracted from such sources, and even higher intensities, up to 11 mA in 200 µs, have been reported for production of polarized protons [3].

Table 5.2: Polarized Ion Source Performance

		JLEIC parameters	**ABPIS** [2], [3]	**OPPIS** [6], [7], [8]
Parameter	**Units**	**Value**	**Value**	**Value**
Ion species	[–]	H^-	H^-	H^-
Pulse current	[mA]	2.0	3.8	1.0
Pulse length	[ms]	0.5	0.17	0.3
Charge per pulse	[μC]	1.0	0.65	0.3
Ions per pulse	[10^{10}]	624	403	187
Repetition rate	[Hz]	5-10	5	1
Emittance (norm.)	[π mm-mrad]	2.0	1.2	0.4
Polarization	[%]	90	91	85

An advantage of this type of source is the ability to provide both H^- and D^- (or their positive counterparts) from a single device. Additionally, development of the RF transition units has made accessible virtually any polarization state for polarized H or D ions, including the tensor polarization states P_{zz} = (+1, -2) of D^+/D^- ions [4]. H^-/D^- ions from ABPIS have demonstrated polarization over 90%. Table 5.2 compares demonstrated parameters for existing ABPIS with the JLEIC requirements for polarized H^-.

Additional R&D is required to demonstrate the desired intensity for both polarized hydrogen and deuteron beams, as well as the feasibility of a modified ABPIS for polarized ^{3}He and Li production. Avenues for optimization of ABPIS devices include increasing both the atomic beam density and the unpolarized ion current density into the charge-exchange region. The polarized ion current available is proportional to the unpolarized ion current from the plasma source, and further optimization of the plasma source and extraction system can result in improved ABPIS performance. Limitations on the pulsed polarized atomic beam density in the ABPIS are not yet fully understood, and improved ABPIS performance may be possible with optimization of atomic beam formation components.

5.1.1.2 Optically-Pumped Polarized Ion Source (OPPIS) As an alternative, Optically-Pumped Polarized Ion Source (OPPIS) type sources, such as that used at RHIC [6], [7], may be considered for the polarized H^- injection. The RHIC OPPIS uses laser pulses to polarize the electron spins of rubidium atoms, and the polarized electrons are transferred to relatively fast (few keV) protons, creating polarized neutral hydrogen atoms. The electron polarization of the neutral hydrogen atom is transferred to the proton by passage through the Sona transition region, where special magnetic field profiles facilitate the polarization transfer. The final step involves the ionization of the polarized atomic hydrogen beam by passage through a cell containing sodium vapor, producing polarized H^- ions.

The RHIC OPPIS has operated succesfully since 2000, and continues to benefit from upgrades for increased intensity. It has also demonstrated polarized H^- performance that is approaching the JLEIC requirements, with parameters also listed in Table 5.2. Maximum measured polarization of 85% at beam energy of 200 MeV, at the linac exit, has been reported.

The RHIC OPPIS is currently only capable of delivering polarized H^- and unpolarized H^-/H^+ beams. Significant modification is necessary to produced polarized D^- ions in an OPPIS type source.

5.1.1.3 Polarized $^3He^{++}$ Source Polarized $^3He^{++}$ beams are of increasing interest and significant progress has been made to develop a source of polarized $^3He^{++}$ ions for RHIC [7], [9]. ^3He atoms are polarized by the metastability-exchange optical pumping (MEOP) process [10] and will be transferred to an EBIS (see following section) for ionization. The source has demonstrated over 80% polarization of ^3He gas, and further development for ionization tests is ongoing. A similar source could be used for JLEIC.

5.1.2 Unpolarized Ion Source

Unpolarized light and heavy ions will be provided by Electron Beam Ion Sources (EBIS) or Electron Cyclotron Resonance (ECR) ion sources. Both types of sources are capable of providing a variety of ion species.

5.1.2.1 Electron Beam Ion Source (EBIS) Electron Beam Ion Source (EBIS) devices, such as that used at RHIC [11] and the EBIS-CB for CARIBU at ANL [12], are reliable sources of high charge state heavy ions. The source can produce mA-level currents for a single charge state, and the charge state distribution is narrow relative to distributions from other charge state breeders. Ions can be extracted from EBIS devices in short, intense pulses, making an EBIS particularly suited for synchrotron injection in a reasonable number of turns.

The basic components of an EBIS generally include an electron gun, solenoid for radial electron confinement, and electron collector. The trap region is the cylindrical volume occupied by and surrounding the electron beam. Ions are created by electron bombardment of gas fed into the trap region, or are injected into the trap region from external ion sources, and are trapped by the space charge of the electron beam (radially) and by potentials on electrodes near the electron gun and collector (axially). Charge breeding occurs as the trapped ions are bombarded by the incident electron beam. External ion sources are necessary for charge breeding of heavy ions in EBIS; the RHIC EBIS uses both hollow cathode ion sources and a laser ion source to provide singly-charged ions for charge breeding, while a ^{252}Cf fission source is used in the EBIS-CB for breeding of radioactive ions.

2×10^9 Au^{32+} ions per pulse in 20 µs pulses have been extracted from the RHIC EBIS, and a similar source should provide the desired unpolarized ion species and intensities for JLEIC. Table 5.3 compares demonstrated parameters for existing EBIS with unpolarized heavy ion requirements for JLEIC.

5.1.2.2 Electron Cyclotron Resonance (ECR) Ion Source Electron Cyclotron Resonance (ECR) ion sources are also commonly used to breed high charge state heavy ions [11], as at CERN [15], FRIB [17], and other machines. In ECR ion sources, the electron cyclotron resonance condition,

$$\omega_{ce} = \frac{eB_z}{m_e}\,, \tag{5.1.2}$$

is satisfied in a volume defined by a magnetic mirror configuration in the axial direction, and externally applied RF power at the resonant frequency. Electrons are resonantly heated in this volume and ignite a plasma through electron impact ionization of background gas or vapor. Radial magnetic fields provide plasma confinement. Charge breeding occurs as ions in the plasma are further ionized through successive electron impact events. ECR ion sources have the ability to generate a wide variety of high charge state ions in a single device, including metallic and radioactive species, but the distribution of charge states within an extracted pulse is broad and the extracted beam tends to be highly divergent. The long ion confinement times allow for very high charge state ions to be produced in the source, and makes the source more suited to CW or long pulse

operation. Pulsed ECR beams can be obtained with a beam chopper or buncher, as well as by pulsing the input RF power and extracting ions from the intense plasma that follows termination of the pulse ("afterglow" operation). Table 5.3 also lists demonstrated parameters for the GTS-LHC ECR ion source.

5.2 Ion RFQs and Linac

The injection system must include a multi-ion linac capable of delivering any ion beam from hydrogen to lead to the Booster. This includes a pulsed linac which consists of several ion sources, a room-temperature (RT) front end, up to 5 MeV/u, and a superconducting (SRF) section for energies > 5 MeV/u. We include beam dynamics and electrodynamics studies performed to design efficient and cost-effective accelerating structures for both the RT and SRF sections of the linac. The current design includes two separate RFQs for heavy-ion and polarized light-ion beams and a common RT section with special DTL tank design downstream of the RFQs. Quarter-wave and half-wave resonators are effectively used in the SRF section.

5.2.1 Design Requirements and Choices for the JLEIC Injector Linac

The baseline design of the JLEIC ion complex calls for the following requirements from the injector linac:

- Capable of accelerating all beams from protons to lead ions, including polarized light ion beams
- Deliver 280 MeV protons and 100 MeV/u lead ions Pb^{67+} for injection to the Booster, and equivalent energies for other ion beams
- Pulsed beam structure with 5–10 Hz repetition rate and 0.2–0.5 ms beam pulse length
- Pulsed beam current of ∼2 mA for light ions and ∼0.5 mA for heavy ions
- Compact and cost-efficient

To satisfy the design requirements listed above, the following design choices were made for the JLEIC injector linac:

Table 5.3: Unpolarized Ion Source Performance

		JLEIC parameters	**EBIS** [13], [14]	**ECR** [15], [16]
Parameter	**Units**	**Value**	**Value**	**Value**
Ion species	[–]	$^{208}Pb^{30+}$	$^{197}Au^{32+}$	$^{208}Pb^{27+}$
Pulse current	[mA]	1.3	0.6	0.21
Pulse length	[ms]	0.01	0.02	0.2
Charge per pulse	[μC]	0.013	0.012	0.042
Ions per pulse	[10^{10}]	0.27	0.23	0.97
Repetition rate	[Hz]	5–10	5	10
Emittance (norm.)	[π mm-mrad]	0.5	0.1	>75†

† Un-normalized RMS emittance

- Due to the significantly different beam parameters from polarized light-ion and heavy-ion sources, the linac includes two separate RFQs, one for mass-to-charge ratio A/q≤2 and one for heavy ions with A/q>2.
- As a consequence, two separate low-energy beam transport (LEBT) lines are required. However, this separate front-end choice allows a special LEBT design for polarized light ions to preserve polarization.
- Based on similar pulsed ion linacs [18, 19], a room-temperature (RT) section up to an energy of ∼5 MeV/u is the most efficient and cost-effective option for the JLEIC linac, followed by a SRF section up to the full linac energy.
- A pulsed SRF linac can be more compact and cost-effective than the full RT option [20, 21]. It also offers wider acceptance and more tuning flexibility for light and heavy ion beams. In addition, taking advantage of state-of-the-art performance of quarter-wave (QWR) and half-wave (HWR) resonators [22, 23], which can deliver higher voltages in pulsed mode, the linac can be even more compact.
- To deliver Pb^{67+} at 100 MeV/u, the optimum stripping energy was found to be ∼13 MeV/u, which is the energy following two QWRs modules made of 7 cavities each.

5.2.2 Design of Different Linac Sections

Figure 5.2 shows the overall layout of the designed JLEIC injector linac with separate front-ends for light ion and heavy-ion beams, a DTL section made of three tanks followed by SRF section made of three QWR cryomodules operating at 100 MHz and nine HWR cryomodules operating at 200 MHz. A stripper section for the heaviest ions is located between the second and third QWR modules.

5.2.2.1 Existing ion sources and expected performance Table 5.4 shows the desired polarized proton and deuteron ion beam parameters in comparison to the beams available from existing polarized sources, namely the atomic beam (ABPIS) and the optically pumped (OPPIS) sources [24].

We notice that while the desired beam parameters are not exactly matched, they are within reach with some R&D effort. For heavy-ion beams, however, both the electron cyclotron resonance

Figure 5.2: Overall layout of the JLEIC injector linac.

Table 5.4: Polarized Light Ion Beam Parameters: Desired vs Available H^-/D^- Beams

	Units	Desired value	ABPIS value	OPPIS value
Beams		H^-/D^-	H^-/D^-	H^-/D^-
Pulse current	mA	2	3.8	4
Pulse length	ms	0.5	0.17	0.3
Polarization	%	100	91	85

(ECR) and the electron beam (EBIS) ion sources are capable of delivering the desired beam current of 0.5 mA for Pb^{30+} and other ions with equivalent mass-to-charge ratios.

One notable difference between the polarized light ions and heavy ions is the beam emittance at the source. While the 90% emittance is typically $0.5\,\pi$ mm mrad for heavy ions, it is $\sim 2\,\pi$ mm mrad for polarized H^-/D^- beams [25]. This significant difference is the main reason to have two separate front-ends for polarized light-ion and heavy-ion beams.

5.2.2.2 Front-end sections: LEBTs and RFQs The design for the polarized light ion LEBT shown in Figure 5.3 (left) is very similar to the BNL LEBT for polarized H^- [26]. It includes two opposite bends to compensate beam polarization. The LEBT is designed for 20 keV/u beams which is the RFQ injection energy.

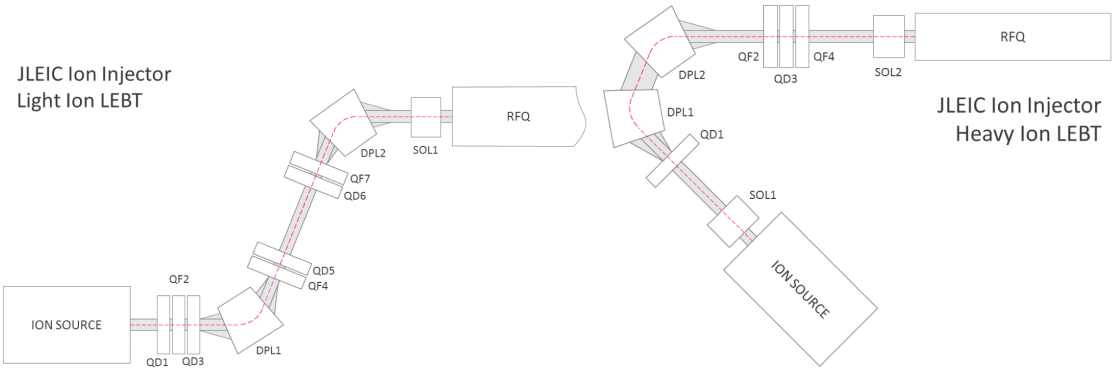

Figure 5.3: LEBT design for polarized light ion beams (left) and heavy ion beams (right).

The heavy-ion LEBT is shown in Figure 5.3 (right). It is based on the CERN Lead Linac-3 injector design [27]. The double-bend is for the selection of the desired charge state for injection into the RFQ. The extraction beam energy from the source is 25 keV/u which is also the RFQ injection energy.

The design parameters for the light ion and the heavy ion RFQs are listed side by side in Table 5.5. Note the ∼100% transmission was achieved for a deuteron beam in order to avoid radio-activation of the RFQ structure by neutrons [28].

For pulsed RFQs, there are different options for the structure design, namely the 4-rod, the 4-vane and the window-coupled designs as shown in Figure 5.4. The structure can be either brazed or bolted. Figure 5.5 shows a conceptual design for a bolted window-coupled structure. For the JLEIC RFQs, we propose the brazed 4-vane window-coupled structure for both its mechanical and field stabilities [29].

5.2.2.3 Room-temperature DTL section Figure 5.6 shows different design options for the accelerating structures in the RT section of the linac. During the design of the RT section [30], we investigated different DTL design options. The first was an IH structure with triplet focusing similar to the BNL EBIS injector [18]. The second was a special DTL design with RF quadrupole focusing [31]. The third option which was selected for the JLEIC linac uses a FODO focusing lattice which offers a large acceptance with limited emittance growth while preserving a good power efficiency.

The design parameters for the three DTL tanks required to reach 5 MeV/u energy for all ion beams are listed in Table 5.6. The DTL section delivers ∼30 MV over ∼11 m and requires ∼1 MW total power. A schematic of the DTL section showing the three tanks made of 19 accelerating gaps and 20 quadrupoles in a FODO arrangement is shown in Figure 5.7.

Table 5.5: Design Parameters for Light-Ion and Heavy-Ion RFQs

Parameter	**Units**	**Light-ion RFQ**	**Heavy-ion RFQ**
Beam A/q Range		1–2	2–7
Input/Output Energy	keV/u	20 / 500	25 / 500
Frequency	MHz	100	100
Average Radius	mm	7	3.7
Voltage	kV	103	70
Length	m	3	5.6
Quality Factor		7200	6600
RF Power Consumption (No Windows)	kW	150	250
Beam Transmission	%	∼100	99
Design transverse normalized emittance	π-mm-mrad	2.0	0.5
Output Longitudinal beam emittance	π-keV-ns	5.0	4.5

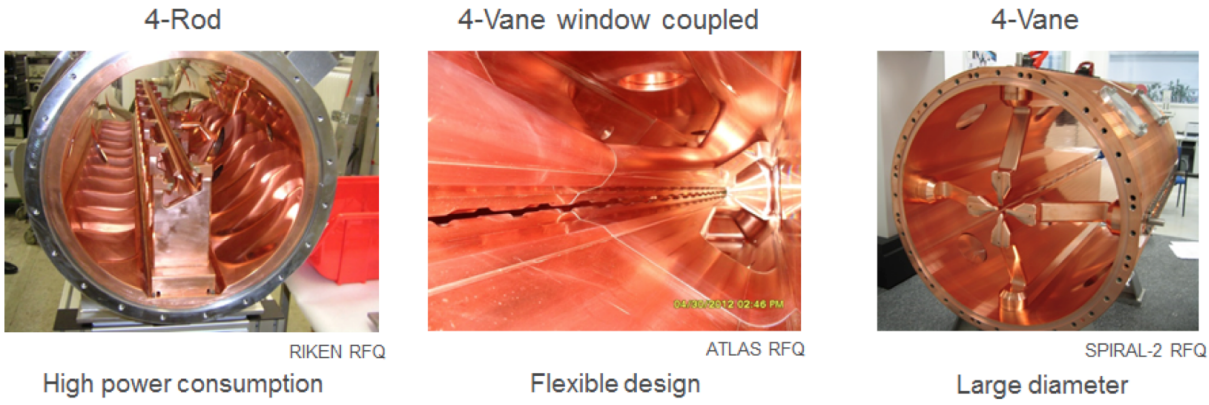

Figure 5.4: Structure design options for ion injector RFQ.

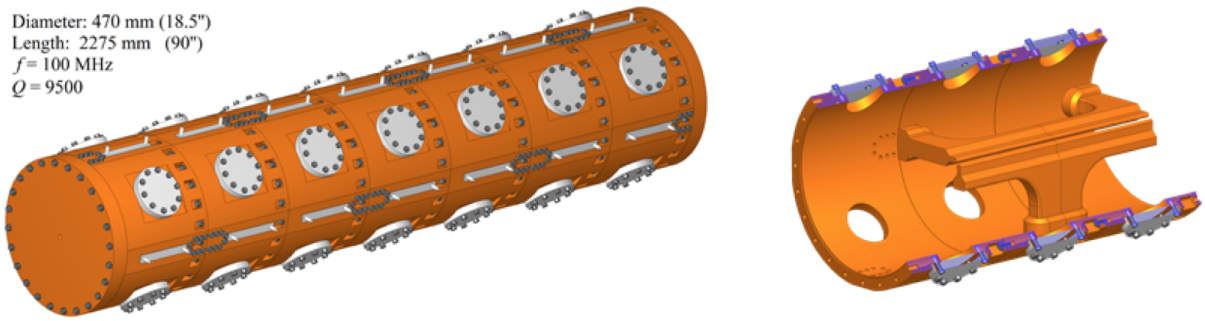

Figure 5.5: Conceptual design for a bolted 4-vane window-coupled RFQ structure.

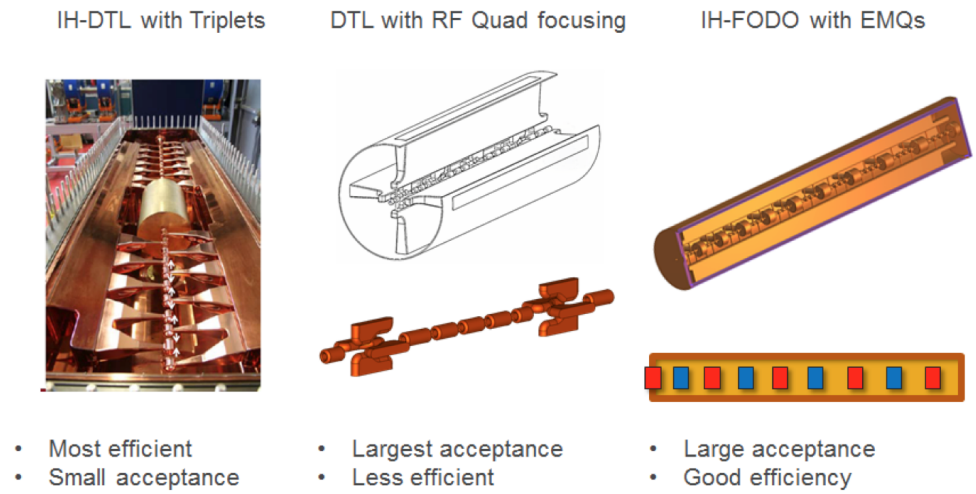

Figure 5.6: Design options for the RT accelerating linac section.

Table 5.6: Design Parameters for the Three IH-DTL Tanks with FODO Focusing

Parameter	**Units**	**DTL-1**	**DTL-2**	**DTL-3**
Input/Output Energy	MeV/u	0.5 / 2.0	2.0 / 3.6	3.6 / 5.0
Accelerating Gaps		10	5	4
Length	m	4.3	3.5	3.4
RF Power Losses	kW	280	400	620

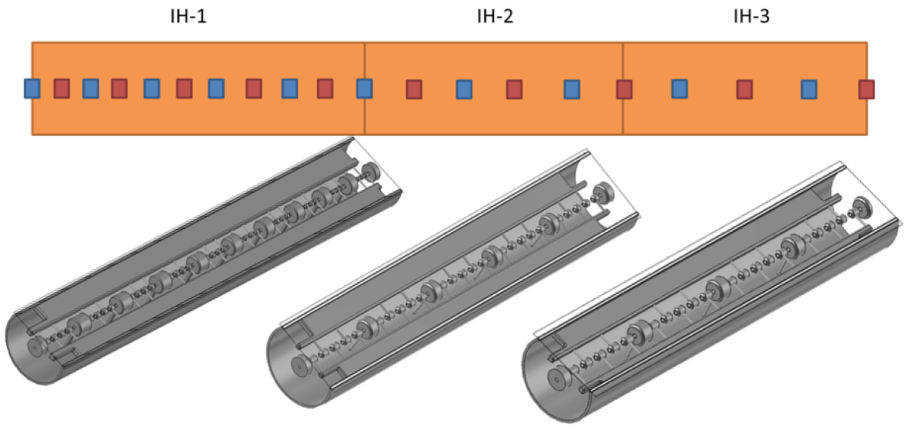

Figure 5.7: Layout of the DTL section made of 3 tanks including 19 accelerating gaps and 20 quadrupoles in a FODO lattice arrangement.

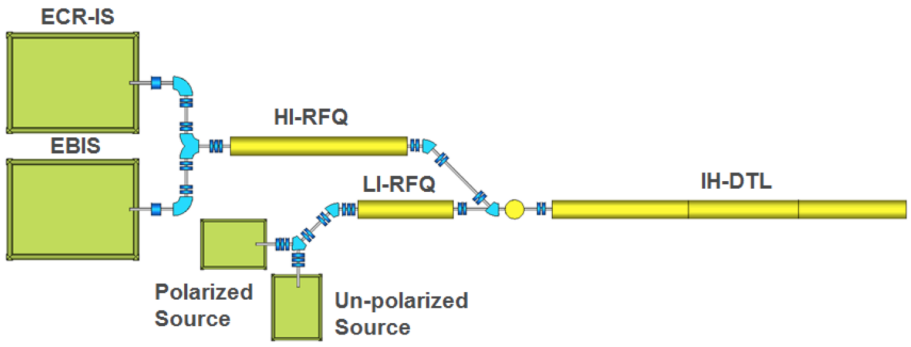

Figure 5.8: A conceptual design of the RT front-end of the JLEIC linac with two heavy-ion sources (one ECR and one EBIS) and two ion sources for light ions (one polarized and one unpolarized).

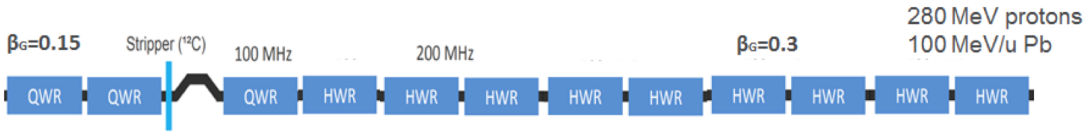

Figure 5.9: Schematic layout of the SRF section including a stripper section after the second QWR module.

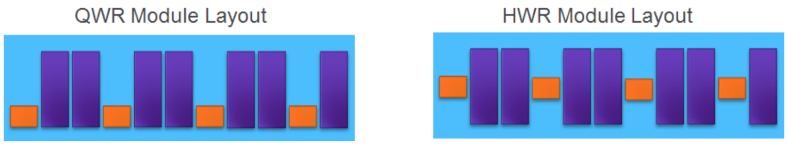

Figure 5.10: Layouts of the QWR and HWR cryomodules, each with seven cavities and four solenoids.

Figure 5.8 shows the preliminary layout of the room-temperature front-end of the JLEIC with possibly one ECR and one EBIS source for heavy ions and one polarized and one unpolarized source for light ions.

5.2.2.4 SRF linac section A schematic layout for the SRF section of the linac is shown in Figure 5.9. It is made of three QWR and nine HWR cryomodules. Each cryomodule is made of seven cavities and four solenoids in the arrangement shown in Figure 5.10 for both the QWR and HWR modules. A stripping section for the heaviest ions is located after the second QWR module at an energy of ∼13 MeV/u for lead ions.

The geometric design of both the QWR and HWR cavities are shown in Figure 5.11 along with their outer dimensions. The corresponding electromagnetic field distributions are shown in Figure 5.12 while their RF design parameters are summarized in Table 5.7.

5.2.2.5 Ion Stripper The optimum stripping energy on a carbon foil to produce lead ions Pb^{67+} for injection to the JLEIC booster is about 13 MeV/u [32]. This energy maximizes the beam fraction in the desired Pb^{67+} charge state which is about 20% and minimizes the total voltage requirements for the linac up to the full-energy of 100 MeV/u for lead ions, see Figure 5.13.

In order to separate the desired charge state from unwanted charge states and other reaction products, a chicane can be used for a straight linac option or a 180° bend for a folded option.

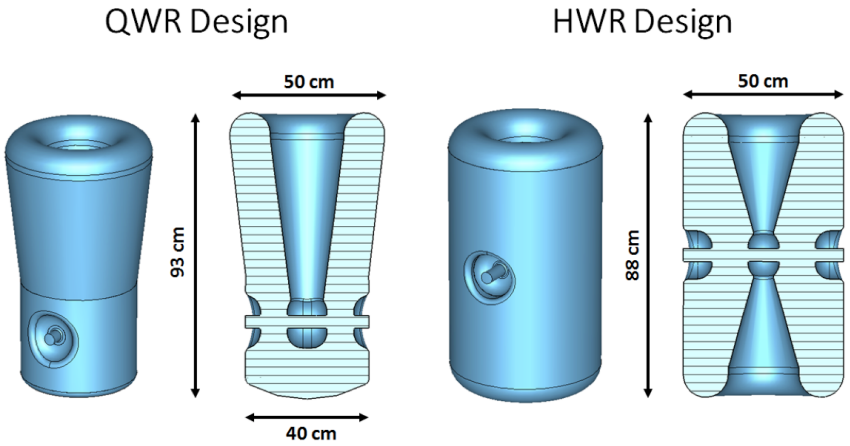

Figure 5.11: Geometrical designs of the QWR and HWR along with their outer dimensions.

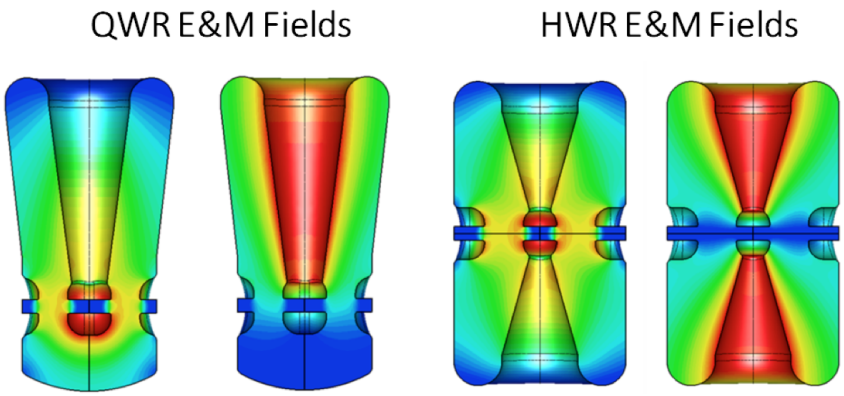

Figure 5.12: Electromagnetic field distributions for the QWR and HWR cavities (electric field on left and magnetic field on right for each cavity.

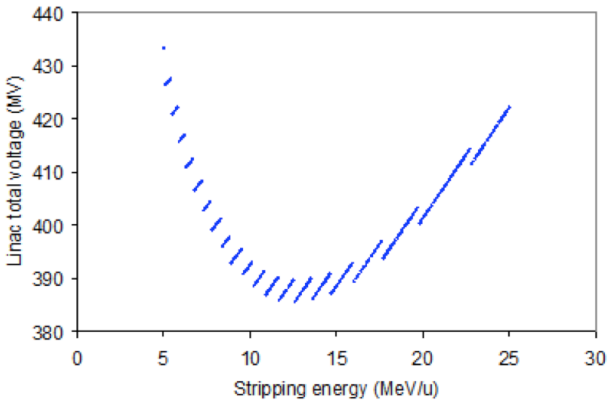

Figure 5.13: Total linac voltage as function of stripping energy for lead ions.

Table 5.7: Design Parameters for the Three IH-DTL Tanks with FODO Focusing

Parameter	**Units**	**QWR**	**HWR**
Design β_{opt}	-	0.15	0.30
Frequency	MHz	100	100
Length ($\beta\lambda$)	cm	45	45
$E_{\text{peak}}/E_{\text{acc}}$	-	5.5	4.9
$B_{\text{peak}}/E_{\text{acc}}$	mT/(MV/m)	8.2	6.9
R/Q	Ω	475	256
G-factor	Ω	42	84
E_{peak} in operation	MV/m	58	52
B_{peak} in operation	mT	86	73
E_{acc}	MV/m	10.5	10.5
Voltage per cavity	MV	4.7	4.7
Cavity phases	deg	15-30	15-30
No. of Cavities	-	21	63

Figure 5.14 shows a preliminary concept of a stripping chicane, where the beam is focused onto the stripper foil using a triplet and the desired charge state is separated and selected using the slits in the middle plane. A rebuncher and another triplet are used at the end of the chicane to longitudinally and transversely match the beam to the following section. Note that the bends can be as strong as required to resolve the selected charge state from other charge states and reaction products.

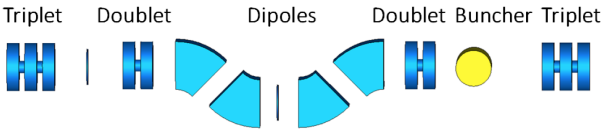

Figure 5.14: A preliminary concept for the stripping chicane to be installed between the second and third QWR cryomodules.

5.2.3 End-to-End Beam Dynamics in the Linac

The beam dynamics design is straightforward for the SRF section of the linac, a focusing period made of two accelerating cavities and one solenoid is the main building block. Exception is made at the end of every cryomodule where a missing cavity accounts for the extra drift space between modules where beam diagnostic devices can be installed. The general design rule is to start with a phase advance below 90° for the zero current beam and maintain periodic focusing for smoothly decreasing phase advance along the linac. The accelerating voltage profile in the cavities is shown in Figure 5.15. It clearly shows that the HWR covers very well the velocity range from 0.2 to 0.35 and no need for a different cavity type at the higher energies. This simplifies the overall design and fabrication of the linac with only two cavity types, one QWR and one HWR. The proposed

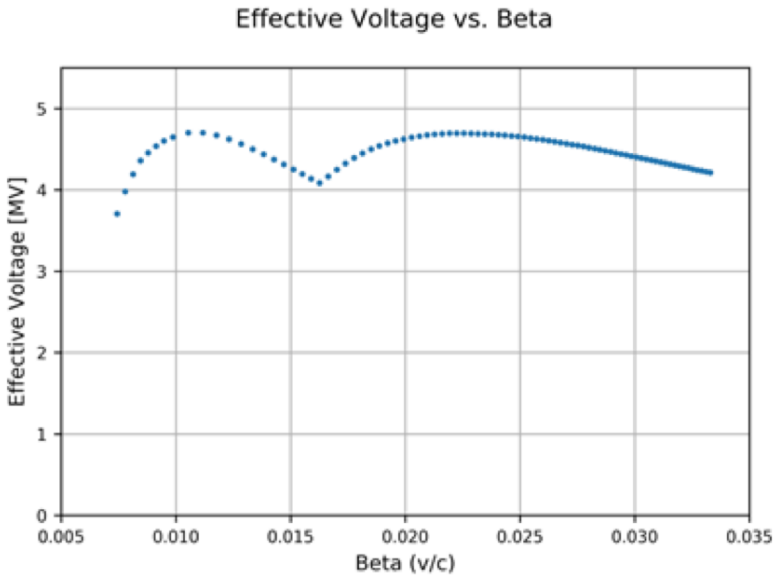

Figure 5.15: Effective cavity voltage as a function of β along the linac, showing that the HWR is fairly efficient up to the full energy of the linac.

operating voltage per cavity of 4.7 MV which will require 9 T superconducting solenoids for lead beam focusing.

Figure 5.16 shows the beam dynamics results for a 2 mA polarized deuteron beam through the RT section and the first part of the SRF section of the linac. In the case, we note a 100% transmission of the large emittance deuteron beam with only about 30% emittance growth. Figure 5.17 shows the same results for a 2 mA polarized proton beam with similar output beam parameters.

Figure 5.18 shows the lead ion beam dynamics in the low-energy section of the linac with close to 100% transmission and ∼30% emittance growth.

The expected beam parameters from the full-energy linac are listed in Table 5.8.

Table 5.8: Linac Expected Beam Parameters

Parameter	**Units**	**Polarized H^-**	**Polarized D^-**	**Pb^{67+}**
Input Emittance	[π mm mrad]	2.0	2.0	0.5
Output Beam Energy	[MeV/u]	280	150	100
Beam Transmission	[%]	99.7	100	98.3
Output Transverse Emittance	[π mm mrad]	3.0	3.0	1.0
Output Longitudinal Emittance	[π keV/u ns]	7.5	7.5	7.0
Energy Spread (rms)	%	0.1	0.1	0.1

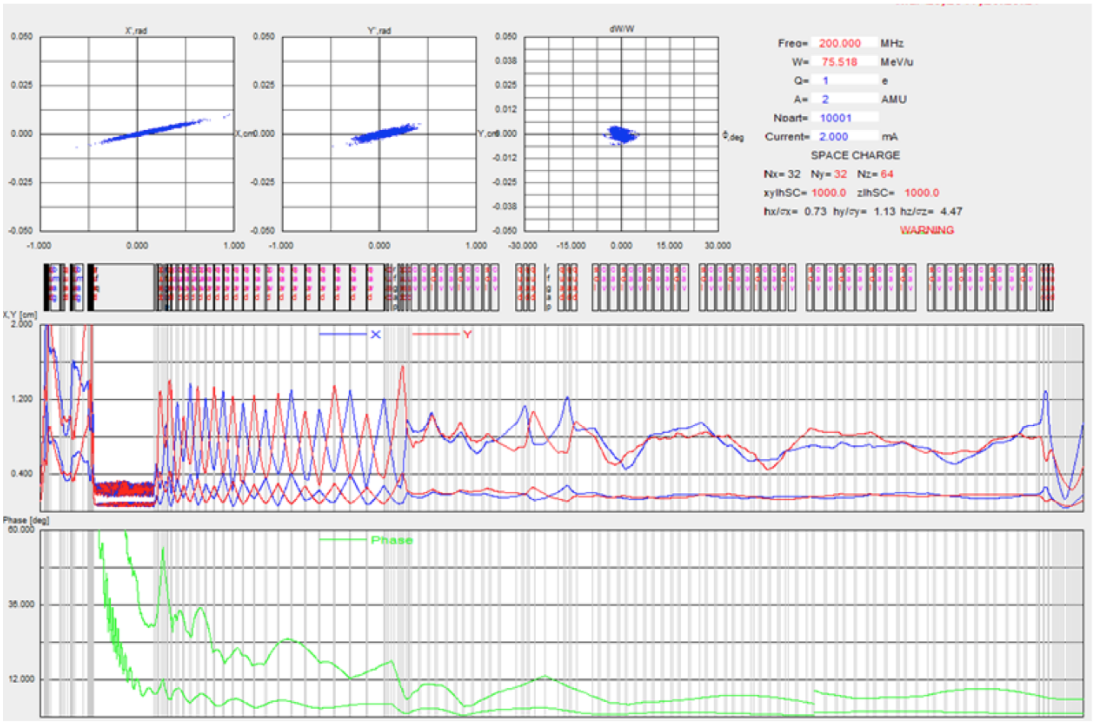

Figure 5.16: Polarized deuteron beam dynamics with 100% transmission through the low energy section of the linac.

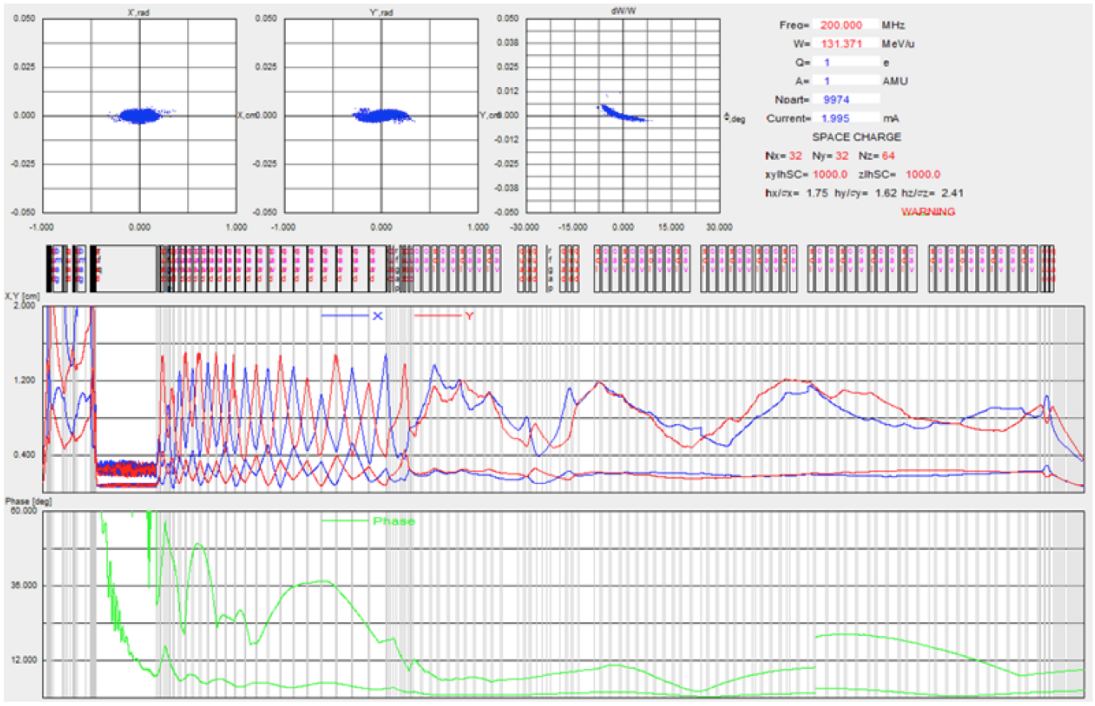

Figure 5.17: Polarized proton beam dynamics through the low energy section of the linac.

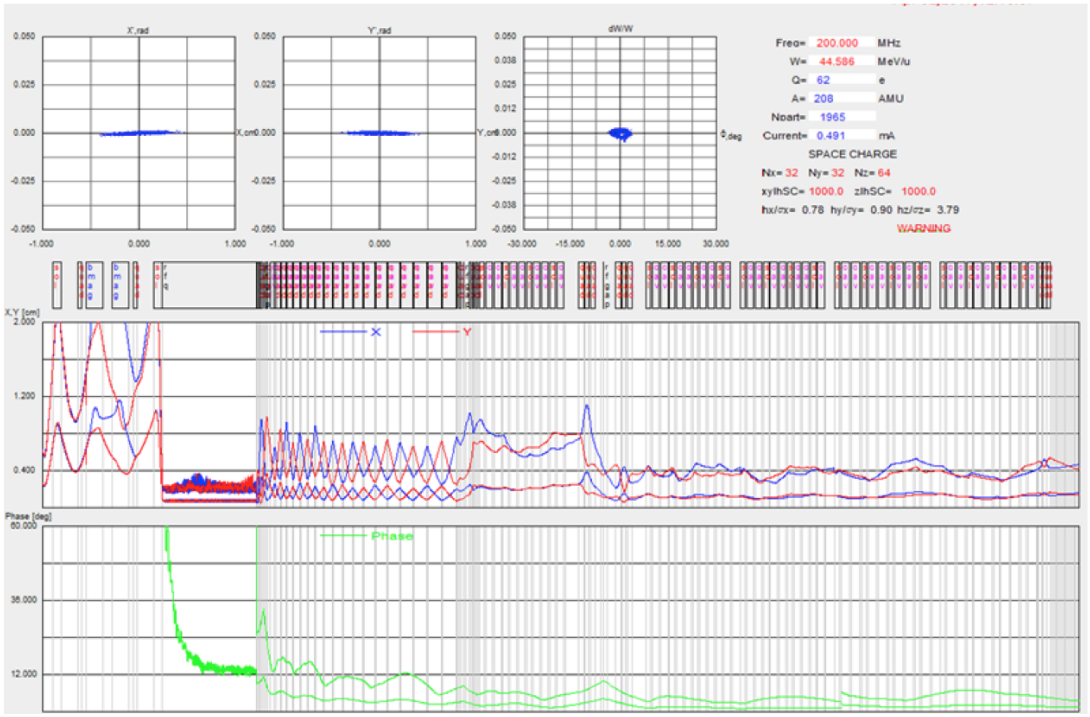

Figure 5.18: Beam dynamics for lead ion beam in the low-energy section of the linac.

5.3 Ion Booster Ring

The JLEIC booster accelerates ions from the linac to the required injection energy for the ion collider ring [33]. The proton energy range is 280 MeV-8 GeV, a ratio of 28 consistent with currently operating machines. The booster also will accelerate light and heavy ions throguh an equivalent rigidity range. Kinematics parameters for the Booster for protons and Pb^{67+} are shown in Table B.1 (Appendix B). The Pb^{67+} charge state is optimum for the linac (Section 5.2); maximizing injected Booster current to minimize stacking time precludes additional ion stripping in the Linac to Booster transfer line.

5.3.1 Booster Design Criteria

The design criteria uses bending dipoles of no more than 3 T at top energy within a maximum circumference of 320 m. The booster accommodates the full energy range without transition crossing, including room for a possible future energy range improvement as detailed in Appendix A. A flexible momentum compaction (FMC) cell is used to "dial in" the desired transition energy [33]. Beam parameters are shown in Table 5.9. A figure-8 shape preserves spin polarization of the ions throughout the acceleration process, as it does in the ion collider ring.

Table 5.9: JLEIC Booster Proton Beam Parameters

	Units	Value
Injection Kinetic Energy	[MeV]	280
Extraction Kinetic Energy	[GeV]	8.0
Horizontal Emittance	[mm-mrad]	1.21
Vertical Emittance	[mm-mrad]	1.21
$\delta p/p$		4×10^{-4}
Bunch Length	[m]	26
Total Number of Particles		8.3×10^{11}

5.3.2 Lattice and Layout

The basic building block of each arc is the FMC cell, shown in Figure 5.19. This particular cell is a 3-cell FODO with the dipoles removed from the central cell, and the phase advance over this "bend free" section changed to give the desired momentum compaction. The dispersion suppressors use the same geometry as the arc cells, but their phase advances are set to suppress the dispersion. This is shown in Figure 5.20.

Sextupoles are used to control non-linear dispersion excited by the FMC cells. The sextupoles are carefully placed to allow for the suppression of the nonlinear dispersions, the control of chromaticities, and the avoidance of nonlinear resonances.

The two opposite bending polarity arcs are joined with straight sections. These sections house an electron cooler, injection, extraction, accelerating RF, spin rotators, and polarimetry. This requires significant empty space, which is maximized by using quadrupole triplets for focusing. This design gives ∼70 m of open drift space in the straights. The lattice for the straight sections is shown in Figure 5.21.

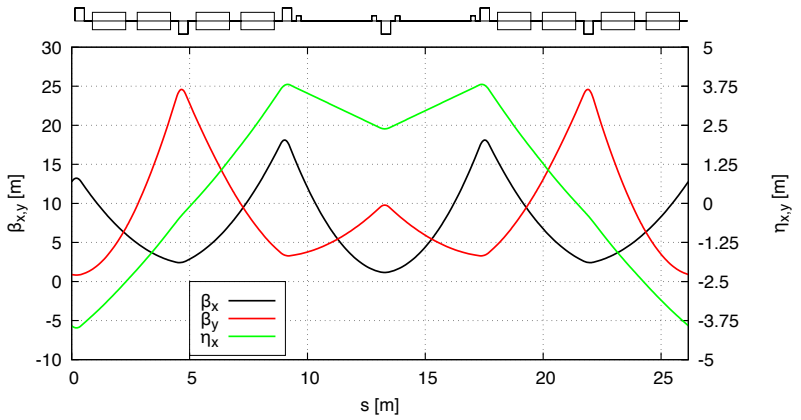

Figure 5.19: Base FMC cell used to make up the arcs of the booster, created by removing the dipoles from the central cell of a three cell FODO lattice, with the phase advance over that cell increased to achieve the desired γ_t.

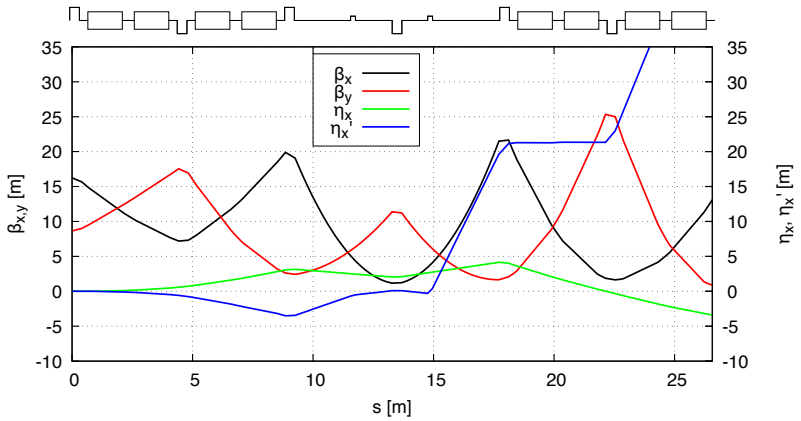

Figure 5.20: Booster dispersion suppressor. The base design is a missing magnet suppressor, with the same geometry as the arc cell.

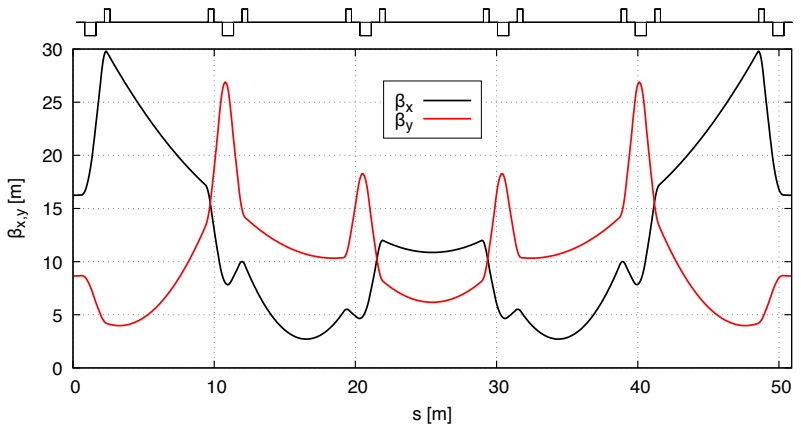

Figure 5.21: One of the straight sections. The middle contains the RF acceleration in this straight, with the injection at the center of the second straight.

The footprint of the total ring is shown in Figure 5.22. The circumference is 313.489 m and the γ_t is 18.647, enough to accommodate possible energy upgrades. The lattice for the full ring is shown in Figure 5.23. The lattice makes use of 40 cm quadrupoles, with some 80 cm units in the straights, as well as 20 cm sextupoles. The counts and maximum values of the magnets are shown in Table 5.10.

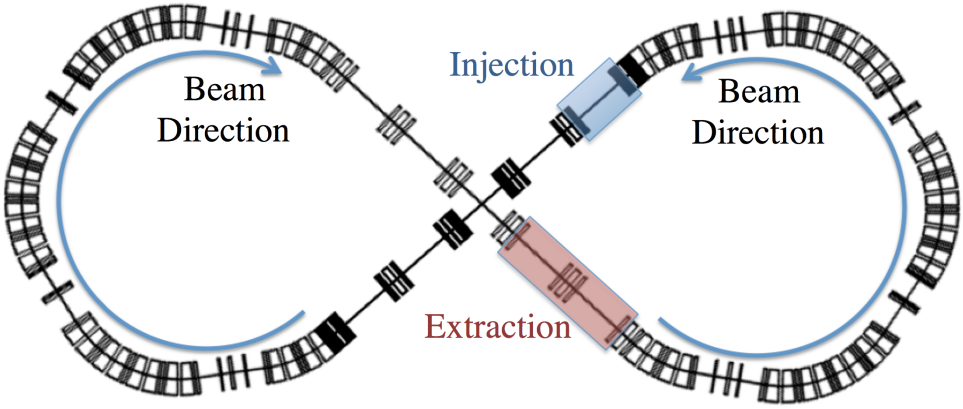

Figure 5.22: Booster physical layout.

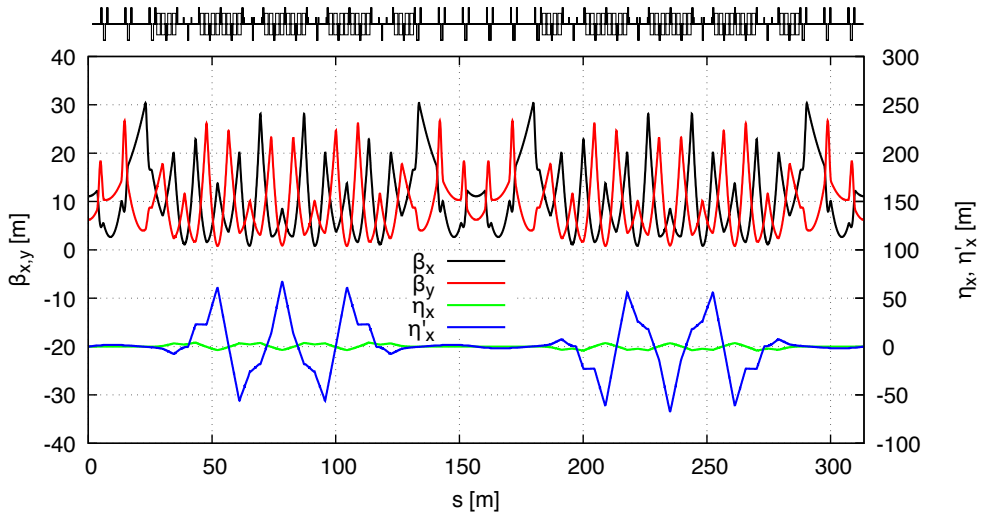

Figure 5.23: Total booster lattice. Note the suppressed linear and nonlinear dispersions.

Table 5.10: Types and Maximum Fields of JLEIC Booster Magnets

Element	Length	Number	T (max)	T/m (max)	T/m^2(max)
Dipole	1.4218 m	64	3	-	-
Quadrupole	40 cm	70	-	29.56	-
Quadrupole	80 cm	12	-	21.68	-
Sextupole	20 cm	24	-	-	305.84

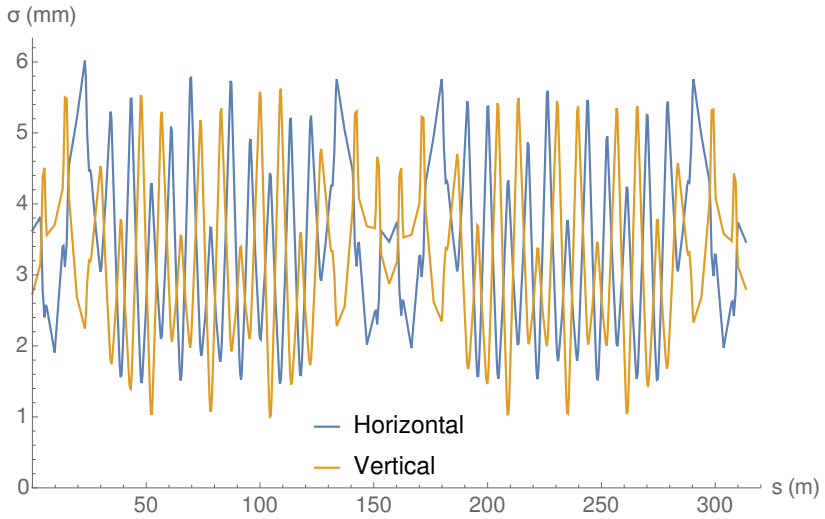

Figure 5.24: Horizontal and vertical standard deviations of the beam throughout the booster, with a 4 cm beam pipe radius for $6\,\sigma$.

5.3.3 Optics and Projected Beam Sizes

The beam sizes were calculated using the space charge code Synergia [34], which is used to perform simulations of the injection and ramping portions of the booster cycle in a later section. The projected beam sizes are shown in Figure 5.24. The maximum sigma value is 6 mm, giving a beam pipe/magnet aperture size of 3.61 cm using injection parameters and assuming $6\,\sigma$ apertures.

The arc cells have two sextupole families in symmetric arrangements around the empty center cell. There are also two more sextupoles in each dispersion suppressor, for a total of four families. These sextupoles were placed in the empty cells to minimize the amplitude dependent tune shifts. Several quadrupoles in the straight sections are designated as a tuning trombone. A detailed optimization of the Booster working point including space charge is ongoing.

The design for the RF uses a single cavity with a peak voltage of 22.8 kV, with the acceleration performed at a 5.8° phase offset. The RF bucket height is approximately $\delta p/p{=}7 \times 10^{-3}$, giving an upper limit on the momentum acceptance. Acceleration is performed with $h = 1$.

5.3.4 RF Ramping Simulations

The software code Synergia is used to simulate the beam under the effects of space charge during the energy ramping process. Synergia is a self consistent particle in cell code which is capable of simulating injection and acceleration [34, 35]. The profile for these simulations involves injecting the bunch at the center of the beam pipe, and accelerating it through a subset of the total ramping.

The ramping profile linearly changes the phase of the RF from storing the beam to accelerating it. For these simulations this is changed over a period of 10 turns. The planned phase difference is 5.8° and the accelerating gradient is 22.8 kV, giving a ΔE per turn of 2.3 kV [36]. The profile involves the bunch starting out, being circulated at injection energy for 100 turns, then ramping the RF phase to acceleration, leveling off afterwards for a total of 20 000 turns. Figure 5.25 shows that the momentum smoothly increases in the simulation. Figure 5.26 shows that the emittances level off after initial space-charge driven growth.

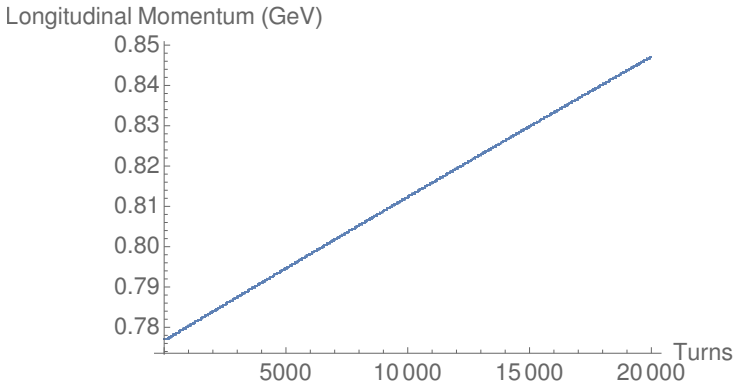

Figure 5.25: Momentum of the beam during the Booster ramping cycle.

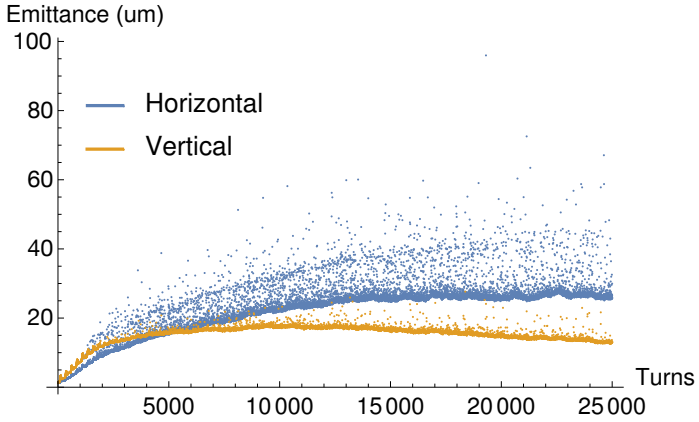

Figure 5.26: Horizontal and vertical emittances of the two beams during the Booster ramping process.

5.3.5 Injection Modeling

H^- injection is performed using charge exchange and transverse phase space painting. The injection model uses a quadratic time dependence of the injection orbit bump amplitude to evenly distribute the transverse beam distribution and minimize space charge effects [37]:

$$x_{\text{bump}}(t) = a\sqrt{\frac{2t}{T_{\text{bump}}} - \left(\frac{t}{T_{\text{bump}}}\right)^2} \tag{5.3.3}$$

where x_{bump} is the injection bump amplitude, a is the maximum amplitude, and T_{bump} is the total time taken by the injection bump.

The maximum offsets have been obtained manually. An example of the injected beam size vs time is shown in Figure 5.27, with a horizontal and vertical offset of 6 mm. The intensity (or particle number) is shown in Figure 5.28. This simulation uses 300 turns. Preliminary optimization of the injection offsets and painting location for phase space painting has been performed [38].

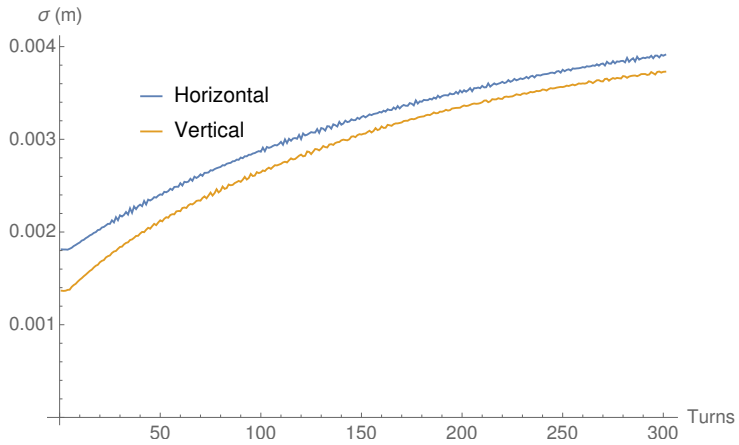

Figure 5.27: Standard deviations of the horizontal and vertical dimensions of H^- beam during booster injection.

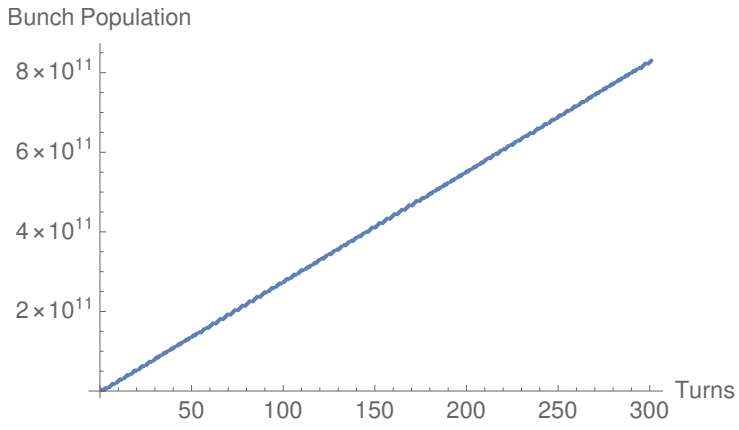

Figure 5.28: Bunch population of the ring during booster H^- injection.

5.4 Ion Collider Ring

5.4.1 Design Requirements, Linear Optics, and Geometric Match

The ion collider ring accelerates protons from 9–100 GeV/c and is designed to provide luminosity above $10^{33}\,\mathrm{cm}^{-2}\,\mathrm{s}^{-1}$ in the beam momentum range from 20–100 GeV/c. Kinematics parameters for the Booster for protons and $^{208}\mathrm{Pb}^{82+}$ are shown in Table B.2 (Appendix B). Final stripping of heavy ions to a fully stripped state is performed in the Linac to Booster transfer line as described in Section 5.7.

The overall layout of the ion collider ring indicating the main components is shown in Figure 5.29. The ring consists of two 257.4° arcs connected by two straight section intersecting at an 77.4° angle. The ion collider ring's geometry is determined by the electron collider ring (Section 4.3. The ion arcs are composed mainly of FODO cells. The last few dipoles at both ends of each arc are arranged to match the geometry of the electron collider ring. One of the straight sections houses a primary interaction region (IR) and is shaped to make a ±25 mrad crossing angle with the electron beam at the interaction point. The second straight is mostly filled with FODO, however, retaining the capability of inserting a second IR. The overall ion ring circumference is near 2256 m. The main building blocks of the ring are described below.

The main building block of the ion arcs is a FODO cell shown in Figure 5.30. It has been designed considering a balance of geometric, engineering and beam dynamical aspects. It has the same average bending radius as the electron arc. The ion FODO cell length is chosen at 22.8 m to be 1.5 times that of the electron FODO cell. Such a size supports use of $\cos\theta$ superconducting magnets [39] to reach a proton momentum of at least 100 GeV/c. Each 8 m long dipole has a field of 3.06 T at 100 GeV/c and bends the beam by 4.2° with a bending radius of 109.1 m.

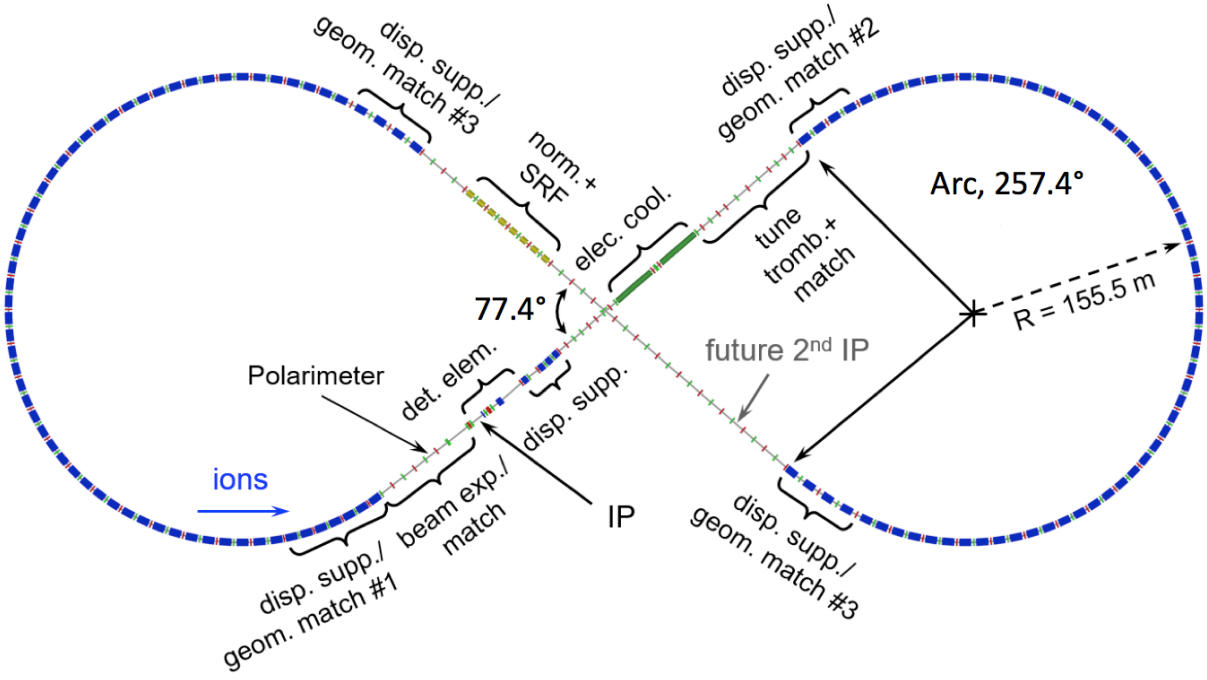

Figure 5.29: Layout and main components of the ion collider ring.

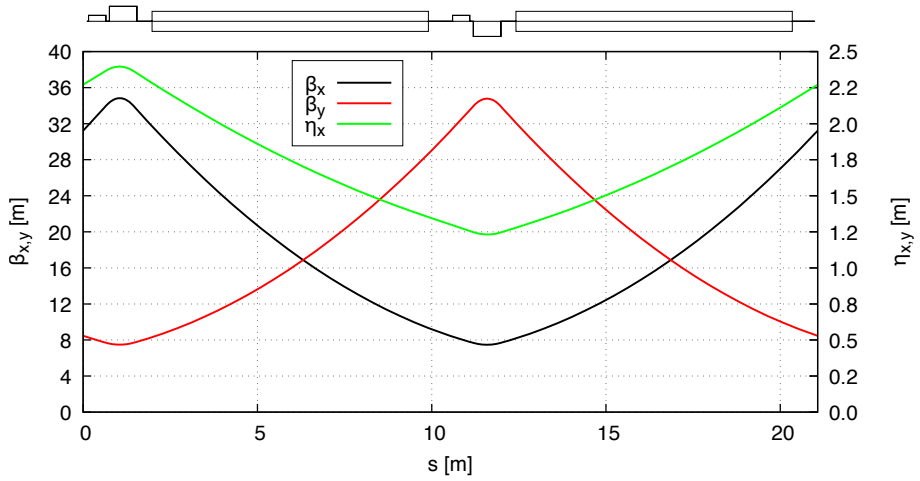

Figure 5.30: Optics of the ion arc FODO cell

The required magnet apertures are determined using a sum of a $\pm 10\sigma$ rms beam size at injection (including betatron and dispersive components), a ± 1 cm closed orbit allowance, and, in case of dipoles, plus or minus half of the orbit arc's sagitta. To make the dipole horizontal aperture size more manageable, each dipole is implemented as two 4 m long straight pieces, reducing the sagitta to a total of 18 mm. The resulting required aperture of all ring magnets is circular with a radius of 4 cm. Sufficient space has been reserved in the lattice for magnet coil extensions: 14 cm at each end of the dipoles and 5 cm at each end of most other magnets.

The required gradient of 0.8 m long FODO cell quadrupoles at 100 GeV/c is 53 T/m for a 90° betatron phase advance in both planes, which is straightforward to achieve with $\cos(2\theta)$ superconducting technology. We place a 0.5 m long corrector package on one side and a 15 cm long Beam Position Monitor (BPM) on the other side of each quadrupole. Each corrector package includes horizontal and vertical orbit correctors, a skew quadrupole, and higher-order multipoles. The sextupoles in the corrector packages located in the dispersive regions are used for chromaticity compensation. With the above FODO cell parameters, the dispersive and betatron components of the beam size are comparable, which allows for an efficient use of the sextupole strength for chromaticity compensation.

The bending angles and the spacing of the seven dipoles at the arc end upstream of the IR are adjusted to match the electron ring geometry and form a ± 25 mrad crossing angle at the IP as shown in Figure 5.31(left). The quadrupole strengths in this section are adjusted to suppress the dispersion while keeping the beta functions under control as shown in Figure 5.31(right). Figure 5.32 shows the geometry (left) and optics (right) of a four-dipole section at the arc end downstream of the IR. It is adjusted to suppress the dispersion and provide a 1.5 m separation between the ion and electron beams. Similarly, four-dipole arc-end sections near the ends of the other straight are used to suppress the dispersion and match the electron ring shape.

The detector region design is described in detail in the Interaction Region and Detector chapter (Chapter 7). Figure 5.33 shows the detector region optics. It starts at the end of one of the arcs and consists of a matching/beam expansion section, upstream and downstream triplet Final Focusing Blocks (FFB), a spectrometer section, a geometric match/dispersion suppression section, and a matching/beam compression section. The matching sections contain a sufficient number of quadrupoles to control both the beta functions at the IP and the betatron phase advance for beta squeeze and chromaticity compensation. The upstream FFB is closer to the IP than the down-

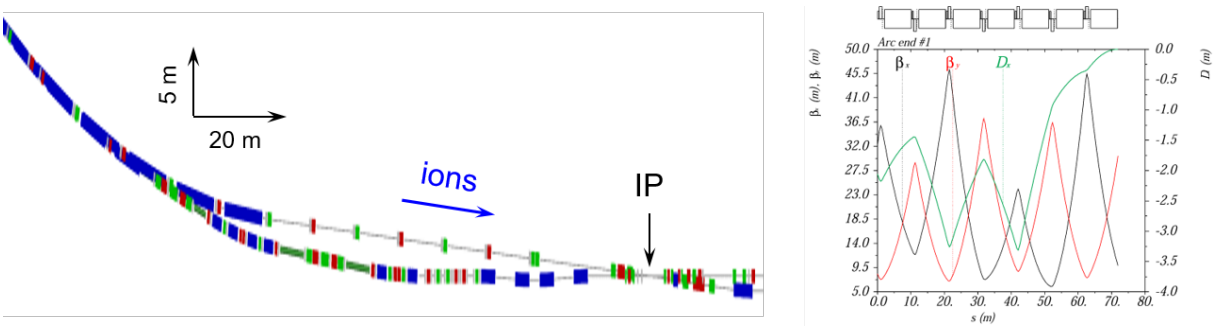

Figure 5.31: Geometry (left) and optics (right) of the arc end upstream of the IR.

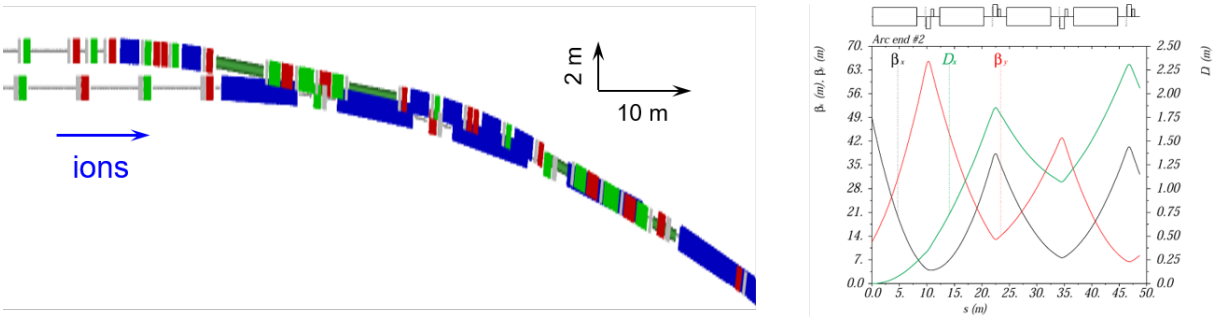

Figure 5.32: Geometry (left) and optics (right) of the arc end downstream of the IR.

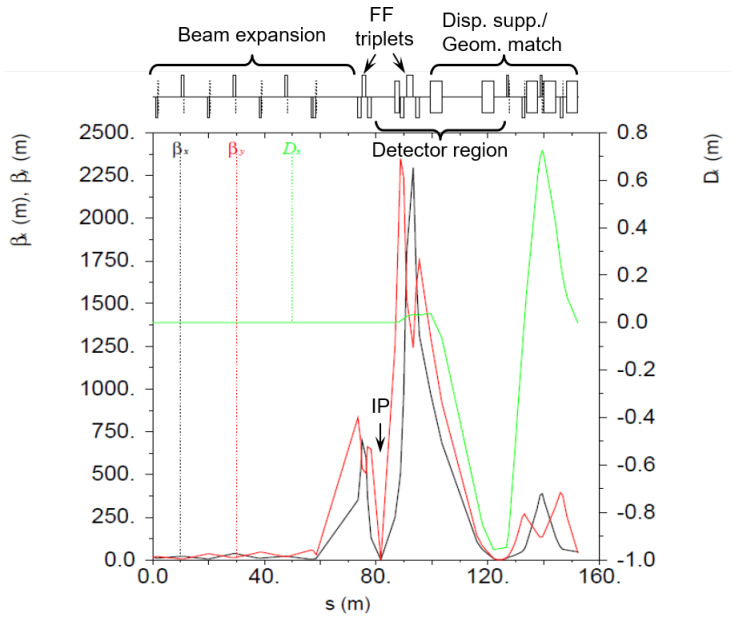

Figure 5.33: Optics of the ion IR.

stream one to minimize their chromatic contribution while satisfying the detector requirements. The nominal horizontal and vertical beta function (beta-star) values at the IP are 10 and 2 cm, respectively. As shown in Figure 5.34, after the downstream FFB, there is a 56 mrad spectrometer dipole followed by a machine-element-free 14.4 m space instrumented with detector elements. The subsequent four-dipole section suppresses the dispersion generated by the spectrometer dipole and adjusts the ion beam to be parallel to and separated by 1.5 m from the electron beam. This separation matches that at the arc end downstream of the IP which is formed by shaping the ion arc end as described above. Such a design makes the IR somewhat modular and decouples from the ring geometry providing for ease of integration into the ring lattice [40].

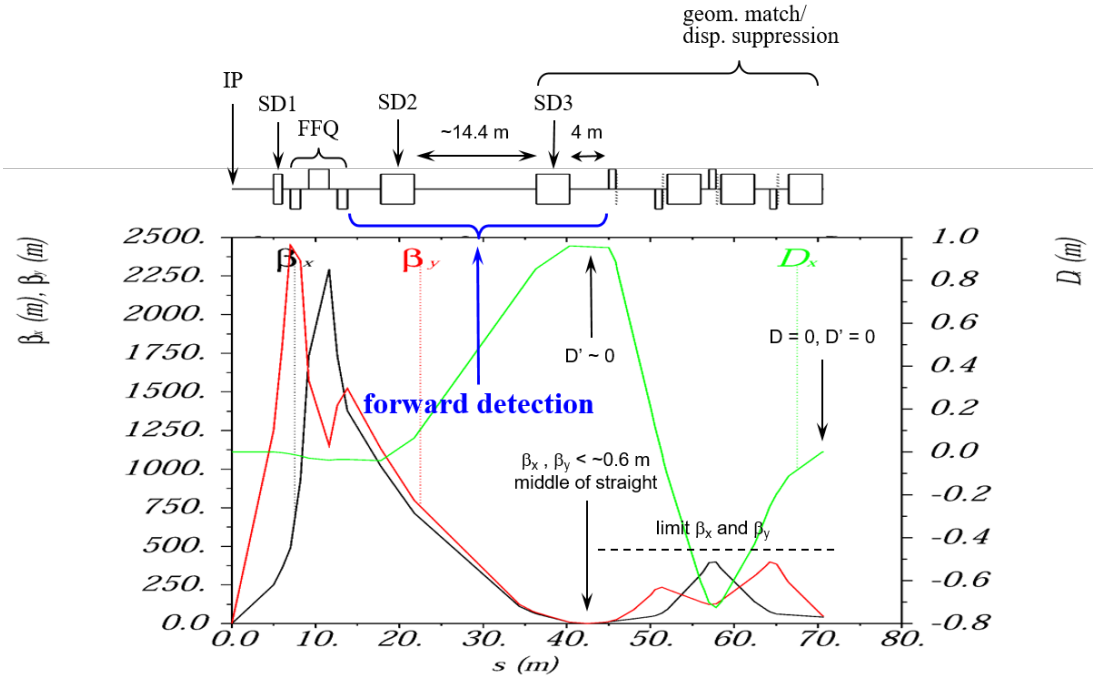

Figure 5.34: Optics of the IR section downstream of the IP.

Another major component housed in the same straight as the interaction region is the electron cooling section (Sections 6.3 and 6.4) shown in Figure 5.35. It contains two 30 m long electron cooler solenoids. The two solenoids have opposite field directions so that their net longitudinal field integral is zero generating no global coupling and having no effect on the ion spin. Since the solenoid focusing effect on the ion beam is relatively small, triplet focusing is used to control the beam optics over such a long straight. There is a matching segment at each end of the cooling section connecting it the IR on one side and a straight FODO of a tune trombone on the other side.

The rest of the IR straight is occupied by a tune trombone for betatron tune adjustment. It consists of two FODO cells surrounded by matching sections. One of the matching sections is shared with the electron cooling section. The other matches FODO to the adjacent arc.

The second straight contains a FODO lattice that reserves space for a second IR. This straight connected to arcs by matching sections as shown in Figure 5.36. Both accelerating and bunching RF cavities [41] are placed in this straight between the quadrupoles of the FODO lattice in areas not reserved for the second IR.

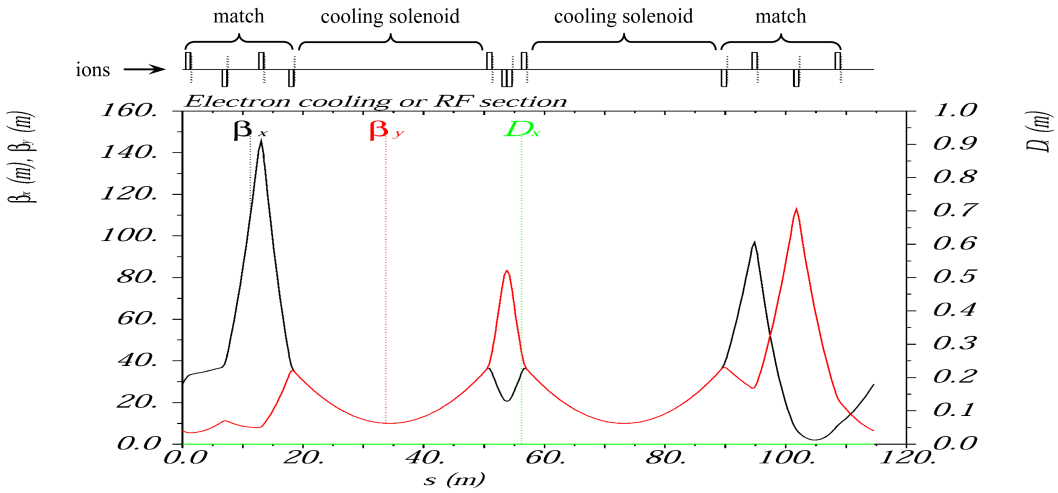

Figure 5.35: Optics of the electron cooling section.

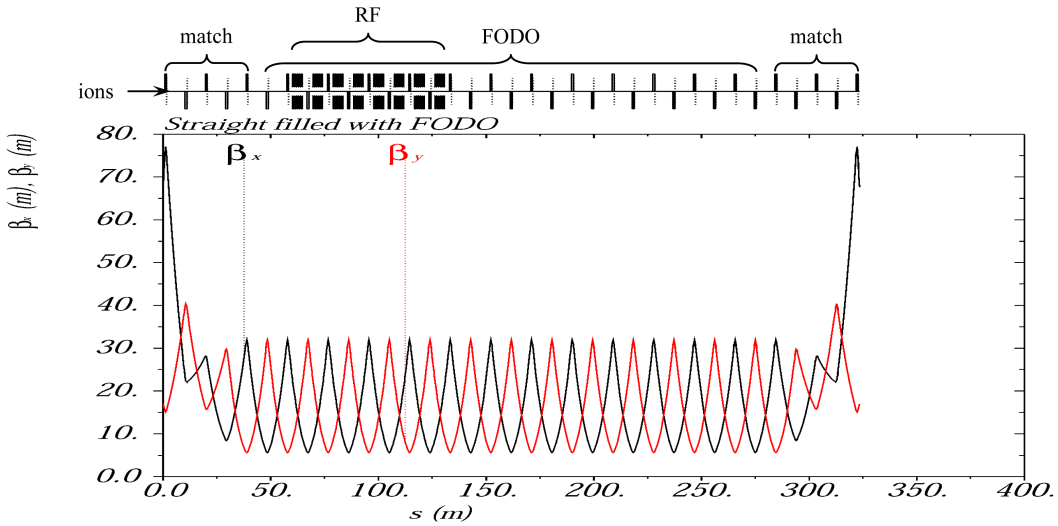

Figure 5.36: Optics of the ion ring's second straight.

The complete ion collider ring optics consisting of the components discussed above is shown in Figure 5.37. Some of the ring's global parameters are summarized in Table 5.11. Note that crossing of the transition energy occurs during acceleration. However, existing experience shows that it can be handled efficiently using standard techniques [42, 43, 44].

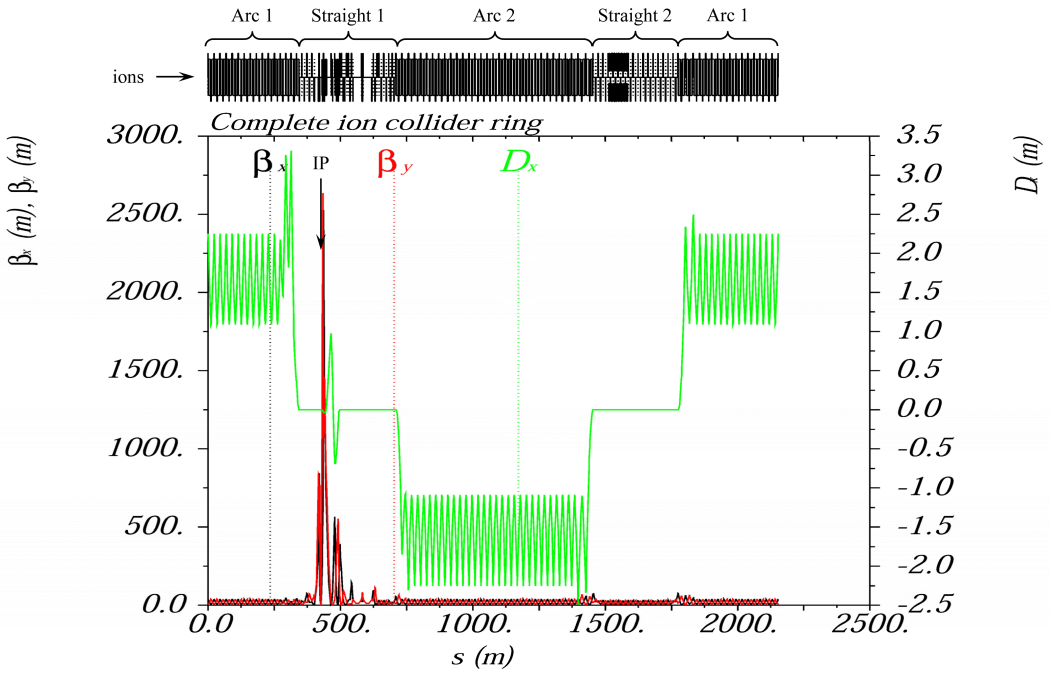

Figure 5.37: Optics of the IR section downstream of the IP.

Table 5.11: Parameters of the JLEIC Ion Collider Ring

Parameter	Unit	Value
Proton momentum range	GeV/c	9–100
Circumference	m	2256
Arc bending angle	deg	257.4
Straights' crossing angle	deg	77.4
β_x^*/β_y^* functions at the IP	cm	10 / 2
Maximum β_x/β_y functions	m	2301 / 2450
Maximum x dispersion D_x	m	3.28
ν_x/ν_y betatron tunes	-	24.22 / 23.16
ξ_x/ξ_y natural chromaticities	-	-101 / -112
Momentum compaction factor α_p	-	6.45×10^{-3}
Transition γ	-	12.46
Normalized $\varepsilon_x^N/\varepsilon_y^N$ emittances	µm-rad	0.35 / 0.07
$\sigma_x^{IP}/\sigma_y^{IP}$rms beam sizes at the IP	µm	18 / 4
$\sigma_{x'}^{IP}/\sigma_{y'}^{IP}$ rms angular beam divergence at the IP	mrad	0.2 / 0.2
Maximum $\sigma_x^{max}/\sigma_y^{max}$ rms beam sizes	mm	2.8 / 1.3

5.4.2 Nonlinear Dynamics Design, Optimization, and Validation

The ion ring before chromaticity correction has the ξ_x/ξ_y natural chromaticities of -101.1/-111.6. They are mostly generated by the large-β FFB quadrupoles in the IR (see, e.g., Figure 5.33). Due to asymmetry of the IR, the β functions in the downstream FFB are a factor of 3 higher than in the upstream one leading to a greater chromatic contribution. Due to the $\sim \pi$ phase advance between the upstream and downstream FFBs their chromatic contributions add up. Moreover, the downstream side includes the detector spectrometer optics with a second focal point, which further increases the chromatic asymmetry of the IR.

The large chromaticities generated by the IR require a dedicated correction. If not locally cancelled, the chromatic beta perturbation would propagate around the ring giving rise to large non-linear momentum dependence of the tune. A conventional solution is to use local sextupoles generating a chromatic beta wave opposite to the one from each FFB, so that they cancel each other. A separate local correction is needed on each side of the IP in order to avoid the chromatic beam smear at the IP. In case of JLEIC, the two FODO arcs are the only dispersive regions suitable for the chromaticity correcting sextupoles. The desired conditions at the sextupoles for an efficient correction are:

1. Large dispersion and β function to achieve compensation with a reasonable sextupole field;
2. $\sim n\pi$ phase advance between the FFQ and the sextupoles (in the correcting plane);
3. Large β_x/β_y and β_y/β_x ratios at the x and y sextupoles, respectively, for orthogonal correction;
4. Minimal optics between the sextupoles and FFQ for minimal distortions due to chromaticity from other quadrupoles in this region.

The non-linear fields of sextupoles also generate 2nd and higher-order geometric (amplitude dependent) aberrations resulting in non-linear tune shift and excitation of 3rd and higher-order resonances. These effects can significantly limit the beam dynamic aperture (DA). A common way to compensate these aberrations is to use non-interleaved pairs of identical sextupoles with $-I$ separation between them. As demonstrated at KEKB [45], a pseudo $-I$ separation can also be used, which differs from $-I$ in that the matrix terms M_{21} and M_{43} are not zero. The latter adds flexibility to the sextupole optics.

Following this general strategy described, we developed a non-linear chromaticity correction scheme for the JLEIC ion collider ring. It is based on non-interleaved $-I$ sextupole pairs as illustrated in Figure 5.38. Two pairs on each side of the IP correct the x and y non-linear chromaticities of the respective FFB. In this case, we use a pseudo $-I$ separation between the sextupoles in each pair. We locally modify the optics of an arc section consisting of 13 FODO cells to create high β functions and large beta ratios at these pairs as shown in Figure 5.39. Only the quadrupole strengths are adjusted in this section. Its geometric layout does not change. β_x is adjusted to

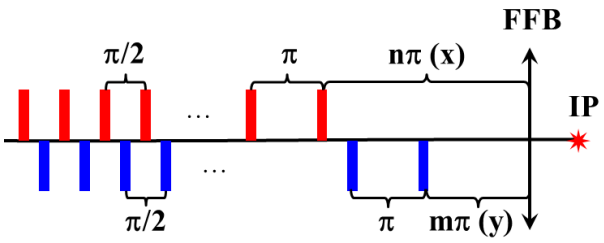

Figure 5.38: Schematic of a non-interleaved $-I$ sextupole pair setup for chromaticity compensation.

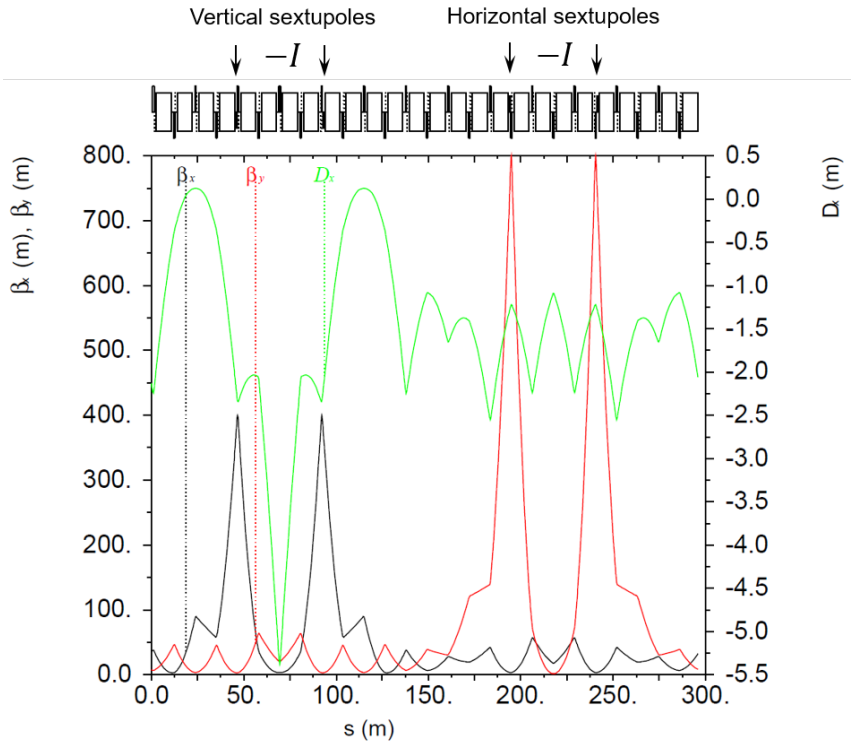

Figure 5.39: Optics of a Chromaticity Compensation Block (CCB) with the sextupoles locations indicated.

about 400 m at the x sextupole locations while β_y at the y sextupole locations is adjusted to a greater value of 800 m due to a smaller dispersion size at those locations. This section, called a Chromaticity Compensation Block (CCB), is matched to the regular FODO lattice on each side. Each CCB is placed in its arc as close as possible to the IP. The optics of the sections between a sextupole pair and the corresponding FFB is adjusted to provide a betatron phase advance of exactly $n\pi + \pi/2$ in the correcting plane. The resulting setup is shown in Figure 5.40. The CCBs correct about 55% and 75% of the horizontal and vertical natural chromaticities, respectively. The remaining linear chromaticity of the machine is canceled using two families of sextupoles in twelve 90◦ FODO cells of each arc. Note that the number of cells is chosen as a multiple of four. This provides compensation of second-order geometric and chromatic effects of the sextupoles [46].

The correcting sextupole strengths are obtained using MAD-X [47]. First, the $-I$ sextupole strengths are set to cancel the chromatic β perturbation $\partial\beta/\partial\delta$ at the IP and minimize its amplitude in the rest of the ring. This way both the chromatic beam smear at the IP and the 2nd-order term of the chromatic tune shift are minimized. In MAD-X, we use the Montague W function as the objective function, since it is linearly proportional to $\partial\beta/\partial\delta$. The sextupoles downstream of the IP are stronger due to the higher FFB beta functions and additional optics on that side. Next, the two families of the periodic sextupoles are set to cancel the remaining linear chromaticity. The required sextupole strengths are quite modest even at the top proton energy (<0.4 T at 4 cm radius). Figure 5.41 shows the final W functions around the ring. One can clearly see the chromatic β waves excited by the sextupole pairs and their compensation of the chromatic kicks produced by the FFBs. The small bumps in the W functions are due to the chromatic kicks of the two periodic sextupole families. These kicks cancel each other.

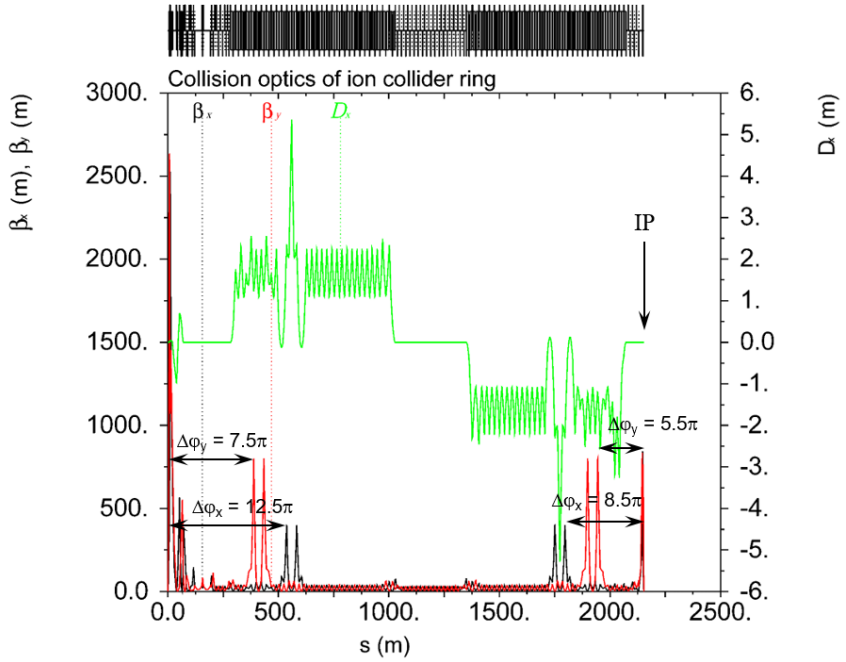

Figure 5.40: Complete optics of the ion collider ring including the CCBs with the betatron phase advance from the sextupole pairs to the IP indicated.

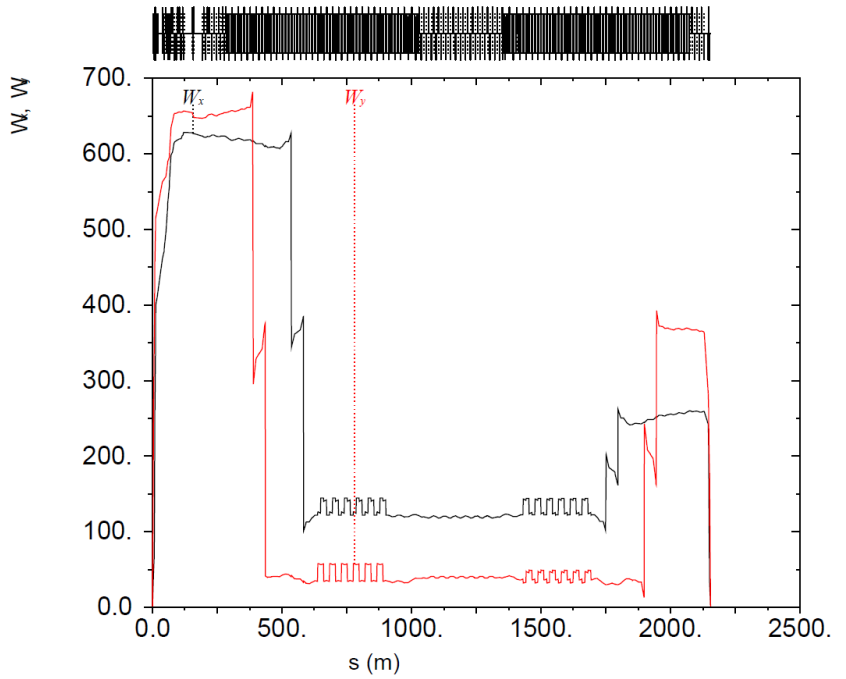

Figure 5.41: Montague W functions of the collider ring after chromatic compensation.

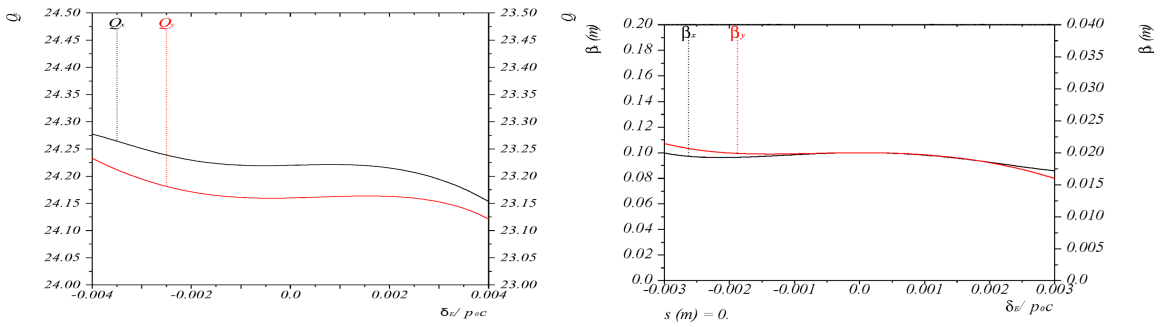

Figure 5.42: Momentum dependencies of $\nu_{x,y}$ (left) and $\beta^*_{x,y}$ (right) after chromatic compensation in the ion collider ring.

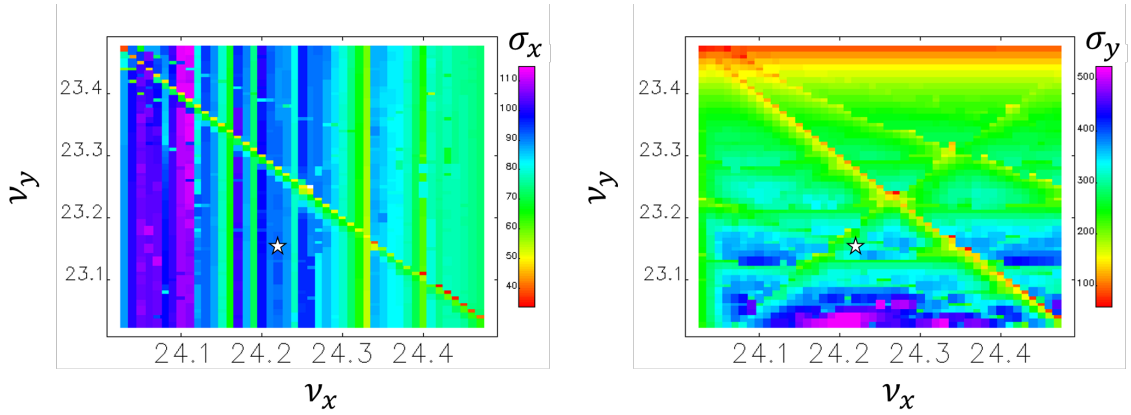

Figure 5.43: Horizontal (left) and vertical (right) sizes of the dynamic aperture in units of the rms σ beam size as functions of the horizontal $\nu_{\rm x}$ and vertical $\nu_{\rm y}$ betatron tunes.

Figures 5.42(left) and 5.42(right) show the momentum dependencies of the betatron tunes $\nu_{x,y}$ and $\beta^*_{x,y}$, respectively. They are sufficiently flat over a $\Delta p/p$ range of about $\pm 0.4\%$. Assuming an rms relative momentum spread $\sigma_{\Delta p/p}$ of 3×10^{-4}, this range corresponds to a momentum acceptance of $\pm 13\sigma$. The $\nu_{\rm x}/\nu_{\rm y}$ betatron tunes are set to 24.22/23.16. The $\xi_{\rm x}/\xi_{\rm y}$ linear chromaticities are both set to +1. The betatron tunes are chosen using the result of a dynamic aperture tune scan. The horizontal and vertical sizes of the dynamic aperture in units of the rms σ beam size are shown in Figs. 5.43(left) and 5.43(right), respectively, as functions of the horizontal $\nu_{\rm x}$ and vertical $\nu_{\rm y}$ betatron tunes. The x and y DA sizes are obtained from an Elegant simulation. A 100 GeV/c proton is tracked for 1000 turns while its initial transverse offset is systematically increased until the particle is lost in less than 1000 turns indicating the edge of the stable motion area. The particle's transverse offset is increased along the positive x and y lines originating at $(x,\ y) = (0,\ 0)$. The tune adjustment in this study is done using a thin lens trombone. One can see that the maximum DA occurs in the first quarter above an integer. The final tune selection indicated by a white star also takes into account the effect on the chromatic tune shift.

We check the tune shift with amplitude using LEGO [48] and find it to be relatively small (<0.03), thus confirming self-compensation of the sextupole geometric effects. The corresponding tune footprint is shown in Figure 5.44 (top). The footprint shows some effect of higher-order resonances. For example, one can see the $3\nu_{\rm x} + 2\nu_{\rm y}$ and $6\nu_{\rm y}$ resonance lines. The dynamic aperture at the IP is shown in Figure 5.44 (bottom) for different $\Delta p/p$ values of up to $\pm 0.5\%$. This result

is obtained for a ring without errors. The DA is plotted in units of the σ beam size at 100 GeV/c. However, the DA is sufficient even for the larger beam size at the lowest collision momentum of 20 GeV/c. The momentum acceptance of $\pm 0.5\%$ is also sufficient ($\pm 16\sigma_{\Delta p/p}$).

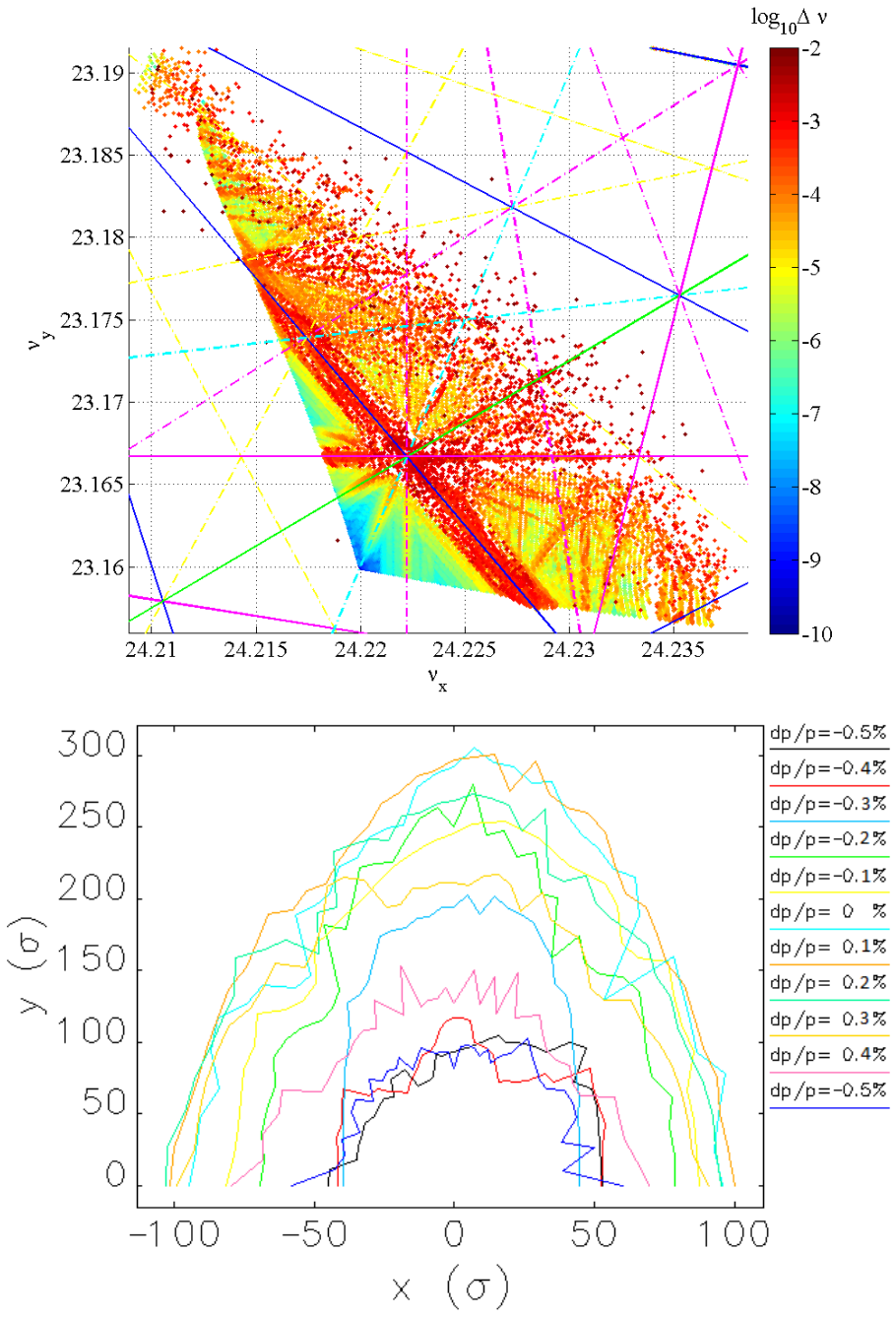

Figure 5.44: Top: tune footprint of the particles surviving from a large initial distribution after 1024 turns. The color reflects the tune diffusion rate $d = \log_{10}(\Delta\nu_x^2 + \Delta\nu_y^2)$. Bottom: DA at the IP for different $\Delta p/p$ of up to $\pm 0.5\%$ obtained using a ring model without errors.

The central solenoid of the JLEIC full-acceptance detector is 4 m long and has a maximum field of 3 T. Its axis is parallel to the electron beam to avoid generation of synchrotron radiation in the detector and makes a 50 mrad angle with the ion beam. The center of the detector solenoid is longitudinally shifted by 0.4 m from the IP in the downstream ion direction [49] so that the ion beam passes through 1.6 m of it upstream and 2.4 m of it downstream of the IP. This shift is implemented to optimize the detection of the forward ion fragments and further complicates compensation of the solenoid effects on the beams. We use a hard-edge model of the detector solenoid to represent its real main field in our simulations presented below, as illustrated in Figure 5.45.

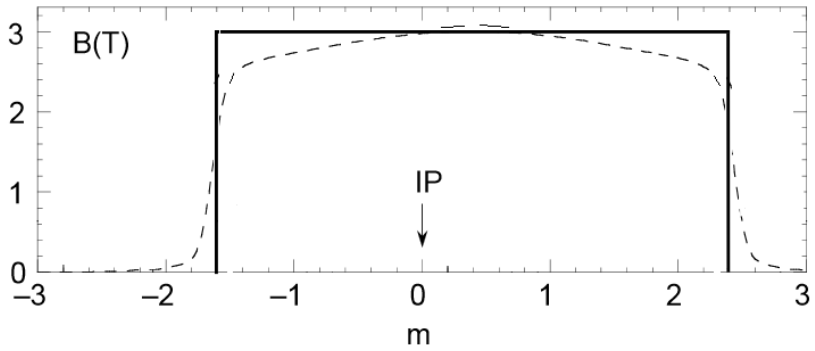

Figure 5.45: Realistic field profile (dashed line) and hard-edge model (solid line) of the JLEIC detector solenoid.

The JLEIC detector solenoid has the following effects on the colliding beams, similar to the Super$B$ Factory [50]:

- Coherent distortion of the ion orbit. The orbit distortion is mostly vertical and is due to the solenoid angle relative to the beam trajectory (50 mrad). The horizontal component of the orbit distortion arises due to the vertical component and coupling.
- Coupling of the x and y betatron motions, which, in the absence of other magnets, rotates the beam transverse plane about the s-axis by an angle $B_{\rm sol}L/(2B\rho)$, where $B_{\rm sol}$ and L are the solenoid field and length. For example, the corresponding rotation angles for 5 GeV electron and 100 GeV proton beams are 359.7 and 17.8 mrad, respectively. This may create a mismatch of the elliptical beam spot sizes at the IP and get the planes of the crab tilt out of alignment for the two beams. Therefore, transverse betatron coupling has to be compensated locally at the IP.
- Vertical and horizontal dispersions due to the y and x orbit bends.
- Perturbation of the β functions, betatron tunes, linear chromaticities and Montague W functions due to the focusing effect of the solenoid.
- Breaking of the figure-8 spin symmetry for both ion and electron polarizations.

The JLEIC detector solenoid coupling must also be compensated. As is well known, the linear matrix of a solenoid can be represented as a product of a rotation part $R(KL)$ and an uncoupled focusing part $M_{\rm sol}^{\rm focus}(KL)$ [51]:

$$M_{\rm sol}(KL) = R(KL)M_{\rm sol}^{\rm focus}(KL) \tag{5.4.4}$$

with

$$R(KL) = \begin{pmatrix} CI & SI \\ -SI & CI \end{pmatrix}, \tag{5.4.5}$$

$$M_{\rm sol}^{\rm focus}(KL) = \begin{pmatrix} C & S/K & 0 & 0 \\ -KS & C & 0 & 0 \\ 0 & 0 & C & S/K \\ 0 & 0 & -KS & C \end{pmatrix}, \tag{5.4.6}$$

where $C \equiv \cos(KL)$, $S \equiv \sin(KL)$, $K = B_{\rm sol}/(2B\rho)$, and I is a 2×2 identity matrix. Since the matrices R and $M_{\rm sol}^{\rm focus}$ commute with each other, the simplest way to decouple a solenoid is to put an anti-solenoid (a solenoid with a field integral equal in magnitude and opposite in sign) next to it. Then

$$\begin{aligned} M_{\rm sol}(-KL)M_{\rm sol}(KL) &= M_{\rm sol}^{\rm focus}(-KL)R(-KL)R(KL)M_{\rm sol}^{\rm focus}(KL) \\ &= M_{\rm sol}^{\rm focus}(KL)^2, \end{aligned} \tag{5.4.7}$$

has no coupling. However, in case of JLEIC, it is not possible to place anti-solenoids next to the central detector solenoid due to space constraints and detection requirements. The nearest spaces available for anti-solenoids are after the Final Focusing Blocks (FFB). Simply placing an anti-solenoid after each of the FFBs does not work because the rotation and FFB matrices do not commute with each other. To restore the coupling compensation, the whole FFB has to be tilted by the solenoid rotation angle KL:

$$\begin{aligned} &M_{FFB}^{tilt} = R(KL)M_{FFB}R(-KL), \\ &M_{\rm sol}(-KL)M_{FFB}^{tilt}M_{\rm sol}(KL) = M_{\rm sol}^{\rm focus}(-KL)M_{FFB}M_{\rm sol}^{\rm focus}(KL). \end{aligned} \tag{5.4.8}$$

This is called a Rotating Frame Method [52].

Nuclear physics studies are planned at JLEIC not only for a single energy combination of the electron and proton beams but require the capabilities of independently adjusting the beam energies in wide ranges and of operating with multiple ion species. The FFB tilt angle should then be adjustable according to the rotation angle of the solenoid. Adjusting the FFB tilt angle for each run setting is, of course, not practical. Therefore, we produce an effect analogous to an FFB rotation by appropriately combining the normal $k_{\rm n}$ and skew k_s strength components of its quadrupoles:

$$\alpha = \frac{1}{2}\arctan\frac{k_s}{k_{\rm n}} = \frac{B_{\rm sol}L}{2B\rho}. \tag{5.4.9}$$

Note that, as discussed above, the beam has to be locally decoupled at the IP. Therefore, this compensation has to be applied separately to the two parts of the solenoid: one from its upstream edge to the IP and the other from the IP to its downstream edge. An important advantage of our chosen coupling compensation scheme over, for example, skew quadrupole compensation is that it restores the figure-8 spin symmetry by compensating the longitudinal field integral of the central detector solenoid.

The complete correction system for the JLEIC detector solenoid is designed based on a hard edge solenoid field model. It includes two anti-solenoids, skew strength components in the FFQ quadrupoles, and orbit correctors for complete compensation of linear coupling and coherent orbit distortion on each side of the IR. The β functions, dispersion, linear chromaticities and W functions are also re-matched by adjusting quadrupole and sextupole settings.

It is best to eliminate closed orbit distortion inside the FFB quadrupoles to keep their multipole effects at the minimum. Therefore, our design of the closed orbit correction system localizes the

orbit distortion caused by the detector solenoid to the region between the nearest quadrupoles upstream and downstream of the IP. An additional constraint is that not only the orbit offset but its slope must be corrected at the IP as required for crabbing. The correction system uses two x/y dipole correctors on each side of the IP as indicated in Figure 5.46. The resulting orbit after correction is shown in Figure 5.46 for 60 GeV protons with a 3 T solenoid. As one can see, the orbit distortion is mostly vertical with a maximum offset of about 3 mm at the 3rd corrector from the left. The 3rd corrector provides the largest vertical kick of about 1.6 mrad.

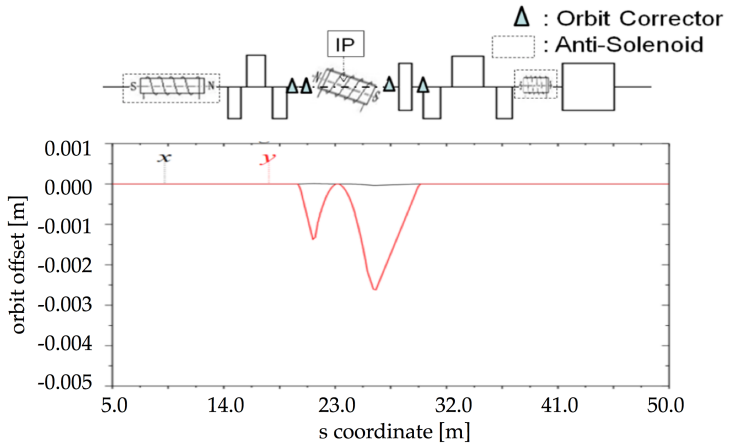

Figure 5.46: Correction of the closed orbit distortion due to the detector solenoid in the ion IR.

We then apply the coupling compensation scheme discussed above using skew field components of the FFB quadrupoles and localizing coupling between the detector solenoid and anti-solenoids. The optics for a 60 GeV proton beam before and after compensation of a 3 T detector solenoid are shown in Figs. 5.47(left) and 5.47(right), respectively. Quantitatively, the amount of coupling can be represented using Ripken's optics parameters [53]. The coupling β's without compensation can be seen in Figure 5.47(left). Before compensation, as shown in Figure 5.47(left), the β_{12} and β_{21} functions related to coupling are about 5% of β_{11} and β_{22}, which are analogous to the usual β_x and $beta_y$ without coupling. After compensation, as shown in in Figure 5.47(right), β_{12} and β_{21} are zero before the first anti-solenoid and after the second anti-solenoid, which means that coupling is localized between them.

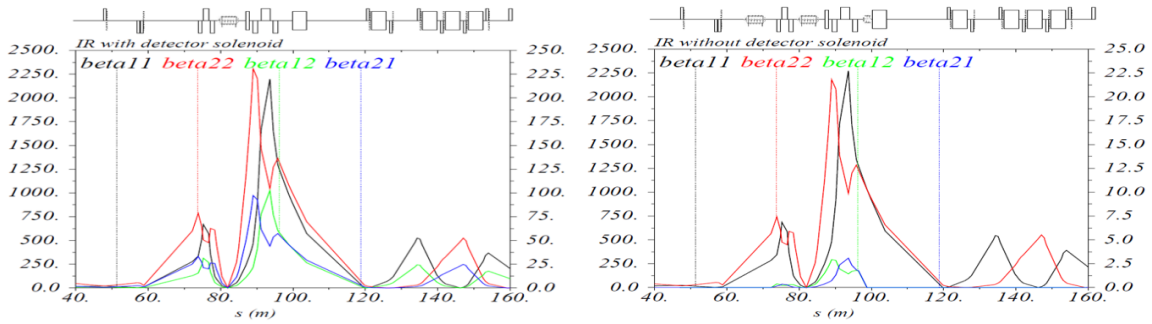

Figure 5.47: IR optics before (left) and after (right) compensation of the coupling effect caused by the detector solenoid in the JLEIC ion collider ring.

The normal and skew strengths components of the FFB quadrupoles are used for simultaneous coupling compensation and optics match in the IR. In addition, we use other ring quadrupoles to compensate effects on the betatron tunes, β functions, dispersion, and linear chromaticities. In particular, we adjust the chromatic sextupoles and their betatron phase advances to restore local and global chromatic compensation and minimize the W functions at the IP. The resulting linear optics of the whole collider ring for 60 GeV protons is shown in Figure 5.48. We do not compensate the vertical dispersion generated by a dipole in the IR at a coupled beam location because it is less than 0.5 m around the ring, which is acceptable.

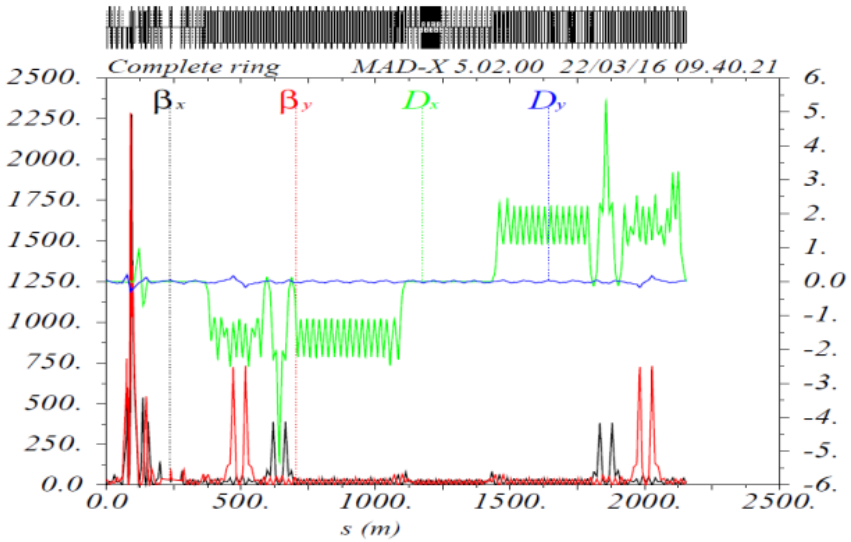

Figure 5.48: β and dispersion functions around the JLEIC ion collider ring after correction of the detector solenoid effects.

The detector solenoid may have to stay at a fixed field of 3 T during the whole beam cycle including injection and acceleration because ramping it with energy may not be practical. However, the compensation requirements are then different. They are more relaxed, since the beam position and slope do not need to be 0 at the IP, the W functions do not need to be small, etc.

Let us now consider the effect of machine element errors on the beam dynamics in the JLEIC ion collider ring. The magnet and Beam Position Monitor (BPM) errors included in our study are summarized in Table 5.12. They can be divided into two types [54]:

- Static error: this type of error is independent of time. It includes displacement, roll and strength errors of all magnets including dipoles, quadrupoles, sextupoles and correctors. Offset of the BPMs is also this type of error but, since it can be determined by beam-based alignment, we do not consider it in our simulations. One important static error is the multipole field content of the main magnets including dipoles, quadrupoles, and sextupoles. The multipole field components, especially, of the IR magnets have a dominant effect on the dynamic aperture. They are considered below.
- Dynamic error: this type of error depends on time. It includes noise signal of the BPMs, field jitter of the magnets, etc. The noise signal level depends not only on the BPM itself but also on the beam energy, beam current, etc. Field jitter of the magnets is usually less than 0.1% of the nominal setting value.

Table 5.12: σ Values of the Random Error Distributions Used in Below Simulations

Machine element	$\Delta x/\Delta y/\Delta z$ (mm)	Tilt (mrad)	Strength error (%)
Dipole	0.3/0.3/0.1	0.3	0.1
Quadrupole	0.3/0.3/0.3	0.3	0.2
FFQ	0.03/0.03/0.03	0.05	0.03
Sextupole	0.3/0.3/0.3	0.3	0.2
BPM noise	0.05/0.05	-	-
Corrector	-	0.1	0.1

We first study the error sensitivity without any corrections. Since the full errors in Table 5.12 without orbit correction will give no stable closed orbit in a simulation, we start by using 50% of these errors to perform the sensitivity study with MAD-X [47] and Elegant [55].

We analyze the sensitivity of the closed orbit distortion to each error type listed in Table 5.12 separately. We assign randomly generated errors of each type to all of the appropriate magnets in the ring and then calculate the rms closed orbit distortion. We repeat this procedure for ten different error sets generated using ten different seeds. We then average the rms closed orbit distortions obtained for the different error sets and use the average as the measure of the closed orbit sensitivity. Figure 5.49(left) compares the sensitivity of the closed orbit distortion to the different error types. The main effect comes from the transverse displacements of quadrupoles and the strength errors of dipoles, which contribute 57% and 34% of the total effect, respectively.

At the same time, we analyze the sensitivity of the dynamic aperture to the different error types. For each error type, in addition to the closed orbit, we simulate the dynamic aperture at the IP and average it over the ten random error sets. We then calculate the relative reduction of the dynamic aperture with respect to the perfect ring case. This reduction serves as a measure of the sensitivity of the dynamic aperture to a particular error type. The relative effect on the dynamic aperture of the different error types is summarized in Figure 5.49(right). The greatest effect on the dynamic aperture comes from the quadrupole strength errors, which constitute about 45% of the total effect. The quadrupole tilt errors and transverse displacements of quadrupoles and sextupoles produce similar effects of about 15% each. We call a simple sum of the individual errors the total effect only for the purpose of relative comparison of effects. When combining different errors, their effects do not simply add up. However, this study suggests the most critical errors that one should pay attention to when correcting the closed orbit and dynamic aperture.

We next implement the following corrections:

- Closed orbit correction with a particular attention to the IR.
- Betatron tune correction. Considering the tune measurement accuracy, the tunes are corrected to within $\pm 0.1\%$ of their design values.
- Correction of β function distortion. Considering the β function measurement accuracy, the β functions are corrected to within $\pm 5\%$ of their design values at all magnets with both beta functions less than 500 m. At all magnets where one of the beta functions is greater than 500 m and in the IR, the beta functions are corrected with $\pm 1\%$ accuracy.
- Correction of transverse betatron coupling. The optimal skew quadrupole locations [56] in terms of the horizontal and vertical betatron phase advances ($\mu_x,\ \mu_y$) between them are $(0,\ 0)$, $(\pi/2,\ 0)$, $(0, \pi/2)$, and $(\pi/2,\ \pi/2)$ (mod π). Since it is not always possible to find locations

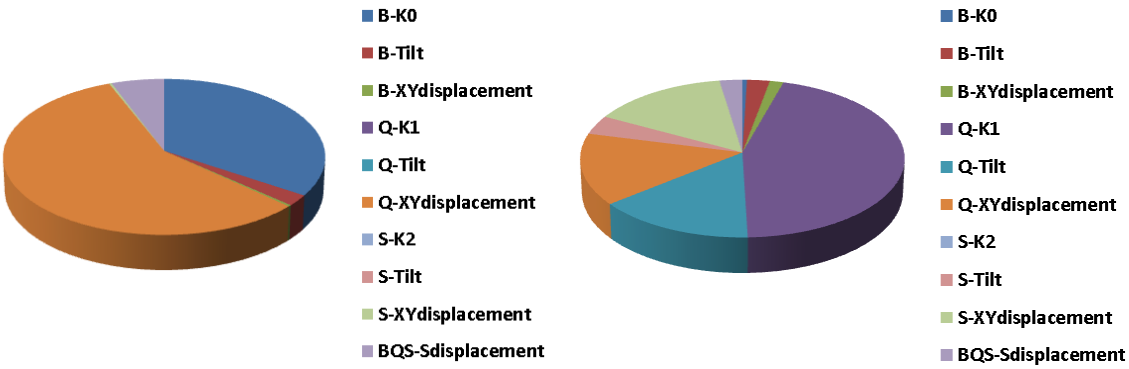

Figure 5.49: Pie chart of the effect of individual error types on the closed orbit distortion (left) and the dynamic aperture (right). We use the rms closed orbit distortion and relative reduction of the dynamic aperture with respect to the perfect ring case as the measures of the error effect.

for skew quadrupoles with those exact phase advances, a larger number of skew quadrupoles is used.

- Chromaticity correction. We correct the linear chromaticities using the two global sextupole families in the arcs. In the future, we plan to also correct the first-order beta chromaticities at the IP by minimizing the W functions at that location.

We simulate the full errors listed in Table 5.12 and their correction using Elegant. Figure 5.50 shows the corrected closed orbit around the whole ring and in the IR for ten different random seeds. We assume that there are a BPM on one side and an x/y corrector dipole on the other side of each of the 205quadrupoles. Sufficient space has been reserved in the lattice for the BPMs and correctors. However, the necessary orbit correction can be achieved with smaller numbers of them. We plan to optimize the BPM and corrector numbers and locations in the future. The final horizontal closed orbit is corrected to $< \pm 25$ µm globally and to $< \pm 1$ µm at the IP. The final vertical closed orbit is corrected to $< \pm 10$ µm globally and $< \pm 0.2$ µm at the IP. It is important to minimize the closed orbit distortion inside the IR quadrupoles to reduce the effect of their multipoles on the dynamic aperture. With the x and y closed orbit offsets of < 2 µm in those quadrupoles, the multipole effect due to the closed orbit offset is negligible.

After correcting the closed orbit distortion, we simulate corrections of the betatron tunes, β function distortion, coupling, and linear chromaticity. We then find the dynamic aperture at the IP for a 60 GeV/c proton beam by tracking a particle for 1000 turns and systematically increasing its initial transverse offset until the particle is lost in less than 1000 turns indicating the edge of the stable motion area. The particle's transverse offset is increased along 41 lines originating at $(x,\ y) = (0,\ 0)$ and uniformly distributed in the top $(x,\ y)$ half plane. The on-momentum dynamic aperture obtained this way for ten different random error seeds is shown in Figure 5.51. The above corrections are independently implemented in the simulation for each error seed. Assuming conservative normalized x/y emittances of 1.2/1.2 mm-mrad, the dynamic aperture is greater than $\pm 27\sigma$ of the beam size, which is acceptable.

Any magnet's field has higher-order multipole components. They can be defined using the following expansion [57]:

$$B_{\mathrm{y}} + iB_{\mathrm{x}} = 10^{-4} B_{\mathrm{N}} \sum_{n=N}^{\infty} (b_{\mathrm{n}} + ia_{\mathrm{n}}) \left(\frac{x + iy}{r_0} \right)^n , \tag{5.4.10}$$

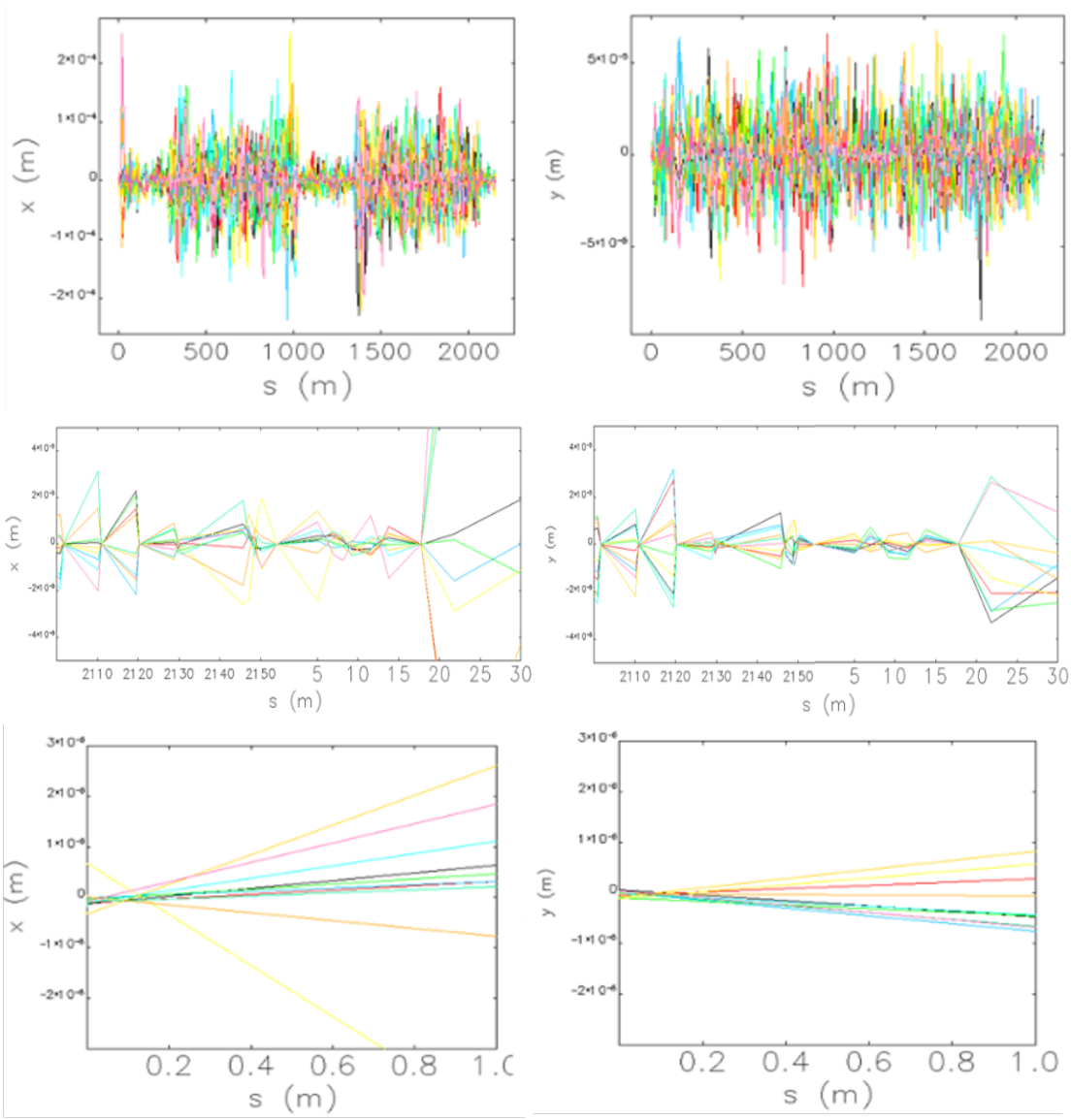

Figure 5.50: Corrected closed orbit around the whole ring (top), in the IR (middle) and within ±1 m around the IP (bottom).

where the b_n and a_n coefficients are the relative values of the normal and skew multipole field components determined at a reference radius r_0 in units of 10^{-4} of the main field B_N at r_0. Furthermore, each of b_n and a_n is composed of the systematic and random terms, where the systematic terms arise from the magnet design and are the same for all magnets of the same kind while the random terms emerge due to random errors in magnet construction and vary from magnet to magnet according to a Gaussian distribution.

For a superconducting magnet, r_0 is usually set to 1/3 of the coil diameter, as an edge of the good field region of the magnet. The multipole terms b_n and a_n scale with the reference radius r_0 and the coil diameter d_c as [57]:

$$b_n,\ a_n \propto r_0^{n-1}/d_c^n. \tag{5.4.11}$$

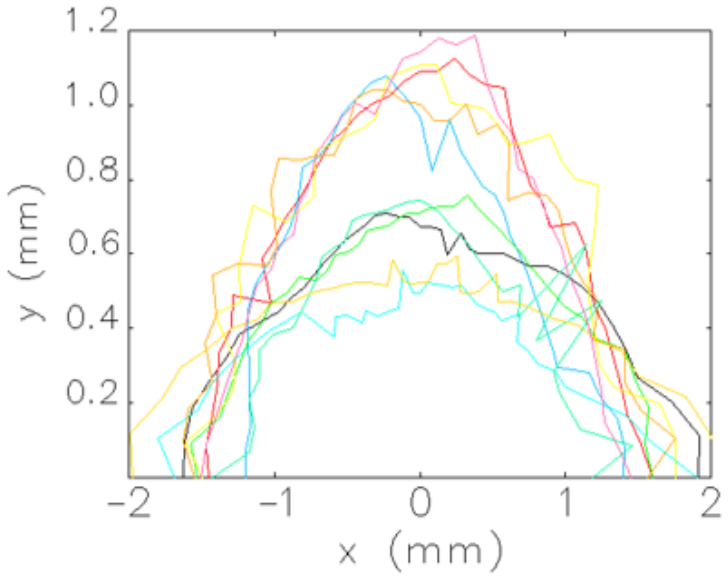

Figure 5.51: On-momentum dynamic aperture after including errors and implementing their corrections for ten different random error seeds.

Furthermore, assuming constant contributions of a magnet's b_n and a_n to the non-linear resonance driving terms, their values scale with β at the magnet location according to [58]

$$b_n,\ a_n \propto 1/\beta^{\frac{n+1}{2}}. \tag{5.4.12}$$

Thus, the reference radius is an important parameter for characterizing the magnet's field quality. It is reasonable to make it 1/3 of the coil aperture or proportional to the beam size. For example, for the IR triplets in the JLEIC ion ring, the three upstream final focus quadrupoles have their reference radii defined using the 1/3-of-the-aperture guidance and are roughly proportional to 10σ of the beam size. According to the full acceptance requirement [59], the physical apertures of the three downstream ion final focus quadrupoles are designed to provide a large acceptance in the forward direction and are greater than needed for simply passing the beam through. The physical apertures and reference radii of the ion FFQs are summarized in Table 5.13. Note that the maximum x and y beam sizes are equal in the conservative normalized x/y emittance case of 1.2/1.2 mm-mrad. In the ultimate normalized emittance case of 0.35/0.07 mm-mrad, the beam size in x is about a factor of 2 larger than in y.

The simulated systematic multipoles of the arc dipoles [60] are listed in Table 5.14. We use these data without any optimization or compensation to study the dynamic aperture in Elegant. The simulations are done for 60 GeV protons, 1000 turns and 41 lines in the $x - y$ phase space. Figures 5.52(left) and 5.52(right) compare the DA simulation results with no multipoles in any of the ring magnets and with the multipoles in Table 5.14 included in all of the ring dipoles, respectively. In each case, the DA is simulated for three values of $\Delta p/p$.

Figure 5.52 suggests that the dipole multipoles should be reduced or corrected. However, this is not necessary for all dipoles. It is sufficient to impose tighter multipole requirements only for magnets at large-β locations because they provide the dominant contributions to the resonance driving terms. To quantify this, we consider the scenarios where the multipoles in Table 5.14 are included only in the dipoles with $\beta < 1$ km and only in the dipoles with $\beta < 200$ m. The numbers of magnets in the different β ranges are summarized in Table 5.15. The resulting dynamic apertures

Table 5.13: Physical Apertures and Reference Radii of the Ion FFQs Listed in the Order They are Passed by the Ion Beam

FFQ	Inner radius (mm)	$\beta_x^{max}/\beta_y^{max}$ (m)	r_0 (mm)
Upstream			
FFQ3us	40	538/-	30
FFQ2us	40	847/-	30
FFQ1us	30	369/767	22
Downstream			
FFQ1ds	90	931/2640	60
FFQ2ds	157	2574/-	90
FFQ3ds	170	1724/-	90

Table 5.14: Simulated Systematic Multipoles of the Arc Dipoles at r_0 =20 mm

Multipole	b_1	b_2	b_3	b_4	b_5
Value (units)	-0.151	-0.537	0.126	0.850	0.714
Multipole	b_6	b_7	b_8	b_9	b_{10}
Value (units)	0.366	-0.464	-0.410	0.009	0.027

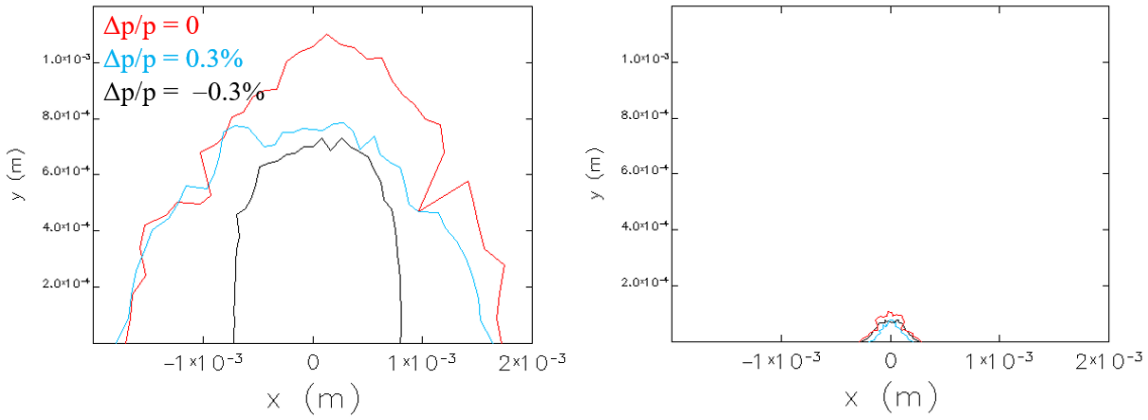

Figure 5.52: DA simulation results with no multipoles in any of the ring magnets (left) and with the multipoles in Table 5.14 included in all of the ring dipoles (right).

for the two scenarios are shown in Figs. 5.53(left) and 5.53(right), respectively. Clearly, excluding the multipoles of the large-β dipoles from the simulation results in a greater dynamics aperture. However, even with the multipoles included in all dipoles, assuming conservative x/y emittances of 1.2/1.2 mm-mrad, the dynamic aperture is still about $\pm 16\sigma$ of the beam size. If needed one may still consider compensation of the multipole effect of a small number of the large-β dipoles. Generally speaking, the present magnet model is adequate for the arc dipoles [61]. So far, we only use the normal b_n multipole field data obtained in magnet modeling. As the magnet design

advances and further data such as the skew multipole values become available, we will conduct a more detailed dynamic aperture study.

Table 5.15: Numbers of Magnets in the Different β Ranges

β range	Dipoles	Quadrupoles	Sextupoles
Any $\beta_{x,y}$	133	205	75
β_x or $\beta_y > 1$ km	2	6	0
β_x or $\beta_y > 200$ m	21	19	8

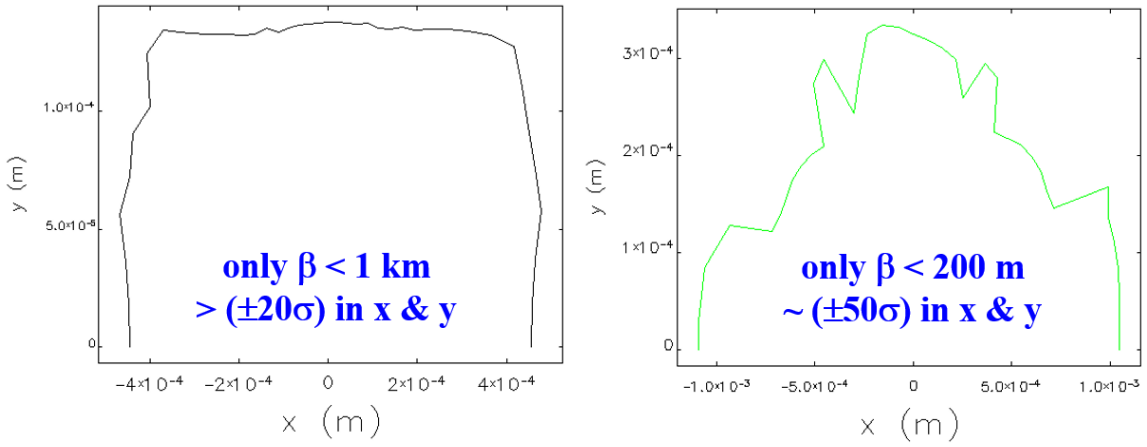

Figure 5.53: DA simulation results when the multipoles in Table 5.14 are included only in the dipoles with β <1 km (left) and only in the dipoles with β <200 m (right).

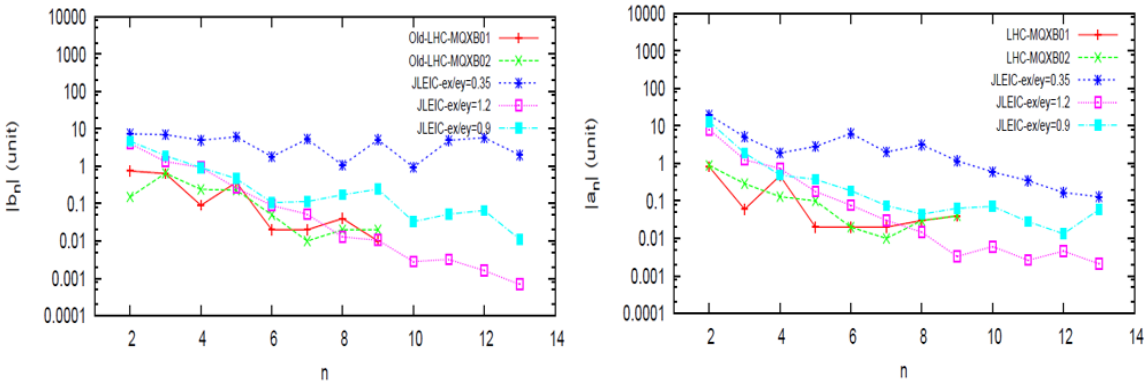

Figure 5.54: Limiting values of the normal (left) and skew (right) multipole components of the JLEIC ion FFQs for the normalized x/y emittances of 1.2/1.2, 0.9/0.9 and 0.35/0.07 mm-mrad. They are compared to the measured multipole values of the LHC FFQs.

In a collider ring, the dynamic aperture is usually dominated by the multipole effect of the final focusing quadrupoles (FFQ) because that is where the β functions reach their largest values. Therefore, we complete both top-down and bottom-up studies of the FFQ multipole requirements.

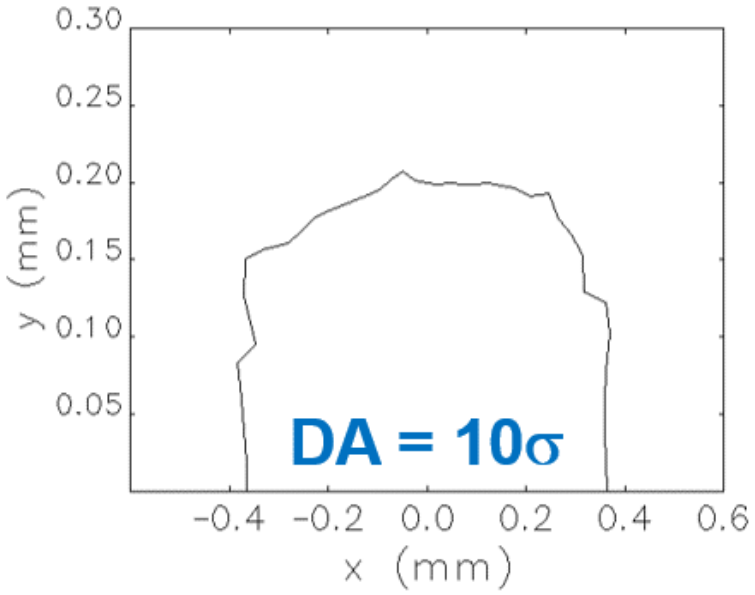

Figure 5.55: On-momentum dynamic aperture simulated with all limiting multipoles combined for the normalized x/y emittances of 1.2/1.2 mm-mrad.

In the top-down study, we require that the final dynamic aperture is at least $\pm 10\sigma$ of the beam size. We increase the value of a single multipole in all FFQs until the dynamic aperture shrinks to about $\pm 20\sigma$. All other multipoles during this study are set to zero. We repeat this study for each of the normal and skew multipoles up to the 13th order. After combining together all of the limiting multipole values obtained this way, the resulting dynamic aperture is about $\pm 10\sigma$ as needed. The value of $\pm 20\sigma$ for an individual multipole was determined empirically. We also verified that assigning different signs to a certain multipole in different FFQs does not change its limiting value. The absolute values of the limiting normal and skew multipoles are plotted in Figs. 5.54 (left) and 5.54 (right), respectively. We complete this study for both the conservative, intermediate and ultimate normalized x/y emittance values of 1.2/1.2, 0.9/0.9 and 0.35/0.07 mm-mrad, respectively. Since we keep the β functions constant, a smaller emittance means a smaller beam size. A smaller beam size with the same number of σ results in a smaller required absolute size of the dynamic aperture and relaxed multipole requirements as shown in Figure 5.54. In Figure 5.54, the multipole requirements of the JLEIC ion FFQs are compared to the measured multipole values of the LHC FFQs. As one can see, the tightest JLEIC multipole requirements are consistent with the measured parameters of the LHC FFQs. Note that in this and other studies, we consider and quote the smallest size of the dynamic aperture, which in our case is always in the horizontal plane. The dynamic aperture simulated with all limiting multipoles combined for the normalized x/y emittance of 1.2/1.2 mm-mrad is shown in Figure 5.55.

We next complete the bottom-up analysis of the FFQ multipole requirements. We find the dynamic aperture of the JLEIC ion collider ring assuming the multipole field data of the LHC IR triplets [62] for the JLEIC FFQs. The resulting dynamic aperture is shown in Figure 5.56. It corresponds to $\pm 16\sigma$ for the normalized x/y emittances of 0.35/0.07 mm-mrad and about $\pm 10\sigma$ for the normalized x/y emittances of 1.2/1.2 mm-mrad. In other words, the measured parameters of the LHC IR triplets are adequate for any emittance scenario. For smaller emittance values, the

luminosity can be improved by stronger focusing at the IP or the FFQ multipole requirements and therefore engineering challenges can be relaxed.

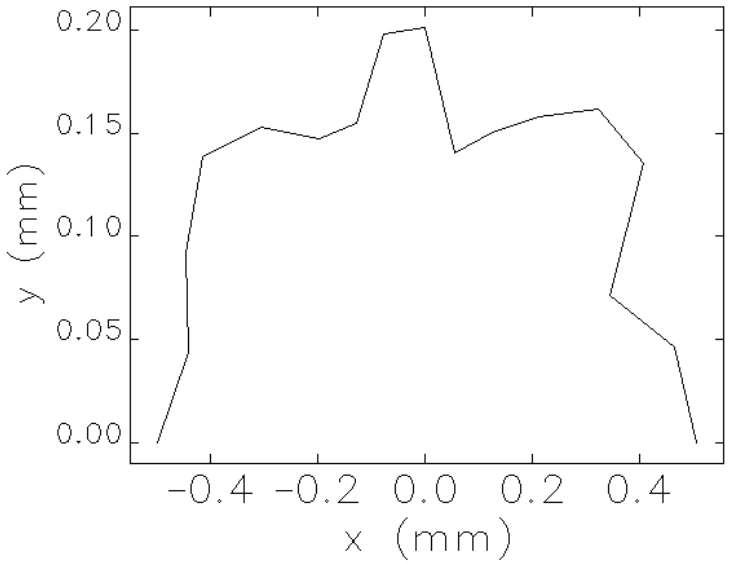

Figure 5.56: Dynamic aperture of the JLEIC ion collider ring simulated assuming the multipole field data of the LHC IR triplets for the JLEIC FFQs.

5.4.3 β Squeeze and Injection Optics

The collision optics of the JLEIC ion collider ring shown in Figure 5.40 has the IP x and y β^* values of 10 and 2 cm, respectively. Such small β^* values in combination with an about 11 m detector space lead to maximum x and y β functions of about 2500 m. The horizontal emittance is typically larger than the vertical one due to the difference in the horizontal and vertical intra-beam scattering rates. Depending on electron cooling performance, the normalized rms horizontal emittance is expected to be as low as 0.35 mm-mrad. Even with such a low emittance, the maximum rms beam size inside the FF quadrupoles reaches about 3 mm at 100 GeV/c. The normalized rms emittance at the injection momentum of 8 GeV/c is expected to be about 1 mm-mrad. There is a factor of 32 difference between the geometric emittances at 8 and 100 GeV/c. Thus, with the same optics, the maximum beam size would be a factor of $\sqrt{32}$ larger at 8 GeV/c than 100 GeV/c. Since the maximum beam size reaches its limit determined by the beam dynamics at 100 GeV/c, the beam optics at 8 GeV/c must be modified.

The beam clearly can not be injected in the collision optics setup. At injection, the maximum β functions in the FFQs have to be brought down ideally by a factor of 32 to keep the maximum beam size manageable. This can only be done by increasing the β^* values at injection by about the same factor. Once the beam is electron-cooled and accelerated to the experimental energy, the β^* sizes are reduced to the design values through the β squeeze procedure commonly used in hadron colliders [63]. During a β squeeze, the betatron tunes must remain constant to avoid crossing of betatron resonances, the phase advances between the IP and the local chromatic sextupoles (see Figure 5.40) should stay fixed, and the dispersion, particularly in the interaction region (IR), should remain suppressed. We use a modular approach to perform the β squeeze [64]. The β functions are reduced in large-β sections independently while connecting sections are used to control the

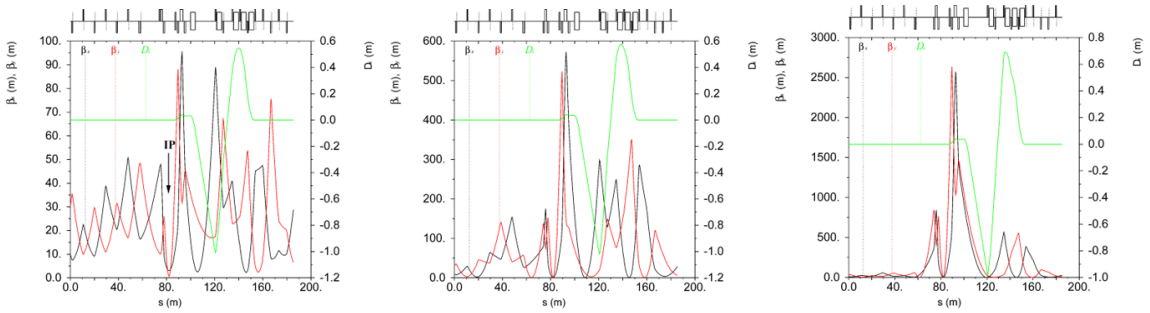

Figure 5.57: IR optics at different stages of β squeeze with $\beta_x^*/\beta_y^* = 3.0/0.6\,\text{m}$ (left), $0.5/0.1\,\text{m}$ (center) and $0.1/0.02\,\text{m}$ (right).

betatron phase advances. This technique involves a large number of quadrupoles but can provide the required range of the β squeeze in the ion collider ring.

The large-β sections of the ion collider ring are the IR and CCBs (see Figure 5.40). At injection, the maximum β functions in these sections are independently reduced resulting in relaxed β^* values. At the final energy, the β^* sizes are gradually squeezed to the collision values increasing the maximum β functions in the IR. The β functions at the locations of the local chromatic sextupoles in the CCBs are increased synchronously with the IR maintaining the local chromatic compensation of the FF quadrupoles throughout the β-squeeze process. Maintaining the chromatic compensation requires that the phase advances between the local sextupoles and the IP are maintained as well. This is done by using the matching sections between the IR and CCBs as tune trombones. Finally, the global betatron tunes are kept constant by a dedicated global tune trombone to avoid crossing of betatron resonances. The optical matching of each section participating in β squeeze is kept fixed decoupling it from the rest of the ring. Thus, β squeeze is done by simultaneously ramping quadrupoles in several independent sections making this a modular approach.

Figures 5.57(left), 5.57(center) and 5.57(right) show the IR optics for three different settings of β_x^*/β_y^* including injection, intermediate and collision values of 3.0/0.6, 0.5/0.1 and 0.1/0.02 m, respectively. Note that the optics remains fixed at the start and end points. Scaling of the upstream IR quadrupoles during the β squeeze is illustrated in Figure 5.58. A relatively large number of quadrupoles is needed to maintain the optical match and adjust the phase advance to the chromatic sextupoles. However, the ranges of the quadrupole strength variations are limited and there are enough knobs to optimize the scaling pattern and simplify the practical implementation. The fully relaxed injection optics of the complete ion collider ring is shown in Figure 5.59. Compared to Figure 5.40, the maximum β function values are reduced by a factor of more than 25.

Figures 5.60(left) and 5.60(right) show the 10σ x and y beam sizes, respectively, at 8 GeV/c injection assuming the normalized x and y rms emittances of $\varepsilon^n_{\text{x inj}} = \varepsilon^n_{\text{y inj}} = 1\,\mu\text{m}$ and a relative momentum spread of $\Delta p/p_{\text{inj}} = 1 \times 10^{-3}$.

We next investigate the nonlinear dynamics in the injection lattice. Figure 5.61 shows the dynamic aperture at the IP of the bare lattice for different values of the relative momentum offset. Since the natural chromaticity of the injection lattice is much lower than that of the collision mode, the dependence of the DA on the momentum offset is quite weak. The DA in Figure 5.61 exceeds $\pm 20\sigma$ in both x and y. Figures 5.62(left) and 5.62(right) show the DA frequency map and tune footprint, respectively.

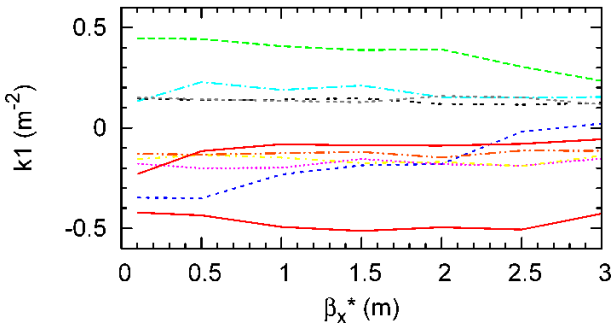

Figure 5.58: Change in the strengths of the upstream IR quadrupoles during β squeeze as a function of β^*_x. β^*_y scales proportionally to β^*_x.

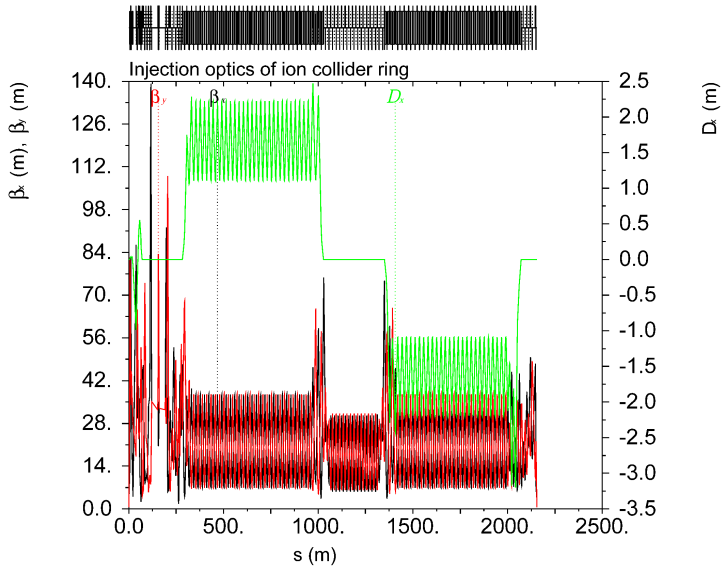

Figure 5.59: Injection optics of the complete ion collider ring.

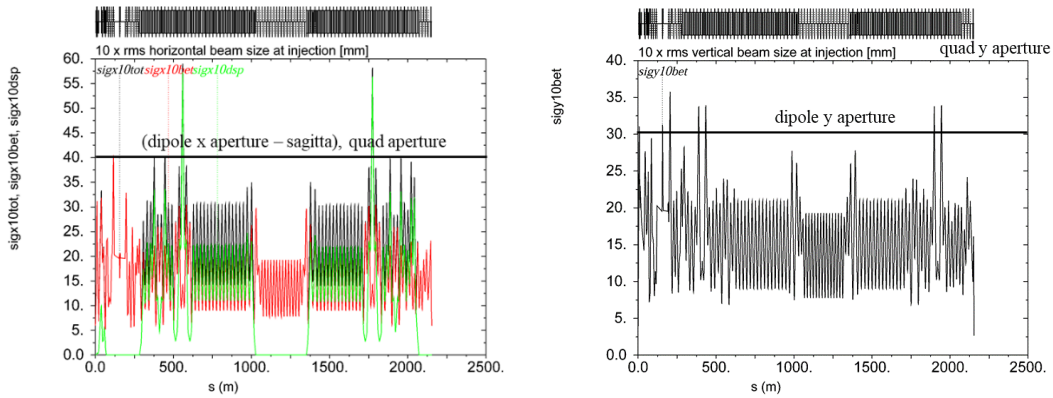

Figure 5.60: 10σ x (left) and y (right) beam sizes at 8 GeV/c injection assuming the normalized x and y rms emittances of $\varepsilon^n_{x\,inj} = \varepsilon^n_{y\,inj} = 1\,\mu$m and a relative momentum spread of $\Delta p/p_{\rm inj} = 1 \times 10^{-3}$.

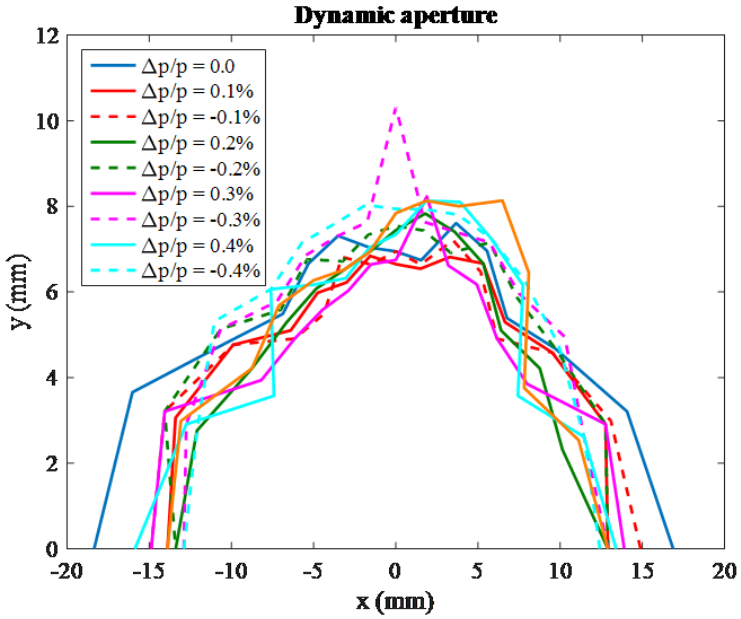

Figure 5.61: Dynamic aperture of the bare injection lattice for different relative momentum offsets.

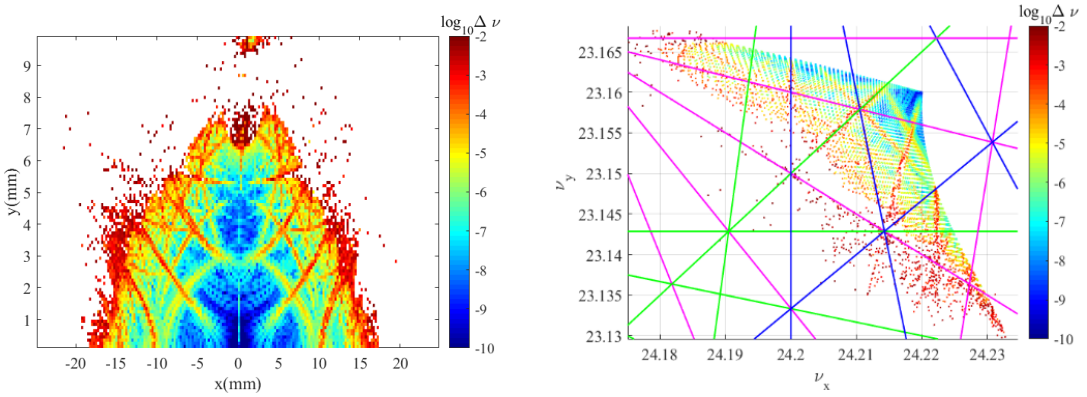

Figure 5.62: DA frequency map (left) and tune footprint (right) of the bare injection lattice.

5.4.4 Energy Ramp

The ion collider ring accelerates an ion beam from the injection momentum of about 8.9 GeV/c (8 GeV KE) to an experimental momentum between 20–100 GeV/c. Some of the ring parameters relevant to the energy ramp design are listed in Table 5.16. As described in Section 5.6, the ion bunches are injected from the booster into the ion collider ring by a bucket-to-bucket transfer. Two collider buckets are filled during each transfer until 52 out of 56 buckets are filled. The empty buckets form two equally-spaced beam gaps to allow for abort kicker rise and electron cloud cleaning.

Table 5.17 summarizes the RF, ramp, and beam parameters during ion acceleration in the collider ring. The ion bunches are relatively long at injection and during acceleration. At injection, 95% of each bunch occupies nearly a half of the stationary bucket length. This keeps the space charge

Table 5.16: Ion Collider Ring Parameters Relevant to the Energy Ramp Design

Parameter	**Units**	**Value**
Circumference	m	2256
Fig 8 crossing angle	deg	77.4
Total ring bend	deg	514.8
Dipole bend angle	deg	∼2.1
$N_{dipoles}$	–	246
Dipole length	m	4
Dipole bend radius	m	109.1
$\beta_{\mathrm{x,max}}$	m	141.3
$\beta_{\mathrm{y,max}}$	m	109.5
α_{C}	–	6.45×10^{-3}
γ_{T}	–	12.45

Table 5.17: Ion Collider Ring RF, Ramp and Beam Parameters

Parameter	**Units**	**Injection**	**Final**
KE	GeV	8	19.1–99.1
E	GeV	8.94	20.02–100.0
γ	–	9.53	21.34–106.6
β	–	0.99448	0.9989–0.99996
v	10^8 m/s	2.9814	2.9946–2.9978
p	GeV/c	8.89	20–100
$B\rho$	T-m	29.7	66.7–333.6
B	T	0.27	0.61–3.06
f_{rev}	kHz	132.15	$132.74 - 132.88$
t_{rev}	µs	7.567	$7.533 - 7.526$
η_{C}	$\times 10^{-3}$	-4.57	$4.25 - 6.36$
h	–	56	
f_{RF}	MHz	7.401	$7.433 - 7.441$
V_{RF}	kV	25	
φ_s	deg	~ 29.5 ($\gamma > \gamma_{\mathrm{T}}$	
rms bunch length σ_{z}	m	3.54	$2.94 - 2.1$
rms relative momentum spread $\Delta p/p$	$\times 10^{-3}$	0.73	$0.39 - 0.11$
rms longitudinal emittance	eV-s	0.078	
Bunch intensity	$\times 10^{11}$	6.8	
$\dot{B}_{max}$	T/s	0.05	
$\ddot{B}_{max}$	T/s^2	0.0125	

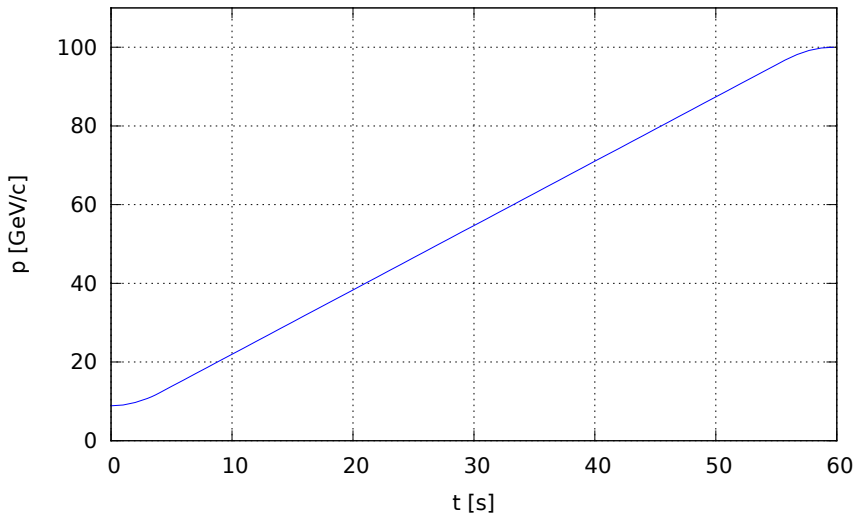

Figure 5.63: Collider ring momentum ramp.

tune shift below the stability threshold and allows for use of relatively low-frequency accelerating stations that can easily provide the necessary frequency tuning range during acceleration. After acceleration, each bunch is sequentially split in half six times as described in Section 5.6 resulting in a ring harmonic number of 3584. Assuming that there is no increase in the longitudinal emittance during splitting and that the design rms bunch length σ_z and relative momentum spread $\Delta p/p$ after splitting at 100 GeV/c are 12 mm and 3×10^{-4}, respectively, the longitudinal emittance of each bunch at injection is 0.08 eV − s.

Ramping the energy of the ion collider ring is a small fraction of the complete ion complex cycle. Therefore, the ramp rate can be kept relatively low at 0.05 T/s relaxing magnet and power supply requirements. For simplicity and ease of parameterization, we choose a symmetric ramp pattern consisting of quadratic, linear, and quadratic parts between sections of constant main dipole field. We chose the second derivative of the magnetic field ramp rate at the beginning and end of acceleration at a value of 0.0125 T/s^2, which is compatible with the linear ramp rate and is easily achievable with existing superconducting magnet technology. Given the initial and final magnetic fields and imposing the continuity requirement of the first time derivative of the dipole field, its first and second time derivatives completely define the ramp pattern. Figure 5.63 shows the resulting momentum ramp from the 8.9 GeV/c injection momentum to the top momentum of 100 GeV/c. Figure 5.64(left) shows the rms bunch length and relative momentum spread evolution during the ramp. The bucket area as a function of time is shown in Figure 5.64(right). It is calculated from the stationary bucket area by multiplying by a factor of 0.33 corresponding to the synchronous phase of 30° [62]. Note that the bucket area is greater than the rms longitudinal emittance by at least a factor of 17. These calculations assume constant V_{RF} of 25 kV.

We estimate the main dipole power supply requirements by calculating the rate of change of the magnetic field energy stored in the apertures of the ring dipoles. This calculation uses the dipole parameters listed in Table 5.16 and assumes a round dipole aperture of ±4 cm. The dipole magnet stored energy and associated transient power needed for this magnet stored energy ramp are shown in Figures 5.65(left) and 5.65(right), respectively. The peak power draw is about 600 kW. This calculation is a lower bound since it does not include stored energy outside of the magnet aperture or any power transfer Ohmic losses. Adding a conservative 50% margin to the required power suggests an ∼1 MW main dipole power supply.

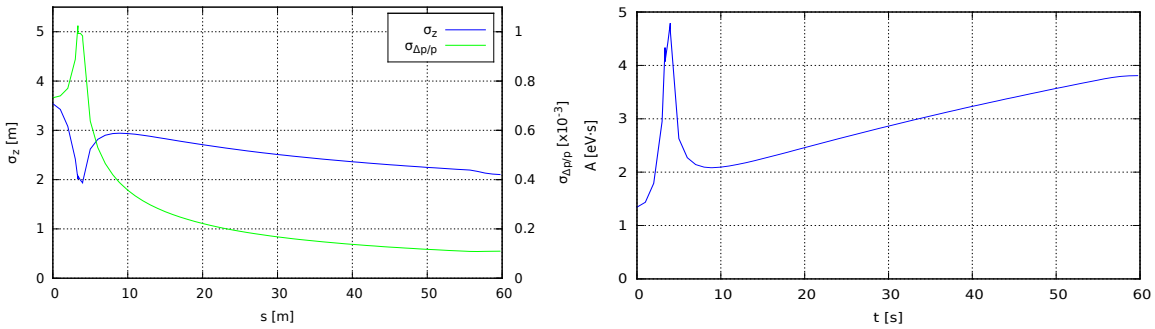

Figure 5.64: Left: σ_z and $\sigma_{\Delta p/p}$ evolution during the ramp. Right: bucket area as a function of time.

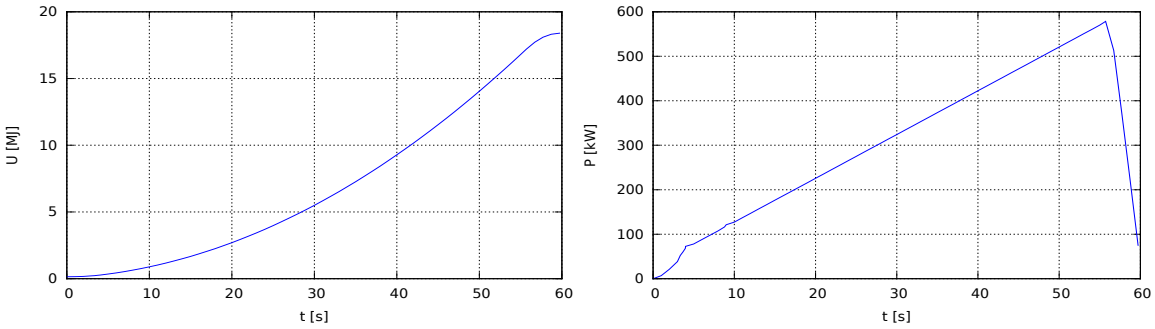

Figure 5.65: Left: Stored dipole energy. Right: Required transient power.

The ion collider ring crosses the transition energy during acceleration. Transition crossing may cause both single-particle and multi-particle dynamics problems. Chromatic non-linearities may cause growth of the bunch area by making different-momentum particles cross transition at different times. Low- and high-frequency self fields may lead to bunch shape mismatch and microwave instability, respectively [42]. An effective way to eliminate these problems is to increase the transition crossing rate of the beam. This can be accomplished by temporarily adjusting the lattice to produce a γ_T jump. This method has been successfully used in many accelerators and provides a large crossing rate enhancement without causing a large mismatch at transition.

Let us estimate the required parameters of a γ_T jump. Transition energy crossing is characterized by two time scales [42]: T_C during which the particle motion is non-adiabatic and T_{nl} during which the second-order dependence of the particle path length on $\Delta p/p$ dominates over the first-order one. Relative growth of the bunch area $\Delta\varepsilon_L/\varepsilon_L$ is determined by the ratio of the two time scales: $\Delta\varepsilon_L/\varepsilon_L \approx 0.76 T_{nl}/T_C$ when $T_{nl} \ll T_C$. For the JLEIC parameters listed in Table 5.17, T_C is about 35 ms. Without a γ_T jump, T_{nl} is about 15 ms, which would result in a significant increase of the bunch area. Assuming a γ_T jump of one unit in 60 ms reduces T_{nl} down to about 1.5 ms and $\Delta\varepsilon_L/\varepsilon_L$ to about 3%.

Changing γ_T of a ring requires modification of the ring's dispersion. At the same time, one must avoid a betatron tune shift and keep the maximum β functions and dispersion below reasonable values. A simple and flexible solution is to use quadrupole doublets with the quadrupoles in each doublet separated by $n\pi$ betatron phase advance in both planes [43, 44]. Such a scheme produces no betatron tune shift and leaves the β functions completely unchanged outside the doublet interval. Due the difference in the periodicities of the dispersion and β waves, the dispersion wave excited

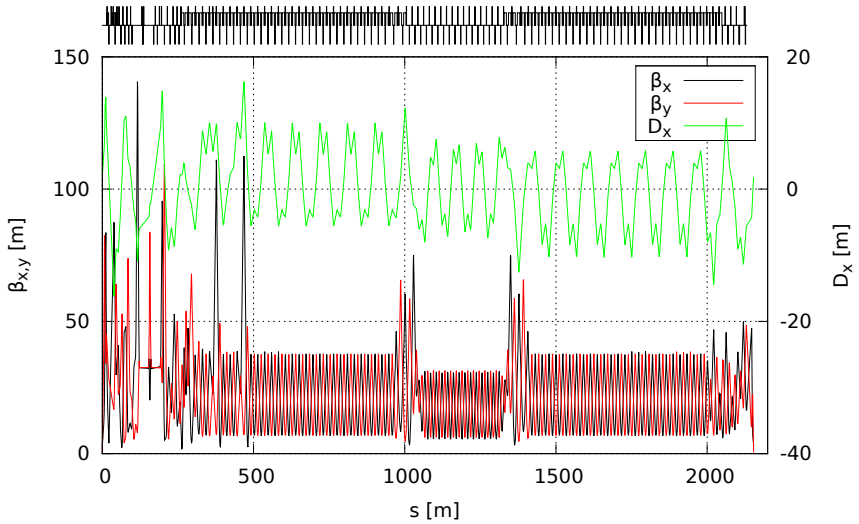

Figure 5.66: Injection optics with γ_T reduced by one unit from 12.45 to 11.45.

by the first quadrupole in a doublet is amplified by the second one while the β wave of the first quadrupole is canceled by the second one. This scheme can be easily implemented in the JLEIC ion collider ring lattice, since its arc FODO cells use 90° betatron phase advance in both planes. Figure 5.66 shows a modified injection lattice with γ_T reduced by one unit from 12.45 to 11.45. The only difference from the original lattice is that the strengths of two pairs of regular quadrupoles in one of the arcs are slightly modified. The maximum dispersion size can be optimized using additional quadrupole pairs.

5.4.5 Collimation

Uncontrolled loss of even a small fraction of a 0.75 A ion beam can quench super-conducting magnets and severely damage machine and detector components. In addition, chronic beam loss may deteriorate the performance of machine components, create high radiation areas making it difficult to service the machine, and generate detector background affecting the physics performance.

During stable operation, beam loss occurs due to constant scrape-off of the beam's peripheral, or halo, particles. The beam halo is continuously repopulated by particles transferred from the beam core due to various processes such as intra-beam scattering, non-linear dynamics, beam-beam interaction, and scattering on the residual gas. The beam halo will be collimated with an ion collimation system.

The ion collider ring collimators will be located at the downstream ends of the long straights where they transition into the arcs. The ring quadrupoles in those areas are separated by about 8 m long warm straight sections that provide sufficient space for collimator installation. If needed a tapered collimator design can be used. To validate our choice of the collimator locations, we have simulated the performance of the collimation system and determine where the beam losses are mostly likely to occur [65].

Each collimator is 20 cm long and consists of graphite. All collimators are set to $\pm 6\sigma$ opening. The beam size varies between injection and different collision energies. Therefore, the collimator opening size must be adjusted during the course of each cycle to follow the changes in the beam size. Both ends of each collimator will be independently adjustable to support tapered setup.

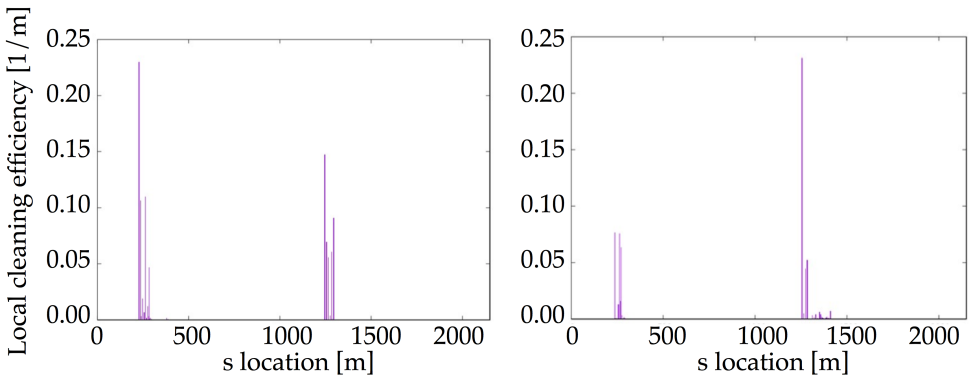

Figure 5.67: Beam loss maps with horizontal (left) and vertical (right) collimation in the JLEIC ion collider ring.

Figure 5.67 shows beam loss maps in the JLEIC ion collider ring with horizontal (left) and vertical (right) collimation. These beam loss maps are a histogram of local cleaning inefficiency, i.e. particle loss density along the ring normalized to the total number of lost particles. The spikes in Figure 5.67 are located near the collimator regions. There seem to be no losses anywhere else around the ring except for a small loss at the entrance into the second arc when collimating vertically.

5.4.6 Abort System and Beam Dump

The ion beam abort system and beam dump must include transmission line kickers with a rise time of one $h = 28$ bucket, or about 270 ns, consistent with the minimal length of the abort gaps. Here we extrapolate from similar hadron beam abort systems, as such beam abort and dump systems have standard designs that are well-established with no technical risk.

Scaling energy and beam power from such systems [66], the JLEIC ion abort kickers will require approximately 2.8–3.0 m of warm straight lattice space allocation. Kick angles should be 1.6–2.4 mrad, easily achievable given gap and rise time requirements using standard Blumlein and transmission line designs.

The drift from the abort kickers to the dump absorber must be ∼24 m, and the dump body itself will be 2.0–2.5 m long. The dump will surround a warm beam pipe downstream of the main experimental region (including all forward tagging) to preclude abort-generated background. This dump length estimate will be refined with Monte Carlo simulations that include effects of range straggling, multiple Coulomb scattering broadening, and heavy ion dissociation. However this estimate is likely conservative given the stronger than linear energy scaling of most relevant quantities.

The peak energy incident on the dump face is quite high; 0.75 A of 100 GeV beam current extracted in one revolution (∼7.5 s) is 600 kJ. The dump window will include water cooling, while the dump body itself requires no additional cooling. It is worth noting that the JLEIC ion ring dump is a pulsed dump, with very different performance requirements than the high-power CW electron beam dumps used in CEBAF 12 GeV oeprations.

Beam power is typically distributed along an area on the dump face by slightly mismatching the transmission line kickers. This results in a variation of the abort kick angle through the extraction, and reduction of local peak power on the dump face.

The estimated ion collider ring dump system requirements are summarized in Table 5.18.

Table 5.18: Ion Collider Ring Dump/Abort System Requirements

Parameter	**Units**	**Value**
Kicker rise time	ns	270
Total kicker length	m	3.0
Number kicker modules	–	2–3
Total extraction angle	mrad	1.6–2.4
Kicker to absorber distance	m	∼20
Absorber length	m	2.1–2.5

5.5 Ion Polarization

5.5.1 Ion Booster

For calculating proton and deuteron polarizations in a figure-8 booster, we chose the booster lattice with the tunes $\nu_x = 7.977$ and $\nu_y = 6.793$ initially developed for 3 GeV/c momentum. To weaken the sensitivity of orbital parameters to lattice element setup errors, the betatron tunes were adjusted away from betatron resonances. The tune shifts were done using the two quadrupole families constituting the triplets of the booster's straight sections. Figures 5.68 and 5.69 show the β-functions and dispersion in an unperturbed lattice of the figure-8 booster, respectively. Figures 5.68 and 5.69 also show the location of the solenoid stabilizing the spin motion. The solenoid is indicated by a yellow rectangle. We have studied the effects of the incoherent and coherent parts of the resonance strength on the proton and deuteron polarizations, and demonstrate their stabilization using the spin tracking code Zgoubi [67].

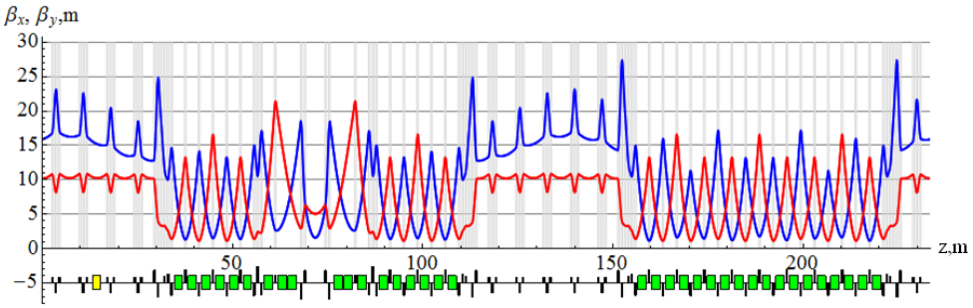

Figure 5.68: β-functions in an unperturbed lattice of the figure-8 booster.

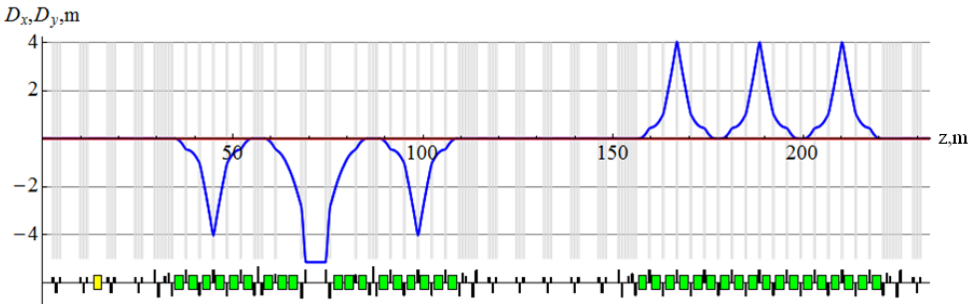

Figure 5.69: Dispersion in an unperturbed lattice of the figure-8 booster.

Proton polarization

The greatest contribution to the zero-integer resonance strength comes from the quadrupole misalignments in the plane transverse to that of the orbit. Figures 5.70 and 5.71 show the diagrams of random quadrupole shifts in the radial and vertical directions, respectively, that were used when calculating the proton spin motion in the figure-8 booster [68]. The sizes of the quadrupole shifts are given in units of their rms deviation equal to 10^{-3} cm.

Figure 5.72 shows the coherent part of the resonance strength versus the energy in units of $\gamma|G|$ obtained by a Zgoubi simulation [68]. The coherent part has a periodic behavior and its maximum value does not exceed 10^{-3}. To stabilize the longitudinal direction of the proton spin in the whole

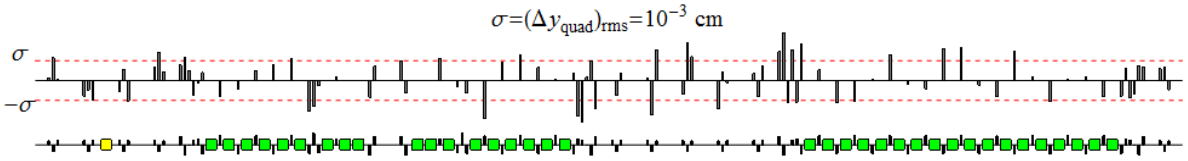

Figure 5.70: Diagram of radial quadrupole misalignments in the booster. The errors are distributed normally with an rms deviation of $\sigma = \Delta x_{quad} = 10^{-3}$ cm.

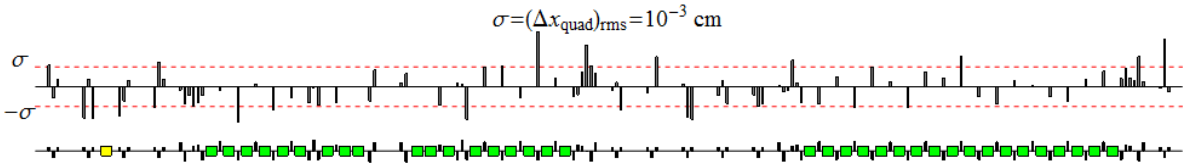

Figure 5.71: Diagram of vertical quadrupole misalignments in the booster. The errors are distributed normally with an rms deviation of $\sigma = \Delta y_{quad} = 10^{-3}$ cm.

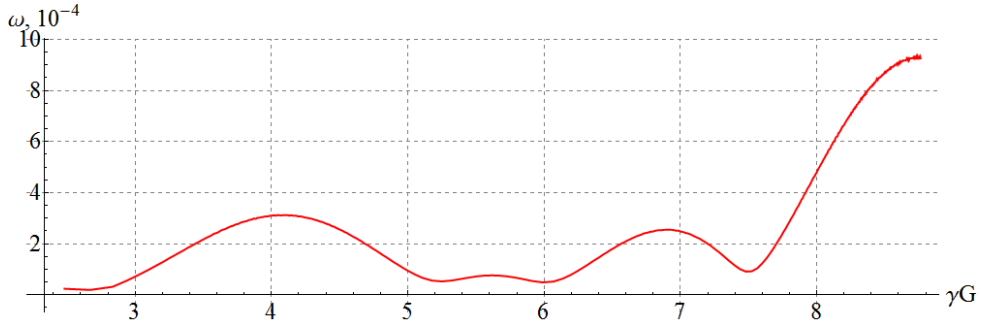

Figure 5.72: Coherent part of the proton spin resonance strength vs. $\gamma|G|$ in the figure-8 booster.

energy range during acceleration, it is sufficient to introduce a "weak" solenoid inducing a spin tune value significantly greater than the resonance strength.

Figure 5.73 shows the change in the proton longitudinal spin component during acceleration in the booster with a stabilizing solenoid. Providing a spin tune equal to 5×10^{-3} requires a field integral changing proportionally to the beam momentum with a maximum value of 0.1 T-m. The longitudinal polarization is stabilized in the whole energy range with a precision better than 3%. In principle, by choosing a stronger spin stabilizing solenoid or an optimal collider injection energy, one can significantly improve the beam polarization. For instance, when extracting the beam at the energy corresponding to a value of $\gamma G \approx 7.5$, the change in the proton longitudinal polarization will be less than 0.1% at the same field strength of the solenoid.

Deuteron polarization

The graph in Figure 5.74 shows the dependence of the deuteron vertical spin component on the energy in units of $\gamma|G|$ when accelerating deuterons with a field ramp rate of 1 T/s in the figure-8 booster. The booster quadrupoles are randomly shifted according to the diagrams presented in Figures 5.70 and 5.71. One can make a rough estimate from the graph that the coherent part of

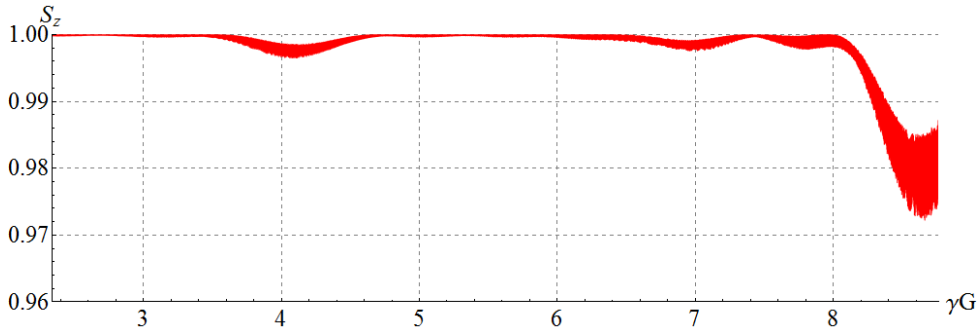

Figure 5.73: Proton longitudinal spin component vs. γG in the figure-8 booster with random quadrupole shifts and with the spin stabilizing solenoid. The initial conditions are: x_0 =1 cm, x_0' =0 rad, y_0 =1 cm, y_0' =0 rad, and $\Delta p/p = 0$.

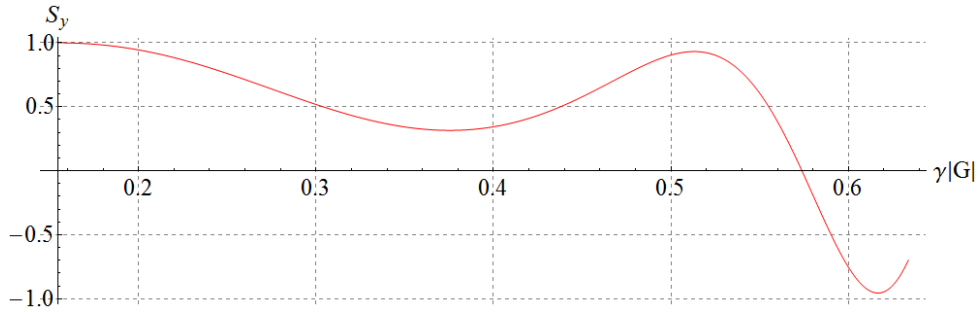

Figure 5.74: Deuteron vertical spin component vs. $\gamma|G|$ for a synchronous particle in the figure-8 booster with random quadrupole shifts. The particle was launched along the distorted closed orbit.

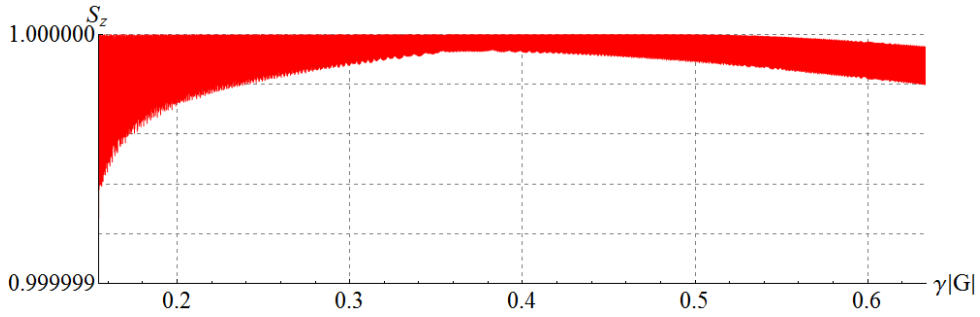

Figure 5.75: Deuteron longitudinal spin component vs. $\gamma|G|$ in the figure-8 booster with random quadrupole shifts and with the spin stabilizing solenoid. The initial conditions are: x_0 = 1 cm, x_0' = 0 rad, y_0 = 1 cm, y_0' = 0 rad, and $\Delta p/p = 0$.

the resonance strength has an order of magnitude of 1×10^{-7} at injection into and 1×10^{-6} at extraction from the booster.

Figure 5.75 shows the change in the deuteron longitudinal spin component in the booster with a stabilizing solenoid. The same solenoid was used in the calculation as in the proton case. As one can see, the longitudinal polarization is stabilized in the whole energy range with a precision better than 5×10^{-7}. The presented examples show an exceptional stability of the deuteron polarization in the figure-8 booster.

5.5.2 Ion Collider

Acceleration of polarized proton and deuteron beams

Polarizations of the proton and deuteron beams in the ion collider ring are preserved during acceleration from 8 GeV/c to 100 GeV/c using a weak solenoid [69]. One must ensure that the spin tune ν induced by the solenoid significantly exceeds the strength of the zero-integer spin resonance w: $\nu \gg w$ [70]. As demonstrated below, a solenoid field integral of 1.2 T-m is sufficient to stabilize the polarization. Such a solenoid does not perturb the design orbit and has practically no effect on the beam's orbital parameters. Polarization is longitudinal at the solenoid location. Such a solenoid induces a spin tune ν of 10^{-2} for protons and 3×10^{-3} for deuterons, i.e., when a particle with a vertical spin makes one turn along the design orbit, its spin tilts by an angle of $2\pi\nu$ from its initial orientation.

Figure 5.76 shows the β functions of the JLEIC collider lattice in the acceleration mode [64] used in our spin dynamics calculations. The origin of the coordinate frame is located at the collider's IP. Figure 5.76 also indicates the location of the solenoid stabilizing the spin during acceleration. The difference from the collision mode [71] where the β functions in the IP region reach 2.5 km is that, in the acceleration mode, the β functions in the detector section do not exceed 150 m.

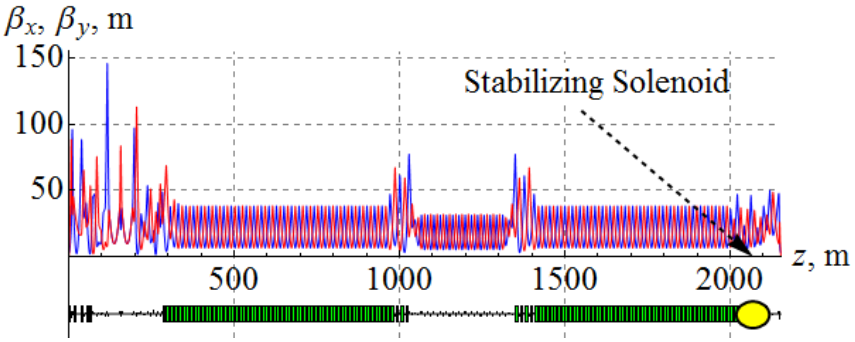

Figure 5.76: β functions of the ion collider ring in the injection mode.

We calculate the coherent part of the spin resonance strength using the statistical model with random shifts of all quadrupoles in the transverse directions [69]. Figure 5.77 shows the coherent part of the proton resonance strength for the injection mode optics of the ion collider ring with random quadrupole misalignments resulting in a transverse closed orbit distortion of about 100 µm rms. The statistical model calculates the most probable magnitude of the coherent part of the resonance strength not specifying its direction, which lies in the collider's plane. The coherent part of the resonance strength has interference peaks whose maximum values do not exceed 1.5×10^{-2}, which has an order of magnitude comparable to the field induced by the stabilizing solenoid. Figure 5.78 shows a graph of the coherent part of the deuteron spin resonance strength calculated using the statistical model of random quadrupole misalignments.

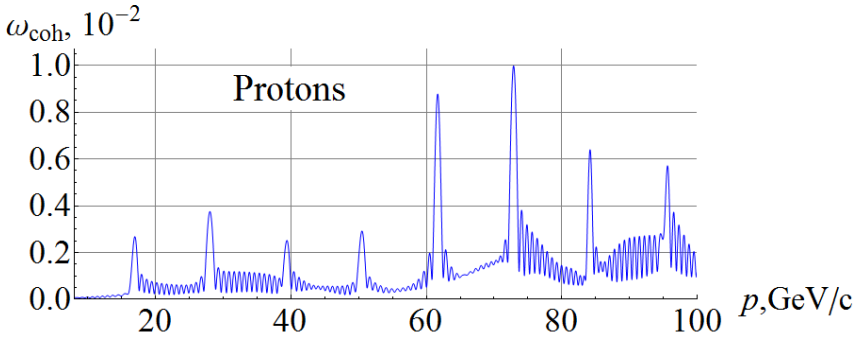

Figure 5.77: Coherent part of the proton spin resonance strength for the injection mode optics of the JLEIC ion collider ring.

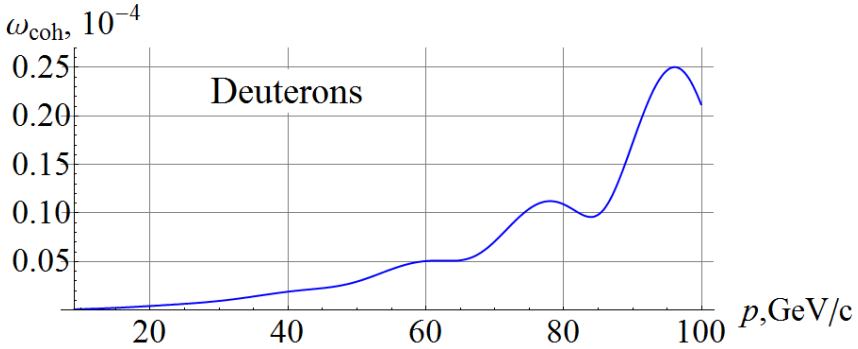

Figure 5.78: Coherent part of the deuteron spin resonance strength for the injection mode optics of the JLEIC ion collider ring.

During acceleration in the ion collider ring, there is a precession about the spin field $\vec{h}$ that consists of the field $\vec{h}_{\rm sol}$ induced by the stabilizing solenoid and the resonance strength $\vec{w}$: $\vec{h} = \vec{h}_{\rm sol} + \vec{w}$. During acceleration the field $vech_{\rm sol}$ is maintained constant while the resonance strength $\vec{w}(t)$ experiences significant changes in the regions of the interference peaks.

The beam polarization substantially depends on the field ramp rate in the arc magnets. When using superconducting magnets with a field ramp rate of $\sim$3 T/min, acceleration happens adiabatically, which means that, in a characteristic time of change in the spin field, the spin makes a large number of turns. During adiabatic acceleration, the spin follows the $\vec{h}$ field direction, which can significantly deviate from the longitudinal direction at the locations of the interference peaks of the coherent part of the resonance strength. However, this does not signify polarization loss, the beam polarization restores its longitudinal direction in places where $h_{\rm sol} \gg w_{\rm coh}$.

Figure 5.79 shows the longitudinal spin components in the ion collider ring during acceleration of 3 protons with $\Delta p/p = 0$ (green line), $\Delta p/p = 10^{-3}$ (red line) and $\Delta p/p = -10^{-3}$ (blue line). The graphs of the longitudinal spin components practically do not differ from each other (the red line covers up the blue and green lines), i.e. the synchrotron energy modulation does not give a noticeable contribution to the ion spin motion when the polarization is stabilized by a weak solenoid in the JLEIC ion collider ring. All particles were launched with the same initial conditions: $S_{z0} = 1$, x_0 =0.61mm, x_0' =0 rad, y_0 =0.27 mm, y_0' =0 rad. The field ramp rate was $\sim$3 T/min (the particles were accelerated in 8.3 million turns). During acceleration, the spin preserves its component along the spin field, which lies in the orbit plane and noticeably deviates from the longitudinal direction

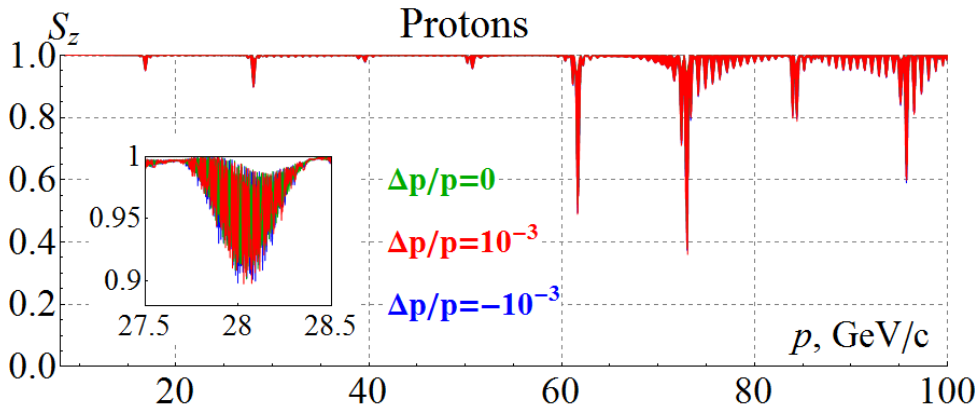

Figure 5.79: Longitudinal spin component during acceleration of three protons in the ion collider ring.

in the regions of the "interference" peaks of the coherent part of the resonance strength at momenta of about 60 GeV/c and 75 GeV/c, where the resonance strength becomes approximately equal to the size of the solenoid spin field. The spin tune induced by the solenoid during acceleration is 10^{-2}.

The simulation in Figure 5.79 is done with a closed orbit excursion of 100 µm rms. If needed the tolerances on alignment of the lattice elements can be relaxed. The strength of the stabilizing solenoid can be increased. One then has to account for the fact that the solenoid itself gives a contribution to the spin resonance strength due to an angle between the distorted closed orbit and the solenoid axis. This results in a transverse magnetic field component, which has practically no effect on the orbital motion but can have a strong effect on the spin motion especially for a proton beam at high energies ($\gamma G \gg 1$). This contribution can be minimized either by a more precise alignment of the solenoid axis or by choosing an appropriate collider lattice, which has a sufficiently small value of the spin response function at the solenoid location [70]. Another option is to compensate the coherent part of the spin resonance strength at the experimental energy using a 3D spin rotator [72].

Similar graphs of the longitudinal components of the deuteron spin are shown in Figure 5.80. The initial conditions and the solenoid field strength during acceleration were chosen to be the same as in the proton case. In contrast to protons, the change in the deuteron longitudinal polarization during acceleration does not exceed $2 \cdot 10^{-5}$ even in the interference peak. This example demonstrates a high stability of the deuteron polarization in figure-8 rings, which can be used for high-precision experiments. To the contrary, in conventional accelerators with preferred periodic spin orientation, control of the deuteron polarization and its preservation during acceleration to 100 GeV/c is not achievable.

The relativistic Lorentz factor of the transition energy in the ion collider ring equals 12.453, which corresponds to a momentum of 11.65 GeV/c for protons and 23.3 GeV/c for deuterons. For our calculations, we choose a conventional model, in which crossing of the transition energy is done by a fast jump of the RF cavity phase at the exact moment of the crossing from the value φ_s to the value $\varphi_s^* = \pi - \varphi_s$ at a constant field ramp rate. The phase space trajectories of two protons with the initial momentum offsets of $\Delta p/p = 10^{-3}$ (red line) and $\Delta p/p = -10^{-3}$ (blue line) are shown in Figure 5.81. As the energy approaches transition, the amplitude of the synchrotron phase deviation from the equilibrium value of $\varphi_s \approx 0.3$ rad reduces while the amplitude of the momentum deviation grows. After crossing the transition energy, the particles are captured inside a new separatrix and

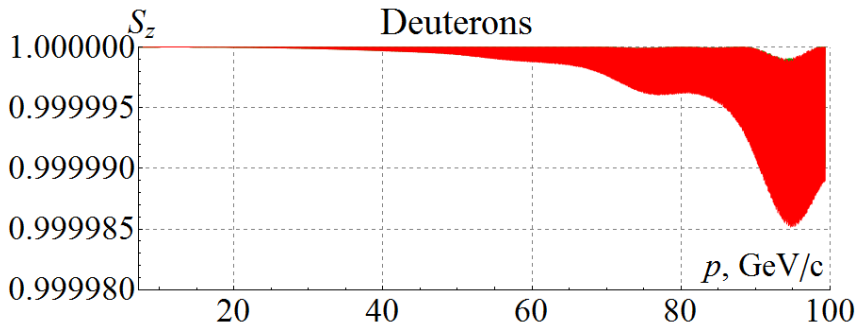

Figure 5.80: Longitudinal spin component during acceleration of three deuterons in the ion collider ring.

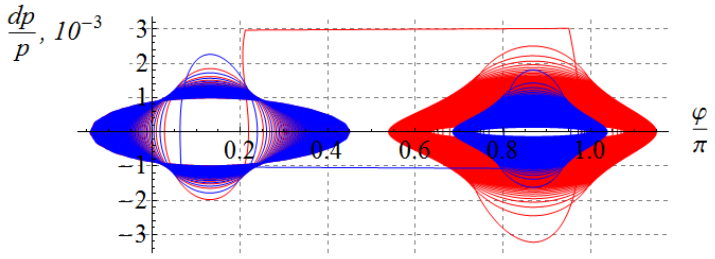

Figure 5.81: Proton phase space trajectories during transition energy crossing.

undergo oscillations about a new equilibrium phase of $\varphi_s^* \approx 2.84$ rad. The amplitude of the momentum deviation dampens as the energy gets further away from transition. Our calculations indicate that, if transition energy crossing is organized without significant excitation of the emittances, its effect on the polarization is negligible [69]. Indeed, our calculations made using a spin tracking code Zgoubi verify the validity of our scheme for preserving the polarization during acceleration of protons and deuterons in the JLEIC ion collider ring with transition energy crossing.

Control of proton and deuteron polarizations the ion collider ring

A 3D rotator is used to control the ion polarization in the ion collider ring. It consists of three modules for control of the radial, vertical, and longitudinal beam polarization components. Figure 5.82(left) shows the module for control of the radial polarization component $n_{\rm x}$, which consists of two pairs of opposite-field solenoids and three vertical-field dipoles producing a fixed orbit bump. The control module for the vertical polarization component $n_{\rm y}$ is the same as that for the radial component except that the vertical-field dipoles are replaced with radial-field dipoles (Figure 5.82(center)). To keep the orbit bumps fixed, the fields of the vertical- and radial-field dipoles must be ramped proportionally to the beam momentum. The module for control of the longitudinal polarization component $n_{\rm z}$ consists of a single weak solenoid (Figure 5.82(right)). There is a substantial flexibility in the placement and arrangement of these modules in the collider.

The formulae for calculation of the spin rotation angles $\varphi_{\rm zi}$ in the control solenoids for a given polarization direction at the 3D spin rotator location $\vec{n} = (n_{\rm x},\ n_{\rm y},\ n_{\rm z})$ and a given value of the

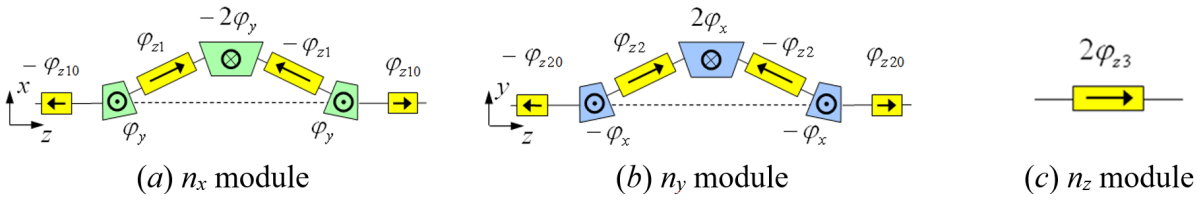

Figure 5.82: Ion collider ring 3D spin rotator modules.

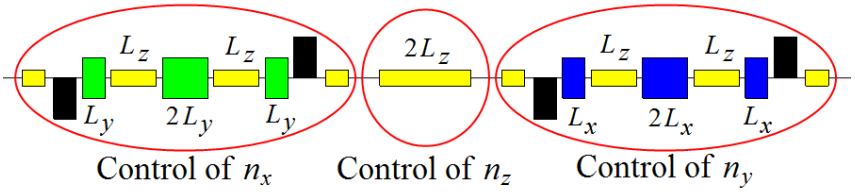

Figure 5.83: Schematic placement of the 3D spin rotator elements.

spin tune ν (linear approximation in ν) are:

$$\begin{aligned}
&n_{\rm x}\text{ module:} \quad \varphi_{\rm z1} = \pi\nu\frac{n_{\rm x}}{\sin\varphi_{\rm y}}, \quad \varphi_{\rm z10} = \frac{\pi\nu}{2}\frac{n_{\rm x}}{\tan\varphi_{\rm y}}, \quad \varphi_{\rm y} = \gamma G\alpha_{\rm orb},\\
&n_{\rm y}\text{ module:} \quad \varphi_{\rm z2} = \pi\nu\frac{n_{\rm y}}{\sin\varphi_{\rm x}}, \quad \varphi_{\rm z20} = \frac{\pi\nu}{2}\frac{n_{\rm y}}{\tan\varphi_{\rm x}}, \quad \varphi_{\rm x} = \gamma G\alpha_{\rm orb},\\
&n_{\rm z}\text{ module:} \quad \varphi_{\rm z3} = \pi\nu n_{\rm z}.
\end{aligned} \tag{5.5.13}$$

The field $B_{\rm zi}$ of a control solenoid of length $L_{\rm zi}$ can be calculated using the formula:

$$B_{\rm zi} = \frac{\varphi_{\rm zi}}{(1+G)L_{\rm zi}}. \tag{5.5.14}$$

The schematic placement of the 3D rotator elements in the collider ring's experimental straight is shown in Figure 5.83 [70, 72, 73]. The lattice quadrupoles are shown in black, the vertical-field dipoles are green, the radial-field dipoles are blue, and the control solenoids are yellow. With each module's length of ∼7 m, the fixed orbit deviation in the bumps is ∼15 mm in the whole momentum range of the collider. The 3D spin rotator can provide any desired polarization orientation at the interaction point. The maximum required dipole and solenoid magnetic field strengths are 3.0 T and 3.6 T, respectively. Figure 5.84 shows placement of the 3D rotator magnetic elements in the ion collider ring with the following parameters: $L_{\rm x} = L_{\rm y}$ =0.6 m, $L_{\rm zi}$ =2 m, $L_{\rm zi0}$ =1 m, $\alpha_{\rm orb} = 0.31°$.

In real conditions, there are always errors in construction of the collider's magnetic lattice elements as well as errors in alignment of these elements along the collider's design orbit. These lattice imperfections lead to a change in the collider's closed orbit. As a result, particle spins experience additional coherent rotations caused by perturbing magnetic fields when the particles are moving along the distorted periodic closed orbit. The combined effect of these magnetic fields on the spin determines the coherent part of the resonance strength.

Random quadrupole shifts resulting in a change in the collider's closed orbit are among the main reasons for appearance of the coherent resonance strength component. Figures 5.85 and 5.86 show diagrams of random quadrupole shifts in the vertical and radial directions, respectively, which are

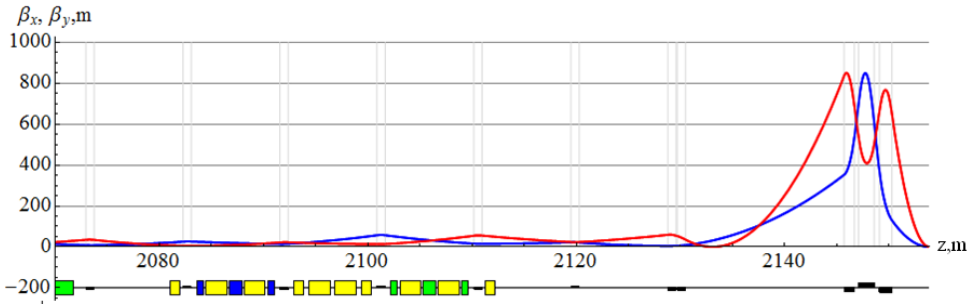

Figure 5.84: Placement of the 3D rotator in the ion collider lattice. The yellow rectangles are the control solenoids, the blue rectangles are the dipoles with radial magnetic field direction, and the green rectangles are the dipoles with vertical magnetic field direction.

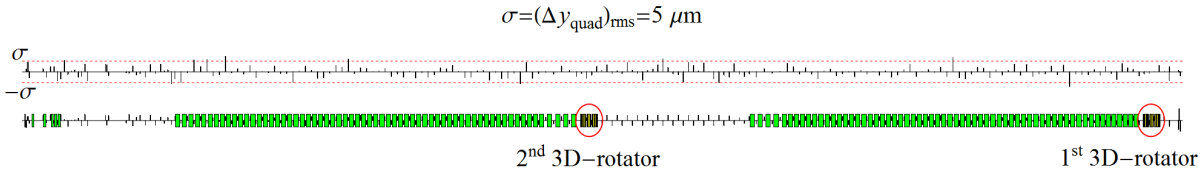

Figure 5.85: Diagram of vertical quadrupole alignment errors in the collider ring distributed normally with $\sigma(\Delta y_{\rm quad})$ =5 µm.

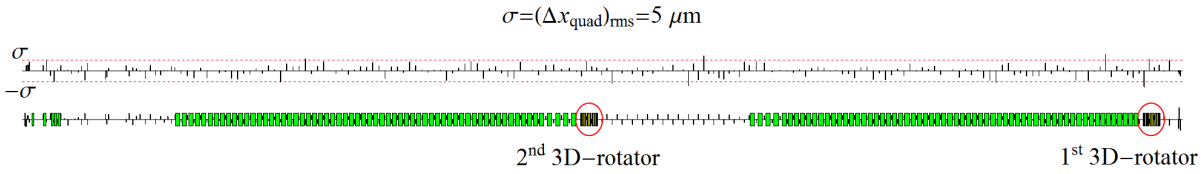

Figure 5.86: Diagram of radial quadrupole alignment errors in the collider ring distributed normally with $\sigma(\Delta x_{\rm quad})$ =5 µm.

used in calculations of the proton spin motion in the collider. The sizes of the quadrupole shifts are given in units of their rms deviation equal to 5 µm. The diagrams also indicate the locations of the control 3D rotator (1st 3D-rotator) and of the compensating 3D rotator (2nd 3D-rotator). The indicated quadrupole alignment errors result in a closed orbit distortion in the arcs of a few hundred µm (see Figure 5.87).

Below we consider compensation of the coherent part of the resonance strength using protons as the example. The deuteron case can be treated similarly. The calculation of the coherent part of the resonance strength in the collider ring shows that its value for protons is $w_{\rm coh}^{prot} \approx 2.5 \cdot 10^{-3}$. This means that using a 3D rotator with a spin tune of 10^{-2} to control the proton polarization already becomes inconvenient, since one should always make a "correction" of the spin field for the coherent part of the resonance strength during a spin manipulation process. Besides, the coherent part grows with increase in energy along with the fields required for its compensation. Nevertheless, the solenoid fields of the control 3D rotator can be left at the same level if one compensates the

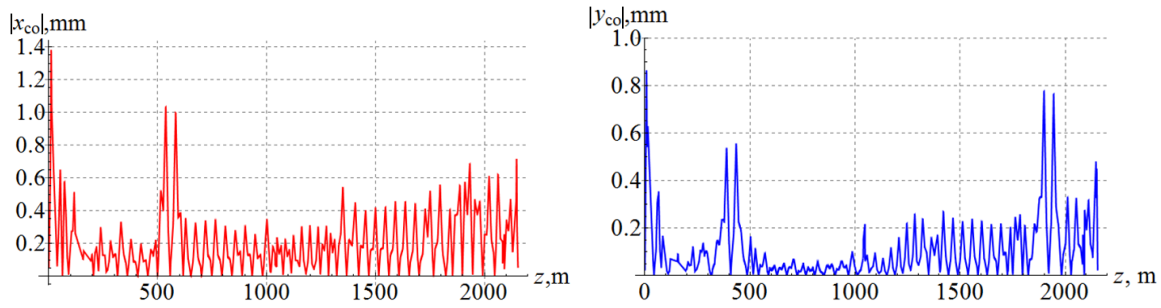

Figure 5.87: Radial (left) and vertical (right) orbit excursions with random misalignments of all quadrupoles in the collider ring according to the diagrams in Figures 5.85 and 5.86.

coherent part of the resonance strength using a second 3D rotator with static field located in the opposite straight (see Figure 5.85).

We determine the direction of the precession axis induced by the coherent part of the resonance strength near the 2nd 3D rotator from a Zgoubi simulation. In practice, it will be measured experimentally. We set the 2nd 3D rotator to cancel the coherent part of the resonance strength. After this compensation, the coherent part of the resonance strength, becomes $2.7 \cdot 10^{-5}$, i.e. decreased practically to the value of the incoherent part of the resonance strength.

Since we set the 3D rotator parameters using formulae derived in the linear approximation in the spin tune ν, the accuracy of the compensation is determined by the square of the spin tune $\nu^2 \sim 5 \times 10^{-6}$. One can further improve the compensation by specifying the 3D rotator parameters up to the second order including the non-commutativity of the spin rotations about the different axes in the 3D rotator modules. One should also analyze the effect of additional fields arising inside the 3D rotator due to random quadrupole misalignments.

Figure 5.88(left) shows a graph of the spin component evolution in a non-ideal collider lattice when setting vertical proton polarization at the interaction point with compensation of the coherent part of the resonance strength. The parameters of the control 3D rotator are: $n_y = 1$ and $\nu_{sol} = 0.01$. The beam momentum is 60 GeV/c. The particle is launched along the closed orbit with vertical spin. For comparison, Figure 5.88(right) shows a similar graph without compensation of the coherent part of the resonance strength. The provided example shows that a non-ideal collider with compensation of the coherent part of the spin resonance strength becomes equivalent to an ideal collider in terms of the polarization control.

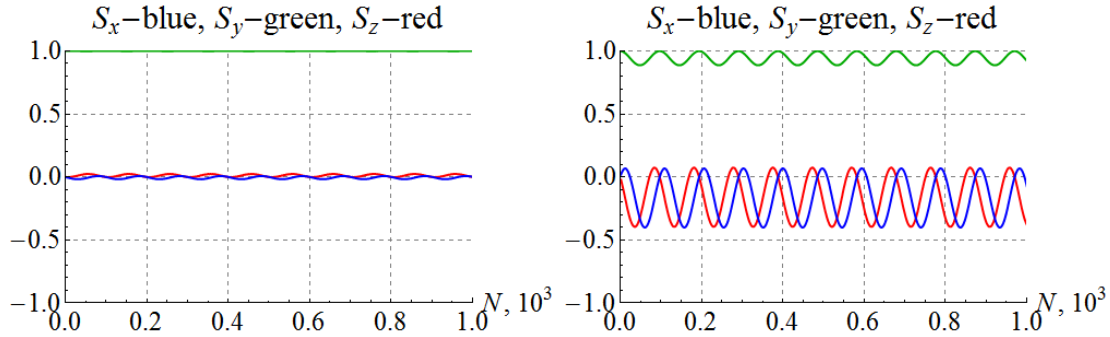

Figure 5.88: Setting vertical proton polarization in a non-ideal collider lattice with (left) and without (right) compensation of the coherent part of the resonance strength.

Spin-flipping ion polarization

A 3D spin rotator allows one to make reversals of the particle spins during an experiment by slowly (adiabatically) changing the solenoid fields of the 3D spin rotator to rearrange the spin motion [74]. To preserve the polarization degree, one must meet the condition of adiabatic change in the spin direction, which has the following form for the number of particle turns $N_{\rm flip}$ necessary to flip the spin:

$$N_{\rm flip} \gg 1/\nu. \tag{5.5.15}$$

We get a limit on the number of turns for a spin flip of $N_{\rm flip}^{prot} \gg 10^2$ for protons and $N_{\rm flip}^{deut} \gg 10^4$ for deuterons, which, in terms of the flip time, means $\tau_{\rm flip}^{prot} \gg 1$ ms for protons and $\tau_{\rm flip}^{deut} \gg 0.1$ s for deuterons. In practice, the adiabaticity condition is automatically satisfied, since the spin reversal time is limited by the field ramp rate in the super-conducting solenoids.

We provide the results of our calculation of the proton spin reversals in the vertical (yz) plane of the collider. The pattern of the spin field change with the number of turns when making spin reversals is shown in Figure 5.89. The number of turns is normalized to N_0, which is the number of turns for rotation of the spin from vertical to longitudinal direction. The vertical $h_{\rm y}$ (green line) and longitudinal $h_{\rm z}$ (red line) components of the spin field are set using the solenoids of the vertical $n_{\rm y}$- and longitudinal $n_{\rm z}$-modules of the 3D spin rotator. The magnitude of the spin field sets the spin tune value. Change in the spin tune normalized to the maximum field $h_{\rm max}$ is shown in Figure 5.90.

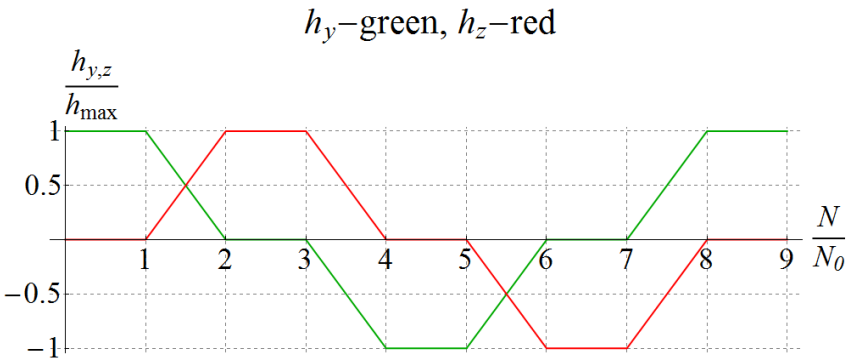

Figure 5.89: Pattern of change in the vertical $h_{\rm y}$ and longitudinal $h_{\rm z}$ spin field components when making spin reversals in the collider ring.

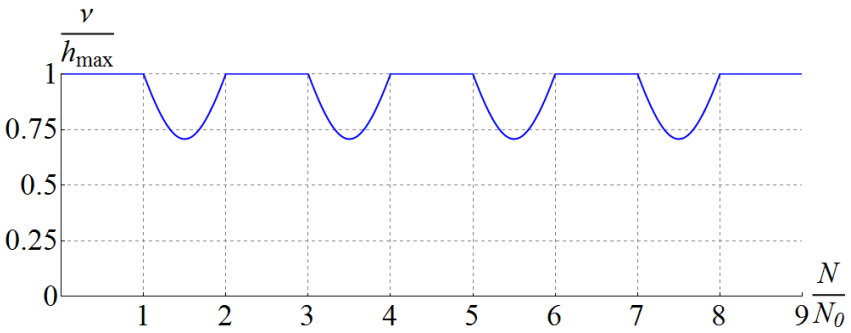

Figure 5.90: Change in the spin tune in units of the maximum spin field $h_{\rm max}$ when rotating the spin in the collider.

Figure 5.91 shows the proton spin components as a function of the number of turns for the indicated pattern of change in the spin field using the 3D rotator. Rotation from vertical to longitudinal direction and back is done in 50 thousand turns. The maximum spin tune value is 10^{-2}. The spin components then follow the shape of the spin field pattern practically everywhere, as it should be in case of adiabatic motion. Exceptions are small regions where the spin field pattern has sharp corners, in which the adiabaticity condition is violated. The spin starts directed vertically up. Then a spin rotation takes place in 50 thousand turns. As we can see, the spin undergoes sequential rotations from the vertical-up direction to the longitudinal direction along the particle velocity, then to the vertical-down direction and finally to the longitudinal direction opposite to the particle velocity.

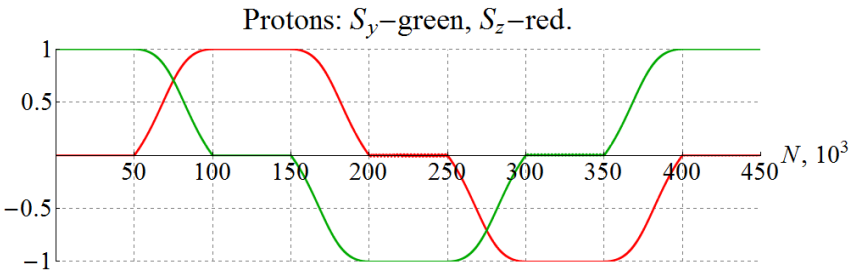

Figure 5.91: Rotating the proton spin in an ideal collider lattice.

To meet the adiabaticity condition for deuterons with a spin tune of 10^{-4} it is sufficient to increase the number of turns for the spin rotation from vertical to the longitudinal direction to 300 thousand. The resulting behavior of the deuteron spin components during the rotations is shown in Figure 5.92. As in the proton case, the spin follows the spin field practically everywhere according to the pattern in Figure 5.89. The presented calculations demonstrate the capability of spin-flipping using a 3D spin rotator. Thus, the figure-8 JLEIC ion collider provides a unique capability of doing high-precision experiments with polarized ion beams.

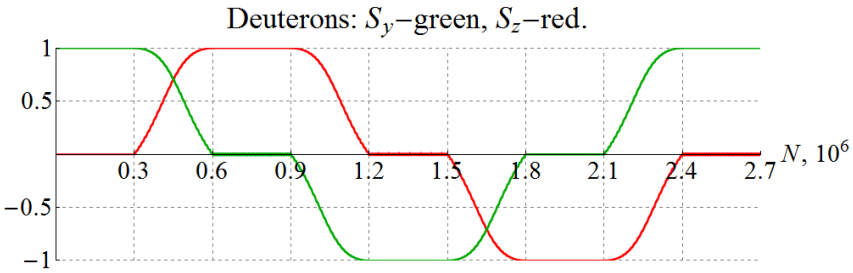

Figure 5.92: Rotations of the deuteron spin in an ideal collider lattice with the adiabatic condition of the spin motion satisfied.

5.5.3 Deuteron Tensor Polarization

The spin-transparency mode of JLEIC allows for acceleration and spin control of a polarized deuteron beam. The deuteron is a spin-1 particle. Its spin component along the magnetic field direction or a quantization axis is specified by a spin quantum number m that takes one of the $+1$, 0, or -1 values. Classically, these correspond to the “up”, “transverse”, and “down” spin

directions, respectively. The degree of the spin alignment of a spin-1 particle beam is described by the "vector" P_V and "tensor" P_T polarizations [75]:

$$\begin{aligned} P_V &= (N_+ - N_-)/N, \\ P_T &= 1 - 3N_0/N, \end{aligned} \tag{5.5.16}$$

where N_+, N_0, and N_- are the numbers of beam particles in the $m = +1$, 0, and -1 states, respectively, and $N = N_+ + N_0 + N_-$ is the total number of beam particles. Note that, according to the definition in Eq. 5.5.16, P_V can take values from $+1$ ($N_+/N = 1$) to -1 ($N_-/N = 1$) while P_T has a range from $+1$ ($N_0/N = 0$) to -2 ($N_0/N = 1$). When all of the beam particles are equally distributed between the three spin states, i.e. the beam is unpolarized, $P_V = 0$ and $P_T = 0$. The vector polarization is completely analogous to the proton polarization. It describes the asymmetry in the populations of the "up" and "down" spin states. The tensor polarization describes the degree of the spin alignment associated with the $m = 0$ state.

The polarization state of a spin-1 beam is specified by a pair of numbers (P_V, P_T) such as $(+1, +1)$, $(-1, +1)$, $(0, -2)$ or any other combination allowed by Eq. 5.5.16. A polarization state is formed by creating the appropriate populations of the three spin states in a polarized deuteron source [76, 77, 78]. In a source, room-temperature molecular deuterium is first dissociated into neutral atomic deuterium beam. The resulting deuterium atoms are equally distributed between the six hyperfine states. In a strong magnetic field, each hyperfine state is determined by the directions of the deuteron and electron spins in a deuterium atom. Three options for the deuteron spin direction and two options for the electron spin direction give the six states. The atomic beam is cooled to a cryogenic temperature to reduce the thermal energy spread below the energy difference between the hyperfine states in a strong magnetic field. The beam then passes through a sequence of sextupoles and RF transition units. A sextupole separates the atoms according to their electron polarization. The three highest-energy hyperfine states are focused while the three lowest-energy ones are defocused. An RF transition unit exchanges the populations of two hyperfine states. Sequentially applying state selections and exchanges, one can generate any desired deuteron polarization state. Moreover, by turning RF transitions on and off, one can quickly alternate between different polarization states. After the deuteron polarization state has been formed, the polarized neutral atomic deuterium beam is negatively ionized by an incoming Cs beam preserving its polarization and goes for further beam formation and acceleration. This technology of polarized deuteron beam generation is well-developed. Polarized deuteron sources have been routinely operated at a few user facilities providing polarized deuteron beams to experiments [76, 77, 78].

The deuteron polarization dynamics is described in the previous sections in terms of the vector polarization. These vector polarization results at the same time uniquely determine the behavior of the tensor polarization. In other words, the ability to preserve and control the tensor polarization follows from the ability to preserve and control the vector polarization. Without going into mathematical details, this can be motivated in the following way. The spin wave function of a spin-j particle can be formally composed of the spin wave functions of $2j$ independent spin-1/2 particles. The description of the spin-j dynamics in electric and magnetic fields then reduces to description of the spin-1/2 dynamics, or the vector polarization dynamics. The spin dynamics in electric and magnetic fields is simply rotation of the spin vector about the field direction. Rotations of the vector and tensor polarizations are uniquely coupled. It has been experimentally demonstrated earlier [79].

Measurement of the deuteron vector and tensor polarizations is based on the azimuthal dependence of the deuteron-target elastic scattering cross-section [80]:

$$\frac{d\sigma}{d\Omega} = \frac{d\sigma_0}{d\Omega}[1 + \frac{3}{2}A_y P_V \cos\phi - \frac{1}{4}A_{zz}P_T - \frac{1}{4}(A_{xx} - A_{yy})P_T \cos(2\phi)], \tag{5.5.17}$$

where $d\sigma_0/d\Omega$ is the unpolarized cross-section, A_y is the vector analyzing power, and A_{xx}, A_{yy}, and A_{zz} are the tensor analyzing powers. The analyzing powers are constants. Equation 5.5.17 shows that the vector and tensor polarizations can be extracted using the $\cos\phi$ and $\cos(2\phi)$ harmonics, respectively, in the azimuthal behavior of the deuteron elastic scattering data. Determination of the absolute values of the vector and tensor polarizations requires knowledge of the analyzing powers. In practice, rather than analyzing the full ϕ count rate dependence, it may be more convenient to split the detector into a few azimuthal segments and measure the asymmetries of scattering into these segments. To measure both the vector and tensor polarizations, a deuteron polarimeter must have at least four segments, e.g. left (L), right (R), top (T), and bottom (B) quadrants. One can then define asymmetries proportional to the $\cos\phi$ and $\cos(2\phi)$ terms such as $\alpha_V \equiv (L-R)/(L+R)$ and $\alpha_T \equiv (L+R-T_B)/(L+R+T+B)$, respectively. One can relate these asymmetries to the vector and tensor polarizations by integrating Eq. 5.5.17 over each quadrant's acceptance and taking into account the detector efficiencies. From these relations, one can obtain P_V and P_T in terms of α_V and α_T. The coefficients of these expressions are determined by the fundamental analyzing powers in Eq. 5.5.17 and are called effective analyzing powers [81].

5.6 Ion Bunch Formation

The JLEIC ion collider ring is designed to provide ion beam with up to 0.75 A beam current (requiring 5×10^{12} stored protons or equivalent ions), high repetition rate (476.3 MHz, with the capability to operate at reduced rate such as 119 MHz and upgradable to 952.6 MHz), low emittance, and short bunch length (∼10 mm). Such bunch repetition rate and bunch length are unprecedented in hadron colliders. The ion species cover the full mass range of stable elements, from proton to lead.

The JLEIC beam formation process has multiple stages to address the large difference in beam properties between the ion sources and the collider ring, especially the beam energy and density. The constraints are multi-dimensional, ranging from beam physics, technology, and cost. One major limit is the space charge tuneshift in the rings, which is strong for beam with high charge density and at low energy. At each critical beam formation stage, such as injection, bunch compression, and cooling, the ion energy needs to be set high enough to avoid Laslett tuneshift exceeding the limit, but still low enough to avoid higher cost and higher technical risk. For example, the maximum kinetic energy for the collider ring injection is chosen at 8 GeV/u, an energy already proven by Tevatron DC electron cooling [82].

The JLEIC ion injection chain contains ion sources, a 285 MeV proton and ion linac with warm front end, and a single figure-8 8 GeV Booster as illustrated in Figure 5.93.

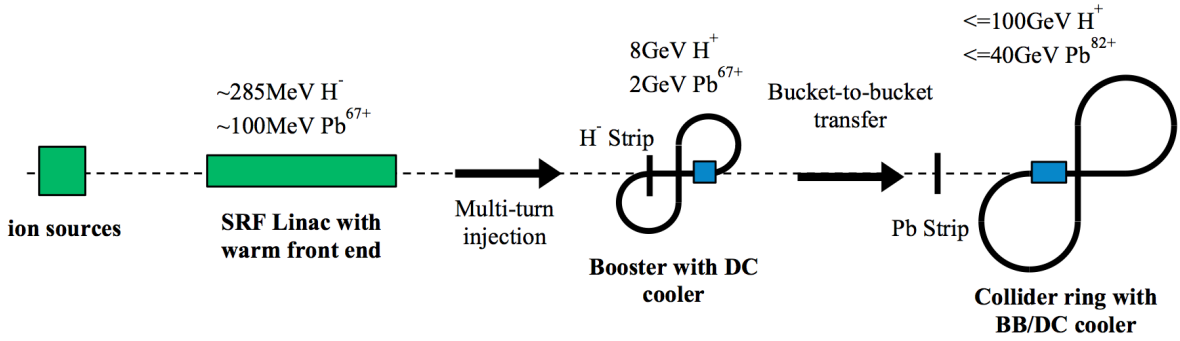

Figure 5.93: JLEIC ion injection chain

The JLEIC luminosity optimization approach is to maximize the collision frequency with moderate charge per bunch, so the bunched beam cooler can effectively maintain the low emittance as well as the short bunch length of the ion bunches. The high bunch repetition rate of up to 476 MHz and short bunch length are unprecedented in hadron colliders. There are a few options of bunch splitting for JLEIC, as described in [83, 84]. Our baseline chose up to 7 stages binary adiabatic RF bunch splitting. The CERN PS forms a train of 72 bunches at 25 MHz bunch repetition rate for LHC through one stage of factor of three adiabatic RF splitting and two stages of binary splitting [85], while the BNL AGS adopts the reverse of the adiabatic RF splitting, merging three bunches into one 9 MHz bunch for RHIC [86].

To maximize the average collision frequency, the total length of gaps in the collider rings needs to be minimized. We choose to inject long ion bunches into the collider ring buckets, using the empty space between two bunches as the kicker rise time. The majority of the bunch splitting has to be performed in the collider ring, so the long gaps reserved for injection will be filled with bunches after splitting. We assume ∼40 ns rise time for the ion injection kicker. Due to the space

charge limit, the JLEIC ion bunch must occupy up to 70% of the bucket length during the collider stacking stage, so the stacking bucket length needs to be ∼130 ns, or 64 times a 476 MHz bucket. The only gap that is required during the collision is the abort gap, and we set it at about twice the stacking bucket length, or ∼270 ns, which is about half of the RHIC abort gap. In the case of polarized ion collision with electron, we may have two gaps in the electron ring to separate the two electron bunch trains with flipping polarization, so an additional gap in the ion ring might be also needed to match the electron ring gaps.

The binary splitting scheme requires the harmonic number of the collider ring to be a multiple of 64, so we choose 3584 for the case without "gear change" beam synchronization, or a circumference of 2255.34 m. The booster ring circumference needs to be 1/7 of that. Future changes of the circumference need to be in the increment of 64 bucket lengths of 476 MHz.

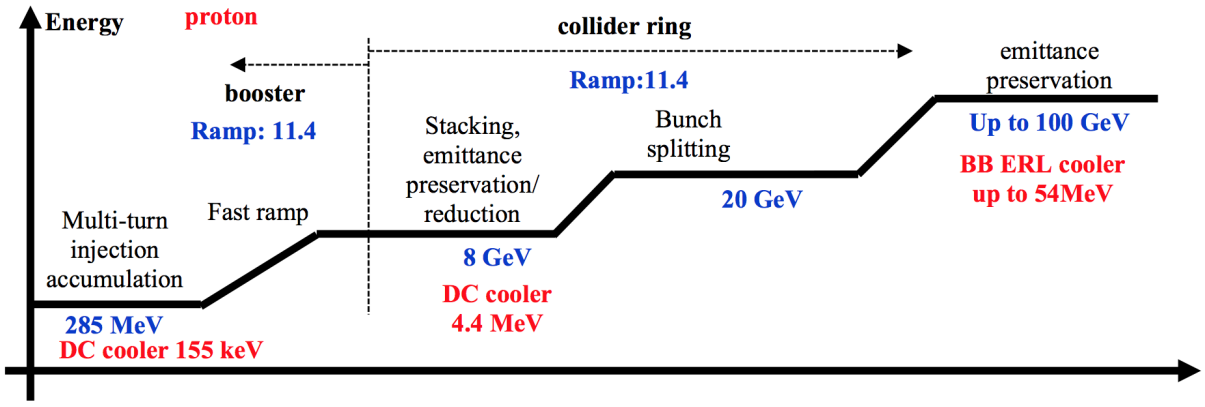

Figure 5.94: Ramping stages for JLEIC proton beam formation

5.6.0.1 JLEIC Beam Formation Cycles The JLEIC ion beam formation ramping cycle for protons is shown in Figure 5.94. Each step of the beam formation cycle is listed below:

1. Eject the used beam from the collider ring, cycle the magnets
2. Multi-turn charge-exchange injection of polarized protons from linac to booster. Low energy DC cooling (155 keV electron) might be needed to maintain the beam size.
3. Capture beam into a long bucket (∼200 m bunch length, rms ∼56 m)
4. Ramp the booster to 8 GeV
5. Raising RF voltage and compress the bunch length to 56 m (rms ∼13 m), adiabatically split to two bunches of ∼40.5 m bucket length and ∼28 m bunch length (rms ∼7 m)
6. Bucket-to-bucket transfer the two long bunches into the collider ring, gap between bunches ∼12 m, ∼40 ns
7. Repeat step 2–6 for **26** times, each cycle ∼1 min, total ∼25 min. During the stacking, operate DC cooler at lower strength to maintain the emittance
8. After the completion of stacking, turn up the DC cooling electron current and reduce the emittance to space charge limit.
9. Ramp collider ring to 20 GeV with slight bunch length compression

10. Perform adiabatic binary RF bunch splitting up to **6** times to harmonic number $h = 3584$. In certain cases that luminosity optimization prefers lower repetition rate (most likely with higher ion energy), the bunch splitting can stop at $h = 796$ or 1792.
11. In case of low energy collision that requires "gear change" collision for beam synchronization, manipulate the beam to create several extra empty buckets (476 MHz) in the gaps ($h = 3585 - -3587$ depending on ion energy). Ramp the beam to collision energy.
12. With 476 MHz RF, compress the bunch length to the acceptance of 952.6 MHz RF. Turn on 952.6 MHz SRF and compress the bunch length further. Turn on bunched beam cooling to maintain the emittance. Start collision.

The beam formation process for other ions is similar to the proton, with an additional ramp from the collider ring injection to 8 GeV/u for DC cooling (emittance reduction). DC cooling electron energy also needs to switch between emittance preservation during stacking and the emittance reduction stages. For heavy ions, the booster can't use charge exchange injection, and has to use phase painting. There will be a final charge stripping when the heavy ion beam is transported from the booster to the collider. Figure 5.95 shows the ramping cycle of Pb ions. Due to the final charge stripping, the ramping ratio in the collider ring is higher for heavy ions, and increases to 13.9 for Pb. The product of the maximum ramp ratio in the booster and collider ring will be

$$R_{\text{booster}} R_{\text{collider}} = \frac{B\rho_{\text{max,collider}}}{B\rho_{\text{min,booster}}} \times \frac{Q_{\text{Pb,collider}}}{Q_{\text{Pb,booster}}} \tag{5.6.18}$$

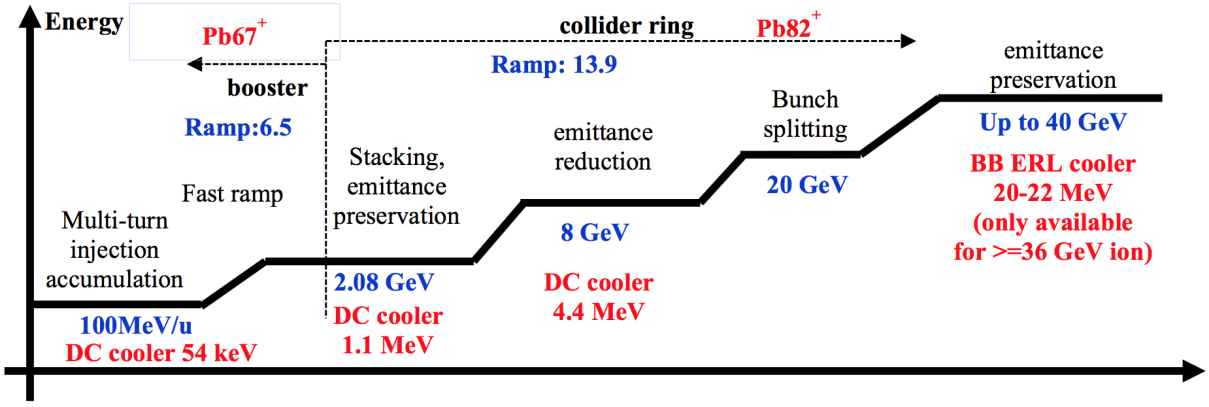

Figure 5.95: Ramping stages for JLEIC lead ion beam formation.

We may consider increasing the booster extraction energy for heavy ions by raising the maximum magnet rigidity in the future optimization, which will improve the space charge tuneshift in the collider ring during stacking, and will better balance ramp ratio between the booster and the collider ring. Another approach is to increase the intermediate Pb charge stripping energy in the ion linac from 13 MeV to 17–21 MeV, which will raise the booster charge state from 67 to 70–72, and enhance the booster extraction energy proportionally. With such strip energy change, the linac will lose a few MeV of Pb energy, and the space charge tuneshift after booster RF capture will increase due to both lower energy and higher charge state. However, calculation for the baseline case shows that the booster Pb injection space charge tuneshift has room to trade for collider ring Pb injection space charge tuneshift.

5.6.0.2 Generating extra empty buckets for harmonic number variation As shown in Section 8.1, JLEIC ion collider ring needs to be able to operate at variable harmonic numbers, a.k.a. "gear change" scheme, to mitigate other challenges caused by beam synchronization. However, with the binary RF splitting, the length of bunch trains and gaps in the collider ring needs to be binary multiple of the RF wavelength (multiple of 64 in the baseline). Although changing to the barrier bucket splitting scheme may provide the flexibility of generating arbitrary harmonic numbers, the beam dynamics and technology for barrier bucket in large size rings needs more extensive study. For the JLEIC baseline, the ion ring harmonic number ranges between 3584 and 3587, and we can generate the few extra buckets by RF phase manipulation.

To insert an extra bucket in the gap, the RF frequency has to ramp from $h \times f_{\rm rev}$ to $(h+1) \times f_{\rm rev}$. To avoid beam loss during the ramp, the synchrotron phase of each bucket with beam has to stay around 0, while the total RF phase advance in one revolution is non-integer multiple of 2π. This can be achieved by an RF phase jump when the gap is passing the cavity. The maximum phase jump will be π, as shown in Table 5.19.

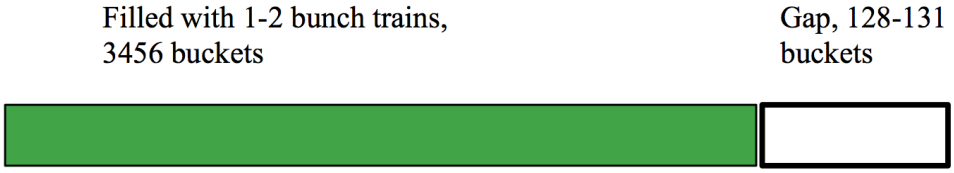

Figure 5.96: Inserting buckets in the ion ring by phase jump in the gap.

Table 5.19: Inserting Buckets in the Ion Ring by Phase Jump in the Gap

Stage	h	$f_{\rm RF}$ **(MHz)**	**RF phase jump in the gap**
before ramping	3584	475.934	0
Start ramping	3584+Δ (Δ=0$\sim$0.5)	475.934$\times$(1+Δ/3584)	-2$\pi\Delta$/3584
ramp half finished	3584.5	476.000	-π
continue ramping	3585-Δ (Δ=0.5$\sim$0)	476.066$\times$(1-Δ/3584)	2$\pi\Delta$/3584
ramping finished	3585	476.066	0

The $Q_{\rm ext}$ of this 476 MHz RF cavity needs to be low enough to allow this phase jump. The estimated RF voltage needed is 150 kV with about 75 mm rms bunch length. The optimized $Q_{\rm ext}$ is around 200. If we use one PEP-II RF cavity with redesigned coupler, the RF power needed is 220 kW. The total RF power can be further reduced with increased number of cavities.

5.6.0.3 Parameters During the JLEIC Ion Bunch Formation Process Table B.3 in Appendix B shows parameters through the JLEIC bunch formation process. Considerations and assumptions include:

- $\sim$20% longitudinal emittance growth during booster ramping/compression/split due to IBS. No additional longitudinal emittance growth during injection stacking.
- To hold transverse emittance and avoid overcooling to the space charge limit, cooling rate is low during stacking. Earlier injected bunches experience larger ΔE growth. This was estimated with the program JSPEC [88].
- Pb ramping reduces the beam energy spread to 1×10^{-4}, but electron cooling rate cannot maintain this energy spread.

- Maximum 952 MHz SRF voltage is 56 MV (Section 9.5).
- IBS will be quite strong at lower energies (40 GeV or below). The ion beam energy spread will increase quickly without cooling in this energy range according to JSPEC [88].

5.7 Transport Lines

Required ion beam transfer lines for the JLEIC ion complex include transport from the source/linac to the booster, and from the booster to the ion collider ring. The booster injection section is in the first long drift of one of the straight sections, while the extraction section is in the final long drift of the opposite straight section. Locations of the booster injection and extraction sections are shown in Figure 5.22.

5.7.1 Linac to Booster

The linac to booster transport line is an 88.93° arc with a total bend radius of ∼30.46 m. This geometry was altered slightly to allow for straight sections to match into and out of the arc. The design uses a FODO lattice, the lattice functions are shown in Figure 5.97. Dispersion suppression is accomplished with a π phase advance over the bending region. Required elements are outlined in Table 5.20.

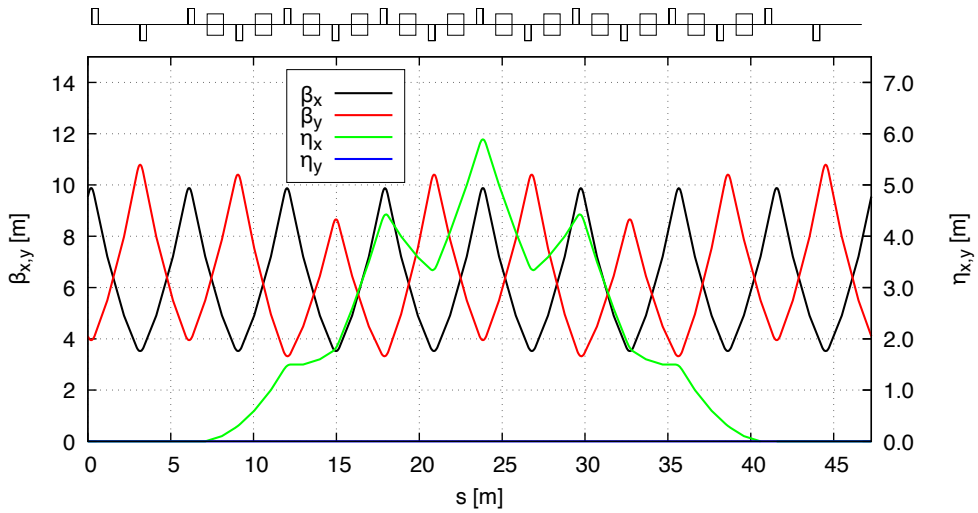

Figure 5.97: Lattice functions of the transport line from the linac to the booster.

Table 5.20: Types and maximum fields of the given magnets in the JLEIC Linac to Booster Transport Line.

Element	Length	Number	T (max)	T/m (max)
Dipole	1.0 m	12	0.34	-
Quadrupole	40 cm	16	-	2.24

5.7.2 Booster to Collider

The Booster to Collider transfer line geometry is a straight section of ∼26.5 m and a 58.1° arc with a bending radius of ∼62.8 m. The straight section also includes a low beta insertion for final stripping of heavy ions. The design uses a β^{strip} of 1.0 m, for an rms spot-size of 0.4 mm at the stripping foil. To facilitate this low-β insert, the straight section uses a triplet lattice, while the arc uses FODO. The lattice for this transport line is shown in Figure 5.98. while the number and strengths of the magnets are shown in Table 5.21. The overall layout of the complex is shown in Figure 5.99.

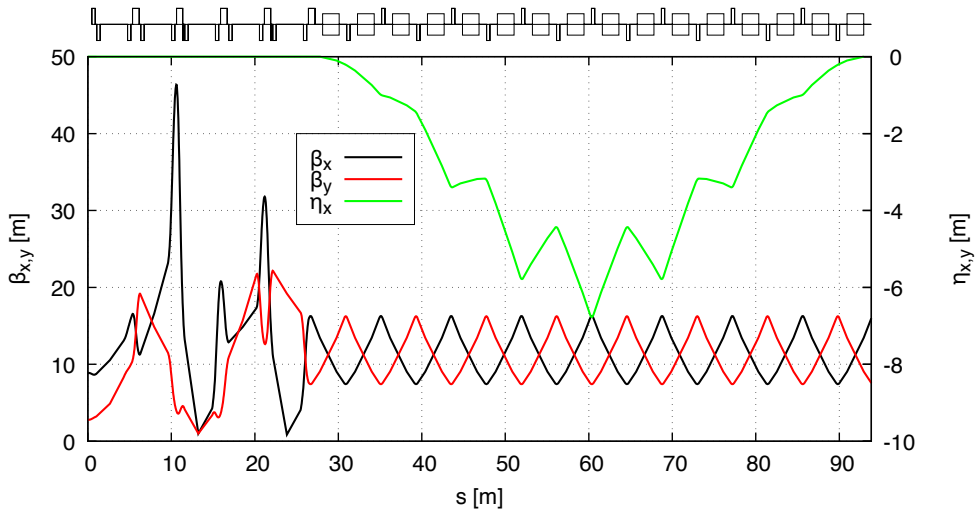

Figure 5.98: Lattice functions of the transport line from the booster ring to the collider ring.

Table 5.21: Types and maximum fields of the given magnets in the JLEIC Booster to Collider Transport Line

Element	Length	Number	T (max)	T/m (max)
Dipole	1.4218 m	12	1.82	-
Quadrupole	40 cm	32	-	98.14

REFERENCES

1. A.S. Belov *et al.*, "High-intensity source of polarized negative hydrogen ions with a resonant charge-exchange plasma ionizer", Rev. Sci. Instrum. 67 (3), 1293 (1996).
2. A.S. Belov *et al.*, "Intensity improvements of pulsed source of polarized negative hydrogen ions", Rev. Sci. Instrum. 77, 03A522 (2006).
3. A.S. Belov, "Production of Polarized Ions with Nearly Resonant Charge-Exchange Collisions in Plasma", AIP. Conf. Proc. 980, 209 (2008).
4. A.S. Belov, *et al.*, "Source of polarized ions for the JINR accelerator complex", J. Phys.: Conf. Ser. 938 012017 (2017).

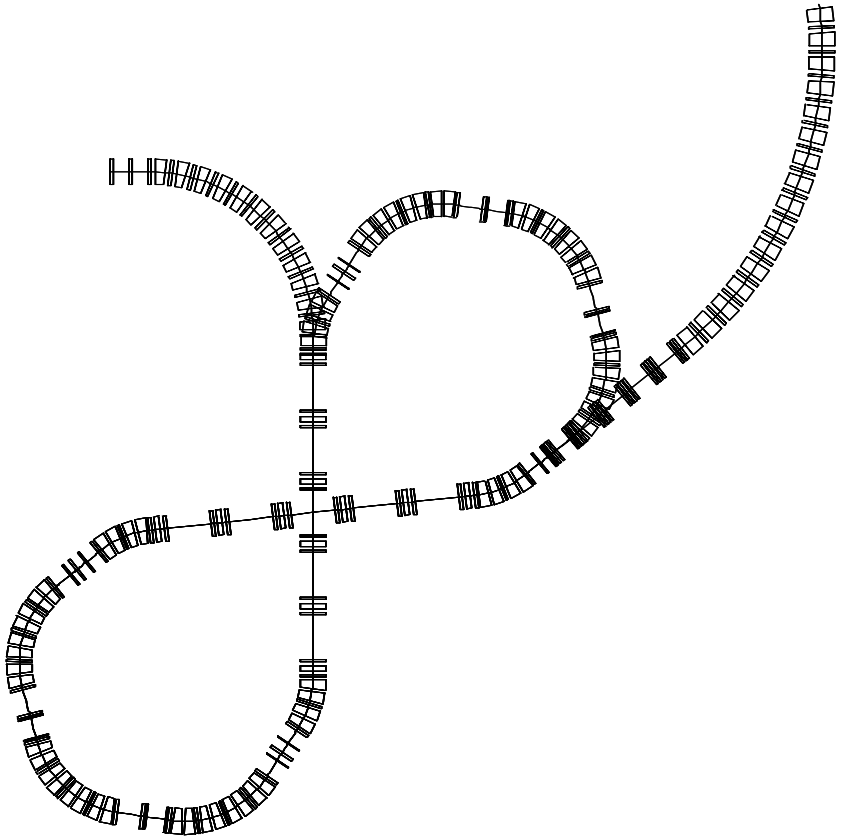

Figure 5.99: Overall footprint of the booster ring with the transport lines.

5. A.S. Belov, "A scheme for a polarized ^{3}He ion source with a resonant charge-exchange plasma ionizer", NIM A 402 (1998) 205-207.
6. A. Zelenski *et al.*, "The RHIC polarized H^- source", Rev. Sci. Instrum. 87, 02B705 (2016).
7. A. Zelenski *et al.*, "Optically-Pumped Polarized H^- and $3He^{++}$ Ion Sources Development at RHIC", Proc. IPAC2018, Vancouver, BC, Canada, TUYGBE4 (2018).
8. A. Zelenski *et al.*, "The RHIC polarized source upgrade", J. Phys. Conf. Ser. 295 (2011) 012147.
9. J. Maxwell *et al.*, "Development of a Polarized Helium-3 Source for RHIC and eRHIC", Int. J. Mod. Phys. Conf. Ser. 40, 1660102 (2016).
10. F. D. Colegrove, L. D. Schearer, and G. K. Walters, "Polarization of ^{3}He Gas by Optical Pumping", Phys. Rev. 132, 2561 (1963).
11. J.G. Alessi, "High-intensity, high charge-state heavy ion sources", Proc. LINAC 2004, MO202 (2004).
12. R.C. Vondrasek *et al.*., "Charge breeding of radioactive isotopes at the CARIBU facility with an electron beam ion source", Rev. Sci. Instrum. **89**, 052402 (2018).
13. E. Beebe *et al.*, "Reliable Operation of the Brookhaven EBIS for Highly Charged Ion Production for RHIC and NSRL", AIP. Conf. Proc. 1640, 5 (2015).
14. J. Alessi *et al.*, "High Performance EBIS for RHIC", Proc. PAC07, Albuquerque, New Mexico, FRYAB02 (2007).
15. V. Toivanen *et al.*, "Upgrade of the beam extraction system of the GTS-LHC electron cyclotron resonance ion source at CERN", Rev. Sci. Instrum. 87, 02B912 (2016).

16. V. Toivanen *et al.*, "Recent Developments with the GTS-LHC ECR Ion Source at CERN", Proc. ECRIS2016, Busan, Korea, WEAO01 (2016).

17. G. Machicoane *et al.*, "Status of ECR ion sources for the Facility for Rare Isotope Beams (FRIB)", Rev. Sci. Instrum. 87, 02A743 (2016).

18. A. Schempp *et al.*, "RFQ and IH accelerators for the new EBIS injector at BNL", Proc. of PAC'07, Albuquerque, New Mexico, USA, paper TUPAN021, pp. 1439–1441.

19. N. Angert *et al.*, "The IH Linac of the CERN Lead Injector", Proc. of LINAC'94, Tsukuba, Japan, pp. 743–745.

20. P. Ostroumov, "Warm and Cold Ion Linac: Comparison and Optimization", Presentation at the MEIC Collaboration Meeting, Jefferson Lab, Spring 2015.

21. R. York, "Status Report on Technology Evaluation for JLEIC Ion Linac", Presentation at the JLEIC Collaboration Meeting, Jefferson Lab, Spring 2016.

22. M. Kelly *et al.*, "Low Beta Cavity Development for an ATLAS Intensity Upgrade", Proc. of SRF'13, Paris, France

23. Z. Conway *et al.*, "Achieving High Peak Fields and Low Residual Resistance In Half-Wave Cavities", Proc. of SRF'15, Whistler, BC, Canada, paper WEBA05, pp. 973–975.

24. A. Sy and V. Dudnikov, "JLEIC Ion Source: Specifications, Design and R&D Prospects", Presentation at the JLEIC Collaboration Meeting, Jefferson Lab, Fall 2016.

25. A. S. Belov, "Polarized Ion Source with Nearly Resonant Charge-Exchange Plasma Ionizer: Parameters and Possibility for Improvements", Proc. of the 15th International Workshop on Polarized Sources, Targets and Polarimetry, September 9–13, 2013, Charlottesville, VA, USA, Proceedings of Science (PSTP 2013) p. 67.

26. J. Alessi *et al.*, "Design of a 35 keV LEBT for the New High Intensity OPPIS at BNL", Proc. of PAC'99, New York, NY, USA, paper WEA33, pp. 1964–1966.

27. N. Angert *et al.*, "CERN Heavy-Ion Facility Design Report", CERN Report 93-01, 28 April 1993, Geneva, Switzerland.

28. R. Ferdinand *et al.*, "Commissioning of SPIRAL2 CW RFQ and Linac", Proc. of IPAC'17, Copenhagen, Denmark, paper WEOAA1, pp. 2462-2465.

29. P. Ostroumov *et al.*, "Development and Beam Test of a Continuous Wave Radio Frequency Quadrupole Accelerator", Phys. Rev. ST Accel. Beams **15**, p. 110101, 2012.

30. A. Plastun *et al.*, "Design of the Room-Temperature Front-End for a Multi-Ion Linac Injector", Proc. of NA-PAC'16, Chicago, IL, USA, paper MOB4CO04, pp. 73–75.

31. A. Kolomiets and A. Plastun, "Spatially Periodic Radio-Frequency Quadrupole Focusing Linac", Phys. Rev. ST Accel. Beams **18**, p. 120101, 2015.

32. A. Leon *et al.*, "Charge State Distributions of Swift Heavy Ions Behind Various Solid Targets", Atomic Data and Nuclear Data Tables **69** pp. 217-238, 1998.

33. E. Nissen and T. Satogata "Revised Optics Design for the JLEIC Ion Booster" *Proceedings of the* 9^{th} *International Particle Accelerator Conference. (IPAC '18)* Vancouver, Canada, May 2018 THPAK126

34. Q. Li and J. Amundson "Synergia CUDA: GPU-accelerated accelerator modelling package," Journal of Physics: Conference series 513 (2014) 052021

35. Synergia Simulation Package `https://cdcvs.fnal.gov/redmine/projects/synergia2`

36. T. Satogata, "JLEIC Booster Ramp Parameters," JLAB, Newport News, USA, internal technical note JLAB-TN-17-034.

37. I. Sakai *et al.*, "Phase-Space Painting of Charge-Exchange Injection in the KEK Booster," Proceedings of the European Particle Accelerator Conference 1998, paper MOP24C.

38. A. Hatfield, E. Nissen, and T. Satogata, "Designing and Optimizing JLEIC Booster Injection," JLAB, Newport News, USA, internal technical note JLAB-TN-19-003.

39. M. Anerella *et al.*, "The RHIC magnet system", Nucl. Instrum. Meth. A **499**, 280 (2003).
40. F. Lin *et al.*, "Interaction region design and detector integration at JLab's MEIC", in Proc. of NAPAC'13, Pasadena, CA, USA, paper TUPAC28, pp. 508-510.
41. S. Abeyratne *et al.*, "MEIC Design Summary", arXiv:1504.07961 [physics.acc-ph] (2016), p. 52.
42. J. Wei, "Transition Crossing in RHIC", BNL Report AD/RHIC-84 BNL-45923 (1991).
43. W. Hardt, "Gamma Transition Jump Scheme of the CPS", Proc. 9th Int. Conf. on High Energy Acc., Stanford, April 1974, (CONF 740522, USAEC, Washington, 1974).
44. T. Risselada, Proc. CERN Accelerator School, CERN-91-04, p. 161, 1991.
45. H. Koiso and K. Oide, "Lattice Design for KEKB Colliding Rings", in Proc. of PAC'95, Dallas, TX (1995), p. 2780.
46. K.L. Brown, "A Second-Order Magnetic Optical Achromat", SLAC-PUB-2257 (1979).
47. MAD-X, `http://madx.web.cern.ch/madx/`
48. Y. Cai, M. Donald, I. Irwin, and Y. Yan, "LEGO: A Modular Accelerator Design Code", SLAC-PUB-7642 (1997).
49. G.H. Wei *et al.*, "Evaluation and compensation of detector solenoid", in Proc. of IPAC'16, Busan, Korea, paper WEPMW015, p. 2454.
50. Y. Nosochkov *et al.*, SLAC–PUB–14469 (2011).
51. K. Brown, "Single Element Optics", Handbook of Accelerator Physics and Engineering, 3rd edition, edited by A.W. Chao and M. Tigner (World Scientific, Singapore, 2006), p. 71.
52. M. Bassetti *et al.*, "Solenoidal field compensation", Frascati Phys. Ser. **10**, 209 (1998).
53. G. Ripken and F. Willeke, "Methods of Beam Optics", DESY 88–114 (1988).
54. G.H. Wei *et al.*, "Error correction for the JLEIC ion collider ring", in Proc. of IPAC'16, Busan, Korea, paper THPMR054, p. 3528.
55. M. Borland, "elegant: A Flexible SDDS-Compliant Code for Accelerator Simulation", Advanced Photon Source LS-287 (2000).
56. Y. Nosochkov *et al.*, "Detector Solenoid Compensation in the PEP-II B-Factory", in Proc. of PAC'95, Dallas, TX (1995), p. 585.
57. B. Bellesia *et al.*, Phys.Rev.ST-AB **10**, 062401 (2007).
58. S. Fartoukh, "Layout and Optics Solutions for the LHC Insertion Upgrade Phase I", sLHC Project Report 0038.
59. V.S. Morozov *et al.*, "Integration of detector into interaction region at MEIC", in Proc. of IPAC'12, New Orleans, Louisiana, USA, paper TUPPR080, p. 2011.
60. J. Breitschopf *et al.*, "Superferric arc dipoles for the ion ring and booster at JLEIC", in Proc. NAPAC'16, Chicago, IL, October 2016, paper MOPOB54, pp. 184-187.
61. G.H. Wei *et al.*, "Influence of magnet multipole field components on beam dynamics in JLEIC ion collider ring", in Proc. of IPAC'16, Busan, Korea, paper THPMR053, p. 3525.
62. D.A. Edwards and M. Syphers, "Longitudinal Motion", Handbook of Accelerator Physics and Engineering, 3rd edition, edited by A.W. Chao and M. Tigner (World Scientific, Singapore, 2006), p. 67.
63. A. Valishev *et al.*, in Proc. of PAC'09, Vancouver, BC, Canada, paper FR1PBC04, p. 4230.
64. V.S. Morozov *et al.*, "Injection Optics for the JLEIC Ion Collider Ring", in Proc. IPAC'16, Busan, Korea, May 2016, paper WEPMW012, pp. 2445-2447.
65. H. Cooper and V. Morozov, "JLEIC Ion Collider Ring Beam Losses and Collimation", JLAB, Newport News, USA, JLAB-TN-19-003.
66. N.P. Abreu, E. Choi, and H. Hahn, "Measurement and simulation of the RHIC abort kicker longitudinal impedance", C-A/AP/362, Sep. 2009, `https://www.bnl.gov/isd/documents/70529.pdf`

67. F. Méot, "The Ray-Tracing Code Zgoubi", Nucl. Instr. Meth A **427**, 353 (1999).
68. A.M. Kondratenko *et al.*, "Ion Beam Polarization Dynamics in the 8 GeV Booster of the JLEIC Project at JLab", in Proc. IPAC'16, Busan, Korea, May 2016, paper WEPMW017, pp. 2460-2462.
69. A.M. Kondratenko *et al.*, "Acceleration of polarized protons and deuterons in the ion collider ring of JLEIC", in Proc. IPAC'17, Copenhagen, Denmark, May 2017, paper WEPIK038, pp. 3014-3017.
70. A.M. Kondratenko *et al.*, "Ion Polarization Scheme for MEIC", arXiv:1604.05632 [physics.acc-ph] (2016).
71. Y. Nosochkov *et al.*, in Proc. IPAC'15, Richmond, VA, USA, May 2015, paper TUPWI032, pp. 2311-2314.
72. A.M. Kondratenko *et al.*, "Baseline Scheme for Polarization Preservation and Control in the MEIC Ion Complex", in Proc. IPAC'15, Richmond, VA, USA, May 2015, paper TUPWI029, pp. 2301-2303.
73. Ya.S. Derbenev *et al.*, "Polarization Preservation and Control in a Figure-8 Ring", Int. J. Mod. Phys. Conf. Ser. 40, 1660090 (2016).
74. A.M. Kondratenko *et al.*, "Spin Flipping System in the JLEIC Collider Ring", in Proc. NAPAC'16, Chicago, IL, October 2016, paper TUPOB30, pp. 558-560.
75. E. Leader, "Spin in Particle Physics", (Cambridge University Press, Cambridge, 2001).
76. V.P. Derenchuk and A.S. Belov, in Polarized Gas Targets and Polarized Beams, edited by R.J. Holt and M.A. Miller, AIP Conf. Proc. **421** (AIP, Melville, NY, 1998), p. 422.
77. R. Weidmann *et al.*, Rev. Sci. Instrum. **67**, 1357 (1996).
78. O. Felden *et al.*, in Proc. of the 9th International Workshop on Polarized Sources and Targets, Nashville, IN, 2001, edited by V.P. Derenchuk and B. von Przewoski (World Scientific, Singapore, 2002), p. 200.
79. V.S. Morozov *et al.*, "First Spin Flipping of a Stored Spin-1 Polarized Beam", Phys. Rev. Lett. **91**, 214801 (2003).
80. Proc. of the 3rd International Symposium on Polarization Phenomena in Nuclear Physics, Madison, 1970, edited by H.H. Barschall and W. Haeberli (University of Wisconsin Press, Madison, WS, 1971), p. xxv.
81. V.S. Morozov, "Using Spin Resonances to Manipulate the Polarization of Spin-1/2 and Spin-1 Particle Beams", Ph.D. dissertation, University of Michigan, Ann Arbor, MI (2007).
82. S. Nagaitsev *et al.*, "Experimental Demonstration of Relativistic Electron Cooling", *Phys. Rev. Lett* **96**, p. 044801, 2006.
83. B.R.P. Gamage, "Ion Bunch Formation Strategies for the JLEIC Collider", Ph.D. Dissertation, Old Dominion University, Aug. 2018.
84. J. Guo, "JLEIC Ion Beam Bunch Formation", Jefferson Lab Tech Note JLAB-TN-18-038, Aug. 2018.
85. W. Bartmann *et al.*, "Impact of LHC and SPS Injection Kicker Rise Times on LHC Filling Schemes and Luminosity Reach", in Proc. of IPAC'17, Copenhagen, Denmark, paper TUPVA007, p. 2043.
86. C.J. Gardner *et al.*, "Operation of the RHIC Injector Chain with Ions from EBIS", in Proc. of IPAC'15, Richmond, VA, paper THPF046, p. 3804.
87. V. Schoefer, "RHIC Injection Kicker Measurement and Emittance Growth Simulation", BNL internal note, C-A/AP/606, June 2018.
88. H. Zhang *et al.*, "Development of the Electron Cooling Simulation Program for JLEIC", in Proc. of IPAC'16, Busan, Korea, p. 2451.

CHAPTER 6

ELECTRON COOLING

There is no synchrotron radiation damping for JLEIC hadron beams, so beam cooling, must be introduced to deliver high luminosity performance. This beam cooling must create a significant reduction of the hadron beam emittance, by up to an order of magnitude in all directions, to deliver a very short bunch with a very small beam spot at the IP. It also must counteract Intra-Beam Scattering (IBS)-induced emittance degradation during beam store to extend the luminosity lifetime [1].

Conventional electron cooling, a proven technology, is chosen for the JLEIC design. We also adopt a scheme of multi-stage cooling [2, 3] for JLEIC, using electron cooling during formation of the ion beam (particularly including an initial cooling at low energy), and during collision. This enhances the overall cooling efficiency. This scheme is based on the observation that cooling time is proportional to ion beam emittance and beam energy, so electron cooling is much more efficient when the ion beam energy is low. At the collision energy, the cooling time is also reduced due to a much smaller ion beam emittance as a result of the initial low energy cooling. Combining both cooling phases, we expect that the total cooling time should be orders of magnitude shorter than cooling at only collision energy.

Table 6.1 summarizes the multiple cooling phases in JLEIC for a proton beam. DC electron cooling is first used to maintain the proton beam emittance in the collider ring at injection energy during stacking of long bunches transferred from the booster ring. After stacking is completed, the proton beam emittance is reduced by DC cooling to the design values of collision. The protons then are boosted to collision energy and promptly cooled by a high energy bunched electron beam from an ERL circulator cooler for conditioning and maintaining the beam emittance. Figure 6.1 provides an illustration of the JLEIC proton beam formation process with electron cooling.

Table 6.1: Multi-phase Electron Cooling Scheme for JLEIC Proton Beam

Ring	Functions	Kinetic Energy [GeV/MeV]		Cooler type
		Proton	Cooling electron	
booster	Injection and accumulation	0.285	—	—
collider	Maintain emittance during stacking	7.9	4.3	DC
	Pre-cooling for emittance reduction	7.9	4.3	DC
	Maintain emittance during collision	Up to 100	Up to 54.5	ERL

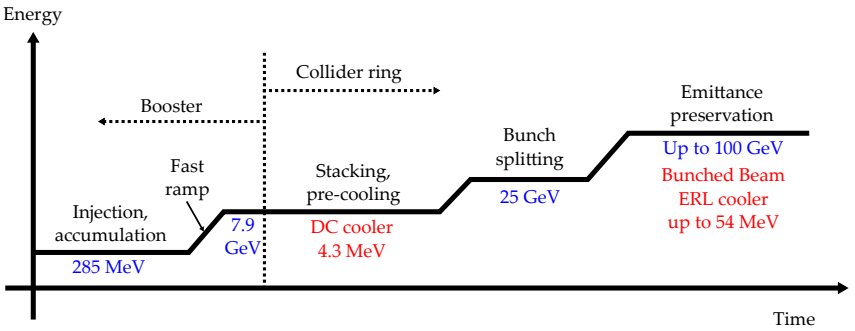

Figure 6.1: An illustration of JLEIC proton beam formation with electron cooling.

The multi-phase cooling of JLEIC heavy ions is similar, except that DC electron cooling is also used for assisting beam accumulation in the booster. As an example, shown in Table 6.2 and Figure 6.2, partially stripped lead ions ($^{208}Pb^{32+}$) are injected from the pulsed warm/SRF ion linac into the booster and accumulated with assistance of low energy DC cooling to increase the beam intensity. The accumulated lead ion beam is boosted to 2 GeV, and transferred to the collider ring for stacking with DC cooling preservation of its emittance. Unlike a proton beam, pre-cooling of lead ions for emittance reduction is performed not at the injection energy (2 GeV) due to the space charge limit, rather after the lead beam energy is boosted to 7.9 GeV, to alleviate the space charge effect. The cooling scheme after that stage is basically the same for proton and all ion beams.

Three electron coolers are required to implement the JLEIC cooling scheme. In the booster, a low voltage DC cooler similar to the one installed at IMP [4] with electron energy up to 55 keV is needed for cooling during ion accumulation. In the collider ring, a modest high voltage DC

Table 6.2: Multi-phase Electron Cooling Scheme for JLEIC Lead Ion Beam

Ring	Functions	Kinetic Energy [GeV/MeV]		Cooler type
		Proton	Cooling electron	
booster	Injection and accumulation	0.1	0.054	—
collider	Maintain emittance during stacking	2.0	1.1	DC
	Pre-cooling for emittance reduction	7.9	4.3	DC
	Maintain emittance during collision	Up to 40	Up to 54.5	ERL

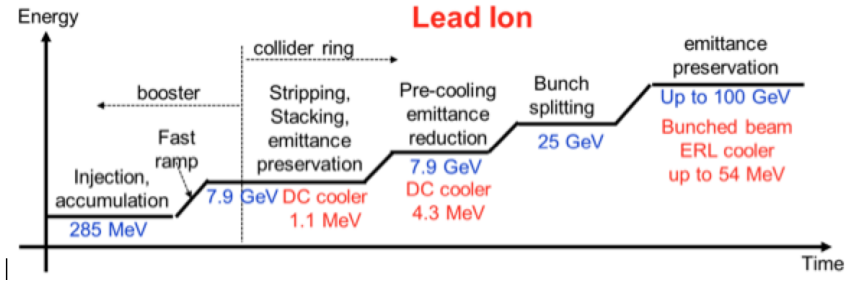

Figure 6.2: An illustration of JLEIC lead beam formation with electron cooling.

cooler similar to the one at COSY [5] but with electron energy up to 4.3 MeV is needed to pre-cool proton and ion beams for emittance reduction. In addition, a high energy bunched beam cooler with electron energy up to 54.5 MeV is needed for cooling of ion beams during collision.

The specifications for the three coolers are shown in Tables 6.3 through 6.7. The parameters are derived in Section 6.1.

Table 6.3: Design Parameters of the Low Energy DC Cooler in the Booster Ring

Parameter	**Units**	**Value**
Effective cooler length	[m]	5
Maximum beam energy	[MeV]	0.055
Maximum beam current	[A]	1
Beam pipe aperture	[mm]	80
Beam size (diameter)	[mm]	13
Longitudinal/transverse temperature	[eV]	0.1/0.1
Maximum magnetic field	[T]	1
Vacuum pressure in cooling section	[Torr]	$<1 \times 10^{-10}$

Table 6.4: Design Parameters of the High Energy DC Cooler in the Ion Collider Ring

Parameter	**Units**	**Value**
Effective cooler length	[m]	30
Maximum beam energy	[MeV]	4.3
Maximum beam current	[A]	3
Beam pipe aperture	[mm]	80
Beam size (diameter)	[mm]	10
Longitudinal/transverse temperature	[eV]	0.1/0.1
Maximum magnetic field	[T]	1
Vacuum pressure in cooling section	[Torr]	$<1 \times 10^{-10}$

Table 6.5: Electron Beam Specifications for the Collider Bunched Beam Electron Cooler. The repetition rate is for the case of highest proton luminosity. For the highest center of mass energy, the repetition rate is lowered to match the proton beam.

Parameter	**Units**	**Value**
Electron energy	[MeV]	20–55
Charge	[nC]	1.6 (3.2)[1]
CCR pulse frequency	[MHz]	476.3
Gun Frequency	[MHz]	43.3
Bunch length (top-hat)	[cm/°]	2/11.4
Thermal (Larmor) emittance	[mm-mrad]	19
Cathode spot radius	[mm]	3.1
Cathode magnetic field	[T]	0.05
Normalized hor. Drift emittance	[mm-mrad]	36
rms Energy spread (uncorr)		3×10^{-4}
Energy spread (p-p corr.)		6×10^{-4}
Cooler solenoid field	[T]	1
Electron beta in cooler	[cm]	36
Solenoid length	[m]	4×15
Bunch shape		Beer can

[1] Cooling simulations assume a charge of 3.2 nC. The emittance in the CCR ends up being a very strong function of charge; however due to CSR effects in the arcs. It is possible to maintain a small emittance for a charge of 1.6 nC.

Table 6.6: Assumed Proton Beam Specifications for Peak Luminosity

Parameter	**Value**	**Units**	**Comment**
Energy	100	[GeV]	
Particles per bunch	1×10^{10}		
Repetition rate	476.3	[MHz]	
Bunch length (rms)	1	[cm]	
Normalized emittance (x/y)	0.5/0.1	[mm-mrad]	
Betatron function in cooler	100	[m]	(at point between solenoids)

Table 6.7: Assumed Proton Beam Specifications for Maximum Center of Mass Energy

Parameter	Value	Units	Comment
Energy	100	[GeV]	
Particles per bunch	4×10^{10}		
Repetition rate	119.1	[MHz]	
Bunch length (rms)	2.2	[cm]	
Normalized emittance (x/y)	0.9/0.18	[mm-mrad]	
Betatron function in cooler	100	[m]	(at point between solenoids)

6.1 Cooling Simulations and Requirements

6.1.1 Simulation Program (JSPEC) Development

JSPEC (Jlab Simulation Package for Electron Cooling) [6, 7] is an open source numerical package for IBS effect and electron cooling process simulation developed at JLab. The goal of JSPEC is to enhance the simulation capability for electron cooling in JLEIC project. It preferentially fulfills the needs of JLEIC design. The program simulates the evolution of the macroscopic beam parameters, such as emittances, momentum spread and bunch length, in different electron cooling scenarios with any combination of bunched or coasting ion beam with DC or bunched cooling electron beam.

The emittance change rate due to the IBS effect can be calculated using several different formulas under different assumptions of the ion beam profile and lattice parameters [8, 9, 10, 11]. JSPEC uses the Martini model [9] for the IBS rate calculation. The Martini model assumes a Gaussian distribution for the ion beam, which is a reasonable assumption at least to first order, and the absence of vertical dispersion of the lattice, which is true for JLEIC booster and collider rings.

The electron cooling rate is defined as the emittance change per unit time due to the electron cooling effect, which is calculated by the Monte Carlo model. The ion beam is sampled as a Gaussian bunch whose rms size is determined by the given emittance and the TWISS parameter at the cooler. The friction force due to the magnetized cooling on each ion will be calculated using the Parkhomchuk formula [12]. Assuming the friction force is constant while the ion passes through the cooler, the change of momentum of each ion can be calculated. Then the new emittance and the rate of change of the emittance can be statistically calculated.

The evolution of the ion beam under the IBS effect and/or electron cooling effect is simulated by a four-step procedure, which can be described as follows: (1) initialize the computational environment; (2) create the sample ions, (3) calculate the IBS rate and the electron cooling rate, and (4) update the beam parameters, such as emittance, momentum spread, and/or bunch length, update the sample ions, and repeat from (3). The ion beam can be represented by the macro-parameters, e.g. emittance, momentum spread, bunch length, etc., assuming it has Gaussian distribution. The ion beam can also be represented by sample particles, which allows to simulate any charge distribution.

JSPEC has been thoroughly benchmarked with BETACOOL [13] for accuracy and efficiency. All cooling simulations detailed here are performed using JSPEC. Each phase of JLEIC cooling is summarized in the following subsections.

6.1.2 DC Cooling in the Booster Ring

Heavy ion beams are injected into the booster ring at 100 MeV/u. During the phase space painting injection process, electron cooling is needed to enhance the ion density in the booster ring. At this energy, traditional DC electron cooling is very efficient and is considered a mature technique. Simulations show that a 5 m long cooling solenoid with 1 A of electron current can easily reduce the emittance to about 0.3 mm-mrad. This is actually so small that it will lead to space charge problems so a hollow beam or lower current will be used to reduce the cooling to a level where the emittance is maintained.

No cooling of the protons in the booster is needed. They will be cooled after acceleration to 8 GeV.

6.1.3 DC Cooling in the Collider Ring

Once the beams have been injected into the collider ring they can be cooled using a DC cooler that overlaps the higher energy bunched beam cooler and uses half of the same 1 T solenoid. The magnetized DC electron beam operates up to 3 A at 4.2 MeV.

Protons are injected at 7.9 GeV and are cooled after stacking and bunch formation before being accelerated to the final energy. At 7.9 GeV and with a peak current of less than 2 A, the IBS is not strong enough to significantly heat the beam during stacking. Once the beam has been formed into bunches with a 2 cm rms bunch length, the DC cooler is used to improve the beam brightness. Equilibrium is reached within 15 minutes. The emittance is reduced to below 0.5 mm-mrad and the momentum spread to 4×10^{-4}. Acceleration to the collision energy does not change the normalized emittance or momentum spread.

Ion beams are injected at 2 GeV and their emittance must be maintained as the beam is accumulated. The IBS rate for an uncooled beam is substantial. Only 0.62 A of electron beam current is necessary to maintain a transverse emittance of 1.5 mm-mrad and a momentum spread of 6×10^{-4} in a lead ion beam. Once the beam has been stacked, it can be accelerated to 7.9 GeV where space charge forces are smaller and then cooled enough that the emittances can be maintained up to the final energy. The transverse emittances of a lead ion beam are reduced to less than 0.4 mm-mrad and the energy spread is reduced to 4×10^{-4} in less than one minute using a 2 A electron beam.

6.1.4 Bunched Beam Cooling in the Collider Ring

JLEIC covers a wide center-of-mass (CM) energy range from 21.9–63.3 GeV. The property of the proton beam varies for different CM energies. In the following, we present preliminary simulation results on the cooling of the proton beam for 44.7 GeV CM energy and for 63.3 GeV CM energy. This is the most challenging part of the JLEIC cooling scheme, due to the high energy and high density of the proton beam. The high particle density results in a stronger IBS effect, while the high energy reduces the cooling effect. The property of both the proton beams is listed in Table 6.8.

Assuming a bunched electron beam with 3.2 nC per bunch is used to cool the proton beam, the initial cooling rates are calculated and shown in Tables 6.9 for both CM energies. Due to the absence of vertical dispersion, the IBS effect in the vertical direction is much weaker than that in the horizontal direction. In both cases, the horizontal IBS expansion rate is more than a factor of ten larger than the vertical one. The cooling in the vertical direction and the longitudinal direction is much stronger than the IBS effect, but in the horizontal direction the cooling is not strong enough to mitigate the IBS effect.

Introducing proton beam dispersion at the cooler transfers the extra longitudinal cooling into the transverse direction. Introducing transverse coupling can translate the horizontal IBS effect

Table 6.8: Proton Beam Parameters for 44.7 and 66.3 GeV CM Energy

Parameter	**Unit**	44.7 GeV	66.3 GeV
Kinetic energy	[GeV]	100	100
Emittance	[mm-mrad]	0.5/0.1	0.9/0.18
Momentum spread	[$\times 10^{-4}$]	8	8
Particle number	[$\times 10^{-10}$]	0.98	3.9
Bunch length	[cm]	1	1

Table 6.9: Initial Expansion Rate for 44.7 (66.3) GeV CM Energy

Rate	**Unit**	**x**	**y**	**z**
IBS	$10^{-3}\,s^{-1}$	12.894 (3.192)	0.669 (0.102)	0.992 (0.618)
Cooling	$10^{-3}\,s^{-1}$	-4.675 (-0.431)	-11.752 (-1.434)	-11.043 (-1.605)
Total	$10^{-3}\,s^{-1}$	8.291 (2.761)	-11.083 (-1.332)	-10.005 (-0.987)

into the vertical direction, which then can be mitigated by the extra vertical cooling. However, it is still very difficult to fully compensate the IBS effect with cooling even after introducing the dispersion and transverse coupling. In the following, a few examples are presented in which the IBS effect and the electron cooling are in equilibrium or close to the equilibrium and the emittance of the proton beam is maintained. The proton beam charge is slightly lowered to reduce the IBS effect. The left side of Figure 6.3 shows the proton beam for 44.7 GeV CM energy cooled by a 3.2 nC/bunch electron beam. The emittance remains constant. The momentum spread decreases very slowly. The current of the proton beam is 82% of the proposed value in Table 6.4 (0.80×10^{10} protons per bunch). Transverse coupling of 40% is assumed.

Figure 6.3 (right) shows the proton beam for 66.3 GeV CM energy cooled by a 3.2 nC/bunch electron beam. The cooling and the IBS are in equilibrium and the emittance and the momentum spread remain constant. The current of the proton beam is 38% of the proposed value in Table 6.5 (1.48×10^{10} protons per bunch). Transverse coupling of around 40% is assumed.

The proposed luminosity is considered achievable after further optimization of the cooling process in future.

6.1.5 Cooling during collision for the heavy ion beam

The heavy ion beam is accelerated to 40 GeV/u for collision. Cooling by the ERL bunched beam cooler is also applied to maintain the emittance. Simulations show that cooling is much easier for the heavy ion beam than for the proton beam. Taking the lead ion, $^{208}Pb^{82+}$, as an example, an electron beam of only 0.8 nC/bunch is used to cool the lead ion beam. Equilibrium is reached within two minutes and the emittance remains close to the proposed value consistently.

6.1.6 Studies on Improving the Cooling Efficiency

The preliminary simulations revealed the following challenges for the high energy bunched beam electron cooling of the JLEIC proton beam:

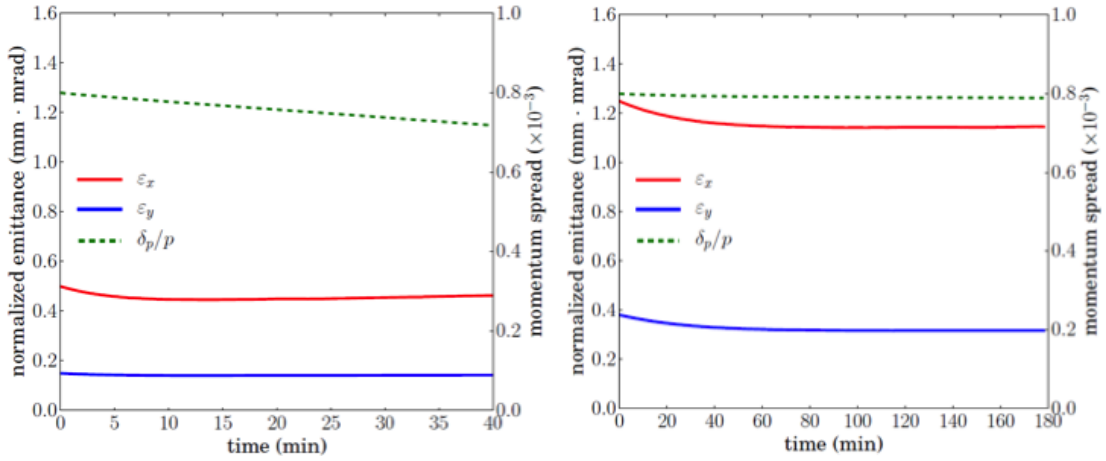

Figure 6.3: Proton beam (44.7 GeV CM energy left, 63.5 GeV CM energy right) cooling during collision with 3.2 nC electron beam.

- Unbalanced IBS effect: the IBS induce emittance growth rate in the horizontal direction is much larger than those in the other two directions;
- Overcooling in the longitudinal direction: the increased phase space density due to the longitudinal cooling enhances the IBS effect in the transverse directions and make the transverse cooling, especially the horizontal cooling, even more difficult;
- Cooler technology gap: the capability of the cathode and ERL, and the collective effects in beam transport in the circulator ring limit the achievable electron bunch charge.

In the following we briefly discuss some measures that may help to overcome the challenges and strengthen the cooling scheme, these concepts and scheme are under investigation.

6.1.6.1 Maintaining a constant proton bunch length during cooling As noted earlier, at collision energies and with very short bunches, the horizontal IBS emittance growth rate is one order of magnitude stronger than the rate in any other directions. The electron cooling rates are close to each other in all three directions. Transverse coupling can only redistribute and balance the transverse IBS. Cooling in the longitudinal direction increases the phase space density of the proton beam, which further increases the IBS growth rates. As an example, Figure 6.4 shows results of a simulation in which an electron beam with 3.2 nC bunch charge is used to cool a bunched 100 GeV proton beam with 70% transverse coupling and up to 0.9 m dispersions at the cooling section. Each bunch has 3×10^{10} protons, about 30% of the JLEIC design value. The simulation shows, due to the fast reduction of the momentum spread and the bunch length, the horizontal IBS emittance growth rate increases to 3×10^{-3}/s and overwhelms the horizontal cooling.

If the RF voltage can be adjusted as the momentum spread goes down during cooling, we can maintain a constant proton bunch length. Figure 6.5 (right) shows a simulation with constant proton bunch length. The number of protons is 0.5×10^{10}/bunch and the transverse coupling is 55% while all the other parameters remain the same as in Figure 6.4 (left). These simulation results suggest that maintaining constant bunch length will make the high energy bunched beam cooling easier, especially in the horizontal direction.

In all the previous simulations, it was assumed that both ion and electron beam have a round transverse cross section inside the electron cooler. The vertical emittance of the ion beam is smaller than the horizontal emittance. To achieve a round beam, the vertical beta function is enlarged

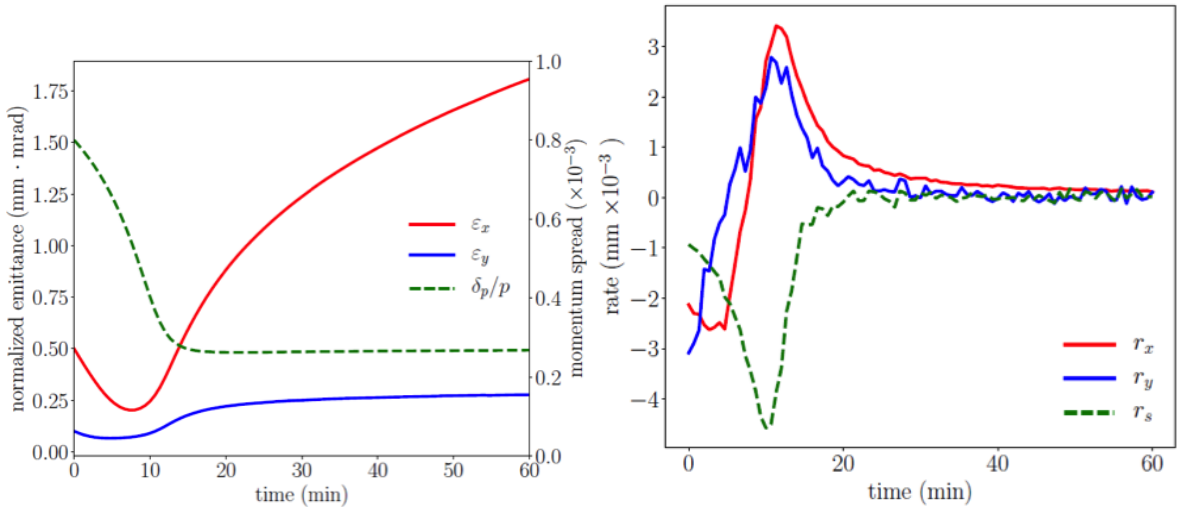

Figure 6.4: Overcooling in the longitudinal direction (left) leads to an explosion in the transverse directions (right).

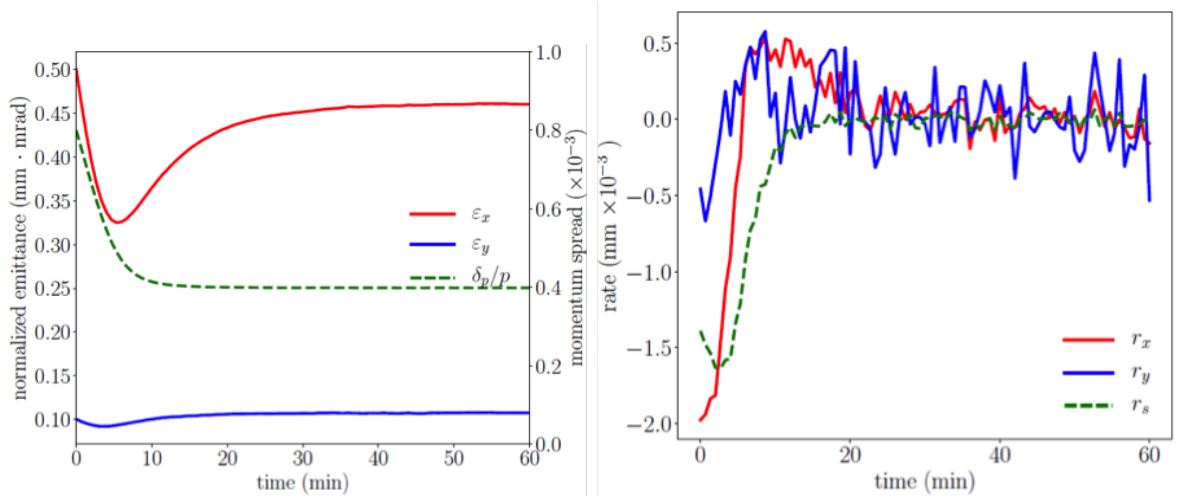

Figure 6.5: Cooling with constant proton bunch length (left) and cooling by a flat electron beam (right).

respectively. However, a round shape does not necessarily provide the best cooling effect, so we studied cooling by a flat electron beam, namely, the vertical size of which is smaller than the horizontal size, on a flat ion beam, assuming the flat magnetized electron beam is achievable.

When cooling with a round electron beam, we assume the ion beam has a Gaussian distribution transversely with an RMS radius of σ and the electron beam has a beer can shape of a radius σ with uniform charge density. When cooling with a flat electron beam, the ion beam has a Gaussian distribution with the RMS sizes σ_{x}, σ_{y} ($\sigma_{\mathrm{x}} = \sigma$,$\sigma_{\mathrm{x}} \gg \sigma_{\mathrm{y}}$) in the horizontal and vertical direction. The cross section of the electron beam will be an ellipse, the semi-major radius of which is $r_{\mathrm{x}} = \sigma_{\mathrm{x}}\sqrt{\sigma/\sigma_{\mathrm{y}}}$ and the semi-minor radius of which is $r_{\mathrm{y}} = \sigma_{\mathrm{y}}\sqrt{\sigma/\sigma_{\mathrm{y}}}$. In such a way, the electron beam emittances remain unchanged in the two cases. We find that the flat beam electron match provides 30% more cooling than does the round beam case.

6.1.6.2 Introducing a velocity gradient to the electron beam In our simulations, it is always assumed velocity of the electron beam has a Boltzmann distribution and that the temperature of the electron beam is uniform inside the bunch. However, a radial gradient of the longitudinal velocity may be created by the space charge field or by a non-adiabatic impact of transverse forces related to imperfections of the electron gun optics. This gradient will therefore lead to a radial gradient of the longitudinal friction force and hence a redistribution of the strength or decrements of the friction between the longitudinal and transverse directions. The redistribution of the cooling can help to mitigate the difficulty due to the imbalance of the IBS effect. When the longitudinal friction force dominates over the transverse forces, the redistribution can speed up the equilibrium.

6.1.6.3 Dispersive cooling Another way to introduce the radial gradient of the longitudinal friction force is to create a transverse gradient of the electron density. A convenient way to create the electron density gradient is to place the electron bunch, assumed to be smaller than the ion bunch, asymmetrically relative to the ion beam center. Generally we can represent the electron density as $n_{\mathrm{e}}(x, y) = n_0 + (\partial n_{\mathrm{e}}/\partial x)x + (\partial n_{\mathrm{e}}/\partial y)y$. Not only the constant part of the density, n_0, contributes to the change of the dynamic invariant; but also the gradient part make a contribution in proportion to $D_{\mathrm{x}}/\beta_{\mathrm{x}}(\partial n_{\mathrm{e}}/\partial x)$ or $D_{\mathrm{y}}/\beta_{\mathrm{y}}(\partial n_{\mathrm{e}}/\partial y)$ respectively, which enhances the electron cooling.

6.1.6.4 Sweeping technique In current simulations, we also assume the electron beam and the ion beam move with the same longitudinal speed. However, intentionally introducing a relative speed between them enhances cooling; this is called the "sweeping" cooling technique. To be specific, if we change the electron beam velocity with time at a rate of $(dv_{(e\|)})/dt = F_{\max}/M$, where $F_{\max}$ is the maximum friction force on an ion and M is the ion mass, and pass through the whole width of $\Delta v_{\|}$, where $\Delta v_{\|}$ is the longitudinal velocity spread of the ion beam, the ion will be sequentially captured into a relatively narrow region of maximum friction and will remain there and thus the cooling will be accelerated. In the case of JLEIC, the electron beam is strongly magnetized. The use of sweeping is usually beneficial and the magnetization can increase its efficiency manyfold. The aforementioned topics provides ideas to enhance the cooling effect by strategically arranging the cooling process and to achieve the desired cooling with lower technical risk on the electron gun, ERL and beam transport.

6.2 Booster DC Cooler

A low energy magnetized DC electron cooler is needed in the JLEIC booster ring for providing electron cooling at very low ion injection energy to assist accumulation of heavy ions. This technique has been used in many ion complexes worldwide. For example, a DC cooler was installed in the CSRe ring of the Heavy Ion Research Facility at Lanzhou (HIRFL-CSR) at Institute of Modern Physics (IMP), China [16]. It supports ion accumulation with ion injection energy from 10–50 MeV, but it could also continuously cool the accumulated ion beam while it is accelerated up to 600 MeV/u, such as U^{91+} at 400 GeV/u and C^{6+} at 600 GeV/u. Similarly, a 100 keV electron cooler was installed for accumulation of injected protons at 45 MeV in the COSY synchrotron accelerator and storage ring at Nuclear Physics Institute (IKP), Juelich, Germany [17].

In the JLEIC ion booster ring, the injection energy of the lead ion beam in the booster is 100 MeV/u. The main parameters of this DC cooler are summarized in Table 6.3. At this low energy range, the conventional magnetized DC electron cooler has been mature since the 1980s. Figures 6.6 shows the magnetized DC cooler EC-35 at CSRe ring at IMP [18]. The compact facility includes the following components: magnetized thermionic electron gun, accelerating tube, electron transport system with two bending toroids, cooing section with a solenoid, decelerating tube and

electron collector. There are also control system and vacuum system. The control system includes a set of dipole steering coils providing corrections of both electron and ion trajectories, and various beam diagnostic equipment such as beam current transformer and x-y beam position monitors. The electron gun generates a magnetized electron beam with desired property, e.g. transverse size, energy spread, etc., then the beam is accelerated in a DC aperture. The magnetized electron beam is guided by a longitudinal magnetic field along the beam transport direction. In the cooling section, the electrons are merged with the ions and move together, while taking heat away from ions through Coulomb collisions. The temperature of the Larmor circle is usually much lower than the temperature of the free electrons, hence the magnetized electron beam provides much stronger cooling than the non-magnetized one. At the end of the cooling section, the electrons are separated from the ions, then decelerated and dumped in the collector. Such a system may be purchased as a turn-key device.

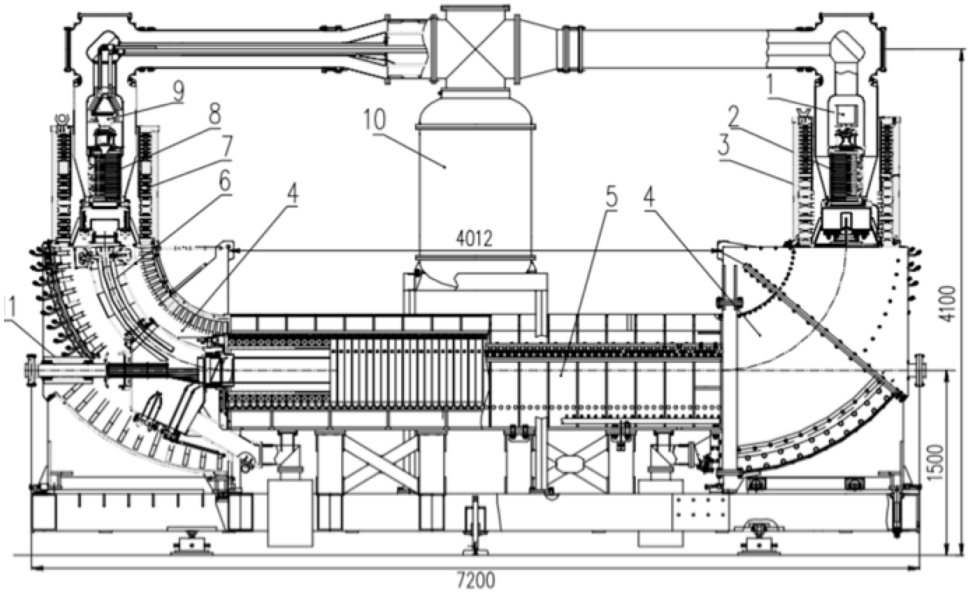

Figure 6.6: A technical drawing of the CSRe DC cooler at HIRFL-CSR of IMP, China.

6.3 Low-Energy Collider DC Cooler

A high voltage DC electron cooler is needed in the JLEIC ion collider ring to suppress IBS-induced emittance growth during stacking of long ion bunches transferred from the ion booster, and for providing a pre-cooling of both proton and ion beams. Since the injection energy of protons and lead ions into the collider ring are 8 GeV and 2 GeV/u respectively, the kinetic energy range of a cooling electron beam is 4.3–1.1 MeV. This DC cooler should be able to provide up to 3 A average current. The length of the cooling channel is 30 m. The cooling electron beam must be magnetized to achieve the required cooling efficiency. The solenoid field in the cooling section is 1 T. Table 6.4 summarizes the main design parameters of the high voltage DC cooler.

Such a high energy relativistic DC cooler is considered near the technological state-of-the-art. The Fermilab recycler DC cooler has been the highest electron beam energy cooler [19] at 4.3 MeV. This is the same energy as the JLEIC cooler; however, the Fermilab electron cooler beam is not magnetized. The newly constructed high voltage DC cooler at COSY, Juelich has a 2 MeV magnetized electron beam [20, 21]. It is at this writing the highest-energy magnetized cooling ring. The COSY cooler started operation in 2013, and has achieved cooling in all three dimensions [22].

The 2 MeV Cooler for COSY-Juelich is shown in Figure 6.7. It is composed of the following major components: electron gun, accelerating tube, electron transport system, cooling section, deaccelerating tube and electron collector, as well as the magnetic system, control system, and vacuum system. Figure 6.8 is a technical sketch of the facility. The basic features of the cooler design are

- the longitudinal magnet field from the electron gun to the collector, in which the electron beam is embedded;
- unlike other low energy coolers, the COSY cooler electron gun and collector are placed at the common high voltage terminal; and
- the power for magnet field coils at accelerating and decelerating column is generated by turbines operated on SF gas under pressure.

Specifically, the cathode of the electron gun is immersed in a magnetic field for magnetizing the beam. The electron beam is accelerated to 2 MeV. After that the electron beam is bent in the toroid and is guided to the cooling section for cooling ions. The electron beam is then returned to the electrostatic column for deceleration and finally absorbed in the collector. Each toroid consists of two parts. The first one bends the magnetized electron beam 90° in the vertical plane. The second one bends the electron beam 180° in a plane which is inclined 45° to the vertical plane. Such a complicated 3D geometry provides the compactness of the system, which is critically important for fitting the cooler into the existing beamline and available space in the COSY facility. The dipole kick for protons in the bending toroids near the cooling section will be compensated by dipole magnets which will be installed as near as possible to the large toroid coils. The electrons receive dipole kicks due to the inhomogeneity of the magnetic field. These kicks are compensated by electrostatic kickers inserted in front of the cooling section. The control system includes dipole steering coils and another special coils to provide corrections of both electron and ion trajectories/profiles. It also includes various beam diagnostic equipment such as a beam current transformer and x-y beam position monitors.

Compared to the 2 MeV COSY cooler, the DC cooler in the JLEIC ion collider ring needs higher energy, higher current and longer cooling section. With accelerator R&D, it is reasonable to expect a magnetized DC cooler similar to 2 MeV COSY cooler could be designed and developed with a similar but improved technique for JLEIC.

6.4 Collider ERL Cooler

6.4.1 Overall Design

The specifications for the bunched beam cooler in the collider are listed in Table 6.5. Note the very high circulating current in the cooler itself of 1.5 A for 1.6 nC bunches. Such a high repetition rate of high charge bunches for an electron source is significantly beyond ERL state of the art. We therefore plan to use a Circulating Cooler Ring (CCR) to lower the average current required from the electron source. A pair of harmonic kickers will be used to inject and extract bunches from the

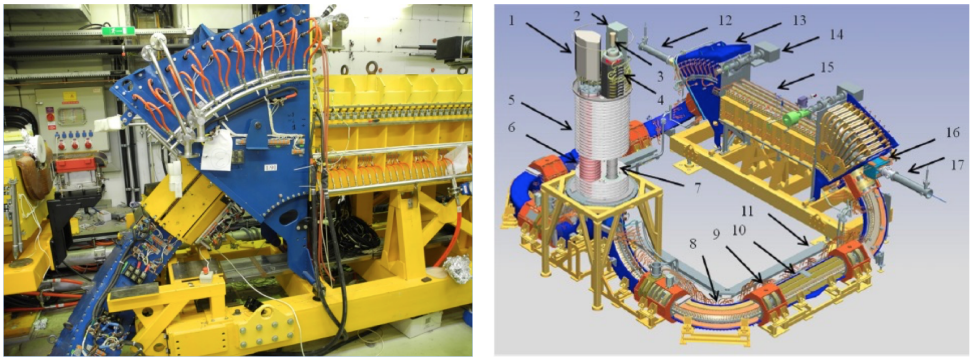

Figure 6.7: 2 MeV COSY cooler (left) and 3D engineering drawing (right). The major components of the cooler are labeled in the drawing: 1. collector PS; 2. SGF system; 3. ion pump of collector; 4. collector with magnetic system; 5. HV section; 6. cascade transformer; 7. acceleration tube; 8. 90 degree bend; 9. straight section; 10. line section; 11. cable path; 12. input of the proton beam; 13. Toroid; 14. vacuum pump; 15. cooling section; 16. ion dipole; 17. output of the ion beam.

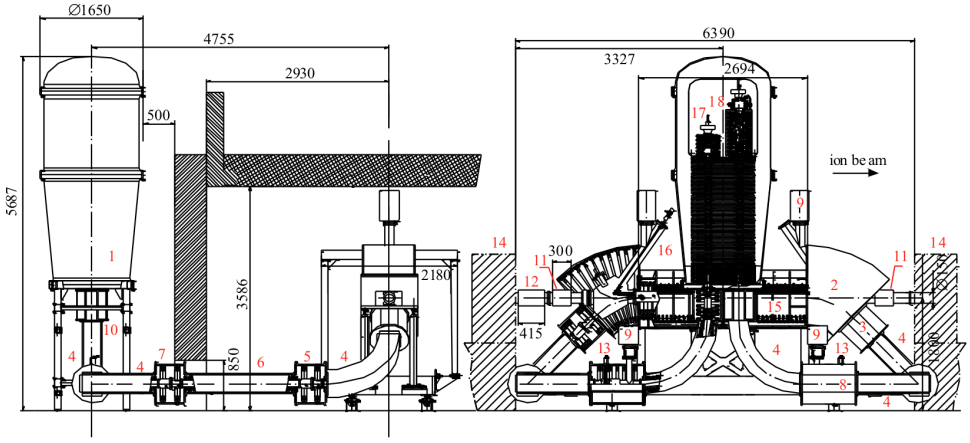

Figure 6.8: Sketch of the 2 MeV Cooler for COSY-Julich. 1. High voltage tank; 2. 45° toroid; 3. magnetic system of the transition section from 45° toroid to the transport channel; 4. magnetic system of the 90° bend; 5. magnetic systems of the straight line 0.5 m; 6. the straight section 1.7 m; 7. 5 magnetic systems of the straight line 0.5 m; 8. the straight section 0.88 m; 9. the pump; 10. the transition section accelerating tube — transport; 11. the dipole correction of the ion beam; 12. the fast ramping kicker; 13. the vacuum gate; 14. the quadrupole lens of COSY ring; 15. the cooling section; 16. the rotary motion feedthrough to the vacuum for the magnetic compass probe; 17. the electron gun; 18. the electron collector.

CCR and deliver them from and to an Energy Recovery Linac (ERL). The number of circulations in the CCR must be coprime with the harmonic number in the CCR so that all bunches are kicked in and out. We have chosen 11 turns as a compromise between injector average current and beam degradation in the CCR. The CCR circumference will be 340 RF periods long at 476.3 MHz. The number of circulations and the number of bunches in the CCR then have no common factors.

As with the lower energy DC coolers, cooling is much stronger when a magnetized beam is used to cool the protons or ions. Unlike the DC coolers however, the magnetized beam must be transported through accelerating sections and asymmetric focusing elements. The magnetization must be

preserved throughout the transport. Simulations have shown that a "beer can" distribution, with a flat top temporal profile and a uniform transverse profile is slightly preferable to a Gaussian-like distribution. We have chosen the edges of this distribution to correspond to the rms dimensions of the proton beam. The uniform distribution survives transport better under the effects of CSR and space charge. A Gaussian bunch would develop more of high frequency energy variation that cannot be corrected by a simple RF cavity. With a flat top bunch, the energy loss and energy slope can be corrected by choosing the phase and gradient in a simple RF cavity in the CCR, though as will be seen, energy tails develop that must be controlled.

The drift emittance is determined by the spot size in the cooler but the thermal emittance specification must be determined by the fall-off of the cooling with increasing thermal emittance. We have found that we can tolerate a rather large emittance of 19 mm-mrad before the cooling falls greatly. The energy spread must be determined by simulations as well. There are two parts of this. There is a specification for the relative energy spread at any position in the microbunch as well as a specification on the variation of the mean energy during the microbunch. The worst case is assumed to be a sinusoid, with peak-to-peak variation equal to the value in Table 6.5.

The length of the cooling solenoid is determined by the field strength and available room on the collider straight section. A stronger solenoid field would provide slightly more cooling but would also make the beam large in the rest of the ring and would make kicking the bunches into and out of the CCR more difficult. We have split up the magnet into several sections with opposite field directions to minimize the effect of the cooler solenoid on the ion or proton spin. We then introduce "helicity swap" sections that introduce a parity reversal in the electron beam. This reverses the sense of the magnetization in the electron beam to match the reversed solenoid polarity. This must be done twice (or an even number of times) in a CCR so that the magnetization on the next pass is correct. We have then chosen to use four segments to make the system symmetric.

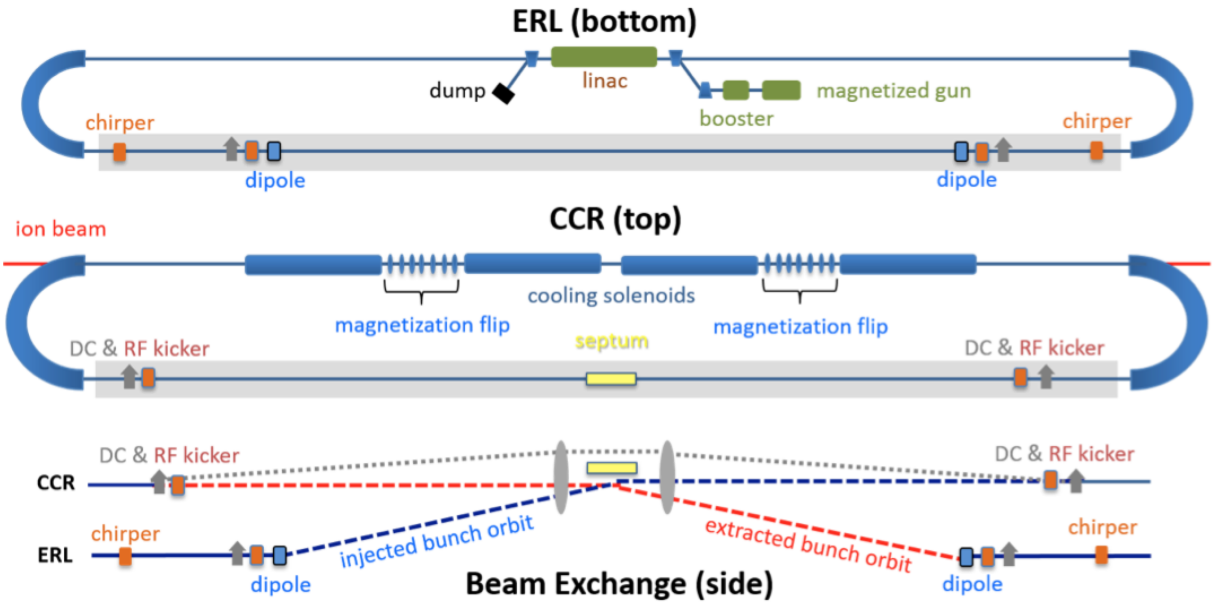

Figure 6.9: Electron cooler layout. See text for full description.

As shown in Figure 6.9, high charge bunches are produced in a magnetized gun, accelerated to greater than 5 MeV, and merged into a linac that accelerates the electrons up to a speed that

matches those of the protons or ions in the collider ring. The bunches are prepared to match the longitudinal phase space necessary for the cooling channel. They are then deflected upwards to a septum and kicker, which injects them into the Circulating Cooler Ring. The bunches are then circulated 11 times in the ring before being kicked out and energy recovered in the original linac structure.

A key design goal is preserving the small projected energy spread and so we must avoid gross distortion due to CSR and longitudinal space charge over a single (or multiple) recirculations. Accurately modeling the relevant collective effects in the system — space charge, microbunching instability, CSR and the effect of CSR shielding — in addition to beam dynamical processes such as halo, presents a formidable challenge. There are no simulations codes that model all of these effects, so we have derived an approach towards the design, analysis and optimization of the accelerator system using a combination of existing codes to estimate the overall behavior of the system.

The foundation upon which the ERL is designed is the longitudinal match, which not only dictates the machine topology, but also clearly defines the specifications of key lattice sections. These include defining the linac energy gain and phase operating point (both accelerating and decelerating passes), the required momentum compactions (first- and higher-order) of the arcs, and the need for components such as chirpers, de-chirpers and/or chicanes for additional longitudinal manipulations.

The longitudinal match is predicated on the initial beam conditions from the injector. The injected bunch length is constrained on the low end by space charge (too short a bunch degrades beam quality) and on the high end by linac phase acceptance (too long and the linac RF-imposed curvature is too great to manipulate downstream). With an injector solution giving a bunch length of 1.8 cm (full), the working longitudinal match has the beam accelerated from 7 to 55 MeV/c while sitting at -20° from crest to impart a phase-energy correlation along the bunch. Because the bunch is already at the ideal length for the cooling channel, the first arc must be isochronous to first-order (R_{56}=0) but use higher-order momentum compactions to linearize the bunch. Upon exiting the arc, there still remains a large phase-energy correlation which must be removed. A de-chirper cavity run at the zero-crossing removes that correlation. To prepare for energy recovery, we need to reverse the process. Following the CCR and its transport back to the ERL, a chirper cavity is run at the other zero-crossing to impart a phase-energy correlation along the bunch. The recovery arc arranges the momentum compactions so that when the beam is decelerated through the linac 180° out of phase (160° from crest), the bunch is linearized and nearly mono-energetic at the dump.

6.4.2 Component Design

6.4.2.1 Injector The design of the CCR injector is demanding due to the need to preserve the magnetization of high charge bunches from the cathode to the linac. Simulations make assumptions that beam charge and current can be delivered from a multi-alkali photocathode inside a 400 kV DC electron gun and this has not been demonstrated at the full required current. Otherwise, components have been chosen conservatively. The complete beam parameters for the injector are listed in Table 6.3 Additionally, cooling simulations indicate that a bunch with uniformly filled cylinder shape produces slightly improved cooling over bunches that have Gaussian longitudinal and transverse characteristics. Therefore a “beer-can” volume is preferred.

A schematic layout of the injector is shown in Figure 6.10. A DC gun is immersed in the field of a Helmholtz coil (magnetizing solenoid), which is assumed to give a uniform longitudinal magnetic field over the diameter of the photocathode. This is followed by an additional traditional solenoid, buncher cavity, further focusing, a capture cavity, a final solenoid and a booster unit containing 4 double-cell cavities. The fundamental frequency of the RF is 952.6 MHz to be compatible with

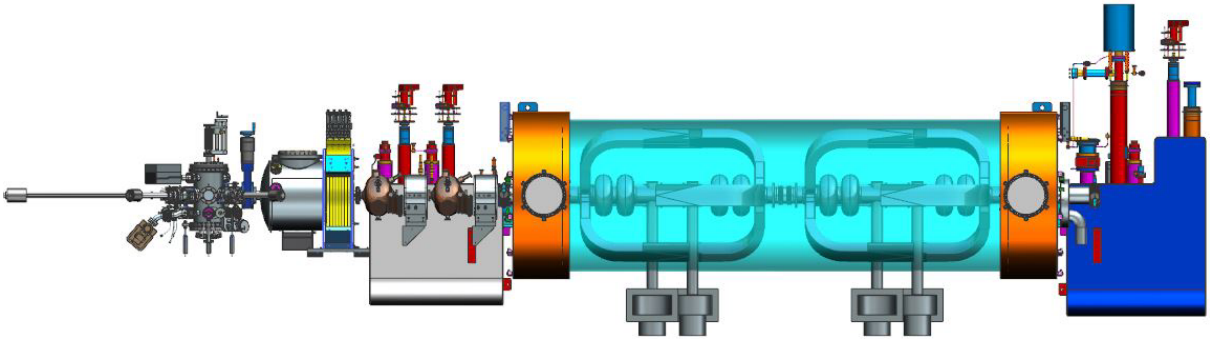

Figure 6.10: ERL cooler injector schematic.

the ion collider ring frequency. The tracking code General Particle Tracer (GPT) was used for the optimization of this injector, and to avoid discrepancies in the off-axis field computation at large radius, 2D or 3D field maps were employed wherever possible in the simulation. The magnetic field on the cathode is chosen specifically, in conjunction with the transverse emitting size to result in a drift emittance, d (that associated with the canonical angular momentum) of 36 µm, calculated using:

$$\epsilon_d = \frac{eB_{\mathrm{cath}}a_0^2}{8m_{\mathrm{e}}c} = 36\,\mu\mathrm{m} \tag{6.4.1}$$

where e is the electron charge, m_{e} is the electron mass, c is the speed of light, B_{cath} is the field at the cathode, and a_0 is the beam transverse radius (assuming a radial, uniform distribution). The drift emittance is chosen so that when the beam arrives at the cooling channel that it is cancelled by the cooling solenoid field, such that:

$$B_{\mathrm{cath}}a_0^2 = B_{\mathrm{cool}}\sigma_{\mathrm{e}}^2 \tag{6.4.2}$$

B_{cool} and e are the field and beam radius at the cooler, fixed at 1 T and 0.7 mm respectively. All other component settings are considered free variables within realistic limits. The objectives of the optimization were to minimize the 4D transverse emittance, minimize longitudinal emittance, and create a long bunch of 2 cm with a small uncorrelated energy spread. The results in Figure 6.11 show the bunch evolution through the injector beamline.

The magnetized gun assumed in the simulations is based on a 400 kV DC gun operating with a multi-alkali photocathode. The gun has a typical Pierce geometry for the electrodes, 10 cm apart and a flat cathode. The magnetizing solenoid in the simulations is from a Helmholtz coil that provides a uniform magnetic field over the emitting area. This gun, along with other components in the injector can satisfy the specification at 1.6 nC and with some transverse emittance degradation, at 3.2 nC also. It is believed that improvements in the 3.2 nC case can be made with a higher cathode gradient and overall gun energy, such as that from a low frequency CW, NCRF gun. This state-of-the-art approach will require more development over the DC option.

To support the choice of a DC gun and to investigate the properties of magnetized beams at low energy, an R&D project has been running for some years at JLab in the Gun Test Stand. Measurement and simulation of this experiment show good agreement, reinforcing our understanding of magnetized beam transport and evolution.

In the JLEIC configuration, the transverse emitting area is rather large with a 8 mm diameter and has an emission time of 24 ps rms. This is required to extract 1.6 nC bunches from the cathode with a surface electric field of 4.3 MV/m.

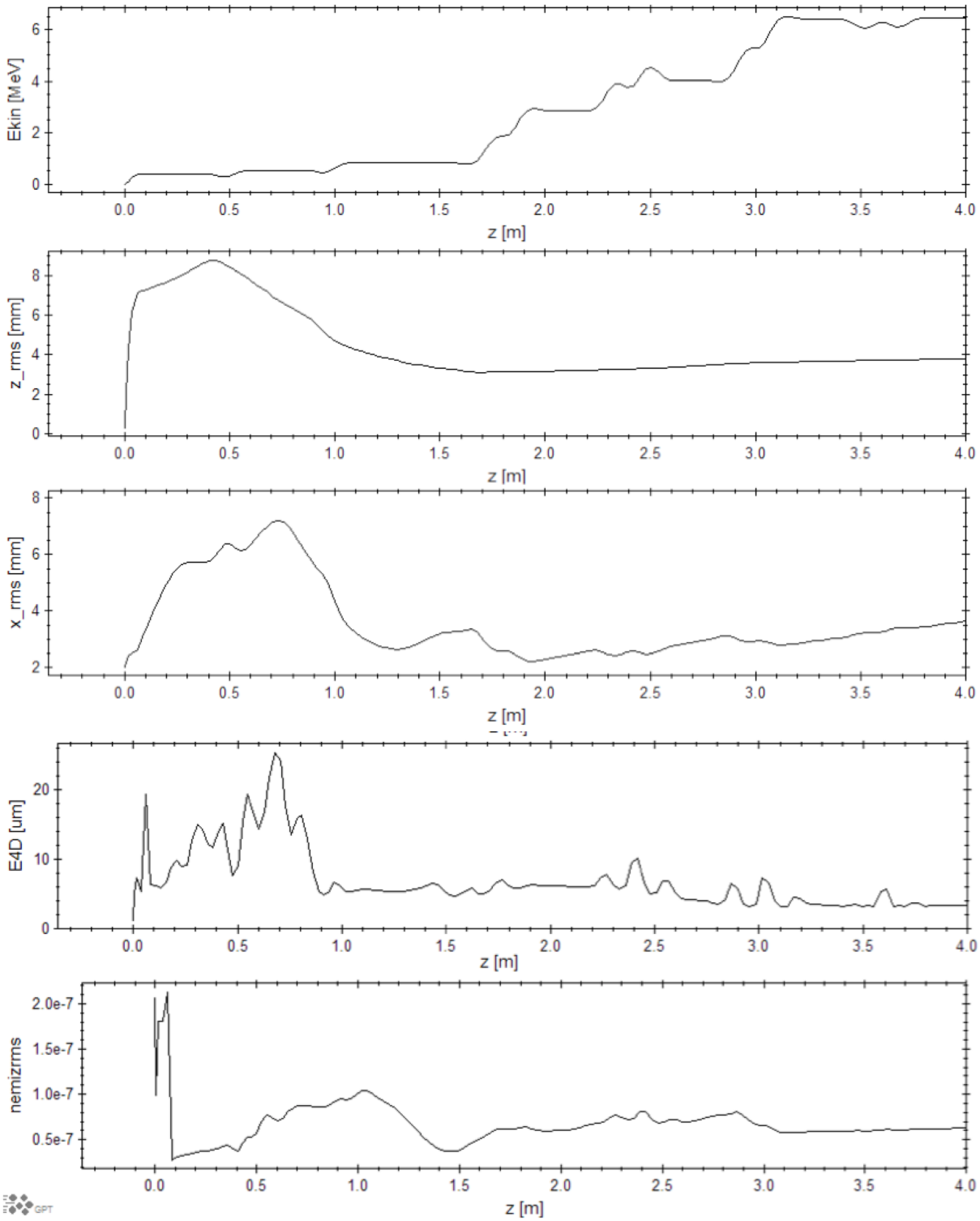

Figure 6.11: Bunch evolution through the injector beamline: (a) average kinetic energy, (b) longitudinal rms beam size, (c) horizontal rms beam size, (d) horizontal normalized rms emittance, (e) longitudinal normalized rms emittance.

As the bunch progresses through the fringe of the Helmholtz coil, which is 1% of peak on-axis value at 50 cm, it acquires angular momentum due to Busch's principle of conservation. Transverse space charge forces, and solenoid focusing are also acting to determine beam properties in this region. While the bunch is at low energy, below ∼2 MeV in this scenario, space charge forces dominate both transversely and longitudinally. Beyond this energy the angular momentum of the beam dominates the transverse dimensions, whilst the longitudinal progression is still affected by space charge.

Longitudinally, the bunch is compressed in both the buncher and capture cavities. The capture cavity is also phased to provide some energy gain that would facilitate better acceleration in the beta=1 cavities of the booster. Each booster cavity increases the kinetic energy by ∼2 MeV resulting in an average of 6.3 MeV with a 0.75 MeV full energy spread. The longitudinal emittance remains small, as shown in Figure 6.11, owing to the small uncorrelated energy spread. The full bunch length, shown in Figure 6.13, is ∼1.7 cm as required. The final cavity of the booster does not serve a function in this particular 1.6 nC set up. However, a solution for 3.2 nC that meets specification has been generated using this same beamline layout, so the cavity was left in the optimization.

In the transverse plane, the beam size is determined by a balance between the angular momentum of the beam and solenoid and RF focusing. At the exit of the injector, the beam has a full ∼1.5 cm diameter. The resulting transverse emittance is 38 µm, which is a combination of thermal, space charge and angular momentum contributions. If all the transverse correlations are removed, and the ultimate 4D emittance calculated, this yields the emittance as will be seen by the ion beam. This has been calculated as 3.5 µm. In an ideal magnetized beam, with no degradation from the cathode, the r-phase space would be a thin line with a small width indicative of a small thermal energy contribution from the photocathode. Here slight degradation from space charge at low energy and non-linear off axis field effects can be seen in Figure 6.12.

Future studies for the injector will further optimize the 3.2 nC solution and look for improvements with using a lower frequency for all cavities in the injector.

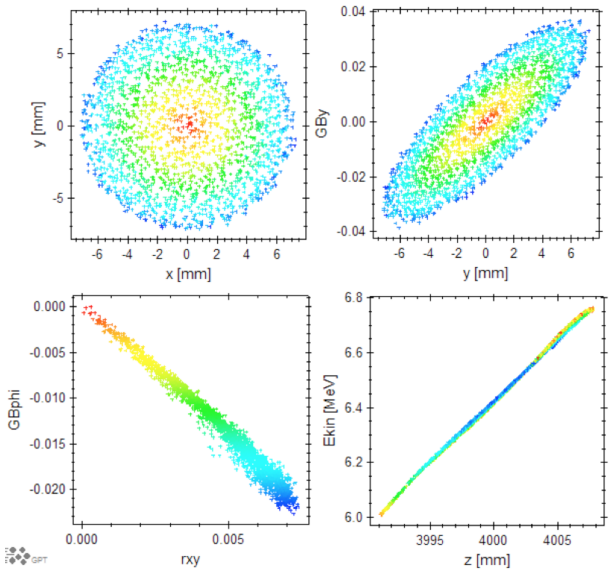

Figure 6.12: Phase space at the exit of the injector for 1.6 nC bunches: (a) configuration space (color scale p), (b) longitudinal phase space, (c) radial phase space, (d) horizontal phase space.

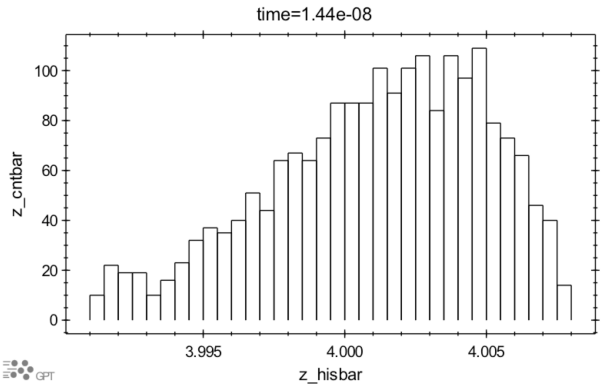

Figure 6.13: Longitudinal histogram of the bunch.

The final part of the injector merges the injected beam with the energy recovered beam from the ERL. This must be done in such a way that both the transverse and longitudinal emittances are not increased significantly and the magnetization is not degraded. We have been looking at several approaches to this:

- Existing coolers transport the electron beam in a long solenoid that keeps the beam contained and magnetized. Since the injector beam energy is not much higher than that in a conventional DC cooler it is tempting to use this approach for the merger. A big issue with this approach is that the ratio of the two merged beam momenta is typically on the order of 2000 or higher. In the JLEIC cooler ERL the ratio could be as low as 3. The effect of the toroidal transport needed to get the beam into the linac on the energy recovered beam must be calculated and the beam quality preserved. Initial simulations indicate that we can preserve both high and low energy beams [23]. Further optimization will be performed.
- Most ERLs use a magnetic merger design. To preserve the magnetization, it is necessary to make the magnets as symmetric as possible between the x and y axes [24]. Further optimization will also be performed here. Space charge forces at such a low energy make such a design very challenging.
- It should be possible to use a transverse deflection cavity similar to those used in pulse measurements systems, combined with a static magnetic field, to allow the injected beam to proceed straight into the linac. The RF and static deflections will cancel to first order. The energy recovered beam, arriving 180° out of phase from the injected beam, will have its RF deflection added to the magnetic deflection. It will be significantly deflected. A septum magnet can then be used to further separate the two beams. We have done some preliminary measurements of such a deflector on a straight-through beam and found the effects on the beam to be in agreement with modeling results [25].

6.4.2.2 Linac The linac is a high-current capable ERL comprised of six 5-cell SRF cavities operating at 952.6 MHz, twice the baseline ion bunch repetition rate. This is a compromise between linearity and acceptance at low frequency and compactness and ease of manufacture at high frequency. The second harmonic is a good balance, is compatible with future upgrades to higher bunch rate, and is in a frequency range where high-power RF sources are available. The cavity shape is an evolution of the JLab Ampere class ERL cavity [26] and uses a similar waveguide end group Higher Order Mode (HOM) damping scheme. This provides strong damping of cavity HOMs to prevent regenerative BBU, and can handle high average HOM power. Although the

average current of 138.6 mA is much less than in storage rings, the sparse filling pattern (every 11^{th} bucket filled) produces a dense current spectrum with many lines, increasing the probability of HOM power being excited. High power broadband absorbers are used to safely dissipate the HOM power at room temperature. For compactness coaxial power couplers are used. A high degree of modularity is employed between the ERL cavity, injector cavities and the ion storage ring cavities. Geometrically similar couplers can be used with the ERL versions requiring only modest power while the injector and storage ring cavities require high power. Significant HOM power will propagate down the beam pipe at high frequency so warm beam-pipe absorbers are envisaged at the ends of the cryomodules.The entire linac is quite compact and measures about 8.0 m in length.

Assuming a phase operating point of 20° before crest (specified from the longitudinal match) and assuming beam is injected at 7 MeV/c, each cavity is operated at a modest gradient of 10.85 MV/m. The main linac parameters are shown in Table 6.10. A first prototype single cell cavity of this shape has been built and tested and comfortably exceeded this specification [27]. A bare five-cell version has also been completed and will be tested soon. Once the HOM and FPC geometries have been finalized these end groups will be added to the five-cell for final design verification. Figure 6.14 shows the ERL cavity concept, while Figures 6.15 and 6.16 show the single cell result and the 5-cell cavity prototype respectively.

Table 6.10: Main Cooler ERL Linac Parameters

Parameter	**Value**	**Units**
Geometry	6	five-cell low-loss cavities
Energy gain	15–48	[MV]
Required gradient	11	[MV/m]
Required Q	10^{10}	
Base frequency	952.6	[MHz]
Aperture	>70	[mm]
Maximum HOM Q	10^4	
Operating temperature	2.0	[°K]

6.4.2.3 Ion Clearing Gaps If ion accumulation is a problem in the ERL or CCR ion clearing gaps can be introduced by periodically interrupting the bunch stream. By eliminating bunches in a specific order a clean gap can be developed in the CCR and then refilled, without introducing a large beam-loading transient in the ERL. However missing bunches in the injector could result in a large transient so it may be better to produce the bunches continuously and kick unwanted bunches out to a dump before injection into the linac. Since the bunch spacing is every 11 buckets at this point and the energy is only 5 MeV the kicker requirements would be modest.

6.4.2.4 Energy Recovery Linac Arc The high bunch charge needed for effective cooling rates forces the optimized injected bunch length to be fairly long (21° at 952 MHz) which in turn forces acceleration of the bunch far enough off-crest so as to not allow the bunch to fall over crest. Consequently, the projected energy spread going into the arc is 9% (full). This requires arc designs for the ERL that have large momentum acceptance in addition to tunable higher-order momentum compactions for linearizing the bunch. Because the bunch only passes through the ERL arcs a single time, the microbunching gain requirements can be slightly relaxed compared to those of the CCR arcs (see

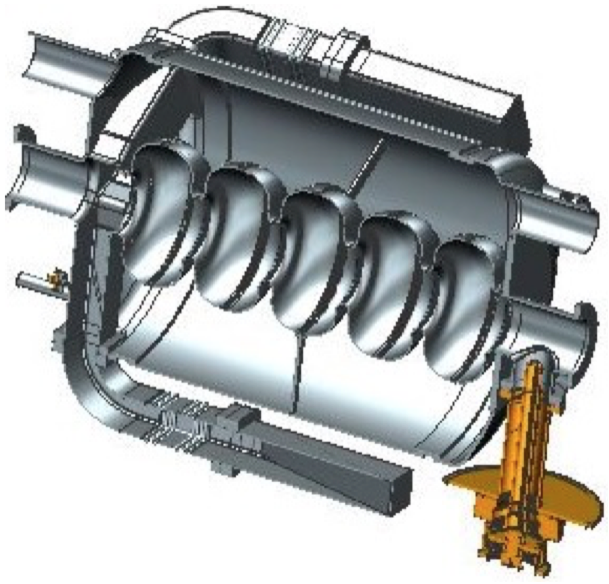

Figure 6.14: Cooler ERL cavity concept.

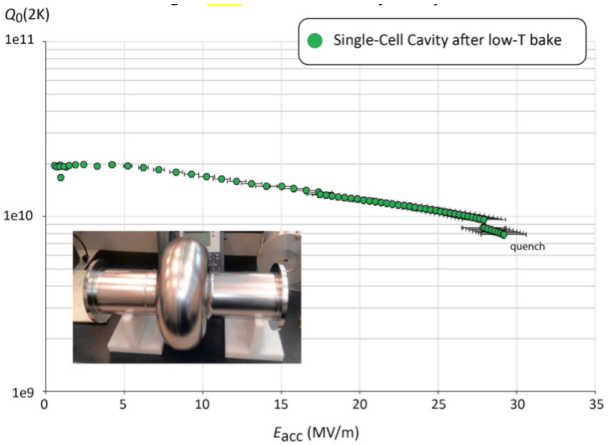

Figure 6.15: Cooler ERL cavity single cell test results.

next section). We have designs for a variety of different recirculation arcs which are currently being assessed for their ability to handle a large energy spread beam.

6.4.2.5 Circulator Cooler Ring Arc The CCR arcs present a unique challenge in that they must preserve beam quality (magnetization, transverse emittance, energy spread) during 3960° (11 recirculations) of bending. The most significant figure of merit when assessing possible architectures is the microbunching instability gain. For multiple passes, the gain scales roughly as: $G^{N\text{passes}}$. Therefore, even a modest gain of 1.5 for a single pass will become unacceptably large (1.5^{11}=471) after 11 recirculations. In terms of momentum compaction management, the arcs must be isochronous (both first- and second-order) to maintain the same 2 cm (full) bunch length at the cooling channel from turn to turn. An arc that meets these requirements has been demonstrated through simulations [28]. The arc was intentionally designed to be simple, in the sense that it does not have high

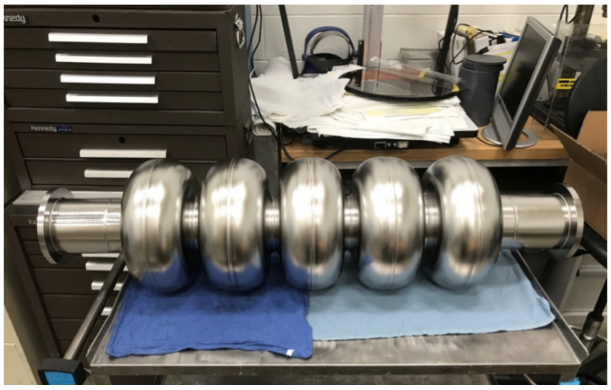

Figure 6.16: Cooler ERL five-cell cavity prototype.

periodicity (it only has 4 dipoles) nor does it try to maintain local axial symmetry throughout (though it is globally axially symmetric) [29]. A schematic is shown in Figure 6.17.

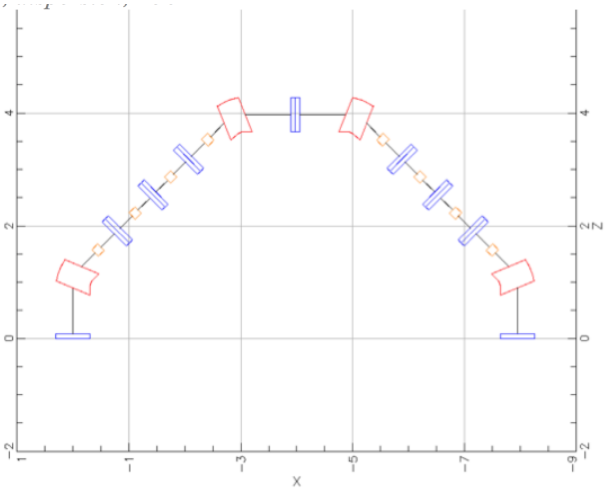

Figure 6.17: Layout of the CCR arc where red markers denote dipoles, blue markers denote quadrupoles and orange markers denote sextupoles.

6.4.2.6 Beam Exchange Region The ERL to CCR beam exchange is based on use of a fast RF kicker to deflect selected bunches, allowing them to betatron oscillate so as to evolve a displacement [30]. This displacement ensures the bunch of interest resides in the high field region of a septum magnet, which is used to bend the exchanged bunch into/out of the circulation beam line.

The basic concept of the exchange is presented in Figure 6.18. An incoming ERL bunch is dechirped after traversing the ERL recirculation arc. It is then bent upward by a vertical dipole, and brought parallel to the plane of the CCR by the field of the exchange septum. It is then focused toward the CCR back-leg axis by the downstream transport, reaching an orbit node at an injection fast kicker. The kicker removes the angle, merging the injected bunch into the CCR bunch train. It is thereafter available for cooling. The process is reversed for the extracted bunch before it is chirped and transported back to the linac.

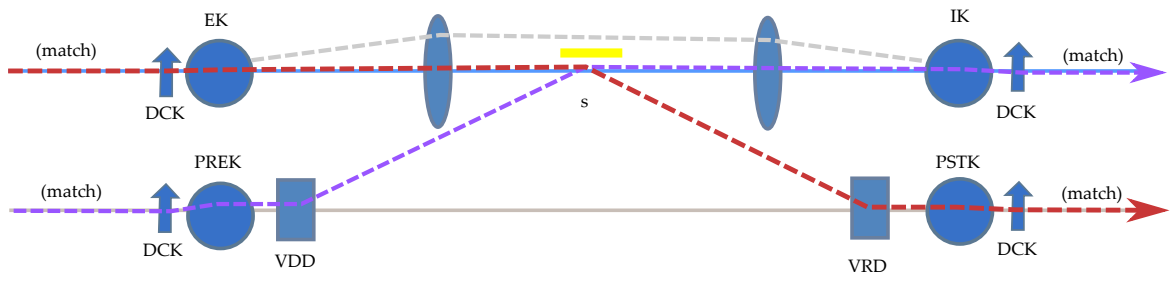

Figure 6.18: Schematic of the beam exchange region.

An extracted bunch is deflected downward by the fast kicker, generating an offset that directs the bunch into the septum, whereupon it is directed toward the plane of the ERL. A vertical bend brings the bunch orbit onto to the plane of the ERL; a re-chirper imposes a phase/energy correlation on the bunch, and the downstream exchange-to-linac recirculation arc compaction is used to recompress the bunch prior to reinjection and energy recovery with energy compression.

6.4.2.7 De-Chirper With a proper choice of momentum compactions, the ERL arc will linearize the bunch. However to meet the energy spread specification for the cooling channel, the phase energy correlation must be removed. This is achieved in the de-chirper which is a single 5-cell 952 MHz cavity operated at zero-crossing. With a gradient of 15 MV/m the phase energy correlation is removed.

6.4.2.8 Harmonic Kicker A harmonic kicker system in the CCR, as shown in Figure 6.19, delivers a transverse harmonic kick. This harmonic kick is a linear combination of 5 odd harmonic modes with the base frequency f_k =86.6 MHz to deflect incoming (outgoing) electron bunches from the injection transport (to the extraction transport) to get them on to (off of) the CCR. The system consists of injection kicker, extraction kicker, pre-kicker, and post-kicker [31]. As for an extraction kicker, the electron bunch at E_e =55 MeV is deflected 2.5 mrad downward to the extraction transport by a total kick of 137.5 keV. Being combined harmonic modes, the kick is sharply peaked at the kick frequency, which corresponds to every 11th incoming bunch.

We have adopted a new waveform synthesis scheme [32] that uses only five odd harmonics of the base frequency and a DC offset voltage so that the number of required cavities for each kicker can be reduced to one at the cost of a slightly higher total RF power and larger voltage slopes for the residual kicks. The waveform is shown in Figure 6.19 (left), and Table 6.11 lists the specification of the harmonic components of the waveform. The small "residual" of the kick on the 10 unkicked bunches can be cancelled out by injection kicker, which is the same device physically separated from the extraction kicker with betatron phase advance of odd harmonics of π. To suppress the emittance growth specially at cooling channel/the ERL, the voltage for the injected/extracted bunches needs to be constant over the whole the bunch length. For that reason a single frequency (952.6 MHz) pre-kicker and post-kicker are conceived in the injection and extraction transport line, respectively, that will linearize the RF curvature imposed by the multi-mode kicker (see Figure 6.19 (right) and Table 6.11).

The simulation using ELEGANT shows in Figure 6.20 that introducing a pre-kicker to kicker system leads to an improved longitudinal structure of angular divergence compared to without pre-kicker case [33].

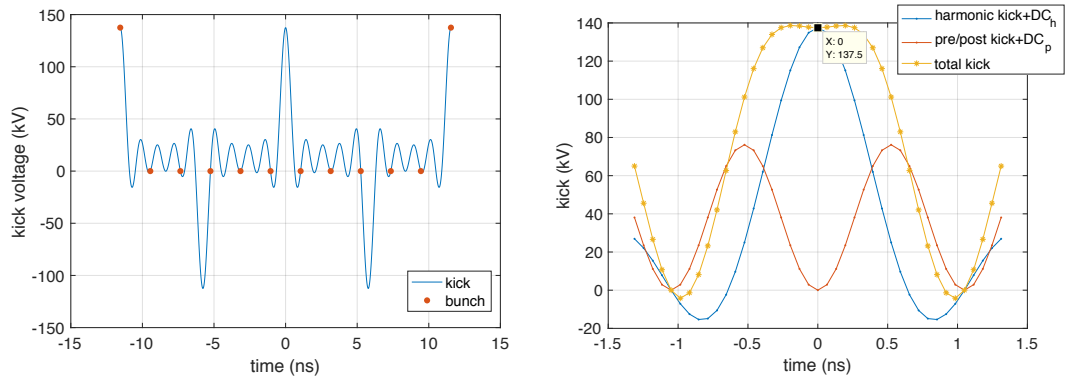

Figure 6.19: Kick profile of the harmonic kicker. (left) Temporal profile of the harmonic kick. (right) Temporal profile of the injection (extraction)-kick with a 952.6 MHz pre (post-) kicker added.

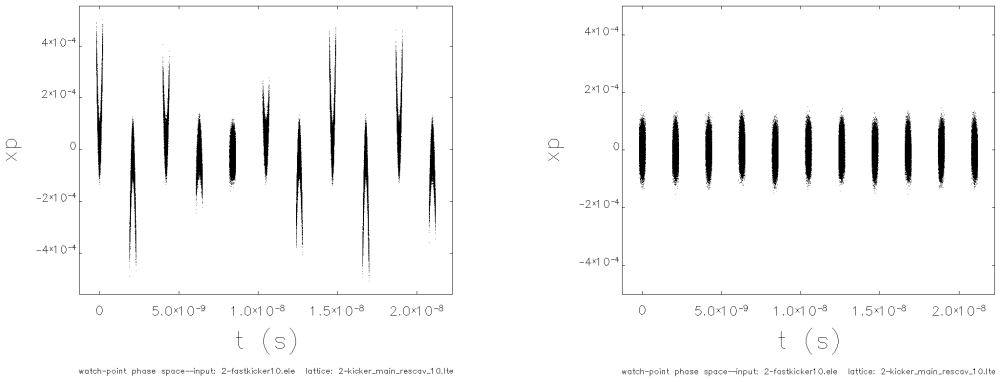

Figure 6.20: Longitudinal profiles of the angular divergence, x_{p}, at the cooling channel for an electron bunch circulating 11 turns. (left) Harmonic kicker only (without pre-kicker). (right) With pre-kicker.

The harmonic kicker is based on a normal conducting quarter wave resonator (QWR) cavity, whose lowest 5 TEM modes constitute a harmonic kick [34]. The structure of the cavity is shown in Figure 6.21 (left). See [35] for a more detailed design description.

To control the beam loss to minimum level, the gap size g and beam pipe aperture R_{a} are determined via beam dynamics simulations to be $\pm 6\sigma$ =0.07 m, where σ is the rms transverse beam size at the kicker. The cavity design was optimized for maximum shunt impedance and tuning range for 5 harmonic frequencies. Based on analytical estimation of RF power [36], a series of numerical simulations with 3D code CST-MWS was done for the optimization with an intense meshing for high accuracy. some representative field profiles are shown in Figure 6.21 (top right) and 6.21 (bottom right). The specification and figures of merit of the cavity is listed in Table 6.11.

A preliminary thermo-mechanical analysis by ANSYS [37] was done with a simplified geometry (3 mm wall thickness) of the kicker cavity [38]. The introduction of (water) cooling channel inside the center conductor, at the top plate, and around side wall of the cavity already reduces temperature to manageable level (∼115 C) at 6.4 kW.

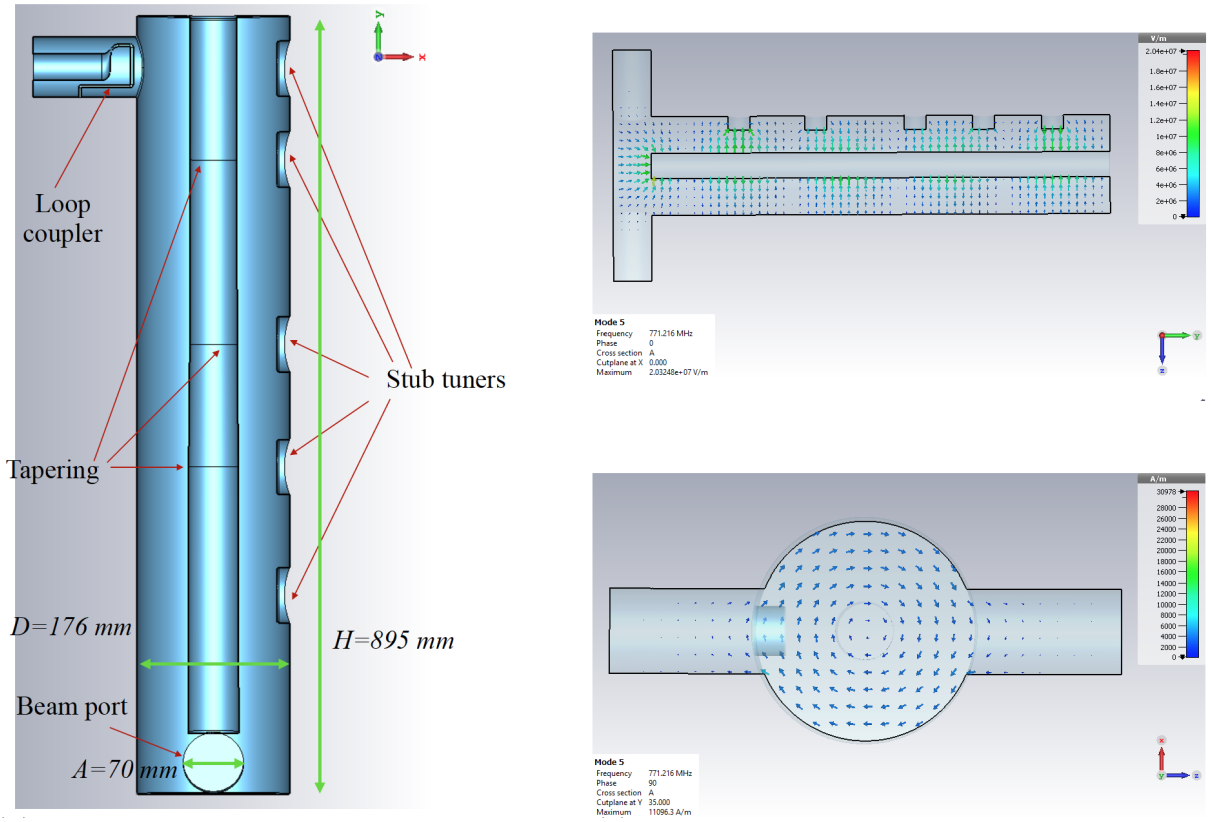

Figure 6.21: The geometry of the QWR and the electromagnetic fields. (left) The view of the QWR and the dimensions. (top right) The electric field distribution of the 5th mode. (bottom right) The magnetic field distribution of the 5th mode.

6.4.2.9 Solenoid The cooling channel is comprised of four 15 m long solenoids with two intervening helicity swaps (see following section). The ion beam and electron beam co-propagate through this channel for a single pass where thermal energy is transferred from the ions to the electrons and are cooled. Naturally, a magnetic element several tens of meters long will present challenges with field uniformity as well as challenges with alignment. These issues will be picked up in a later study. At present we assume idealized 1 T solenoids.

6.4.2.10 Helicity Swap Two of the four solenoids need to run with opposite signs to preserve the polarization of the ion beam through the cooling channel. However the electron beam has a specific sign of angular momentum which must be matched to the sign of the solenoid. When one of the solenoids changes sign, the challenge is to swap the sign of the angular momentum (i.e. "helicity swap") between solenoids while at the same time transversely matching the electron beam to the entrance of the next solenoid. One possible design is based on four FODO cells, each with eighth integer horizontal and quarter integer vertical tunes and rolled 45° [39]. The net result is an exchange of the horizontal and vertical phase spaces with the 4×4 transverse matrix taking the form

$$\begin{pmatrix} 0 & I \\ I & 0 \end{pmatrix} \tag{6.4.3}$$

Table 6.11: The figures of merit for harmonic kicker cavity. The middle box is for harmonic kicker and the bottom box is for pre-/post kicker. n_{h} is harmonic number, f is frequency, V is kick voltage amplitude. P_{wall} is wall loss, Q_0 is unloaded quality factor, $R_{\mathrm{sh},\perp}$ is transverse shunt impedance of harmonic kicker. $\mathrm{DC_h}$ and $\mathrm{DC_p}$ refer to DC magnet field associated with harmonic kicker and pre-/post-kicker and kick voltage translates to 0.1 and 0.3 mT for 0.4 m long magnet, respectively.

Modes	f	V	P_{wall}	Q_0	$R_{\mathrm{sh},\perp}$
	MHz	kV	kW	–	MΩ
1	86.6	25	0.43	5785	1.44
2	259.8	25	0.80	10026	0.78
3	433	25	1.42	13043	0.44
4	606.2	25	1.22	15540	0.51
5	779.4	25	2.54	17452	0.24
0	$\mathrm{DC_h}$	12.5	-	-	-
Total	-	137.5	6.4	-	-
0	$\mathrm{DC_p}$	38.1			
11	952.6	38.1			

where each element represents a 2×2 matrix and I represents the identity matrix. Not only is the sign of the angular momentum swapped, but the module also images the incoming beam to the same values at the exit so that it is matched. And the fact that the transverse phase spaces are swapped will naturally help in suppressing the multipass beam breakup (BBU) instability [40]. With an average current of 140 mA (3.2 nC×476 MHz), we will need to take extra precautions to mitigate BBU using all the means available.

6.4.3 Performance Summary

Simulations of the cooling process have identified a beer-can distribution as optimal for the electron beam [41]. Generating an initial magnetized beam is achieved by defining a flat beam and then invoking a flat-to-round beam transform [42]. The longitudinal phase space is shown in Figure 6.22. To avoid unphysical hard edges on the temporal distribution, a script was used to generate a flat-top with Gaussian edges.

The entirety of the CCR ring was modeled in elegant [43]. Because of the amount of bending, CSR is expected to be the main contributor to beam degradation. And although elegant uses a 1D, ultrarelativistic CSR model, it has proven to be remarkably robust across many accelerators and over a broad range of parameter regimes. Transverse rms beam sizes through the CCR are shown in Figure 6.23.

A number of beam dynamical manipulations occur in the CCR exchange region. A schematic of the region showing the relative locations of lattice elements is displayed in Figure 6.24. The beam is circulating from left to right in the image. After a transverse matching section (denoted by the quadrupoles qccrm1-8) a circulating bunch will encounter a section containing the DC and RF kickers, CSR correction and collimation schemes. For these initial simulations, the kickers are modeled as zero-length, impulse kicks of the appropriate magnitude. Likewise, the CSR correction scheme, which will be realized with an RF cavity, is modeled as a matrix element with an appro-

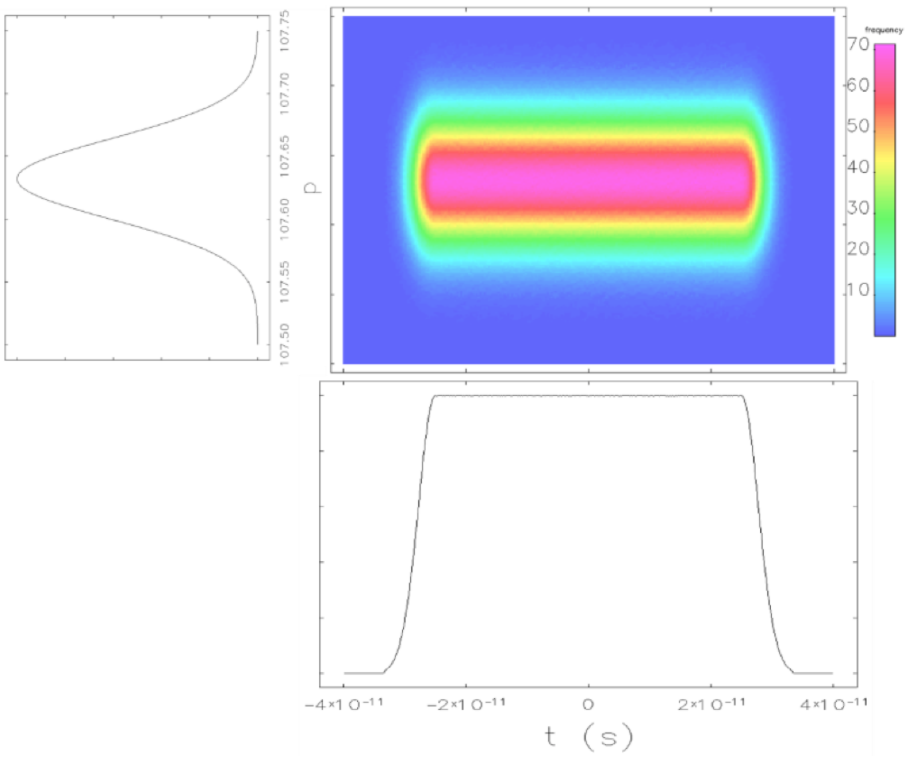

Figure 6.22: Intensity plot of the initial, idealized longitudinal distribution with projections in each plane. Temporally the beam is a flat-top with Gaussian edges. The full bunch length is 2.0 cm (66.7 ps).

priately tuned R_{65} element which mimics the effect of running at zero-crossing in a cavity. Finally, the collimation refers to an element which removes particles from the distribution that exceed a user-specified relative energy spread (3×10^{-3} in this case). As the design matures, these elements will be modeled with increasing levels of realism (i.e. finite length kickers and RF cavities).

Figure 6.25 displays the longitudinal phase space after each turn in the CCR (for clarity they are each plotted on the same scales). Note that while CSR causes the ends of the bunch to develop a high energy head and tail (which is "collimated") the core of the beam is effectively corrected by the RF cavity and remains useful for cooling through all passes. Note that the effectiveness of the CSR compensation is predicated on a uniform longitudinal distribution. Deviations from this will require other, possibly more involved, correction schemes.

To get a feel for how well the magnetization is preserved, so-called "quiver" plots of the physical phase space depicting the rotation of the bunch after selected turns are shown in Figure 6.26. It is not yet clear how to quantify the magnetization required at the cooling channel to maintain effective rates or the effect that degraded magnetization has on those rates.

The transverse phase space was characterized in two complementary ways. First, the horizontal and vertical emittance of the magnetized beam were computed as a function of turn number in the CCR. This is shown in the left plot of Figure 6.27 where the dotted black line denotes the ideal, unperturbed emittance value. Secondly, the magnetized beam was converted to a flat beam (via a round-to-flat matrix transform) after each turn, and the drift and Larmor emittances were plotted as a function of turn number. These results are displayed in the right plot of Figure 6.27 Note that

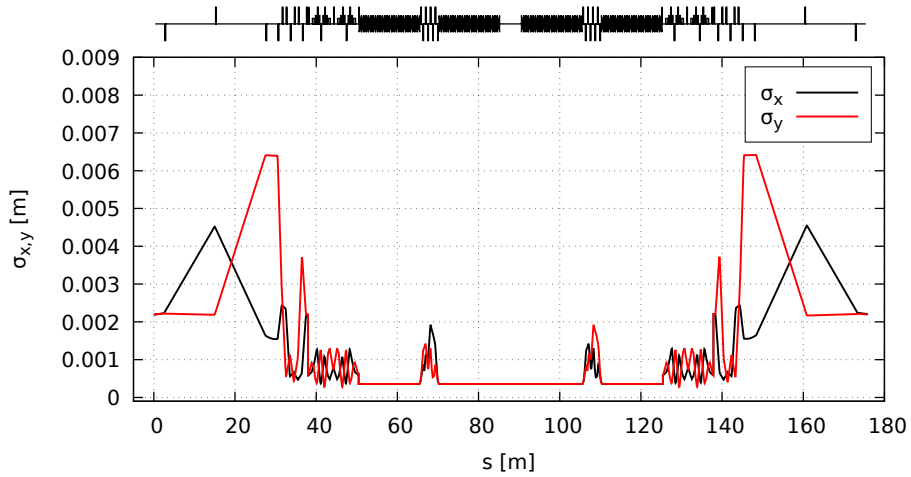

Figure 6.23: Transverse RMS beam sizes through a single turn of the CCR, starting from the septa. The cooling channel starts at roughly 50 m and extends to 125 m.

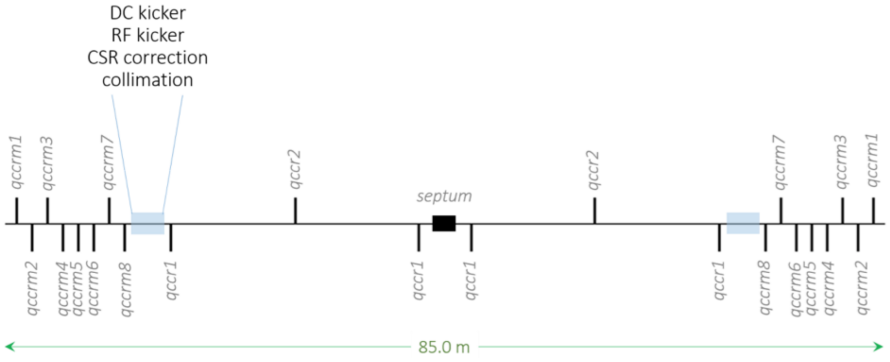

Figure 6.24: Schematic of the CCR exchange region showing locations of relevant lattice elements.

the Larmor emittance specification of 19 mm-mrad (see Table 6.5) is met for all but the last few turns in the CCR. While there is still work to do, these are encouraging preliminary results.

6.4.4 Beam Dynamics

6.4.4.1 Space Charge The aggressive bunch charge means that space charge — both transverse and longitudinal — needs to be managed. This is most true during the beam formation process and has been discussed in detail in the injector description. Fortunately, by invoking a magnetized beam the space charge forces are reduced due to the relatively large transverse beam size. And simulations using Tstep [44] to model the CCR arc show that there is negligible effect from space charge through 180° of bending [29].

6.4.4.2 Coherent Synchrotron Radiation Coherent synchrotron radiation poses a significant challenge for accelerators using high brightness beams. When a bunch travels along a curved orbit, fields radiated from the tail of the bunch can overtake and interact with the head. Rather than the more conventional class of head-tail instabilities where the tail is affected by the actions of the head, CSR is a tail-head instability. The net result is that the tail loses energy while the head gains energy leading to an undesirable redistribution of particles in the bunch. Because the interaction

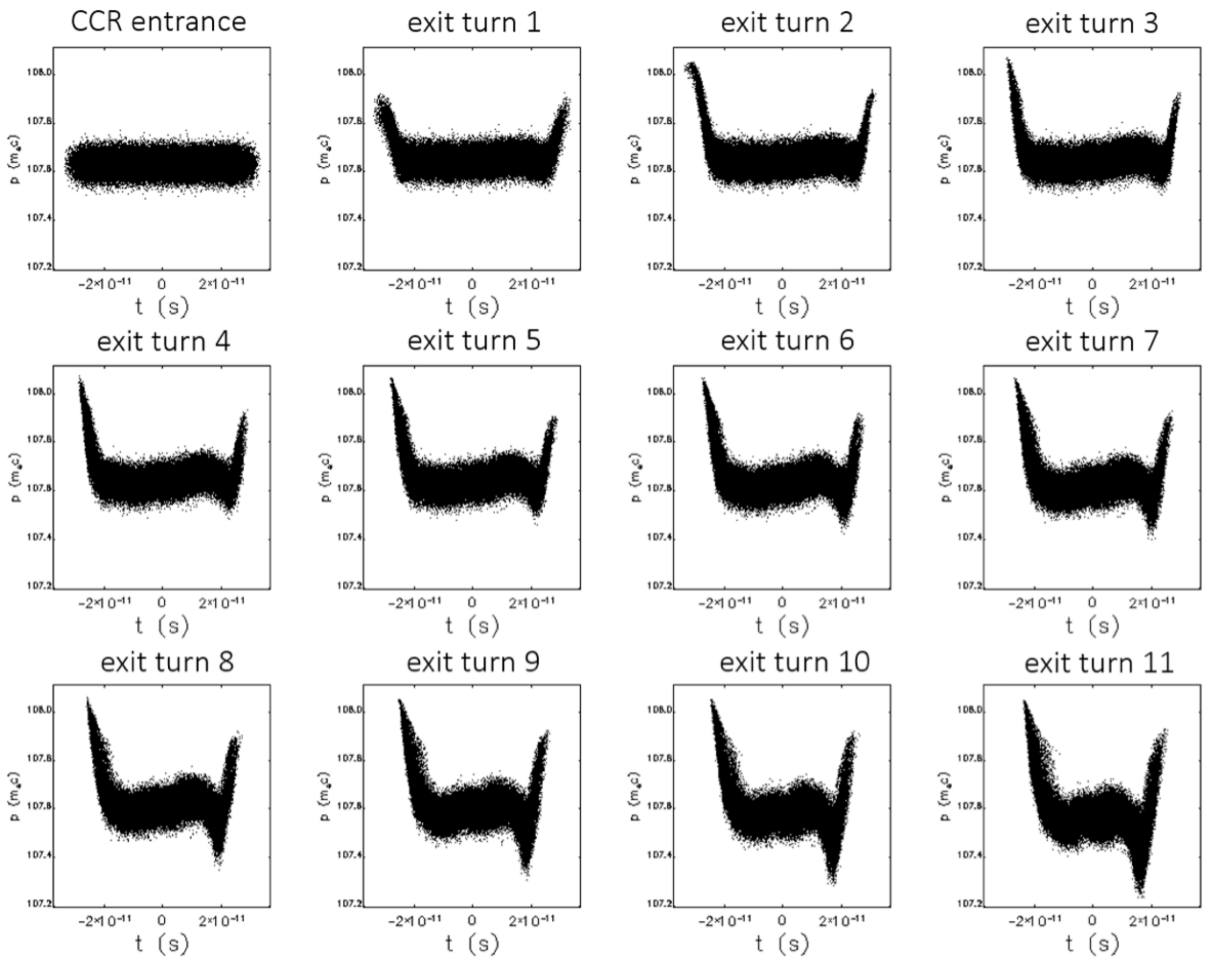

Figure 6.25: Evolution of the longitudinal phase space after each pass through the CCR.

takes place in a region of dispersion, the energy redistribution is correlated with the transverse positions in the bend plane and can lead to projected emittance growth. Managing CSR in a single recirculation arc can be challenging enough, let alone through nearly 4000° of bending which the beam experiences in the CCR.

There has been much progress in recent years to undo the effects of CSR in the bend plane with an appropriate choice of beam optics [45]. Though possible to control the transverse emittance growth, it is more difficult to undo the gross longitudinal distortion caused by the CSR wake — particularly in applications where the intrinsic energy spread is small and/or where the effect can accumulate over multiple recirculations. One possible mitigation is shielding of the CSR wake from the beam pipe. Therefore a proper treatment of both CSR and shielding in the codes is essential. Only a handful of codes exist that model CSR shielding; one of them is Baby MAD (Bmad), which was developed at Cornell University [46]. Figure 6.28 shows the horizontal and longitudinal phase spaces at the exit of the arc with and without CSR shielding. The full aperture is assumed to be 2 inches (5.08 cm) for the shielding computations. The effect on the longitudinal phase is striking. Rather than a linear energy slew across the bunch, shielding modifies the CSR wake so that the center of the bunch remains unscathed while the head and tail show a modest decrease in energy.

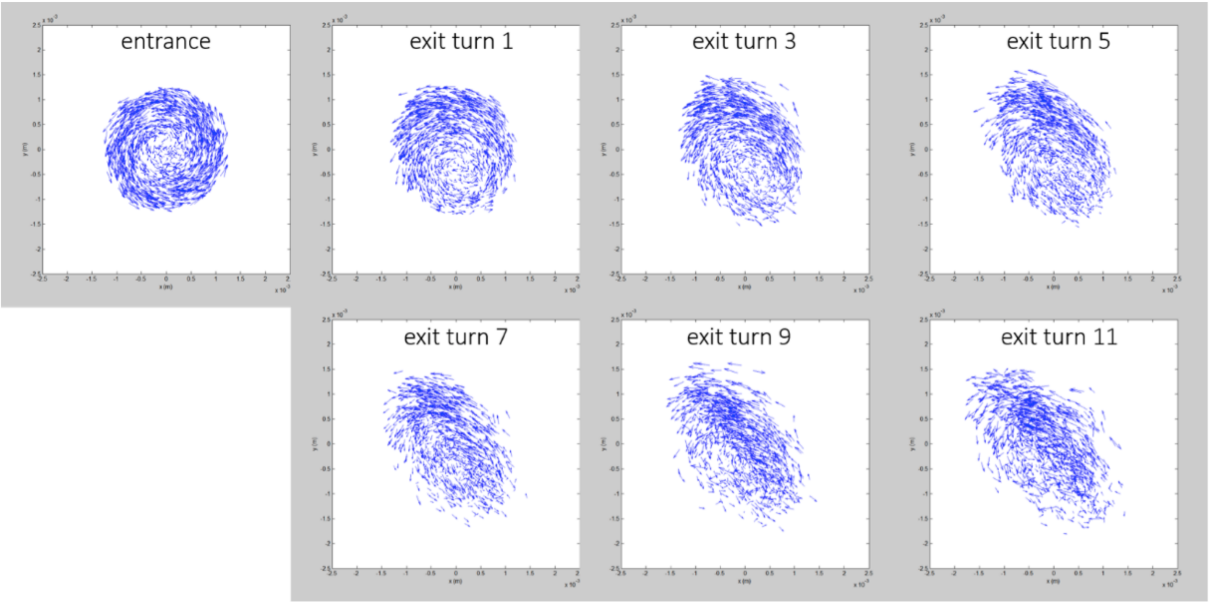

Figure 6.26: Plots of the physical phase space (x,y) depicted with vectors to show bunch rotation after selected turns in the CCR.

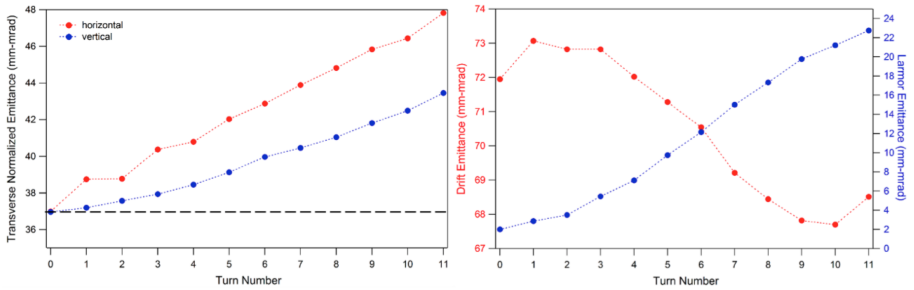

Figure 6.27: Transverse emittances as a function of turn number in the CCR. The right plot shows the horizontal and vertical emittances of the round beam whereas the left plot shows the drift and Larmor emittances of the beam.

Similarly, the horizontal phase space with shielding lacks the spray of particles (upper right) that normally evolve.

While some of the CSR effects on the beam is ameliorated by CSR shielding, active compensation is needed for multiple recirculations, namely using an RF cavity run far off-crest to restore energy lost by CSR and to remove the energy chirp.

6.4.4.3 Microbunching Instability The amount of bending in the CCR alone raises concern about the microbunching instability developing. The situation, however, is further aggravated by the necessarily small intrinsic energy spread (3×10^{-4} rms). Even modest microbunching gains, if they are above unity, are unacceptable in systems where multiple recirculations are required since the total gain goes as the gain for a single pass raised to the number of passes. All this to say, the ability to control microbunching is critical.

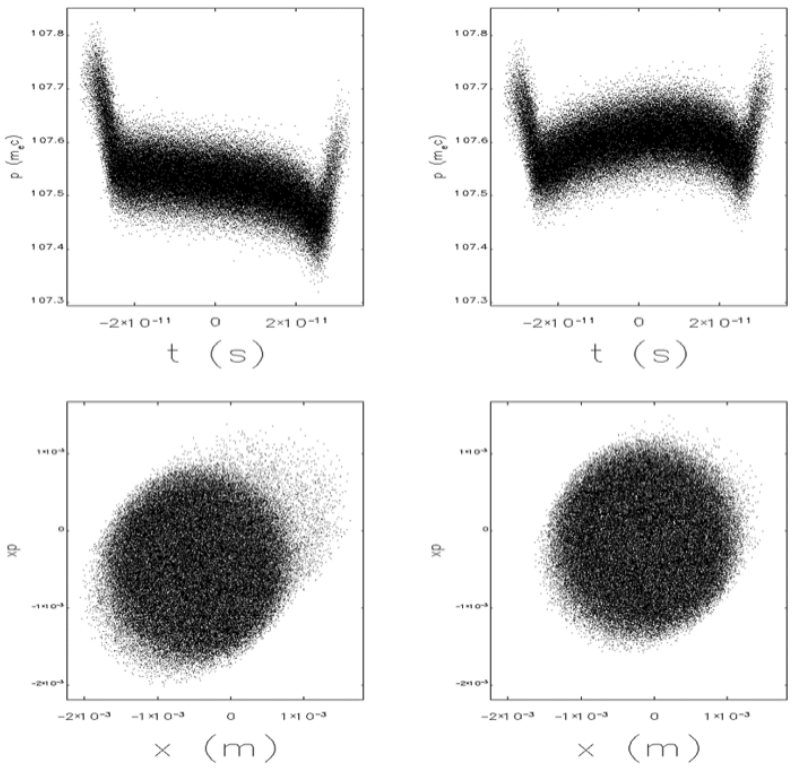

Figure 6.28: Longitudinal (top) and horizontal phase space (bottom) after a single traversal through the arc without (left) and with CSR shielding (right). The full aperture is 5.08 cm. (The simulation used 500 bins and 8 image charges).

Studying the microbunching instability in the time-domain (i.e. via particle tracking) is a computational burden that makes it difficult to exercise parametric studies and/or model an entire accelerator complex. On the other hand, a semi-analytical Vlasov-solver that works in the frequency-domain and models relevant collective effects such as LSC, CSR and linac geometric effects using analytic impedance expressions allows faster analysis (by orders of magnitude) and has already led to insights on lattice constraints for control of the microbunching instability [47].

The microbunching gain curves for 3- and the full 11-passes through the CCR are given in Figure 6.29. Note that for 3-passes the gain remains just below unity over a broad range of wavelengths. For 11-turns the gain reaches a maximum of about 1.9 at a wavelength of 5 mm which is perfectly acceptable.

6.4.4.4 Halo It is well known that halo represents one of the most difficult operational challenges for ERLs [48]. To adequately assess the impact of halo particles requires simulating initial distributions that are as realistic as possible and pushing large numbers of particles. For instance, even in a 1M particle distribution even a single rogue particle represents significant beam power. To get an accurate representation of possible beam loss mechanisms requires not only tracking a large distribution, but tracking many variations (simulating the effect of bunch to bunch variation in a real machine) of that distribution. Processes that may generate halo particles include intra-beam,

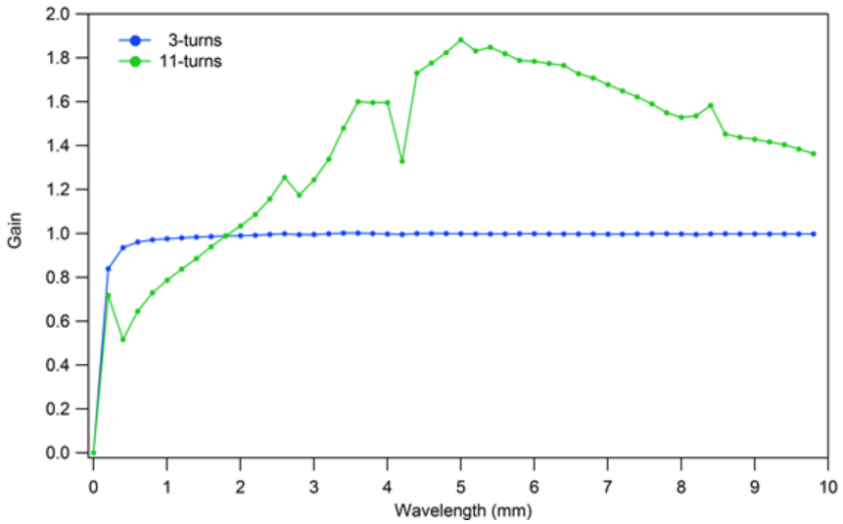

Figure 6.29: Microbunching gain curves for 3-turns (blue) and 11-turns (green) in the CCR.

Touschek and beam/gas scattering. As the lattice becomes better defined, these various beam dynamical processes will be studied.

REFERENCES

1. Y.S. Derbenev, G. Krafft, B. Yunn, and Y. Zhang, "Achieving High Luminosity in an Electron-Ion Collider", in Proc. of HB'10, Morschach, Switzerland, paper MOPD06.
2. Y.S. Derbenev, "Electron Cooling for ELIC — a High Luminosity Electron-Ion Collider", in Proc. of COOL'07, Bad Kreuznach, Germany, paper THAP12, p. 187.
3. Y.S. Derbenev, "Electron Cooling for a Future Electron-Ion Collider at JLab", in Proc. of COOL'09, Lanzhou, China, paper FRM2MCCO01, p. 181.
4. L.-J. Mao *et al.*, "Electron cooling system in the booster synchrotron of the HIAF project", NIM A **786**, pp. 91-96, 2015.
5. D. Prasuhn *et al.*, "Technical Features and Final Electron Beam Tests of the COSY Electron Cooler and First Proton Beam Cooling", in Proc. of COOL'93, Montreux, CERN Report 94-03, pp. 317 - 321, 1994.
6. H. Zhang *et al.*, "Development of the Electron Cooling Simulation Program for JLEIC", in Proc. of IPAC'16, Busan, Korea, p. 2451.
7. JSPEC source code, `https://github.com/zhanghe9704/electroncooling`
8. A. Piwinski, "Intrabeam Scattering", Proc. of 9th Int. Conf. on High Energy Accelerators, p. 105, (1974).
9. M. Martini, "Intrabeam Scattering in the ACOL-AA Machines", CERN PS/84-9 AA (1984).
10. J.D. Bjorken and S.K. Mtingwa, "Intrabeam Scattering", Particle Accelerators, Vol. 13, p. 115, (1983).
11. J. Wei, "Evolution of Hadron Beams under Intrabeam Scattering", Proc. of PAC'93, p. 3651, (1993).
12. V. V. Parkhomchuk, "New Insights in the Theory of Electron Cooling", Nucl. Instr. and Meth. A **441**, pp. 9-17 (2000).
13. I. Meshkov *et al.*, BETACOOL Physics Guide, Dubna, 2007.
14. Radiasoft LLC, `http://radiasoft.net`

15. JSPEC Sirepo web interface, `https://beta.sirepo.com/#/jspec`
16. J.-W. Xia *et al.*, "The Heavy Ion Cooler-Storage-Ringc Project (HIRFL-CSR) at Lanzhou", NIM A **488** 1–2, pp. 11-25, 2002.
17. H. Stein *et al.*, "Present Performance of Electron Cooling at COSY-Julich", `https://arxiv.org/pdf/1101.5963`, 2011.
18. J. W. Xia *et al.*, "Lanzhou Cooler Storage Ring Commissioning", Proc. of IPAC'10, Kyoto, Japan, paper THYMH01, p. 3611.
19. S. Nagaitsev *et al.*, Phys. Rev. Lett. **96**, p. 044801, 2006.
20. J. Dietrich and V. Parkhomchuk, "The Proposed 2 MeV Electron Cooler for COSY-Juelich", in Proc. of EPAC'06, Edinburgh, Scotland, 2016.
21. Electron Cooler COSY 2 MeV, Conceptual Design Report (CDR), Novosibirsk, 2009.
22. N. Alinovskiy *et al.*, "2 MeV Electron Cooler for COSY and HESR — First Results", in Proc. of IPAC'14, Dresden, Germany, 2014.
23. A. Sy, "Toroidal Merger Simulations for the JLEIC Bunched Beam Electron Cooler Ring", in Proc. of IPAC'18, Vancouver, Canada, paper THPAK127, p. 3540.
24. A. Burov, S. Nagaitsev, A. Shemayakin, and Ya. Derbenev, "Optical Principles of Beam Transport for Relativistic Electron Cooling", Phys. Rev. Spec. Topics Accel. Beams **3**, p. 094002 (2000).
25. K. Deitrick *et al.*, "Development of a Magnetized Injector for Proof of Principle Experiments", in Proc. of Linac'18, Beijing, China, paper TUPO108, to be published.
26. J. Guo, R. Rimmer, S. Williams, M. Neubauer, "Muon Inc. High Power Coaxial SRF Coupler Phase II Project Summary", JLAB Tech note, JLAB-TN-14-010 .
27. F. Marhauser and R. Rimmer, "Progress on the Design of the JLEIC Ion Ring Cavities", JLAB-TN-18-041, September 2018.
28. C. Tennant and D. Douglas, "Analysis of a 'Simple Arc' for Use in the CCR for Strong Cooling in JLEIC", JLAB-TN-18-001, January 2018.
29. D. Douglas, S. Benson and C. Tennant, "A Simple Achromatic/Isochronous CCR Arc Design", JLAB-TN-18-009, January 2018.
30. D. Douglas, S. Benson and C. Tennant, "ERL to CCR Beam Exchange Region Design, Revision 1.0", JLAB-TN-17-012, March 2017.
31. Y. Huang, H. Wang, R. A. Rimmer, S. Wang, and J. Guo, *Phys. Rev. Accel. Beams* **19**, 122001 (2016).
32. A. Dotson, "Minimizing the average slope and kick of intermediate bunches for electron cooling", REU report, Jefferson Laboratory (2017)
33. G. Park. "Beam dynamics study of the harmonic kicker", JLAB-TN-18-044, October 2018
34. Y. Huang, H. Wang, R. A. Rimmer, S. Wang, and J. Guo, *Phys. Rev. Accel. Beams* **19**, 084201 (2016).
35. G. Park. "RF design of the harmonic kicker", JLAB-TN-18-046, October 2018
36. H. Wang, "The RF power scaling of the harmonic kicker with kicking angle and beam path aperture", JLAB-TN-18-047, October 2018
37. Ansys Inc., http://www.ansys.com
38. M. Marchlik, "Thermal and structural analysis of the harmonic kicker", JLAB-TN-18-048, October 2018
39. D. Douglas, "Flipping Magnetization Helicity", JLAB-TN-16-035, October 2016.
40. D. Douglas *et al.*, "Experimental Investigation of Multibunch, Multipass Beam Breakup in the Jefferson Laboratory Free Electron Laser Upgrade Driver", Phys. Rev. Accel. Beams **9**, p. 064403 (2016).
41. H. Zhang, "Cooling with an Electron Bunch of Cylinder Shape", slides dated November 19, 2015.
42. D. Douglas, "Twiss Parameterization of Flat Beam Transforms Including Beam Divergence", JLAB-TN-15-022, July 2016.

43. M. Borland, "elegant: A Flexible SDDS-Compliant Code for Accelerator Simulation", Advanced Photon Source LS-87 (2000).

44. TStep, Homepage: `http://tstep.lmytechnology.com/TSTEP.html`

45. S. Di Mitri, M. Cornacchia, and S. Spampinati, "Cancellation of Coherent Synchrotron Radiation Kicks with Optics Balance", Phys. Rev. Lett. **110**, p. 014801 (2013).

46. Bmad, Homepage: `https://www.classe.cornell.edu/bmad/`

47. C.Y. Tsai, "Investigation of Microbunching Instabilities in Modern Recirculating Accelerators", Ph.D. Dissertation, Virginia Tech, April 2017, `https://vtechworks.lib.vt.edu/handle/10919/77429`

48. D. Douglas *et al.*, "Architectural Considerations for Recirculated and Energy-Recovered Hard XFEL Drivers", Proc. of IPAC'18, Vancouver, Canada, paper THPMK106, to be published.

CHAPTER 7

INTERACTION REGION AND DETECTOR

7.1 Introduction to Interaction Region and Detector Design

Measurements at the EIC have very stringent requirements on high luminosity as well as on the acceptance of the final state particles of the collisions, particularly in the directions along the beamline, equivalently extremely high rapidity. Accessing the EIC physics of interest requires unprecedented integration of the interaction region (IR) and detector designs.

The basic process at the EIC, deep inelastic scattering, is illustrated in Figure 7.1. An ion, composed of nucleons, in turn composed of partons (quarks and gluons), moves to the right and collides with an electron moving to the left. The electron interacts with a parton within the ion in a hard collision and excites the ion to a state with high invariant mass. We can, qualitatively, define three classes of particles in the final state:

1. The scattered electron,
2. Particles associated with the initial state ion, and
3. Particles associated with the struck parton.

All three classes of final-state particles carry information about the inner structure of the ions in the collisions and allow to investigate the quark-gluon structure of the nucleons and nuclei. Therefore it is essential that the IR and the detector at the EIC are designed so that all three classes of particles are measured at as close to 100% acceptance as possible, and with necessary resolutions and particle identification purities.

We define the concept of a total acceptance detector as one that achieves close to 100% acceptance for all three classes of particles. The final state electron and the particles associated with the struck parton are scattered at relatively high angles with respect to be beam direction and can be detected

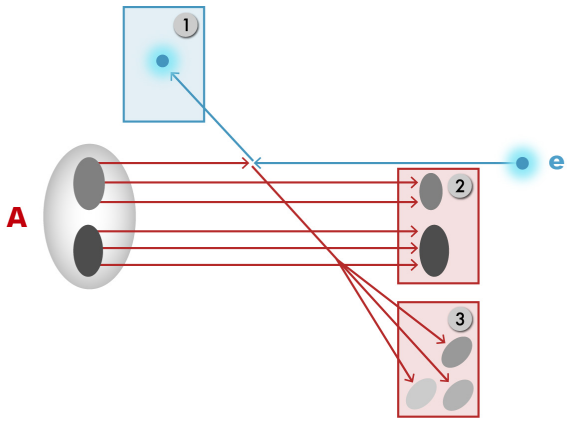

Figure 7.1: Classification of the final-state particles of a DIS process at the EIC: scattered electron (1), the particles associated with the initial state ion (2), and the struck parton (3).

in a conventional collider detector using a solenoidal magnetic field. The particles associated with the initial-state ion, however, tend to be nearly collinear with the ion-beam direction. Collider detectors in the recent past have had rather small acceptance for these particles.

The luminosity at the interaction point (IP) is (to first order) inversely proportional to the distance between the last upstream and first downstream Final Focus Block (FFB) around the IP. However, the closer the beam elements are to the IP, the more they restrict the size of the detector and compromise the measurements. At shallow angles with respect to the beam axis (high rapidities), the FFBs begin to severely restrict the measurability of the final-state particles associated with the initial-state ion, and eventually would make many of the physics aims of the EIC inaccessible. The solution to achieve the necessary high average luminosity of 10^{33}–$10^{34}\,\mathrm{cm}^{-2}\mathrm{s}^{-1}$ while maintaining a total acceptance detector, is to let the small-angle particles pass through the nearest machine elements, which perform the function of angle and momentum analyzer for the small angle reaction products. A significant challenge of this approach is that it must consistently reconcile often contradictory detector and machine optics requirements. A central detector space of $-3.5\,\mathrm{m}$ and $+7.0\,\mathrm{m}$ around the IP has been chosen, taking these consideration into account as well as the asymmetric collisions at JLEIC.

We have chosen a crossing angle of 50 mrad between the electron and ion beams to accommodate the FFBs with large enough aperture, particularly in the ion-forward direction, and field strength consistent with the detector space of 10.5 m. With this design, the beam elements of the electron and ion beams are interleaved but independent, reducing engineering complexity. The crossing angle also eliminates parasitic collisions of closely-spaced bunches and reduces the detector background by shortening the section of the detector beam pipe common for both beams.

The schematic layout of the JLEIC interaction region containing a total-acceptance detector is shown in Figure 7.2. At small angles with respect to the beam directions, the detection regions extend 30–40 m in either direction from the central detector. The central detector is built around a 4 m long solenoid extending 2.4 m on the outgoing ion side and 1.6 m on the opposite side. The solenoid field is adjustable independently of the beam energies to optimize the detection for various processes. The maximum field is expected to be 3 T. The electron beam is aligned with the detector solenoid axis to avoid additional synchrotron radiation generation.

This IR design implies several accelerator design challenges addressed elsewhere:

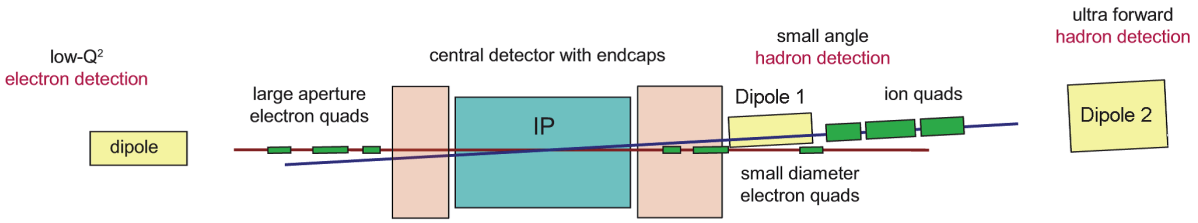

Figure 7.2: Schematic layout of the JLEIC full-acceptance detector region.

1. The beam crossing angle is arranged by shaping the end section of the ion arc upstream of the IP. The ion beamline segment downstream of the IP is designed to produce a 1.5 m transverse separation between the ion and electron beams. This section produces a high dispersion secondary focus 40 m downstream of the IP, before matching to the ring lattice. The electron detector region has no net bend or shift. It is aligned with the detector axis to avoid generation of synchrotron radiation by the detector solenoid field. The challenge associated with a beam crossing angle is that, without compensation, its geometric effect would reduce the luminosity by about an order of magnitude compared to the head-on collision scenario. This problem is solved by integrating local crab crossing systems into both the electron and ion collider rings (Section 8.2). They include high-voltage deflecting crab cavities that tilt the bunches at the IP to effectively restore head-on collisions and the respective luminosity (Section 9.6).

2. Strong focusing at the IP leads to a large chromatic betatron tune spread and chromatic beam smear at the IP. Without compensation, the chromatic betatron tune spread overlaps many beam resonances leading to beam loss and restricted momentum acceptance. The chromatic beam smear increases the beam spot size at the IP potentially causing a luminosity loss. Thus, we develop a chromaticity compensation scheme and optimize the dynamic aperture and momentum acceptance as discussed in Section 5.4.2.

3. The detector solenoid with a field of up to 3 T has a significant impact on the beam dynamics, which must be compensated. For electrons, the main effect of the solenoid field is coupling of the transverse degrees of freedom. It may lead to beam instabilities due to coupling resonances. Since the beams have 5-to-1 horizontal-to-vertical size ratios at the IP, coupling may lead to a mismatch of the beam sizes at the IP. In addition, it may rotate the planes of crab tilt of the colliding bunches bringing them out of mutual alignment. Thus, coupling must be compensated not only globally but also locally at the IP. One must also consider the solenoid effect on electron and ion polarizations. Without compensation, the solenoid breaks the figure-8 spin symmetry nullifying its important properties. In addition to these problems common to the electron and ion beams, the ion beam crosses the solenoid at a 50 mrad angle. This results in distortion of the ion closed orbit and generation of vertical dispersion due to the transverse component of the solenoid field on the ion orbit. A solenoid compensation scheme that addresses all of these issues is also presented in Section 5.4.2.

4. The beams must have sufficiently long life times to reach the luminosity goal. One of the prerequisites for a long beam lifetime is a large dynamic aperture. The dynamic aperture of a bare lattice was presented in Section 5.4.2, including the effects of magnet misalignments, strength errors and multipole components on the dynamic aperture. We specified tolerances to the magnet alignment and strength errors and demonstrated closed orbit correction. Due

to a large expansion of the beams in the final focusing quadrupoles, the dynamic aperture is dominated by the quality of these magnets. By requiring a dynamic aperture of at least $\pm 10\sigma$ of the RMS beam size, we have completed a top-down analysis of the maximum acceptable magnetic multipoles of the final focusing quadrupoles.

5. Injection into the JLEIC electron collider ring is done from CEBAF at full energy. The ion beam is injected into the ion collider ring at 8 GeV. It is then accelerated to an experimental energy between 20 GeV and 100 GeV. Due to the low energy and space-charge limit, the geometric emittance of the injected ion beam is a factor of 32 greater than in collision. This means that injection cannot be done with collision optics. Section 5.4.3 describes the design of injection mode optics that has maximum values of the β functions in the interaction region reduced from about 2500 m to about 100 m. The beam is accelerated with these optics and, at the experimental energy, the β functions at the IP are reduced to their collision values through a β-squeeze procedure.

This chapter is organized in the following sections. Section 7.2 discusses the IR and far-forward optics, including a section on the beampipe design and background considerations. Section 7.3 discusses the main detector design concept, including auxiliary measurements. Section 7.4 presents early results of detector and physics performance studies to validate the design choices and preliminary detector layout.

7.2 IR and Far-Forward Optics

7.2.1 Ion Optics

The optics of the IR must be flexible enough to support the β-squeeze and optimization of the luminosity and detection in different collider configurations, including different beam energies, ion species, and detector solenoid strengths. The ion IR optics designed to support these requirements is shown in Figure 7.3. Each ion FFB is a quadrupole triplet. We optimized parameters of the downstream final focusing quads including their strengths, length and positions for maximum acceptance to the forward scattered collision products. We adjusted the quadrupole strengths to fall off with the distance from the IP so that, with their pole-tip fields not exceeding 6 T at 100 GeV, their apertures form a cone with an opening angle of about ± 10 mrad. The resulting parameters of the detector region magnets at 100 GeV are listed in Table 7.1.

As illustrated in Figure 7.2, there is a 6 mrad spectrometer dipole, Dipole 1 (iBD61), before the downstream ion FFB and a 56 mrad spectrometer dipole, Dipole 2 (iBDS2), after the FFB. Dipole 1 is used for momentum analysis of the forward scattered particles in the low-momentum-resolution region of the solenoid near its axis. Dipole 2 momentum-analyzes small-momentum-offset particles that are moving very close to or within the ion beam. From the optics point of view, the dispersion generated by Dipole 1 is small and only creates a small perturbation of the dispersion generated by Dipole 2. Dipole 2 is followed by a 14.4 m long drift space instrumented with forward detectors. By the end of the drift, the horizontal dispersion reaches about 1 m, making off-momentum collision products come out of the beam stay clear area. To separate the small momentum offset products from the beam core even more and therefore improve the detector's momentum acceptance, the ion beam is focused towards the end of the drift space near the point of maximum dispersion as shown in Figure 7.3. The horizontal and vertical beta functions are less than 0.7 m at the focal point. Implementation of the secondary focus leads to additional chromatic contributions, but it is necessary for forward detection. A combination of small beam size and large dispersion allow one to place Roman Pot detectors close to the beam and detect smaller momentum offset particles

Table 7.1: Parameters of the ion detector region magnets at the maximum ion momentum of 100 GeV.

Name	Type	Length (m)	GFHA[1] (cm)	IHA[2] (cm)	OR[3] (cm)	Dipole field		Quad gradient		Solenoid (T)	Position and orientation[4]		
						B_x (T)	B_y (T)	$\frac{\partial B_y}{\partial x}$ ($\frac{T}{m}$)	$\frac{\partial B_x}{\partial x}$ ($\frac{T}{m}$)		x (m)	z (m)	θ (rad)
Upstream ion IR elements													
iASUS	Sol	1.6	3	4	12	0	0	0	0	3.0	0.455	−9.089	0.05
iQUS3	Quad	1	3	4	12	0	0	−115.8	−1.666	0	0.385	−7.690	0.05
iQUS2	Quad	1.5	3	4	12	0	0	149.0	2.144	0	0.302	−6.042	0.05
iQUS1	Quad	1.2	2	3	10	0	0	140.5	−2.022	0	0.210	−4.195	0.05
iCUS1	Kicker	0.2	2	3	10	−0.949	0.144	0	0	0	0.155	−3.096	0.05
iCUS2	Kicker	0.2	2	3	10	1.548	−0.148	0	0	0	0.095	−1.898	0.05
iDSUS	Sol	1.6	2	160	210	0	0	0	0	−3.0	0.040	−0.799	0.05
Downstream ion IR elements													
iDSDS	Sol	2.4	2	160	210	0	0	0	0	−3.0	−0.060	1.199	0.05
iBDS1	Dipole	1.0	4	23.5	31	1.477	2.098	−7.630	−5.370	0	−0.276	5.493	0.0530
iCDS2	Kicker	0.5	4	25.25	33	−2.637	−0.160	0.511	8.439	0	−0.317	6.242	0.0560
iQDS0S	Quad	0.1	4	7	17	0	0	0	53.47	0	−0.356	6.941	0.0560
iQDS1	Quad	1.2	4	8.5	17	0	0	−77.94	0	0	−0.392	7.590	0.0560
iQDS1S	Quad	0.1	4	10	25	0	0	0	−34.28	0	−0.479	9.137	0.0560
iQDS2	Quad	2.4	4	12.6	25	0	0	52.39	0	0	−0.549	10.385	0.0560
iQDS2S	Quad	0.1	4	12	27	0	0	0	−17.90	0	−0.619	11.633	0.0560
iQDS3	Quad	1.2	4	14.8	27	0	0	-46.09	0	0	−0.706	13.181	0.0560
iQDS3S	Quad	0.1	4	15	27	0	0	0	19.02	0	−0.742	13.830	0.0560
iASDS	Sol	2.4	4	17	29	0	0	0	0	3.0	−0.840	15.577	0.0560
iBDS2	Dipole	4.0	4	40	90	0	−4.670	0	0	0	−1.019	19.773	0.0280
iBDS3	Dipole	4.0	4	30	47	0	4.670	0	0	0	−1.131	38.319	0.0280
iQDS4	Quad	0.8	3	4	20	0	0	71.828	0	0	−1.472	45.400	0.0560

[1] GFHA stands for Good-Field Half Aperture.
[2] IHA stands for Inner Half Aperture.
[3] OR stands for Outer Radius.
[4] Position and orientation are specified for the center of each magnet.

than without the secondary focus. Performance of this design from the forward detection point of view is quantified below. A third dipole at 40 m flattens the dispersion at the secondary focus.

The beam parameters at the IP and secondary focus are determined by the lattice optical functions, transverse beam emittances, and beam momentum spread. At the points where the derivatives of β and dispersion (D) are zero, the rms transverse beam size $\sigma_{x,y}$ and angular spread $\sigma_{x',y'}$ are given by:

$$\begin{aligned} \sigma_{x,y} &= \sqrt{\beta_{x,y}\varepsilon_{x,y} + (D_x \Delta p/p)^2}, \\ \sigma_{x',y'} &= \sqrt{\varepsilon_{x,y}/\beta_{x,y}}, \end{aligned} \tag{7.2.1}$$

where $\beta_{x,y}$ are the horizontal/vertical β functions, $\varepsilon_{x,y}$ are the horizontal/vertical geometric beam emittances, D_x is the horizontal dispersion, and $\Delta p/p$ is the relative beam momentum spread. The geometric beam emittances can be expressed in terms of the invariant normalized beam emittances $\varepsilon^N_{x,y}$ as:

$$\varepsilon_{x,y} = \varepsilon^N_{x,y}/(\beta\gamma), \tag{7.2.2}$$

where $\beta\gamma = p/mc$ is the relativistic parameter. The beam parameters indicated in Figure 7.3 are calculated for a proton beam assuming (p =100 GeV), $\varepsilon^N_{x,y}$ = 0.5/0.1 µm, and $\Delta p/p$ =3×10^{-4}.

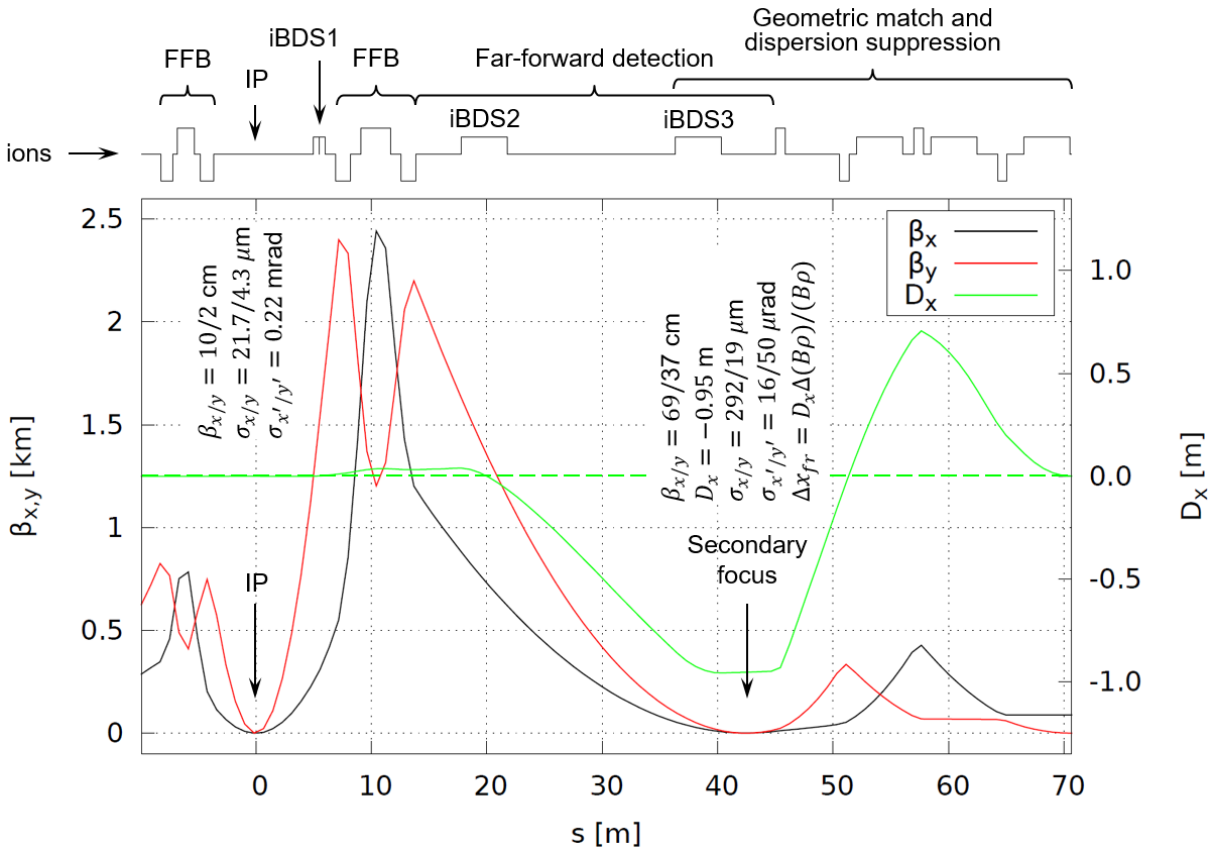

Figure 7.3: Beam optics of the ion detector region. Also shown are the positions of the IP and secondary focus, and the beam parameters at those locations.

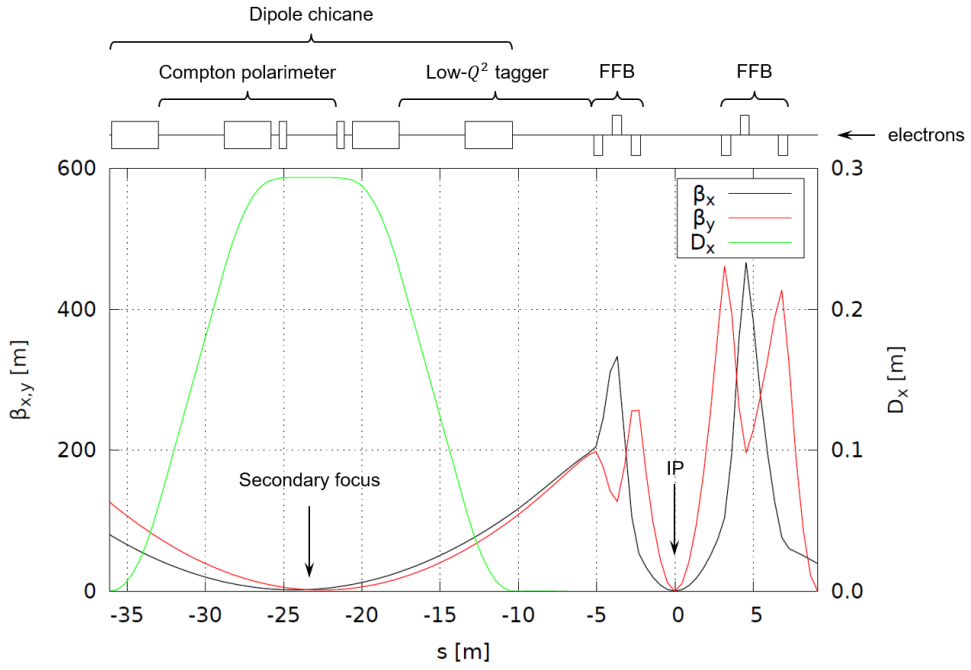

Figure 7.4: Electron collider ring detector region optics. (Also see Figure 4.14.)

Since the collision products originate with a small offset from the IP and the optics provides point-to-point focusing from the IP to the secondary focus, the transverse offset of a collision fragment at the secondary focus is determined primarily by a combination of the dispersion at that location and the fragment's relative magnetic rigidity offset:

$$\Delta x_{\mathrm{fr}} = D_{\mathrm{x}} \Delta(B\rho)/(B\rho), \tag{7.2.3}$$

where $B\rho = p/(Ze)$ is the magnetic rigidity. A fragment can be detected if it comes out of the beam stay-clear area: $\Delta x_{\mathrm{fr}} > 10\sigma_{\mathrm{x}}$. Reducing σ_{x} by focusing the beam the second time and maximizing D_{x} at the secondary focus improves the detector's momentum acceptance. Large dispersion also provides a high resolution in the magnetic rigidity offset.

To keep the IR design modular, the dispersion generated by the spectrometer dipoles is suppressed by a section consisting of a number of dipoles and quadrupoles as shown in Figures 7.3. The geometry of the section is adjusted so that the ion beam exits it parallel to the electron beam and is transversely separated from it by 1.5 m. This provides the design with enough flexibility to allow changes in the geometry of the IR without affecting the geometry of the rest of the ring and simplifies optimization of the IR separately from the rest of the ring.

7.2.2 Electron Optics

The detector region optics in the electron collider ring, shown in Figure 7.4, is optimized to meet the detection requirements. Strengths, sizes and positions of the machine elements are optimized to reduce the technical challenge of the magnet design and avoid interference with the ion detector region elements. The downstream final focusing quadrupoles (FFQs) are designed with large apertures and followed by spectrometer dipoles for forward low-Q^2 tagging. In addition, the electron beam is focused towards the end of the element-free spaces downstream of the respective spectrometer dipoles to allow closer placement of the detectors at those locations. Such a design, in

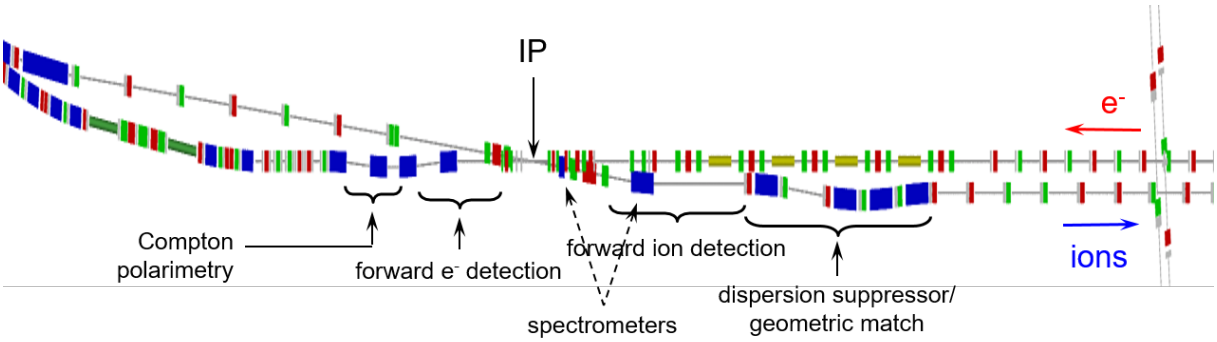

Figure 7.5: JLEIC design and extended detector: Accelerator elements in the IR and downstream the electron and ion beams are shown. The dark blue elements are dipoles whereas red and green elements are beam quadrupoles. The central detector is placed asymmetrically around the IP. Forward electron (ion) detectors will be installed in the downstream electron (ion) area. The locations for the electron (labeled as Compton polarimetry) and ion polarimetry are also shown. (Also see Figure 5.31.)

combination with relatively large dispersion values, enhances momentum resolution of the forward detectors. The dispersion generated by the spectrometer dipoles is suppressed by a simple dipole chicane structure whose parameters are chosen to avoid a significant impact on the electron equilibrium emittance. The resulting parameters of the electron detector region elements at 10 GeV are listed in Table 7.2.

The center of the chicane is a convenient place for a Compton polarimeter. The whole chicane serves as spectrometers providing resolution of scattered electrons down to very small momentum offsets. Because there is no net spin rotation between the polarization measurement point and the interaction point (IP), the polarimeter allows for continuous non-invasive monitoring of the electron polarization at the IP. The polarimeter is shifted from the electron beam axis at the IP eliminating the background due to the synchrotron radiation coming from the IP. Figure 7.15 shows the schematic of the low-Q^2 tagger and electron polarimeter setup downstream of the IP.

To mitigate the synchrotron radiation in the Compton detectors from the upstream dipoles in the chicane, two soft dipoles are placed in the middle of the chicane. Decreasing the solid angle acceptance of the detector and adding ante-chambers to absorb the synchrotron radiation photons further reduce the number of photons incident on the beam pipe and detectors.

The minimum relative momentum offset, which makes particles come out of the beam stay clear, can be calculated using the following formula.

$$\left(\frac{\Delta p}{p}\right)_{\min} = \frac{10\sigma_{\mathrm{x}}}{D_{\mathrm{x}}}. \tag{7.2.4}$$

Here $\sigma_{\mathrm{x}} = \sqrt{\beta_{\mathrm{x}}\epsilon_{\mathrm{x}} + (D_{\mathrm{x}}\frac{\Delta p}{p})^2}$ is the rms value of the beam size, and D_{x} is the horizontal dispersion. The minimum relative momentum offsets are 0.11 and 0.006 at the end of the first dipole and in the middle of the chicane, respectively.

Measurements of particles down to the beam- line in the electron-beam direction are also needed. The detector/IR design is expanded in the forward electron direction, as shown in Figure 7.15 (see also Figure 7.5) to monitor the luminosity and polarization of the electron beam and significantly increase the low-Q^2 detector coverage.

Table 7.2: Parameters of the electron detector region magnets at the electron momentum of 10 GeV.

Name	Type	Length (m)	GFHA[1] (cm)	IHA[2] (cm)	OR[3] (cm)	Dipole field		Quad gradient		Solenoid (T)	Position and orientation[4]		
						B_x (T)	B_y (T)	$\frac{\partial B_y}{\partial x}$ ($\frac{T}{m}$)	$\frac{\partial B_x}{\partial x}$ ($\frac{T}{m}$)		x (m)	z (m)	θ (rad)
Downstream electron IR elements													
eBDS6	Dipole	3	1.8	4.5	11	0	0.445	0	0	3.0	−0.030	−34.491	−0.02
eBDS5	Dipole	3	1.8	4.5	11	0	−0.417	0	0	0	−0.260	−27.295	−0.02125
eBDS4	Dipole	0.5	1.8	4.5	11	0	−0.167	0	0	0	−0.293	−25.045	−0.00125
eBDS3	Dipole	0.5	1.8	4.5	11	0	−0.167	0	0	0	−0.293	−21.345	0.00125
eBDS2	Dipole	3	1.8	4.5	11	0	−0.417	0	0	0	−0.260	−19.096	0.02125
eBDS1	Dipole	3	1.8	4.5	11	0	0.445	0	0	0	−0.030	−11.900	0.02
eASDS	Sol	1.2	2.2	4.5	11	0	0	0	0	−4.0	0	−6.3	0
eQDS3	Quad	0.6	2.4	4.5	10	0	0	−13.629	−1.974	0	0	−4.9	0
eQDS2	Quad	0.6	2.8	4.5	8.5	0	0	43.466	6.298	0	0	−3.7	0
eQDS1	Quad	0.6	1.7	4.5	8	0	0	−44.780	−6.489	0	0	−2.5	0
eDSDS	Sol	1.6	2	160	210	0	0	0	0	3.0	0	−0.8	0
Upstream electron IR elements													
eDSUS	Sol	2.4	2	160	210	0	0	0	0	3.0	0	1.2	0
eQUS1	Quad	0.6	2	4.5	10	0	0	−37.263	8.171	0	0	3.26	0
eQUS2	Quad	0.6	3.2	4.5	11	0	0	42.511	−9.321	0	0	4.46	0
eQUS3	Quad	0.6	1.5	4.5	11	0	0	−29.391	6.444	0	0	6.91	0
eASUS	Sol	1.2	2.2	4.5	11	0	0	0	0	−6.0	0	8.21	0

[1] GFHA stands for Good-Field Half Aperture.
[2] IHA stands for Inner Half Aperture.
[3] OR stands for Outer Radius.
[4] Position and orientation are specified for the center of each magnet.

7.2.3 Beam-pipe design and background

The types and levels of background influence the detector design and the size of the systematic uncertainties of any physics measurement and are a direct consequence of the arrangement of beam magnets and other beam parameters and optics. Experience at earlier accelerator facilities, especially the previous HERA electron-proton collider, indicates the importance of background studies in the early design phase. Primary sources of machine-induced background are:

- **Synchrotron radiation**
  Various sources of synchrotron radiation must be considered in detailed background studies. Any time the trajectory of a charged particle is bent, synchrotron photons are emitted tangential to the particle's path. Bending and focusing of the electron beam is the main cause of synchrotron radiation within the IR. However, contributions from the upstream electron beam scattering off residual gas must be assessed as well. It is important to place the IP far away from strong bending magnets in the arcs to minimize synchrotron radiation. The tracking detectors in the central detector as well as the calorimeter have to be properly shielded against synchrotron radiation, therefore a number of absorbers and masking must be applied along the electron beam direction. Synchrotron radiation also deposits several kilowatts of power into the beam pipe in the central detector region, which must then be cooled. Additionally, synchrotron radiation can degrade vacuum quality by causing material desorption from vacuum chamber walls and/or heating residual gas. Synchrotron radiation is also a direct and indirect source of background in the Compton polarimeter, the luminosity monitor, and low-Q^2 tagger located on the downstream electron side of the IR.
- **Beam gas interactions**
  Beam-gas interactions might occur when proton or ion beam particles collide with residual beam gas. Ion beam interactions with gas cause beam loss and halo which may reach detectors. This may be an important source of neutrons that thermalize within the detector hall. The large synchrotron radiation load could heat the beam pipe and residual gas particles from the beam pipe walls could be released, which would lead to a degradation of the vacuum. A crossing angle and short section of shared beam pipe in the JLEIC design minimize the beam-gas problem.
- **Beam halo**
  Particles formed from elastic collisions of both electron and proton beams with residual gas or beam-beam interactions can form a halo distribution around the beam. Often the result is an on-momentum electron or ion with large scattering angle. These particles can then generate additional background by interacting with the beam pipe and can impact the stability of the beam. Beam halo must be studied to determine whether "scraping" the halo with collimators is required, as well as proper placement of those collimators.
- **Neutron flux**
  Neutrons with energies around a few hundred keV can be detrimental to detector components like silicon photo-multiplier tubes which are especially vulnerable. A quantitative estimate of the neutron flux is needed for detector development and placement. To achieve this, modeling the experimental hall and collaborating with the Radiation Control Group has been initiated.

.

The beam pipe near the IR is considered to have three regions. The 50 mrad crossing angle, a 10σ beam-clear requirement, as well as a need to operate with various beam energies, set a constrain on a beampipe radius and also on a shape of beampipe elements. The straight section of

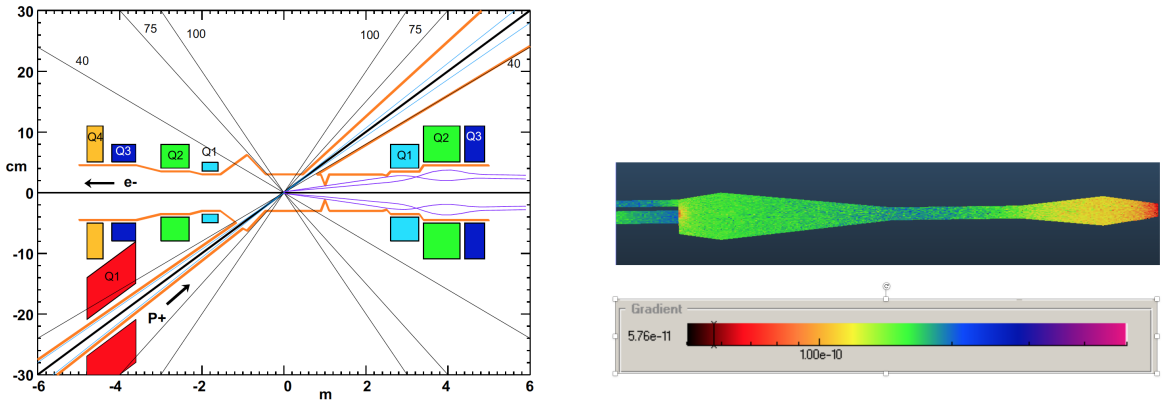

Figure 7.6: The beampipe design (left panel), including the masking for synchrotron radiation, and the simulation vacuum distribution in the IR with a static vacuum level in the order of 10^{-10} Torr (right panel) is shown

the beam-pipe, surrounding the IP, has a common volume for both electron and ion beams and is envisioned to have an inner radius of about 3.2 cm. The material for this beampipe section will be beryllium, to minimize the multiple scattering for outgoing particles as well as the energy-loss for low-P_T particles. The next section of the beampipe design has a conical shape to accommodate the crossing angle. Both beams also share the volume here. The material requirements are not so strict in this area, therefore aluminum will be used. Further up- or downstream from the IP the electron and ion beams are separated. Copper parts will be used for better absorption/masking of synchrotron radiation. An illustration of a possible beam pipe design near the IR is shown in the left panel of Figure 7.6.

The vacuum and synchrotron radiation induced gas load have been estimated using the Molflow+ and SynRad vacuum modeling software. The Molflow+ simulation shows that by placing pump with speeds about 100 L/s at either end of the central interaction region and outside the quadrupole cryostat, the static vacuum in the interaction region should be maintained at the anticipated 10^{-10} Torr. The right panel of Figure 7.6 shows the simulated vacuum distribution with the cryopumping for the cold beamline sections, showing much lower pressures in the cryostats.

The SynRad software suite is useful for determining synchrotron radiation loads. At electron beam energy of 10 GeV and 1 A of electron current a power of up to 100 W/cm^2 is deposited in the collimator block near the aperture. The preliminary Synrad simulations show very little power deposited downstream of the IP on the scattering chamber.

7.3 Detector Design Concept

The integrated JLEIC IR and detector concept to detect all three classes of final-state particles as defined in Section 7.1 is illustrated in Figure 7.7. The crossing angle moves the ion beam away from the electron beam elements and makes room for dipoles and FFBs located just downstream of the central detector area. The dipoles serve two purposes. First, they shape the ion beam orbit so that there is 1 m distance between the two beams 42.5 m away from the IP, making room for detectors. Second, the dipole systems allow momentum analysis of the particles with small transverse momentum with respect to the beams. The particles with large transverse momenta are

analyzed using the solenoidal field in the central detector. The IR/detector area can be divided into three main parts.

1. Central Region (−3.5 m, +7 m) around the IP. This is the region in which predominantly the final state particles from the hard collisions between the electron and the struck parton are measured (particles of types 1 and 3 in Figures 7.1 and 7.7).
2. Far-Forward Hadron Region (+7 m, +40 m) downstream of IP in the ion direction. This is the region in which predominantly the particles associated with the initial ion are measured (particles of type 2 in Figures 7.1 and 7.7).
3. Far-Forward Electron Region (−3.5 m, −30 m) downstream of IP in the electron direction. This is the region in which electrons at very small angles are detected (particles of type 1 in Figures 7.1 and 7.7). In this region, also the luminosity and electron-beam polarization is measured as described in Sec. 7.3.4.

The JLEIC design and the extended detector with a total length of 70 m is shown in Figure 7.5.

7.3.1 The Central Detector Design Considerations

The central detector is designed mainly to measure the final state particles of types 1 and 3. It is very much like a traditional collider detector with large transverse acceptance.

The longitudinal kinematics of DIS is shown in the left panel of Figure 7.8. The basic kinematic variables of DIS are $Q^2 = -q^2$, the virtuality of the exchanged photon, x , the fraction of the longitudinal momentum carried by the struck parton, and y , the inelasticity of the collision. The three variables are related by $Q^2 = sxy$, where s is the center-of-mass energy of the collision. Thus, measuring any two of x, y, or Q^2, specifies completely the longitudinal kinematics of DIS. While

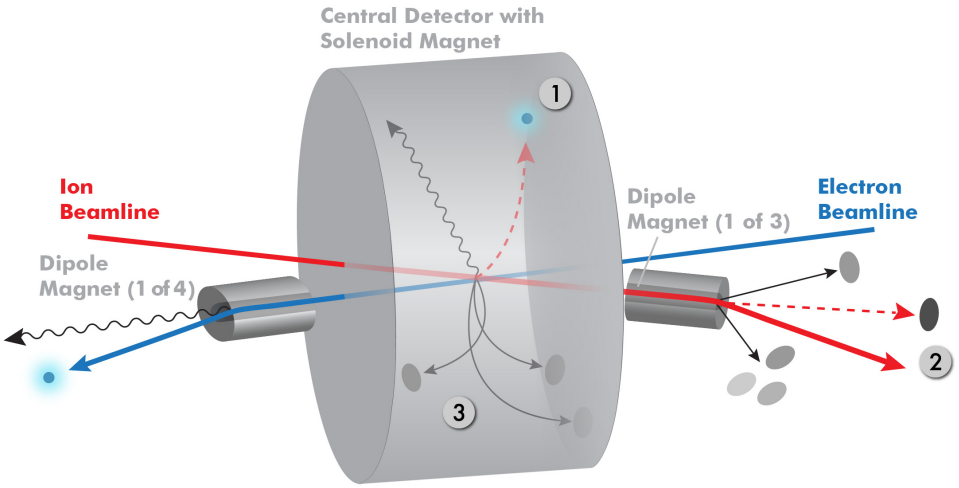

Figure 7.7: JLEIC IR and detector concept illustrating the crossing angle between the electron and ion beams and the dipole magnets downstream and upstream of the central detector. Circled numbers correspond to the three classes of particles in the final state.

this measurement of two variables (taken to be x and Q^2) is not enough for much of the physics program at the EIC, they need to be measured for almost all events to be used for physics analyses.

The scattered electron energy E'_{e} and the scattering angle θ_{e} can be used to reconstruct the longitudinal kinematics, x and Q^2. The angle of the scattered parton and its energy (substituted with the angle and energy of the associated jet, θ_{jet} and E'_{jet}) can also be used. Conversely, specifying x and Q^2 completely determines the four measurable variables, θ_e, θ_{jet}, E'_{e}, and E'_{jet}. Therefore, the energy of the scattered electron or jet that point towards any particular region of the central detector (i.e. fixed θ) is predicted from simple kinematics and can be taken into account in the detector design.

Access to the transverse kinematics, transverse momentum k_t and transverse position or impact parameter b_t of the parton, as well as flavor identification of the partonic collision is central to the nucleon and nuclear structure measurement program planned for the EIC. The energy scale of transverse kinematics is in the order of a few hundreds MeV or less. This means identification and precise angular and momentum measurements of single hadrons among the particles associated with the scattered partons (particles of type 3 in Figure 7.1) are needed. The momentum range of these particles in various parts of the central detector must be understood to determine the detector requirements. This follows from understanding of the jet energy that is expected for a fixed θ_{jet} and the momentum distribution of particles within that jet.

To provide a full solid angle (4π) coverage for all outgoing particles, the central detector is divided into three sections, the barrel, the electron endcap and the hadron endcap, as shown in the top panel of Figure 7.9. Far-forward sections (both electron and hadron) will be discussed in Sec. 7.3.2 and 7.3.3. The three different central detector sections that correspond to different x and Q^2 regions for the scattered electron or jet are shown in Figure 7.9 along with lines of constant scattered electron energy E'_{e} and E'_{jet} respectively.

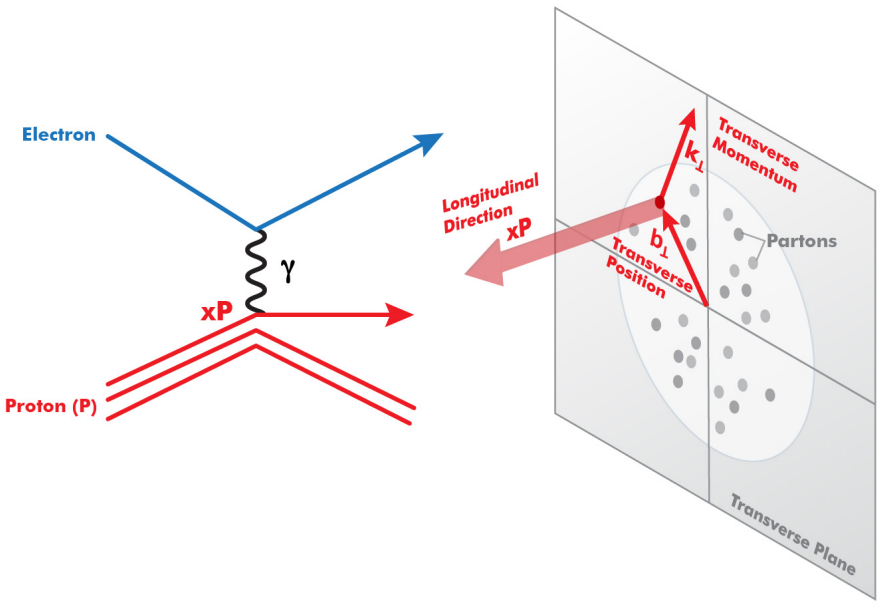

Figure 7.8: The basic process of the EIC, DIS, is illustrated in the left panel. In the right panel, the transverse momentum and transverse position information is shown in addition to the longitudinal momentum.

From these figures, the range of energies E'_{e} and E'_{jet} in each section of the central detector can be read. Using Monte Carlo simulation the momentum range of hadrons detected in each detector section can be estimated. Table 7.3 gives, then, a rough estimate of the momenta for each of dectected particle in each section.

Table 7.3: Estimated Momentum Ranges in the Central Detector

Detected Particle	Electron Endcap	Barrel	Hadron Endcap
E'_{e}	$< 8\,\mathrm{GeV}$	8–50 GeV	$> 50\,\mathrm{GeV}$
E'_{jet}	$< 10\,\mathrm{GeV}$	10–50 GeV	20–100 GeV
E'_{hadrons}	$< 10\,\mathrm{GeV}$	$< 15\,\mathrm{GeV}$	15–50 GeV

These energy ranges inform the choice of technologies needed in the central detector for tracking, calorimetry and particle identification. To provide complete coverage in all regions, for all expected particle momenta, the central detector will be instrumented with several high-performance particle identification (PID) detectors, such as energy-loss or cluster counting measurements with tracking

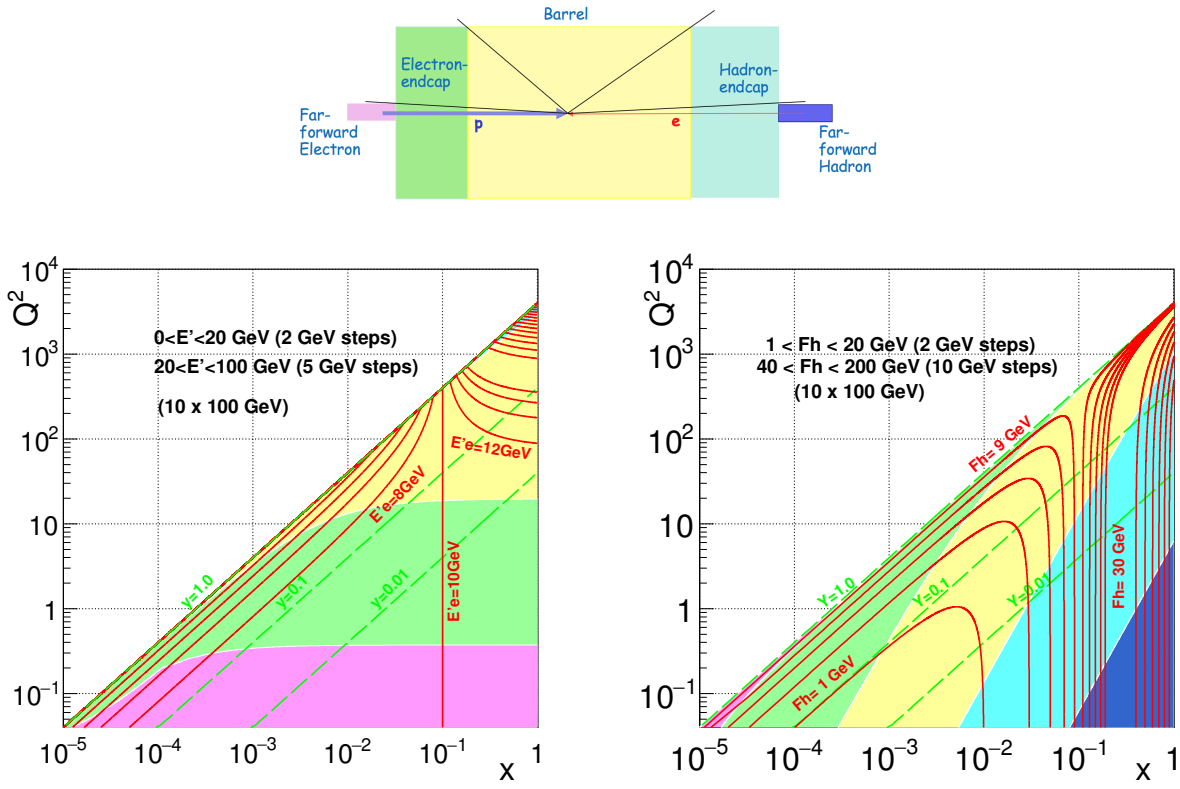

Figure 7.9: Isolines of the scattered electron (bottom, left panel) and jet (bottom, right panel) in the JLEIC central detector for the collision of 10 GeV electrons and 100 GeV protons. The color coding corresponds to the electron endcap, barrel, and hadron endcap regions in the JLEIC central detector (top panel).

detectors dE/dx, time-of-flight measurements (TOF), Cherenkov detectors. An overview about the PID system is provided in Figure 7.10.

The current JLEIC central detector design concept is shown in Figure 7.11. In some cases, a provisional choice has been made for specific sub-detector technologies taking the performance requirements into account.

7.3.1.1 Barrel The barrel is the volume around the IP defined by the dimensions of the solenoid, 4 m in length and 3.2 m in diameter. The solenoid is centered along the electron beam axis to limit synchrotron radiation and shifted 40.0 cm upstream of the hadron beam direction to increase the rapidity coverage for outgoing hadrons (particles of type 3 in Figure 7.1). The solenoid magnet will operate with a 1.5–3.0 T field with the lower field improving the acceptance for low-P_T particles, e.g., slow pions originating from D^* decay with transverse momenta below 100 MeV.

The tracker inside the barrel region makes precise momentum measurements of high-P_T particles and covers a rapidity range of about $-1.1 < \eta < 1.5$. Approximately 20 cm of radial space are reserved for the vertex detector. The radial dimension of the barrel tracking detector is a compromise between the tracking performance (number of layers or drift volume) and spatial restrictions due to the inner radius of the solenoid and the requirement of a vertex detector around the IP as well as for PID detectors.The simulated barrel tracker design, using straw tubes, is shown in Figure 7.12. The energy loss information in the straw tubes will provide PID information for low-momentum particles ($P < 1$ GeV) and high-momentum particles. Silicon discs based on MAPS technology are placed along the beam pipe for tracking of particles along the electron and ion beams.

The vertex detector for the reconstruction of primary and secondary vertices is placed as close to the IP as possible. Due to the 10σ stay-away constraint for the beam envelope at injection energies, the outermost radius of the beam pipe will be 3.2 cm. Possible technologies for the vertex detector are silicon pixel detectors based on MAPS or DEPFET technology. The small pixel size with relatively high readout rate will allow to limit the occupancy of background events, e.g., from synchrotron radiation or beam gas events. Also the endcaps of the vertex detector for the reconstruction of forward and backward going particles are placed as close to the IP as possible.

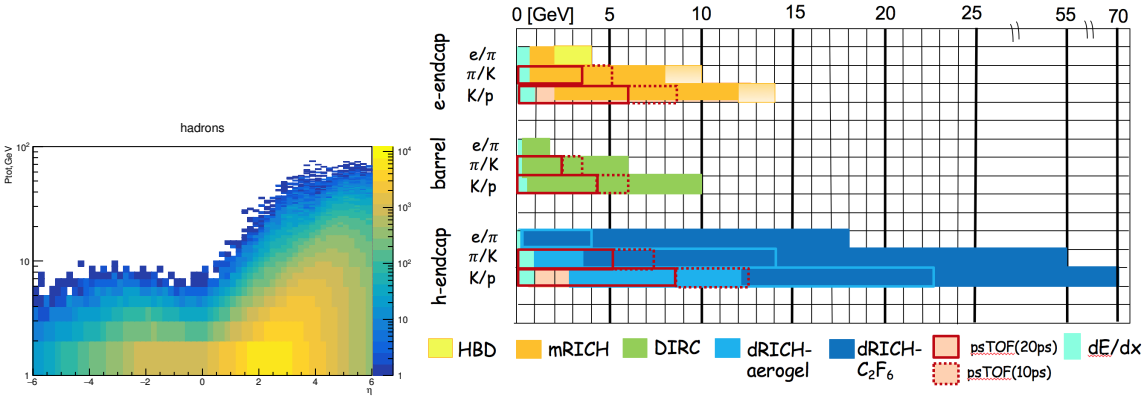

Figure 7.10: Due to a wide range of hadron momenta in various regions of the detector (left panel), several PID detectors are selected for the identification of hadrons at JLEIC. The technologies used in the barrel, electron endcap, and hadron endcap regions and their momentum range are summarized (right panel).

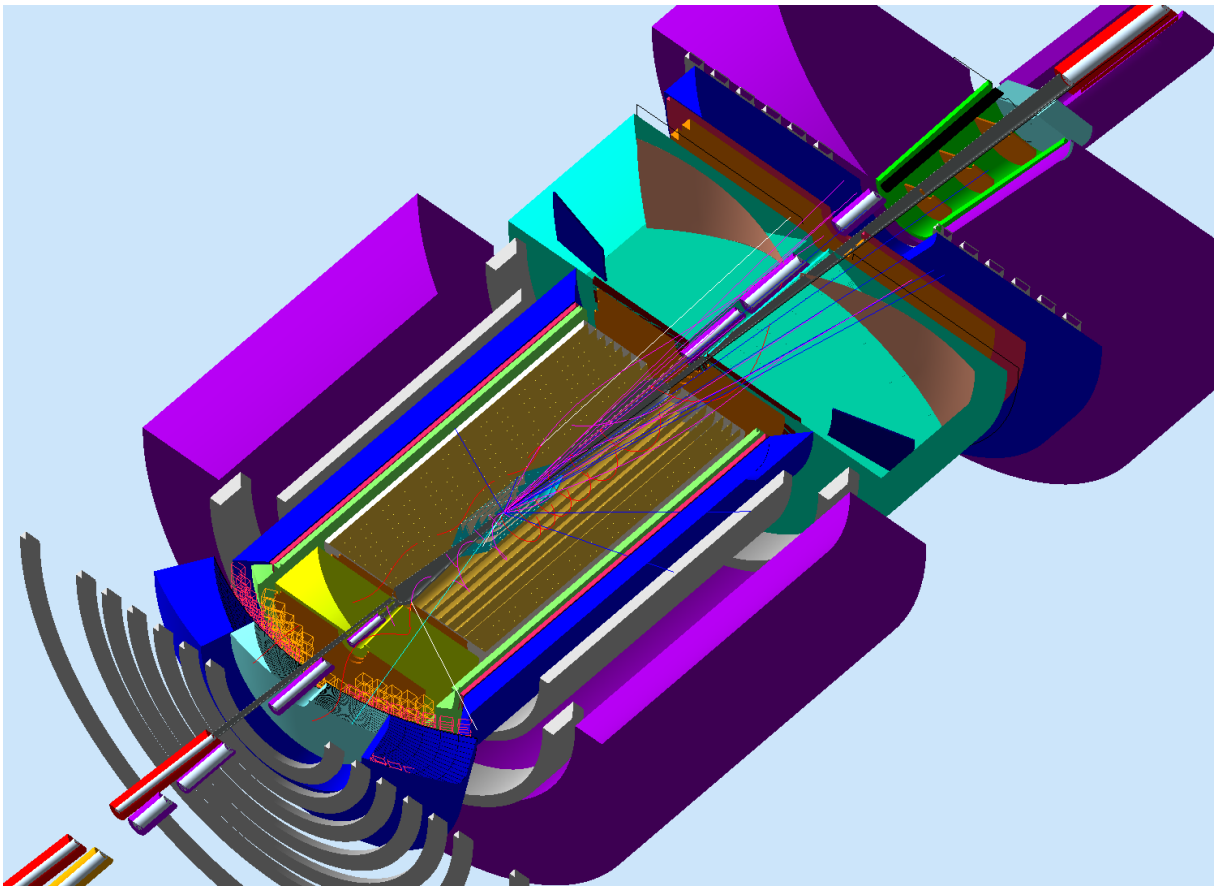

Figure 7.11: Simulation of the JLEIC Central Detector

A detector of internally reflected Cherenkov light (DIRC) is implemented as the main PID detector in this region due to the restricted space. A 3σ separation of e/π, π/K and K/p can be achieved for particle momenta up to 1.8 GeV, 6 GeV and 10 GeV, respectively.

For high-Q^2 measurements in the barrel where the energy of the scattered electron is typically above 10 GeV, a sampling shashlik calorimeter with an energy resolution of about 10% is used. The barrel electromagnetic calorimeter provides particle identification for scattered and secondary electrons as well as for photons from the DVCS process, or π^0 mesons from the electromagnetic part of jets.

7.3.1.2 Electron Endcap The electron endcap is mainly designed for the high-precision measurement of the scattered electron (particles of type 1 in Figure 7.1) whose energy is below a few GeV. It is thus equipped with a tracker, based on the GEM technology, and a crystal calorimeter ($PbWO_4$) with a constant term in the order of 0.5 % and a stochastic term in the order of 1.0–1.5 %. As PID detector in this region, a modular RICH (mRICH) is adopted. With a current mRICH prototype, using a 6" focal length Fresnel lens and 3x3 mm^2 photosensors a 3σ separation of e/π, π/K and K/p could be achieved up to 2 GeV, 8 GeV and 12 GeV, respectively.

7.3.1.3 Hadron Endcap Due to asymmetric beam energies at the EIC, final state particles will be boosted towards the hadron endcap. While the expected multiplicity of particles per event is only a

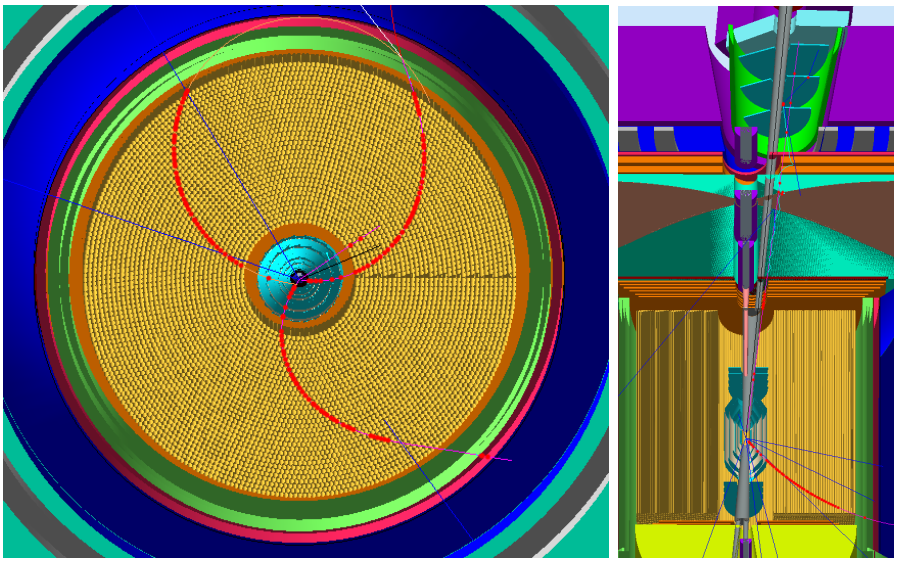

Figure 7.12: Simulation of the central tracker: XY view (left panel) and top view including hadron endcap and first dipole area (right panel).

few, the large cross-section of low-Q^2 events implies that several hundred particles with momentum nearly up to the ion beam energy are expected every µs. Therefore a high granularity tracker will be needed for efficient multiple track separation. A system of GEM discs will be used for this purpose. To improve the momentum measurements, an additional dipole is used to cover the area along the beam pipe and the GEM discs are placed within it, as shown in Figure 7.12).

The dual-radiator RICH (dRICH) will cover the wider momenta expected to be required in the hadron endcap. It incorporates two different radiator materials, aerogel and C_2F_6 gas, with different refractive indices n to cover different momentum ranges. The aerogel provide 3σ separation of e/π, π/K and K/p in the momentum range $0.003(0.8) < e/\pi < 4$GeV, $0.8(2.84) < \pi/K < 14$GeV and $2.84(5.4) < K/p < 22$GeV, where number in a brackets correspond to a effective threshold. For the C_2F_6 gas the corresponding momentum coverage are $0.01(3.48) < e\pi < 18$GeV, $3.48(12.3) < \pi/K < 55$GeV and $12.3(23.4) < K/p < 70$GeV,respectively. The time-of-flight system could be used for hadron separation for the low momentum particles.

To detect high-x SIDIS particles and the electromagnetic part of high-x jets, an electro-magnetic calorimeter with high resolution, to separate, e.g., DVCS photons from high π^0 background in this region, is required. The calorimeter will be also used to measure the energy of the particles at rapidities $\eta < -2$, where due to the lack of magnetic fields, the tracking resolution is poor compared to the energy resolution of $PbWO_4$ crystals (3% or better).

7.3.2 Far-Forward Ion Region Detector Design Considerations

Charged particles that traverse the FFB apertures are detected either between Dipole 1 (iBD61) and Dipole 2 (iBDS2; see Figure 7.13) or downstream of Dipole 2. Tracking detectors within Roman pots will be used to reconstruct these particles in a similar manner to those used by the TOTEM experiment.

We estimated the particle position at a few locations along the beam line as a function of its momentum and angles at the IP. The results are shown in Figure 7.14. The top panels shows

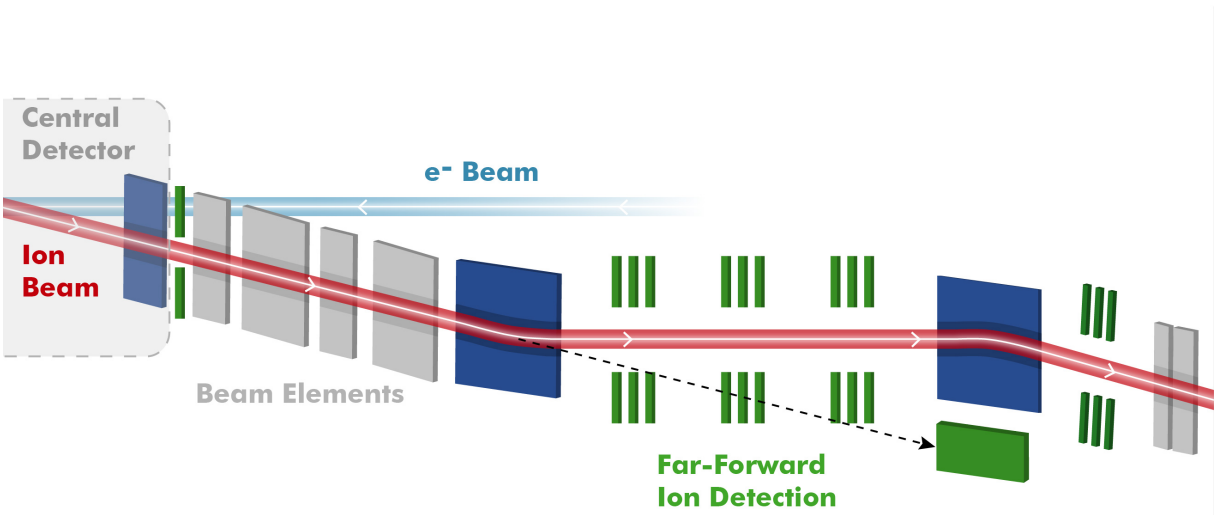

Figure 7.13: Schematic illustration of the IR and detector design in the far-forward ion region.

the particle's radial position at the beam focal point 16 m downstream of Dipole 2 as a function of the particle's $\Delta p/p$ for a number of different initial θ_x and θ_y angles. The top right graph in is an expanded version of the left figure focusing on small values of $\Delta p/p$ and x. The red band indicates the nominal $\pm 10\sigma_x$ beam stay-clear region where a particle cannot be detected. The points where the curves cross the red band boundaries determine the $\Delta p/p$ limits, while the slopes of the curves determine the momentum measurement precision. The graph indicates, e.g., that a particle initially moving along the beam, i.e. $\theta_{x,y} = 0$, can be detected as long as its $\Delta p/p$ is greater than about 5×10^{-3}.

Similarly, we investigate the dependence of the particle's radial position on the initial θ_x and θ_y angles for a characteristic set of $\Delta p/p$ including 0, ± 0.01, ± 0.1, and ± 0.5. At the secondary focal point 16 m downstream of Dipole 2, in the first order, there is no dependence of the particle's transverse position on its initial angle at the IP. Therefore, we move the observation point 4 m upstream to a location 12 m downstream of Dipole 2. The bottom panel of Figure 7.14 shows the calculated dependence of the particle's radial deflection at that point as a function of the initial θ_x for the different $\Delta p/p$. The graph on the bottom right is a version of the left-hand side figure with a greatly expanded vertical scale. The red band is the nominal $\pm 10\sigma_x$ beam stay-clear area. The bottom right plots of Figure 7.14 indicates that a particle of the same rigidity of the beam can be detected if its initial angle exceeds about ± 3 mrad.

These studies demonstrated that a relatively modest position resolutions of a few hundred microns for the tracking detectors are needed. Such a performance can be achieved with a variety of techniques including silicon and fiber trackers.

The forward ion FFB is designed so that there is clear line of sight from the IP through the FFQ apertures within a cone with a ± 10 mrad opening angle. Zero-degree calorimeter placed downstream will be needed to measure the neutral particles produced along the beamline. As

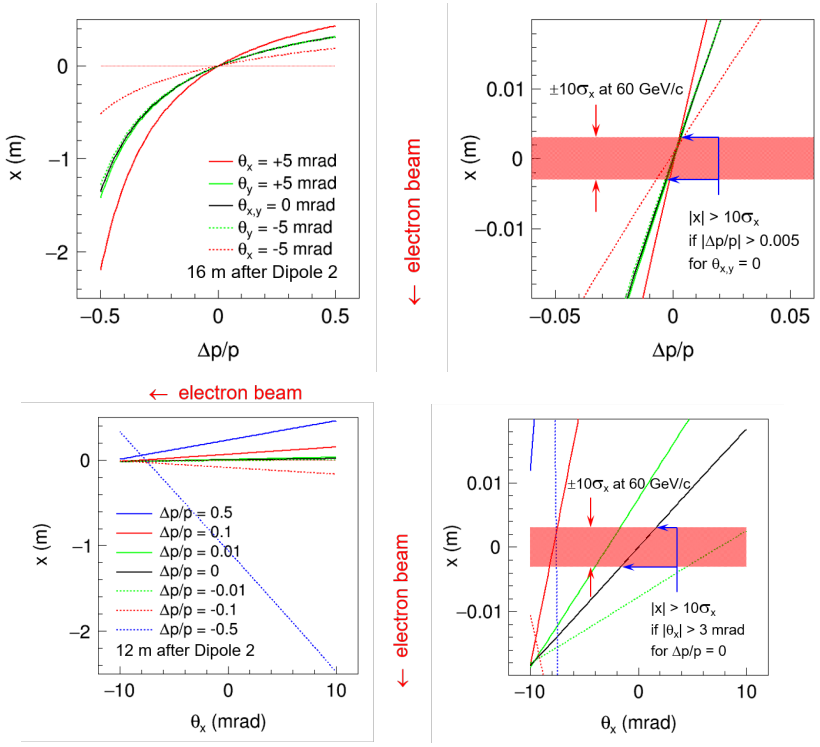

Figure 7.14: Momentum (top panel) and angular resolutions (bottom panel) of the far-forward ion detection: In the top panels, the particle's radial position 16 m downstream of Dipole 2 (iBDS2) is shown as a function of the particle's $\Delta p/p$ for a characteristic set of different initial θ_x and θ_y angles. In the bottom panels, the particle's radial deflection 12 m downstream of Dipole 2 (iBDS2) is shown as a function of the initial θ_x for a characteristic set of different $\Delta p/p$. The right plots are an expanded version of the left figures. The red band is the nominal $\pm 10\sigma_x$ beam stay-clear region.

outlined below, the desired performance of this detector is rather stringent, with hadronic energy resolution in the range of $35\,\%/\sqrt{E}$ as well as good position resolution for neutrons in the range of 50–100 GeV, as well as the ability to count photons in the range of hundreds of MeV. A highly granular calorimeter as well as a dual readout calorimeter combined with an electromagnetic section in front are candidates for the zero-degree calorimeter.

7.3.3 Far-Forward Electron Region Detector Design Considerations

Measurements of particles down to the beamline in the electron-beam direction are also needed. The IR and detector design is expanded in the forward electron direction, as shown in Figure 7.3 and Figure 7.15 to significantly increase the low-Q^2 coverage. The far-forward electron detector design is also used to monitor the luminosity and polarization of the electron beam as described in Sec. 7.3.4.

The detector configuration for the low-Q^2 electron tagger is still under study. The configuration will be driven by the required acceptance and energy resolution for the processes of interest. The electron tagger places certain constraints on the geometry of the chicane. For example, the dipoles should be "C-type" to allow the scattered electrons to exit the beampipe unimpeded. In addition,

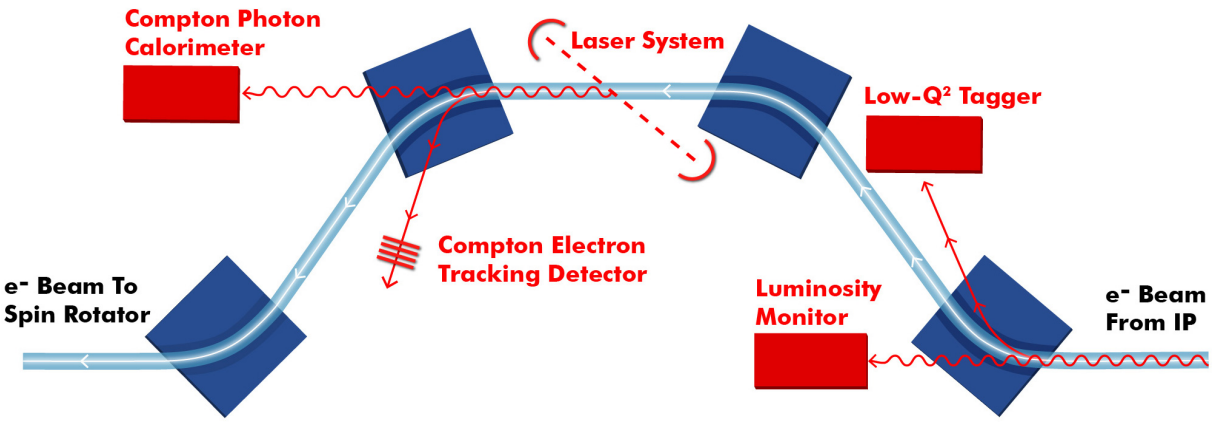

Figure 7.15: Illustration of the concept for detecting low-Q^2 events and measuring the polarization of the electron beam and the luminosity at the IP.

the pipe itself should have a relatively thin window on the side facing the detector to minimize multiple scattering.

7.3.4 Auxiliary Measurements

7.3.4.1 Luminosity Measurement The Bethe-Heitler process , where the incoming or outgoing electron radiates a high-energy photon in the field of the proton, was used very successfully at HERA for luminosity measurement and we plan to do the same at JLEIC. The high-energy photon is produced at the electron-ion collision point and propagates along the electron beam direction until it is detected after the first dipole of the Compton polarimeter/forward electron detection chicane.

Due to the high electron current at JLEIC, the synchrotron radiation as well as event rates are expected to be high. Luminosity monitors based on calorimetric detection of the primary photon from the Bethe-Heitler process will suffer from radiation damage as well as pile-up (multiple events). The luminosity monitor at JLEIC will be based on the luminosity "spectrometer" concept used at the ZEUS detector in HERA run II. The spectrometer counts bremsstrahlung photon conversions in the beam pipe exit window using two small calorimeters symmetrically placed away from the synchrotron radiation plane. The photon conversion rate is measured by counting electron-positron coincidences in the calorimeters. The electron-positron pair is separated by a small dipole magnet.

7.3.4.2 Electron Polarimeter We plan to measure the electron beam polarization using a Compton polarimeter with the detection of the scattered electron from a laser. As shown in Figure 7.15, the polarimeter is integrated in the dipole chicane downstream of the electron-ion interaction region. The first two dipoles shift the electron beam (horizontally) about 29 cm. The integrated fields in these two bending magnets are equal and opposite, so the net precession of the longitudinal electron spin is zero thus guaranteeing that the polarization measured by the Compton polarimeter is the same as at the IP. The region between the 2nd and 3rd large dipoles incorporates the laser system that will collide with the electron beam. The backscattered photons from the laser and electron collisions pass through the beam pipe in the 3rd large dipole and eventually exit the vacuum system through a thin window where they are detected by a photon detector. Because the scattered electrons have lower energy, they will be bent more by the 3rd large dipole than

the unscattered electrons, achieving a separation on the order of several mm to a few cm at the position of an electron detector, just upstream of the fourth dipole.

The electron detector for the JLEIC Compton polarimeter are highly segmented in the direction of the dipole bend to be able to fully map the electron energy and asymmetry spectrum, and will be large enough to cover the asymmetry spectrum from the kinematic endpoint to at least the "zero-crossing" of the asymmetry. Solid-state detectors such as silicon and diamond, segmented into strips 100 to 200 µm can be constructed to accommodate the geometry required.

At JLEIC, the very high current electron beam will create large RF power levels inside the vacuum chamber, likely rendering the detector unusable if placed in the vacuum chamber. For this reason, the JLEIC detector will be placed in a "Roman Pot" (a thin windowed "container", external to the beamline vacuum system).

7.3.4.3 Ion Polarimeter Experience in proton polarization measurement for high energy beams comes exclusively from RHIC. High energy proton polarimetry is performed in the RHIC-Spin program with primarily two types of polarimeters: Polarized Hydrogen Atomic Beam Polarimeters (ABP) and proton Carbon elastic scattering. Both use the transverse polarization single-spin asymmetry in the low momentum transfer region of the Coulomb-Nuclear Interference (CNI).

The absolute polarization is measured using a target that is a free atomic H-beam jet, which crosses the RHIC beam in the vertical direction with a maximum target thickness of about 0.9×10^{-12} atoms/cm^2. The counting rate is less than 100 events/s at RHIC. Therefore, an integration time of about 10 h is required for 2% statistical accuracy. The systematic uncertainty of 2%, is dominated by uncertainty in the contamination due to unpolarized molecular hydrogen.

Fast beam polarimetry at RHIC is based on pC elastic scattering at very small proton scattering angles. pC elastic scattering events are identified by detecting the recoil carbon ions. For very small angle scattering the elastic reaction dominates and the measurement of the recoil ions gives predominantly elastic events with very small backgrounds. The largest systematic uncertainty in extracting the polarization comes from the uncertainty in the absolute energy scale in determining the energy of the recoil carbon ions.

JLEIC bunch spacing of 2 ns compared to 100 ns at RHIC means that a significant R&D is required for JLEIC polarimeters both for background rejection and for measuring the polarization structure of the stored beam. Ultrafast Si detectors, enhancement of beam-background reduction, and viability of bunch averaged polarization measurements are being investigated.

The JLEIC complex will also accelerate polarized d, ^{3}He, and Li ions. The weak energy- and target-dependence of the CNI asymmetry suggest that the analyzing powers for $\vec{d}$C, $\vec{d}$H, $^3\overrightarrow{\text{He}}$C *etc.* will be similar. In addition, tagging the diffractive channels such as $\vec{d}\text{C} \to pn\text{C}$ is possible, and may offer additional tools for timing and background subtraction. Additional R&D could also demonstrate the feasibility of absolute deuteron and ^{3}He polarimetry with polarized atomic deuterium and ^{3}He beams, respectively.

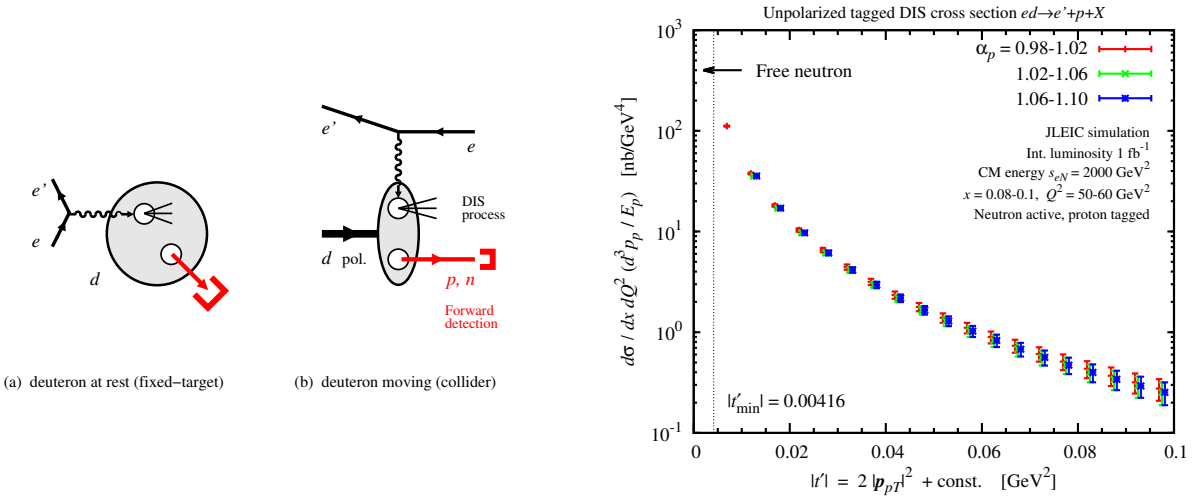

(a) deuteron at rest (fixed–target) (b) deuteron moving (collider)

Figure 7.16: DIS on deuteron with spectator tagging, $e + d \to e' + X + N$. (a) Deuteron rest frame (fixed-target experiments). The spectator nucleon is released with momenta ∼few 10–100 MeV. (b) Moving deuteron (collider experiments). The spectator moves in the deuteron direction with ∼1/2 the beam momentum and is detected with forward detectors. (c) Unpolarized neutron structure measurement with JLEIC. The tagged DIS cross section is measured as a function of the spectator proton momentum (transverse, longitudinal) and extrapolated to $p_{pT} \to 0$. The drop of the cross section with increasing p_{pT} reflects the nucleon momentum distribution in the deuteron.

7.4 Physics Performance Studies

The performance of the current IR and detector configuration are evaluated using specific physics studies. A selected subset of studies that illustrate particular aspects of the IR and detector designs are briefly described below.

7.4.1 Extraction of the spin structure of the neutron

The spin structure of the neutron is, arguably, best studied in polarized deuteron DIS at a collider. This is due to the well understood nuclear structure of the deuteron as well as the good control of the nuclear configuration achieved by using tagging of the spectator proton in the far-forward ion region detectors described in Sec. 7.3.2. The concept of spectrometer tagging is illustrated in the left panel of Fig. 7.16. In the right panel, the unpolarized tagged DIS cross section obtained by using the far-forward ion detectors to extrapolate the neutron structure to the physical point is shown.

Neutron spin asymmetry measurements have been simulated and are shown in Fig. 7.17. These measurements require the high-luminosity capability of the current design (100 fb^{-1} of data) as well as the availability of a highly polarized deuteron beam and high acceptance far-forward ion region detectors.

7.4.2 Extraction of gluon densities using Charm particles

While inclusive measurements access gluon distributions in nucleons and nuclei indirectly through scaling violations, the measurement of charm production directly access gluons via the photon-gluon

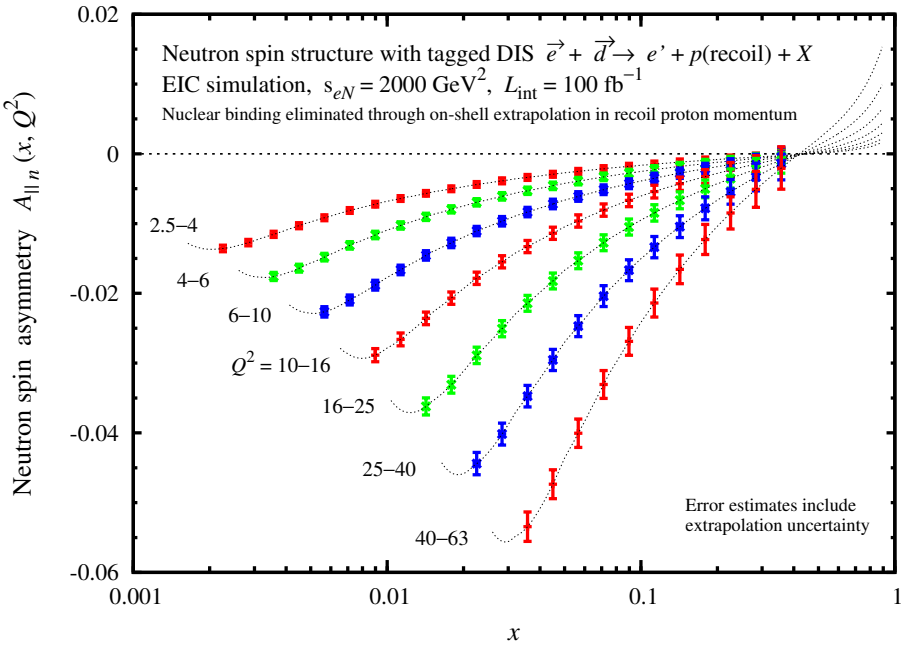

Figure 7.17: Simulated measurement of the neutron spin asymmetry $A_{n\parallel}(x, Q^2)$ in polarized electron-deuteron DIS with spectator proton tagging at JLEIC (integrated luminosity 100 fb^{-1}). The double spin asymmetry of the tagged cross section is measured as function of spectator proton momentum and extrapolated to on-shell point. The method eliminates both nuclear binding effects and D-wave corrections. The spin asymmetry $A_{n\parallel}$ gives access to the neutron structure function ratio g_{1n}/F_{1n}.

process. Charm production measurements depend on the capability of the detector to identify the charm-decay vertex which is separated from the primary vertex, as well as to the ability to tag the decay products of charm particle using particle-ID detectors. The current implementation of these detectors were described in Sec. 7.3.1.

Fig. 7.18 shows the mass distribution of a reconstructed D^0 particle and the effect of using the vertexing and particle ID capabilities. Fig. 7.19 shows a simulation of the extraction of the nuclear charm structure function and the nuclear gluon ratio determined using such an extraction.

7.4.3 Geometry tagging of heavy ions

Electron-nucleus collisions form an essential part of the science program at the EIC [2] including studies of gluon anti-shadowing, studies of parton propagation, attenuation and hadronization in the nucleus, and ultimately the search for parton saturation. The study of electron-nucleus collisions greatly benefits from geometry tagging [3], which is an experimental analysis technique for selecting event samples where one can, on a statistical basis, control the geometry of the collision. Using geometry tagging, one can select an event sample in ePb collisions with a saturation scale or an average path length equivalent to a minimum bias nucleus of size $A = 600 - 900$. In the case of the saturation scale, this is also equivalent to a minimum bias ePb collision at more than 3 times the baseline energy.

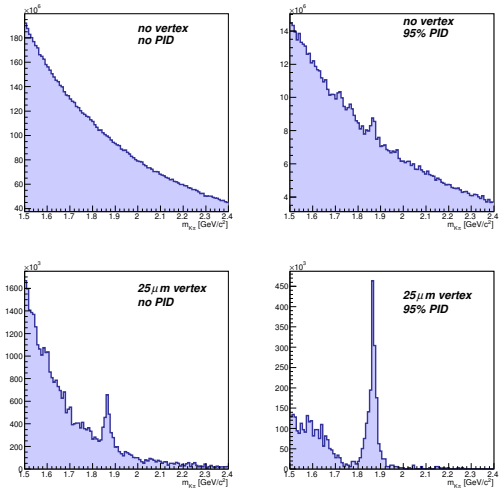

Figure 7.18: Impact of particle identification and vertex cuts on reconstruction of exclusive $D^0 \to K^-\pi^+$ decays.

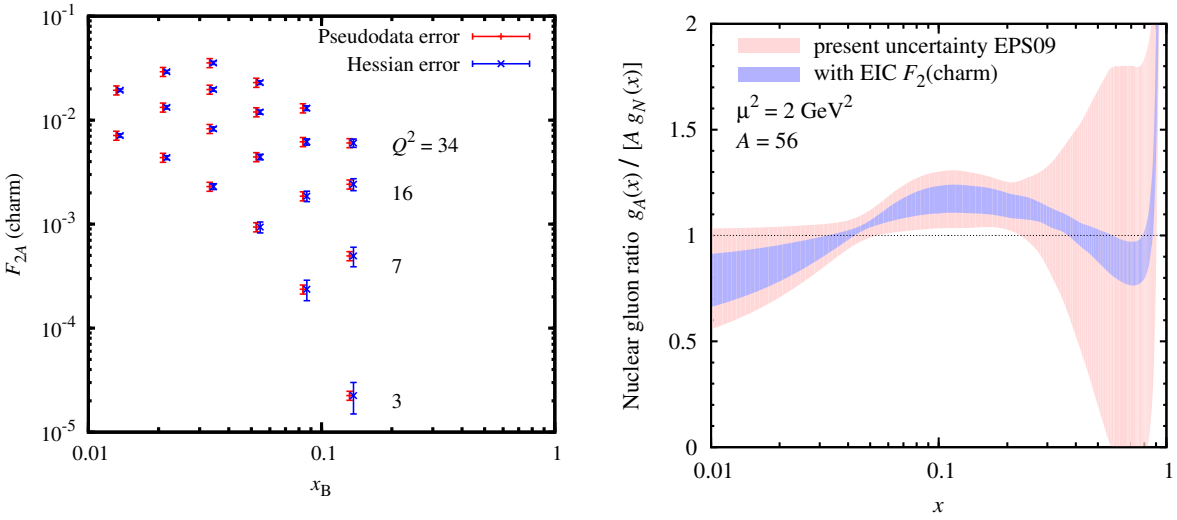

Figure 7.19: (a) Set of pseudo data in the nuclear charm structure function F_{2A}^c used in the impact study. The two error bars show the assumed pseudo data errors and the present theory error, estimated with the Hessian uncertainty of the EPS09 parameterization [1]. (b) Impact of charm pseudo data on nuclear gluon density.

Geometrical tagging depends on the identification and measurement of the forward reaction product of the heavy ions in the far-forward ion region as described in Sec. 7.3.2. The BeAGLE [4] simulation is used in this study. Fig. 7.20 shows the simulated tracks in the detector.

Using these techniques, we find that while the average thickness for geometrically tagged ePb events is 10.62 fm, it is 7.50 fm for the minimum bias distribution. This results in a thickness enhancement by a factor of 1.42.

So-called oomph factor [2] for gluon saturation posits that DIS measurements on nuclei enhances the saturation scale Q_s^2 as:

$$Q_s^2 \sim A^{1/3} x^{-\lambda}. \tag{7.4.5}$$

The factor $A^{1/3}$ represents the minimum bias geometrical factor. The thickness enhancement of 1.42 corresponds to an effective energy enhancement factor of 3.2 in the ion beam energy. It should also be noted that according to the white paper [2], estimates of λ range from $0.2 - 0.3$, which implies that an effective energy enhancement factor could be as high as 5.7. In terms of the nominal electron-proton $\sqrt{s}$ figure of merit, this corresponds to an increase of factor 1.8 to 2.4. For example a configuration with $\sqrt{s}$= 100 GeV, for ep, would correspond to $\sqrt{s}_{effective}$ = 180 - 240 GeV.

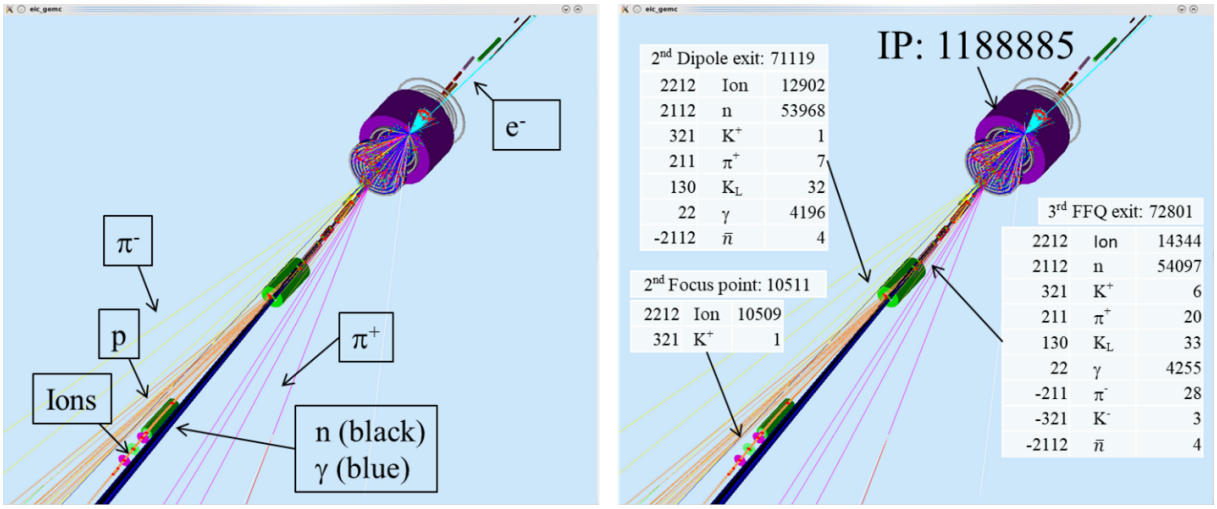

Figure 7.20: Snapshot of the GEMC event display showing the detector region with tracks from a few BeAGLE events.

REFERENCES

1. K. J. Eskola, H. Paukkunen and C. A. Salgado, JHEP **0904**, 065 (2009) [arXiv:0902.4154 [hep-ph]].
2. A. Accardi *et al.*, *Electron Ion Collider: The Next QCD Frontier*, arXiv:1212.1701v3 [nucl-ex] (2014).
3. BRAHMS, PHOBOS, STAR, and PHENIX Collaborations, Nucl. Phys. **A757** (2005) 1, 28, 102, 184.
4. `https://wiki.bnl.gov/eic/index.php/BeAGLE`

CHAPTER 8

COLLIDER DYNAMICS

8.1 Beam Synchronization

JLEIC is an asymmetric collider providing a wide range of beam energy, colliding 3–12 GeV electrons with 20–100 GeV protons or up to 40 GeV per nucleon heavy ions. Protons or ions with energy below 20 GeV also must be considered. In the medium ion energy range of 20–100 GeV, have relativistic β varying from 0.999 to 0.999957, while the velocity of the electrons is effectively the speed of light.

To ensure collision, each pair of electron/ion bunches need to arrive at the IP(s) at the same time, so the two beams need to have the same bunch time interval T_0:

$$T_0 = L_{0\mathrm{e}}/(n_{0\mathrm{e}}c) = L_{0\mathrm{i}}/(n_{0\mathrm{i}}\beta_{\mathrm{i}}c)\,, \tag{8.1.1}$$

where the index 0 refers to a synchronized situation. $L_{0\mathrm{e}}$ and $L_{0\mathrm{i}}$ are the circumferences of the electron and ion rings, respectively. $n_{0\mathrm{e}}$ and $n_{0\mathrm{i}}$ are bunch slot numbers in both rings, usually same as the RF harmonic number $h_{0\mathrm{e}}$ and $h_{0\mathrm{i}}$ if every RF bucket is filled. However, for JLEIC's initial phase with 476 MHz RF in the electron ring and 952 MHz RF in the ion ring, $n_{0\mathrm{i}}$ would be half of RF harmonic number, $h_{0\mathrm{i}}/2$.

$$T_0 = L_{0\mathrm{e}}/(h_{0\mathrm{e}}c) = (2L_{0\mathrm{i}})/(h_{0\mathrm{i}}\beta_i c) = 1/f_{(\mathrm{RF},0\mathrm{e})} = 2/f_{(\mathrm{RF},0\mathrm{i})} \tag{8.1.2}$$

8.1.1 Choices of synchronization option

To keep Equation 8.1.2 valid with different ion velocity β_i, we need to vary machine circumferences, frequencies, or harmonic number. The possible options to synchronize JLEIC's colliding beam with different ion energy are compared in detail in [1, 2].

Table 8.1: Required Magnet Movement for Electron Ring Pathlength Chicanes

# of FODOs	Length	# of Magnets Moved	Pathlength Change	Radial Shift Range	Inter-magnet Gap Change
3	68.4 m	4 dipoles, 5 quads	±10 cm	52/ − 69 cm	20 mm
4	91.2 m	6 dipoles, 7 quads	±10 cm	36/ − 39 cm	14 mm
5	114 m	8 dipoles, 9 quads	±10 cm	28/ − 29 cm	11 mm

We have chosen to synchronize the JLEIC electron/ion beams by

- varying the electron ring circumference, and
- varying ion ring harmonic number,
- varying the collider RF frequency.

The ion ring circumference will remain constant.

8.1.2 Electron Ring Circumference Variation

Varying electron ring circumference by moving the electron ring magnets is more straightforward than moving superconducting magnets in the ion ring to vary the ion ring circumference. We anticipate at most one or two configuration changes per year that require changes to the electron ring circumference; the JLEIC design therefore assumes motion and realignment of several FODO cells, rather than addition of extra long pathlength chicanes.

Required movement for this scheme is shown in Table 8.1 for options to move three, four, or five FODO cells. Figure 8.1 is a diagram of lateral motion required to adjust pathlength when moving three FODO cells. Figure 8.2 is a diagram of lateral motion required to adjust pathlength when moving five FODO cells.

8.1.3 Ion Ring Harmonic Number Variation

Varying the ion ring harmonic number poses more challenges to the ion bunch formation scheme; this is addressed in Section 5.6) on ion bunch formation. Incremental changes to the ion ring harmonic number will be accomplished with barrier buckets after the binary splitting operation.

8.1.4 Varying Collider RF Frequency

An RF frequency change of 0.028% is still higher than the CEBAF frequency tuning range limited by the path length adjustment chicane. However, Section 4.1 shows that the longitudinal acceptance of the 476 MHz electron ring RF systems accommodate a long bunch train of half the ring circumference injected with ±0.014% mismatched bunch spacing. When electron ring upgrades to 952.6 MHz, the acceptance is reduced by half, and we may need to reduce the length of injected bunch train by half.

8.1.5 Parameters

Tables 8.2 and 8.3 list the variation of circumference and RF parameter for different JLEIC subsystems affected by beam synchronization. Electron ring harmonic number is set at h_e=3584 (28×2^7), and a primary ion ring harmonic number of h_i =7168 (3584×2) is chosen for the highest ion energy range of 36–100 GeV, so for this wide range of energy there is no need to squeeze in

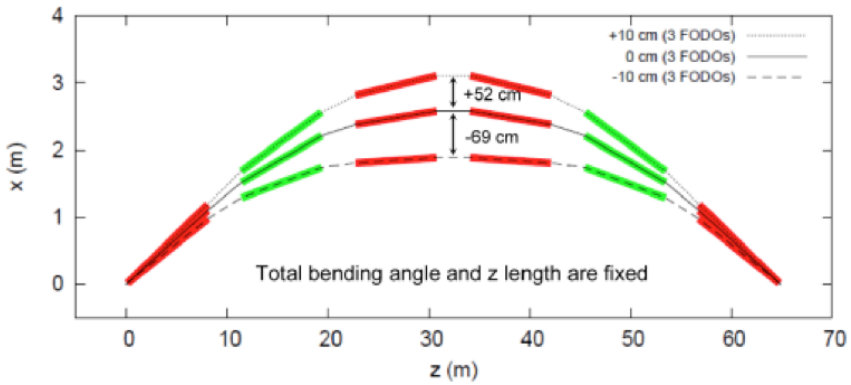

Figure 8.1: 3-FODO pathlength adjustment scheme for JLEIC beam synchronization.

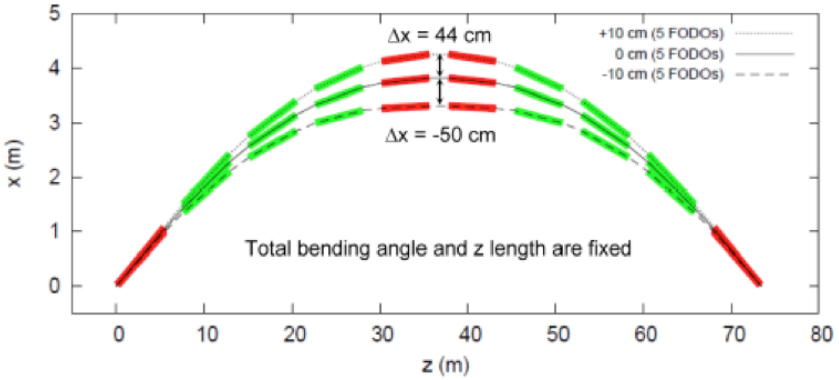

Figure 8.2: 5-FODO pathlength adjustment scheme for JLEIC beam synchronization.

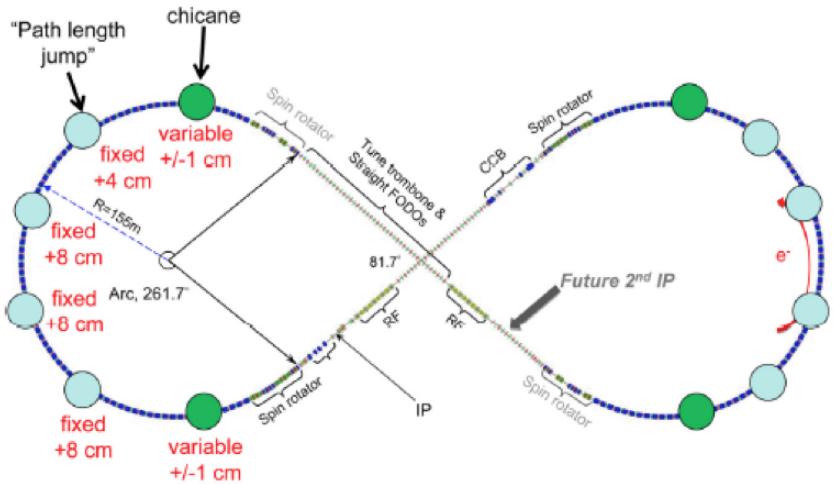

Figure 8.3: Electron ring FODO chicane motion for the JLEIC beam synchronization scheme.

Table 8.2: Fixed Parameters and Range of Variable Parameters for JLEIC Synchronization

Parameters	**Value**	**Note**
Top ion energy $E_{\mathrm{k,max,ion}}$ (GeV/u)	100	
Ion $\beta_{\max}$ at top energy	0.9999568	
h_{e}	3584	282^7
h_{i}	7168–7184 (or more)	increment by 2
h_{CCR}	680	=22×31-2, divisible by 8
$f_{\mathrm{RF,e}}$ (MHz)	476.318±0.066	1497 MHz×7/22×(1±1/3584/2)
Collision rate (MHz)	476, 238, 119	binary sub-harmonics of $f_{\mathrm{e,RF}}$
Nominal $\lambda_{0,\mathrm{e}}$ (m)	0.629395	
$f_{\mathrm{RF,i}}$, f_{CCR} (MHz)	952.636±0.133	$f_{\mathrm{RF,e}} \times 2$
Nominal $\lambda_{0,\mathrm{i}}$, λ_{CCR} (m)	0.314698	
L_{e} (m)	2255.753±0.315	minimum range $\pm\lambda_{0,e}/2$
L_{i} (m)	2255.34	
ion booster circumference (m)	322.19	1/7 of L_{i}, $8\times128\lambda_{\mathrm{i}}\beta_{\mathrm{i}}$

Table 8.3: JLEIC parameters at different ion energies and ion ring harmonic numbers h_{i}

i-ring Nh	ion E_k (GeV/u)		ion β	e-ring circum (m)	e-ring f_{RF} (MHz)	i-ring/CCR f_{RF} (MHz)	CCR Circum(m)	CCR Energy(MeV)
7168	Max	100	0.99996	2255.438	476.385	952.769	213.955	54.46
	Min	36.03	0.99968	2256.068	476.252	952.503		19.62
7170	Max	36.03	0.99968	2255.438	476.385	952.769	213.896	19.62
	Min	26.13	0.99940	2256.068	476.252	952.503		14.23
7172	Max	26.13	0.99940	2255.438	476.385	952.769	213.836	14.23
	Min	21.44	0.99912	2256.068	476.252	952.503		11.67
7174	Max	21.44	0.99912	2255.438	476.385	952.769	213.776	11.68
	Min	18.56	0.99884	2256.068	476.252	952.503		10.11
7176	Max	18.56	0.99884	2255.438	476.385	952.769		
	Min	16.57	0.99856	2256.068	476.252	952.503		
7178	Max	16.57	0.99856	2255.438	476.385	952.769		
	Min	15.09	0.99829	2256.068	476.252	952.503		
7180	Max	15.09	0.99829	2255.438	476.385	952.769		
	Min	13.93	0.99801	2256.068	476.252	952.503		
7182	Max	13.93	0.99801	2255.438	476.385	952.769		
	Min	12.99	0.99773	2256.068	476.252	952.503		
7184	Max	12.99	0.99773	2255.438	476.385	952.769		
	Min	12.21	0.99745	2256.068	476.252	952.503		

extra RF buckets after binary splitting and no "gear change" involved. However, squeezing RF buckets requires more RF power when it is closer to transition energy, especially for heavy ions.

The ion booster needs to match the RF frequency of the booster and the collider rings during injection. The binary bunch formation scheme requires both rings' circumferences to be multiple

of the long bucket length when long bunches are transferred from the booster to the collider, which is set to $128\lambda_i\beta_i$, or 40.274 m.

For the bunched beam electron cooler circulating ring (CCR), the bunch spacing needs to exactly match with the ion ring, and the CCR circumference is determined by $L_{CCR} = (L_i h_{CCR}/h_i$. Since the ion ring has a fixed circumference, the CCR circumference only changes when ion ring harmonic number jumps. The nominal operation energy range of the bunched beam is 20–55 MeV, which is approximately same as the ion ring energy range of the first harmonic number 7168. As a result, the CCR circumference does not need to be changed in the reference design. If the energy reach of the cooler ERL can be lowered in the future, the CCR circumference needs to be adjusted by ~6 cm for each harmonic jump.

8.2 Crabbing Dynamics

One of the key concepts of the JLEIC high luminosity strategy is the use of bunch crabbing in the interaction region (IR) [3]. Crab crossing is implemented in the JLEIC collider rings to prevent a potential luminosity loss due to a non-zero crossing angle between the two beams [4, 5, 6, 7]. In JLEIC, the full acceptance detector requires a large crossing angle of ±25 mrad. Without compensation, this angle would reduce the luminosity by about an order of magnitude compared to the head-on collision scenario. Crab crossing effectively restores head-on collisions and the corresponding luminosity. It is essential technology of the JLEIC design, responsible for a factor of ten in JLEIC luminosity. Crab crossing in JLEIC is implemented as a so-called local crab scheme, where crab cavities are placed on both sides of the IR. The first set of the crab cavities produces a longitudinal-dependent transverse kick along each bunch such that it is zero in the middle and has opposite directions at the head and tail of the bunch. This kick transforms into a longitudinal-dependent transverse particle offset at the interaction point (IP) resulting in a bunch tilt at the IP and therefore recovering a head on collision. The second set of the crab cavities is used after the IP to cancel the initial kick, thus avoiding crab induced effects anywhere else in the ring such as synchro-betatron coupling. A schematic of a local crabbing scheme for an EIC is shown in Figure 8.4. A local crab scheme is also convenient as it could be implemented in a future second interaction region of JLEIC.

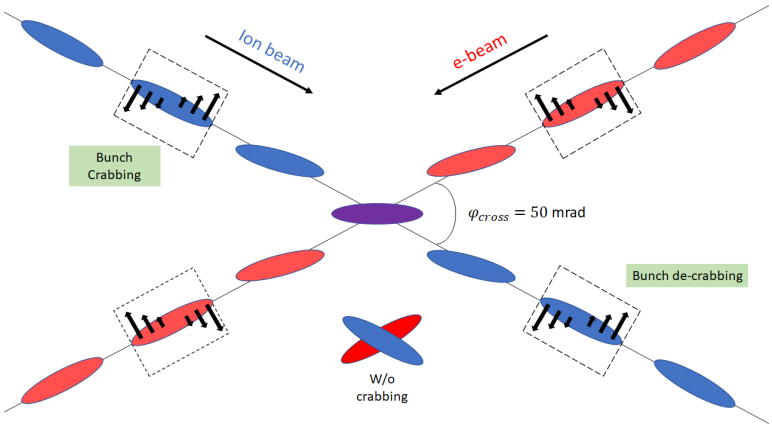

Figure 8.4: Local crabbing scheme for an EIC.

8.2.1 JLEIC Bunch Crabbing Scheme

The crab cavities must produce a crabbing voltage $V_{\rm crab}$ to produce the required tilt at the IP [7]:

$$V_{\rm crab} = \frac{cE_{\rm b}}{e2\pi f\sqrt{\beta_{\rm x}^{\rm crab}\beta_{\rm x}^{*}}}\tan\left(\frac{\phi_{\rm cross}}{2}\right), \tag{8.2.3}$$

where $E_{\rm b}$ is the beam energy, $\phi_{\rm cross}$ is the crossing angle between the two colliding beams, f is the cavity frequency, $\beta_{\rm x}^{\rm crab}$ is the horizontal beta function at the crab cavity location and $\beta_{\rm x}^{*}$ is the horizontal beta function at the IP. Note that in Eq. 8.2.3 a higher $\beta_{\rm x}$ value lowers the required crab voltage.

For optimum operation of the crab cavities, they can only be placed at very specific locations in the ring, which satisfy the following condition for their relative phase advance to the IP

$$\Delta\psi_{\rm CC\rightarrow IP} = n\pi + \frac{\pi}{2}, \tag{8.2.4}$$

i.e. an odd number of quarter-integer horizontal betatron oscillations.

The design of the JLEIC IR includes horizontal and vertical Chromaticity Compensation Blocks (CCB) [8], designed to cancel the chromatic kick from the Final Focusing Quadrupoles (FFQ). These sections have locations with high $\beta_{\rm x}$ values and the same phase advance requirements as for the crab cavities. Therefore, they are convenient for placement of the crab cavities. The crab cavity locations are indicated in Figures 8.5 and 8.6 for the ion and electron rings, respectively. Based on the these considerations, a set of parameters required for bunch crabbing in JLEIC are summarized in Table 8.4.

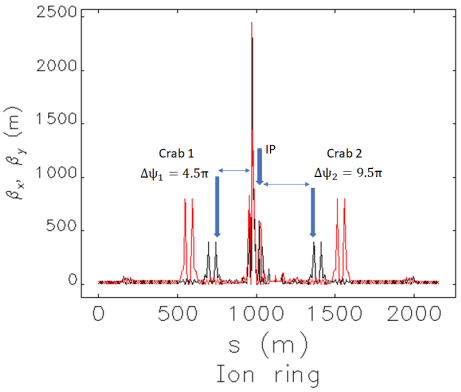

Figure 8.5: Horizontal and vertical beta functions of the ion ring lattice.

8.2.2 Particle Tracking Simulations

Using the parameters in Table 8.4, we set up a local crab scheme in the JLEIC rings and perform particle tracking studies using the accelerator code elegant [9, 10]. In particular, elegant tracks the 6D phase space of the beam through each of the ring components and over many turns. The crab cavities are modeled as a thin deflecting rf element RFDF that changes each particle's transverse momentum by

$$\Delta p_x = \frac{eV_{\rm crab}}{mc^2}\cos(\omega t + \phi_c), \tag{8.2.5}$$

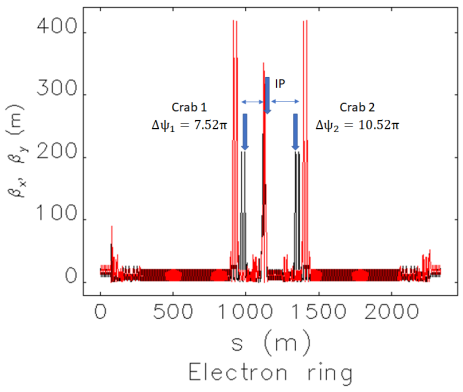

Figure 8.6: Horizontal and vertical beta functions of the electron ring lattice.

Table 8.4: General JLEIC crabbing parameters.

Parameter	**Electron ring**		**Ion ring**			**Units**
Energy	5	10	20	60	100	GeV
Frequency	952.6					MHz
Crossing angle	± 25					mrad
β_x^*	0.1					m
β_x^{crab}	200		363.44			m
Crab voltage	1.4	2.8	4.18	12.50	20.82	MV

The cavity phase φ_c is set up so that the field is zero at the bunch center, i.e., at the crabbing phase of $\pi/2$. Particles with a matched Gaussian distribution are generated outside of the crabbing region, $s = 0$ in Figure 8.5, and tracked turn by turn through the ring. For the ion beam, a normalized emittance $\epsilon_{x/y} = 0.35/0.07$ μm·rad is assumed, which corresponds to an ion beam with strong cooling.

In Figure 8.7, we first demonstrate bunch crabbing at the IP, where the required tilt of 25 mrad per beam is successfully produced for an electron beam at 5 GeV and a proton beam at low, medium and high energies of 20, 60, and 100 GeV. Similarly, Figure 8.8 shows the stable evolution of the crab angle at IP for a proton bunch over a few thousand turns.

Considering that the high energy ion beam requires more stringent crab cavity parameters, we study other effects on the dynamics of the proton beam at 100 GeV. In Figure 8.9, we study excitation of the beam emittance by the crab cavity voltage turn on at different rates. To verify that the observed emittance increase is uncorrelated, we turn the crab cavities off at the same rate as the initial turn on after 5,000 turns. We see that the faster the cavities are turned on, the greater the increase in emittance is when the cavities are turned back off. This suggest a minimum turn-on rate of a few hundred turns (milliseconds) for minimum uncorrelated emittance impact.

In Figure 8.10, we present the effect of a transversely-uniform crab kick on the ion ring dynamic aperture (DA). When the crab cavities are turned off, the horizontal DA spans $\pm 90.7\sigma_x$. When the crab cavities are turned on, the DA is reduced to $\pm 68\sigma_x$. Note there is no effect on the vertical DA, since crabbing is done in the horizontal plane.

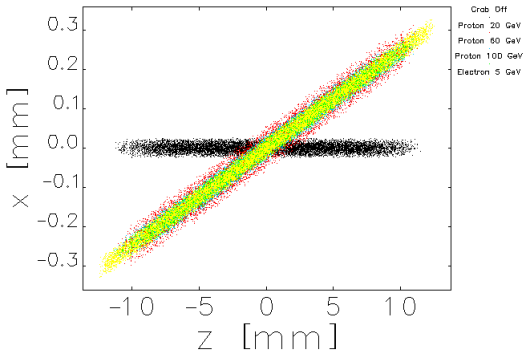

Figure 8.7: Crabbed electron and ion bunches at the IP at different energies.

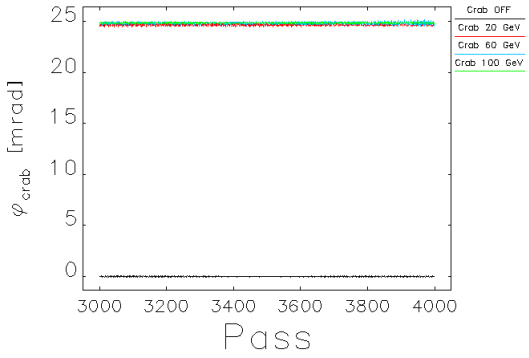

Figure 8.8: Evolution of the bunch tilt at the IP produced by crabbing in the ion ring lattice. The angle is shown for low, medium and high energy proton beams.

8.2.3 Crab Cavity Multipoles

Compact crab cavities like the ones currently being considered for JLEIC can have different geometries. A consequence of the cavity shape is that the produced field in the fundamental mode is non-linear, i.e. not exactly transversely uniform. It is then convenient to describe the field of the crab cavity using a multipolar expansion. In elegant, a crab cavity with multipolar field content can be modeled using a thin element MRFDF, which allows a field expansion of up to the decapole term ($n = 5$). We study the effects of the crab cavity multipoles on the ring's dynamic aperture [11]. The multipole terms of the different crab cavity designs are modeled in CST Microwave Studio[12, 13]. In Figure 8.11, we present single-cell, 3-cell and squashed crab cavity designs for JLEIC, with a 70 mm beam pipe aperture. Analysis of the multipoles also includes cavities with 60 mm apertures and 2 variations of the single and 3-cell cavities, namely, cavities with flat and curved inner pole tips, where our motivation for curving the poles initially was to minimize the sextupole term $n = 3$.

Figure 8.12 shows the resulting ion ring DA produced by the different crab cavity concepts. The DA spans about $\pm 50\sigma_x$ for the squashed and flat-pole dipole cavities and is reduced to $\pm 35\sigma_x$ for curved-pole cavities. In Figures 8.13 and 8.14, we present a comparison between the flat and curved pole designs of a 3-cell crab cavity with a 70 mm aperture. The impact on the DA is studied

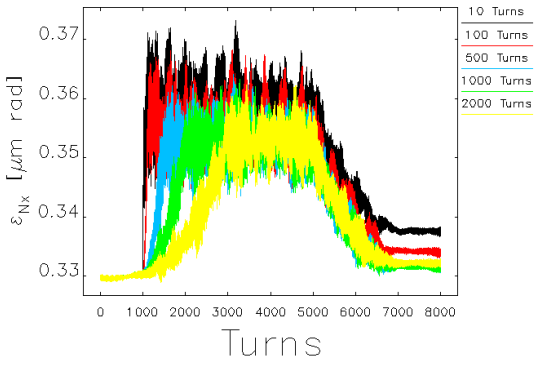

Figure 8.9: Projected normalized horizontal beam emittance in the ion ring. The growth is due to the establishment of a new matched phase space ellipse. The voltage of the crab cavities is ramped over 10, 100, 500, 1000 and 2000 turns for comparison. The impact on emittance is negligible with a turn-on time of at least 500 turns.

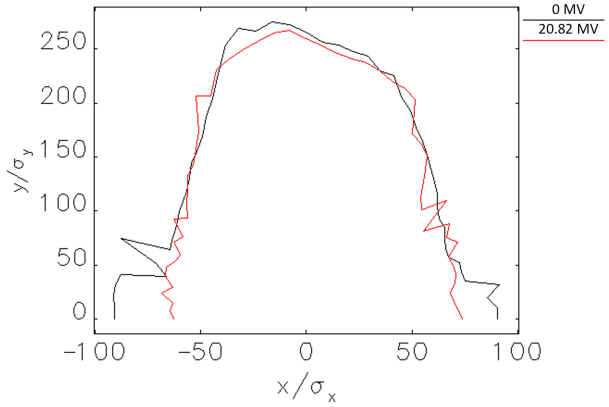

Figure 8.10: Reduction of the DA due to transversely-uniform bunch crabbing in the JLEIC ion ring.

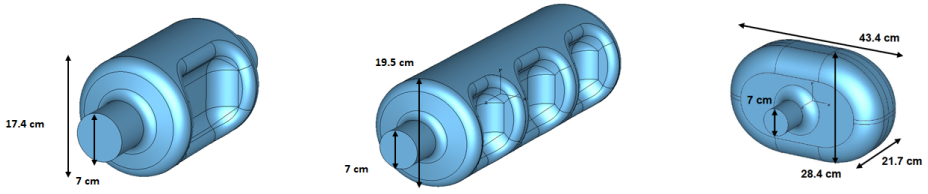

Figure 8.11: Designs of crab cavities for JLEIC including single- (left) and 3-cell (center) dipole and squashed (right) cavities.

individually for each multipole and for all multipoles combined. Note that in the curved-pole cavity, the decapole term b_5 dominates in the effect on the DA while b_3 has been minimized.

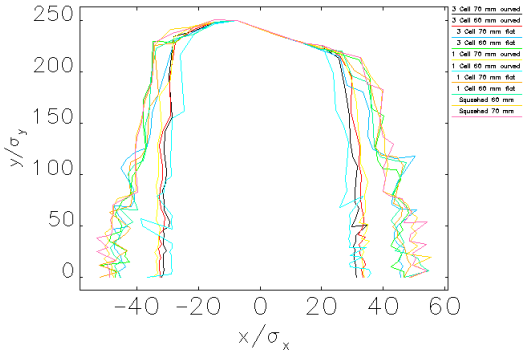

Figure 8.12: DA of the JLEIC ion ring with the multipoles of the different crab cavity designs. For each design, the multipole terms of up to decapole ($n = 5$) are included.

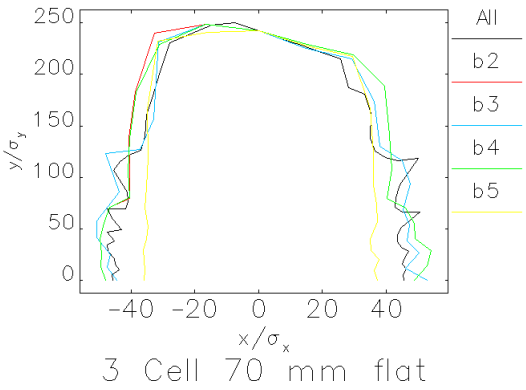

Figure 8.13: DA with the multipoles of a 3-cell flat-pole crab cavity with a 70 mm aperture.

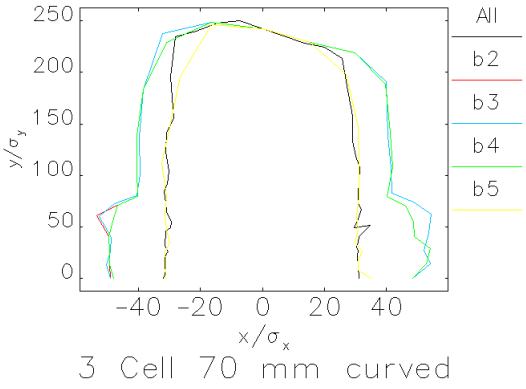

Figure 8.14: DA with the multipoles of a 3-cell curved-pole crab cavity with a 70 mm aperture.

Nonetheless, all of the presented crab cavity designs are acceptable in the sense that their effect is not what limits the ring DA. The main impact on the DA comes from the multipole fields of the FFQ magnets, which limit it to about $\pm 10\sigma_x$[14].

8.2.4 RF Noise

Noise in the amplitude and phase of the crab cavity voltage needs to be controlled precisely to avoid degradation of the beam emittance, particularly of the cooled ion beam. Noise in the voltage amplitude translates into variation of the bunch tilt angle at the IP. From the luminosity point of view, a sufficient requirement on the voltage amplitude noise is for the transverse projection of the bunch length $\sigma_z \tan\Delta\phi_c$ due to the bunch tilt angle error $\Delta\phi_c$ to be much smaller than the uncorrelated bunch width σ_x [5],

$$\frac{\Delta V}{V} \ll \frac{1}{\tan\left(\frac{\phi_{\rm cross}}{2}\right)}\frac{\sigma_{\rm x}^*}{\sigma_{\rm z}}. \tag{8.2.6}$$

Assuming a JLEIC bunch with $\sigma_{\rm x}^*$=18 μm and σ_z= 1.2 cm, Eq. 8.2.6 gives $\Delta V/V \ll 5\%$. In elegant, we can introduce different noise levels in the ring and evaluate the long-term stability. First, we fully ramp the cavity voltage over 1000 turns, then introduce a fractional rms noise of 0.1%, 0.05% and 0.01% in both crab cavities. For each noise setpoint, we track a bunch of 100 particles over 5×10^4 turns. In Figure 8.15 we present the distribution of the produced bunch angle at the IP corresponding to each noise level. For $\Delta V/V = 0.1\%$, we get an rms spread of the produced tilt of σ =0.85 mrad. For $\Delta V/V = 0.05\%$, σ =0.42 mrad and for $\Delta V/V = 0.01\%$, σ =0.15 mrad. Figure 8.16 shows evolution of the beam emittance tracked over a number of turns for the different noise levels. These results suggest that the voltage amplitude noise should be controlled at a level below 0.01% for negligible impact on the emittance.

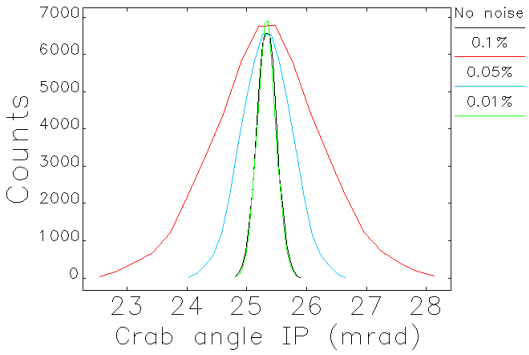

Figure 8.15: Distribution of the crabbing angle at the IP over 5×10^4 turns with the fractional rms noise level in the voltage amplitudes of the crab cavities of $\Delta V/V$ =0.1%, 0.05% and 0.01%.

A shift in the cavity phase produces a transverse offset of the bunch at the IP [15] given by

$$\Delta x_{\rm IP} = \frac{c\phi_{\rm cross}}{\omega_{\rm rf}}\Delta\phi. \tag{8.2.7}$$

Again, from the luminosity point of view, this offset is tolerable if it is much smaller than the transverse beam size at the IP [5],

$$\Delta\phi \ll \frac{\omega_{\rm rf}\sigma_{\rm x}^*}{c\tan\frac{\phi_{\rm cross}}{2}}. \tag{8.2.8}$$

With the JLEIC bunch parameters, $\Delta\phi \ll 20$ mrad $\simeq 1.1$ deg. We introduce different levels of noise in the phase of the cavity voltage and track a bunch over many turns to evaluate its effect.

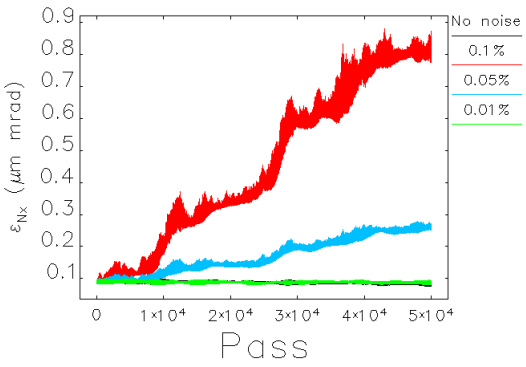

Figure 8.16: Emittance increase due to the different noise levels in the cavity voltage amplitudes.

In Figure 8.17 we show the beam emittance as a function of the number of turns for 0.5, 1 and 5 mdeg rms phase noise levels. This suggests that the phase jitter needs to be controlled to a level of less than 1 mdeg to have negligible effect on the beam emittance. Following Eq. 8.2.7, a 1 mdeg phase shift produces a 0.04 μm transverse offset at the IP, which is about 0.2% of the bunch size.

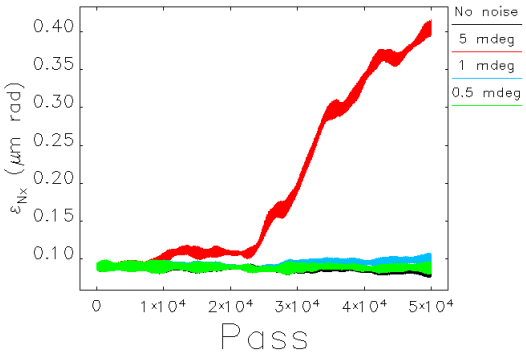

Figure 8.17: Beam emittance as a function of the number of turns for the three indicated rms noise levels in the cavity voltage phase.

8.2.5 Higher Order Modes

The beam passing through a cavity can excite oscillations in multiple electromagnetic higher order modes (HOM) of the cavity. Short JLEIC bunches of 1 cm can potentially excite HOMs with frequencies of up to ∼30 GHz. Particularly, HOMs with frequencies below the beam pipe cutoff frequency are trapped modes of the cavity and can resonate long enough to interact with the subsequent bunches. The cavity HOMs can then drive coupled bunch oscillations. Assuming that the beam is formed by M equally spaced bunches, there are μ possible coupled bunch modes (CBM) of oscillations with $0 \leq \mu < M$. $2\pi\mu/M$ gives the phase shift between oscillations of adjacent bunches. A resonant build-up of the amplitude of a coupled bunch oscillation can become a coupled bunch instability (CBI) and needs to be estimated.

To evaluate the CBI growth time and identify particular HOMs that need to be suppressed, we use preliminary estimates of longitudinal HOMs of 2-cell and 3-cell crab cavities with coaxial couplers shown in Figure 8.18. The impedance of the longitudinal HOMs of the two cavities is shown in Figure 8.19 for modes of up to 3 GHz.

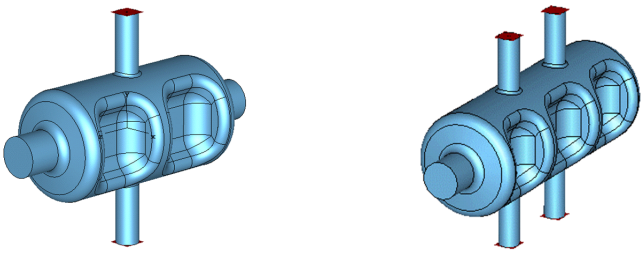

Figure 8.18: 2-cell and 3-cell crab cavities with 70 mm aperture and coaxial couplers used in the HOM analysis.

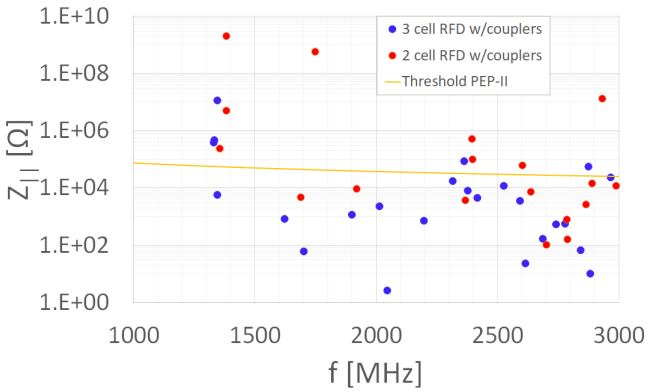

Figure 8.19: Impedance of the longitudinal HOMs of the 2-cell and 3-cell crab cavities with 70 mm aperture and coaxial couplers.

We estimate the characteristic growth times of the CBIs corresponding to different CBMs and evaluate their stability [16, 17]. In the frequency space, the frequency-dependent impedance of a cavity HOM couples it to a particular frequency in the beam current spectrum and can potentially drive CBI. A simple model of narrow-band impedance, such as a cavity HOM k with ω_k, R_k and Q_k, is

$$Z_{||}(\omega) = \sum_k \frac{R_k}{1 + iQ_k\left(\frac{\omega_k}{\omega} - \frac{\omega}{\omega_k}\right)}, \tag{8.2.9}$$

where the sum runs over all cavity HOMs. This impedance couples the HOMs to the beam spectrum given by $\omega_{p,\mu} = (pM + \mu)\omega_0 + \omega_s$ where p is an integer, ω_0 is the beam revolution frequency and ω_s is the synchrotron frequency. The CBI is characterized by its growth time, which can be calculated using [18]:

$$\tau_{||}^{-1} = \frac{I_b \omega_0^2 \eta}{6\,(L/2\pi R)^3\, 2\pi\beta^2\,(E/e)\,\omega_s} \sum_p \frac{Re\{Z_{||}(\omega_p)\}}{(\omega_p/\omega_0)} \frac{h_a(\omega_p)}{S_a}. \tag{8.2.10}$$

This is a weighted bunch power spectrum sampled at the different beam frequencies. For our calculation, we assume that $h_a(\omega)$ is a parabolic bunch power spectrum and $S_a = \Sigma h_a$, $a = 1$ for the dipole mode of oscillations [16, 17]. In Figure 8.20, we present the resulting CBI growth rate as a function of the CBM number for the HOMs of both cavities. The negative rates represent damped modes of oscillations. Once we determine which CBMs give the highest growth rates, we can identify the cavity HOMs driving them. This is presented in Table 8.5.

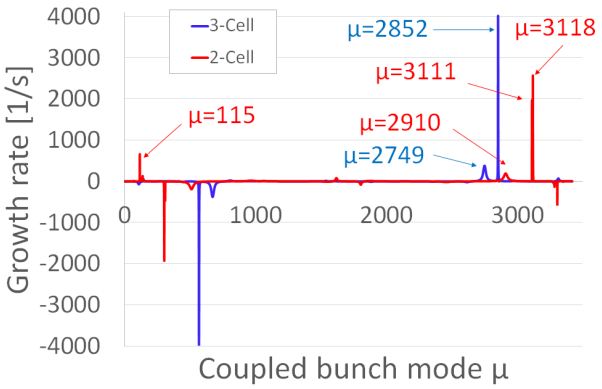

Figure 8.20: Coupled bunch instability growth rate for the 2-cell and 3-cell crab cavities with coaxial couplers.

Table 8.5: Beam frequencies matched to cavity HOMs. The top (bottom) values correspond to the 2(3)-cell cavity.

Mode	μ	p	Beam $f_{\mu,p}$ [MHz]	HOM f [MHz]
1	3118	2	1384.17	1385
2	3111	2	1383.2	1385
3	115	6	2868.27	2866
4	2910	2	1355.26	1357
1	2852	2	1347.2	1349
2	2749	2	1332.89	1334
3	2749	5	2759.02	2743

For both cavities, the fastest CBI growth time is only a fraction of a millisecond. We are in the process of optimizing the crab cavity designs and developing HOM dampers to increase the CBI growth times to the levels where they can be handled by Landau damping in the ion collider ring and by a feed-back system that is within the state of the art in the electron collider ring, e.g. ∼5 ms demonstrated at PEP-II. Future analysis of CBI will include a more realistic beam structure containing gaps as well as estimation of CBI due to transverse HOMs.

8.3 Beam-Beam

8.3.1 Nominal Lattice Design

JLEIC is designed to meet the requirements laid out by the white paper on the science program [19]. It is a ring-ring electron-ion collider. It departs from traditional colliders by adopting a figure-8 layout to preserve the beam polarization, allowing it to remain above 70% for both electrons and ion beams and longitudinal at the interaction points by means of energy-independent spin rotators, a consequence of the figure-8 design.

The electron ring will permit electron accumulation and collisions over energies ranging from 5–12 GeV. The ring is based on warm magnet technology to permit higher synchrotron radiation loads. The ion collider is based on superconducting magnets and will enable the use of ion species ranging from proton and deuteron to lead.

There are three broad center of mass kinematic energy ranges that should be considered, all having different implications in terms of the beam-beam effects (see Table 3.1 in Section 3.4).

8.3.2 Beam-Beam Parameters

The low energy range ($\sqrt{s}$=21.9 GeV) is limited by space-charge and requires a longer bunch length to be able to stay within a reasonable range for the Lasslett tune shift. This in turn gives raise to stronger geometric hourglass effects. It is also challenging in terms of beam synchronization for some of the kinematics where the ion momentum is low [20].

The middle energy range is $\sqrt{s}$=44.7 GeV, where the luminosity peak is limited by the beam-beam effect. The high energy range of $\sqrt{s}$=63.3 GeV is restricted by the maximum synchrotron radiation load tolerable in the electron ring.

Here we concentrate the beam-beam studies on the middle kinematic range which is where the beam-beam effects are most prevalent.

8.3.2.1 Determination of Working Point We employed a variety of techniques to perform the initial searches for the working points. In these studies, we make use of BeamBeam3D [21], a beam-beam simulation code which uses a self-consistent approach based on a shifted integrated Green function method to solve the Poisson equation on a grid surrounding the beam bunches. It is a massively parallel code that can run on a large number of processors. It has been extensively benchmarked and used to investigate beam-beam effects at many high-energy colliders such as RHIC, Tevatron, LHC, and KEK-B [22, 23, 24, 25].

The search for an optimal working point was first carried out by performing tune scans with a linear lattice model for both the electron and proton ring. Figure 8.21 shows an example of such a weak-strong tune scan. We obtained a few candidates working points and selected ($\nu_x = 0.53, \nu_y = 0.567$) for the electron beam for further studies. The proton ring working point, we initially selected to be ($\nu_x = 0.23, \nu_y = 0.14$) as a result of previous studies.

The head-on collision simulations showed adequate initial behavior. The current JLEIC design relies upon short bunches and high repetition rates to achieve the desired luminosity unlike most ion colliders which rely on longer bunches with higher space charge. This design choice implies that one has relatively strong longitudinal focusing. Given that the JLEIC design also has a crossing angle of ±25 mrad, it is important to check for synchro-betatron resonances.

8.3.2.2 Strong Longitudinal Focusing and Synchro-Betatron The design calls for a proton bunch length of around 1 cm, corresponding to a longitudinal tune ranging from from $\nu_s = 0.045$ (σ_z =1.4 cm) to $\nu_s = 0.058$ (σ_z =1.1 cm). Stronger values yielding a smaller bunch length are possible but require

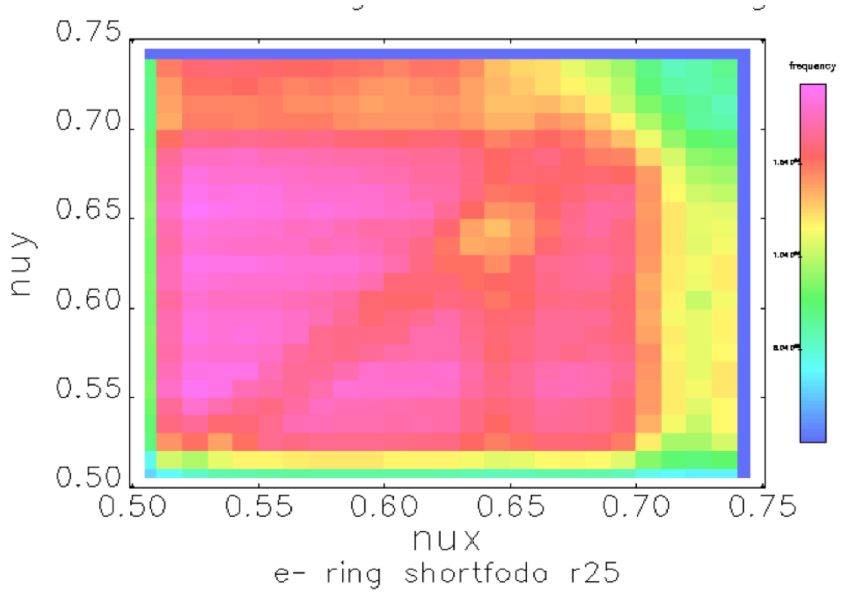

Figure 8.21: Weak-strong scan for the electron ring.

a costly increase of RF cavity power. We scanned the synchrotron tune between these values and examined the tune footprint of the proton bunch in the first 1024 turns. As can be clearly seen in Figure 8.22, there is a synchro-betatron resonance. Scanning the longitudinal tune produces similar results in the resonance moving to other areas of the tune space.

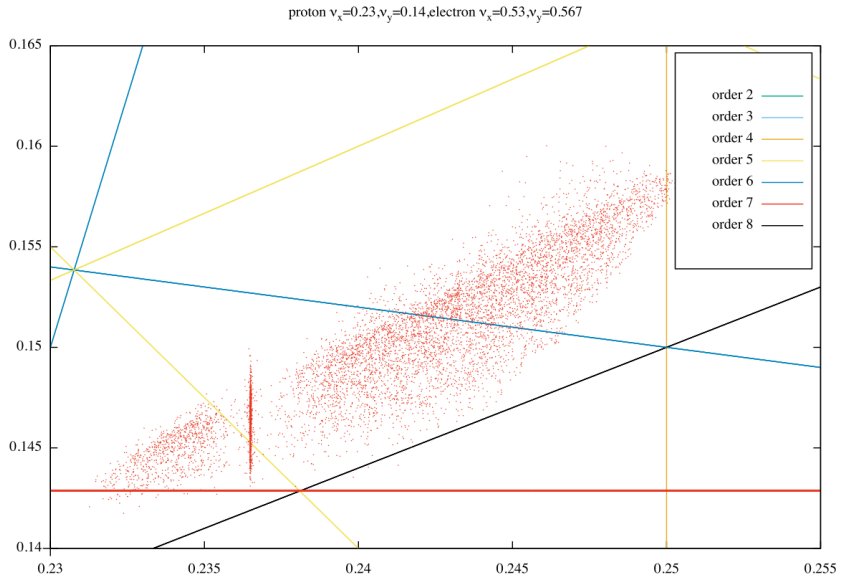

Figure 8.22: Tune footprint for proton with initial working point.

8.3.2.3 Alternate Working Point This prompted us to consider another working point in the lower quadrant, (0.08,0.14). Further optimizations for the higher order resonances ultimately resulted in converging to (0.078,0.132). The tune diagram in shown in Figure 8.23. This optimized de-

sign for head-on collisions easily reached the design luminosity of $2.1 \times 10^{34}\,\mathrm{cm}^{-2}\,\mathrm{s}^{-1}$ as shown in Figure 8.24.

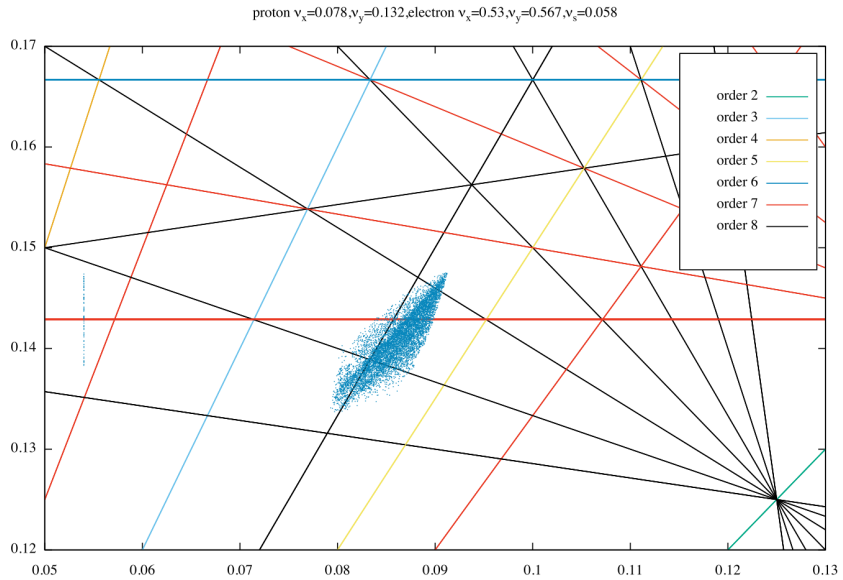

Figure 8.23: Tune diagram up to 8th order for protons.

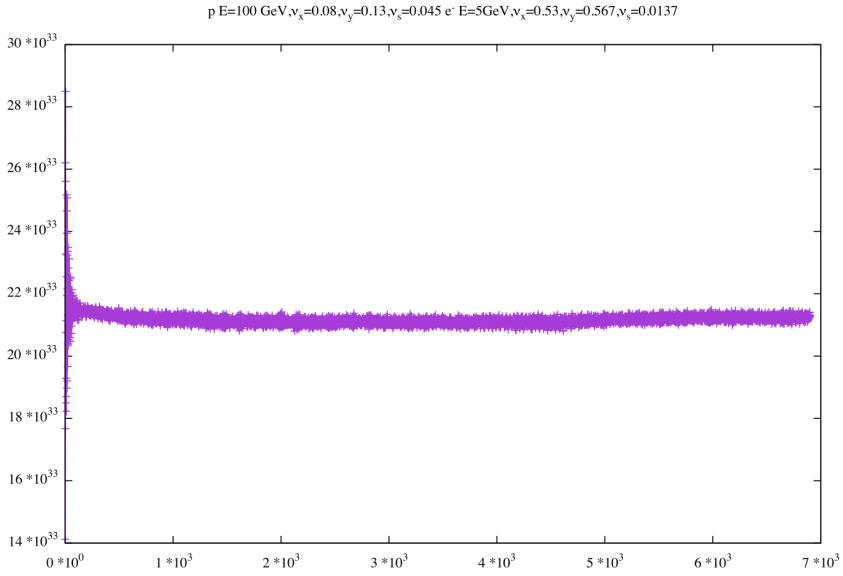

Figure 8.24: Head-on luminosity after optimizations.

8.3.3 Crabbing Effects

The JLEIC design features a crossing angle of ±25 mrad, leading to a Piwinsky angle of 13.8 (unitless) which would result in an unacceptable loss of luminosity due to the beam-beam kicks generating synchro-betatron resonances.

Originally proposed by R. Palmer [26], the crab-crossing scheme consists of imparting a transverse kick to the particles in the beam proportional to their longitudinal position in the bunch. It can be viewed an rotation of the bunches restoring the head-on collision.

One can choose to implement it as a global scheme where the bunches are tilted across the whole ring or a local scheme where crab-cavities are placed before and after the IP to "crab" and "decrab" allowing for the bunches to only be tilted at the IP. The former was succesfully implemented at KEK-B [27] while the latter is being considered for HL-LHC.

It should be noted that there is another scheme, namely the crab-waist scheme that has been proposed and implemented in electron-positron colliders such as DAΦNE [28, 29].

Our initial studies have focused on implementing a local crabbing scheme for JLEIC. The global crabbing scheme, while potentially leading to lower values on the crab cavity gradients give raise to a host of complicated beam dynamic issues since the head and tail of the bunches now travel around the ring with different closed-orbit distortions. In particular, coupling and chromatic corrections have to be controlled with a high degree of accuracy [30, 31, 32].

8.3.3.1 Crabbing requirements The crabbing system must be capable of providing a transverse RF kick of magnitude

$$V_\perp = \frac{c\tan(\theta/2)}{2\pi q\sqrt{\beta_c\beta^\star}}$$

for cavities located at a phase advance of $\frac{\pi}{2} + n\pi$ from the IP. The phase and gradient stability of these cavities has to be controlled to avoid emittance growth. Any noise on the phase for example, will change the transverse beam offset of the bunches at the IP.

The non-linearity of the beam-beam force will eventually damp these transverse oscillations at the expense of the emittance. This mechanism also holds true for non-linear kicks induced by higher order multipoles in the crab-cavity RF field. We are currently carrying out studies to determine these constraints (Section 8.2).

Finally, in a local crabbing scheme, we strive to cancel the transverse kick from one side of the IP with those on the other side. This cancellation does not occur if there is dispersion at the crabbing cavities. This can lead to transverse emittance growth as well as synchro-betatron resonances. A stability criterion was given in [33]. Future studies will examine this for the case of JLEIC.

8.3.3.2 Crabbing Implementation We made use of the BB3D implementation which models the crab cavities as thin-lens kicks in the x-z plane. One such cavity is placed on each side of the IP for both the proton and ion beam. The actual implementation will use several cavities to make up for the required gradient of 20.1 MV for a crossing angle of ±25 mrad.

The location at which these cavities are placed in the lattice is still being under consideration. For the subsequent studies we assumed that they would be in a dispersion free region with transverse beta function of 600 m.

The frequency was chosen to be 952 MHz to produce compact crab cavities. We note that since the bunch length of the ion and electron beam is small (of the order of 1 cm) compared to the RF wavelength of the crab cavities, there is no significant degradation of the longitudinal bunch phase space.

8.3.3.3 Initial Studies and Synchro-Betatron Crabbing Mode The initial calculation showed that with nominal crabbing voltage we have a slow decline of the luminosity over time (Figure 8.25).

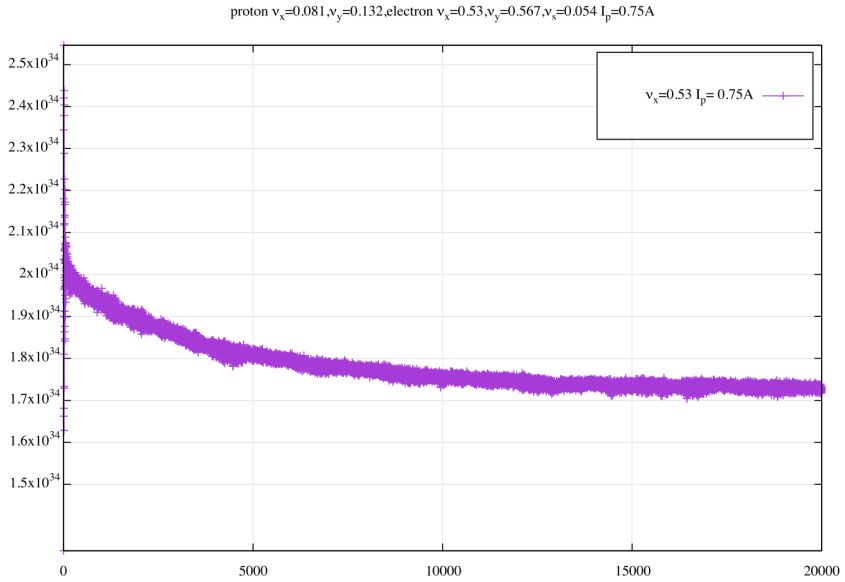

Figure 8.25: Luminosity reduction from crabbing.

8.3.3.4 Luminosity After Crabbing Optimization To address this luminosity reduction, we performed longitudinal tune scans of the electron beam until we found a setting which adequately pushed the resonances away from the tune footprint.

After adjusting the synchrotron tune to 0.02, we were able to eliminate the loss and increase the proton beam current pushing for higher luminosity (Figure 8.26) which shows values well above our design goal of $2.1 \times 10^{34}\,\mathrm{cm}^{-2}\,\mathrm{s}^{-1}$.

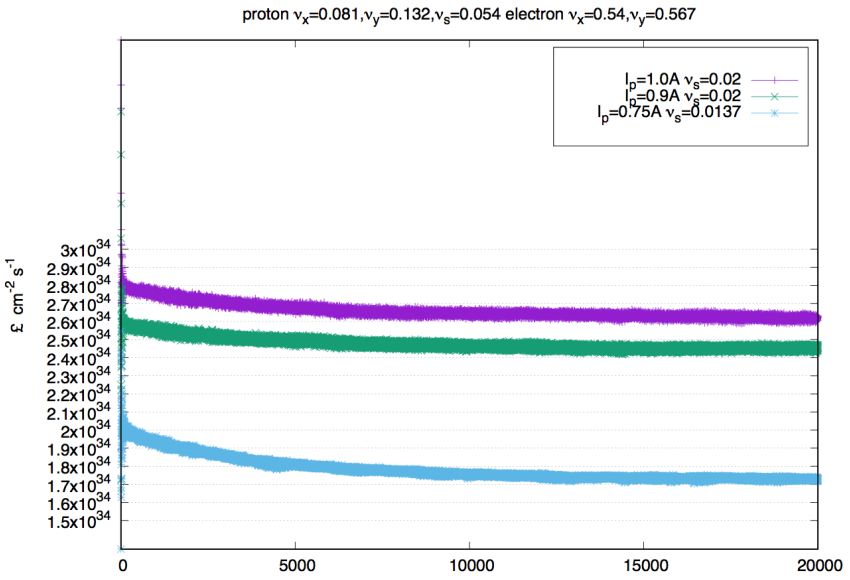

Figure 8.26: Luminosity versus current after crabbing optimization.

We did not observe any beam-beam limit within the range of the proton currents we investigated. The upper limit for the proton current was given by limiting the Lasslett tune shift to keep the space-charge effects in the ion ring under control.

Future work in this direction will consider the effect of dispersion leakage at the location of the crab cavities as well as the tolerances required on the cavity white noise, voltage stability and higher order field components. Some of these effects can be compensated via a transverse feedback system.

8.3.4 Two Interaction Points

In a head-on single Interaction Point (IP) situation, the beam-beam forces cause the particles in the bunches to oscillate incoherently in the phase space, producing a tune spectrum extending out a distance of the beam-beam tune shift parameter from the tune at the working point. In collider rings with beams of similar tune, intensity and type, coherent modes where all the particles move together can also occur during head-on collisions.

These coherent oscillations will also happen when running with several interaction points under certain conditions [34]. It is possible to mitigate them to some extend by a judicious choice of the phase advance between the IPs.

Fortunately, for the JLEIC design, since the beams have different intensity, particle mass, and working points, we are already in a situation where the symmetry between the two beams is broken, preventing the formation of coherent beam motions.

However, running with the design parameters at nominal crossing and crabbing does give raise to a set of synchro-betatron resonances in the proton tune spectrum as shown in Figure 8.28 for two different values of the proton synchrotron tune.

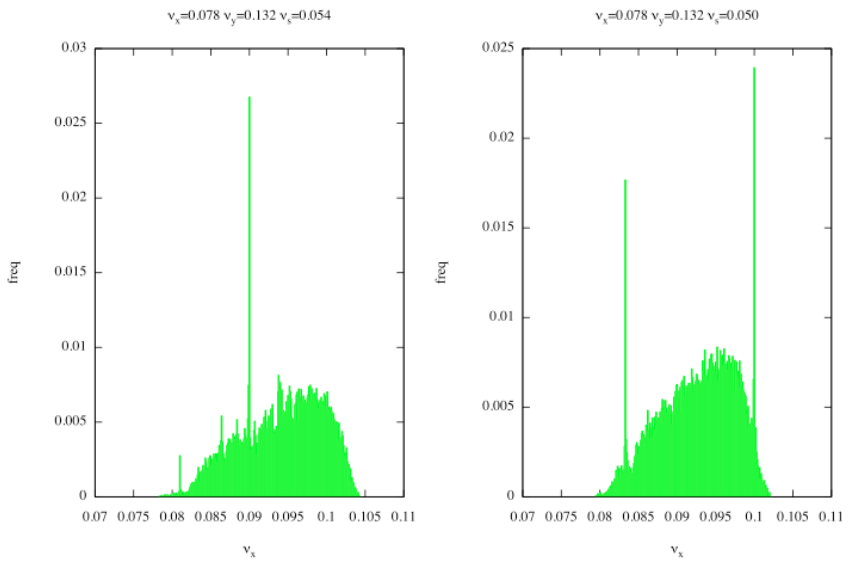

Figure 8.27: Proton tune spectrum for two IPs with crabbing. The left plot is for ν_s=0.054; the right plot is for ν_s=0.050.

A way to investigate this behavior was suggested in [35]; increase the momentum of the electron beam and adjust the number of pseudo-particles in the proton beam to keep the beam-beam parameters the same. This "freezes" the electron motion by making it a very strong beam. Doing

so make the synchro-betatron resonances present in the proton tune spectrum disappear indicating that the phenomenon is not merely some numerical noise artifact but instead a real coupling between the transverse electron beam motion and the proton longitudinal beam motion.

This initial assessment assumed a smooth phase advance transition between the two interaction points placing the second one ($\frac{2\pi}{2}Q_x$, $\frac{2\pi}{2}Q_y$) from the first one. We also configured the two IPs identically.

The extended electron and proton incoherent tune spectra will now cover $+2\xi$, where ξ is the linear beam-beam tune shift parameter. This is shown in Figure 8.28 for the electron beam, and is far enough away from resonances.

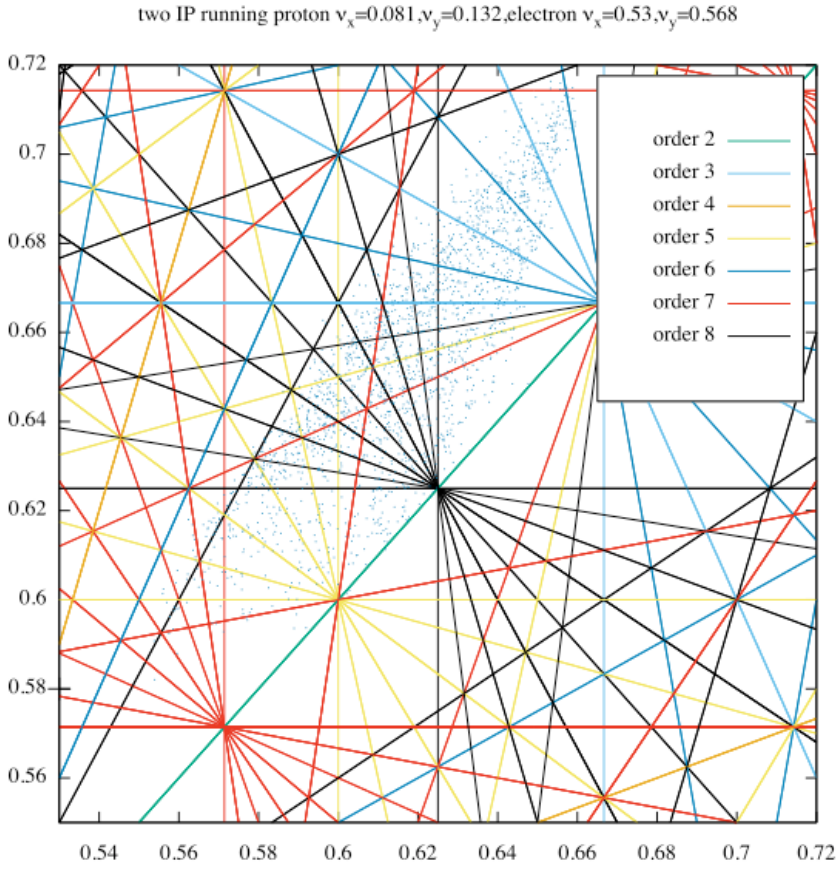

Figure 8.28: Electron tune footprint for two IPs.

Future studies will explore the possibility of optimizing this two IP configuration by investigating the nature of these synchro-betatron resonances induced by the crabbing.

8.3.5 Long-Range Beam-Beam Effects

For JLEIC, with a crossing angle of ±25 mrad and a time between bunches of 2 ns, the closest bunches are separated transversally by 1.5 cm which is hundreds of beam sizes, ruling out any long-range effects.

8.3.6 Injection and Beam Abort Gaps

The bunch train in JLEIC will include abort gaps, injection gaps, and ion clearing gaps.

The outcome of that is that not all bunches see the same beam-beam forces if the gaps are not at the same location in the bunch trains of the electron and ion beams. In machines like LEP or LHC, this phenomenon also occurs in the long-range interactions and was dubbed the PACman effect when first discovered [36].

The final specification of the bunch pattern has not yet been decided. Beam-beam effects are being considered concomitantly with the requirements from the abort systems, injection scheme, and ion clearing gaps.

8.3.7 Depolarization Due to Beam-Beam Effects

Spin depolarization due to the beam-beam collisions has been studied in colliders using both analytical and numerical approaches [37, 38]. It was observed experimentally in PETRA [39].

The effect is mostly suppressed if one stays away from spin resonances and below the beam-beam limit. JLEIC also has spin-rotators which can be used to compensate for this small effect as necessary. Estimates were carried out both analytically and numerically for the case of JLEIC. The method is based on the concept of the spin response function (see Section 5.5) introduced by A. Kondratenko [40].

A real collider lattice always contains additional perturbing radial fields δB_x, which cause distortion of the particle vertical motion. Therefore, even with a local perturbation of the radial field, the particle spins experience an additional effect of the whole ring when moving along the distorted orbit. For a figure-8 ring, the periodic spin response function $F(z) = F(z+L)$ is determined by the ideal linear ring lattice and accounts for the resonance strength contribution due to a "response" of the whole collider ring to a periodic radial field perturbation.

Below we provide an example of how the response function technique allows one to account for the impact on the polarization of the dipole component of the opposing beam, which we model as a 2 cm long dipole field located at the interaction point.

Figure 8.29 shows the absolute value of the proton response function at the interaction point of the JLEIC ion collider ring versus momentum in the range from 45–55 GeV/c.

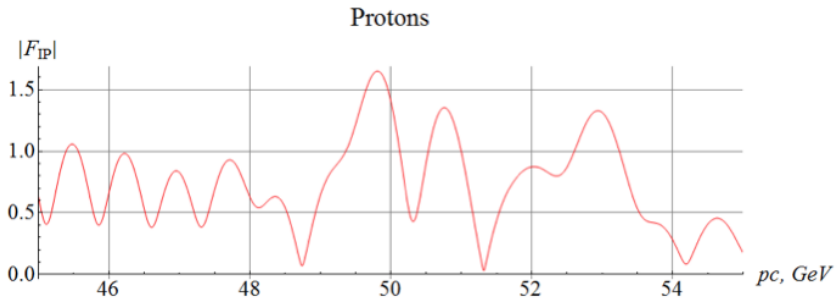

Figure 8.29: Proton response function at the IP vs momentum offset in the collider ring.

We use a spin tracking code Zgoubi [41] to calculate the resonance strengths for the two momenta of 51.32 and 52.94 GeV/c, which correspond to the points of local minimum and maximum of $|F_{\rm IP}|$ with the values of 0.0322 and 1.329, respectively. The resonance strength is determined by the number of particle turns $N_{\rm flip}$ that it takes an initially vertical spin to flip $w = 1/(2N_{\rm flip})$.

Figure 8.30 shows the vertical spin components versus the number of particle turns for the selected momenta. In the calculations, we set the field strength of the radial dipole to $2 \times 10^{-3}\,\mathrm{m}^{-1}$ in units of magnetic rigidity. The spin makes a complete revolution in about 54 thousand particle turns at 51.32 GeV/c and in about 1.17 thousand turns at 52.94 GeV/c, which correspond to resonance strengths values of $w_1 \approx 1.85 \times 10^{-5}$ and $w_2 \approx 8.54 \times 10^{-4}$, respectively. A calculation using the response function gives resonance strengths of $w_1 \approx 2.01 \times 10^{-5}$ and $w_2 \approx 8.56 \times 10^{-4}$, which are in good agreement with the numerical modeling. The discrepancy in the resonance strengths at the small value of the response function is about 8%. This discrepancy may be due to the fact that the resonance strength in this case is already determined by higher orders of the spin motion expansion. Another reason is related to excursion of the closed orbit due to the radial dipole, which leads to a "shift" of the interaction point.

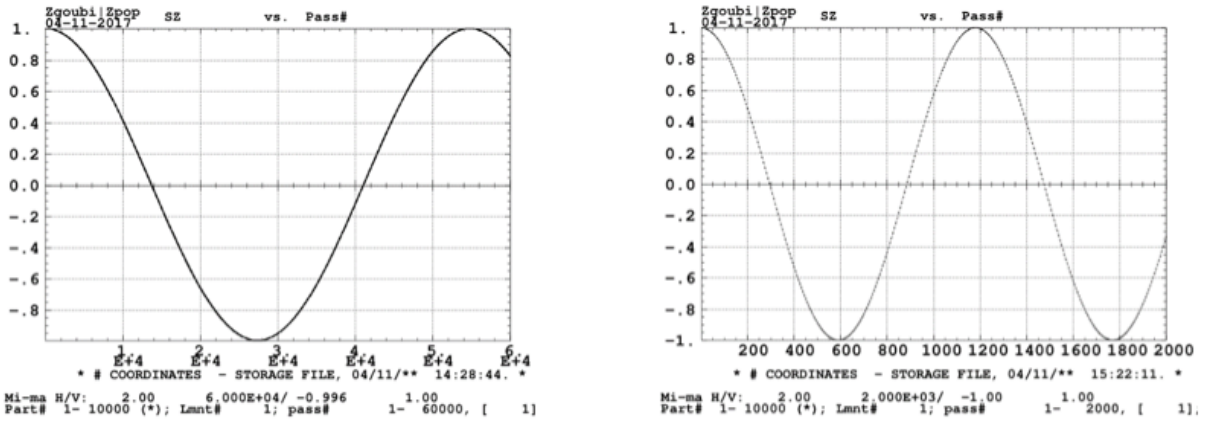

Figure 8.30: Vertical proton spin components versus the number of particle turns at momenta of 51.32 GeV/c (left) and 52.94 GeV/c (right).

The numerical modeling confirms the analytic calculation that the resonance strength is proportional to the response function. In the above example, we are able to reduce the spin resonance strength by a factor of about 40 by choosing momentum with a minimum response function.

The above example demonstrates the possibility of reducing the impact of the opposing bunches on the beam polarization by a few orders of magnitude by adjusting the response function and its derivative to zero at the interaction point by the choice of the collider's magnetic lattice. This problem is similar to designing an interaction point with a zero dispersion function.

The same conclusion is valid when analyzing the depolarizing effect of the incoming ion beam on the electron polarization at the interaction point.

8.3.8 Beam Synchronization and Gear Changing

In the JLEIC design for an electron-ion collider, broad adjustments in the momentum of the ion beam are required to span the appropriate kinematical range. Consequently, because of the non-relativistic nature of the ion beam at low momentum, one has to adjust the relative timing between the relativistic electron beam and non-relativistic ion beam. This can be accomplished by adjusting the RF frequency, ring sizes or harmonic numbers of either or both rings at the same time.

The method is attractive because it alleviates the needs for expensive hardware adjustments and has some benefit for polarization measurement.

As described in Section 8.1, we choose to synchronize the two rings by adjusting the harmonic number of the ion ring and the circumference and RF frequency of the electron ring. This becomes necessary when the ion momentum falls below 36 GeV/u.

However, it has dynamical issues for the beam-beam interaction that have to be carefully evaluated. Namely, this "gear changing" scheme will generate a large number of additional resonances due to the uneven collision pattern which results in each bunch colliding with every other bunch in a repeating pattern giving rise to coherent oscillations ranging from dipole to higher order modes.

The problem was examined in [42] by treating it in a simplified 4D framework. We propose to carry out more detailed studies using full 6D tracking with a greater number of bunches. Dedicated software, the GPU-optimized High Order Symplectic Tracker (GHOST) is being developed to do a large scale many-bunch beam-beam tracking [21, 43]. It is implemented to take advantage of modern high-performance computing infrastructure using Graphical Processing Units (GPU).

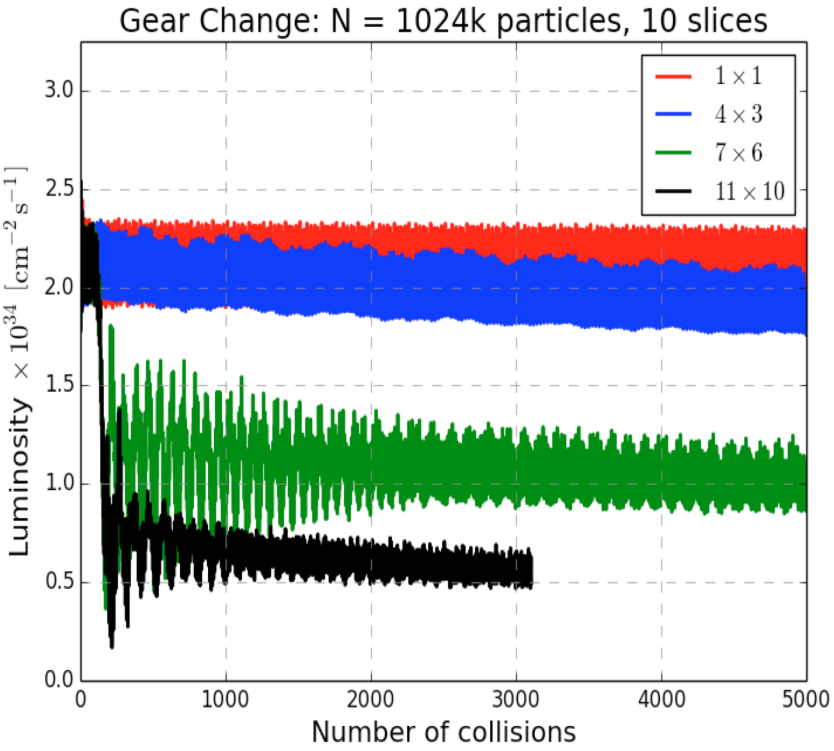

Figure 8.31: Initial tests of gear changing with GHOST.

8.3.8.1 Initial results for gear changing Each beam is simulated by a set of point particles, sampling their initial distributions. Beam-beam effects of one beam on the other are simulated using the generalized Bassetti-Erskine approximation [44]. This treatment, which is valid for an infinitesimally short bunch, is generalized to beams of finite size by considering a number of slices. In between the consecutive collisions, the beams are transported through the rings using symplectic maps which can be of any order.

For purposes of testing and benchmarking of the new beam-beam code, we use the reference collider parameters shown in Section 3.4, and performed strong-strong simulations.

Figure 8.31 shows the 1×1 result in red which is to be compared with the BB3D result in Figure 8.24.

Subsequent runs with uneven number of bunches were carried out. It shows a drop in luminosity when the bunch number increases. This is expected since N_1 bunches will produce an array of resonances separated by $1/N_1$ and is similar to what was shown in [42] using a simple beam-beam model.

We also ran a BB3D simulation for a 7x6 configuration in head-on collision mode and compared with the GHOST result. This is shown in figure 8.32 and show a good agreement between the two codes.

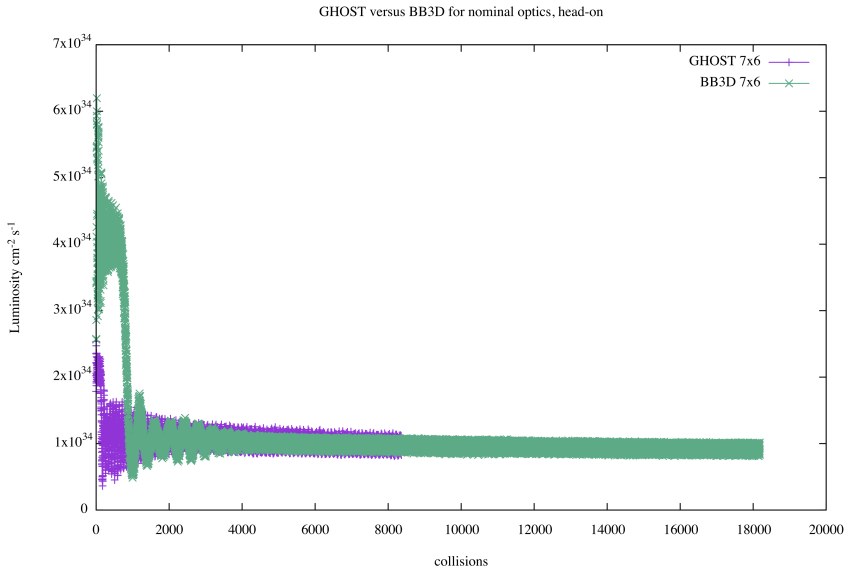

Figure 8.32: Comparison between GHOST and BB3D for a small number of bunches.

Future work will carefully examine the characteristics of the resonance pattern and its dependency on bunch number and beam-beam parameters for increasing values of bunches. The nominal JLEIC parameters for synchronization can be found in Table 8.2.

8.3.8.2 Specifications for a transverse feedback system To damp the coherent dipole kicks, one can make use of a transverse damping system similar to the LHC system [45]. Extrapolating from estimates in [42], it can be seen that it would require a state of the art system capable of damping the oscillation in less than 10 turns. The JLEIC figure-8 design is particularly favourable to implementing such a feedback since the distance between the kickers and pickup is minimal when cutting across the figure 8. Future work will involve the modelling of such a system and the refinement of its specifications.

8.3.8.3 Exploiting Landau damping As suggested in [42], we will investigate the possibility of suppressing the higher order coherent modes by exploiting Landau damping [46]. These studies are computationally intensive and require exploring the various mechanisms available to enhance the damping, notably the nonlinearities in the lattice and the chromaticities.

8.4 Collective Effects

The JLEIC reference parameters [47] are conceived based on the unique luminosity concept of the design, featuring small bunch emittance, relatively low bunch charge, and very high bunch repe-

tition rate. These features further determine the behavior of collective instabilities in the collider rings [17]. It implies less significant single-bunch instabilities; yet it poses strong requirements on the bunch-to-bunch feedback systems to mitigate the longitudinal and transverse coupled bunch instabilities. These collective effects need to be assessed for a wide range of beam energies and ion species, and also for the entire ion bunch formation processes. Ideally, the wakefield-induced beam instabilities can be analytically and numerically studied once the machine impedance budget is available. However, developing impedance budget and performing instability estimations are an iterative and gradually refining process. A preliminary estimation of impedance thresholds, for various coherent instabilities, is necessary for the engineering design to make choices to minimize machine impedance and ensure beam stability. In this section, we discuss the current status of the JLEIC impedance studies, and present our initial back-of-envelope estimations for single and coupled bunch instabilities using the recent JLEIC reference design parameters. The estimated impedance threshold will be compared with the expected machine impedances for the JLEIC collider rings, as inferred from the impedance budgets of some existing machines. We will also give preliminary accounts of the two-stream instabilities, i.e., the electron cloud effect in the ion ring and the ion effects in the electron ring.

8.4.1 Status of Impedance Estimation

The single and coupled bunch instabilities are respectively driven by the interaction of the beam current with the machine broadband and narrowband impedances. The estimation of the broadband impedance budget requires engineering drawings of the vacuum chamber. Yet for JLEIC, presently the machine engineering design has just begun, and no details are available except for the elements count for most of the impedance-generating components in both rings (see Table 1). Lacking component designs at this stage, we use impedance budgets for some existing machines, such as PEP-II and RHIC, as references. One reason for using PEP-II for reference is that the JLEIC e-ring will reuse the PEP-II HER vacuum components, such as BPMs and RF cavities. Another reason is that the bunch length ($\sigma_z \approx 1\,\mathrm{cm}$) for JLEIC is comparable to that in PEP-II (the effective impedances are bunch-length dependent). With the PEP-II impedance budget [48] and the JLEIC component counts in Table 1, and assuming these components are identical with those used in the PEP-II HER, we get $L \approx 99.2\,\mathrm{nH}$, $|Z_\parallel/n| \approx 0.09\,\Omega$, and $|Z_\perp| \approx 0.03\,\mathrm{M\Omega/m}$. If components in SUPERKEKB [49] are used as reference, the JLEIC e-ring impedance estimation becomes $L \approx 22.6\,\mathrm{nH}$, $|Z_\parallel/n| \approx 0.02\,\Omega$, and $|Z_\perp| \approx 6.5\,\mathrm{k\Omega/m}$, with the note that the smaller bunch length ($\sigma_z \approx 0.5\,\mathrm{cm}$) for SUPERKEKB than that in JLEIC may cause underestimation of the effective impedance.

For the JLEIC ion ring, the short ion bunch ($\sigma_z \approx 1\,\mathrm{cm}$) is made possible only with the envisioned high-energy electron cooling [50], which is unprecedented for ion beams in existing ion rings. If $\sigma_z \sim 7\,\mathrm{cm}$ for the JLEIC ion bunches, we can use the vacuum components in RHIC [51] to estimate the broadband impedance for JLEIC ion ring, yielding $|Z_\parallel/n| \approx 0.71\,\Omega$ and $|Z_\perp| \approx 0.2\,\mathrm{M\Omega/m}$. We note that on one hand, with the much shorter bunch length in JLEIC, the impedance budget for RHIC rings is NOT a suitable reference for the JLEIC ion-ring impedance estimation; and on the other hand, for RHIC, the measured impedance [52] is 3–5 times larger than the impedance-budget estimation [51]. Accurate impedance budgets of both the electron and ion rings require careful electromagnetic field calculations, which generates the full impedance spectrum for each impedance-generating components. As the JLEIC design improves and becomes more complete, the counts for certain elements in Table 8.6, such as collimators, feedback kickers, and clearing electrodes, will be further modified. In addition, some special components unique to the JLEIC

Table 8.6: Impedance-Generating Components in JLEIC

Elements	**e-Ring**	**ion-Ring**	**e-Cooler**
Flanges (pairs)	1215	234	104
BPMs	405	214	49
Vacuum ports	480	92	62
Bellows	480	559	74
Vacuum valves	23	14	–
Tapers	6	6	26
Collimators	16	16	–
Forks	0	0	4
Fast kickers	0	0	2
DIP screen slots	470	–	–
Crab cavities 2	8	0	
RF/SRF cavities	32	40	2
RF/SRF bellows	0	60	0
RF/SRF Valves	68	24	–
Feedback kicker 2	2	–	
IR chamber	1	1	–

design, such as the crab cavities and IR chamber, require detailed impedance modelling and cannot use references to impedances from existing machines.

8.4.2 Single Bunch Dynamics

For the electron and ion beams, beam stability needs to be assessed for all the collision scenarios and the entire ion bunch formation process, and for all the ion species. At the present stage, we focus only on the beam stability at the collision scenarios for the electron beam at energy E_e=3, 5, and 10 GeV and for the proton beam at E_p=100 GeV.

8.4.2.1 Longitudinal Microwave Instability (LMWI) With the Boussard approximation, the LMWI instability threshold is given by the Keil-Schnell criterion:

$$\left|Z_{\parallel}(n)/n\right|_{\text{eff}}^{\text{th}} \approx 2\pi|\eta|(E_e/e)\sigma_\delta^2/I_p \tag{8.4.11}$$

For the JLEIC reference parameters, when the electron and proton beams at collision energy E_e=3, 5, and 10 GeV and E_p=100 GeV, the instability thresholds are listed in Table 8.7. Unlike the PEP-II LER, which was a separate ring and had a different dipole configuration from the HER, the JLEIC e-ring uses the same dipole configuration for a wide range of beam energy, with both the dipole strength and the energy spread from synchrotron radiation scaling with the beam energy. As a result, the energy spread for beam at 3 GeV in the JLEIC e-ring is much smaller than that for the PEP-II LER beam, and thus the former is vulnerable to LMWI while the latter is not. This estimation indicates the necessity to employ suppression mechanisms against the microwave instability for the JLEIC e-ring at low energy, such mechanisms include use of an alternative dipole

configuration, damping wigglers, or a Landau cavity. For the ion ring, the machine impedance is expected to be much smaller than the threshold impedance, so the beam is safe from this instability. Detailed simulation is to be performed on the bunch lengthening due to potential-well instability below the LMWI threshold, and turbulent bunch lengthening and energy-spread increase beyond the instability threshold.

8.4.2.2 Transverse Coupled-Mode Instability TCMI The impedance threshold for the transverse mode coupling instability (TMCI) is estimated by

$$|Z_\perp|^{\rm th}_{\rm eff} \approx F(E_{\rm e}/e)v_{\rm s}/\left(\langle B_\perp\rangle I_{\rm p}\right), \tag{8.4.12}$$

with F the bunch form factor. For Gaussian bunches, $F = 16\sqrt{2}/3$, yielding threshold results as shown in Table 8.7 for both the JLEIC electron and proton beams at collision scenarios. In Table 8.7, the expected machine impedances are estimated from impedance budget of existing machines, such as PEP-II or RHIC. More accurate estimation will be available as the JLEIC engineering design progresses. For more complete studies of TMCI, we need to resort to an eigenmode solver of the Vlasov equation that also accounts for bunch lengthening caused by potential-well distortion. In particular, the Christmas-tree-like equilibrium longitudinal charge distribution [53] for the proton bunch under strong electron cooling, with dense core and long tail, requires special care for its role in stability assessment.

Table 8.7: Threshold for Single Bunch Instability

Parameter	**PEP-II (LER)**	**JLEIC e-Ring**			**JLEIC p-Ring**
E [GeV]	3.1	3	5	10	100
$I_{\rm p}$ [A]	113	59.0	59.4	50.6	15.6
η [10^{-3}]	1.31	1.09	1.09	1.09	6.22
σ_δ [10^{-4}]	7.7	2.78	4.55	9.28	3.0
$\nu_{\rm s}$ [10^{-2}]	3.7	0.88	1.46	2.51	0.053
$\langle\beta_\perp\rangle$ [m]	20	13	13	13	18
$\lvert Z_\parallel/n\rvert^{\rm ring}_{\rm eff}$ [Ω]	~ 0.1	≤ 0.1 (expected)	≤ 0.5		
$\lvert Z_\parallel/n\rvert^{\rm th}_{\rm eff}$ [Ω]	0.145	0.027	0.125	1.16	1.12
LMWI	stable	unstable		stable	stable
$\lvert Z_\perp/n\rvert^{\rm ring}_{\rm eff}$ [Ω]	¡0.5	≤ 0.5 (expected)			5
$\lvert Z_\perp/n\rvert^{\rm th}_{\rm eff}$ [MΩ/m]	~ 1.2	0.81	2.25	9.0	22.5
TMCI	stable	stable			stable

8.4.3 Coupled Bunch Dynamics

Narrow-band impedances from RF cavities can cause longitudinal or transverse coupled-bunch instabilities (LCBI or TCBI). For the JLEIC electron ring, we expect to use PEP-II RF cavities, with the detailed parameters of HOM impedances listed in Tables 1 and 2 of [54]. For the JLEIC ion ring, an initial RF cavity design is recently developed, featuring 2-cell cavity with HOM damping. Detailed parameters for the HOM impedances for the new ion-ring RF cavity are shown in Tables 8.8 and 8.9 [55]. In the following, we present estimations of the growth rate for the

coupled-bunch instability using ZAP [56] under the assumption of even bunch filling pattern. This assumption gives an upper bound of the instability growth rate for general filling patterns. Since the growth rate is much faster than the natural damping rate, the design will rely on fast feedback system (FBS) to control the instabilities. Consequently, we will assess the stability by comparing the instability growth time with the damping time of advanced bunch-by-bunch FBS, which can be in the range of one millisecond.

Table 8.8: Ion Ring Longitudinal HOM Parameters

f [MHz]	$R_s^{\parallel}$ [Ω]	Q
940.8	7.98e06	2.98e06
1771.9	2.25e04	5643.9
1814.0	1.00e05	5265.5
2894.8	3.33e04	9172.4
3079.4	2.23e02	2.65e04

Table 8.9: Ion Ring Transverse HOM Parameters

f [MHz]	$R_s^{\perp}$ [kΩ/m]	Q
792	42.0	115
1063	38.0	27
1133	1.82	54
1202	12.2	871
1327	76.7	611
1420	126.9	1138
1542	0.89	92
1595	1.39	145
1676	64.5	783
1749	2.31	1317

With the JLEIC machine and beam parameters, and the RF HOM parameters in Ref. [54] for the electron ring and in Tables 8.8 and 8.9 for the ion ring, the growth rates for coupled bunch instabilities are obtained by ZAP and shown in Table 8.10. Here in the TCBI calculations for both the electron and the proton beams, we assume a nonzero chromaticity and a finite betatron tune spread of 3×10^{-4}.

In Table 8.10, $\tau_{a=1}^{\parallel}$ and $\tau_{a=2}^{\parallel}$ are the growth time for the longitudinal dipole and quadruple mode respectively, and $\tau_{a=1}^{\perp}$ and $\tau_{a=2}^{\perp}$ correspond to the growth time for the transverse rigid and dipole mode. $\tau_{damp}^{\parallel}$ and $\tau_{damp}^{\perp}$ for the e-ring each represents the natural longitudinal and transverse damping time due to synchrotron radiation, while $\tau_{damp}^{\parallel}$ and $\tau_{damp}^{\perp}$ for the p-ring are the damping times for the proton beam due to electron cooling [57]. Note that for the electron ring, the lowest energy of 3 GeV yields the fastest growth time of $\tau_{a=1}^{\parallel}$=6.1 ms for LCBI, and $\tau_{a=0}^{\perp}$=1.6 ms for TCBI, which are expected to be mitigated by advanced FBS as used in modern electron storage

rings. The fast growth times of $\tau^{\parallel}_{a=1}$=2.3 ms and $\tau^{\perp}_{a=0}$=8.6 ms for the proton beam require the longitudinal and transverse FBS in the proton ring working as effectively as those in an electron ring. This, however, requires much stronger kicker strength than those found in modern proton-ring FBS, implying higher broadband impedance due to kicker cavities. Additional efforts are needed to further damp the HOM of the p-ring cavities and alleviate these excessive demands on kicker strength. The Landau damping effect on transverse coupled bunch instability, from either chromaticity and beam-beam tune shift spread, are the subject of further studies.

Table 8.10: Growth Time for the Coupled Bunch Instabilities in the JLEIC Design

	e-Ring	p-Ring		
E [GeV]	3	5	10	100
$\tau^{\parallel}_{a=1}$ [ms]	6.1	8.5	16	2.2
$\tau^{\parallel}_{a=2}$ [ms]	118	163	199	12
$\tau^{\parallel}_{damp}$ [ms]	187	40.5	5.1	¿30 min
$\tau^{\perp}_{a=0}$	1.6	2.7	6.4	8.6
$\tau^{\perp}_{a=0}$	25	39	58	74
$\tau^{\perp}_{damp}$	375	81	10.1	¿ 30 min

8.4.4 Electron Cloud in the Ion Ring

In an ion ring, the ionization of residual gas and the beam-loss induced surface emission provide the source for the primary electrons, while the electron cloud build-up comes mainly from the secondary electron production [58]. Unlike the trailing-edge effect of electron cloud for long ion bunches in conventional ion rings, here the high rep rate and short bunches of the ion beam in JLEIC renders the electron cloud build-up process similar to those in positron rings of modern lepton colliders. For the proton beam at $E_{\rm p}$=100 GeV, the electron cloud density rapidly rises, and then saturates at around the neutralization density of

$$\rho_{\rm sat} = \frac{N_{\rm b}}{\pi b^2 L_{\rm sep}} = 2 \times 10^{12}\ {\rm m}^{-3}, \tag{8.4.13}$$

with the number of protons per bunch $N_{\rm b} = 0.98 \times 10^{10}$, the average pipe radius $b = 4.86$ cm, and the bunch separation $L_{\rm sep} = 0.63$ m. Such saturation behavior is modelled in Ref. [58] for a similar set of parameters. The electron-cloud induced single-bunch transverse mode coupling instability (TMCI) threshold can be estimated using two-particle model [59],

$$\rho_{\rm th} = \frac{2\gamma Q_{\rm s}}{\pi r_{\rm p} C \langle \beta_{\rm y} \rangle} = 1.7 \times 10^{13}\ {\rm m}^{-3} \tag{8.4.14}$$

for the synchrotron tune $Q_{\rm s} = 0.053$, ring circumference $C = 2154$ m, and $\langle \beta_{\rm y} \rangle = 64$ m. With $\rho_{\rm sat} < \rho_{\rm th}$, the bunch is stable from the electron-cloud induced strong head-tail instability. The electron-cloud induced coupled-bunch instability for the JLEIC ion beam can cause more concern, which is yet to be assessed by computer modelling.

Electron cloud build-up simulations have been performed with PyECLOUD [60] for the proton beam, magnet, and vacuum parameters shown in Table 8.11. Secondary electron yield (SEY)

parameters corresponding to different materials are given in Table 8.12. Stainless steel and copper values are reported for technical materials as received. Black stainless steel and black copper refers the process of laser treating surfaces, and results in both surfaces having a comparable δ_{max} to the non-evaporable getter (NEG) coating. It should be noted that the feasibility of laser treating or NEG-coating the beam pipe is low — these values are only included for comparison.

Simulations were run for three cases — stainless steel, copper, and partially scrubbed copper. The simulation effort was limited to the arc dipoles, which is the anticipated location of highest electron cloud density — future simulations will be performed to verify this. The electron line density build up for the three cases is shown in Figure 8.33. It is clear that in all three cases, the electron density saturation value is reached within the first bunch train and returns to this value for subsequent bunch trains.

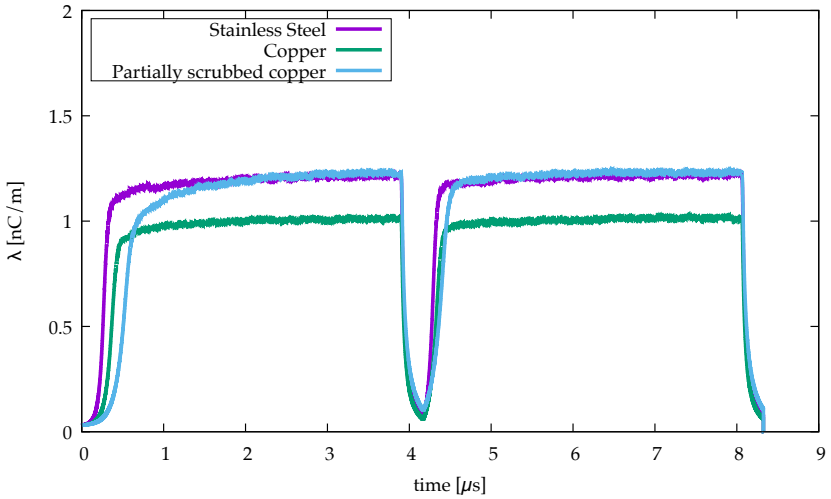

Figure 8.33: Electron line density as a function of time for beam pipes of stainless steel, copper, and partially scrubbed copper. Simulations were for two bunch trains of 1856 bunches.

It is possible to calculate the estimated horizontal tune shift per unit length with the formula

$$\Delta\nu_x/L = \frac{r_p\bar{\beta}_x\rho_e}{2\gamma_b} \tag{8.4.15}$$

where $r_p = 1.535\times10^{-18}$ m is the classical proton radius, ρ_e is the electron cloud density, $\bar{\beta}_x = 49$ m is the average horizontal beta function, and $\gamma_b = 106.6$ is the typical relativistic factor of the proton beam. The formula for the estimated vertical tune shift per unit length is similar, simply replacing $\bar{\beta}_x$ with $\bar{\beta}_y$, which is 66 m. Taking L to be 2257 m, the circumference of the ion ring, we can estimate the vertical and horizontal tune shift per turn — these results are given in Table 8.13. All three estimated tune shifts per turn fall below 2×10^{-3}, which does not indicate that electron cloud effects will have a significant impact on the performance of the machine. Additionally, these values overestimate the electron cloud density of the entire machine, by taking the presumed highest density and assuming it applies throughout the entire machine.

However, this approach assumes that the highest electron cloud density occurs in the dipoles. Using the machine parameters given in Table 8.11 and the magnet settings given in Table 8.14, electron cloud densities in each type of magnet were simulated for stainless steel [65]; the electron cloud densities and estimated tune shifts are given in Table 8.15 while the build up over the first

Table 8.11: Proton Beam, Magnet, and Vacuum Parameters used in the Simulations

Parameter	Symbol (Unit)	Value
Beam energy	E_b (GeV)	100
Circumference	C (m)	2257
Collision frequency	f_c (MHz)	476
Beam pipe cross-section	-	Circular [61]
Beam pipe radius	r_b (mm)	40 [61]
Number of bunches per train	K_B	1856
Bunch spacing	s_b (ns)	2.1
Bunch population	N_p (10^{10})	0.98
Bunch length	σ_l (cm)	1
Bunch profile	-	Gaussian
Empty bunches between trains	-	126
Normalized emittance	$\epsilon_x^N, \epsilon_y^N$ (µm-rad)	0.5, 0.1
Residual gas pressure	P (nTorr)	5
Temperature	T (K)	4.5
Simulation section	-	Dipole magnet
Length of simulated region	L (m)	8.0
Dipole magnetic field	B (T)	3.06

Table 8.12: SEY Parameters Corresponding to Different Materials

Material	Peak SEY $\delta_{max} \equiv \delta(E_{max})$	Energy at peak SEY E_{max} (eV)	Ionization cross-section σ_i (Mbarns)
Stainless steel [62]	2.25	300	2
Copper [62]	1.90	300	2
Partially scrubbed copper [63]	1.55	125	2
Black stainless steel [62]	1.12	900	2
Black copper [62]	1.12	600	2
Non-evaporable getter (NEG) [64]	1.1	230	2

bunch train is shown in Figure 8.34. In Table 8.14, the total magnetic length of the drift is the circumference minus the total magnetic lengths of the other elements listed.

In Table 8.16, instead of using the entire circumference as the length parameter to calculate the estimated tune shifts, the total magnetic length given in Table 8.14 is used. The final line gives the average line and volume densities with the total estimated tune shifts, horizontal and vertical, over the entire machine. These values are within 10% of estimates using only dipoles, assuming a constant electron cloud density over the entire ring. Consequently, quick estimates using only

Table 8.13: Simulation Results for Different Beam Pipe Materials

Material	λ_e (nC/m)	ρ_e (m^{-3})	$\Delta\nu_x$	$\Delta\nu_y$
Partially scrubbed copper	1.24	1.54×10^{12}	1.22×10^{-3}	1.65×10^{-3}
Stainless steel	1.23	1.53×10^{12}	1.21×10^{-3}	1.64×10^{-3}
Copper	1.02	1.27×10^{12}	1.01×10^{-3}	1.36×10^{-3}

Table 8.14: Magnetic Properties for Electron Cloud Simulations

Element	Absolute Field Strength	Unit	Count	Magnetic Length (m)	Total Magnetic Length (m)
Drift	-	-	-	-	971.4
Dipole	3.06	T	254	4	1016
Quadrupole	85	T/m	302	0.8	241.6
Sextupole	450	T/m^2	56	0.5	28

Table 8.15: Electron Cloud Simulation Results for Different Magnetic Elements in a Stainless Steel Beam Pipe

Material	λ_e (nC/m)	ρ_e (m^{-3})	$\Delta\nu_x$	$\Delta\nu_y$
Drift	1.09	1.36×10^{12}	1.07×10^{-3}	1.45×10^{-3}
Dipole	1.23	1.53×10^{12}	1.21×10^{-3}	1.64×10^{-3}
Quadrupole	2.40	2.99×10^{12}	2.37×10^{-3}	3.20×10^{-3}
Sextupole	3.11	3.87×10^{12}	3.07×10^{-3}	4.15×10^{-3}

the dipoles can give guidance in future considerations of bunch train structures and beam pipe materials.

Table 8.16: Simulation Results for Different Magnetic Elements in a Stainless Steel Beam Pipe. These use the total magnetic length of each element. Total machine parameters are averages (line and volume densities) or totals (estimated tune shifts).

Material	λ_e (nC/m)	ρ_e (m^{-3})	$\Delta\nu_x$	$\Delta\nu_y$
Drift	1.09	1.36×10^{12}	0.462×10^{-3}	0.623×10^{-3}
Dipole	1.23	1.53×10^{12}	0.547×10^{-3}	0.738×10^{-3}
Quadrupole	2.40	2.99×10^{12}	0.254×10^{-3}	0.342×10^{-3}
Sextupole	3.11	3.87×10^{12}	0.038×10^{-3}	0.051×10^{-3}
Total Machine	1.32	1.64×10^{-12}	1.30×10^{-3}	1.75×10^{-3}

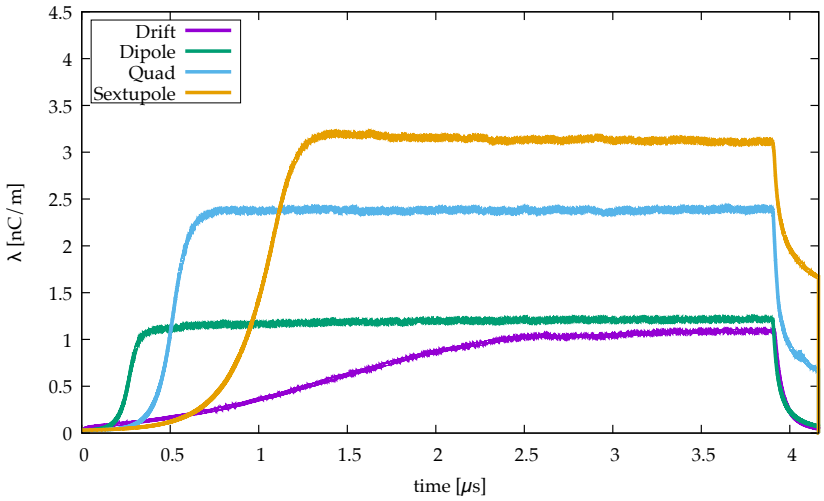

Figure 8.34: Electron line density as a function of time for a single bunch train (1856 bunches, followed by 126 empty buckets) with a beam pipe of stainless steel.

8.4.5 Ion Effects in the Electron Ring

The ionization scattering of the electron beam with residual gas molecules in the vacuum chamber can cause ion trapping in the electron ring. The trapped ions can cause many undesirable effects for the stability of the electron beam, such as emittance growth, halo formation, and coherent coupled bunch instabilities. For a symmetric bunch pattern, the critical ion mass for the ions to be trapped is given by [66]

$$A_{\mathrm{x,y}}^{\mathrm{trap}} = \frac{r_{\mathrm{p}} N_{\mathrm{b}} L_{\mathrm{sep}}}{2\sigma_{\mathrm{x,y}}(\sigma_{\mathrm{x}} + \sigma_{\mathrm{y}})} \,. \tag{8.4.16}$$

For the JLEIC electron ring, with L_{sep} the bunch separation distance, $N_{\mathrm{b}} = 3.7 \times 10^{10}$, the critical ion masses in Table 8.17 indicate that all ion molecules ($A \geq 2$) will be trapped for even bunch fill.

Table 8.17: Critical Ion Mass for Trapped Ion

E [GeV]	3	5	10
L_{sep} [m]	0.63	0.63	2.52
σ_{x} [mm]	0.15	0.26	22.2
σ_{y} [mm]	0.07	0.12	0.51
$A_{\mathrm{x}}^{\mathrm{trap}}$	0.5	0.2	0.24
$A_{\mathrm{y}}^{\mathrm{trap}}$ 1.1	0.4	0.4	

Bunch clearing gaps in electron rings are often used to clear the ions to prevent them from accumulating turn after turn. For a single gap, with h the harmonic number and n the number of bunches in the train, the stability criteria for the ion motion is [67],

$$|\mathrm{Tr}\,(M_{\mathrm{x,y}})| \leq 2 \tag{8.4.17}$$

for

$$M_{\mathrm{x,y}} = \left[\begin{pmatrix} 1 & L_{\mathrm{sep}} \\ 0 & 1 \end{pmatrix} \begin{pmatrix} 1 & 0 \\ -k_{\mathrm{x,y}} & 1 \end{pmatrix} \right]^n \begin{pmatrix} 1 & L_{\mathrm{sep}} \\ 0 & 1 \end{pmatrix}^{h-n} , \tag{8.4.18}$$

which is the one-period transport matrix of the ion particle phase-space vector, with

$$k_{\mathrm{x,y}} = \frac{2N_{\mathrm{b}} r_{\mathrm{p}}}{A\sigma_{\mathrm{x,y}}(\sigma_{\mathrm{x}} + \sigma_{\mathrm{y}})} . \tag{8.4.19}$$

For the JLEIC electron ring, the A vs. n for the x-motion (y-motion) is displayed in Figure 8.35 (Figure 8.36), where dots are marked when the stability (or ion trapping) condition is satisfied. These results show that almost all ions are trapped as n approaches h, and a gap of a few percent of the ring circumference will help clear up the ions.

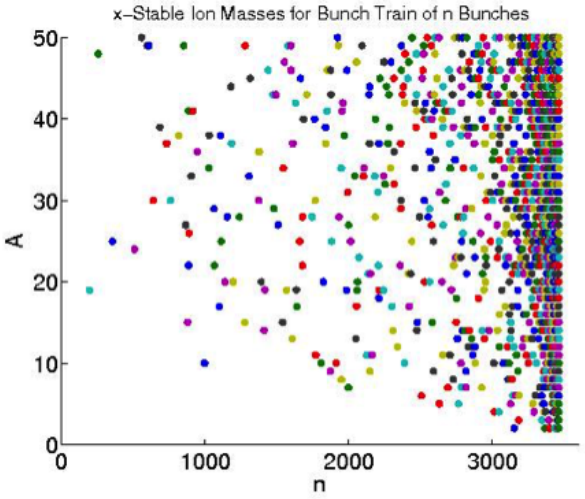

Figure 8.35: Ion stability in the A vs n plot for the x-motion.

With the ions being cleared after each turn by a clearing gap or gaps (under multi-train operation), there is still the fast beam-ion instability (FBII) [68] that could cause coupled transverse dipole motion of the electron bunches, with the dipole amplitude increases in time and along the bunch train. Under the assumptions that (1) the force between the ion and electron beam is linearly proportional to their dipole offsets and (2) constant frequency for all ion oscillations, the FBII is characterized by the growth time

$$y_{\mathrm{b}}(t) \propto (t/\tau_{\mathrm{g}})^{-1/4} \ \mathrm{e}^{\sqrt{t/\tau_{\mathrm{g}}}} \tag{8.4.20}$$

$$\tau_{\mathrm{g}}^{-1}[\mathrm{s}^{-1}] = 5p[\mathrm{Torr}] \left(\frac{N_{\mathrm{b}}^{3/2} n_{\mathrm{b}}^2 r_{\mathrm{e}} r_{\mathrm{p}}^{1/2} L_{\mathrm{sep}}^{1/2} c}{\gamma \sigma_{\mathrm{y}}^{3/2} (\sigma_{\mathrm{x}} + \sigma_{\mathrm{y}})^{3/2} A^{1/2} \omega_\beta} \right) . \tag{8.4.21}$$

For realistic beams, one needs to include the Landau damping effect of the ion oscillation frequency spread. Then the dipole amplitude growth is characterized by the e-folding time [69, 70]

$$y_{\mathrm{b}} \propto \mathrm{e}^{t/\tau_{\mathrm{e}}} , \tau_{\mathrm{e}}^{-1} \approx \tau_{\mathrm{g}} \left(\frac{c}{4\sqrt{2\pi} L_{\mathrm{sep}} n_{\mathrm{b}} a_{\mathrm{bt}} f_{\mathrm{i}}} \right) \tag{8.4.22}$$

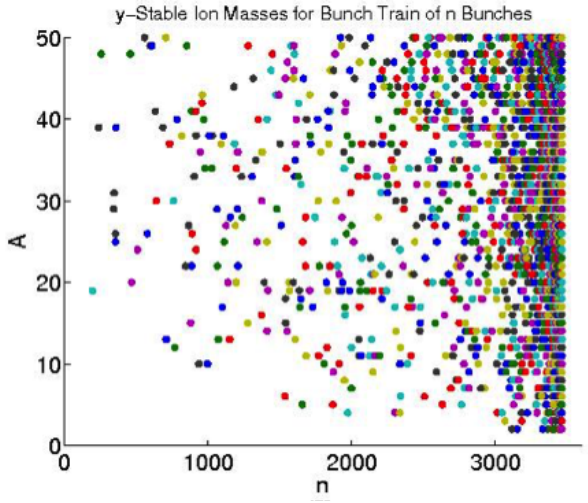

Figure 8.36: Ion stability in the A vs n plot for the y-motion.

for $f_{\rm i}$ being the coherent ion oscillation frequency, and $a_{\rm bt}$ the ion frequency variation. For the JLEIC electron ring, $\tau_{\rm g}$ and $\tau_{\rm e}$ are shown in Table 8.18 (for $a_{\rm bt}$=0.5). For $E_{\rm e}$ = 10 GeV, the growth time is comparable to that of the PEP-II HER beam. However, for $E_{\rm e}$=3-5 GeV, the growth time is orders of magnitude faster and is consequently a serious concern for the electron beam stability. Possible mitigation methods include using chromaticity to Landau damp the FBII, or using multiple bunch trains to reduce the growth amplitude. Comprehensive numerical modelling of FBII will be performed, along with its joint effect with beam-beam induced tune spread and coupled bunch beam-beam instability in the case of gear change scenario [1].

Table 8.18: Growth Time of FBII for the JLEIC e-Ring

$E_{\rm e}$ [GeV]	3	5	10
$\tau_{\rm c}$ [µs]	0.01	0.11	13.9
$\tau_{\rm e}$ [ms]	0.02	0.1	3.2

8.4.6 Summary

We have presented the status of our initial back-of-envelope estimations for the JLEIC beam stability at a set of selected collision energies. Our estimation shows that for the current design, the low energy electron beam is vulnerable to the longitudinal single bunch instability. In addition, to mitigate the coupled bunch instabilities, both electron and proton beam require the state-of-art longitudinal and transverse fast bunch-by bunch feedback systems—as strong as those employed in PEP-II or modern storage-ring light sources. As the engineering design progresses and when more details of impedance spectrum are available for the JLEIC collider rings, a more in-depth modeling will be conducted for the impedance-induced single and coupled bunch instabilities, including the effects of chromaticity and uneven bunch filling on the coupled bunch instabilities. The HOMs from both the accelerating/focusing RF cavities and the crab cavities are to be considered. We also need to model the electron-cloud buildup and its effect on the ion beam stability, in particular

the e-cloud induced coupled bunch instability, as well as the effects of chromaticity and multi-bunch train on the mitigation of fast beam-ion instability for the electron beam.

REFERENCES

1. V. Morozov *et al.*, "Study of Beam Synchronization at JLEIC", ArXiv:1606.09117 [physics.acc-ph], June 29 2016.
2. J. Guo, "Variation of JLEIC RF Frequencies and Circumferences due to Synchronization Requirements", JLAB-TN-17-036, 2017.
3. S.Abeyratne *et al.*, "MEIC Design Summary", arXiv:1504.07961, 2015.
4. R. B. Palmer, SLAC Report No. SLAC-PUB-4707, 1988.
5. K. Oide and K. Yokoya, "Beam-beam collision scheme for storage-ring colliders", *Phys. Rev. A* 40, No.1, p. 315 , 1989.
6. Y.-P. Sun *et al.*, *Phys. Rev. ST Accel. Beams* 12, 101002, 2009.
7. F. Zimmermann and U. Dorda, in *Proc. LHC-LUMI-05*, CERN-OPEN-2006-036, CERN, 2005.
8. V.S. Morozov *et al.*, *Phys. Rev. ST. Accel. Beams*, 16, 011004, 2013.
9. S. Sosa, V. Morozov and J. R. Delayen, WEPIK043, IPAC2017, Copenhagen, Denmark (2017).
10. M. Borland, "elegant: A Flexible SDDS-Compliant Code for Accelerator Simulation", Advanced Photon Source LS-287, September 2000.
11. S. Sosa, H. Park, S. U. De Silva, V. Morozov and J. R. Delayen, WEPIK044, IPAC2017, Copenhagen, Denmark (2017).
12. H. Park, A. Castilla, J. R. Delayen, S. U. De Silva and V. Morozov, WEPMR034, IPAC2016, Busan, Korea (2016).
13. S. U. De Silva, H. Park, and J. R. Delayen, WEPMW022, IPAC2016, Busan, Korea (2016).
14. G.H. Wei, V.S. Morozov, F. Lin, Y. Zhang, F. Pilat, THPMR053, IPAC2016, Busan, Korea (2016).
15. R. Calaga, "Crab Cavities for the LHC Upgrade", in Proceedings of Workshop on LHC Performance, Chamonix (2012).
16. S. Sosa, R. Li, H. Park, S. U. De Silva, V. Morozov and J. R. Delayen, THPAK070, IPAC2018, Vancouver, BC, Canada (2018).
17. R. Li, "Estimations of Coherent Instabilities for JLEIC", Proc. of IPAC17, pg. 3903, paper THPAB080, 2017.
18. Chao, A. W., & Tigner, M. in Sec. 2.4.10. of Handbook of accelerator physics and engineering, 2nd ed.: World Scientific (2012).
19. S. Abeyratne *et al.*, "Science requirements and conceptual design for a polarized medium energy electron-ion collider at Jefferson lab", edited by Y. Zhang and J. Bisognano, arXiv:1209.0757 (2012)
20. V.S. Morozov *et al.*, "Study of Beam Synchronization at JLEIC", arXiv:1606:0.9117 (2015)
21. K. Arumugam *et al.*, "GPU-Accelerated High-Fidelity Simulation of Beam-Beam Effects in Particle Colliders", Proceedings of the Summer Computer Simulation Conference, article 5, 2017.
22. J.Qiang *et al.*, Nucl. Inst. & Meth. in Phys. Rev. vol. A558,p.351, (2006)
23. J. Qiang *et al.*, Proc. HALO'03, May 19-23, Montauk, NY p. 278, (2003)
24. J. Qiang *et al.*, Proc. of IPAC 2015, p. 2210
25. J. Qiang *et al.*, Proc. of Particle Accelerator Conf., Portland, Oregon, May 12-16, p3401 (2003)
26. R. B. Palmer, SLAC-PUB-4707 (1988)
27. T. Abe *et al.*, "Compensation of the Crossing Angle with Crab Cavities at KEKB", arXiv:0706.3248 (2007)

28. Raimondi, P. *et al.*, "Status on SuperB effort", in 2nd SuperB Workshop, Frascati, Italy, 16-18 March 2006.
29. Zobov M. *et al.*, "Test of crab-waist collisions at DAΦNE Φ-factory", Phys. Rev. Lett. **104** 174801 (2010)
30. D. M. Zhou *et al.*"Simulations of beam-beam effect in the presence of general chromaticity", Physical Review ST-AB 13, 021001 (2010).
31. Y. Ohnishi *et al.*"Measurement of chromatic x-y coupling", Physical Review ST-AB 12, 091002 (2009).
32. Y. Funakoshi *et al.*"Orbit feedback system for maintaining an optimum beam collision", Physical Review ST-AB 10, 101001 (2007).
33. Y. H. Chin, "Effects of Non-Zero Dispersion at Crab-Cavities on the Beam dynamics", LBL-29581, (1991)
34. W. Herr and M.P Zorzano, "Coherent dipole modes for multiple interaction regions", LHC Project Report 462 (2001).
35. Y. Hao, "Dynamics with Crab-Crossing for EIC", EIC Accelerator Collaboration Meeting, Brookhaven National Laboratory, Oct 2017.
36. D. Neuffer and S. Peggs, "Beam-Beam Tune Shifts and Spreads in the SSC: Head-on, Long-range and PACMAN conditions", SSC-63 (1986)
37. Y. K. Batygin and T. Katayama, "Spin Depolarization Due to Beam-Beam Collisions", Phys. Rev. E **58**, 1019 (1998)
38. M. Boge and T. Limdberg, "Calculation on Depolarization in HERA Due to Beam-Beam Effects", " Proceedings Particle Accelerator Conference, Dallas, TX, 1995, pp. 2901-2903 vol.5.
39. H.D. Bremer *et al.*, DESY Report No. M-82-26, 1982.
40. A. Kondratenko *et al.*, private communication.
41. F. Méot, "The Ray-Tracing Code Zgoubi", Nucl. Instr. Meth A **427**, 353 (1999).
42. Y. Hao *et al.*, "Beam Beam Effects of Gear Changing in Ring-Ring Colliders", arXiv:1309.1739v1 (2013)
43. R. Majeti "Multi-GPU Accelerated High-Fidelity Simulations of Beam-Beam Effects in Particle Colliders", Masters Thesis, Old Dominion University, 2017.
44. M. Bassetti and G. Erskine, "Closed Expression for the Electrical Field of a Two-Dimensional Gaussian Charge", CERN Report CERN-ISR-TH/80-06, 1980.
45. V. Zhabitsky *et al.*, "LHC Transverse Feedback System: First Results of Beam Commissioning", CERN-LHC-Project- Report-1165, CERN, Geneva (2008)
46. W. Herr, "Introduction to Landau Damping", Proceedings of the CAS-Accelerator School, Trondheim (2013)
47. Y. Zhang, "JLEIC Baseline Update and New Parameters", `https://www.jlab.org/indico/event/210/`, 2017.
48. "PEP-II an Asymmetric B Factory", Conceptual Design Report, SLAC-418, 1993.
49. D. Zhou, SuperKEKB mini optics meeting, 2015.
50. S. Benson, Proc. of COOL'17 Workshop, 2017.
51. S. Peggs and W.W. MacKay (editors), "Collective Instabilities in RHIC", RHIC/AP/36, 1994.
52. S.Y. Zhang *et al.*, "Transverse Impedance Measurement at the RHIC", Proc. of EPAC'02, 2002.
53. A. Sidorin *et al.*, THAP01, Proceedings of COOL 2007, 2007.
54. R. Rimmer, J. Byrd, and D. Li, PRST-AB 3, 102001, 2000.
55. F. Marhauser, private communication, 2017.
56. M. Zisman, S. Chattopadhyay, and J.J. Bisognano, "ZAP USER'S MANUAL" LBL-21270, 1986.
57. H. Zhang, "Cooling Simulation Studies", `https://www.jlab.org/indico/event/210/`, 2017.
58. K. Ohmi *et al.*, PRSTAB **5** 114402, 2002.
59. K. Ohmi and F. Zimmermann, *Phys. Rev. Lett.* **85**, p. 3821, 2000.

60. G. Iadarola, "Electron cloud studies for CERN particle accelerators and simulation code development", Ph.D. Dissertation, Università degli Studi di Napoli Federico II, 2014, CERN-THESIS-2014-047, http://www.fedoa.unina.it/id/eprint/9957

61. T. Michalski, R. Fair, R. Rajput-Ghoshal, and P. Ghoshal, "JLEIC SC Magnets: Replace SF and High CM Energy Needs", 2018.

62. R. Valizadeh *et al.*, "Low secondary electron yield engineered surface for electron cloud mitigation", Applied Physics Letters, **105** 23, p. 231605, 2014, https://doi.org/10.1063/1.4902993

63. R. Cimino *et al.*, "Can Low-Energy Electrons Affect High-Energy Physics Accelerators?", Phys. Rev. Lett. **93** 1, p. 014801, 2004, https://link.aps.org/doi/10.1103/PhysRevLett.93.014801

64. W. Fischer *et al.*, "Electron cloud observations and cures in the Relativistic Heavy Ion Collider", Phys. Rev. ST Accel. Beams **11** 4, p. 041002, 2008, https://link.aps.org/doi/10.1103/PhysRevSTAB.11.041002

65. K.E. Deitrick, V.S. Morozov, and T. Satogata, "Electron cloud estimates for the Jefferson Lab EIC", Proc. of LINAC'18, Beijing, China, paper TUPO109.

66. Y. Baconnier and G. Brianti, CERN/SPS/80-2, 1980.

67. M.Q. Baron, *NIM:A* **243**, p. 278, 1986.

68. T.O. Raubenheimer and F. Zimmermann, *Phys. Rev. E* **52**:5, pp. 5487–5498, 1995.

69. G. Stupakov, T.Raubenheimer, and F. Zimmermann, *Phys. Rev. E* **52**:5, pp. 5499–5504, 1995.

70. F. Zimmermann *et al.*, SLAC-PUB-7617, 1997.

CHAPTER 9

TECHNICAL SUBSYSTEMS

To achieve the required performance defined in the preceding sections, numerous technical systems must be fully integrated and operate seamlessly. State of the art technologies have been selected as the foundation for these systems. Each has been technically proven either through application in an existing accelerator or prototyped and tested to appropriate levels of performance to reduce technical risk.

9.1 Superconducting Magnets

The superconducting magnet systems for JLEIC mainly encompass the ion complex: the booster ring and ion collider ring. There are superconducting solenoids in the electron collider ring. The interaction region contains final focusing quadrupoles, skew quads, correctors, and anti-solenoids. The details of all IR magnets are documented in Section 9.3.

The magnets in the ion complex consist primarily of superconducting dipole, quadrupole, and sextupole magnets for guiding and focusing the ion beam into well-defined orbits in the machine lattices for the Booster and Ion Collider figure-eight rings. These magnet systems are designed to allow operation in the energy range of 285 MeV to 8 GeV in the Booster Ring and 8 GeV to 100 GeV in the Ion Collider Ring. The superconducting magnets must achieve the required field range as well as meet stringent requirements on field quality, reproducibility, and long-term reliability. To satisfy all these requirements without increasing technical risk, existing, proven superconducting magnet technology is used for the magnet design/analysis, construction, test measurement, cooling, quench protection, instrumentation, and quality control standards. The performance requirements are very similar to the cosine-theta magnets used in RHIC [1], manufactured by Northrup Grumman. Therefore, the magnet designs, conductor selection, and fabrication are guided by these magnets.

Additionally, they have the reputation of being a cost effective design and successful production magnet program. The Booster magnets have the added requirement of fast ramping requiring adaptations to standard Rutherford conductor are required as demonstrated in magnets developed for the SIS 300 program at GSI [2, 3]. All magnet designs for JLEIC are based on readily available superconductor materials. Functionality of all magnets is within state-of-the-art, as validated by production magnets in existing accelerators or in tested prototypes with published results.

9.1.1 Ion Collider Ring Magnets

The JLEIC Ion Collider Ring magnet lattice is designed to fit into a figure-8 tunnel of 2257 m beam path length. Table 9.1 gives the Ion Collider Ring inventory. The magnets are designed around a common aperture to minimize impedance effects. This aperture is sized to account for sagitta in the dipoles and extended to other magnets in the ring.

Table 9.1: Ion Collider Ring Superconducting Magnets Inventory

Magnet Type	**Number of Magnets**	**Magnet Strength [T, T/m, T/m^2]**	**Magnetic Length [m]**	**Coil Aperture Radius [mm]**	**Beam Pipe Aperture Radius [mm]**	**Operating Current [A]**
Dipole	254	3.06 T	4.00	50	40	5838
Dipole	5	4.67 T	4.00	50	40	
Quadrupole	41	20–30 T/m	0.80	50	40	208
Quadrupole	34	30–40 T/m	0.80	50	40	312
Quadrupole	28	40–50 T/m	0.80	50	40	417
Quadrupole	155	52.9 T/m	0.80	50	40	551
Quadrupole	44	82.2 T/m	0.80	50	40	558
Sextupole	56	528.7 T/m^2	0.50	50	40	200
Solenoid	4	1 T	15.00	50	40	

Table 9.2 lists the dipole multipole errors for the Ion Collider Ring magnets which have been used to analyze the dynamic aperture.

Table 9.2: Projected Ion Collider Ring Multipole Errors. These are multipole errors relative to the main dipole field at a reference radius of 20 mm, in units of 10^{-4}.

Multipole Type	$\frac{\Delta B_1}{B_0}$	$\frac{\Delta B_2}{B_0}$	$\frac{\Delta B_3}{B_0}$	$\frac{\Delta B_4}{B_0}$	$\frac{\Delta B_5}{B_0}$	$\frac{\Delta B_6}{B_0}$	$\frac{\Delta B_7}{B_0}$	$\frac{\Delta B_8}{B_0}$	$\frac{\Delta B_9}{B_0}$	$\frac{\Delta B_{10}}{B_0}$
Systematic	-0.151	-0.537	0.126	0.850	0.714	0.366	-0.464	-0.410	0.009	0.027
Random										

9.1.2 Booster Ring Magnets

The JLEIC Booster magnet lattice is designed to fit into a figure-8 tunnel of 313.5 m beam path length. Table 9.3 gives the Booster inventory. Fast ramping of the magnets is required due to the number of times the Booster must be cycled to the Ion Collider Ring. A ramp rate of 1 T/s for the dipoles is the guiding specification for the entire ring of magnets. A ramp rate of 1 T/s for the dipoles is the guiding specification for the entire ring of magnets. However, the need for fast ramping requires a modified conductor design to address AC losses. The conductor design will therefore follow the fast ramping designs developed and validated for the GSI 001 and SIS300 magnets.

Table 9.3: Ion Collider Ring Superconducting Magnets Inventory

Magnet Type	**Number of Magnets**	**Magnet Strength [T, T/m, T/m^2]**	**Magnetic Length [m]**	**Coil Aperture Radius [mm]**	**Beam Pipe Aperture Radius [mm]**	**Operating Current [A]**
Arc Dipole	64	3.0 T	1.42	50	40	5100
Straight Quads (F)	20	24.3 T/m	0.40	50	40	2616
Straight Quads (D)	12	-19.8 T/m	0.80	50	40	-2137
Arc Quads	50	29.6 T/m	0.40	50	40	3187
Sextupole	64	210.0 T/m^2	0.20	50	40	100

9.1.3 Superconductor Cable

9.1.3.1 NbTi Rutherford Cable A 30-strand (or wire) superconductor cable is planned in the fabrication of all of the dipole magnets in the Ion Collider Ring (see Figure 9.1). Due to similar magnet size and conductor requirements, this cable is expected to be very similar to what has been used in the RHIC dipole and quadrupole magnets. The wire and cable fabrication methods are well developed and will be acquired from various sources.

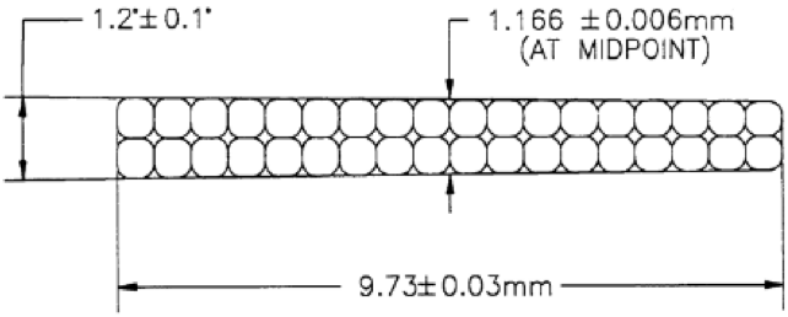

Figure 9.1: 30 strand, keystoned NbTi Rutherford cable

9.1.3.2 Fast-Ramp NbTi Rutherford Cable To achieve the requisite ramp rate, a modified Rutherford cable [4, 5, 6] with 30 strands is chosen for the Booster dipole and quadrupole magnets (see Figure 9.2. This conductor is characterized by several features, chosen to provide low AC losses: 1) reduced filament size; 2) reduced twist pitch of filaments in the strand; 3) change the filament matrix to CuMn; 4) separate cable layers using a thin stainless steel foil (25 µm); 5) coat the strands with SnAg solder. This conductor has been demonstrated in the GSI 001 prototype, and 4.5 T and 6 T versions of SIS300 magnet prototypes.

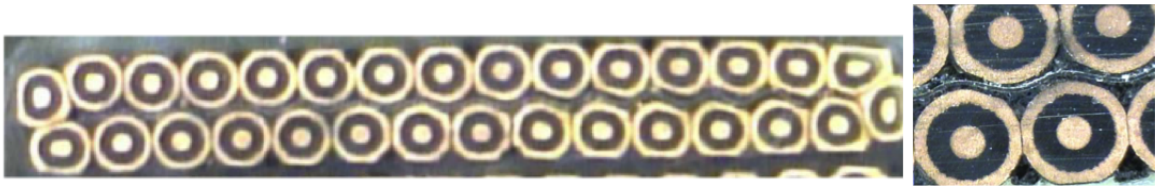

Figure 9.2: Fast ramping NbTi Rutherford cable with stainless steel foil between layers

9.1.3.3 Sextupole Conductor The sextupoles have requirements which allow for using MRI style rectangular cross-section superconductor. This material is readily available from multiple sources and is very cost effective.

9.1.3.4 Dipole Design and Construction Figure 9.3 shows a cross-section of the superconducting dipole cold mass. The dipole design is based on a 100 mm aperture diameter, single-layer cosine-theta coil, wound from a keystoned, NbTi superconducting Rutherford cable and mechanically supported by a laminated cold steel yoke. A stainless steel outer shell is welded around the yoke and acts as the helium vessel. The helium vessel is also a load bearing part of the yoke assembly. The nominal diameter of the cold mass is 276.5 mm. The nominal dipole operating temperature is between 4.5 and 4.7 K. The dipoles are built as straight magnets.

The dipole cold mass design incorporates a cold beam tube (80 mm diameter) to accommodate the beam dynamic aperture and associated sagitta. The Ion Collider Ring coil uses standard Rutherford cable and the Booster Ring coils are made using the modified Rutherford cable for fast-ramping. Insulator material surrounds the coil assembly and interfaces with the yoke. The steel yoke serves as a magnetic return path and acts as a shield to reduce stray field. The yoke laminations contain holes for the necessary busses and for the flow of helium. The yoke and outer shell provide the structure to counteract the forces of the energized coils. End bells are added to complete the helium vessel.

9.1.3.5 Quadrupole Design and Construction The quadrupole coil design is based on a single-layer cosine two-theta coil, wound from a keystoned, NbTi superconducting cable and mechanically supported by a laminated cold steel yoke. A stainless steel outer shell is welded around the yoke and acts as the helium vessel for the magnet. The helium vessel is also a load bearing part of the yoke assembly. This cold mass assembly, along with that of the sextupole, is mounted within a common helium vessel. The nominal diameter of the cold mass is 276.5 mm. The nominal quadrupole operating temperature is between 4.5 and 4.7 K. Figure 9.4 shows a cross-section of the quadrupole magnet cold mass.

The quadrupole cold mass design incorporates a cold beam tube (80 mm diameter) to accommodate the beam dynamic aperture. Maintaining a common beam tube diameter also aids in minimizing impedance in the ion complex. The Ion Collider Ring coil uses standard Rutherford cable and the Booster Ring coils are made using the Modified Rutherford cable for fast-ramping.

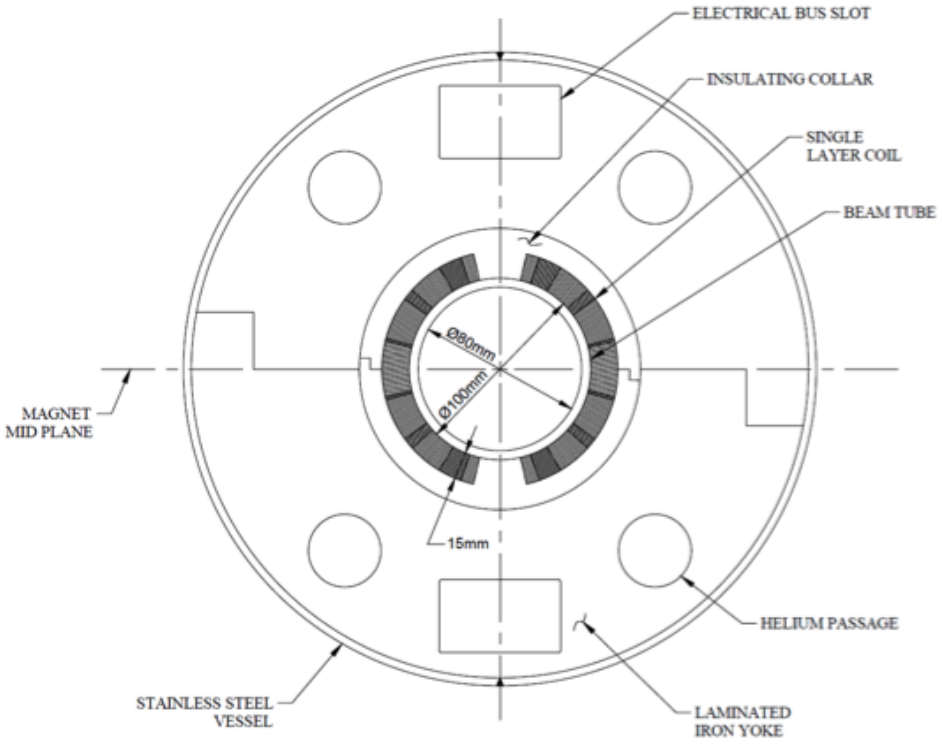

Figure 9.3: Cross section view of an Ion Collider Ring dipole.

Insulator material surrounds the coil assembly and interfaces with the yoke. The steel yoke serves as a magnetic return path and acts as a shield to reduce stray field. The yoke laminations contain holes for the necessary busses and for the flow of helium. The yoke and outer shell provide the structure to counteract the forces of the energized coils. End bells are added to complete the common quadrupole-sextupole helium vessel.

9.1.3.6 Sextupole Design and Construction Sextupole magnets are required to compensate for chromaticity and correct for the sextupole field generated in the dipoles. The coils are wound from NbTi MRI type conductor. The laminated cold steel yoke incorporates the poles of the magnet as well. A stainless steel outer shell is welded around the yoke/poles and acts as the helium vessel for the magnet. This cold mass assembly, along with that of the quadrupole, is mounted within a common helium vessel assembly. The nominal diameter of the cold mass is 276.5 mm. The nominal sextupole operating temperature is between 4.5 and 4.7 K. Figure 9.5 shows a cross-section of the sextupole magnet cold mass.

The sextupole cold mass design incorporates a cold beam tube (80 mm diameter) to accommodate the beam dynamic aperture. The yoke laminations contain holes for the necessary busses and for the flow of helium. The yoke and outer shell provide the structure to counteract the forces of the energized coils. End bells are added to complete the common quadrupole-sextupole helium vessel.

9.1.3.7 Magnet Cryostat and Final Assembly For economy of space and construction cost, all magnets in an arc half-cell will be placed in a single cryostat. For the Ion Collider Ring, the cryostat is

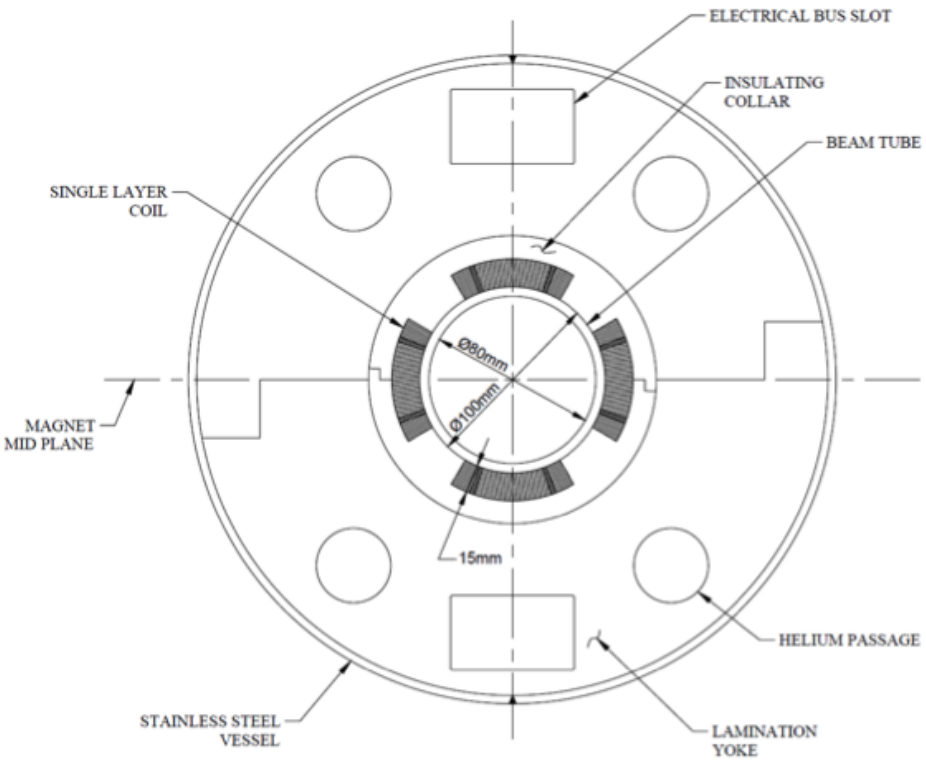

Figure 9.4: Cross section view of an Ion Collider Ring quadrupole.

11.4 m long × 0.61 m diameter, and contains 2×4 m dipole magnets, 1 quadrupole magnet, and 1 sextupole magnet. The 2×4 m dipoles are canted at 2 degrees to account for a portion of the sagitta over their combined length. The quadrupole and sextupole magnets will be closely coupled, mounted on a single beam pipe, and sharing a common helium vessel. Shielded bellows will be placed between the quadrupole-sextupole cold mass and the 2×4 m dipole cold mass assemblies. Pre-alignment will be performed in the warm condition prior to installing into the long cryostat. Magnets in the straight sections of the ion collider will be housed in individual cryostats.

The cryostats for the Booster Ring magnets will have the same diameter but lengths will vary for different groupings. In the arcs, 2 dipoles and a quadrupole will be housed in a single cryostat. Similarly, the triplets in the straights will be housed in a single cryostat.

The cryostat structure serves several purposes. First, it thermally shields the magnet cold mass and minimizes heat transfer from the surrounding environment. This is achieved via an insulating vacuum, MLI, a thermal shield, and a tortuous thermal conduction path in the cold mass support posts. The cryostat must accurately position the magnet cold mass to a given point in the accelerator lattice. Within the cryostat, in addition to the magnet cold mass, are cryogenic headers, a magnet power conductor bus, an instrumentation bus, and support posts. The power conductor bus and instrumentation bus are placed inside conduits within the magnet cryostat assembly. The electrical connections between bus conductors and magnet leads are at the ends of the magnets. The support posts carry the cold mass weight to the wall of the vacuum vessel.

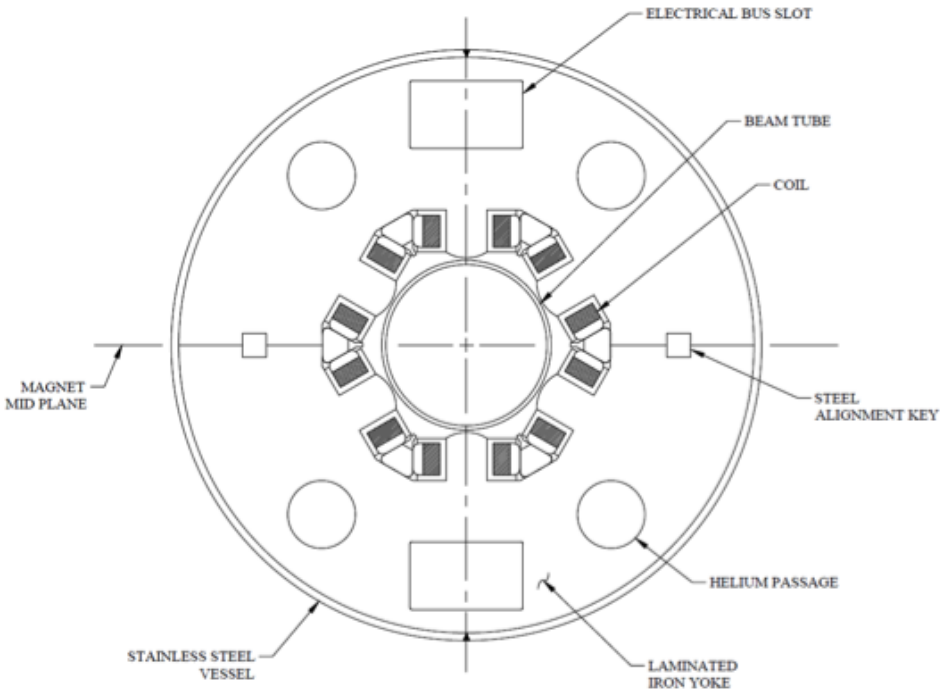

Figure 9.5: Cross section view of an Ion Collider Ring sextupole.

9.1.4 Specialty Magnets

9.1.4.1 Cooling Solenoids The region within the Ion Collider Ring designated for both DC and Bunched Beam Cooling requires a series of 4×15 m solenoids. The cooling solenoid parameters are shown in Table 9.4.

Table 9.4: Cooling Solenoid Operating Parameters. Polarity of the solenoid fields will alternate between adjacent magnets.

Parameter	**Units**	**Value**
Quantity	each	4
Length	[m]	15
Field	[T]	1.0
Field Straightness	$[\times 10^{-4}$	1
Operating Current	[A]	TBD
Coil Aperture Diameter	[mm]	100
Beam Tube Aperture Diameter	[mm]	80

The coils for the solenoids will be wound using NbTi Rutherford cable. Solenoids of this field strength are well within state of the art. The solenoid coils will be bath cooled. The solenoids

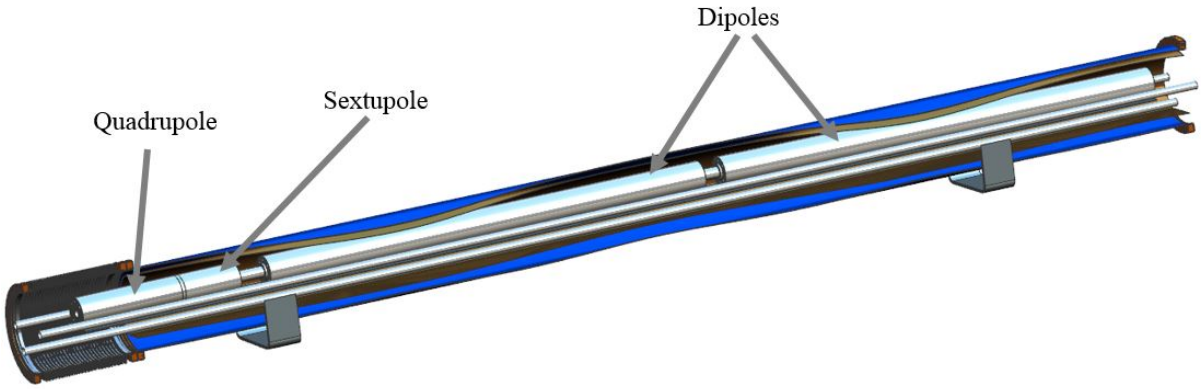

Figure 9.6: Section view of an ion collider ring arc half cell.

will be constructed with a warm bore, allowing access for the precision measurement of the field straightness.

The 15 m solenoids will be divided into 3 segments allowing for ease of manufacturing as well as installation. Final alignment of the segments will be achieved within the collider tunnel via measuring the field within the solenoids with a needle and mirror test mole [7, 8] and associated laser measurement system to measure field straightness.

Precision alignment with each solenoid segment is critical. Therefore several methods of construction are being investigated. Accelerator Technology Corporation is currently working under a 2018 DOE Phase I SBIR [9] in developing a precision washer and epoxy potting scheme for precision assembly of solenoid coils. Detailed assessment of the design may require corrector coils at either end as an additional means of fine tuning the field within the assembled solenoid.

9.1.4.2 Spin Rotator Solenoids The Electron Collider Ring requires superconducting solenoid magnets for spin rotation. These solenoids are located at the ends of the straight with the active Interaction Point. The quantities and performance parameters for these solenoids are included in table below.

The coils for the solenoids will be wound using NbTi Rutherford cable. Solenoids of this field strength are well within state of the art. Due to proximity to the adjacent beamline and associated magnets, additional shielding on these solenoid magnets is required. Figures 9.7 and 9.8 show the peak field in the coil and the effects of active and passive shielding on the ion beamline for one of these solenoids.

9.1.4.3 Electrical Connections and Quench Protection The design of the machine uses a superconducting bus-bar (SC bus-bar) system to connect strings of magnets (i.e. series-connected magnets) to their respective power supplies. A cross-sectional view of a typical SC bus-bar is shown in Figure 9.9.

Each lead within a SC bus will be stabilized with additional copper and will also incorporate a bus expansion joint to allow for movement during cool down and warm up. Each magnet and its current leads will be instrumented with temperature sensors and voltage taps. Each magnet will also be protected with its own cold quench protection diode connected in parallel with the magnet

Table 9.5: Spin Rotator Solenoid Operating Parameters. Solenoids will be warm bore with water cooled beam tube to address synchrotron radiation. This also requires insulating vacuum encapsulation so as not to transmit heat into the magnet coils.

Parameter	**Units**	**Family 1**	**Family 2**
Quantity	each	8	8
Length	[m]	1.25	2.5
Field	[T]	5.0	7.6
Operating Current	[A]	TBD	TBD
Coil Aperture Diameter	[mm]	228.2	232
Beam Tube Aperture	[mm]	140	140

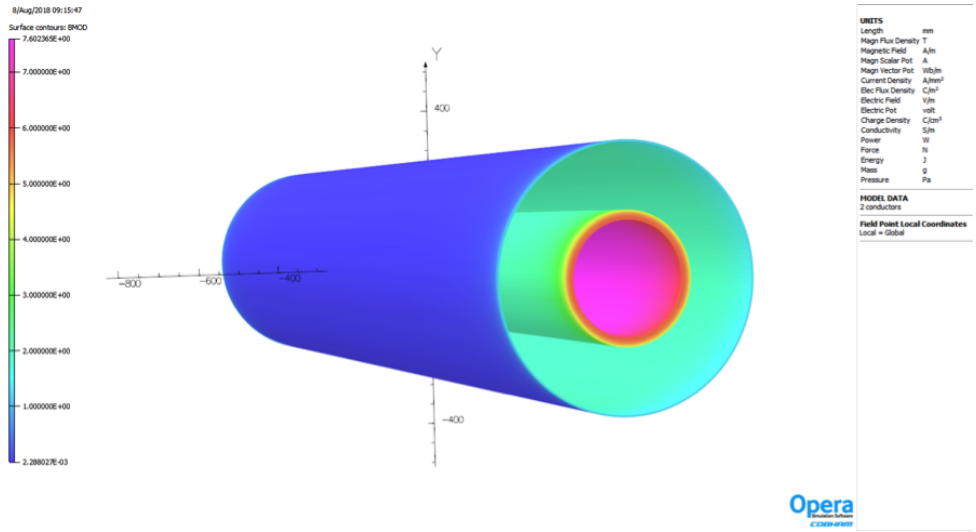

Figure 9.7: Maximum field in the coil for a 7.6 T solenoid (with active shield).

(i.e. between its current leads). If one magnet in a string quenches, the current flow bypasses the quenched magnet via the cold diode and voltage taps trigger the magnet power supply to rapid de-energize the unquenched magnets in the string, by switching in external dump resistors.

9.2 Normal Magnets

9.2.1 Electron Collider Ring

The requirements for the Electron Collider ring are given in Sections 4.3 and 9.2. This section breaks out the magnets by families and discusses designs and quantities as required. Superconducting solenoids required in the electron ring are also discussed here. Also needed in the electron collider ring are a number of superconducting quadrupoles and solenoids in the Interaction Region (Section 9.3).

9.2.1.1 Dipoles There are 258 dipoles required in the electron collider ring, which can further be broken down into six designs based on the effective length, Table 9.6. The largest family includes

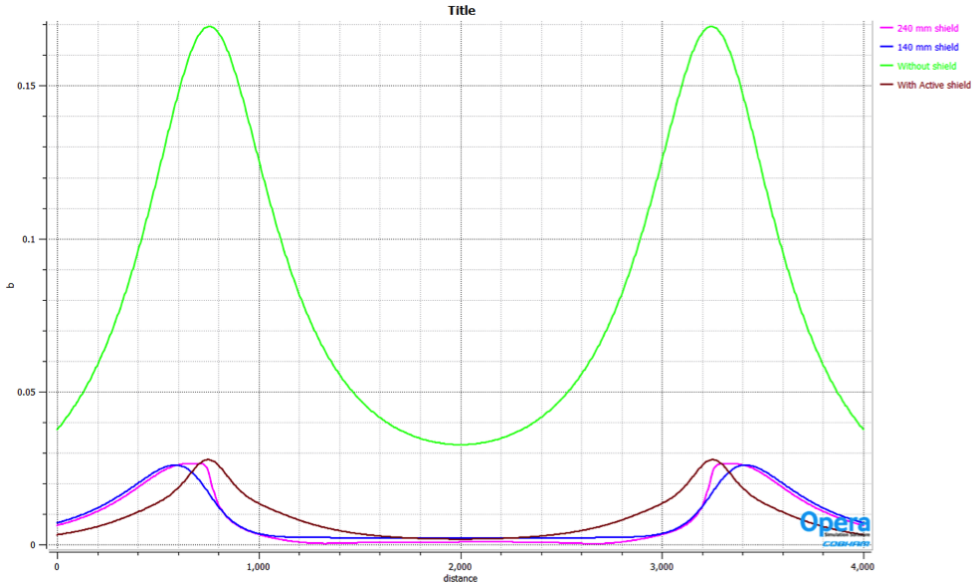

Figure 9.8: Shielding effectiveness of 7.6 T solenoid on the ion beamline.

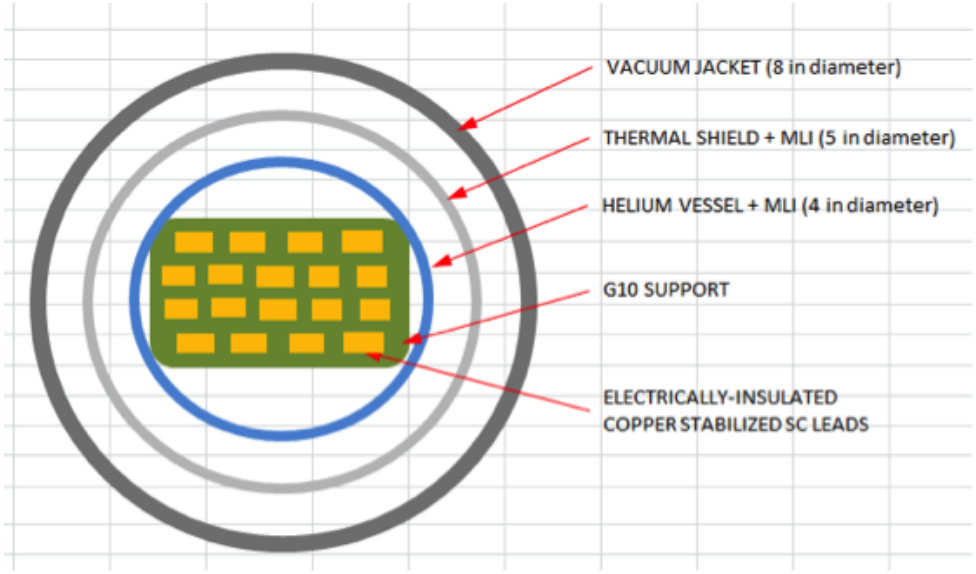

Figure 9.9: Cross section view of a superconducting bus bar.

180 dipoles for the arcs. To maintain compatibility with the PEP-II vacuum system, a dipole full gap of 7.0 cm is used for all of the dipoles. The required field strengths are well within conventional designs.

The majority of the dipoles were specified to keep the synchrotron radiation at or below the 10 kW/m design value used in PEP-II and the total below 10 MW. Sixteen of the dipoles currently exceed this value as listed in Table 9.7. Detailed design work is needed to confirm that the vacuum system, cooling and thermal stress requirements are not exceeded in these areas.

Table 9.6: JLEIC Collider Ring Dipole Requirements

Region	**Magnet Count** [#]	**Effective Length** [m]	**Design Field** [T]	**Bend Angle** [rad]	**Bend Radius** [m]	**Sagitta** [cm]
Chicane #1	2	0.5	0.17	0.14	200	0.016
Chicane #2	4	3.0	0.45	2.29	75	1.5
Spin Rotator	8	2.0	0.64	2.2	52.1	3.8
Spin Rotator	8	4.0	0.64	4.4	52.1	3.8
CCB	32	3.19	0.2	1.05	174	0.73
Arcs, Dispersion Suppression	204	3.6	0.34	2.1	98.2	1.65
Total	258					

Table 9.7: Synchrotron Radiation Values for Each Dipole Design at Maximum Beam Power

Region	**Magnet Count** [#]	**Effective Length** [m]	**Design Field** [T]	**Bend Angle** [rad]	**Bend Radius** [m]	**Beam Current** I [A]	**Beam Energy** E [GeV]	**Synchrotron Radiation** [kW/m]	Total kW
Total	258								
Chicane #1	2	3.0	0.42	2.15	80	3	6.98	15.63	93.8
Chicane #2	2	0.5	0.17	0.14	200	3	6.98	2.50	2.5
Chicane #3	2	3.0	0.45	2.29	75	3	6.98	17.78	106.7
Spin Rotator	8	2.0	0.64	2.2	52.1	3	6.98	36.85	589.5
Spin Rotator	8	4.0	0.64	4.4	52.1	3	6.98	36.85	1179.1
CCB	32	3.19	0.2	1.05	1.74	3	6.98	3.30	337.6
Arcs,Dispersion Suppression	204	3.6	0.34	2.1	98.2	3	6.98	10.37	7616.8
Total	258								

9.2.1.2 Quadrupoles There are 596 quadrupoles of varying lengths and strengths needed in the electron collider ring as listed in Table 9.8. The quads are listed by gradient with two of the length families divided into less than 18 T/m and greater than 18 T/m groupings. Two of the PEP-II quadrupole designs where investigated to see if they could meet some of the requirements [10]. These quads are rated for 18 T/m and can be used up to 20 T/m, by running 20% into saturation. There are 94 to 202 of the 4Q22 (0.56 m) quadrupoles and around 81 of the 4Q29 (0.73 m) of the PEP-II quads available for use in the collider. There is some discrepancy in the available number so the exact numbers are still to be verified. Two of the families in the table are based on these designs. Additional magnets will have to be purchased to make up the difference and additional designs are required. In some cases the required gradients will be met by doubling up on the magnets and work remains to reduce the number of families to help reduce the per item cost.

The PEP-II magnets were made with aluminum conductor, which necessitates a separate cooling system. The use of copper conductor will be investigated to lower operating costs and to simplify the cooling water system needed for JLEIC. Preliminary power requirements have been generated for all of the magnets in the table based on the standard PEP-II design with aluminum conductor.

9.2.1.3 Sextupoles The sextupole requirements are listed in Table 9.9. These are all located in the machine arcs. There are enough excess PEP-II sextupole magnets available to satisfy the 0.25 m long sextupoles. To meet the 302 T/m^2 requirement they will be run at about 17% saturation. These sextupoles can just meet a 12 GeV requirement but with over 30% saturation. To meet the higher gradient design a new sextupole will be designed and manufactured with a ∼430 T/m^2 gradient. This is a similar gradient to the ones installed in the Super KEKB main ring [11].

Table 9.8: Quadrupole Requirements for the Electron Collider

Family	**Name**	**Count** [#]	**Effective Length** [m]	**Max Gradient** [T/m]	**Notes**
1	QSRM201	8	0.15	12.6	
3.a	QSBCC06H	132	0.28	16.6	LT 18 T/m
10.a	QAEL2CHC7	82	0.73	17.3	LT 18 T/m
5.a	QDS02	222	0.56	17.6	LT 18 T/m
4	QSRMT408	2	0.39	17.8	
14	QSRDC03	8	1.9	17.9	
6	QSRM306_H	8	0.6	18.3	
13	QSRDC02	32	1.4	18.9	
9	QSRM30S	16	0.7	19.0	
8	QSRM204_H	8	0.68	19.8	
7	QSRM207	8	0.66	21.1	
12	QAEL2CHC4	3	1.3	24.7	
11	QSRMT406	4	0.9	26.2	
2	QSRMT405	2	0.22	26.7	
5.b	QDS2SB03	8	0.56	27.5	Between 21.1 and 27.5 T/m
10.b	QAEL2CHC6	17	0.73	35.2	Between 19.9 and 35.2 T/m
3.b	QSBCC207H	36	0.28	35.4	Between 19.1 and 35.4 T/m
	Total	596			

Table 9.9: Sextupole Requirements for the Electron Collider

Family	**Name**	**Count** [#]	**Effective Length** [m]	**Max Gradient** [T/m^2]
1	SXTARCR01	80	0.25	302.0
2	SXTARCL01	80	0.25	650.0

9.2.1.4 Correctors There will be 431 corrector dipoles required in the electron collider. The exact requirements for the correctors are still to be determined. Beamline space (0.3 m) has been reserved for each installation. The designs needed will be similar to those used in the PEP-II machine.

9.2.2 Additional normal magnets in JLEIC

9.2.2.1 Transport line from CEBAF to JLEIC The transfer line design is described in Section 4.2. The transfer line has been designed based on reusing the PEP-II dipoles and quadrupoles and so no new magnets will be needed. Reusing the PEP-II dipoles was evaluated at the same time the PEP-II quadrupoles were considered and found to be acceptable [10].

9.2.2.2 Miscellaneous normal magnets Other normal magnets are needed in various locations throughout the JLEIC complex. All of these magnets are well within conventional magnet designs.

9.3 Interaction Region Magnets

9.3.1 Design Summary

A preliminary design is complete for all the quadrupole, skew quadrupole, correctors, solenoid and higher order multipole magnets. Most of these magnets are only optimized to the first order and still need further investigation. The maximum peak field in the coils before optimizing is 11.5 T, which is comparable to some of the LARP high gradient quadrupole magnets. The bore aperture of this magnet is bigger than the LARP magnet, but preliminary stress analysis shows that the peak stresses are not too high compare to LARP magnet [12]. The design summary for all the magnets is given in Tables 9.10 and 9.11 The higher order multipole magnets are not included in these tables, as the requirements for these magnets are still being finalized.

Table 9.10: Design Summary of Ion Beam Quadrupole and Skew Quadrupole Magnets

		Requirements					**Design**				
Magnet location	Magnet Type	Magnet Strength (T, T/m, T/m^2)	Magnetic length (m)	Good field region radius	New Inner Radius (cm)	Outer radius (cm)	Inner radius (mm)	Coil inner radius (mm)	Coil width in radial direction (mm)	Coil outer radius (mm)	Peak field from VF (T)
Interaction region Ion (IR)	Quadrupole QFFB3_US	-116	1	3 cm	4	12	40	45.0	18	63.0	8.93
	QFFUS03S***	-0.99	0.1		4	12		67.0	2	69.0	0.22
	Quadrupole QFFB2_US*	149	1.5	3 cm	4	12	40	45.0	30	75.0	8.0
	QFFUS025***	0.35	0.1		4	12		77.0	2	79.0	0.2
	Quadrupole QFFB1_US	-141	1.2	2 cm	3	10	30	34.5	18	52.5	7.9
	QFFUS01S***	-1.2	0.1		3	10		57.0	2	59.0	0.24
	QFFDS01S	8.6	0.1		8.5	17.1	85	90.8	10	100.8	1.6
	Quadrupole QFFB1**	-88	1.2	4 cm	8.5	17.1	85	90.8	43.6	134.4	11.5
	QFFDS02S***	-3.7	0.1		12.6	24.7	126	133.4	10.0	143.4	1.8
	Quadrupole QFFB2**	51	2.4	4 cm	12.6	24.7	126	133.4	45.0	178.4	10.3
	QFFDS22S***	-5.5	0.1		12.6	24.7	126	133.4	10.0	143.4	1.8
	Quadrupole QFFB3	-35	1.2	4 cm	14.8	26.7	148	155.0	38.0	193.0	8.5
	QFFDS03S***	4	0.1		14.8	26.7	148	155	10	165.0	1.84

* First order electromagnetic optimization done and optimized design presented here.

** First order electromagnetic optimization done and optimized design presented in separate section.
Magnet interaction done without optimized design.

*** Peak field values are for skew quad alone; this value is higher when operated with main quad.

9.3.2 Lattice and Magnet Requirements

In the interaction region there are the following magnets:

- Dipole: These are part of the detector and described in the detector section.
- Quadrupoles: 6 main quadrupole magnets in the electron ring and 6 in the ion ring.
- Skew Quadrupoles: electron ring skew-quadrupoles are combined with the main quadrupole, in the ion ring upstream skew quadrupole will be nested on top of main quadrupoles, but the downstream skew-quadrupoles will be independent.
- Higher Order Multipole Magnets: there will be some higher order multipole magnets, number of these magnets is not yet final, but these will have sextupole, octupole and decapole magnets

Table 9.11: Design Summary of Remainder of IR Magnets

		Requirements					Design				
Magnet Location	Magnet Type	Magnet Strength (T, T/m, T/m^2)	Magnetic length (m)	Good field region radius	New Inner Radius (cm)	Outer radius (cm)	Inner radius (mm)	Coil inner radius (mm)	Coil width in radial direction (mm)	Coil outer radius (mm)	Peak field from VF (T)
Interaction Region Electron (IR)	Common Quad Design based on new requirement January 2018, combined with skew Quads	**Quad** 45** (varies from 13.63 to 44.78)	0.6	3.2	4.5	8	45	49.5	10	59.5	3.51
		Skew-Quad* 9.5** (varies from 1.97 to 9.3)	0.6	3.2	4.5	8	45	61.5	3.25	64.8	1.248
Electron IR	Solenoid AASOLEUS	6	1.2		4		40	60	20	80.0	6
	Solenoid AASOLEDS	6	1.2		4		40	60	20	80.0	6
ION-IR	Solenoid AASOLEUS	6	1.2		4		40	60	20	80.0	6
	Solenoid AASOLEDS	3.6	2		17		170	190	12	202.0	3.614
Corrector	IPUSCORR1	-0.14 B_y -0.95 B_x	.2					34.5	9	43.5	3.06 in X coil
	IPUSCORR2	0.15 B_y 1.55 B_x	.2					50	3	53	1.36 in Y coil (both coils on)

* First order electromagnetic optimization done and optimized design presented here.

** First order electromagnetic optimization done and optimized design presented in separate section. Magnet interaction done without optimized design.

*** Peak field values are for skew quad alone; this value is higher when operated with main quad.

- Corrector Magnets
- Solenoid Magnet: there are 4 solenoid magnets in the IR region, 3 of these will be identical magnets and 4th one has a larger bore

The physics requirements of these magnets are given in Tables 9.12 and 9.13.

9.3.2.1 Design Tools Preliminary electromagnetic design is complete for all the IR region magnets. OPERA simulation software from Cobham is used for all electromagnetic simulations. ANSYS Maxwell is used to calculate the electromagnetic forces in the coils and ANSYS stress solver is used for preliminary stress analysis for one of the magnets. OPERA simulation software has the capability of calculation the field using Biot-Savart's law for the coil only model; therefore, results are very accurate and quick when there is no other material included in the model. ANSYS Maxwell also has the electromagnetic simulation capability, but results are always mesh dependent, therefore, wherever ANSYS Maxwell is used mesh size is finalized while comparing the results with OPERA and that mesh size is used for further analysis in ANSYS Maxwell and ANSYS Stress module. OPERA from Cobham, ANSYS Maxwell and ANSYS are the main software used so far for all the design work. OPERA optimizer module and ROXIE (the optimization tool from CERN) will be used for further optimizing the coil geometry.

9.3.3 Quadrupoles and Skew Quadrupoles

9.3.3.1 Quadrupoles Interaction Region (IR) Quadrupoles: There are 6 main quadrupoles in the Ion ring and 6 main quadrupoles in the electron ring. The layout of the IR region and position of these quadrupoles is show in Figure 9.10. One of the main concerns in the IR region is spacing between the magnets and spacing between the two beam lines. Due to the close proximity of these magnets, there is strong interaction between magnets in one beamline and stray field from the other beamline. This effect has been studied for certain magnets.

Electron Beam IR Quadrupoles: The electron beam has 6 main quadrupoles, all these quadrupoles have same magnetic length but need different gradients. Required gradients vary from 13.7 T/m to

Table 9.12: Specifications for Ion Beam Quadrupole and Skew Quadrupole Magnets

		Requirements				
Magnet location	Magnet Type	Magnet Strength (T, T/m, T/m^2)	Magnetic length (m)	Good field region radius	New Inner Radius (cm)	Outer radius (cm)
Interaction region Ion (IR)	Quadrupole QFFB3_US	-116	1	3 cm	4	12
	QFFUS03S	-0.99	0.1		4	12
	Quadrupole QFFB2_US	149	1.5	3 cm	4	12
	QFFUS025	0.35	0.1		4	12
	Quadrupole QFFB1_US	-141	1.2	2 cm	3	10
	QFFUS01S	-1.2	0.1		3	10
	QFFDS01S	8.6	0.1		8.5	17.1
	Quadrupole QFFB1	-88	1.2	4 cm	8.5	17.1
	QFFDS02S	-3.7	0.1		12.6	24.7
	Quadrupole QFFB2	51	2.4	4 cm	12.6	24.7
	QFFDS22S	-5.5	0.1		12.6	24.7
	Quadrupole QFFB3	-35	1.2	4 cm	14.8	26.7
	QFFDS03S	4	0.1		14.8	26.7

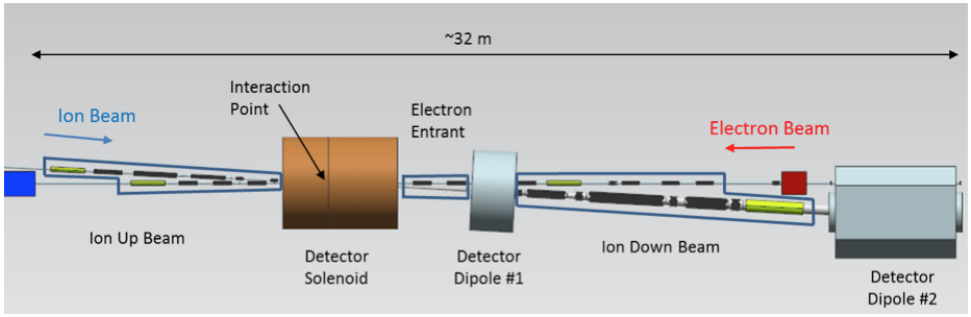

Figure 9.10: Locations of the main quadrupoles and regions in the interaction region.

44.8 T/m for electron energies of 10 GeV. All these quadrupoles uses the same coil design, operate at different current for the required gradient, and are capable of supporting the higher gradients required for 12 GeV operation. The coil layout for this magnet is shown in Figure 9.11. The peak field in the coil is approximately 3.5 T (shown in Figure 9.12). The coils will either be operated at about 600 A of current and will use standard MRI NbTi conductor (e.g. 1.625 mm × 1 mm rectangular conductor) or at about 4000 A of current and will use 9.73 mm × 1.2 mm Rutherford cable. All the electron beam quadrupoles will be operated at 4.5–4.7 K. The field gradient along

Table 9.13: Specifications of Remainder of IR Magnets

		Requirements				
Magnet Location	Magnet Type	Magnet Strength (T, T/m, T/m^2)	Magnetic length (m)	Good field region radius	New Inner Radius (cm)	Outer radius (cm)
Interaction Region Electron (IR)	Common Quad Design based on new requirement January 2018, combined with skew Quads	**Quad 45** (varies from 13.63 to 44.78)	0.6	3.2	4.5	8
		Skew-Quad 9.5 (varies from 1.97 to 9.3)	0.6	3.2	4.5	8
Electron IR	Solenoid AASOLEUS	6	1.2		4	
	Solenoid AASOLEDS	6	1.2		4	
ION-IR	Solenoid AASOLEUS	6	1.2		4	
	Solenoid AASOLEDS	3.6	2		17	
Corrector	IPUSCORR1	-0.14 B_y -0.95 B_x	.2			
	IPUSCORR2	0.15 B_y 1.55 B_x	.2			

the magnet axis is shown in Figure 9.13. The calculated effective length of the magnet is 0.6 m. These quadrupoles are not fully optimized yet; also we have to look at the mechanical analysis of these magnets.

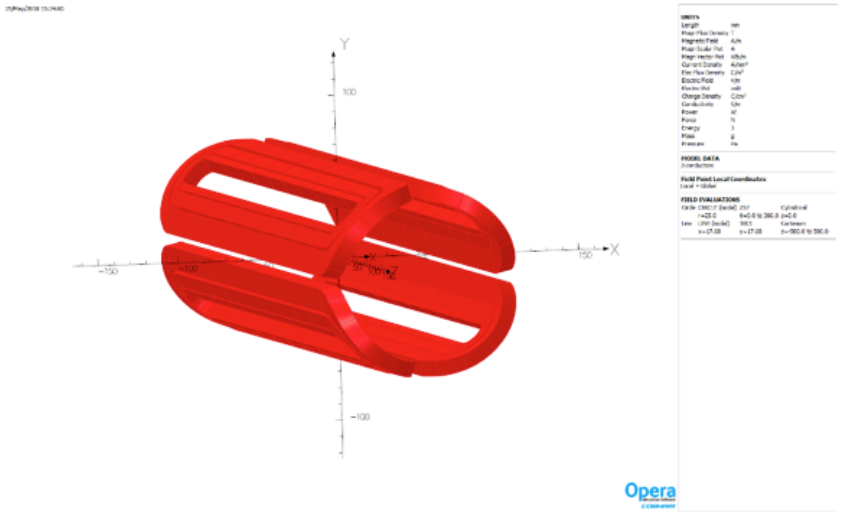

Figure 9.11: Coil layout for electron beam main quadrupole.

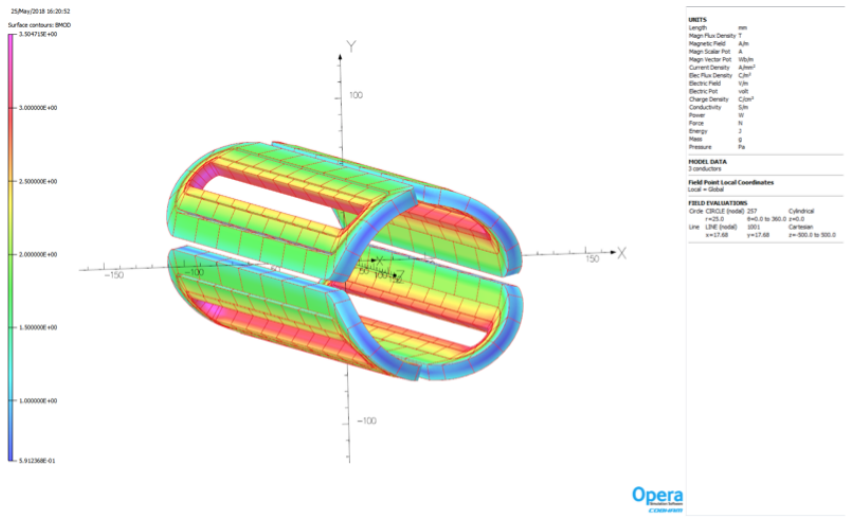

Figure 9.12: Coil field for electron beam main quadrupole.

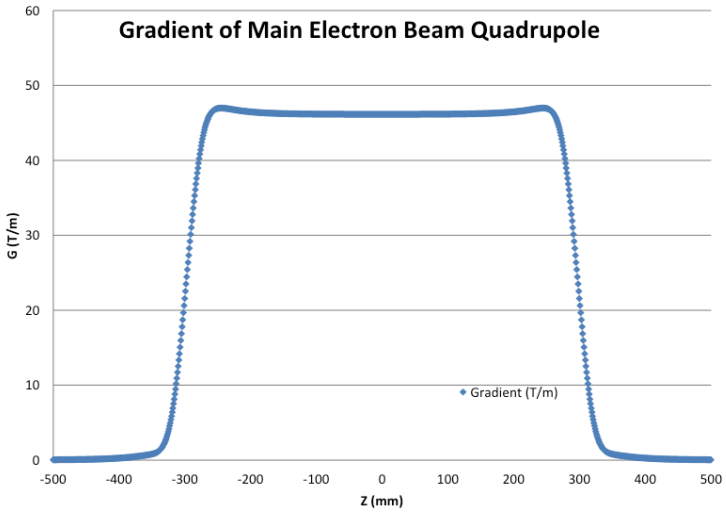

Figure 9.13: Gradient along magnet axis for electron beam main quadrupole.

Ion Beam IR Quadrupoles: The ion beam has 6 main quadrupoles, 3 upstream and 3 downstream. The upstream quadrupole has relatively smaller aperture compare to downstream quadrupoles, but all the upstream quadrupole are stronger than the downstream ones. All these quadrupole have different magnetic lengths and need different gradients, the required gradient varies from 35 T/m to 149 T/m.

The coil field for all the Ion beam IR quadrupoles is relatively high, all these magnets will use Nb_3Sn conductor and will be operated at 4.5 K. The conductor is not fully designed for these magnets, but it will be stranded Nb_3Sn cable with 20–30 strands per cable using 0.7 mm strands. The detailed conductor stability calculations will be done after further optimization of the coil cross section. All of these magnets will be operated between 5–8 kA of current. This Nb_3Sn is also being used for LARP magnets, so it is well established and well proven conductor.

All the upstream quadrupoles have a good field radius of 30 mm and the required beam aperture is 40 mm. All the magnets will have cold bore, therefore coil inner radius is taken as 45 mm. The middle quadrupole in the upstream side QFFB2_US needs the highest gradient of 149 T/m. This coil design is optimized to the first order but not fully optimized yet. The coil layout for this magnet is shown in Figure 9.14. The peak field in the coil is approximately 8 T (shown in Figure 9.15). The field gradient along the magnet axis is shown in Figure 9.16.

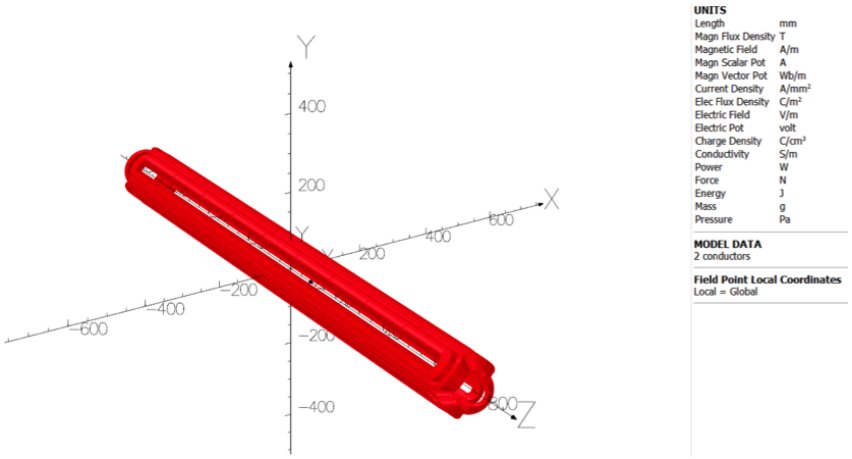

Figure 9.14: Coil layout for ion beam upstream middle quadrupole.

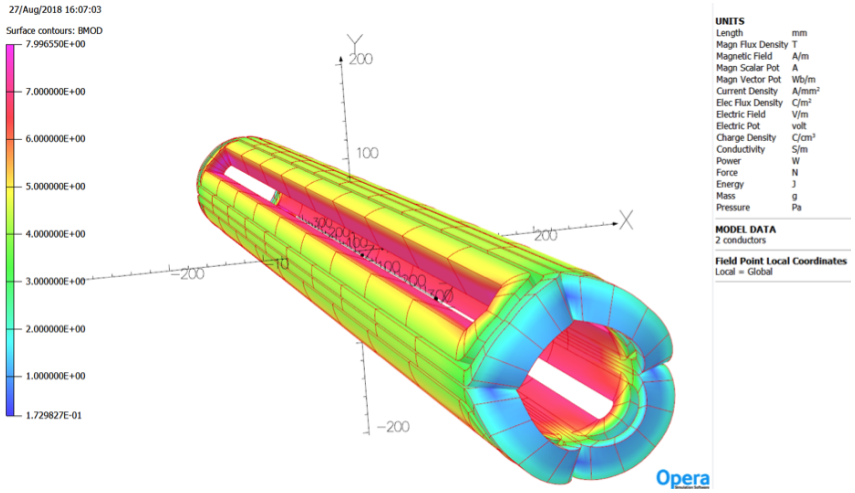

Figure 9.15: Coil field for ion beam upstream middle quadrupole.

The first quadrupole in the downstream side QFFB1 needs the gradient of 88 T/m and the required beam aperture is 8.5 cm radius, the middle quadrupole QFFB2 needs the gradient of 51 T/m and has a beam aperture requirement of 12.6 cm radius. This coil design is optimized to the first order but not fully optimized yet. The coil layout for this magnet is shown in Figure 9.17. The peak field in the coil is approximately 10.3 T (shown in Figure 9.18). The field gradient along the magnet axis is shown in Figure 9.19.

Preliminary stress analysis is complete only for this magnet, as this has high gradient requirement and bigger aperture as well. ANSYS Maxwell is used to calculate the electromagnetic forces in

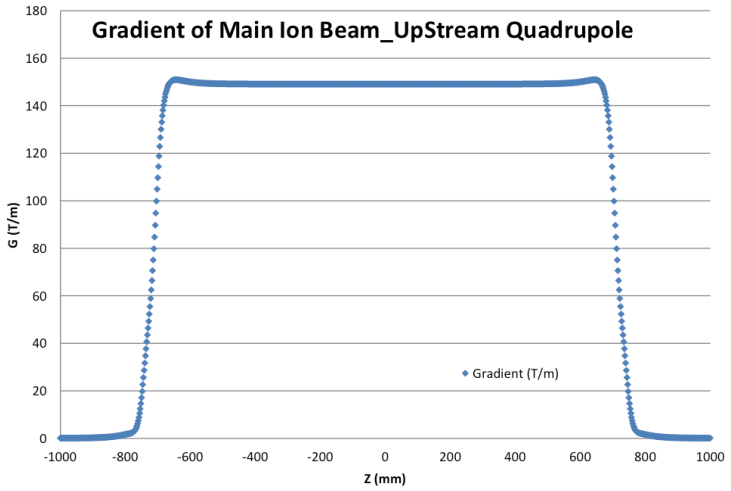

Figure 9.16: Gradient along magnet axis for ion beam upstream middle quadrupole.

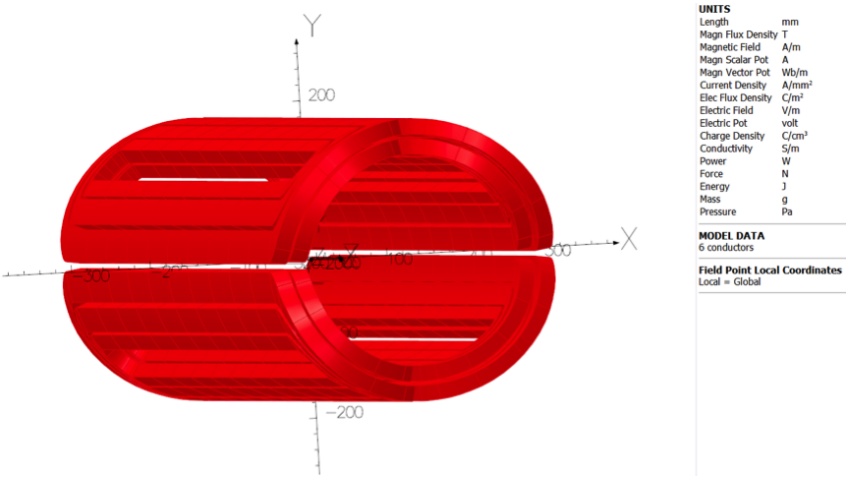

Figure 9.17: Coil layout for ion beam downstream middle quadrupole.

the coils, the results from ANSYS Maxwell are compared with OPERA. The 1/16th FEA model is shown in Figures 9.20 and 9.21 [13]. Lorentz forces in the coils are calculated using ANSYS Maxwell. For this preliminary analysis isotropic material properties are used, the Key 1 and Key 2 are assumed of Titanium and inner and outer keys are assumed to be made of G10 and Titanium. The von-Mises stress in coil is shown in Figure 9.22.

The maximum von-Mises stress is 212 MPa and max azimuthal (tangential) stress is ∼216 MPa; these are comparable to some of the other quadrupole magnet made and tested (ref LARP magnet). The coils ends have not yet been optimized and the final support structure and design of the magnet remains to be performed.

9.3.3.2 Skew Quadrupoles Electron ring skew-quadrupoles are combined with the main quadrupole, in the ion ring upstream skew quadrupole will be nested on top of main quadrupoles, but the downstream skew-quadrupoles will be independent. The skew quad nested over main ion beam quad is shown in Figure 9.23 (the highlighted coil is skew quad). The coil field in the skew quad

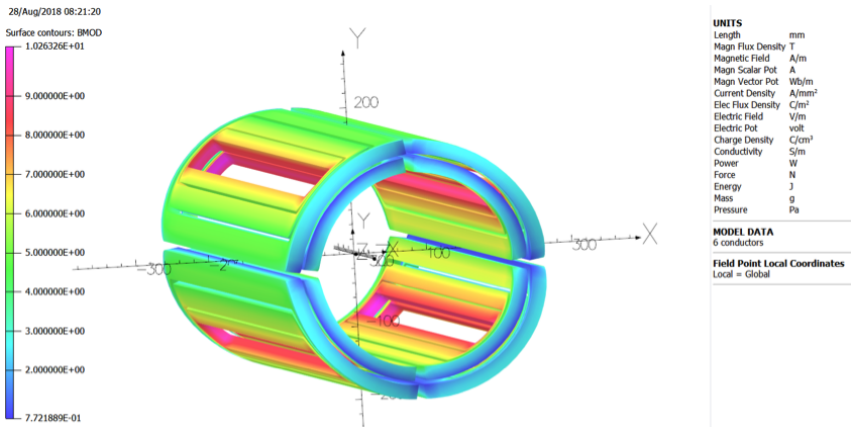

Figure 9.18: Coil field for ion beam downstream middle quadrupole.

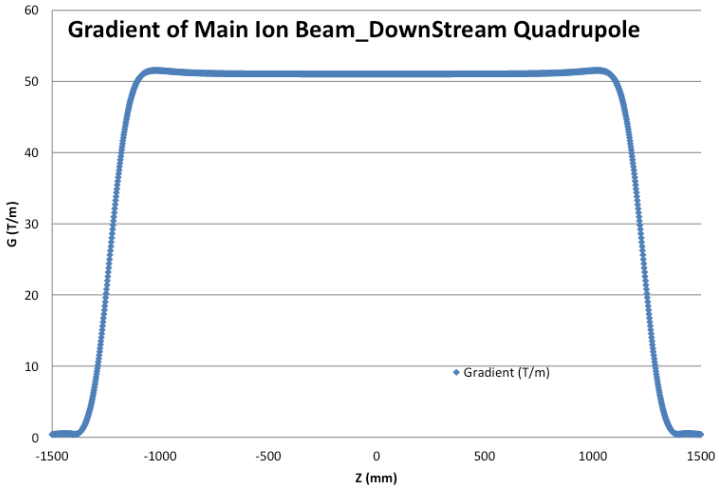

Figure 9.19: Gradient along magnet axis for ion downstream beam middle quadrupole.

in the presence of the main quad field is shown in Figure 9.24. The skew quad nested over main ion beam upstream middle quad is shown in Figure 9.25 (the highlighted coil is skew quad). The coil field in this skew quad in presence of main quad field is shown in Figure 9.26. Figure 9.26 also shows the coil field in ion beam downstream independent skew quad.

The coil field in all the skew quadrupoles is relatively low to moderate, all these magnets will use NbTi conductor and will be operated at 4.5 K. The conductor is not fully designed for these magnets, but either it will be standard MRI rectangular conductor or standard round conductor.

9.3.3.3 Higher Order Multipole Magnets There will be some higher order multipole magnets. The number of these magnets is not yet final, but may include sextupole, skew-sextupole, octupole, skew-octupole, decapole, skew-decapole, dodecapole and skew-dodecapole magnets. The position and strength of all the corrector magnets still needs to be finalized. If these correctors are nested over the skew quads, that will save some space in the lattice. Figure 9.28 shows the coil layout for the nested higher-order multipole correctors. The inside layer represent the skew-dodecapole and the outer most layer is skew-sextupole. These will be nested on the top of the skew-quad on

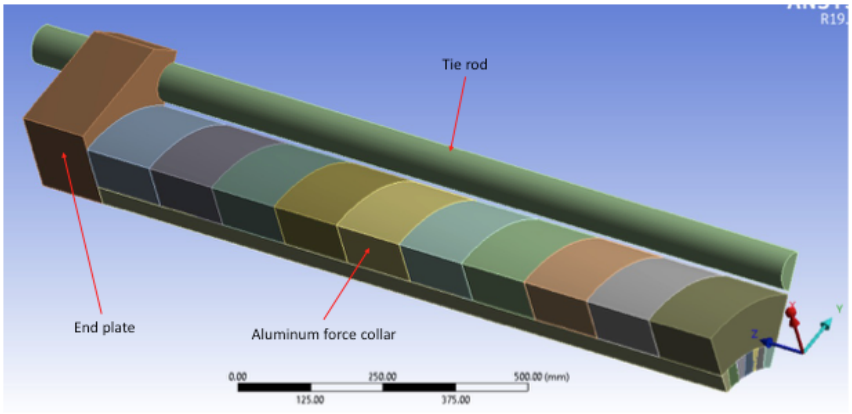

Figure 9.20: FEA model used for stress analysis.

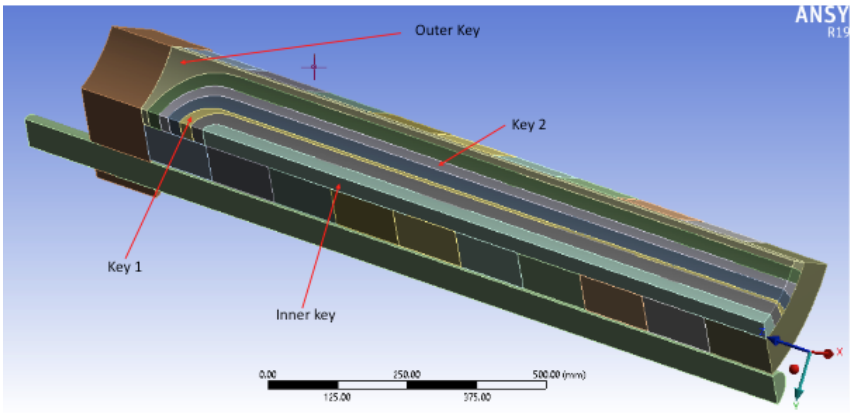

Figure 9.21: FEA model used for stress analysis.

ion beam upstream magnets. Because of the aperture size on the downstream magnets, a different design will be used for the higher order multipole magnets.

All these correctors will be wound using 0.3 mm (bare)/0.33 mm (insulated) standard conductor, operating around 120 A. All eight correctors will be energized independently. A detailed mechanical analysis and electromagnetic analysis will be done after finalizing the requirement specifications. There will be strong electromagnetic and cryogenic interaction between these magnets; therefore, detailed quench analysis will also be done.

9.3.4 Solenoid Magnets

There are 4 solenoid magnets in the IR region, 3 of these (2 for the electron beam and one for the upstream ion beam) will be identical magnets and 4th one (downstream ion beam) has slightly lower central field but large bore. The small bore solenoids have a central field of 6 T; the coil inner radius is 60 mm. The larger bore solenoid has a central field of 3.6 T and the coil inner radius is 190 mm. The coil field for both these solenoids is shown in Figures 9.29 and 9.30.

All these solenoids will be operated at 4.5 K and will be wound with NbTi conductor. The detail conductor design will be done after further optimization and after looking into the shielding

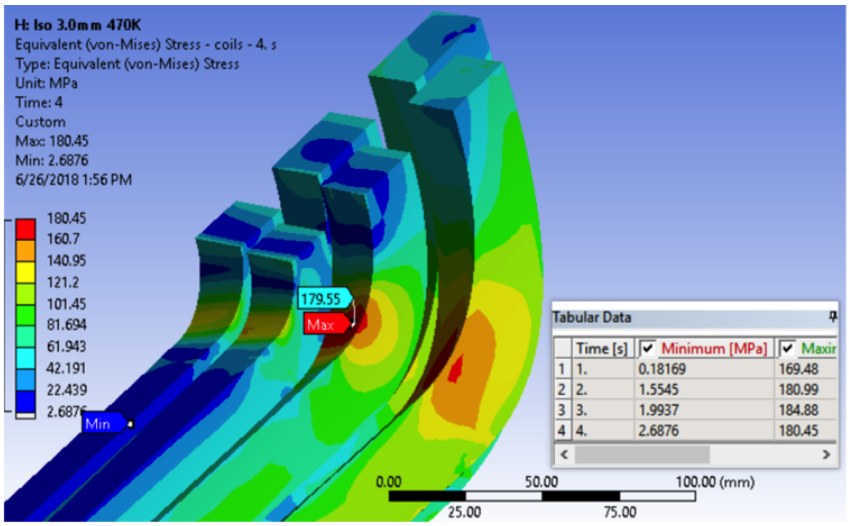

Figure 9.22: The von-Mises stress in the coils.

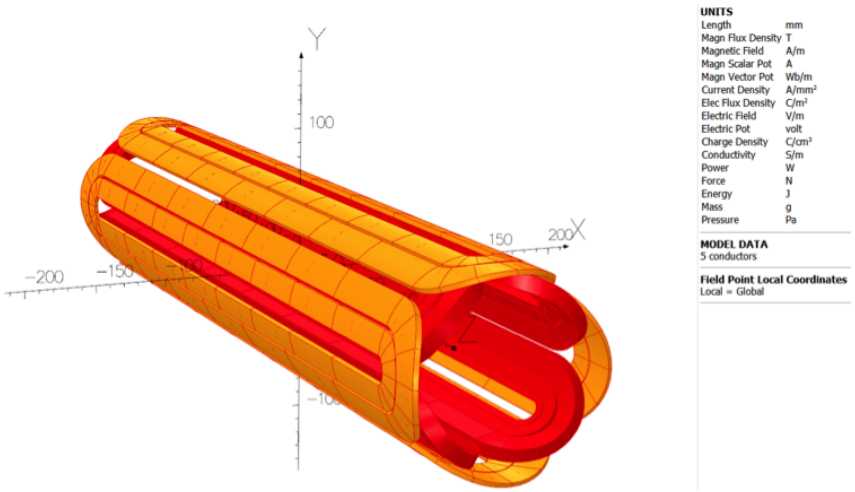

Figure 9.23: Skew quad nested with electron beam main quad.

requirements. The solenoid magnets will be operated at about 400 A of current and will use standard MRI NbTi conductor (e.g. 1.625 mm × 1 mm rectangular conductor).

9.3.5 Corrector Magnets

The corrector magnets IPUSCORR1 and IPUSCORR2 have slightly different field requirement, also IPUSCORR1 have both field components negative and IPUSCORR2 has both components positive. But for the sake of convenience, both these magnets will be identical and worse performing will be used as IPUSCORR1. The coil layout and coils field are shown in Figures 9.31 and 9.32 respectively.

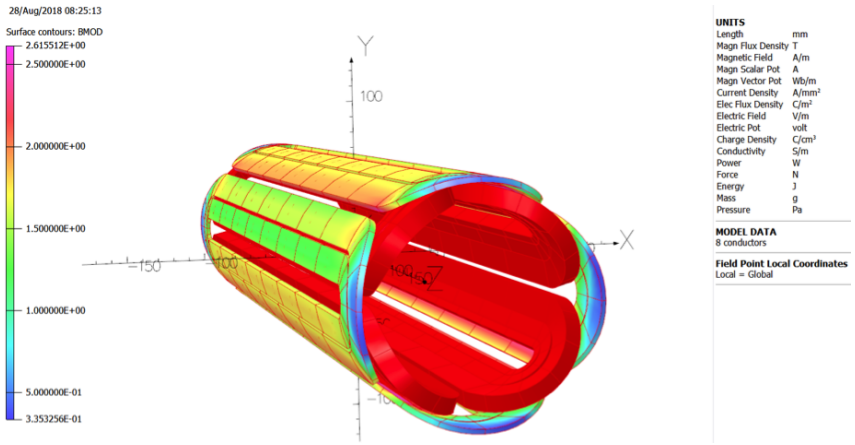

Figure 9.24: The coil field in electron skew quad in presence of electron main quad field.

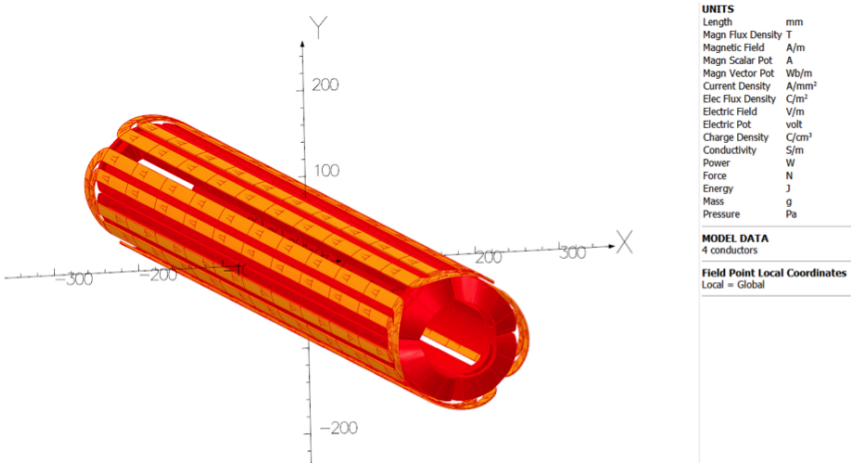

Figure 9.25: Skew quad nested with ion beam upstream middle quad.

9.3.6 Magnet Optimization

The design summary presented in Tables 9.10 and 9.11 show some of the magnets as optimized to first order for the electromagnetic design. The magnet QFFB2_US is further optimized and reported in this document. QFFB1, QFFB2 and the electron quads are optimized recently and those results are only reported in this section. The first order electromagnetic optimization has been performed to reduce the peak fields in the coils while maintaining the gradient and magnetic length.

The VF Opera optimizer is used for this electromagnetic optimization. The optimizer is integrated with Opera and uses an optimization algorithm that combines the deterministic and stochastic methods to solve single and multi-objective optimization problems. Figures 9.33 and 9.34 show the comparative peak field in the coils of QFFB1 and QFFB2 before and after optimization.

After electromagnetic optimization the peak field in the QFFB1 coil reduces from 11.5 T to 9.7 T and the peak field in QFFB2 reduces from 10.3 T to 8.8 T. A similar field reduction is expected for all other magnets after optimization.

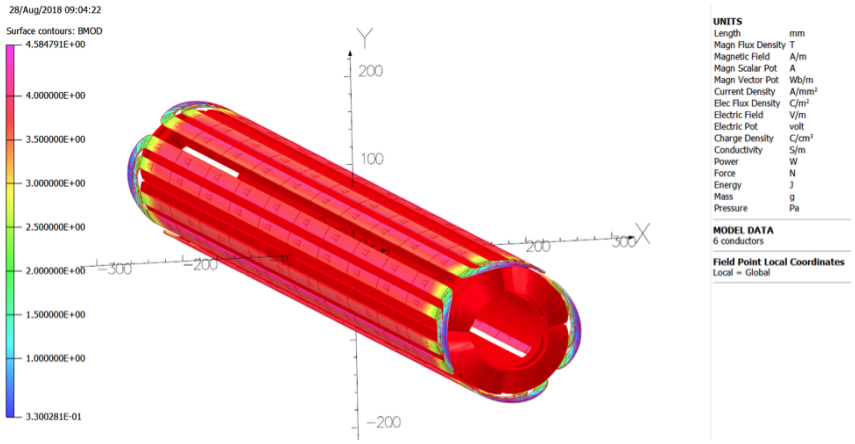

Figure 9.26: The coil field in skew quad ion beam upstream middle quad.

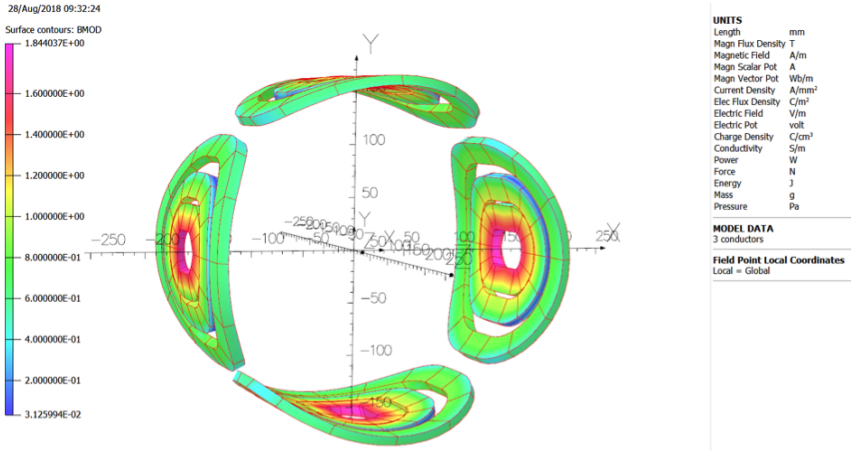

Figure 9.27: The coil field in ion beam downstream skew quad.

These magnets will be optimized further to reduce the higher order multipole components. The optimization is an iterative process. Optimization will change the magnet-magnet interaction and shielding requirements; all these calculation will be updated after further magnet optimization.

9.3.7 Magnet-Magnet Interaction and Shielding

There are more than 30 different magnets in the IR region; these magnets are very close to each other. These magnets will have some electromagnetic interaction with each other. To study the magnet-magnet interaction following sections are considered for the initial study:

1. QFFB2 with electron beamline
2. QFFUS1 with Ion beamline
3. QFFB1, QFFUS3 and EL SOL_ANTI_US
4. QFFDS2 and QFFB1_US

9.3.7.1 QFFB2 with Electron Beamline The QFFB2 magnet is very close to the electron beamline, especially at one end. The effect of this magnet on the electron beam is simulated using VF and

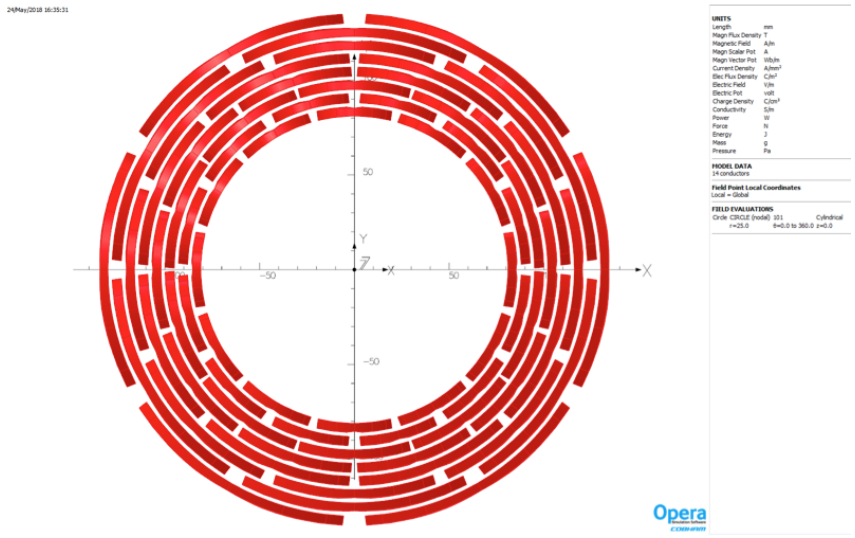

Figure 9.28: Cross-sectional view of the coil layout for multipole correctors.

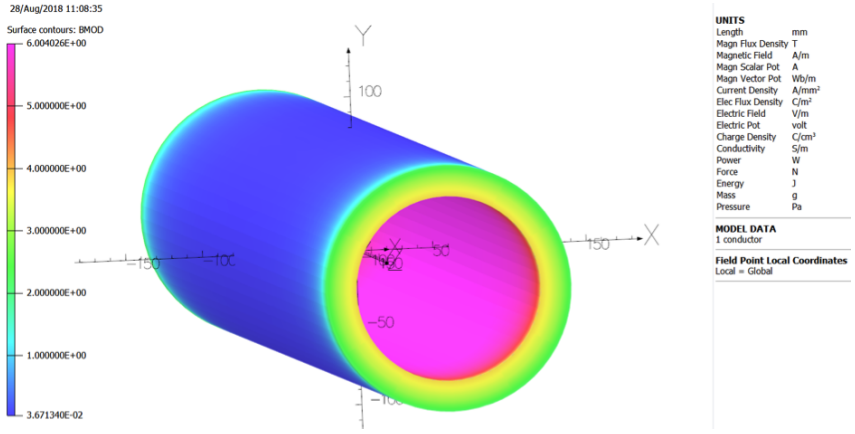

Figure 9.29: Coil field for the electron beam and upstream ion beam solenoid.

shown in Figure 9.35. This magnet is also simulated with the return yoke thicknesses of 200 mm and 250 mm around the magnet, Figure 9.36. The active shield is also tried to reduce the field on the electron beam axis, Figure 9.37. Note that neither the passive shielding nor active shield coil have been optimized yet and that work is ongoing. Figure 9.38 shows the field on the electron beam axis with and without shielding (various options) and Figure 9.39 shows the field on the electron beam axis without any shielding and with combination of active and passive shields.

The 200 mm thick return yoke reduces the field on the electron axis, it also increases the field at the magnet axis, therefore, the coil current and therefore peak field in the coils will be less than without return yoke. But 200 mm thick does not shield the field completely, two more simulations are done (i) with splitting the 200 mm shield in two sections with a 10 mm gap and (ii) increasing the yoke thickness to 250 mm (236 mm is minimum shield thickness calculated based on the design bound tool developed at JLab by R. Fair [14]. Increasing the yoke from 200 mm to 250 mm reduces the peak field on the electron beam from ∼800 G to ∼250 G. However even at 200 mm the resultant magnet structure may have interferences with the electron beamline and electron

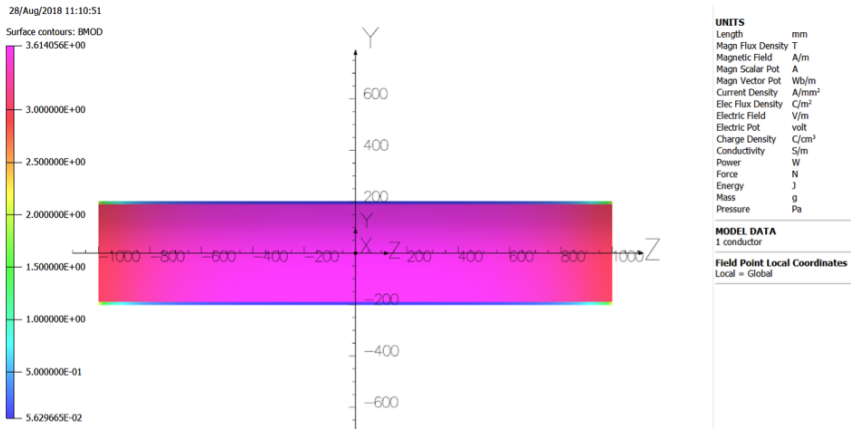

Figure 9.30: Coil field for the downstream ion beam solenoid.

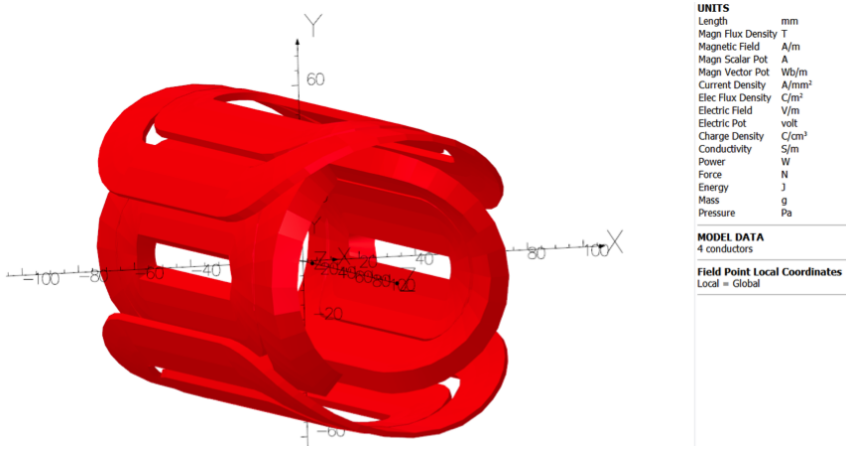

Figure 9.31: IR corrector magnet coil layout.

transport magnets, so further thickening of the yoke may not be practical. More detailed designs are just started to further explore the space available for the yokes.

The active shield coil is based on Brett Parker's shield coil philosophy [15] and reduces the radial dimensions of the magnet to values that avoids the interference with the electron line. The active shield reduces the main field of the coil as well (to about 90%), and to achieve the required gradient, the coil operating current will be increased. Then a combination of active and passive shield is also simulated (model shown in Figure 9.40), with results shown in Figure 9.38.

It is clear from the Figure 9.38, that various shielding techniques could be applied to shield the field at the electron beam. The combination of active and passive shield might give a better solution; this will be explored in detail and optimized later.

9.3.7.2 QFFUS1 with Ion Beamline The QFFUS1 magnet is very close to the ion beamline, especially at one end. The effect of this magnet on the ion beam is simulated using VF. A number of simulations are done for shielding the ion beam from QFFUS1:

1. Ion beam is wrapped with 5 mm shield on the beam tube
2. The vacuum vessel around the QFFUS1 is assumed to be made of mild steel

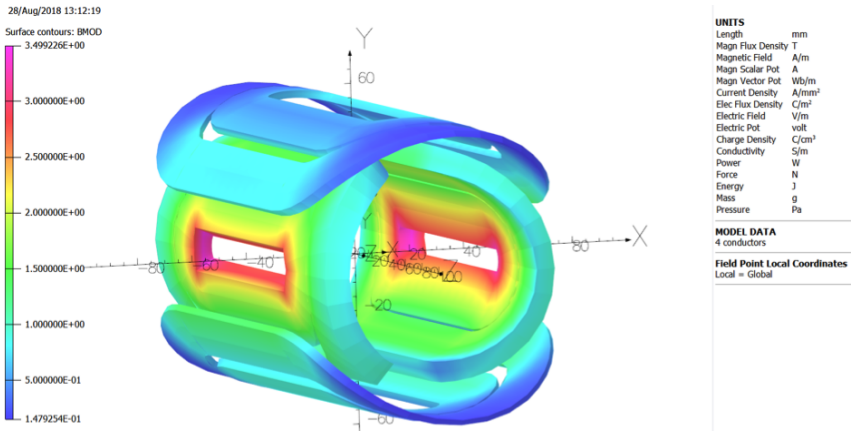

Figure 9.32: IR corrector magnet coil fields in corrector coils.

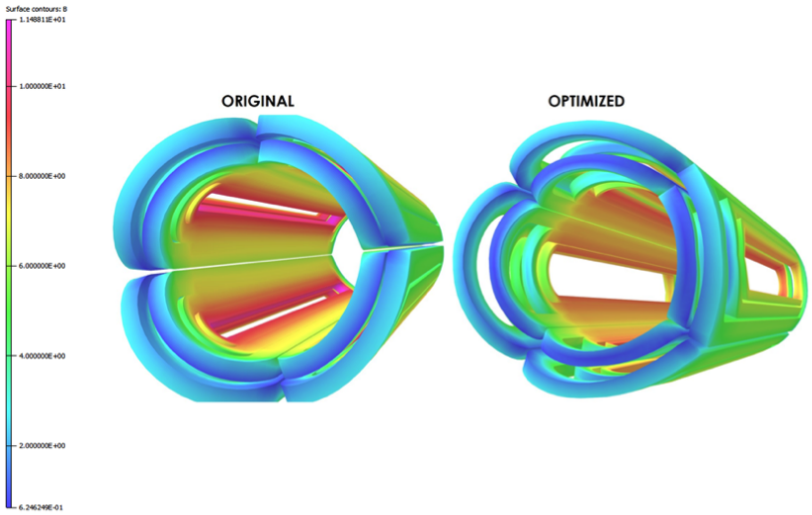

Figure 9.33: The peak coil field in QFFB1 before (left) and after (right) optimization.

3. Combination of the above two

Figure 9.41 shows the layout of this magnet in the lattice.

9.3.7.3 QFFDS2 and QFFB1_US The ion beam magnet QFFB1_US is very close to two of the magnets in the electron beam namely QFFDS2 and QFFDS3. The separation between QFFB1_US and QFFDS3 is bigger compare to the separation between QFFB1_US and QFFDS2, therefore, only the interaction between QFFB1_US and QFFDS2 is studied. Figure 9.43 shows the position of these magnets in the lattice.

To study the effect of these magnets on each other, following parameters are studied:

- Field from one magnet on the axis of the other magnet
- Field from one magnet on the good field radius of the other magnet
- Effect of one magnet on the gradient of the other magnet
- Effect on higher order multipoles

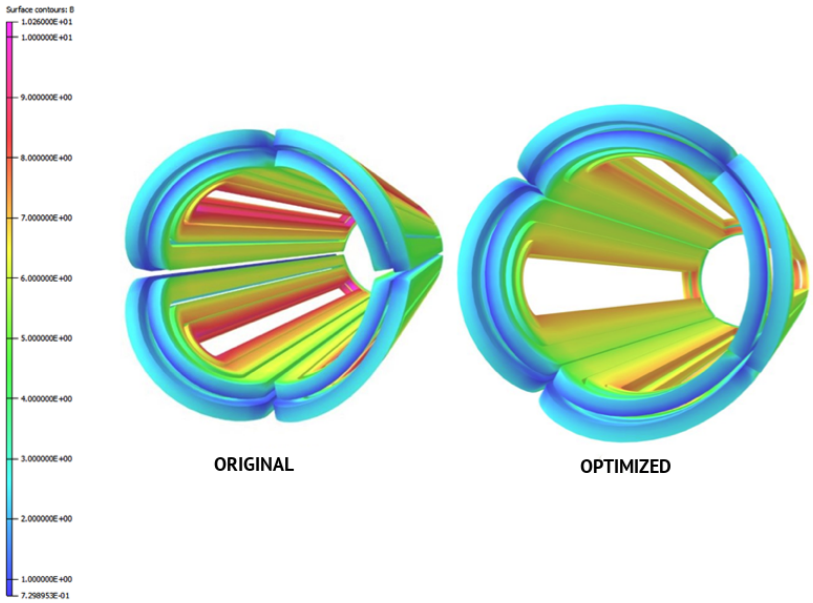

Figure 9.34: The peak coil field in QFFB2 before (left) and after (right) optimization.

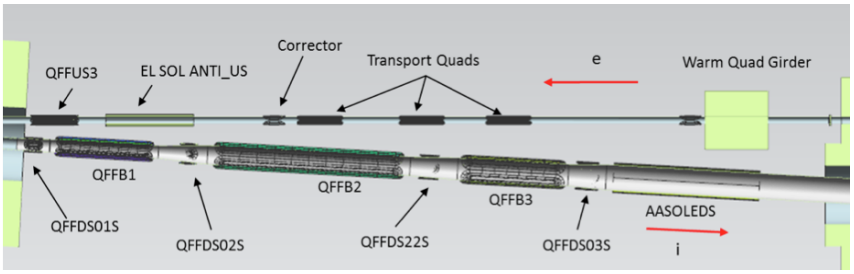

Figure 9.35: Position of QFFB2 with respect to the electron beam.

- Effect of passive shielding on the interaction between both the magnets

Both the magnets are simulated in VF first without any shielding and then using 20 mm thick shield around both the magnets. Figure 9.44 shows the coil layout in VF, and Figure 9.45 shows the coils and shield layout in VF.

9.3.7.4 Summary The magnets in the interaction region are very close to each other and they influence the field/gradient of other magnets. We have studied the effect of passive shield, active shield and a combination of passive and active shield. It is clear from the above studies that effect of a magnet on the other magnet will be nullified using passive/active/combination shields.

Another option for shielding could be using the superconducting shield; this option is being investigated under a SBIR proposal by a company "Particle Beam Lasers Inc." in collaboration with BNL. Jefferson Lab is following that research and will investigate the use of superconducting shields further.

Also still to be done is to look at the interaction between the detector magnets, solenoid and two dipoles, and the transport magnets described in this section.

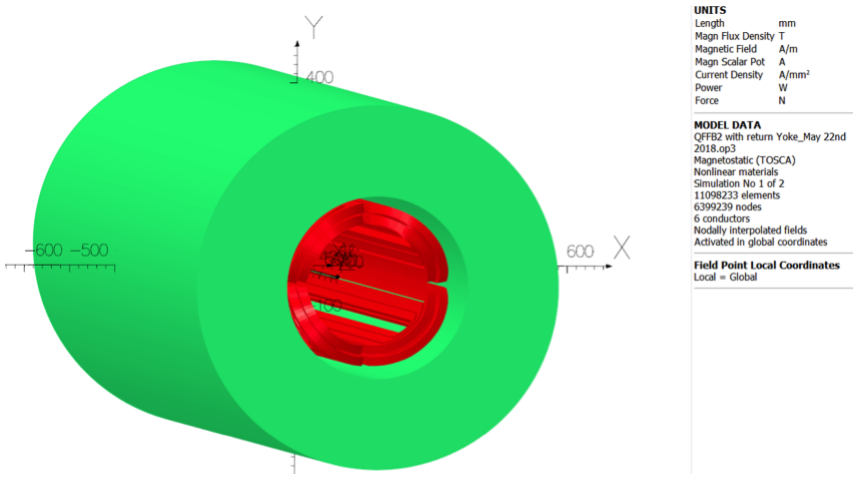

Figure 9.36: Coils and 200 mm thick return yoke for QFFB2.

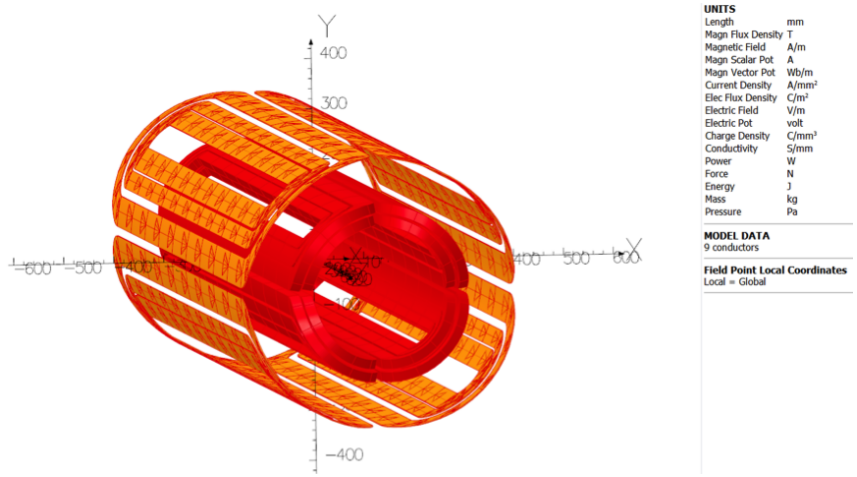

Figure 9.37: The main coil and active shield coils (highlighted) for QFFB2.

9.3.8 Cryostat Designs

9.3.8.1 Cryostat Overview The transport magnets in the IR region will be divided into three cryostats as shown in Figure 9.46. They are divided by the IR with the detector solenoid and the two detector dipole magnets in the ion beamline downstream of the IP ("ion down"). The whole area covers some 32 m. The two detector dipoles are described in Section 7.2 and the detector solenoid magnet is described in Section 7.3. The detector dipole #1 is a combined function magnet. In addition to the dipole, it also provides a quadrupole and two pairs of horizontal and vertical correctors for the Ion beam transport. The final design of the transport magnet cryostats will have to be closely coordinated with the detector elements in the area. This section describes the preliminary designs for those cryostats.

All of the magnets for both the ion and electron beamlines are based on cold bore designs. This is primarily to lower the field requirements on the ion beam quadrupoles. The magnets in the electron beamline could be either warm or cold bore. The cold bore designs reduce the radial space needed, an advantage as one moves closer to the IP.

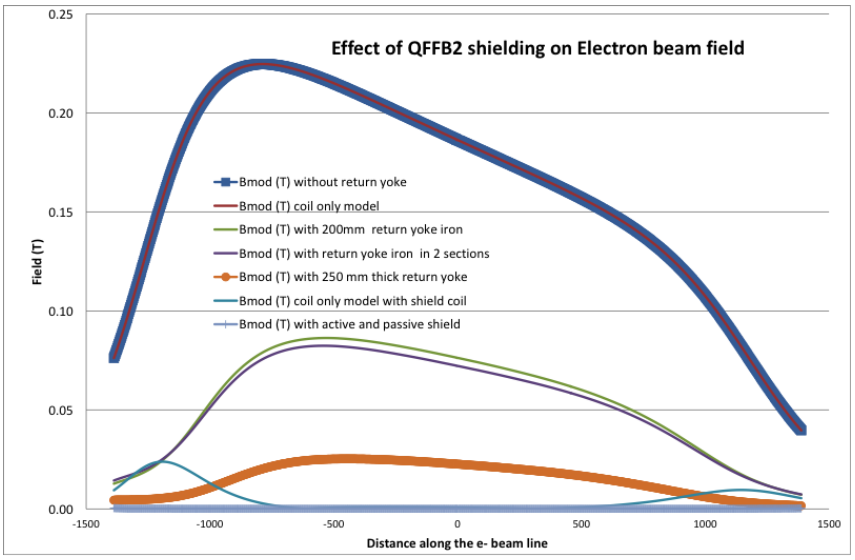

Figure 9.38: Field on the electron beam axis with and without QFFB2 shielding.

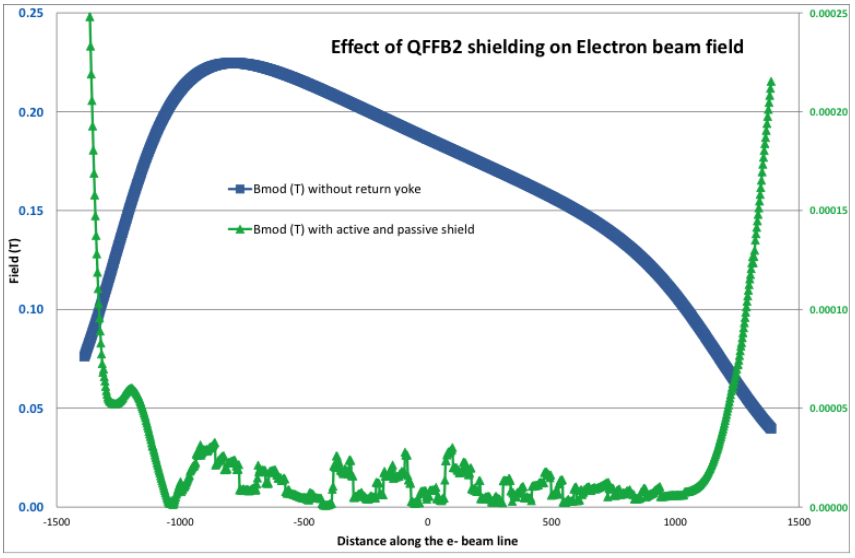

Figure 9.39: Field on the electron beam axis without QFFB2 shielding, with combination of active and passive shields.

The beamline vacuum in the IP chamber and through the two detector dipoles will be warm so that detectors will be put in close proximity to the chambers. The beamline vacuum in this area will not be segmented so that it will all have to be treated as cold bore sections. All of the vacuum pumping will be placed in the warm section at the ends of the cryostats. At the end of each cryostat, room has been reserved for a warm to cold transition to minimize the heat leak. There will also need to be room for an RF shielded bellows to facilitate installation and allow for the thermal contraction of the beamline. The vacuum beamlines and bellows will also have to be studied to insure there are no trapped modes that could lead to localized power being dissipated in the area.

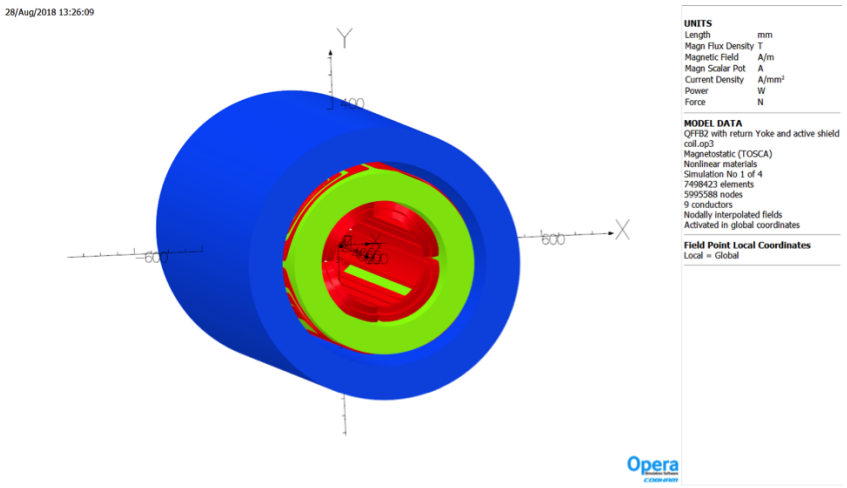

Figure 9.40: The model showing active and passive shields for quadrupole QFFB2.

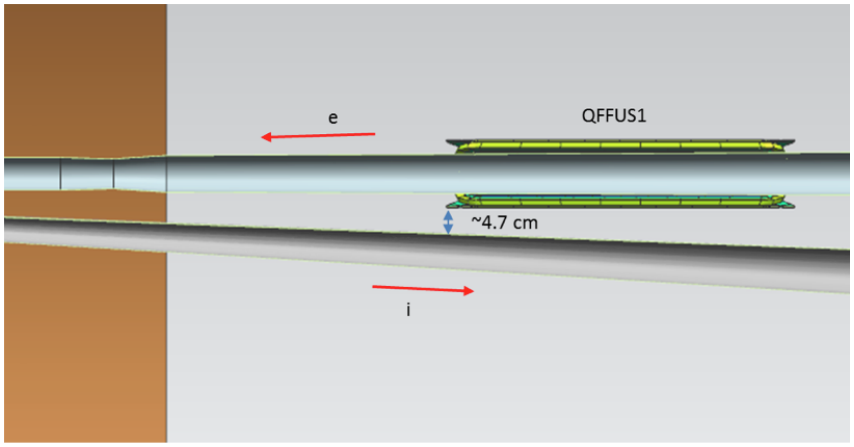

Figure 9.41: Position of QFFUS1 with respect to the ion beam.

9.3.8.2 Ion Up Beam Area with Principal Magnets The ion beamline upstream of the IP ("ion up") cryostat will be approximately 8.7 m long in the ion beamline, 5.9 m of the electron beamline and have a minimum of eighteen super conducting magnets, Figure 9.47. There are three quadrupoles and one solenoid magnet in each of the beamlines. A skew quad is also added around each of the main quadrupoles. There are also two horizontal/vertical corrector pairs just up beam of the interaction point. Multipole correctors are being studied for the ion beamline, but will not be needed in the electron beamline. The need for shielding coils is also being evaluated. That means there will be a minimum of eighteen magnets in this cryostat. As a point of reference, the Super KEKB IR cryostats have 25 and 30 superconducting magnets for the QCSL and QCSR respectively [16]. A single vacuum cryostat is required as there is no room to provide a warm to cold transition between the magnets. As such, there will be a single warm to cold transition at the inlet and exit of each beam line. Near the IR these transition will extend into the detector solenoid. The vacuum vessel will be tapered toward the interaction region to maximize the space for detectors around the cryostat (Figure 11362.02).

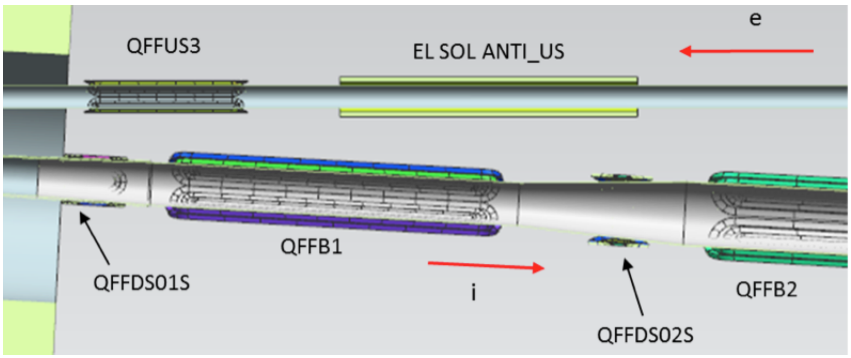

Figure 9.42: Position of QFFB1, QFFUS3, and EL SOL_ANTI_US in the lattice layout.

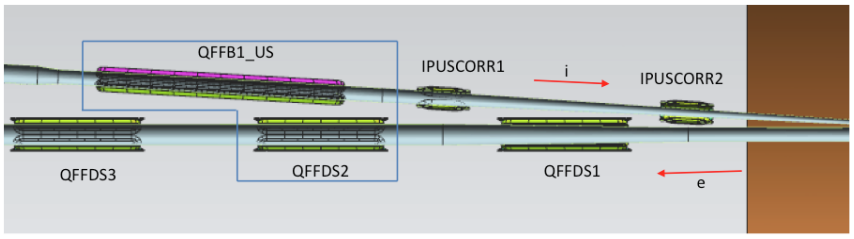

Figure 9.43: The positions of QFFB1_US and QFFDS2 magnets in the interaction region.

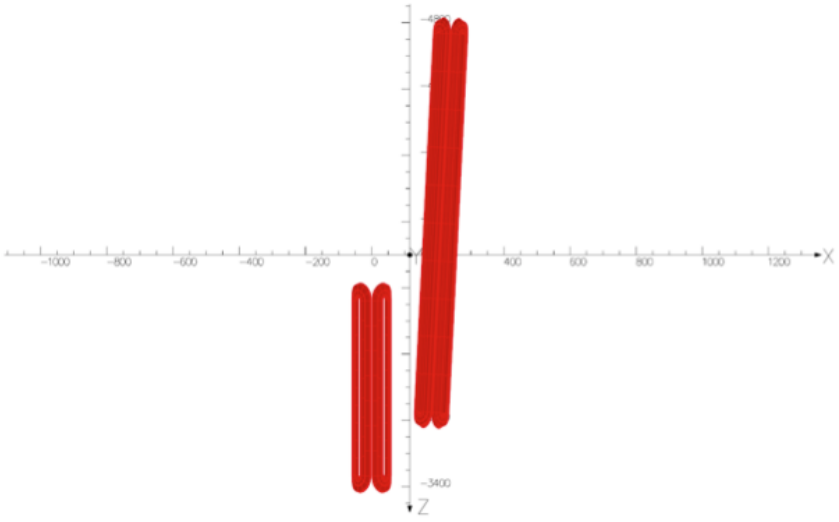

Figure 9.44: Coil layout in VF.

The two corrector magnets and three to four of the quad magnets nearest the IP will be housed in a single helium vessel capturing both beamlines. For the rest of the magnets there may be multiple helium vessels inside the cryostat if that will ease the assembly of the overall structure. The support structure will have to accommodate the cool down contraction and resist the magnet-to-magnet interaction in this area. The whole cryostat will also have to be supported against the fields from the detector solenoid. Both the cryostat and cold mass will have to be supported in at least three locations with a minimum of twelve typical support rods on the cold mass. A

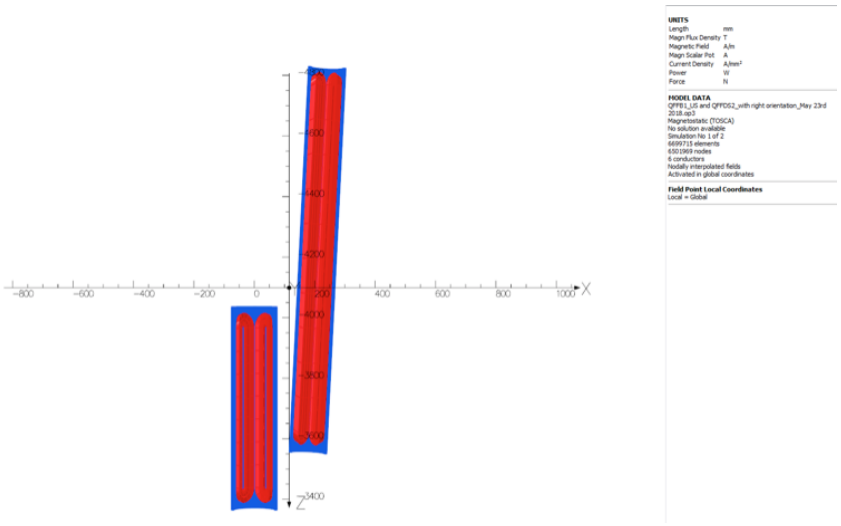

Figure 9.45: Coil and shield layout in VF.

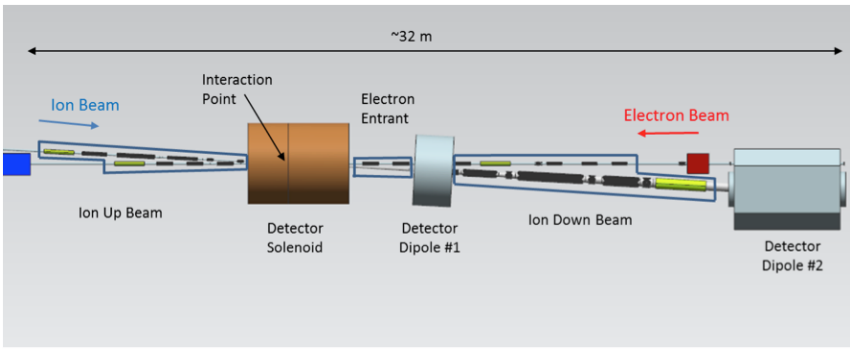

Figure 9.46: Overview of all elements in the IR area.

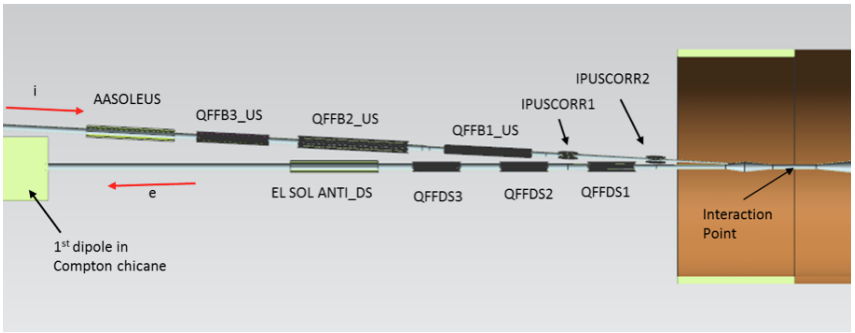

Figure 9.47: Ion up beam area showing the principal magnets.

thermal shield will be included inside of the vacuum vessel and surround the entire cold mass. The cryogenic feed and magnet lead can will be positioned away from the detector elements.

The worst-case estimated synchrotron radiation that will enter this cryostat from the up beam quads in the electron beamline is about 1 to 2 W, which is an acceptable heat load along the

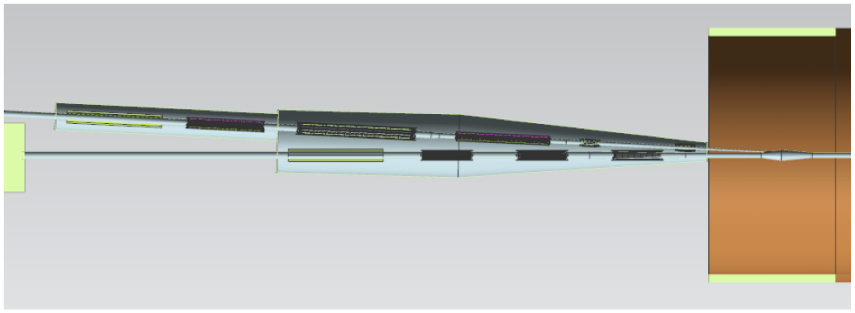

Figure 9.48: Ion up beam cryostat.

beamline [17]. This SR will be reduced by adding a down beam mask just up beam of the cryostat, but this introduces other problems so is not included in the baseline. The effect of the SR on the beam vacuum is currently being studied.

9.3.8.3 Electron Entrance Cryostat Between the detector solenoid and the first detector dipole magnet will be a small cryostat containing four superconducting magnets in the electron beamline and will be approximately 2.6 m long (Figure 9.49). The magnets include two quads with corresponding skew quads around them. The cryostat will be tapered near the IP to avoid interference with the ion vacuum beam line and to allow for the maximum acceptance angle for the detector elements (Figure 9.50). To avoid interference with the ion beam vacuum line, the vacuum vessel and thermal shield will centered eccentrically from the cold mass. The warm to cold transition will extend into the detector dipole on one end and stop just short of the detector solenoid on the other. The vacuum vessel may be made of normal iron to better shield the ion beamline from stray fields. The cryostat and magnets will have to be supported against the fringe fields from both the detector solenoid and dipole. Eight typical magnet support rods will be needed for the cold mass in two locations. The cryogenic feed can and leads will be routed to a location compatible with the detector.

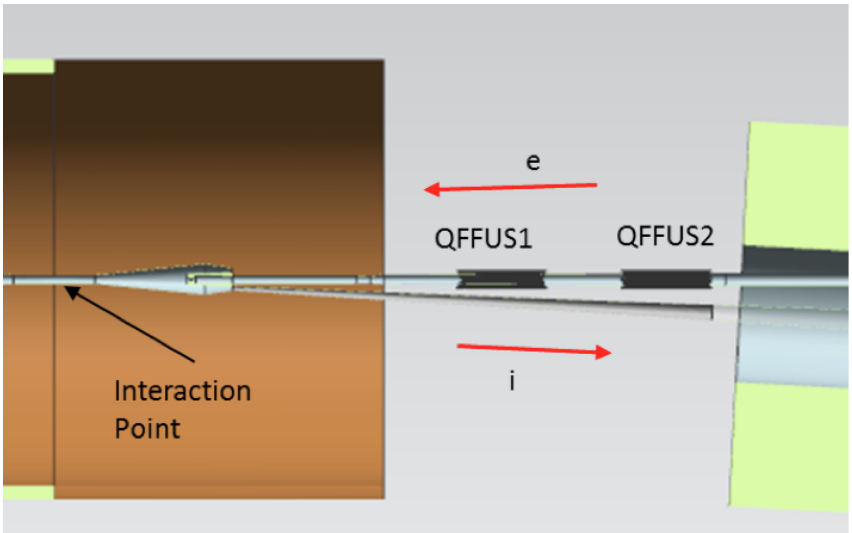

Figure 9.49: Ion up beam cryostat magnet on the electron beamline. A small taper may be included to localize the synchrotron radiation for cooling.

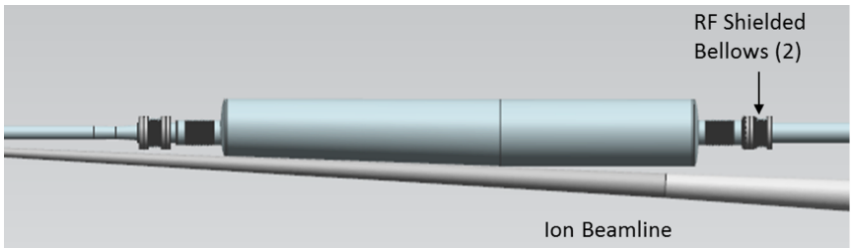

Figure 9.50: Ion up beam vacuum vessel showing taper to avoid the ion beamline.

A preliminary look at the synchrotron radiation from the final focusing quads in the electron line has been completed. No direct synchrotron radiation will impinge on the cold bore of the magnet beamline. Less than a watt will be distributed along the warm beam line from the cryostat to the detector vacuum chamber. A small taper is shown in the figure that may be used to concentrate this power into a single location as required. Backscattering of photons remains to be studied and some small amount of forward scattering may be possible that will contribute to the cryogenic heat load.

9.3.8.4 Ion Down Beam Cryostat The final cryostat for the beam transport will be located between the two detector dipoles. The ion beamline magnets are all large bore with little room between the coils and will be installed as one unit, 10.1 m long. This includes three quads, four skew quads, and a solenoid magnet. The electron beamline requires a single superconducting quad with skew quad around it and a solenoid. Also in the electron line between the dipoles are four additional quads and two correctors. These magnets could be normal magnets, but due to the proximity of the ion line, three of them will be made superconducting, as there is not radial room for the warm iron that would be required in the magnets. The quads will be the same design as the other quads in the electron line. One of the correctors will also be made superconducting. The electron and ion beamlines will be separately supported inside the single vacuum cryostat. The cold electron beam line will be ∼7.6 m in length and the ion line about 10.4 m. The warm to cold transitions from both lines will extend into the first detector dipole. Due to the length of the two separate lines, it is anticipated that a minimum of twelve typical supports will be needed for each line, twenty-four total. As the designs progress it may prove advantages to combine the two cold masses. A thermal shield will surround both cold masses. The total number of magnets is a least 15 magnets plus multiple correctors and shielding coils to be added as required.

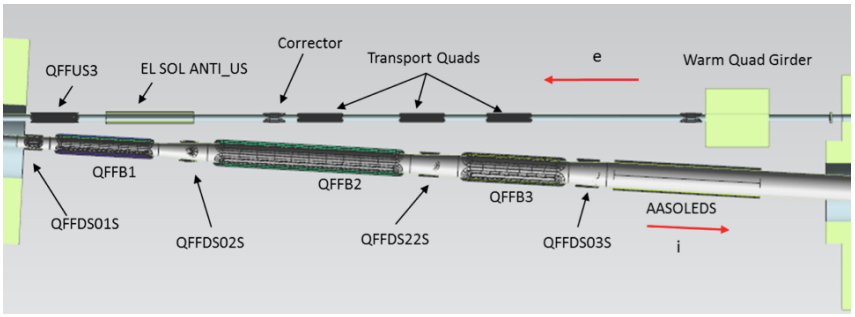

Figure 9.51: Ion down beam area showing the required magnets.

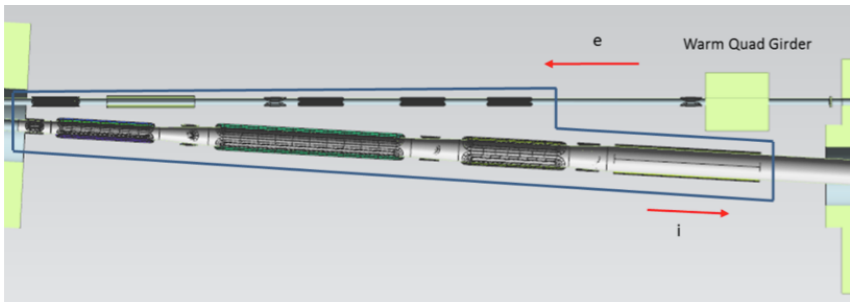

Figure 9.52: Preliminary design of the cryostat.

9.4 Power Supplies

The JLEIC magnet power systems will meet the requirements for currents, controls and safe operation for the electron collider ring, the ion collider ring, the booster ring, transfer line and special use magnets. Each of these subsystems is briefly described below.

9.4.1 Electron Collider Ring magnets

The power systems for the electron ring will be based on existing power supplies in the CEBAF machine. The requirements are divided into three general classes: normal conducting main magnet strings, individual trim and corrector magnets, and IR superconducting magnets.

Power systems for normal conducting dipole, quadrupole, and sextupole magnets will provide current for magnet "strings" wired in series. The string arrangements and buswork will be finalized once magnet design is complete. These will likely be strings in each arc of the figure 8, with one string for main dipoles, and separate strings and tuning shunts for the focusing and defocusing main quadrupole magnets, and focusing and defocusing sextupole buses. Typical protection schemes will be employed for these power systems.

The power systems for room temperature focusing and trim corrector magnets will be based on existing CEBAF style power supplies. The focusing and correction magnets will be powered in series, wherever possible, to reduce the total number of power supplies.

The superconducting temperature solenoids, quadrupoles and sextupoles for the interaction region of the electron ring will also be based on proven power and protection systems. The systems engineer for the magnets will have to integrate the powering scheme into their design.

Several power system parameters will be optimized once the magnet designs are underway. The optimizations for the room temperature magnets will include minimizing the power converter output ranges, determining the required magnetic field stability and configuring magnets in series. The superconducting magnet power systems will be optimized for peak power and having a control scheme common to the ion collider and booster rings.

The power systems for the warm magnets in the electron ring are considered to have low technical risk. The technology for power converters will be similar to existing CEBAF units or equivalent. Topologies for the power supply will be driven largely by peak power, stability and ripple requirements.

The power systems for the interaction region superconducting magnets are also considered to have low technical risk. The technology for power converters will be similar to existing CEBAF units or equivalent. The risks are mostly in the integration of the various electro-mechanical interfaces for typical superconducting magnet installations.

9.4.2 Ion Collider Ring (ICR) magnets

The power systems for the ion ring magnets will be based on superconducting magnet powering schemes already in use at Jefferson Lab or proven technology that exists for similar applications. The requirements are divided into two general classes: superconducting main and IR magnet buses, and individual trim and corrector magnets.

Power systems for superconducting dipole, quadrupole, and sextupole magnets will be configured to provide current for magnet "strings" wired in series. The string arrangements and buswork will be engineered in coordination with magnet design. As in the electron collider ring, these will likely be strings in each arc of the figure 8, with one string for main dipoles, and separate strings and tuning shunts for the focusing and defocusing main quadrupole magnets.

The power systems for focusing and trim corrector superconducting magnets will be based on already existing technology [18, 19]. The trim and correction magnets will be powered in series, wherever possible, to reduce the total number of power supplies.

Several power system parameters will be optimized once the magnet designs are underway. The superconducting magnet power systems will be optimized to minimize peak power, peak voltage during ramping, stored energy in strings, and the number of transitions needed for high temperature-to-superconducting temperature. The controls scheme between the ion collider ring and electron collider ring must be standardized for reliable operations. The magnetic field tuning requirements for the ion ring will have to be defined during machine design and will dictate the powering schemes for focusing and correction magnets.

Protection schemes for superconducting magnets will require detailed engineering effort once the magnet design is completed [20]. The superconducting magnet power busbar distribution will be carefully engineered to minimize risks and points of failure.

The power systems for the ion collider ring magnets are considered to have low technical risk. The risks are mostly in managing the integration of the large-scale electrical, mechanical, and cryogenic interfaces that arise in distributed superconducting magnet installations.

9.4.3 Booster Ring Magnets

The Booster ring magnet systems will consist of ramping power supplies providing power to superconducting magnets. The details of the magnet-powering scheme will be defined once the initial magnet design is completed.

The design of the Booster ring power systems are considered low-to-medium as a technical risk. The power systems for the booster will be challenging because of ramping and output current waveform requirements. The voltage slew rate required to achieve the Booster current ramp rates may require special power electronics components and converters. The effect of the Booster output power ramps on the incoming utility power grid will be evaluated and compensated. Magnet protections schemes will also be specialized to accommodate the ramping schemes.

The power conversion scheme will be achievable, as there are examples of similar powering schemes at many accelerators. The timing and coordination for dipoles, quadrupoles and correction magnet currents must be engineered to meet the stringent beam arrival and injection requirements. The timing systems for the power converter controls are part of the global timing systems being developed for JLEIC, as discussed in Section 9.11. Systems engineering including cryogenic connections for series magnets, mechanical packaging of busbar around the ring and protection systems will have to be well coordinated.

9.4.4 Transfer Line Magnets

Three transfer lines will be present in the JLEIC machine: the CEBAF to electron collider ring line, the ion linac to booster line, and the booster to ion collider ring line.

The power systems for the CEBAF to Electron Collider Ring will power main bus normal conducting dipoles, families of quadrupoles, and smaller individual trim and corrector magnets. The power supplies for this application will be based on existing CEBAF style power converters with a low technical risk.

The Ion Linac to Booster Ring magnets are normal conducting, and expected to have power converters similar to existing CEBAF units. These systems are similar to existing CEBAF units and have a low technical risk once the magnet designs are finalized.

The power systems for the Booster to Ion Collider transfer line magnets will be similar to the ones planned for the ion collider ring. The systems will be engineered to standardize the hardware as much as possible for ease of operations.

9.4.5 Other Magnet Power Systems

The Spin Rotator Magnets at the ends of the straight sections of the arcs will consist of superconducting solenoid magnets. The powering system for these magnets are envisaged to be like the IR region magnets in scope and technical requirements.

The DC cooler and ERL for the collider ring will operate magnets with fields lower than 1 T (Chapter 6, Table 6.3 and Table 6.4). Power supplies for these low field magnets are well understood and lie within the scope of the existing technologies for the electron or ion collider rings.

The DC cooler for the Booster Ring will require careful design, in concert with the requirements for the Booster performance. Timing and controls requirements will need design engineering effort, but is within the realm of existing technology.

9.4.6 Power Systems Interface

Power systems interfaces with the incoming AC grid power utilities and floor space requirements will be co-ordinated with facilities engineering and the project. The large power supplies will be water cooled to minimize floor space and meet efficiency requirements. The physical placement of power supplies, the utility grid power arrangements and cooling water requirements will be optimized as designs are underway.

9.5 Superconducting RF

9.5.1 Introduction

JLEIC requires a number of new SRF cavity designs for the ion collider ring, cooler ERL and booster and eventually for the electron ring. Existing and proposed high current colliders typically operate storage ring RF systems in the frequency range ∼350 MHz to 800 MHz. The proposed JLEIC frequency of 476.3 MHz is the second harmonic of the e-ring normal-conducting systems (see Section 9.7) and is chosen as a practical cavity size for existing global fabrication capabilities, availability of reasonably priced RF power and to provide a built in upgrade path to a future luminosity upgrade by doubling the number of bunches. Early analysis and prototyping indicate that cavities at this frequency can meet all the JLEIC design requirements while allowing for the highest possible bunch collision rate in the future. An SRF linac is proposed for the ion complex,

see Chapter 5. New strongly HOM damped single cells are also envisioned for the electron ring or future upgrades of the electron ring, or as a replacement for the PEP-II copper cavities as needed.

Table 9.14 lists the main parameters for the JLEIC collider ring RF systems. Table 9.15 summarizes all the SRF cavity types. The principal challenges for these designs include the need for strong HOM damping, high fundamental mode power couplers and high HOM power. Initial focus has been on the cooler ERL five-cell cavity as this is a critical component for the strong, high energy, bunched-beam cooling concept, see Chapter 6. One-cell and five-cell Nb prototype cavities have been designed and fabricated that already meet the gradient and Q_0 requirements for the project.

Table 9.14: High Level RF Parameters for JLEIC Rings

	electron ring (NCRF)		**ion ring**	
Energy	4	10	100	GeV
Frequency	476.3	476.3	952.6	MHz
Average Current	3.00	0.684	0.75	A
Syn. Rad. Power	1.03	9.15	-	MW
E-Loss Per Turn	0.342	13.4	-	MeV
V_{peak}, total	1.20	20.5	57	MV
Syn. Phase	16.5	40.6	0.0	deg
V_{gap}	0.301	0.790	1.19	MV
Gradient	1.0	2.5	7.55	MV/m
P_{beam} per cavity	257	352		kW
Cavity Wall Loss	12.9	89.1		kW
P_{fwd} per Cavity	432	441	64	kW
$P_{\mathrm{reflected}}$	163	0.01	64	kW
Q_{ext}	6000	6000	5.2×10^4	
Cavity Number	4	26	48	cells

The high circulating currents in both collider rings require careful design of all components for low impedance. In particular all RF cavities must be designed with strong HOM damping and high power fundamental mode couplers. The RF systems must also tolerate beam gaps for abort kickers and injection or between trains of bunches with opposite polarization. The high average beam current and non-uniform filling pattern will produce a complex beam spectrum that may result in very high beam-induced HOM power. This must be carefully analyzed and mitigated in the cavity design.

The exact ion ring frequency will depend on the energy and the cavities must therefore be tunable over at least one harmonic and at a rate that is consistent with the energy ramp. All other RF systems must also be tunable to track this frequency to maintain synchronization. This tuning range is somewhat higher than is typical in SRF systems but should be achievable with appropriate mechanical design.

9.5.1.1 Storage Ring Cavities High current storage rings such as PEP-II, KEK-B and CESR used heavily HOM-damped single-cell cavities with high-power fundamental mode couplers. For the electron ring JLEIC will re-use the successful PEP-II copper cavities, slightly retuned to 476.3 MHz

Table 9.15: SRF Cavity Parameters

Complex	Cavity	Freq. [MHz]	Volts / cell [MV]	Cells /cav baseline	Power /Cavity [kW]	Gradient [MV/m]	Total Cavity Cell Number	Q_{loaded}	Total RF Power	Total Voltage [MV]	Total cavity RF heat [W2K]
Ion Linac (pulsed, 4K)	QWR	100	4.7	1	20* (0.5-1kW av.)	10.5	21		420kW	100	small, pulsed operation
	HWR	200	4.7	1	20* (0.5-1kW av.)	10.5	63		1.26MW	300	
Ion Ring (2K)	elliptical	952.6	1.2	2	480	7.6	48	30000-60000	11.5MW	57.6	79
	Crab	952.6	1.15	2	small	∼7.4	36			∼40	209
Cooler ERL	Elliptical ERL linac	952.6	1.67	5	small	10.6	30			50	90
	Elliptical booster	952.6		2	240	∼4	8		1MW	5	3
	Elliptical chirper	952.6		2	100	9	4		100kW	5.6	9
E-ring	Crab	952.6		1	small	∼6	6			∼6	60
E-ring upgrade	elliptical	952.6		1	300	∼8	∼40		∼12 MW	48	66

* For JLEIC operation, each booster cycle requires 1–10 linac pulses in 5–10Hz. Each booster cycle takes 0.5-1 minute. Each ion injection cycle contains 8–26 booster cycles. Ion injection repeats every 1–8 hours.

to facilitate injection from CEBAF (Section 4.1). To minimize impedance only enough cavities for the energy required will be installed for each running energy. As upgrades are required or older systems are retired new high-current capable SRF cavities will be installed. In the ion ring all new 2-cell SRF cavities will be used from day one [21].

SRF Cavity Design

The cavity design concept is based on the JLab "high current" cell shape in which the cell profile is optimized to position strong HOMs away from harmonics of the bunch frequency thereby minimizing beam-induced HOM power. Strong cell to cell coupling and strong end group HOM damping ensures low HOM Q's for all dangerous modes. At the same time a reasonable efficiency and moderate peak surface fields must be maintained for reliable and cost-effective operation. This favors a vertical cell wall and generously rounded iris. A flat equator section minimizes impact energy in the multipacting barrier for easier conditioning and allows for trimming. By tuning the length of the end cell in multi-cell designs to achieve field flatness an efficient shape will be achieved using a common cell profile and one associated die set.

In the ion ring the primary function of the high frequency SRF system is bunching, and this is aided by operating at the second harmonic. Higher voltage and lower fundamental power are needed compared to the e-ring, however with 0.75 A circulating current strong HOM damping is still essential. A 2-cell design is chosen as a compromise between high peak voltage and good HOM damping. Beam gaps may require additional power to overcome reactive beam loading transients.

For the new cavity designs several HOM damping options are considered. For a detailed discussion on HOM damping options see also [21].

HOM Damping Options

SRF cavities have been shown to work well at high current using enlarged or fluted beam-pipe dampers, Figure 9.53a, e.g. at KEK-B and CESR, however these are rather long and result in a low packing factor in the cryomodule. Hook type HOM couplers, Figure 9.53b, are compact have been used e.g. in HERA and LEP-II but are typically limited to about 1 kW per coupler even with active cooling. JLab has developed beam-pipe mounted waveguide dampers, Figure 9.53c, that are both compact and designed for high power capability, although they do add some complexity to the cryomodule. A new HOM damping scheme is under development using on-cell waveguides, Figure 9.53d, that produces extremely low HOM Q's and will handle high HOM power in a compact module. The penalty for this is a local magnetic field enhancement around the waveguide iris, Figure 9.54, however this has been minimized by design to allow operation at the desired gradient. Figure 9.55 shows the longitudinal broad-band HOM spectra of these options. Clearly the on-cell damper version produces the best result. The transverse spectrum Figure 9.56 follows a similar trend. The on-cell waveguide damper concept was first used successfully on an SRF cavity for the ANL short pulse X-ray (SPX) prototype [22].

For the ion ring voltage requirements a 2-cell cavity is beneficial while still allowing good HOM damping using the waveguide end group to handle HOM power. For the cooler ERL, where the current is lower, a 5-cell version is optimal, also using the waveguide end group (see Chapter 6) For the cooler injector, which is not energy recovered, one- or two-cell cavities will be used with high power HOM and fundamental couplers similar to the storage ring design. For future upgrades of the e-ring the on-cell damper configuration is preferred, Figure 9.57.

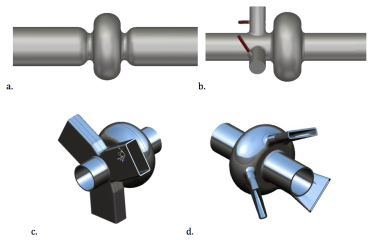

Figure 9.53: Options for strong HOM damping: a) enlarged beam pipes, b) three coax dampers, c) three waveguides, d) three on-cell dampers.

Cavity R&D

The first single-cell 952.6 MHz cavity is complete, Figure 9.58, and has been tested successfully. The first result is shown in Figure 9.59. The gradient and Q_0 both exceed requirements, validating the cell shape design. Once the HOM and FPC configuration have been finalized the cavity will be modified to add these features. A five-cell cavity for the cooler ERL has also been fabricated and is presently in processing. The new on-cell damper concept is also being developed, however this is not needed for the day one configuration.

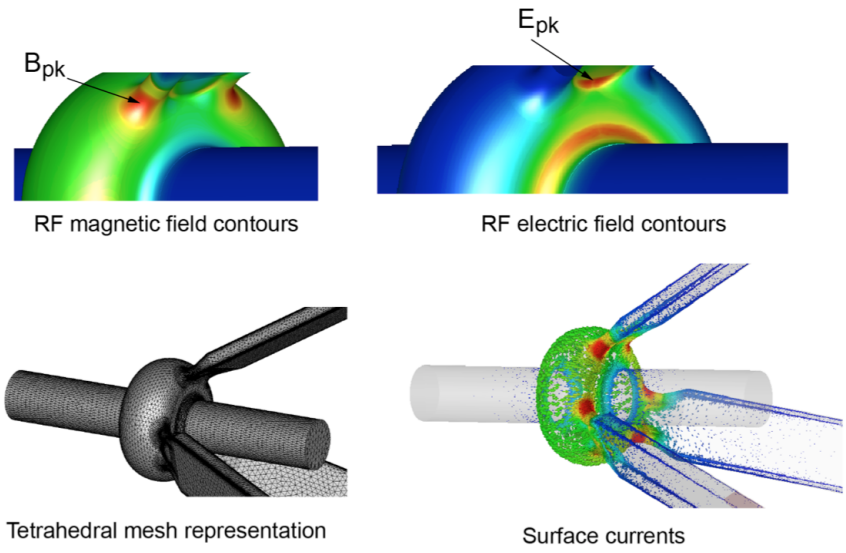

Figure 9.54: Field enhancements around on-cell dampers.

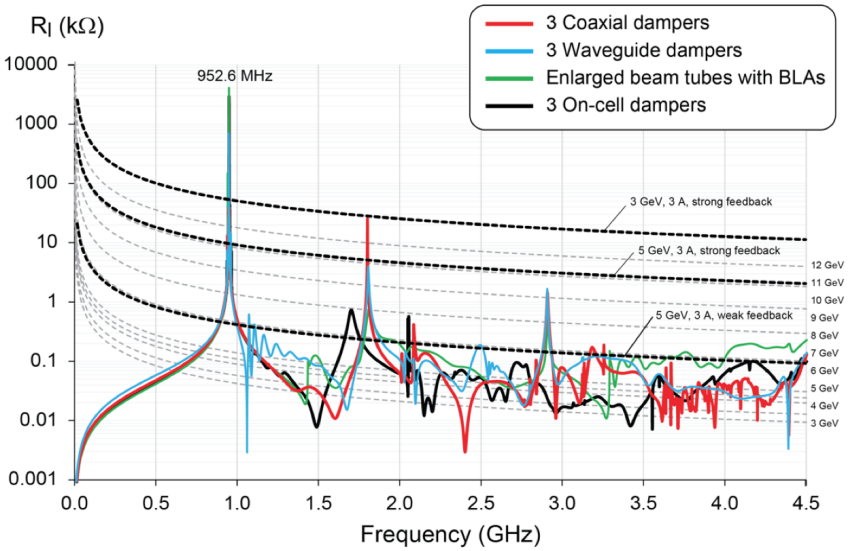

Figure 9.55: Longitudinal broad-band HOM spectrum of different damping schemes applied to a single-cell SRF cavity and e-ring BBU threshold at different energies [21].

9.5.1.2 Cryomodules **Cryostat concept**

To control costs and provide maximum flexibility and interchangeability of parts a highly modular cryostat concept is envisaged. This takes the best features of previous JLab designs for CEBAF, SNS and the 12 GeV upgrade and uses a high degree of modularity and commonality of ancillary components such as tuners and couplers to minimize development and construction costs. Simple concepts and low parts count are used wherever possible to reduce costs. The design is flexible

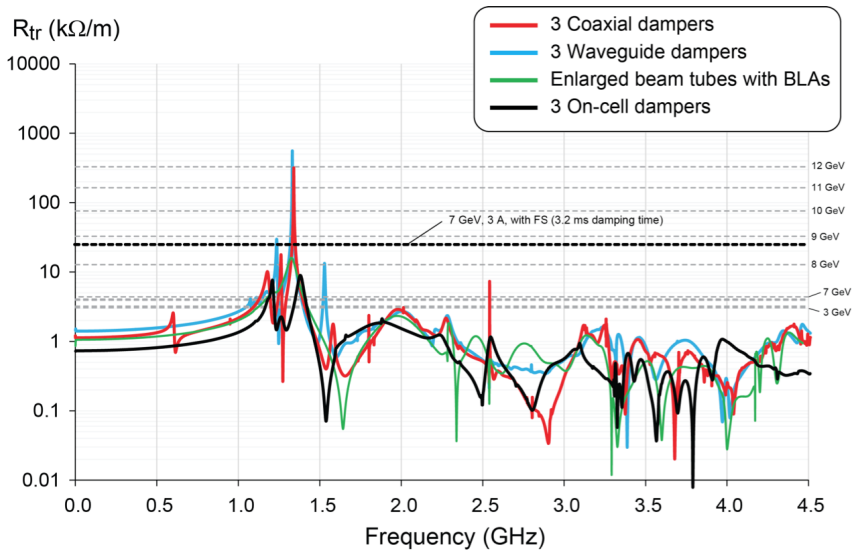

Figure 9.56: Transverse broad-band HOM spectrum of different damping schemes applied to a single-cell SRF cavity and e-ring BBU threshold at different energies [21].

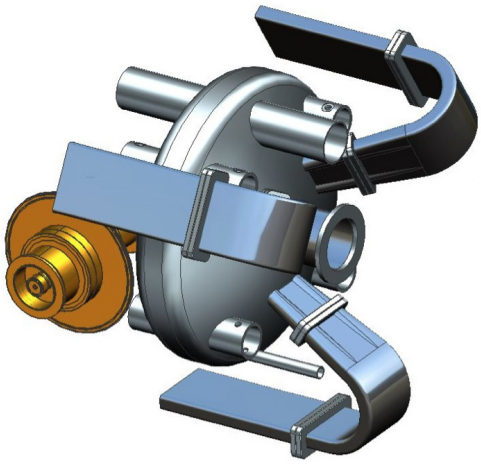

Figure 9.57: On-cell damper storage ring cavity concept.

and may accommodate various different types of cavities, including storage ring, cooler and crab cavities and is suitable for industrial production. The SNS-type cryogenic distribution scheme is proposed, which has small heat exchangers in each supply end can. Figure 9.60 shows such a modular approach housing 5-cell ERL type cavities. Figure 9.61 shows some other possible configurations and Figure 9.62 shows a variety of cavity types that may be accommodated.

9.5.1.3 High Power RF The main SRF system power requirements are listed in Table 9.15. In the ion ring the RF power is dominated by the need to cancel transients induced by the gaps in the beam needed for abort kickers. Even using the techniques developed for LHC [23], the high beam current means this is the dominant term. If shorter gaps or fill pattern shaping can be achieved, for example by use of barrier buckets, this power level may be reduced. For the crab systems the RF power is determined by how well the cavities are aligned since an offset of the dipole mode will

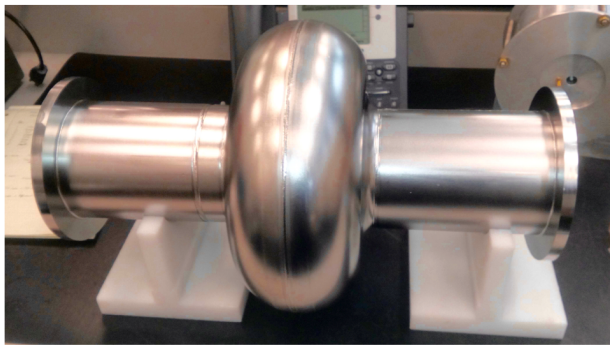

Figure 9.58: First 952.6 MHz cavity produced and tested at JLab.

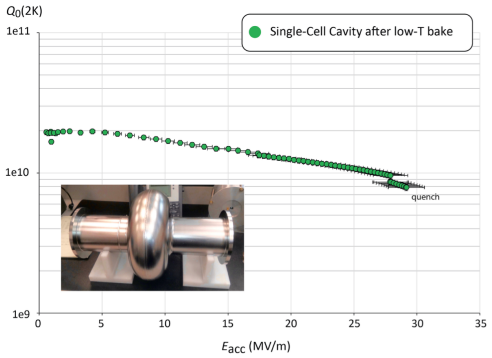

Figure 9.59: Preliminary results of 952.6 MHz 1-cell cavity.

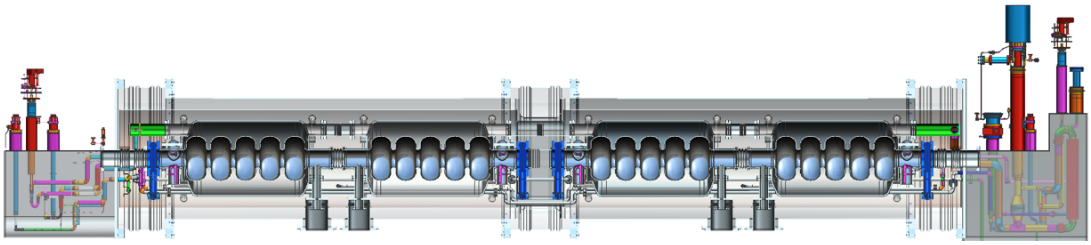

Figure 9.60: Modular cryostat concept with four 5-cell cavities.

couple beam power at the operating frequency (see Section 8.4). In the cooler ERL the beam is energy recovered so only modest RF power is needed to fill and control the cavity. However, the cooler injector and booster are fully beam loaded so also require high power sources.

For the MW class systems new high-power klystrons or magnetrons will be required. For the cooler ERL and possibly the crab systems small klystrons, IOTs or solid state may be sufficient.

9.5.1.4 Low Power RF The low level RF systems for the new SRF stations will be a modular digital-RF systems incorporating standard storage ring controls, plus the additional features developed for high current operation in PEP-II, including comb filters to reduce the impedance at the revolution frequency sidebands, adaptive feed-forward, linearization etc., as well as a digital interface to the bunch by bunch feedback system to suppress the lowest longitudinal coupled-bunch modes driven by the detuned fundamental impedance. Timing and synchronization requirements are not considered

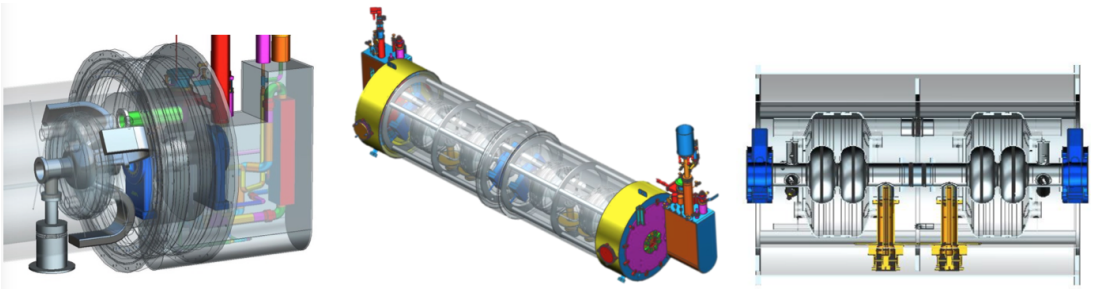

Figure 9.61: Different types of cavity in the modular cryostat: a) single cell with on-cell HOM dampers and warm loads, b) four 2-cell cavities , c) section showing 2-cell cavities in "pair configuration.

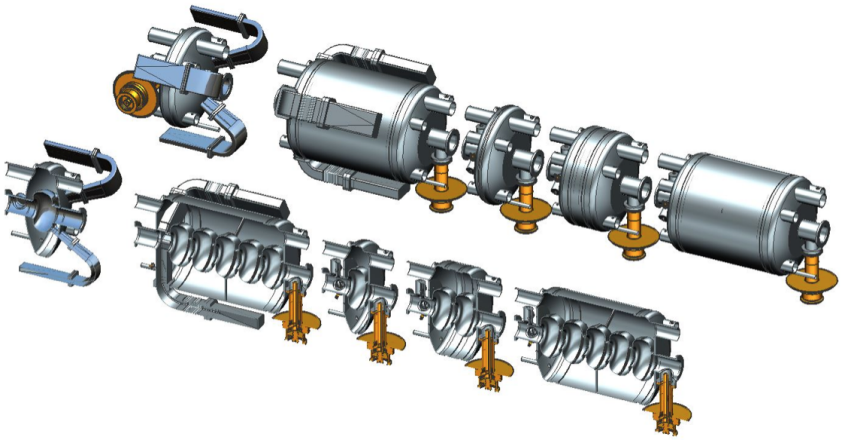

Figure 9.62: Variety of cavity types with modular helium vessel and FPC.

extraordinary with the exception of the crab cavity timing across the IP which will need careful synchronization (see Section 9.6). The JLEIC LLRF system is based on the JLAB LLRF 3.0 RF controls that has its roots in the LCLSII LLRF collaboration.

9.6 Crab Cavities

A local crabbing scheme will be installed to increase the collider luminosity. The crabbing system restores head-on collision of the proton and electron bunches, hence increasing the luminosity by increasing the number of interactions between the colliding particles [24].

Two frequency options of 476.3 MHz and 952.6 MHz are considered for the crabbing system. The 476.3 MHz option will be the operating frequency of the initial stage of the collider. 952.6 MHz will be the frequency of operation of the upgraded machine. The proton beam energy of the baseline design of JLEIC is 100 GeV where the upgrade will be at 200 GeV, which also doubles the required total crabbing kick. The required total crabbing kicks per side per interaction point for both electron and proton beams at 476.3 MHz and 952.6 MHz are given in Table 9.16 [25]. The beam parameters of the crabbing system are given in Table 8.4 in Section 8.2.

The beam aperture of the crabbing cavities is determined by the transverse bunch size of the proton beam at the time of the injection to the collider ring. Therefore, the beam aperture of

Table 9.16: Required Total Crabbing Kick Per Side Per Interaction Point for JLEIC

	476.3 MHz		952.6 MHz	
	e beam	p beam	e beam	p beam
	Baseline Design			
Beam Energy [GeV]	10	100	10	100
Total Crabbing Kick (V_t) [MV]	5.6	37.34	2.8	18.67
	Upgrade Design			
Beam Energy [GeV]			10	200
Total Crabbing Kick (V_t) [MV]			2.8	37.34

the crabbing cavities for JLEIC is selected to be 70 mm. Several superconducting crabbing cavity geometries were studied to achieve a compact crabbing cavity system as shown in Figure 9.63. Dimensional constraints and design requirements related to peak surface fields, impedance threshold, and higher multipole components are taken into consideration in designing the crabbing cavity geometry.

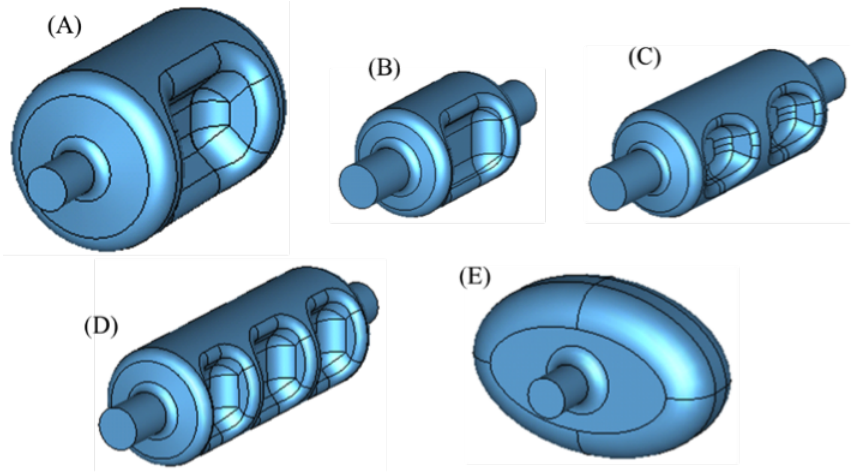

Figure 9.63: Crabbing cavity geometries considered for JLEIC. (A) 476.3 MHz Single Cell RFD Cavity, (B) 952.6 MHz Single Cell RFD Cavity, (C) 952.6 MHz 2-Cell RFD Cavity, (D) 952.6 MHz 3-Cell RFD Cavity, and (E) 952.6 MHz Squashed Elliptical Cavity.

9.6.1 Cavity Design Selection

The RF-dipole cavity design operates in a TE_{11}-like mode where the transverse electric field provides the primary contribution to the crabbing kick. A 400 MHz RF-dipole crabbing cavity is under development for the LHC-High Luminosity Upgrade [26]. Similarly, a single cell RF-dipole geometry is considered for JLEIC at 476.3 MHz. RF properties and cavity dimensions are listed in Table 9.17. The low peak surface fields allow the 476.3 MHz cavity design to be operated at a high transverse kick.

At higher operating frequencies, the RF-dipole design is compact in size where the cavity frequency inversely proportional to the cavity diameter. Therefore, RF-dipole design is also favorable at 952.6 MHz operating frequency. At 952.6 MHz frequency single cell, 2-cell and 3-cell geometries were considered. The rf-properties of the 3 geometries (along with a comparison with the squashed elliptical cavity type) are listed in Table 9.17 [27]. The 952.6 MHz operating frequency results in relatively high peak surface field ratios in the RF-dipole design. Therefore, a single cell RF-dipole cavity would require a large number of cavities, which would raise a challenge in the beamline space available. The 3-cell cavity results in the lowest number of cavities however, this cavity will have a high number of trapped higher order modes (HOMs) that would complicate the damping scheme. Therefore, the 2-cell RF-dipole cavity design is considered for the 952.6 MHz design.

Table 9.17: RF Properties of the JLEIC Crabbing Cavity Designs

Parameter	(A) 476.3 MHz Single Cell RFD	(B) 952.6 MHz Single Cell RFD	(C) 952.6 MHz 2-Cell RFD	(D) 952.6 MHz 3-Cell RFD	(E) Squashed Elliptical	Unit
Frequency	476.3	952.6	952.6	952.6	952.6	MHz
Beam Aperture			70			mm
Cavity Height	28.7	18.7	17.5	19.6	30	cm
Cavity Width	28.7	18.7	17.5	19.6	45.9	cm
Cavity Length	69.0	44.0	66.5	71.0	35.8	cm
LOM	–	–	845.5	756.8, 862.2	691.9	MHz
LOM Mode Type	–	–	Dipole	Dipole	Monopole	
1st HOM	746.2	1411.5	1379.5	1335.4	1040.8	MHz
E_p/E_t	3.7	5.4	5.7	5.6	2.2	
B_p/B_t	6.5	13.6	11.7	11.4	7.7	mT/(MV/m)
G	130.3	165.7	169.0	178.9	339.8	Ω
$[R/Q]_t$	357.2	50.0	147.5	218.8	49.8	Ω
$R_t R_s$	4.7×10^4	8.3×10^3	2.5×10^4	3.9×10^4	1.7×10^4	Ω^2

⋆ At $E_t = 1$ MV/m

9.6.2 Crab Cavity Designs

Two cavity geometries are chosen for the JLEIC crabbing system. The single cell 476.3 MHz RF-dipole cavity design is in the baseline design. The 952.6 MHz 2-cell RF-dipole cavity design is feasible for both the baseline and upgrade JLEIC.

The cavity properties for the JLEIC design with 10 GeV electron beam and 100 GeV proton beam are listed in Table 9.18. The transverse kick per cavity is determined with the cavities operating at a maximum peak surface magnetic field of 70 mT. At both operating frequencies the electron beam only requires two cavities.

The upgrade design with a 200 GeV proton beam will be operating at 952.6 MHz. The higher beam energy would require the cavity to deliver a high transverse kick per cavity. Therefore, the

Table 9.18: Cavity Properties of 476.3 MHz and 952.6 MHz RF-dipole Cavities (10 GeV Electron Beam and 100 GeV Proton Beam)

	protons		electrons		Units
Frequency	476.3	952.6	476.3	952.6	MHz
Total kick	37.34	18.67	5.6	2.8	MV
V_t per cavity	3.4	1.9	2.8	1.4	MV
No. of cavities	11	10	2	2	
Peak electric field (E_p)	40.3	34.2	33.2	25.2	MV/m
Peak magnetic field (B_p)	70.4	70.3	58.0	51.8	mT
Surface resistance (R_s)	22.0	95.0	22.0	95.0	nΩ
Shunt impedance (R_t)	2.11	0.26	2.11	0.26	MΩ
P_{diss} per cavity	5.5	13.8	3.7	7.5	W

Table 9.19: Cavity Properties of 952.6 MHz RF-Dipole Cavities (10 GeV Electron Beam and 200 GeV Proton Beam)

	protons	**electrons**	**Units**
Frequency	952.6	952.6	MHz
Total kick	37.34	2.8	MV
V_t per cavity	2.7	1.4	MV
No. of cavities	14	2	
Peak electric field (E_p)	48.6	25.2	MV/m
Peak magnetic field (B_p)	99.9	51.8	mT
Surface resistance (R_s)	95.0	95.0	nΩ
Shunt impedance (R_t)	0.26	0.26	MΩ
P_{diss} per cavity	27.8	7.5	W

cavities are considered with a less conservative maximum peak surface magnetic field of 100 mT, to reduce the number of cavities.

9.6.3 Input RF Power

Crabbing cavities do not require heavy beam loading as in accelerating cavities. However, bunches which are offsets see an accelerating component and therefore, require additional rf power to compensate. The input rf power [28] required by the RF-dipole crabbing cavities is determined by:

$$P_g = \frac{(1+\beta)^2}{4\beta R_t}\left[\frac{1}{\cos\alpha_L}\left(|V_t| + \frac{I_b R_t}{(1+\beta)} k\Delta x \sin\phi_c\right)\right]^2$$

where I_b is the beam current, V_t is the transverse voltage per cavity, R_t is the transverse shunt impedance of the cavity, Δx is the beam offset, β is the coupling coefficient, and Q_L is loaded

quality factor. The cavity will be at a phase offset ϕ_c=90° from the beam and will be in phase with the generator ($\alpha_L = 0$).

The maximum proton beam current at 100 GeV beam energy is 0.75 A and for the electron beam at the maximum beam energy of 10 GeV the beam current is also 0.75 A. However, at a lower energy of 7 GeV the electron beam current will be as high as 3 A (Table 4.5). Therefore, the input rf power for the electron beam is dominant at 7 GeV with a 3 A beam current. A beam offset of 1.0 mm is considered for the proton beam. For the electron beam a lower beam offset of 0.5 mm is considered as the beam will be controlled effectively with only two cavities per electron beam. Figure 9.64 shows the input power variation with Q_L for both beams with both 476.3 MHz and 952.6 MHz frequencies. Table 9.20 lists the corresponding input power required at the cavity and the optimum Q_L.

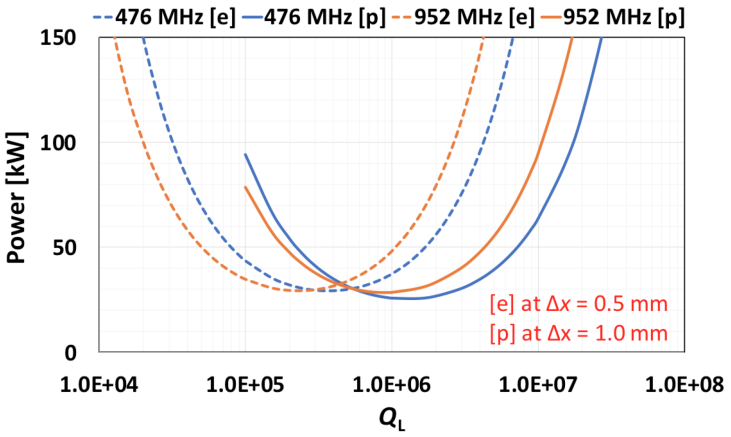

Figure 9.64: Input rf power as a function of Q_L for 10 GeV electron beam and 100 GeV proton beam operating at both 476.3 MHz and 952.6 MHz.

Table 9.20: Input rf power and optimum Q_L for the RF-dipole crabbing cavities operating at both 476.3 MHz and 952.6 MHz frequencies

	protons		**electrons**		**Units**
Frequency	476.3	952.6	476.3	952.6	MHz
Beam energy	100.0	100.0	7.0	7.0	GeV
Total kick	37.34	18.67	3.92	1.96	MV
V_t per cavity	3.4	1.9	1.96	0.98	MV
Beam current	0.75	0.75	3.0	3.0	A
Beam offset	1.0	1.0	0.5	0.5	mm
Optimum Q_L	1.5×10^6	1.0×10^6	4.5×10^5	2.5×10^5	
Power	30	35	35	35	kW

The upgrade design operating at a proton beam energy of 200 GeV and transverse voltage per cavity of 2.7 MV will increase the rf input power up to 45 kW per cavity. Figure 9.65 shows the

input power variation for both the electron and proton beams. Table 9.21 lists the corresponding input power required at the cavity with optimum Q_{L}.

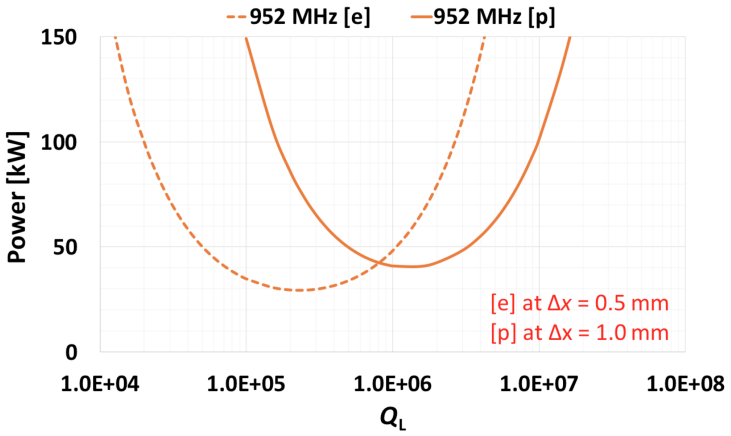

Figure 9.65: Input rf power as a function of Q_{L} for 10 GeV electron beam and 200 GeV proton beam operating at 952.6 MHz.

Table 9.21: Input rf power and optimum Q_{L} for the RF-dipole crabbing cavities for high energy JLEIC operating at and 952.6 MHz frequencies

	protons	**electrons**	**Units**
Frequency	952.6	952.6	MHz
Beam energy	200.0	7.0	GeV
Total kick	37.34	1.96	MV
V_{t} per cavity	2.7	0.98	MV
Beam current	0.75	3.0	A
Beam offset	1.0	0.5	mm
Optimum Q_{L}	1.5×10^6	2.5×10^5	
Power	45	35	kW

9.6.4 Higher Order Mode Analysis

Higher order modes up to 3 GHz of all considered designs were analyzed during the design evaluation process. The following graphs show R/Q, indicating each mode's interaction with the beam. To avoid detrimental effect on the beam, low R/Q for HOM is desired but the values are design dependent. Coupler designs have to be applied to the cavity to get the coupling strength (Q external values) to each mode. The product of R/Q and Q_{ext} will provide the first order beam impedance.

9.6.4.1 HOM Properties HOM properties of all considered design were analyzed. They are categorized 1) transverse horizontal mode, 2) transverse vertical mode, and 3) longitudinal mode.

Transverse horizontal (vertical) modes mean the combined electric and magnetic field effect kicks the beam in horizontal (vertical) plane respectively. Longitudinal modes have the effective field in the direction of the beam, which spreads the bunch energy.

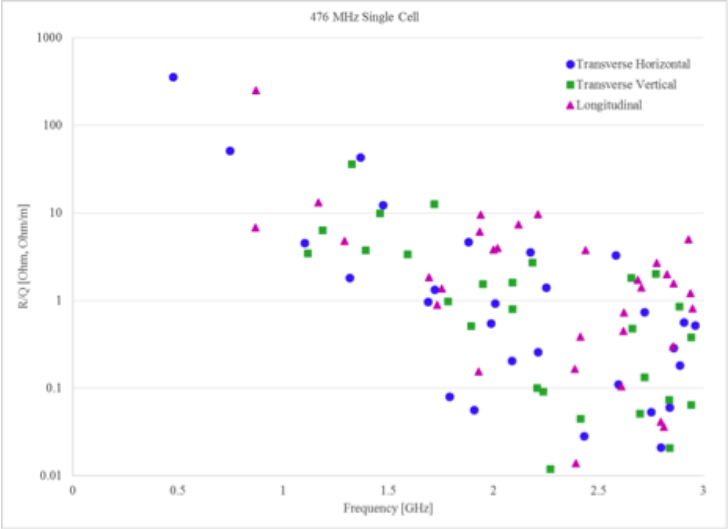

Figure 9.66: HOMs for single-cell 476.3 MHz rf dipole cavity design.

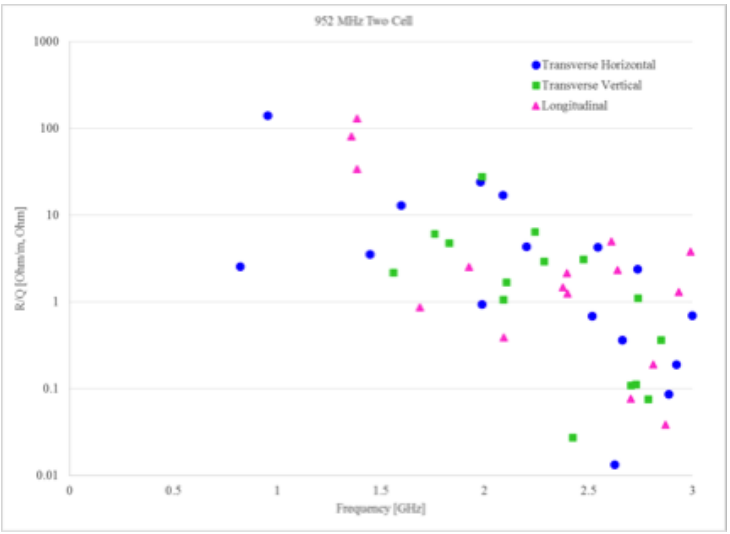

Figure 9.67: HOMs for double-cell 952.6 MHz rf dipole cavity design.

9.6.4.2 HOM Damping Options HOM couplers are designed to couple the HOMs and dissipate the energy as a heat outside of beamline enclosure. Typical HOM damping schemes use waveguide or coaxial couplers. Coaxial couplers interact with electrical, magnetic, or both fields of the modes. HOM couplers are desired not to couple with the operating mode. The studied options are described below. After evaluation, further study will follow for a chosen damping scheme. On-cell waveguide couplers provide a reasonable damping on the RFD crab cavity, which has space available on cell.

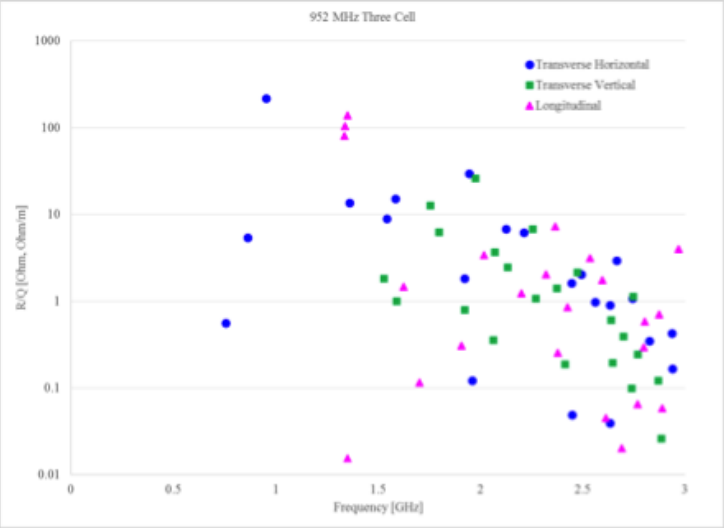

Figure 9.68: HOMs for three-cell 952.6 MHz rf dipole cavity design.

9.6.5 Multipole Analysis

In deflecting/crabbing cavities the rf field of the fundamental operating mode varies across the beam aperture leading to field non-uniformity. This field non-uniformity corresponds to higher order multipole components that may lead to perturbations in beam dynamics such as linear tune shift, chromaticity shift, and chromatic coupling [29]. The higher order multipole components also affect the long term stability in colliders, storage rings and synchrotron machines especially with proton or heavy ion beams. The higher order multipole components are calculated as follows using the Panofsky-Wenzel Theorem:

$$a_n + ib_n = \frac{in}{\pi\omega} \int_{-\infty}^{\infty} \int_0^{2\pi} \frac{1}{r^n} E_z(r, \phi, z)\, \mathrm{e}^{in\phi} \mathrm{e}^{i\omega z/c}\, d\phi\, dz \tag{9.6.1}$$

where a_n and b_n are skew and normal multipole components [30]. E_z in the longitudinal electric field at an offset of r. The higher order multipole components of the 476.3 MHz single cell RF-dipole cavity and 952.6 MHz 2-cell RF-dipole cavity are shown in Table 9.22. The designs with flat poles meet the requirements of HOM components up to b_5 (see Figure 8.12). Curved poles permit reduction of multipole components in case they exceed design requirements.

9.6.6 Cryomodules

The crab cavities will be housed in a version of the same modular cryostat developed for the other SRF systems. Due to the compact dimensions of the RFD either 952.6 or 476.3 MHz versions will be accommodated (see Figure 9.69). The cavities will require strong HOM damping and high power HOM loads which may be similar to the ion ring bunching cavities. Multiple cavities will be packaged in each cryostat consistent with available lattice spacing, see Figure 9.70. External alignment of the cold mass may be required to minimize beam induced power at the operating frequency, which must be cancelled by the high power RF system. A system of external tensioners for the nitronic rods in the cryostat will be used to fine tune the cold mass position, as was proposed for the ANL SPX cryostat [22]. A beam-based measurement will be the best way to establish this alignment, but optical fiducials on the cold mass visible from outside the module may also be

Table 9.22: Higher Order Multipole Components Cavity at V_t =1 MV

Component	476.3 MHz **Design**	952.6 MHz **Design**	**Unit**
b_1	3.33	3.33	mT-m
b_2	-3.1×10^{-4}	-2.4×10^{-4}	mT
b_3	385.7	965.0	mT/m
b_4	0.7	0.5	mT/m2
b_5	-8.6×10^4	-4.6×10^4	mT/m^3
b_6	-1.1e3	-8.1×10^2	mT/m^4
b_7	-1.8×10^7	-7.1×10^7	mT/m^5

useful. With such a system transverse alignment of the electrical center to better than 100 µm is expected. The system probably does not need to be remotely activated, one or more manual adjustments after beam-based measurement should be sufficient to center the cavities.

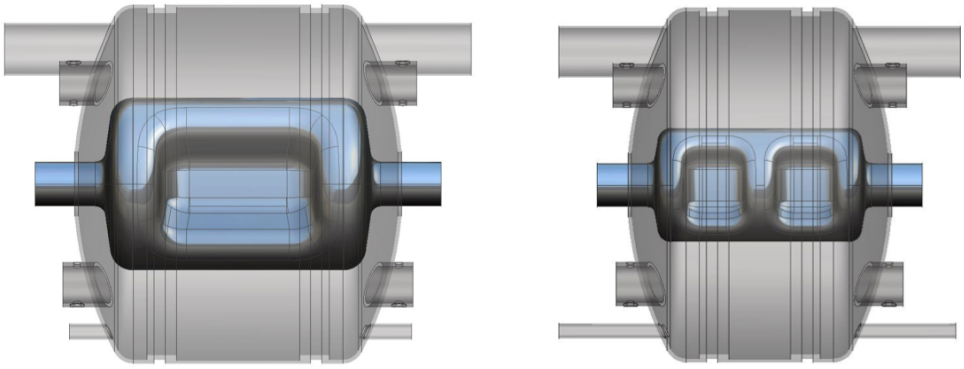

Figure 9.69: 476.3 MHz single gap and 952.6 MHz 2-gap RFD crab cavities in modular helium vessel. Length will be adjusted once HOM damper and FPC arrangements are known. Additional ports may be required for transverse tuners and HOM loads.

9.6.7 High Power RF

The RF power requirements are dominated by the need to cancel beam-induced power at the operating frequency. The magnitude of this power is determined by the alignment tolerance of the cavities and the HOM components as discussed in Section 9.6.4. With external adjustment and beam-based measurement this will be on the order of 1 mm for proton crab cavities and 0.5 mm for electron crab cavities as shown in Tables 9.20 and 9.21. Operation with an incomplete bunch filling pattern (at least two gaps are foreseen) will produce a transient in the residual beam loading that may require an additional RF power overhead. RF power sources may be small klystrons, IOTs or possibly magnetrons or solid state.

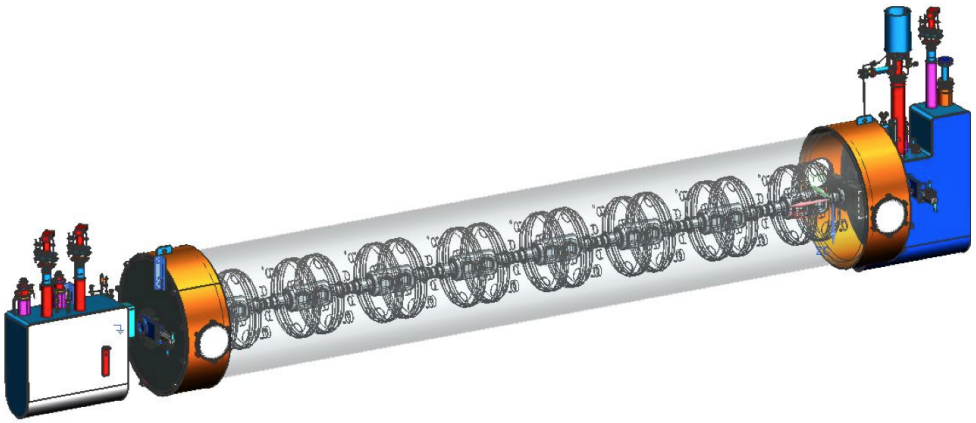

Figure 9.70: Multiple RFD cavities packaged in a modular cryostat. Individual cavity alignment may be fine tuned using external tensioners for the nitronic rods on each helium vessel (not shown in this picture).

9.6.8 Low Power RF

The LLRF for the crab cavities will be similar to that for the bunching system (Section 9.7) however the accuracy of the synchronization system between crabbing systems either side of the IP will have to be much tighter to ensure complete cancellation of the crab kick on each pass. A detailed synchronization scheme was developed by LBNL for ANL's Advanced Light Source SPX project and this will be used as a guide for JLEIC [31]. Incomplete cancellation results in global crab motion in the rest of the ring, possibly leading to particle losses, and emittance dilution. The LLRF system will be based on the JLAB LLRF 3.0 RF controls that has its roots in the LCLSII LLRF collaboration.

9.7 Normal Conducting RF

9.7.0.1 Cavities A number of conventional normal-conducting RF systems are needed in JLEIC for bunch capture and acceleration in the booster and collider rings and for bunch splitting. These will be adapted from similar existing technologies in use at JPARC, CERN and elsewhere. Table 9.23 lists all the NCRF system requirements.

For the electron ring JLEIC will re-use the successful PEP-II copper cavities since they have demonstrated up to 3A operation with ∼0.5 MW power per coupler. The total ring current is limited by the cap of 10 MW of synchrotron radiation losses at high energy. At lower energy the current is limited by other factors such as space charge or BBU but at least 3 A will be achievable from low energy until the power limit is reached.

The cavities themselves will be retuned to 476.3 MHz by adjusting a fixed tuner by 300 kHz (the fixed and movable tuners each have ±500 kHz tuning range). This frequency adjustment allows trains of polarized bunches to be injected from CEBAF to facilitate rapid filling and top-off. The cavities can otherwise be used as is with only light refurbishment. To optimize the use of available RF power the input beta will need to be adjusted. On the PEP-II cavities the input coupling is by waveguide and is not dynamically adjustable, however the input waveguide is demountable and the coupling factor will be changed by inserting a quarter-wave matching section between the cavity and the RF window. The entire cavity assembly is mounted on a raft for installation, Figure 9.71.

Table 9.23: NCRF Cavity Parameters

Complex	**Cavity**	**Freq. [MHz]**	**Voltage / cavity**	**RF power per cav**	**Number of cavities**	**Klystron power**	$Q_{\mathbf{loaded}}$	$Q_{\mathbf{ext}}$	R/Q **per cav**
Ion Linac	RFQ light ion	100	∼1 MV	105 kW⋆	1				
	RFQ heavy ion	100	∼3.5 MV	250 kW⋆	1				
	IH DTL-1 (10 gaps)	100	∼10 MV	280 kW⋆	1				
	IH DTL-2 (5 gaps)	100	∼10 MV	400 kW⋆	1				
	IH DTL-3 (4 gaps)	100	∼10 MV	620 kW⋆	1				
e-ring	Re-entrant	476.3	0.8 MV	500 kW	34	1.2 MW	30000	∼8000	217
Booster capture/ acc	magnetic alloy loaded	0.4–0.92	∼20 kV	∼200 kW	1		Q_l ∼2		∼1000
Booster split /accelerate	magnetic alloy loaded	3.2–7.4	∼20 kV	∼200 kW	1		Q_l ∼2		∼1000
Ion ring accel	MA loaded	7.05–7.44							
Ion ring splitting	button	14.87	6 kV		1				
	button	29.75	11 kV		1				
	QWR	59.49	23 kV		1				
	QWR	118.98	45 kV		1				
	QWR	237.96	90 kV		1				
Ion ring	bucket insertion/acc	475.9–476.4	∼70 kV	∼200 kW	2			$Q_l \sim 100$	∼200
Cooler CCR	Compression to 952 MHz acceptance	476.3	∼800 kV	150 kW	2–3		∼30000	∼15000	∼200
	Injector buncher and capture	476.3	∼800 kV	150 kW	2	150 kW	30000	∼8000	217
	Harmonic kicker	86.6×1, 3,5,7,9	25 kV/mode, 125 kV total	5 kW	2		6000–18000	6000–18000	282–39 (T)
	DQW kicker	952.6	32.5 kV	0.5 kW	2		∼7000	∼7000	324 (T)

⋆ 1 ms, 5–10 Hz; slow means ramp in a few or 10s of seconds

Figure 9.72 shows the station layout in the tunnel and surface building for PEP-II for a station with four cavities driven by one 1.2 MW klystron.

For the ion linac front end a normal-conducting RFQ and DTL will be used. These are described in Section 5.2.

For the booster and ion ring capture low frequency inductively loaded cavities will be used similar to those at JPARC, Figure 9.73 and CERN, Figure 9.74. The cavities will capture the the injected bunches in the ion ring, store them at low energy while they are cooled with the DC cooler, and accelerate them to the splitting energy. The power requirement is determined by the ramping rate. The cavities must be broad band or tunable to accommodate the large velocity change during initial ramping. At the bunch splitting energy a series of binary bunch separations is performed. Each of these systems requires only a modest NCRF system since the bunch length is still quite long at this stage. These cavities may also be inductively loaded, or may be capacitively loaded like those in the CERN PS used during LHC bunch formation, Figure 9.75. Figures 9.76 and 9.77

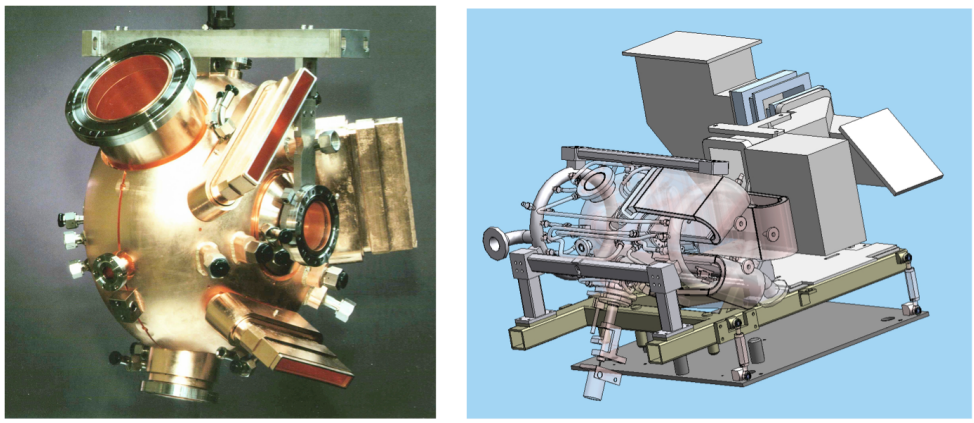

Figure 9.71: PEP-II NCRF cavity and raft assembly.

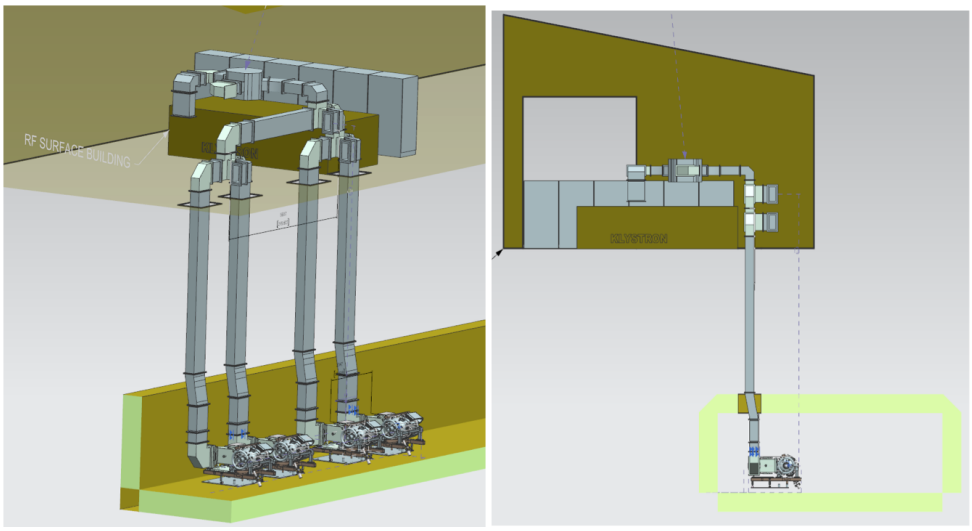

Figure 9.72: PEP-II RF station layout in tunnel and surface building.

show possible variants for JLEIC. These cavities can potentially have gap shields incorporated allowing the impedance to be shorted out when not in use. The highest splitting frequencies may use conventional QWR cavities. Once split to the desired number of bunches a 476.3 MHz copper or the 952.6 MHz SRF system will be used to compress the bunches and accelerate to the collision frequency. The final compression to collision bunch length is performed by the SRF 952.6 MHz system.

9.7.0.2 High Power RF The PEP-II based stations will use the same 1.2 MW klystrons which have been preserved at SLAC. These should be usable with light refurbishment but will also be rebuilt either at SLAC or by a commercial vendor. 13 existing tubes are available, which is sufficient to supply the necessary voltage and beam power up to 12 GeV (a few new cavities would be needed to provide sufficient bucket height above 10 GeV). The SLAC 2 MVA switching power HV supplies for the klystrons are also available.

9.7.0.3 Low Power RF The LLRF system is based on the modular JLAB LLRF 3.0 RF controls that has its roots in the LCLS-II LLRF collaboration. It will incorporate features from the original

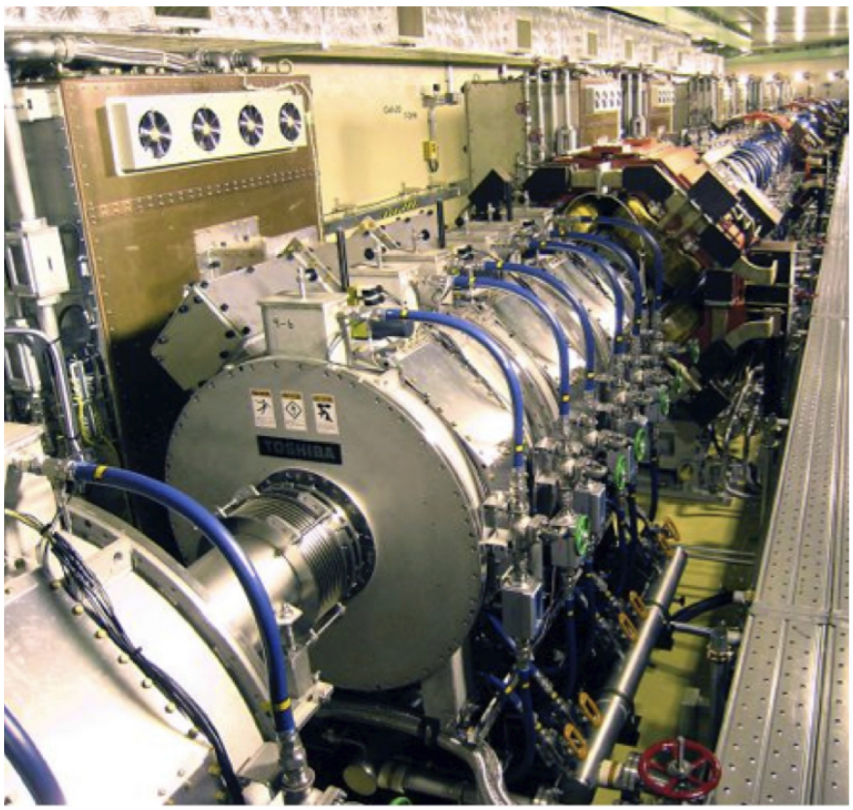

Figure 9.73: JPARC cavity (Metglass loaded).

PEP-II LLRF system such as adaptive feed-forward, klystron linearization, saturation and ripple control, double comb notch filter and links to the bunch by bunch LLRF system.. Figure 9.79 shows a block diagram of the PEP-II RF system [32]. Figure 9.80 illustrates the effect of the direct and double comb loops on the system impedance as seen by the beam. The direct loop reduces the peak impedance but spreads it out over a wider frequency span. The double notch filter further reduces the impedance at the anti-damping sidebands allowing the growth rate to be then counteracted by the bunch by bunch feedback system using the RF system as a low mode kicker (so-called "sub-woofer") [33]. These features were essential for PEP-II operation and will be incorporated in JLEIC.

One limitation of the RF system in any high-current ring is the susceptibility to transients caused by uneven filling or gaps in the beam. At 3 A beam current, it is impractical to cancel this by brute force using RF power alone. In PEP-II this was mitigated by using the shortest abort gap possible (about 1%), but even then the RF power overhead would have been prohibitive. In that case they chose to match the residual transient in both rings by using the same loaded Q for the cavities and balancing the systems. This resulted in the collision point moving back and forth in the detector, but with head-on collisions that was acceptable. In JLEIC this may not be possible due to the very different characteristics of the electron and ion rings and because of the crossing angle, so we have investigated using fill pattern shaping as proposed by Byrd et al. [34]. In this scheme the missing charge from the gap is distributed to bunches either side so that the average current over a longer time period is constant. This results in a strong transient locally around the gap but no transient for the rest of the turn. Figure 9.81 shows the problem. Figure 9.82 shows

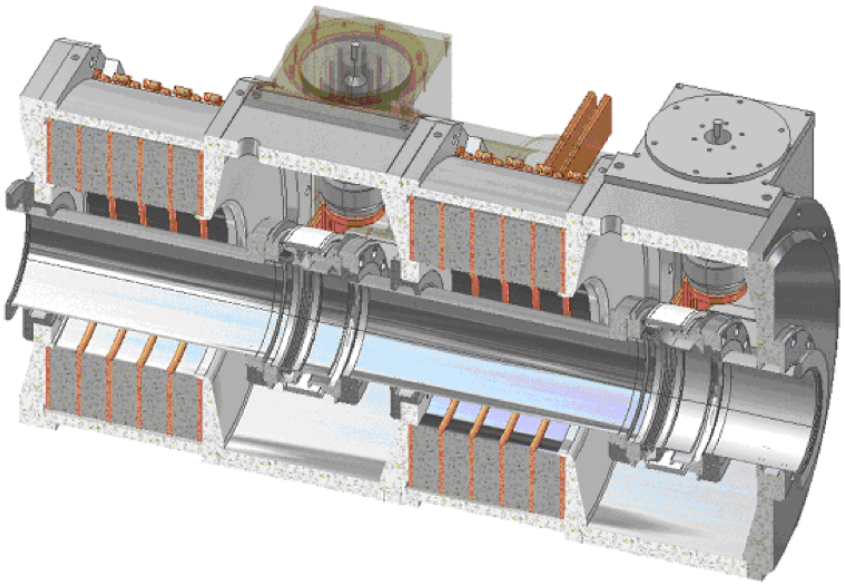

Figure 9.74: CERN PS 13.3–20 MHz low Q Ferrite loaded cavity.

experimental results from a test performed in the Advanced Light Source (ALS) in Berkeley in which bunches either side of the gap were filled with double charge to compensate for the gap. The phase shift for most of the fill is greatly reduced. Fill pattern shaping is straightforward to achieve in the electron ring with top-off injection. In JLEIC the electron beam gaps (at least 2 per turn) will be similarly short, and compensated by nearby bunches provided that higher charge per bunch will be achieved by top-off. This transient portion of the fill is well within the longer ion ring gaps that result from the ion bunch formation scheme.

9.8 Feedback Systems

Bunch by bunch feedback systems are used in most modern storage rings and were essential in allowing PEP-II to run above the CSI threshold. A schematic of the PEP-II longitudinal system is shown in Figure 9.83. Such systems are now commercially available and are used by storage ring light sources to provide stable high intensity beams to users with very good reliability. JLEIC will use a similar system adapted to the final ring frequency and bunch spacing. New reliable high-power kickers are needed. The longitudinal kicker will be based on the DAΦNE style damped cavity kicker, Figure 9.84. The transverse system is shown in Figure 9.85. New transverse kickers are being developed based on the successful APS design, Figure 9.86. The total system gain and number of kickers and feedback power required will be derived from the impedance model of the machine which is still being developed, see Section 8.4.

9.9 Vacuum

Vacuum system requirements for JLEIC are still being generated but are anticipated to be similar to requirements already demonstrated by other machines. The designs will then be similar and updated as needed to take advantage of improvements in vacuum harder and cleaning methods.

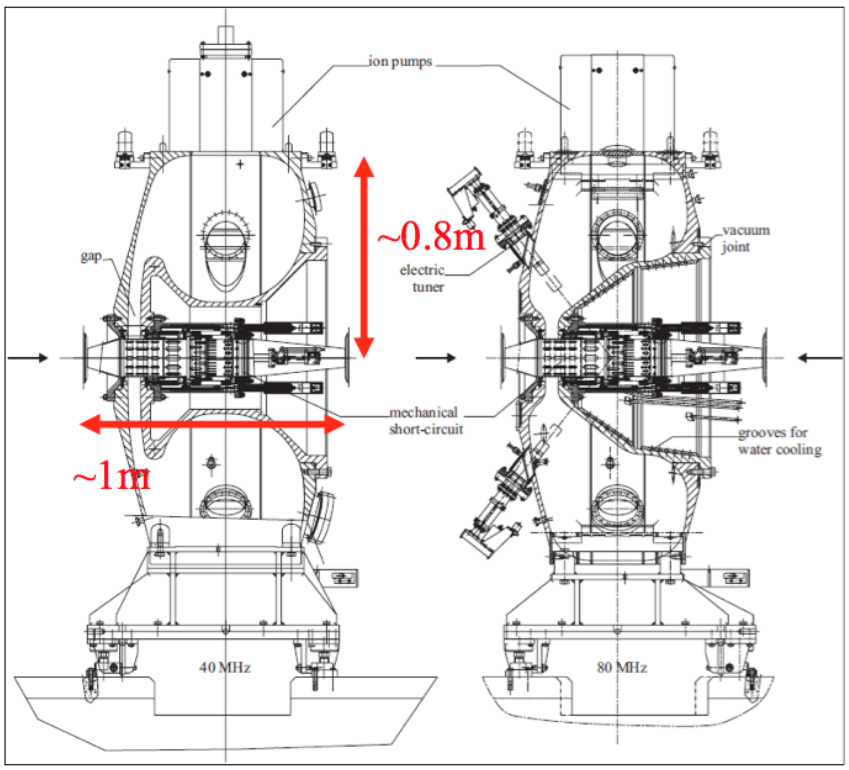

Figure 9.75: CERN PS 40 MHz and 80 MHz capacitively loaded cavities used for LHC bunching.

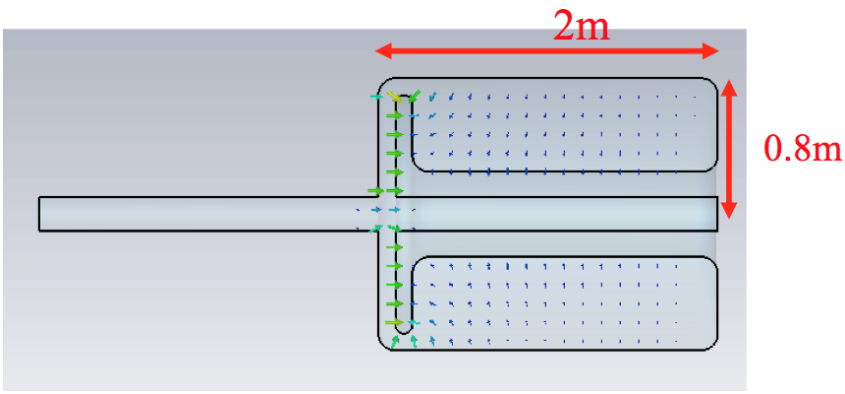

Figure 9.76: JLEIC 15 MHz "button" cavity concept.

Little detailed design has been done on the vacuum systems to date and only select details are presented here.

9.9.1 Electron Collider Ring

The JLEIC beam lifetime from beam-gas scattering is about 6 hours at a gas pressure of 5 nTorr. The vacuum system will be designed to produce this preliminary value of 5 nTorr pressure of background gas [35, 36]. There may also be an electron cloud generated coupled bunch instability to be considered. The strengths of these instabilities are similar to those of B-factories (smaller

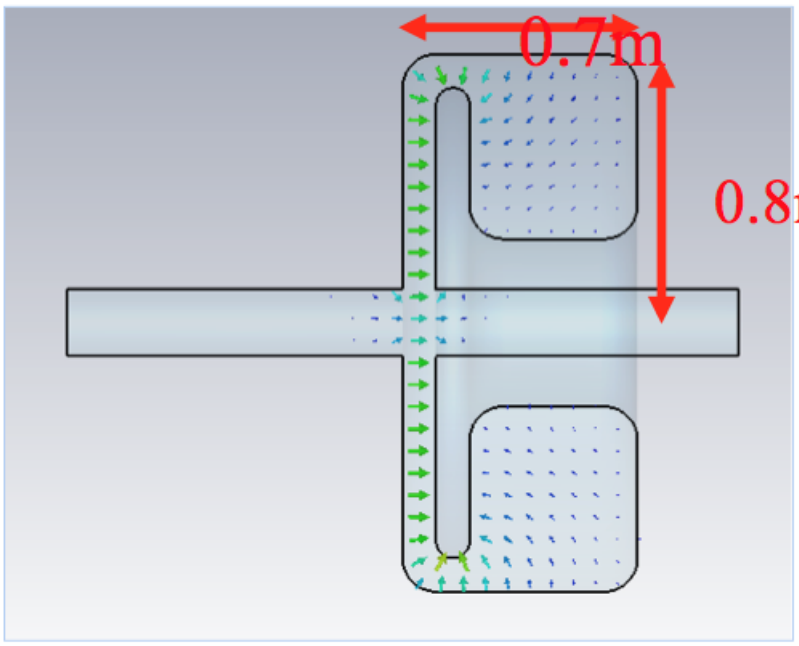

Figure 9.77: JLEIC 30 MHz "button" cavity concept.

Figure 9.78: PEP-II 1.2 MW klystron and 2 MVA switching power supply.

number of particles per bunch is compensated by shorter bunch spacing). A rough estimate gives the growth time of about 0.2 ms for the instability. JLEIC will use various measures (solenoid coils, coating the vacuum chamber with TiN or NEG, etc.) that have been taken at B-factories to control electron cloud effects.

With the design of the vacuum chamber following the example of B-factory ring colliders, JLEIC will be safe from the single bunch instabilities. No bunch lengthening and widening due to the longitudinal microwave instability and no current limitations from the transverse mode coupling

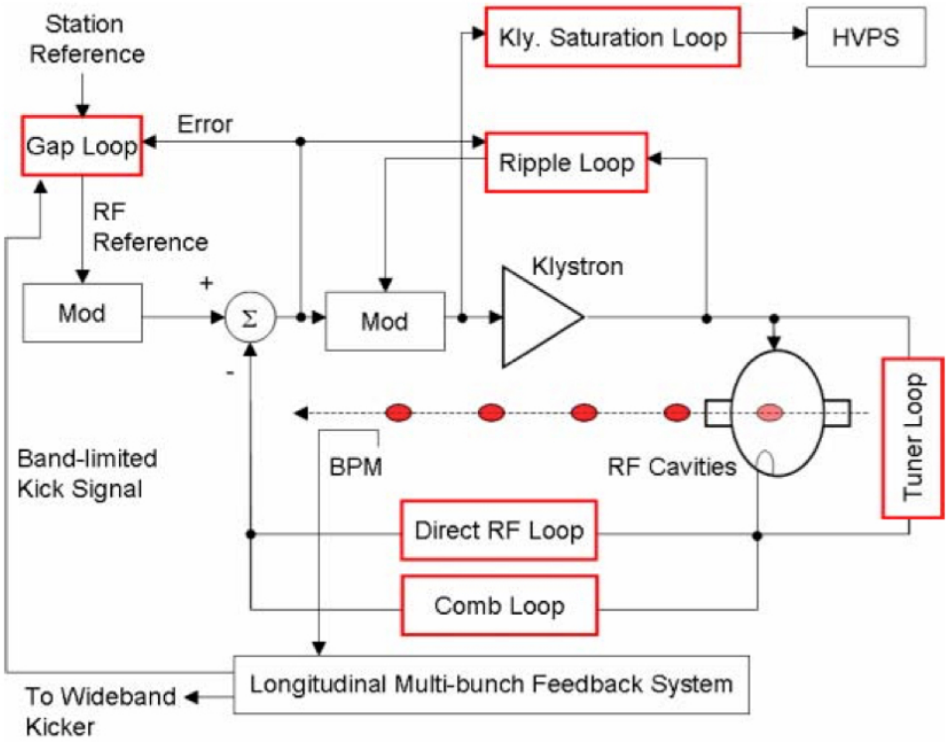

Figure 9.79: PEP-II type digital LLRF system which will be recreated in a current and sustainable hardware platform, JLab 3.0.

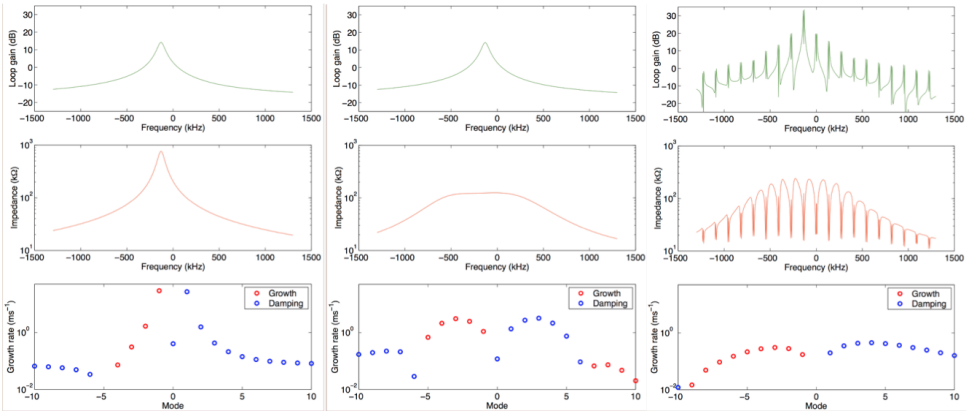

Figure 9.80: Effect of the double-notch comb loop in minimizing the driving impedance for low-mode coupled-bunch instabilities.

instability are expected. The performance of the JLEIC e-ring is most likely to be limited by multi-bunch instabilities that will be handled by feedback systems that well within the state-of-the-art.

The design of the vacuum system for the electron collider ring is based on the design of the PEP-II high energy ring vacuum system. That system was designed for a vacuum pressure of 1×10^{-8} Torr in the arc regions where there was a high synchrotron radiation load and 3×10^{-9} Torr in the straights [37]. The system was based on all an all ion pump system. Distributed Ion Pumps (DIP)

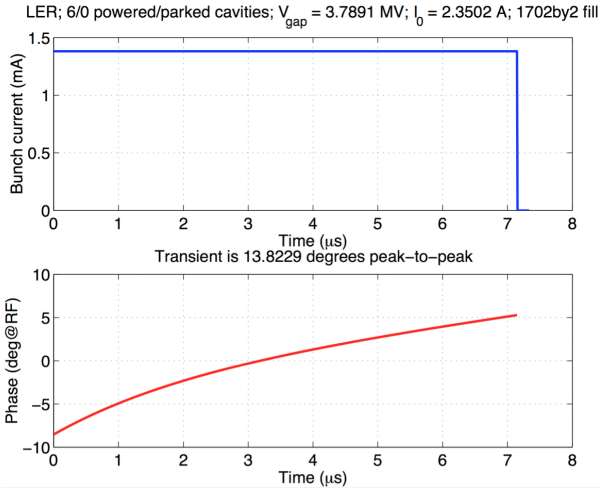

Figure 9.81: Typical beam loading transient in PEP-II without compensation.

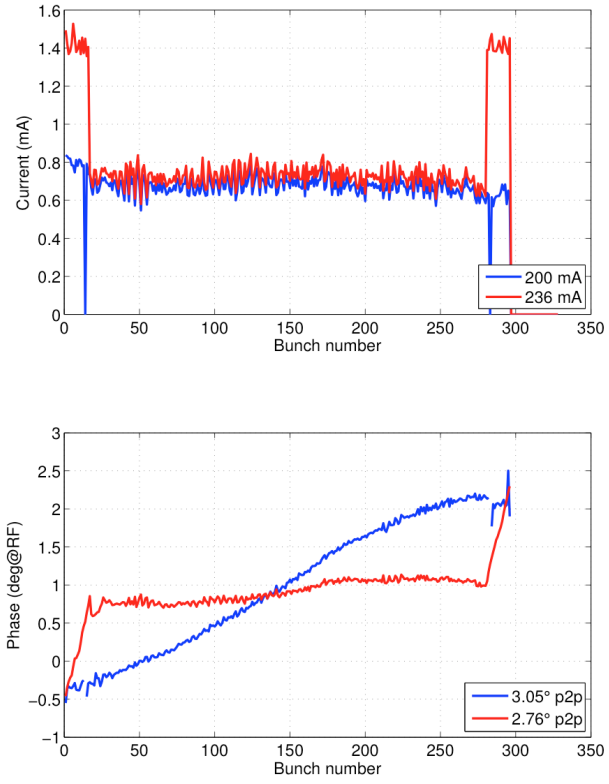

Figure 9.82: Gap transient suppression experiment in ALS using a shaped fill pattern, April 7 2017.

are used in the arcs to deliver greater than 130 L/s/m of pumping. Differential ion pumps are used in the quadrupole girders in the arcs (60 L/s) and straight sections and provide noble gas pumping for the system. After some amount of scrubbing, the average pressure in the HER ring was about

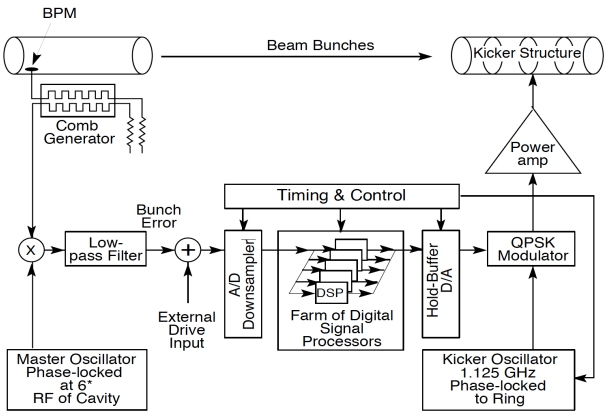

Figure 9.83: PEP-II longitudinal feedback system.

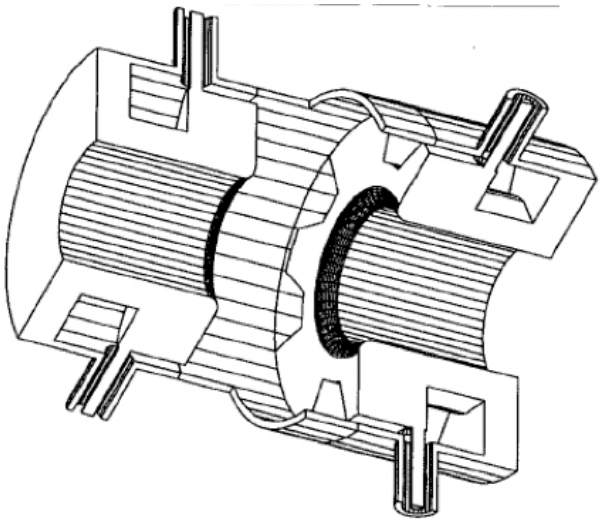

Figure 9.84: DAΦNE type damped cavity longitudinal kicker.

0.5 nTorr, exceeding the design goals for PEP II and JLEIC [38]. NEG pumps and coatings will be included in areas as needed to provide additional pumping.

The vacuum system will reuse chambers from PEP-II as much as possible, and new chambers will be based on the PEP-II design. Straight sections of the ring will be fabricated out of stainless steel with the arc chambers out of half hard C10100 oxygen free copper. The arcs have been designed to limit the local SR to 10.2 kW/m to match the PEP-II design. A few of the magnets have initial designs that exceed this value (Table 4.8). The chambers near these dipoles will need additional design work to meet thermal and localized fatigue stress limits. If designs on the chambers cannot meet the higher loads then it is possible to change the dipole designs to limit the amount of radiation produced.

The PEP-II RF shielded bellows will also be repurposed in the arcs and straights as well. Initial impedance calculations for JLEIC have been based on these designs (Figure 9.87). Special designs are anticipated for the IR region and will be developed once the final geometry has been established.

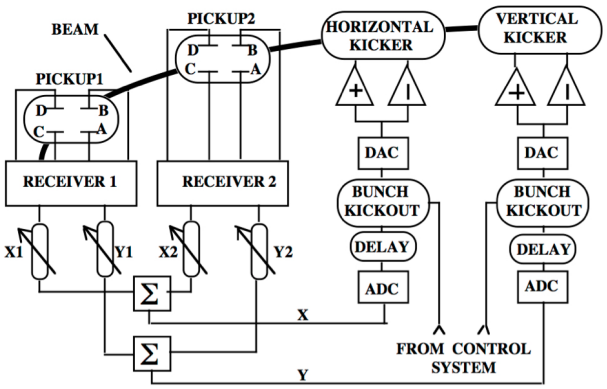

Figure 9.85: PEP-II transverse feedback system concept.

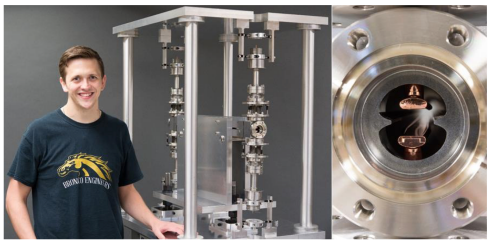

Figure 9.86: APS transverse feedback kicker.

9.9.2 Ion Collider Ring

The ion collider ring will mostly be a cold line except in the warm straight sections, where the warm RF cavities are installed and a few other select locations. Shielded bellows in the ion ring will be based on RHIC design and modified as needed for the JLEIC beam.

Cold bore vacuum systems will be pumped down to better that 1×10^{-8} Torr by turbomolecular pumps prior to cool down. SRF beamline vacuum systems will be better than 1×10^{-9} Torr prior to cool down. The vacuum pressure in the warm beamlines will be monitored by ion pumps. The vacuum pressure in the magnet interconnect regions in the arcs will be monitored by cold cathode gauges. beamline welds and connection will be located outside of the helium space when possible to limit the possibility of helium leaks into the beamline vacuum system.

Both the ion and electron collider rings will have beamline vacuum pipes to keep the impedance as low as possible. This means limiting the number of size variations to a minimum, and designing all components with impedance in mind. Vacuum valves will be shielded and kept to the minimum required for operations.

9.9.3 Ion Booster

In the ion booster ring the vacuum will be required to have a low 1×10^{-11} Torr vacuum to minimize beam loss of partially stripped heavy ions. This is the same requirement set and achieved for the AGS Booster Vacuum Systems at Brookhaven [39]. The same methods used to achieve those levels will be used for JLEIC. This includes having the warm vacuum chambers chemically cleaned, vacuum fired, baked and treated with nitric oxide. The vacuum systems will be baked in situ to minimum of 200 C with select components up to 300 C. Ion pumps and titanium sublimation pumps will be used throughout. NEG pumps will also be considered as needed. Much of the line

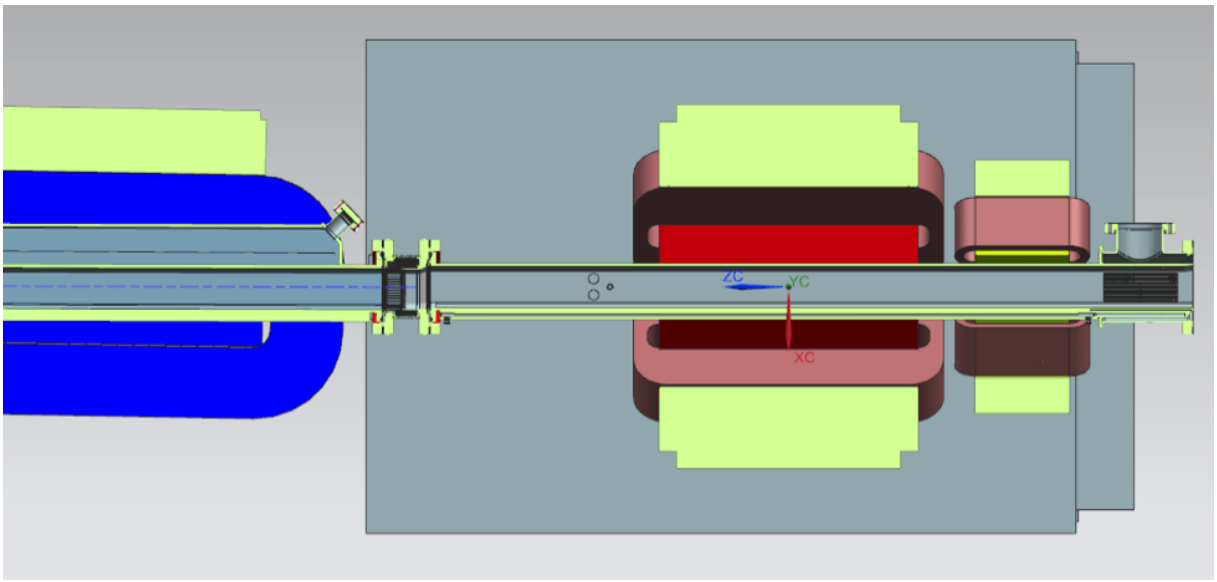

Figure 9.87: CAD cross sectional view of a PEP-II style quadrupole vacuum beam pipe with button BPMs, and slots for ion pumping in the cross. Also show is the connecting RF shielded bellows and dipole vacuum chamber. The vacuum model is being used for initial impedance calculations.

for JLEIC will be inside superconducting magnets and so the cryopumping through those sections will help lower the overall vacuum levels.

9.9.4 Interaction Region

The requirements and design of the interaction regions are being studied as part of the detector design. Simulations will be used to determine what vacuum levels are acceptable for the physics requirements. Simulations will also be done to determine the size and locations of vacuum pumping in the area. This system design has to account for the synchrotron radiation from the final focusing quadrupoles and that fact that the beamline will be a combination of cold beamline through the accelerator magnets and warm beamline through the detectors. The beamlines also have to have be designed for low impedance to limit any trapped modes that could cause beam induced heating in the area.

9.9.5 Other Vacuum Lines

The transport line vacuum from CEBAF to JLEIC will also be based on PEP-II LER and reuse parts as possible. Vacuum requirements will be similar to those needed in the PEP-II LER and CEBAF ARCs and principally pumped by ion pumps. New vacuum chambers made of stainless steel are required.

9.9.6 Insulating Vacuum

Insulating vacuum systems for the SRF cryomodules and superconducting magnet cryostats will be pumped down to better that 1×10^{-4} Torr by turbomolecular pumps prior to cool down. The vacuum pressure will be monitored by cold cathode gauges. Pirani gauges will also be used to

monitor pressure while warm and to establish the pressure prior to cool down. After cool down the insulating vacuum will be isolated and not actively pumped.

9.10 Safety Systems

An additional element of radiation control associated with the intense prompt ionizing radiation discussed above is the process of protecting personnel by keeping beam away from people and people away from beam. Personnel protection from prompt ionizing radiation at Jefferson Lab relies on a reasoned combination of active and passive engineered and administrative safeguards. These safeguards, or Credited Controls, are discussed in the FSAD and identified in the ASE as requirements for operation. The active engineered safeguards are collectively referred to as the Personnel Safety System (PSS). The PSS is a comprehensive, redundant, fail-safe system used to provide employee protection from prompt ionizing radiation. Because of the radiation levels associated with beam transport, personnel are excluded from the accelerator enclosure and experimental halls when they are configured to receive beam.

ODH conditions will be present in the accelerator enclosure. Three are two specific ES&H programs serve as the basis for the Jefferson Lab ODH management program. These requirements apply to each accelerator and any other area where the uncontrolled release of compressed and/or liquefied gasses can result in cryogenic burns and lead to a reduction in the concentration of available oxygen in the work area resulting in an ODH condition. There are potentially serious health effects associated with exposure to decreased oxygen concentrations.

9.10.1 Machine Protection Systems

The MPS is a hardware-based system used to shut off the beam in cases where sustained beam, or energy directly related to the beam, could damage beamline components. MPS subsystems include beam loss monitors (BLM), the beam loss accounting system (BLA), and the fast shutdown system (FSD).

The backbone of the MPS system is the FSD system, which has the ability to shut off the beam from anywhere in the accelerator complex in less than 100 microseconds - short enough to prevent equipment damage. The FSD system aggregates status signals from various sources around the accelerator BLM, BLA, BELS, and several other key systems: vacuum valve status, beam dump cooling systems status, target protection system etc. The FSD interrupts a permission to injector hardware capable of terminating the beam.

BLMs detect increased ionizing radiation levels beam caused by beam steering problems and protect the various beamline components from potential damage or activation by triggering the FSD.

The BLA system consists of beam current cavity monitors and associated electronics. Each cavity generates a signal proportional to the beam intensity. One of these cavities is located at the exit point of each injector and the remaining cavities are located at different beam locations around the accelerator. The BLA system continuously monitors and compares these beam current signals to detect beam losses. There are independent current loss limits for continuous and for pulsed beam, which when exceeded will interrupt beam delivery. Additionally the BLA system can turn off the accelerated beam when the beam current reaches a user-specified threshold. The system triggers the FSD before the accelerator reaches the user-specified threshold. BELS ensures that beam power in the accelerator and in the collider ring does not exceed the designed beam power envelope. This system measures the beam energy and current for each segment of the electron complex and ion complex, combines the results for each complex, and alerts the control room staff

when beam power reaches its operational limit. BELS also has the ability to turn off the beam before operational limits are exceeded if this feature is enabled.

9.10.2 Personnel Safety System

The PSS design follows the Beam Containment and Access Control Policy [40]; it is designed to keep "beam away from people and people away from beam". To achieve a high level of performance, the PSS uses redundant and diverse safety functions that minimize the likelihood of common cause failures. The PSS also includes sensors that independently monitor the status of devices and incorporates logic that compares the monitored status to the command status. PSS component failures are mitigated by the redundant and fail-safe nature of the PSS design, which assures that, in the event of a PSS failure, the accelerator will default to a predetermined (fail-safe) condition.

The PSS has the highest level of configuration management of any engineered system at JLab. Operation, maintenance, and system changes are carefully monitored to ensure high-reliability.

The PSS also serves to integrate numerous safety functions which are not Credited Controls but provide additional layers of protection. For example, the PSS receives trip signals from the Controlled Area Radiation Monitors (CARM). CARMs monitor gamma and neutron levels at locations outside the installed radiation shielding, and through the PSS, terminate the beam if preset thresholds set by the Radiation Control Department (RCD) are exceeded. As well, the PSS will not allow RF power supplies to be energized in an RF zone where waveguides will not hold air pressure. This eliminates RF leakage from waveguides. In addition, the PSS may be used to control access temporarily as a means of limiting access to a hazardous condition, e.g. a High Radiation Area with whole body dose rate in excess of 1000 mrem/hr.

Personnel Safety Systems functions include, but are not limited to:

- Safety Interlock Systems to protect personnel from hazards directly associated with accelerator and accelerator support facility operations, such as:
  - High Power RF Amplifier, Power Supply Control Circuits
  - High Power RF Amplifier, Power Supply ON/OFF Status Readback Circuits
  - High Power RF Amplifier Waveguide Pressure Interlocks
  - Magnet Box Supply, Class II or Higher, Power Supply Low Level Control Circuits
  - Magnet Box Supply, Class II or Higher, Power Supply Contactors
  - Magnet Box Supply, Class II or Higher, Power Supply ON/OFF Status
  - Magnet Power Supplies (Any Class) Power Control Circuits used as a PSS Critical Device
  - Magnet Power Supplies (Any Class) ON/OFF Status Readback Circuits
  - Other Energy Control Devices Interlocked with the Personnel Safety Systems
- Access Control Systems to allow access to and egress from areas controlled for the purpose of containment of hazards directly associated with accelerator and accelerator support facility operations.
- Safety System Operator Control Stations and Equipment
- Public Address Systems used in conjunction with the Personnel Safety Systems
- Video Systems used in conjunction with the Personnel Safety Systems
- Warning and Alarm systems associated with the mission of the Personnel Safety Systems
- All items and contents of items designated under Personnel Safety System Configuration Control (labeled or tagged).

- All interconnections, wiring, cable ways, communication paths, equipment racks, and other support elements associated with the above.

The PSS for JLEIC will be designed as a segmented system. A segmented system allows beam delivery in part of the accelerator complex while other parts of the accelerator complex will be made accessible to personnel. There are eight logical segments of the PSS in CEBAF, and one segment each for the electron transfer line/BSY, ion source and ion LINAC, Booster, Collider Ring Tunnel, and ERL Cooler in JLEIC.

Every access point in a defined PSS segment of the CEBAF and JLEIC enclosure that can be configured to accept beam, including exit stairs, service elevators, and crane hatches, is redundantly monitored and interlocked by the PSS. The PSS is designed to prevent beam transport to a particular segment unless all conditions necessary for transport are satisfied. Any unauthorized access to an interlocked segment will cause the PSS to shut off the beam at the gun and will shut off other potentially hazardous devices within the affected PSS segment in less than one second.

The PSS functions ensure that people cannot enter an area configured to receive beam:

- Shut off of beam (and other devices) when interlocked physical barriers are breached;
- Signal unsafe conditions by means of visual and audible indicators;
- Deter unauthorized entry during Controlled Access by means of magnetically locked physical barriers; and
- Inhibit radiation-generating devices when radiation dose rates in occupied areas exceed Jefferson Lab limits.

The PSS functions ensure that the beam cannot enter an occupied area:

- Three devices using diverse technologies such as a combination of beam blocks and beam steering devices.

The PSS includes features that facilitate "sweeps" of segments to ensure all personnel have exited prior to establishing a configuration that makes beam transport to the segment possible. Once excluded, personnel are prevented from entering these areas when they are configured to receive beam. The PSS also provides for access to already swept areas by a limited number of staff for problem troubleshooting and repair. This entry procedure is referred to as Controlled Access procedure. This allows limited access without the need to repeat a sweep.

Any access to a segment that is configured to accept beam will also cause the PSS to render safe other potentially hazardous devices within a beam enclosure. The PSS serves to integrate numerous safety functions which are not Credited Controls but serve as defense-in-depth. For example, the PSS receives trip signals from the Controlled Area Radiation Monitors (CARM). CARMs monitor gamma and neutron levels at locations beyond the installed shielding, and through the PSS, terminate the beam if preset thresholds set by the Radiation Control Department (RCD) are exceeded. As well, the PSS will not allow RF power supplies to be energized in an RF zone where waveguides will not hold air pressure. This eliminates RF leakage from waveguides. In addition, the PSS may be used to control access temporarily as a means of limiting access to a hazardous condition, e.g. a High Radiation Area with whole body dose rate in excess of 1000 mrem/hr.

9.10.3 Oxygen Deficiency Hazard (ODH) Management

Areas where an ODH may be present are classified and posted according to risk. ODH risks are mitigated by a combination of both passive and active safeguards and administrative controls.

Passive engineered safeguards include lintels and helium removal vents situated in key locations. Administrative controls include training and specialized Personal Protective Equipment (PPE) and monitoring equipment. Active controls include engineered safeguards such as door and ceiling mounted ODH monitors that are part of a monitoring system that results in workplace audible and visual alarms and, in some cases, can initiate high volume air exchange to mitigate ODH conditions. The ODH a monitoring system is also a Credited Controls and share the same level of configuration management as the PSS.

The ODH System functionality is certified every two years by physical testing of the system. ODH monitoring systems in the CEBAF accelerator, Ion Source/LINAC, Booster, and Electron and Ion Colliders are considered Credited Active Engineered Controls.

9.11 Controls

The JLEIC control system covers the entirety of the JLEIC complex, including the ion sources and linac, ion booster, both collider rings, and associated transfer lines.

The architecture of the control system is a traditional three-layer controls system, using EPICS [41] as the main control platform due both to its broad industry support and its centrality to the CEBAF control system [42]. EPICS includes input-output controllers (IOCs), software programs running on front-end computers (FECs) and other network-accessible devices to pass data and messages between high- and low-level controllers. EPICS Channel Access supports TCP/IP for clients to transparently access data in the real-time databases of the distributed IOCs.

The overall facility controls requirements are similar to other facilities of similar size, with on the order of hundreds of thousands of control points throughout the complex. EPICS has demonstrated scalability to this level at other major accelerator installations.

9.11.1 High Level Applications

High-level applications for JLEIC are consistent with those required for operations of other collider complexes. These include:

- Beam loss monitoring and display
- Orbit threading and correction
- Magnet and ramp control
- Injection and extraction setup
- Tune and chromaticity measurement and control
- Beam and bunch current monitoring
- Facility and timeline sequencing
- Real-time and archived stripline, correlation, and analysis displays
- Alarm management and response
- Specialty diagnostic interfaces

The existing CEBAF facility mostly relies on the well-established EPICS Display Manager, with web extensions developed by Jefferson Lab personnel [43]. Specialty applications have also been developed for highly sequenced activities such as qsUtility [44]; these are data- and model-driven through their interfaces to the controls database CED (Section 9.11.2).

Existing expertise in application development at other collider facilities will be leveraged to implement these and other high-level applications for commissioning and operations. These high-level applications will leverage information in the

9.11.2 Database

A large database for element configuration, inventory, controls, and hardware checkout called CED [45] (CEBAF Element Database) has been in use at CEBAF as part of the facility 12 GeV upgrade. This database is used to configure online models [46] using elegant [47], linac energy management and superconducting RF gradient optimization, configure data-driven EPICS operations screens, and track hardware checkout.

The JLEIC element database, JeDi [48], is an extension of CED for the JLEIC complex. JeDi contains facility component and lattice databases for the entirety of the JLEIC accelerator complex. JeDi is used to collect element counts for costing and configuration optimization, and to manage lattices for beam dynamics studies. JeDi will also be used to generate survey information for the overall facility for site planning, and evaluate controls scenarios for synchrotron power supply ramp control.

9.11.3 Timing/Master Reference

Several distributed event and timing links will be implemented for JLEIC:

- RF-synchronous clock (each synchrotron)
- Event link (facility)
- Injection synchronization lines
- Line-synchronized ramping data link (each synchrotron)
- Abort link (each synchrotron)
- Machine and personnel safety links

The RF-synchronous clocks provide timing for distributed instrumentation triggering. These clocks are typically half the frequency of the RF system clock to permit edge encoding. They must encode a high-priority revolution fiducial with less than 100 ps of short term jitter, and permit encoding of up to four other events per turn to permit triggering of diagnostic circular buffer start/stop events, beam aborts, and other activity within the synchrotrons that must be correlated to individual turns.

The event link provides a facility-wide distribution channel for events that are not synchronous with synchrotron RF systems. These include events associated with sequencing the ion complex injection process, synchrotron acceleration ramps, time markers for data archiving, other supercycle events, and non-synchronous triggers for other facility activity. This event link will use commercially available encoders and decoders to improve reliability and decrease cost, with a (constant) reference clock of 10–100 MHz.

Three injection synchronization lines are required to coordinate injection requests from downstream synchrotrons with their upstream injectors. These include a dedicated line from the ion collider ring RF system to the Booster RF to synchronize cogging and beam transfer, and similar lines between the Booster and ion linac, and electron collider ring and CEBAF. Each line should have low jitter and drift (less than 1/10 of the receiving RF bucket), with the highest requirements given by the electron transfer from CEBAF.

Three line-synchronized ramping data links are required, one for each synchrotron. These links are each line-locked, and distribute multiple data frames at 1.44 kHz to waveform generators and diagnostic receivers to coordinate magnet ramping and minimize influence of line fluctuations. These links may also broadcast high-level accelerator parameters (such as $\beta^\star$ and $B\rho$) to control magnet configuration at various stages of a JLEIC cycle.

Three abort links are required, one for each synchrotron. These are each repeated high-frequency token rings, with distributed semaphore stations. Any encoder station may drop its semaphore, stop the token ring carrier, and trigger an immediate beam abort coordinated with the nearest abort gap. Low latency must be ensured to ensure that the token ring distribution is comparable to machine revolution time; this is made somewhat easier by the figure-8 topology of the JLEIC synchrotrons.

Machine and personnel safety systems and links are separated from accelerator control and abort systems, and are described in Chapter 12.

9.11.4 Network

The control system network will be a core redundant design with 100 Gb/s interface to the different aggregation switches. Edge switches are connected to the aggregation switches to provide communication to the devices. Links of 10 Gb/s will be provided to the different devices by the aggregation switches. Links of 40–100 Gb/s will be provided to the different devices by the edge switches.

A 100 Gb/s backbone is selected due to current technical capabilities and the potential large data rate, both for continuous monitoring and for rapid dumps and analysis of abort circular buffers. A higher bandwidth helps to decrease packet transmission latency, improving system stability and operator interface responsiveness. This may also permit some controls network involvement in slow real-time control loops, such as those that are used for slow orbit locks at CEBAF.

REFERENCES

1. Brookhaven National Laboratory, Collider Division, Collider-Accelerator Department (2006). *Configuration Manual for RHIC* (Relativistic Heavy Ion Collider), Retrieved from: `https://www.bnl.gov/cad/accelerator/docs/pdf/RHICConfManual.pdf`
2. Kozub, S, Bogdanov, I., Pokrovsky, V., Seletsky, A., Shcherbakov, P., Shirshov, L., Smirnov, V., Sytnik, V., Tkachenko, L., Zubko, V., Floch, E., Moritz, G., and Mueller, H. (2010), *SIS 300 Dipole Model*, IEEE Transactions on Applied Superconductivity, Vol. 20, No. 3, June 2010 (pp. 200-203)
3. Alessandria, F., Angius, S., Gellomo, G. Fabbricatore, P., Farinon, S., Gambardella, U., Marabotto, R., Musenich, R., Repetto, R., Sorbi, M., Volpini, G., Istituto Nazionale di Fisica Nucleare, Sezione di Genova (2013). *Technical Design Report of the Superconducting Dipole for FAIR SIS300.*SIDS-Pubbliciazioni, Laboratori Nazionali di Frascati. Retrieved from: `https://www.researchgate.net/publication/309007337_Technical_Design_Report_of_the_Superconducting_Dipole_for_fair_SIS300`
4. Kaugerts, J., Moritz, G., Wilson, M. (member, IEEE), Ghosh, A., den Ouden, A., Bogdanov, I., Kozub, S., Shcherbakov, P., Shirshov, L., Tkachenko, L., Richter, D., Verweij, A., Willering, G., Fabbricatore, P, Volpini, G. (2007). *Cable Design for FAIR SIS 300,* IEEE Transactions on Applied Superconductivity, Vol. 17, No. 2, June 2007 (pp. 1477-1480)
5. Kaugerts, J.E., Moritz, G., Muehle, C., Ageev, A., Bogdanov, I., Kozub, S., Shcherbakov, P., Sytnik, V., Tkachenko, L., Zupko, V., Tommasini, D., Wilson, M.N., Hassenzahl, W. (2005). *Design of a 6T, 1T/s Fast-Ramping Synchrotron Magnet for GSI's Planned SIS 300 Accelerator,* IEEE Transactions on Applied Superconductivity, July 2005 (pp 1225-1227). Retrieved from: `https://www.researchgate.net/publication/3312818`

6. Volpini G., Alessandria, F., Bellomo, G., Sorbi, M., Fabbricatore, P., Farinon, S., Musenich, R., Gambardella, U., Kaugerts, J., Moritz, G., Wilson, M.N., (2009). *Low-Loss Wire Design for the DiSCoRaP Dipole,* WAMSDOProceedings, January 2009. Retrieved from: `https://www.researchgate.net/publication/277246308`
7. Jain, A., Brookhaven National Laboratory (2015). *Field Straightness Measurements in Electron Lens Solenoids for RHIC,* 19th International Magnetic Measurement Workshop (IMMW19), June, 2013.
8. Bryzgunov, M., Bubley, A., Cheskidov, V., Fedotov, M., Gosteef, V., Meshkov, O., Panasyuk, V., Parkhomchuk, V., Reva, V., BINP Novosibirsk, Russia, Kamerdzhiev, V., Langenberg, G., FZJ, Julich, Germany (2013). *Compass for Measuring the Magnetic Lines Straightness at the Cooling Section in Vacuum,* Proceedings of COOL2013, Murren, Switzerland, October, 2015.
9. Sattarov, A., Accelerator Technology Corporation (2018). *Micro-Aligned 1 Tesla Solenoid for High-Energy Bunched-Beam Electron Cooling*, DOE, Office of Science, Small Business Innovation Research (SBIR) 2018 Phase I, Release 1 Awards.
10. J. Crumpler, C. Johnson, and T. Hiatt, "PEP-II Magnet Feasibility in the MEIC Electron Collider Ring", JLAB-TN-15-031, 2015.
11. M. Masuzawa *et al.*, "SuperKEKB Main Ring Magnet System", Proccedings of IPAC'16, Busan, Korea, 2016.
12. "Magnet Design of the 150 mm Aperture Low-β Quadrupoles for the High Luminosity LHC", P. Ferracin *et al.*, CERN-ACC-2014-0031.
13. "Status Report of QFFB2", Eric Sun, Presentation dated June 29, 2018.
14. "Design Bounds for SC Accelerator Magnets v2.xlsx", R. Fair, June 13, 2018.
15. "Fast Track Actively Shielded Nb3Sn IR Quadrupole R&D", B. Parker *et al.*, Presented at the 2017 EIC Collaboration Meeting, October, 11, 2017.
16. "Design and Construction of the Magnet Cryostats for the SuperKEKB Interaction Region", Norihito Ohuchi *et al.*, IEE Transaction on Applied superconductivity, Vol. 28, No. 3, April 2018.
17. "3_2_18 SR Background Update for JLEIC", M. Sullivan (SLAC), Talk presented at Jefferson Lab on March 2, 2018.
18. E. Coulinge, J. Burnet, and D. Dujic, "High-Current Low-Voltage Power Supplies for Superconducting Magnets", 19th International Symposium on Power Electronics, (2017)
19. "Proceedings CAS Power Converters". 22 lectures, 460 pages, published as CERN Yellow Report. CERN. Geneva: CERN, 2015.
20. P. Ghosal *et al.*, "Superconducting Magnet Power Supply and Hard Wired Quench Protection at Jefferson Lab for 12 GeV Upgrade", IEEE Transaction on Applied Sc. **27** Issue 8, pages 1-6, (2017).
21. F. Marhauser and R.A. Rimmer, "Progress on the Design of the JLEIC Ion Ring Cavities", JLAB-TN-18-041, Jefferson Lab internal tech note, September 2018.
22. H. Wang *et al.*, "Design, Prototype and Measurement of a Single-cell Deflecting Cavity for the Advanced Photon Source", in Proc PAC'09, Vancouver, Canada, May 2009, paper WE5PF059.
23. T. Mastoridis *et al.*, "Coupled-Bunch Instabilities Due to Fundamental Cavity Impedance", CERN-ACC-NOTE-2017-0009, Feb 2017.
24. B. Palmer, SLAC Report No. SLAC-PUB-4707, 1988.
25. Y-P. Sun *et al.*, Phys. Rev. Accel. Beams **12**, 101002 (2009).
26. G. Apollinari *et al.*, "High Luminosity Large Hadron Collider HL-LHC", CERN Yellow Report, p. 19, May, 2017.
27. S.U. De Silva, H. Park, and J.R. Delayen, in Proc. IPAC 2016, Busan, Korea (2016), p. 2469.
28. K. Akai and Y. Funakoshi. in Proc. EPAC 1996, Barcelona, Spain (1996), p. 2118.
29. J.. Barranco Garcia *et al.*, Phys. Rev. Accel. Beams **19**, 101003 (2016).
30. S.U. De Silva, H. Park, J.R. Delayen, in Proc. IPAC 2017, Copenhagen, Denmark (2017), p. 1177.

31. G. Huang *et al.*, "LLRF Control for SPXAPS Demonstration Experiment", in *Proc. of IPAC'12*, paper TH-PPC089, pp. 3491-3, 2012.
32. P. McIntosh *et al.*, "PEP-II RF System Operation and Performance", Proc. of EPAC'04.
33. D. Teytelman, "Beam Loading Compensation for Super B-factories", Proc. of PAC'05.
34. J. Byrd *et al.*, Phys Rev ST Accel. Beams 5, 092001 (2002).
35. S. Abeyratne *et al.*, "MEIC Design Summary", January 2015.
36. "Science Requirements and Conceptual design for a Polarized Medium Energy Electron-Ion Collider at Jefferson Lab", Various authors, 2012, pages 51–52.
37. "Vacuum System Design for the PEP-II B Factory High-Energy Ring", C. Perkins *et al.*, SLAC-PUP-6546, June 1994.
38. "Vacuum Performance and Beam Life Time in the PEP II Storage Rings", U. Wienands, SLAC-PUP-9447, August 2002.
39. "The AGS Booster Vacuum Systems", H.C. Hseuh, Presented at XI Intl. Vacuum Congress, Cologne, F.R. Germany, September 25-29, 1989.
40. Jefferson Lab, "Thomas Jefferson National Accelerator Facility Beam Containment and Access Control Policy", `https://jlabdoc.jlab.org/docushare/dsweb/Get/Document-111187/Beam%20Containment%20and%20Access%20Control%20Policy%20Rev1.pdf`, December 2015
41. `http://www.aps.anl.gov/epics/index.php`
42. `https://www.jlab.org/accel/documents/epics_doc2.html`
43. `https://github.com/JeffersonLab/wedm`
44. D. Turner, "Software Tools for Emittance Measurement and Matching in 12 GeV CEBAF", in Proc. IPAC'16, Busan, Korea, paper WEPOR053, 2016, `doi:10.18429/JACoW-IPAC2016-WEPOR053`
45. T. Larrieu *et al.*, "The CEBAF Element Database and Related Operational Software", in Proc. IPAC'15, Richmond, Virginia, paper MOPWI045, 2015, `doi:10.18429/JACoW-IPAC2015-MOPWI045`.
46. D. Turner, "eDT and Model-Based Configuration of 12 GeV CEBAF", in Proc. IPAC'15, Richmond, Virginia, paper MOPWI046, 2015, `doi:10.18429/JACoW-IPAC2015-MOPWI046`.
47. M. Borland, "elegant: A Flexible SDDS-Compliant Code for Accelerator Simulation", Advanced Photon Source LS-287, September 2000.
48. `https://jed.acc.jlab.org` (internal).

CHAPTER 10

CONVENTIONAL FACILITIES

10.1 Introduction

Jefferson Science Associates (JSA) manages the Thomas Jefferson National Accelerator Facility (Jefferson Lab) under contract with the United States Department of Energy (DOE). Jefferson Lab is a low-hazard, nuclear physics accelerator facility chartered to conduct unclassified research into the fundamental nature of matter. Jefferson Lab is located on a 169-acre federal reservation in Newport News, Virginia and consists of 66 DOE-owned buildings, plus roads and utilities.

Jefferson Lab is undergoing development of conceptual plans for a new electron-ion collider (EIC) that will greatly expand physics research capabilities. Development of the conceptual plans is the initial phase to be reviewed and considered by DOE. Upon final determination by the DOE, funding and construction of the EIC will be awarded to the best-suited proponent. If awarded and constructed, the EIC will fulfill one of the high-priority recommendations contained in the 2015 Long Range Plan for Nuclear Science (titled: Reaching for the Horizon). The 2015 Long Range Plan was developed by the Nuclear Science Advisory Committee (NSAC) which was charged by the DOE Office of Science and the National Science Foundation Directorate of Mathematical and Physical Sciences to determine opportunities, assess priorities, and provide recommendations for the coordinated advancement of U.S. nuclear science programs over the next decade.

10.1.1 Setting

Jefferson Lab is located in Newport News, Virginia. Newport News is bounded on the east by York County and the City of Hampton; on the north by James City County and the City of Williamsburg; on the west by the James River; and, on the south by the Hampton Roads waterway. Jefferson Lab is located just east of Jefferson Avenue and is less than one mile to the west of Interstate 64. The

site is just south of Oyster Point Road and just north of Middle Ground/City Center Boulevard. Two schools and railroad tracks serving the local rail system are located within one mile of the site. Newport News-Williamsburg International Airport is located two miles to the north.

The weather of the Jefferson Lab site is affected by the nearby marine environment. The Chesapeake Bay moderates the climate and weather of the site, with land-sea breezes dominating the wind patterns during much of the year: The mean monthly temperature for the Newport News area ranges from -0.1° C (32° F) in January to 32° C (90° F) in July. The record low temperature is -19° C (-3° F) and the record high is 40° C (105° F). Note that temperature values are based on information from the NOAA National Environmental Satellite, Data, and Information Service (National Center for Environmental Information) compiled from 2007–2016.[1]

10.1.1.1 Current Configuration The site is composed of 6 parcels of land totalling approximately 99 acres comprised primarily of undeveloped and wooded areas. There are some structures and asphalt paved parking areas on site which are used by the Thomas Jefferson National Accelerator Facility and the City of Newport News Service Center for Operations and Transportation (SCOT Center). Access to the site can be gained from Jefferson Avenue, a six-lane divided highway, and Hogan Drive, a two-lane paved road.

The area north of the subject site consists of other parts of the SCOT Center, and a commercial development called The Tech Center Marketplace. The SCOT Center is currently being redeveloped into a large research park. Canon Boulevard is east of the subject site which is a four-lane asphalt paved roadway. The Canon Virginia Campus is located across Canon Boulevard from the site. Several businesses are located along Jefferson Avenue west of the site. South of the site is the underground Jefferson Lab Continuous Electron Beam Accelerator (CEBAF). Access to this area is controlled. There are four existing structures, and associated hardscape/parking areas, along the northern border of the proposed JLEIC site.

Ground surface elevations vary by approximately 10 feet across the site, with an average elevation of approximately 34.5 feet above mean sea level.

10.1.1.2 Area Geology The geologic stratigraphy generally consists of recent sediments and man-placed fill at the surface underlain by fluvial and estuarine sand, clay, organic soil, and peat of the Shirley Formation which is further underlain by the Yorktown Formation consisting of fossiliferous marine silty fine sand and cross-bedded, bio-fragmental sand. The position of the groundwater table was measured at multiple locations and was encountered at depths below the ground surface ranging from about five (5) to eight (8) feet corresponding to Elevations 25 to 37 feet. The new EIC tunnel would be sited within the Yorktown Formation. The anticipated conditions of the various stratified formations are within the range of construction conditions typically encountered, and can be handled by available construction methods.

10.1.1.3 Groundwater The accelerators at Jefferson Lab, CEBAF, and the LERF, were designed and constructed below ground with self-contained beam dump systems that absorb ionizing radiation and careful attention to groundwater shielding from prompt ionizing radiation due to accelerator operations. The EIC will have a similar design to shield groundwater from radiation exposure.

Baseline groundwater quality for the Jefferson Lab Accelerator Site has been monitored under the direction of Jefferson Lab's radiation control staff since 1989 using a series of monitoring wells. These monitoring wells were positioned along the groundwater gradient at three different distances from the CEBAF accelerator enclosure (tunnel and experimental halls). The wells closest

[1] https://www.nesdis.noaa.gov/

to the accelerator enclosure are designated "A-ring" wells and "C-ring" wells are farthest from the enclosure. These wells were initially installed in 1989 in accordance with a Virginia Pollution Abatement(VPA) permit (VPAO1001) to provide a pre-construction water quality baseline on the distribution of groundwater constituents. Background data through 1995 were compiled for pH, conductivity, hardness, trace metals, and radionuclides. These data are documented in the VPA permit modification request and addendum 5.

The concentrations of radioactive pollutants and limits to the radiological effluent water discharges in the environment at Jefferson Lab are governed by the Virginia Pollutant Discharge Elimination System (VPDES) and the Hampton Roads Sanitation District (HRSD). VPDES permit #VA0089320 addresses groundwater quality, both in-situ (well monitoring) and related to discharges of groundwater to the surface (end station dewatering). The de-facto limit for the surface discharges is the EPA drinking water standard (at the point of dewatering sump discharge). HRSD permit #0117 addresses discharges to the sanitary sewer. The primary limit is 5 Ci of H-3 and 1 Ci of all other gamma emitting nucleides. In addition, a monthly average H-3 concentration limit of 0.1 uCi/ml applies to these discharges, not to exceed 10 mCi/day.

The details of the Jefferson Lab's infrastructure, and ground water monitoring procedures, including ALARA action limits may be found in Ref. [1]

The existing monitoring system will be extended to cover the the new JLEIC facility; new wells will be installed around the site to monitor for accelerator produced radionuclides in ground water and the VPDES and HRSD permits will be modified to establish requirements for JLEIC operation.

check

10.1.1.4 Site Plan The new Jefferson Laboratory Electron Ion Collider (EIC) is proposed to be located in the northeastern portion of the current Jefferson Lab campus (Figure 10.1). The EIC is proposed as a ring-ring collider in which the colliding electron and ion beams are stored in two figure-8 shaped collider rings covering approximately 94 acres, requiring approximately 3 km of tunnel. The existing CEBAF will be integrated with the collider and used as a full-energy electron injector. No further upgrade of the CEBAF for energy, beam current, or polarization is anticipated.

10.1.1.5 Roads and Access The present access road from Jefferson Avenue, called Hogan Drive, will continue to serve as the main entrance to the existing CEBAF and proposed EIC. A new gatehouse entry is proposed along Hadron Drive to provide secure access to the fenced collider campus. This restricted technical entrance, for use by scientists, engineers, technicians and service vehicles, will be identified with appropriate signs on Jefferson Avenue and on the internal road system. Due to the size of the collider ring, Hadron Drive may need to be relocated to the west in some areas. Within the fenced collider area, an internal road network provides access to all facilities by means of a perimeter road, access roads and service drives, and vehicle parking at each building

10.1.2 Tunnels

The existing oval-shaped CEBAF accelerator tunnel was constructed from 1987 through 1991 and is approximately 4,175 feet long. The tunnel was constructed with cut and cover technology. The tunnel cross section is 10 feet x 13.5 feet (inside height and width) with an approximately 2' thick bottom and top slab and 1.75' thick walls. The concrete structure is waterproof and constructed on a mud slab with a finished floor elevation of approximately 11.2 feet based on the Jefferson Lab datum. This structure is covered by approximately 14 feet of earth and when combined with the concrete walls, radiation protection is provided. The bottom of the trench is geologically located over the Yorktown Formation.

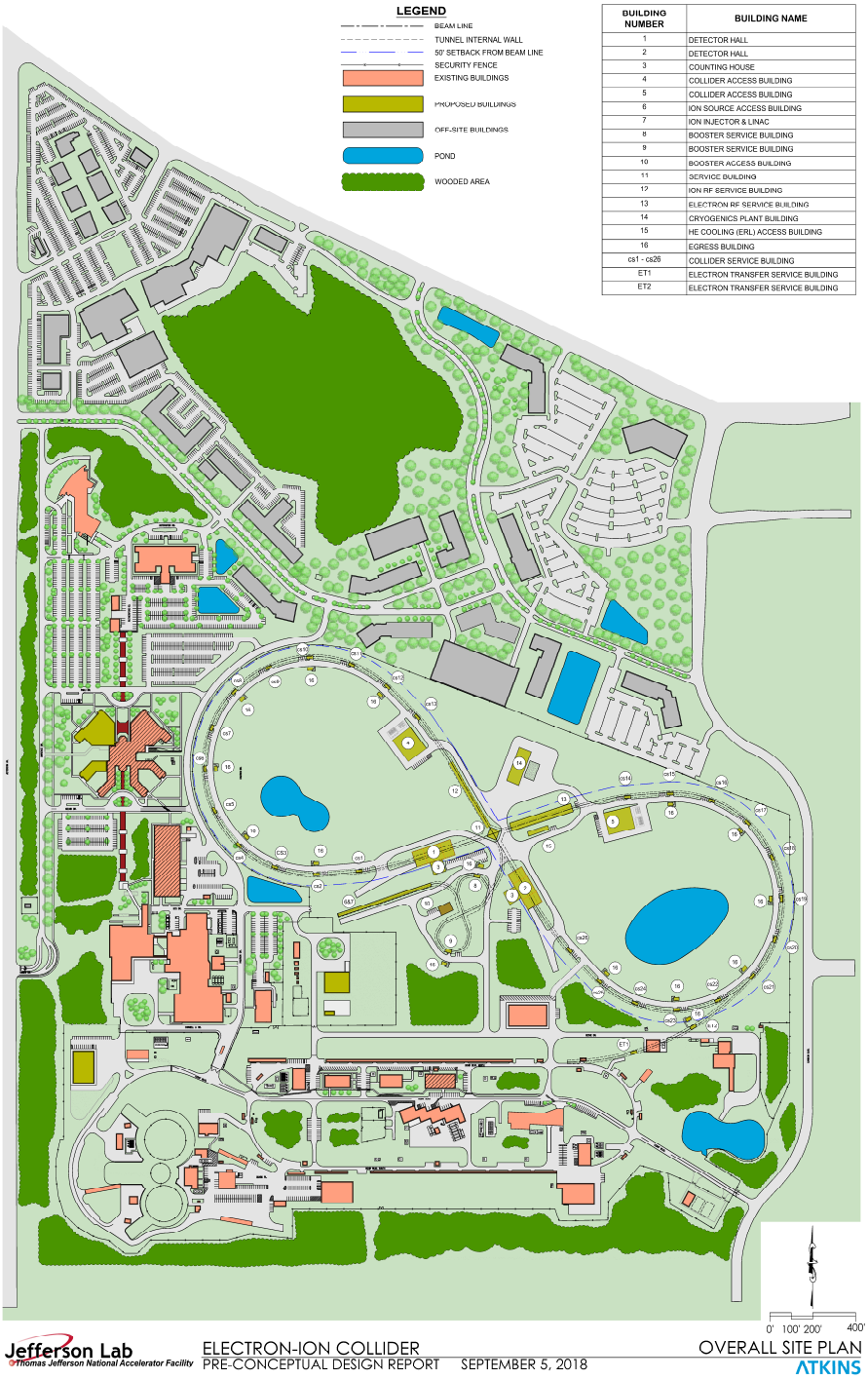

Figure 10.1: JLEIC site plan on Jefferson Lab site.

The new EIC tunnel consists of multiple tunnel structures, including 1) collider, 2) ion booster, 3) ion transfer, 4) ion source/injector, 5) electron transfer 6) helium cooler energy recovery LINAC. All the tunnel sections have the same top of foundation elevation, although they vary in width and height. The entirety of the tunnel is buried and rests on soil-supported mat foundations.

The new tunnel can either be cast-in-place concrete, precast concrete or a combination of both. It could be a viable option to construct the tunnel out of precast concrete. This option could reduce the overall excavation time by limiting the cut, decrease dewatering time and reduce the overall project timeline, compared to cast-in-place concrete work. Drawbacks would include transportation cost, issues with tunnel curvature and means and methods of installation

10.1.3 Buildings and Structures

Similar to the existing CEBAF accelerator, a number buildings and structures, both above and below grade, will intersect with the various tunnel structures of the electron-ion collider. The new buildings and structures include experimental, support, service and miscellaneous facilities.

The experimental facilities include the detector halls which house the detector equipment, and a contiguous counting house which will contain space for data collection. These below grade concrete structures are built to shield radiation. The counting house will be a one-story above-grade structure built in close proximity to the detector hall.

The support facilities include the cryogenics plant, the access buildings, the Ion Injector and Ion LINAC. These above-grade structures produce environmental conditions that are essential to the science, provide personnel and equipment access to the tunnel or allow access to the scientific equipment. These structures generally include conveying equipment such as bridge cranes or elevators.

The service buildings house the power supplies, instrumentation, control racks and other equipment that connect with the below-grade tunnel equipment. These above-grade structures also provide periodic access to the power and data conduits that interconnect the EIC.

The miscellaneous structures include the egress buildings and the gatehouse.

All the above grade structures are proposed as light steel-framed structures with a deep rib, metal panel exterior enclosure. The design of the exterior enclosure will conform with the architectural theme of the existing CEBAF.

10.2 Site Preparation and Development

10.2.1 Site Condition Surveys

The proposed EIC site was surveyed in December 2015 and a record set of documents was developed dated January 5, 2016. The survey shows that the land is relatively flat. The average elevation is about 35 feet above mean sea level and the vertical distance between the highest point and the lowest point is approximately 10 feet.

Although the site is primarily wooded or undeveloped, there are a number of existing structures on the site including a one-story residence facility for CEBAF visiting scientists and a one-story metal warehouse as well as two (2) one story block buildings at the SCOT Center. Hardscape and parking areas are associated with each structure.

10.2.2 Environmental Site Assessment

A Preliminary Environmental Evaluation and Environmental Checklist dated June 15, 2017, was prepared by a subcontractor in accordance with 10 CFR Part 1021 of the National Environmental Policy Act (NEPA) and DOE Quality Assurance Plan and Procedures for the proposed project. The Environmental Compliance Checklist was prepared for submission to the DOE NEPA Compliance Officer. This subcontractor also prepared the federal information consistency package for Coastal Zone Consistency for submission by Jefferson Lab's DOE Site Office to Virginia Department of Environmental Quality (DEQ).

This preliminary environmental document was prepared to present information and a preliminary analysis of the project that can be used as a foundation for a future environmental analysis if an Environmental Assessment (EA) is later deemed necessary. The document was developed pursuant to Section 102 of the National Environmental Policy Act (NEPA) of 1969 (Public Law 91-190), as implemented by regulations promulgated by the President's Council on Environmental Quality (CEQ) [40 Code of Federal Regulations (CFR), Parts 1500—1508, November 1978 and changes] and DOE NEPA Implementing Procedures (10 CFR Part 1021, April 1992 and changes) as much as possible with existing information in hand.

The provided impact analysis is balanced around (1) the temporary impacts due to construction actions on surface water, air quality, and noise concerns; (2) the development, fabrication, and operation activities related to EIC and its associated actions, and the potential for radiological impacts to the public and workers and the potential for activation in the surrounding (on and off site) environment during operations; and, (3) the ultimate changes in site land and resource use due to these actions, including effects on terrestrial resources, stormwater management, and from building operations.

Based on this preliminary evaluation, there is little potential for adverse impacts from any of the following focus areas: long-term non-radiological air quality, floodplains, or community resources, including cultural and socioeconomic effects.

The proposed action is expected to have moderate to minor temporary environmental impacts due to land disturbance during construction of the EIC; moderate to minor impacts to groundwater from EIC operation and resource usage; and minor additional impacts due to long-term land use, traffic, and building usage. In addition, the action is expected to have temporary minor impacts due to noise, non-radiological air quality, and stormwater quality during construction. Potentially negligible to no impacts are expected on ecology, floodplain and threatened/endangered species during long term facility use.

The Jefferson Lab has developed and implemented numerous procedures and policies to assure the protection of the surrounding environment and neighboring areas, protect their workers, and handle and dispose of incidental low level radioactive emissions. The lab has demonstrated competency and diligence in monitoring and maintaining strict adherence to the policies and regulations. The proposed EIC is anticipated to be constructed and operated with minimal impacts to the environment but with great gains in the areas of research and development. With the existing policies, procedures and guidelines in place, strict adherence to regulations from federal, state and local agencies, and development of further project-specific guidelines as design progresses, the EIC is anticipated to have no significant impact on the parameters examined in this preliminary document.

The Phase I Environmental Site Assessment prepared by Environmental Specialties Group (ESG), dated March 10, 2016 identified several unknown areas of potential environmental concern located in the proposed Jefferson Labs project expansion area. These unknown areas included: earthen mounds, a suspect cistern, buried utilities and abandoned steam tunnels at the SCOT

Center. A Phase I Advanced Environmental Site Assessment was conducted to investigate the unknown areas to determine if they could be an impediment to future construction. ESG conducted a records search of potential documents that were not readily available for review during the Phase I Environmental Site Assessment process. ESG also researched engineering plans and contract documents at the SCOT Center and at the City of Newport News to locate documents pertaining to the above listed areas of concern. A Phase I Supplemental Package and report of findings was prepared by ESG dated February 7, 2017 and was included in the discussion of the findings in the Preliminary NEPA Document.

10.2.3 Stormwater Management

Soils: The current condition of the proposed site which will be disturbed by construction of the facility is open cleared or wooded land. In general, the soils are poorly drained. Best Management Practices (BMP) should be installed with underdrains to drain water from the systems. Soil infiltration testing should be performed to obtain site specific infiltration rates for use in the design of BMPs.

Existing Conditions: There are approximately 11 inflow points where drainage from adjacent land enters the site, and combines with the runoff from the site itself. The existing site drains in the southeast direction through two series of man-made ditches, one located to the north and one to the south, that discharge through two sets of culverts under Canon Boulevard. After crossing the right-of-way, the drainage from the two ditches combines and flows into the pond on the Canon property, then into Brick Kiln Creek, and eventually into the Big Bethel Reservoir. The reservoir feeds the Northwest Branch Back River, which discharges into the Chesapeake Bay. An overall drainage area to the site is included in Appendix A.

The estimated limits of disturbance for the project is 71.6 acres. A majority of the area is either wooded or grass with some existing building and associated impervious surfaces in the northwest portion of the site. The existing site conditions are summarized in Table 2-2.

Proposed Conditions: In general, the existing hydrology of the site will be maintained with discharge through the existing culverts under Canon Boulevard. The ditches will need to be reconfigured during design to reroute the water through the site. Natural stream techniques should be used when designing the conveyance system to enhance water quality and provide an aesthetically pleasing result. The use of storm drainage pipes will be minimized and culverts will be installed to convey water under roadways as necessary.

Due to the extent of construction that will be occurring, it is anticipated that most of the development area will be disturbed. The construction will include:

- the cut and cover tunnel; the necessary excavation of the side slopes;
- the buildings;
- roads and parking lots;
- the stockpiling and storage requirements;
- and erosion and sedimentation basins.

Due to the anticipated construction methodologies, the entire area within the tunnel perimeter is assumed to be disturbed. The development area is considered as one drainage area as the flow from the two sets of culverts merge just downstream of the property.

Stormwater Quality and Quantity: A SWCGP must be obtained from VA DEQ for the proposed construction. The project will be required to comply with the following regulations:

- Virginia Stormwater Management Act

- Virginia Stormwater Management Program (VSMP) Regulation (9VAC25-870)
- General VPDES Permit for Discharges of Stormwater from Construction Activities (9VAC25-880)
- Virginia Erosion and Sediment Control Law
- Virginia Erosion and Sediment Control Regulations (9VAC25-840)

In addition to the State requirements, as a federal facility, Jefferson Lab will also be required to comply with Section 438 of the Energy Independence and Security Act (EISA 438). EISA 438 was enacted by Congress to "require federal agencies to reduce stormwater runoff from federal development projects to protect water resources".

Proposed BMPs: In the stormwater management concept, it was assumed that the 32.7 acres of pervious area internal to the collider loop would drain to the proposed constructed wetland. Calculations also included restoring 21 of those acres to open space rather than managed turf. The open space is self-crediting as it does not result in an additional pollutant load over the baseline level, so no treatment of that area is considered in the VRRM Compliance Spreadsheet. Treatment was calculated for 22 acres that were assumed to be managed turf that would drain to the proposed constructed wetland. The open space area will also help to reduce the runoff volume from the site as it allows for more evapotranspiration of runoff.

10.2.4 Site Development

10.2.4.1 Vehicular Circulation A secure perimeter road that follows the figure-8 shape of the tunnel will provide access to all the buildings by means of service drives and parking areas. This road will be accessed via a gatehouse on a new vehicular connection to Hadron Drive. The perimeter road will also connect with the existing CEBAF road system. several of the buildings will require truck access including the detector halls, access buildings and cryogenics plant.

10.2.4.2 Parking Parking areas will be distributed throughout the EIC complex, adjacent each of the above grade structures.

10.2.4.3 Pedestrian Circulation Walks, bicycle paths and jogging trails will be provided to minimize the on-site usage of automobiles.

10.2.4.4 Security and Fencing The secure areas of the site will be enclosed by a chain link security fence that is 6 feet high. Controlled access gate will be provided at the Gate House.

10.2.4.5 Landscaping Disturbed areas that are not paved, or otherwise covered, will be landscaped with shrubs, trees, grass or other types of ground cover. Landscape vegetation will be compatible with local conditions to minimize the excess use of either fertilizers or water. Where essential, sprinkler devices will be used to establish and maintain vegetation. Ground cover will be planted on the earth berms to provide a maintenance-free slope stabilization.

10.3 Utilities Design Criteria

10.3.1 Potable Water

10.3.1.1 Summary The water distribution system will distribute water to the new JLEIC facilities for use as a potable water supply, a cooling water system for industrial use and as fire protection.

The largest demand and driving component for the pipe sizes is fire protection. Potable water is obtained from the Newport News Water works by way of a new connection to their transmission line. At this time, there is no anticipated connection between the existing CEBAF facility and the new JLEIC system. The connection will be made at a 24" Water works transmission main, located in an easement approximately 1,200 feet to the south of the new development area. This is the same line currently used for one of the existing Jefferson Lab connections. The new connection will parallel this existing connection.

Potable water is to be provided to all buildings with sanitary facilities and/or eye wash stations. Eye wash stations are located in the Cryogenics building, the Low Conductivity Water building, and at all cooling towers. All facilities will be served by fire suppression systems and shall be "Ordinary Hazard Group 1 or 2" . Fire hydrants have been located a minimum 50 feet from any building and all building exteriors are within 350 feet of the nearest fire hydrant. Make-up water needs to be available for the cooling tower systems, but in the interest of reducing water use, secondary sources will be explored during the design to include water from stored rainfall runoff.

10.3.1.2 Assumptions The materials of construction will be similar to the existing piping, fittings and valves. Ductile iron will be the material for the distribution pipe. The pipe will be cement lined and wrapped with Polywrap for corrosion control due to the aggressive soil conditions commonly found at the site.

The materials of construction, standards, and codes adhere to the City of Newport News Waterworks Distribution standards. Jefferson Lab does not have a specific standard for their water systems. The requirements for the water distribution systems were provided by Jefferson Lab are as follows:

- The system will be connected directly to the Newport News Water works mains with a new and separate connection point.
- The new system will be metered separately from the existing system, with no interconnection.
- Reduced Pressure Zone (RPZ) type backflow prevention will be provided just after the main water meter pit.
- The main water distribution supply line serving the tunnels will be a 12-inch line. The minimum size line on a loop will be an 8-inch line, with 6-inch service lines for the fire hydrants. Fire service lines to the buildings will be sized according to the demands of each particular building and the minimum potable service lines will be 2 inches.
- All underground piping will be provided with a tracer wire and warning tape for both metallic and non-metallic. Trace wire shall be 10-gauge solid copper and trace wire shall terminate at both ends of pipe accessible in a structure or at the service riser inside the structure.
- The demand for potable water is based on a full-time staff of approximately 60 people.
- Fusion epoxy coated resilient wedge gate type isolation valves will be provided so all buildings can be isolated for maintenance. All valves shall be provided with a cast iron valve box.
- FDCs will be free standing and not connected to buildings.
- Fire pumps are not desired, but if required, only diesel pumps will be used.
- All fire suppression systems will be water based systems, unless specific building requirement dictate otherwise.
- Double interlocked pre-action type systems are necessary in the beam tunnel.
- Conventional wet pipe systems may be used in all above ground offices and equipment sheds.

10.3.1.3 Design Requirements Domestic and industrial water demands have been determined from the sanitary sewer flow rates provided by Jefferson Lab and account for both the domestic and industrial uses for the site. Monthly sanitary sewer flow rates were provided for the months of July 2015 through June 2016. Based on the maximum monthly flow, a peak sewer flow rate of 517 gpm was determined, based on an 8-hour typical working day and a peaking factor of 4. Fire flow demands were determined based on the existing facilities. The largest single fire flow demand for an existing facility is 1,341 gpm for the MCC building. This same building will be used for the new test facility and water for fire service will be provided by the existing system. The second largest fire flow demand is 886 gpm for one of the general-purpose buildings. This is the fire flow demand used in this preliminary study. Adding both the domestic/industrial use with the fire flow demand, a total demand of 1403 gpm will be used for the assessment of the water service for the proposed facilities. Preliminary calculations have been run to determine the water main size and ensure that there will be adequate pressure for fire demands.

The water distribution system consists of approximately 3,600 feet of 12-inch water main that runs from the Newport News Water Works connection, through the new site and in relatively close proximity to the major facilities and approximately 6150 feet of 8-inch water main that runs around the remaining length of the tunnel alignment. The 8-inch line will primarily provide potable water and fire service to the egress buildings. The current layout includes 22 fire hydrants. 15 Isolation valves have been assumed to meet the DOE requirements.

10.3.2 Sanitary Sewer

10.3.2.1 Summary The Sanitary sewerage collection system will collect the sanitary sewage, condensate, ground water infiltration that penetrates the tunnel, and cooling water blowdown from the buildings in the new facility. The system will be a new system and will have no contributions of flow from the existing CEBAF facility. The system will consist of a gravity system with a centrally located pump station to pump the sewage through a force main to an existing manhole located at the intersection of Lawrence Drive and Kelvin Drive. Sanitary facilities are to be provided in all buildings which have full time or part time staff. In addition, sanitary facilities are provided at the ground level for all tunnel egress facilities around the tunnel alignment.

The gravity collection system will consist of approximately 6,900 feet of gravity mains and 36 manholes. The gravity system will generally follow the centerline of the figure eight roadway layout, branching out into all four directions from the central crossing point. The pump station will then transport the sewage through approximately 2580 feet of 6-inch force main.

10.3.2.2 Assumptions The materials of construction will be similar to the existing piping, manholes, laterals and appurtenances. PVC pipe will be used for the gravity sewer collection piping (appropriate pipe specifications to be developed during design). Ductile Iron pipe will be used for the force main. Ductile Iron pipe will be minimum Thickness Class 52 with a corrosion resistant interior lining and standard bituminous exterior with Polywrap. All pipe and fittings will be lined with double cement lining and seal coat or a ceramic epoxy lining.

The materials of construction, standards and codes will be the Hampton Roads Planning District Commission, Regional Construction Standards (RCS), with the City of Newport News Special Provisions to these RCS, Virginia Department of Health and the Jefferson Lab standards. The requirements for the sanitary sewerage collection system were provided by Jefferson Lab as follows:

1. The system will be connected directly to the existing internal system and not directly to the Newport News' or Hampton Roads Sanitation District's system. It is to be assumed that the existing system has capacity.

2. A flow acceptance letter will be required from Newport News or HRSD.
3. The collection system serving the tunnels will be 8 inch and 12 inch gravity mains. The minimum size gravity main will be an 8-inch line. The minimum building service lateral will be a 4-inch line.
4. The Sanitary sewage flow is based on a full-time staff of approximately 60 people.
5. Jefferson Lab wants duplex pump station(s).
6. All underground piping will be provided with a tracer wire and warning tape whether metallic or non-metallic. Trace wire shall be 10-gauge solid copper and trace wire shall terminate at both ends of pipe accessible in a structure or at the service riser inside the structure.

10.3.2.3 Design Requirements Sanitary sewer flows are based on the flow rates generated at the existing Jefferson Lab site. Monthly sewer flows were provided for the year from July 2015 through June 2016. The month with the greatest flow, November 2015, was used to predict the average and peak flow rates. A monthly flow of 1,860,579 gallons was recorded for this month. This flow rate was then divided by the 30, for the days of the month, divided by 3, to represent the concentrated flows generated in the typical 8 working hours of a 24-hour day and then a peaking factor of 4 was applied. The average and peak flow rates calculated were 129 gpm and 517 gpm, respectively.

The sanitary sewer collection and transport system will consist of approximately 6,900 feet of 8 and 12-inch PVC gravity mains with 36 manholes. The gravity system will transport the sewage to a centrally located submersible wastewater pump station where the sewage will then be pumped and transported through 2,580 feet of 6-inch ductile iron force main to a gravity sewer manhole located on the existing facility, at the intersection of Lawrence Drive and Kelvin Drive. Service laterals will be 4 inches minimum in size with 6-inch laterals from some of the larger facilities.

10.3.3 Electrical Power

10.3.3.1 Summary The primary power distribution system will deliver electricity from a central metering point and disperse it to the various buildings. Primary distribution will be conducted through direct-buried, underground cables to liquid-filled, pad-mounted transformers situated near the serviced buildings. Distribution will be done in loops to service the various areas of the JLEIC. The Cryogenics Plant building will be served by two separate 100% Dominion Virginia Power (DVP) sources to allow for maintenance. Equipment in the Cryogenics Plant building will be split between the two services for survivability in the event that one source on either the primary or secondary side is lost.

10.3.3.2 Assumptions Based on meetings with Dominion Virginia Power (DVP), the primary distribution system and the transformers will be owned and maintained by DVP.

10.3.3.3 Design Requirements The conventional power requirements for the buildings are minimal in comparison to the technical (process or science) loads. For planning purposes, lighting loads were taken at 0.25W/gsf for tunnels, 0.7W/gsf for plant areas such as LCW and He, and 1.0W/gsf for areas for science such as the detection halls, which is typical for performance of LED type fixtures. For planning purposes, the conventional building receptacle loads were taken at 0.25W/gsf for tunnels, 0.7W/gsf for plant areas such as LCW and He, and 3.5W/gsf for areas for science such as the detection halls. Requirements for technical power are taken from the spreadsheet provided by the Lab.

10.3.3.4 Ancillary Requirements Standby generators, associated diesel fuel storage, standby power distribution, and controls will be provided as part of the building conventional construction or the specific science requirements. Standby power distribution will be accomplished by various branch circuits which loop into each building to pick up standby loads.

10.3.3.5 Automatic Transfer Switches Generator systems and associated automatic transfer switches (ATS) shall be provided in each building as part of the standby power distribution system for the conventional facilities construction project.

10.3.4 Communications

10.3.4.1 Summary The communications system has two primary goals: connect the various buildings together for voice, basic data, security, fire alarm, mechanical controls, machine controls, and similar IP systems; and provide a pathway for data collection from the target halls to the counting house, and from the counting house to the data center where the data will be stored and analyzed.

10.3.4.2 Assumptions The largest quantities of data will need to move from the target halls to the counting house, and from the counting house to the data center. Two independent pathways for data will be provided to each designated critical building.

10.3.4.3 Design Requirements The new data system will tie into existing manholes. Sufficient space is available for the addition of new cables. Because of the distances between buildings, single mode fiber will be used. 72 or 96 strands (36 or 48 pair) will connect the target halls to the counting house and the Machine Control Center (MCC), Building 85. 24 strands (12 pair) will connect to other buildings for voice (phone), data, fire alarm, security, video and similar functions.

10.3.5 Low Conductivity Water (LCW)

10.3.5.1 Summary The Low Conductivity Water (LCW) system will provide cooling water to LINAC power supplies, beam magnets and RF cavities located within the new Collider Facility. The cooling water chemistry can have a detrimental effect on the performance of beam magnets, RF cavities, and electronic devices, therefore, the cooling water must be continually treated to maintain the conditions specified by Jefferson Lab.

The LCW will also be cooled to maintain a maximum supply temperature of 95° F. Cooling of the LCW water will be provided by shell and tube heat exchangers using an open condenser water system for heat transfer from the LCW. The open condenser water system will include cooling towers for heat rejection, base mounted horizontal split case circulating pumps, and cooling tower water treatment systems.

LCW water and open condenser water central systems will be provided with N+1 equipment redundancy.

Each Collider Access Building will be provided with:

- A dedicated system will be provided for cooling above grade power supplies and above grade system components.
- A dedicated system will be provided for cooling below grade magnets, cavities and associated components.
- Each of the systems will be provided with an independent pumping and piping distribution system.

The approximate total LCW recirculation rate required is estimated by Jefferson Lab to be 20,000 GPM with a system ΔT=12° F, representing an approximate side-stream treatment flow rate of 2,000 GPM or 2.88 MGD (based on the assumption that 10% of LCW flow is treated continuously).

The makeup water, will be obtained from the on-site potable water distribution system. The initial filling of the system will be provided by the contractor to meet the quality specifications indicated, and as such, the make-up water will not be designed to facilitate this type of loading. Make-up water for this system is estimated to be between 10 to 12 gallons per minute and will be provided by Newport News Waterworks. Once tapped from the potable water system, the water will be treated to remove the various contaminants and impurities detrimental to the LCW system.

10.3.5.2 Assumptions The following LCW systems assumptions were provided by Jefferson Lab:

- The demand for LCW to serve the proposed facility is based on the demands of the existing accelerator and an assumed multiplier of 3.3 was applied to the existing flows to account for a doubling in approximate power usage and the physics of the heat transfer and hydraulics processes.
- It is assumed that there will be two (2) closed loop LCW treatment buildings on-site (Buildings 4 and 5). For the purposes of this report, a typical design was shown to indicate all major treatment systems which will be modified as required as additional information becomes available.
- Nitrogen required for the system de-aeration process is assumed to be generated either on site by a nitrogen generator or by the Cryogenics Plant building and a system designed to convey the gas to the LCW facilities.
- Once the LCW supply and return lines are run to the tunnel, the scientists will provide the remaining supply and return lines within the tunnel.
- pH will be manually monitored and adjusted.
- The system will be controlled by a local PLC based control system. The control system will be designed to match the existing systems and sole source justification may be required to facilitate this.
- LCW plants will be designed as utilitarian, un-manned, structures with restrooms, and a utility work area.
- A roll-up access door will be provided at each facility for equipment lay down and maintenance
- Plain concrete floors will be suitable for service in LCW buildings. Chemical resistant flooring will be provided in cooling tower treatment areas which will be designed as separate roomed facilities in the LCW treatment building.
- The facilities which will use LCW are as follows:
  - Bldg. 1 & 2 — Detector Halls
  - Bldg. 3 — Counting House
  - Bldg. 7 — Ion Injector & Linac Service Building
  - Bldg. 11 — Collider Service Building (Magnets)
  - Bldg. 12 & 13 — Collider Service Buildings (RF).
  - Bldg. 15 — HE Cooler Energy Recovery Linac (ERL)
  - Booster Access Building

- Booster Service Building
- DC Cooler Building
- Collider and Booster Tunnel

10.3.5.3 Design Requirements Each Collider Access Building will be provided with two LCW systems as follows:

- A system which will be dedicated to cooling above grade power supplies and above grade system components.
- A system which will be dedicated to cooling below grade magnets, cavities and associated components.
- Each of the systems will be provided with an independent pumping and piping distribution system.

The approximate total LCW recirculation rate required is estimated by Jefferson Lab to be 20,000 GPM with a system ΔT=12° F, representing an approximate side-stream treatment flow rate of 2,000 GPM or 2.88 MGD (based on the assumption that 10% of LCW flow is treated continuously).

The makeup water, will be obtained from the on-site potable water distribution system. The initial filling of the system will be provided by the contractor to meet the quality specifications indicated, and as such, the make-up water will not be designed to facilitate this type of loading. Make-up water for this system is estimated to be between 10 to 12 gallons per minute and will be provided by Newport News Waterworks. Once tapped from the potable water system, the water will be treated to remove the various contaminants and impurities detrimental to the LCW system.

The systems will operate continuously to prevent bacterial growth, and remove contaminants from the LCW water loops. Bacterial growth within the system can cause microbiologically influenced corrosion (MIC). The treatment process will match existing treatment systems, including activated carbon filtration, cation resin softeners, mixed bed ion bed exchangers using 9-inch resin type bottles, membrane de-aeration, reverse osmosis make-up water treatment, ultra violet make up water treatment, and in-line 0.5-micron particle filtration on make-up and process water.

The LCW will be cooled to maintain a maximum supply temperature of 95° F. Cooling of the LCW water will be provided by shell and tube heat exchangers using an open condenser water system for heat extraction from the LCW. The open condenser water system will include cooling towers for heat rejection, base mounted horizontal split case circulating pumps and cooling tower water treatment systems.

The materials of construction will be similar to the existing piping, fittings and valves. Stainless steel will be the material for the supply and return piping system, pumps, air separators, expansion tanks, and make-up water tanks. The particular metallurgy of the stainless steel and the joining of the pipe will be determined during design. The materials of construction, standards and codes will be similar to the existing LCW at the existing accelerator site. All underground piping will be provided with a tracer wire and warning tape whether metallic or non-metallic.

RPZ Backflow prevention in accordance will all local and AWWA codes will be provided on all incoming potable water services.

A separate and independent air compressor system will be provided at each LCW facility to provide dried air service to all actuated valving in addition to providing dried only air to various processes.

LCW water and open condenser water central systems will be provided with N+1 redundancy.

10.3.6 Chilled Water

10.3.6.1 Summary Chilled water will be provided to cool and dehumidify the Collider Facility. Two chilled water plants are proposed with each plant serving approximately one-half of the Collider Facility to minimize system pumping energy consumption. Chilled water will be produced by electric water-cooled centrifugal chillers. The total facility chilled water cooling demand is estimated by Jefferson Lab to be approximately 1,500 tons. Chilled water will be distributed to the cooling and dehumidification equipment serving the facilities using direct buried, pre-insulated underground chilled water piping.

10.3.6.2 Assumptions The facilities which will use chilled water for cooling and dehumidification are listed below:

- Bldg. 1 & 2 — Detector Halls: Cooling and dehumidification.
- Bldg. 3 — Counting House: Cooling occupied facilities and server room.
- Bldg. 7 — Ion Injector & Linac Service Building: Cooling above grade areas housing power supplies and electronics.
- Bldg. 11 — Collider Service Building: Cooling above grade areas housing magnet power supplies and electronics.
- Bldg. 12 & 13 — Collider Service Buildings: Cooling above grade areas housing RF power supplies and electronics.
- Bldg. 14 — Cryogenics Plant: Control Room cooling.
- Bldg. 15 — HE Cooler Energy Recovery Linac (ERL)
- Collider Tunnel — Dehumidification units

10.3.6.3 Design Requirements Each chilled water plant will consist of electric water cooled centrifugal chillers, constant flow primary chilled water pumping system, variable flow secondary chilled water pumping system and open condenser water system for heat rejection. The open condenser water system will consist of cooling towers, condenser water pumping system, filtration and water treatment system. The secondary pumping system will be controlled to maintain adequate differential pressure at each facility served. Chilled water will be distributed to the cooling and dehumidification equipment serving the facilities using direct buried, pre-insulated underground chilled water supply and return piping. Each facility chilled water service lateral will be provided with isolation valves. Each chilled water plant will be provided with N+1 equipment redundancy. Each plant will be controlled by a local PLC based control system. The control system will be designed to match the existing systems and sole source justification may be required to facilitate this.

10.3.7 Natural Gas

Heating for the existing Accelerator Facility uses resistant electric heating. It is assumed that heating for the new Collider Facility will also be provided by resistant electric heating and therefore, natural gas service will not be required.

10.3.8 Cryogenic Casings

10.3.8.1 Summary The Cryogenics casing pipe utility for this project consists only of the casing pipe. It does not include any of the cryogenic distribution system or the manifolds, valves, or

instrumentation. The function of the casing pipe is to house and protect the cryogenic distribution piping from the central cryogenic cooling facility (Bldg. 14) to the underground facilities requiring cryogenic cooling. The internal diameter of the casing piping will be sized to allow cryogenic piping installation and accommodated insulation system and piping contraction during system start-up.

10.3.8.2 Assumptions The casing and material of which it is made is to be the same as originally used in the earlier CBAF project. The requirements for the Cryogenics system were provided by Jefferson Lab as follows:

1. 4 degrees Kelvin (4K) liquid for the magnets in the arcs of the collider tunnel.
2. 2 degrees Kelvin liquid (2K) for the cryomodules in the linear accelerator of the collider tunnel. Modules are located in north side of tunnel.
3. 2K for the cryomodules in the ion booster tunnel.
4. Approximately 1000 square feet in the collider tunnel cross (X) area on the north side will be needed for cryogenics distribution – manifolds, valves and instrumentation.

10.3.8.3 Design Requirements The casing system is a series of carbon steel piping in which the cryogenic transfer lines are installed. The internal diameter of the casing piping will be sized to allow cryogenic piping installation and accommodated insulation system and piping contraction during system start-up; casing sizes indicated are preliminary and must be verified when the system is designed. Since the casing pipe will house the distribution pipes, it is preferable to have the casing as straight as possible with minimal bends. This will enable easier installation, maintenance, and replacement of distribution piping. The casing piping is placed within a trench of sufficient width to hold the necessary number of casing pipes arranged in a side-by-side configuration. They will emanate from the Cryogenics Plant to the points of entry into the tunnels for further distribution. Two trenches are assumed to be dug. The first trench starts at the Cryogenics Plant and travels directly to the north wall of the collider tunnel cross (X) area. The schematic plan shows the pipe in a straight line (both in plan and profile); however, some alignment variations from this straight alignment may be necessary to avoid other structures. Site optimization will review the location of the various facilities in an effort to eliminate the need for any bends in these lines. This casing system contains 7 sleeves:

1. 2K: One 24” and one 12” diameter sleeve.
2. 4K: Two 12” diameter sleeves.
3. Shield (30–50K): Two 12” diameter sleeves.
4. Utilities: One 12” diameter sleeve.

The second trench starts at the Cryogenics Plant and travels to the north wall of the ion booster tunnel north arc. Site optimization will review the location of the various facilities in an effort to eliminate the need for any bends in these lines. This casing system contains 5 sleeves:

1. 2K: One 24” and One 12” diameter sleeve.
2. Shield (30-50K): Two 12” diameter sleeves.
3. Utilities: One 12” diameter sleeve.

A typical cross section of each trench with the pipe layout and spacing is shown below based on the information provided on the CEBAF HT-101 as-built drawings dated 11/15/91.

Casing Pipe Material is to be the same as used in the original CEBAF structures. The pipe is carbon steel pipe of 3/8" wall thickness, galvanized coated conforming to ASTM A 120 or latest edition with butt welded joints conforming to ASTM 135/135M or latest edition. After welding pipe joints, coat and wrap with corrosion protection material to be developed during design. Trench excavation and backfill will conform to appropriate specifications to be developed during design.

10.4 Buildings and Structure Design Criteria

The new electron-ion collider is being built on a site adjacent to the existing collider facility. The collider tunnel will be bearing at a depth of 20 to 30 feet below the existing grade. The experimental Detector Halls will be located at a similar below-grade elevation as the tunnel. In addition, there will be numerous small support and access structures located at-grade. Some of these structures are located directly over the collider tunnel below while some are located outside the tunnel footprint.

Due to the unsuitability of the topsoil on the site, a cut of 6 to 18 inches will need to be removed from the site, extending deeper in some isolated areas. The tunnel and below-grade structures will be founded on a concrete mat foundation that bears on the Yorktown formation, a geological strata of reasonable bearing strength located approximately 30 feet below grade. The above-grade structures located within the tunnel's excavation area will bear on structural fill. Building located outside of the tunnel construction area will need to have the soil capacity verified by a geotechnical engineer or be founded on piles. All the foundation systems will need to account for the high water-table which is located approximately 12 feet above the bottom of the tunnel foundation.

The below grade structures, tunnels and detector halls, will be concrete with thicknesses that account for radiation shielding. The above-grade structures will typically be constructed of a steel braced frame with metal joist roof and metal deck. An independent steel structure will be provided for support of bridge cranes.

The character of the above grade structures will follow the architectural theme employed at the CEBAF, including the use of horizontally-corrugated metal panels and flat roofs. Thermal, acoustic, and fire protection systems will be employed as required for each building type.

10.4.1 Tunnels

The new EIC tunnel consists of multiple tunnel structures, including:

1. Collider,
2. Ion booster,
3. Ion transfer,
4. Ion source/injector,
5. Electron transfer,
6. Helium cooler energy recovery LINAC, and
7. DC Cooler.

All the tunnel sections have the same top of foundation elevation, although they vary in width and height.

10.4.1.1 General The beam tunnels will contain the cryomodules, magnets and other machine-related equipment required to accelerate and guide the electron, or ion beam.

This facility will be a continuous horizontal underground tube having the shape of a figure-eight in plan. It will be rectangular in cross section and constructed out of reinforced concrete.

The beam tunnels will include reinforced concrete labyrinths at access/egress buildings, which will provide protected access into the beam tunnels for personnel and equipment.

There will be numerous openings into the beam tunnels to admit ducts, pipes, conduits and waveguides. Most of these openings will be located under the buildings that sit directly above the beam tunnels; the openings in the beam tunnels will be connected to openings in the building floor slabs above by means of vertical concrete-encased PVC pipes.

The beam tunnels will have a crowned cast-in-place concrete floor, sloping to continuous drainage channels along each side. These channels will drain to sumps located at the access / egress labyrinths.

The finish of the floor of the beam enclosure and of the interior surfaces of the concrete segments will be exposed sealed concrete to preclude or limit dusting.

10.4.1.2 Structural **Geotechnical Site Setting:** The upper soil strata of the CEBAF site exhibit significant variation. These soils are classified as SP, SM or SC, in accordance with the Unified Soil Classification System. There is considerable concern regarding rates of differential and creep settlement in these soils. Based on the geotechnical consultant's recommendation, the beam tunnel is to be supported on the Yorktown formation, which is considered to be stable, thus, reducing concern about differential settlement.

Foundation: The tunnel foundation will consist of a 2 foot to 2.5 foot thick cast-in-place continuous mat supported by the Yorktown formation. The anticipated loads include the self-weight of the tunnel, soil back fill, roller compaction, hydrostatic, HL93 vehicle and future buildings. Based on the evaluation in the geotechnical report, the beam tunnel foundation will be located at elevation 11.2 feet $+n$ -.

Beam Tunnel Structure: The beam tunnel will be a rectangular structure built of cast-in-place reinforced concrete or a similar structure built of precast concrete sections, or a combination of both. The designs will be developed for the beam tunnels, based on code and standard criteria and design loads and cost.

Construction joints will occur at the top and bottom of each wall, and also around the entire tunnel section at approximately 50-foot intervals. These joints will have standard PVC water stop, or other approved water stop products. Additionally, the tunnel exterior (sides and bottom) will be covered with a waterproof barrier system.

10.4.1.3 Mechanical **Heating Ventilation and Air Conditioning (HVAC)** HVAC indoor design conditions are summarized in Table 10.1:

Table 10.1: HVAC Indoor Design Conditions: Beam Enclosure

Room/Area	Occ'd Cooling (°F)	Unocc'd Cooling (°F)	Occ'd Heating (°F)	Unocc'd Heating (°F)	Relative Humidity (%)
Collider Tunnel (Beam Enclosure)	95	95	55	55	55 max.

Outdoor design conditions will be based on ASHRAE 2017 Fundamentals Handbook weather data for Norfolk, Virginia.

Overview: The HVAC systems will provide control of temperature, humidity, helium levels and air circulation during normal facility operations (beam on and beam off). A smoke removal

system will be provided in accordance with NFPA 92, NFPA 204 as amended by the local AHJ; the control of the smoke removal system will be integrated with the existing Accelerator Tunnel smoke removal system.

Dehumidification System: Recirculating type dehumidification units which will maintain space temperature and humidity below the maximum allowable conditions within the beam enclosure. The dehumidification units will be located at the beam enclosure level of the facility, at locations where egress structures and/or service building structures connect to the beam enclosure structure. The dehumidification systems will operate continuously during normal collider operations.

Normal Ventilation System: The normal ventilation system will include outside air supply and exhaust systems to meet the code ventilation requirement of the beam enclosure. The system will consist of 100% outside air units to supply tempered outside air to the space and exhaust fans which will purge air from the space. The system exhaust fans will be located within egress structures and/or service building structures which connect to the beam enclosure structure. The exhaust fans intakes will be ducted down to the beam enclosure level and terminated with an exhaust grille. The 100% outside air unit supply will be ducted down to the beam enclosure structure and terminated with a supply air grille. Exhaust and supply grilles will be strategically located throughout the beam enclosure to provide highly efficient air dilution and prevent short circuiting of supply and exhaust air. The normal ventilation system will operate when the beam is off and the smoke evacuation system is off.

Helium Venting System: The helium venting system will be a passive venting system which will include helium venting ductwork which will communicate from the beam enclosure to the outdoors. Because helium gas is less dense that air, it rises due to the buoyancy effect of the air.

Gas Monitoring System: The system will continuously monitoring helium gas levels in the beam enclosure air. When helium gas levels reach a high limit, the helium vent dampers will be automatically opened to relieve helium gas accumulation within the beam enclosure. The helium venting system will be active only when the beam is off and the smoke evacuation system is off.

Air Circulation System: An air circulation system will be provided to maintain uniform temperature and humidity throughout the length of the beam enclosure. The system will consist of air circulation fans located throughout the length of the beam enclosure. The system will be designed to maintain uniform airflow velocities within the beam enclosure, based on the requirements of Jefferson Lab.

Smoke Removal System: Based on NFPA 101, the underground facility will require a smoke control/removal system if the lowest floor elevation of the underground structure is more than 30 feet below the lowest level of exit discharge or if there is more than one level located below the lowest level of exit discharge. The existing Accelerator Facility include a smoke removal system. It is therefore assumed that the new underground facility will require a smoke removal system.

A smoke removal system will be provided in accordance with NFPA 92, NFPA 204 as amended by the local AHJ; the control of the smoke removal system will be integrated with the existing underground Accelerator Facility smoke removal system.

The smoke removal system exhaust fans will be located adjacent to egress structures and/or service building structures which connect to the beam enclosure structure. The exhaust fans intakes will be ducted down to the beam enclosure level and terminated with an exhaust grille. Un-temperature outside make-up air will be provided via louvered openings communicating with the outdoors. The existing Accelerator Facility uses egress stair enclosures as make-up air plenums to the underground beam enclosure; use of egress stair enclosures as smoke removal system make-up air plenums will require approval by the AHJ.

The smoke removal system will be controlled to operate when local smoke is detected or when a local manual push button switch is activated. When local smoke is detected or when the local push button switch is activated, the local smoke removal fan will be energized, the local make-up air intake will remain closed, and make-up air intakes within adjacent above ground egress structures/service buildings will open.

Plumbing

Tunnel sump pits will be provided in egress structures and/or service building structures which connect to the beam enclosure structure to provide sanitary drainage within the tunnel. Each sump pit will be provided with a sewage ejector which will discharge to the sanitary sewer system.

Fire Protection

The tunnel will be provided with an approved, supervised automatic sprinkler system.

The fire alarm for the tunnel exits will connect to the ground level structure above. Fire alarms manual pull stations will be installed at each egress alcove

10.4.1.4 Electrical / Communication An illumination level of 30 foot-candles will be provided in the beam enclosure by LED lighting fixtures. Double duplex 120V receptacles, fed from 30A circuits, will be spaced every 20 feet in the tunnels. 100A three phase outlets, suitable to serve a welding machine, will be located every 300 feet in the tunnels. Cable trays will be provided by CEBAF for accelerator power and control cables. High-water alarms in the sump pit will be connected to the site-wide supervisory system. Battery-operated emergency lighting units will be provided in each access labyrinth, with remote heads mounted in the beam enclosure.

Tunnel spaces will be provided with telephone service from the structures above using VoIP and copper cabling. No additional communications are required.

10.4.2 Experimental Areas

The experimental areas include the detector halls and the associated counting house.

10.4.2.1 Detector Halls - Buildings 1 & 2 Building dimension: 100’ long x 80’ wide x 50’ high.

General The Detector Halls house the experimental detector equipment. There will be counting house Provision will also be made for parking for experimenters’ counting houses along with the required umbilicals to the high-bay experimental hall and counting house.

Because low energy experiments will be conducted in the Detector Halls, the shielding requirements for the building construction do not require the use of thick reinforced concrete walls and roof. Each Detector Hall has the following requirements:

- Floor of high-bay area is substantially below centerline of beam.
- ton-capacity bridge with hook height of feet above the beamline.
- Exterior shielded access doors are 16 feet wide x 16 feet high. These doors are roller mounted with electric drive mechanism to facilitate the operation.
- Hinged platform at grade level to permit drive-in service by vehicles for unloading by the interior cranes.

Personnel access will be provided by a shielded opening at the Detector Hall floor level at the entry to the counting house.

Structural The Detector Halls will be founded on a concrete mat foundation approximately 3 to 3.5 feet thick. The superstructure includes concrete walls of 2 to 2.5 feet thick up to grade with a steel moment frame supporting steel roof joists and metal roof deck. A bridge crane will be supported from the steel frame structure.

Mechanical Heating Ventilation and Air Conditioning (HVAC)
HVAC indoor design conditions are summarized in Table 10.2:

Table 10.2: HVAC Indoor Design Conditions: Detector Hall

Room/Area	Occ'd Cooling (°F)	Unocc'd Cooling (°F)	Occ'd Heating (°F)	Unocc'd Heating (°F)	Relative Humidity (%)
Detector Hall	95	95	55	55	55 max.

Outdoor design conditions will be based on ASHRAE 2017 Fundamentals Handbook weather data for Norfolk, Virginia.

A single zone constant volume air handling unit will provide heating, cooling and ventilation to the area. The air handling unit will be equipped with a mixing box, filter section, preheat coil, cooling coil, reheat coil and supply fan. Supply air will be distributed to the area via a low pressure galvanized sheet metal ductwork using ceiling supply air diffusers and/or side wall supply air registers to introduce conditioned supply air to the space. Minimum outside ventilation air will be ducted from an outdoor air intake opening to the unit mixing box. Return air will be ducted from the area to the unit mixing box. The return air fan will recirculate space air back to the air handling unit mixing box. The space will be mechanically exhausted. Radiation shielding will be provided for exhaust and intake air openings.

The HVAC system will be controlled by a direct digital control system which will be networked to a centrally located operator's interface.

Plumbing
Sump pits will be provided in Detector Hall egress structures to provide sanitary drainage within the Detector Hall. Floor drains at the Detector Hall floor slab will provide floor drainage and will be connected to the sump pit. Each sump pit will be provided with a sewage ejector which will discharge to the sanitary sewer system.

No other plumbing systems are anticipated for the facility.

Fire Protection
The facility will be provided with an approved, supervised automatic sprinkler system. Detector Hall truck access overhangs will be protected with an automatic dry-pipe sprinkler system for freeze protection, and access ramps will be waterproofed.

A self-contained fire alarm and mass notification panel will be provided for the building. The fire alarm will be an extension of the existing site wide fire alarm system a standalone system for the JLEIC sub-campus, and will be monitored in the security office.

Electrical / Communication Power from two 2500kVA utility transformers will each terminate in one or more vertical sections of service entrance rated drawout switchgear, with a maximum of six breakers. Air insulated power circuit breakers will serve 600A to 800A distribution panels, which will in turn serve branch circuit panelboards or dry type transformers to provide 120V/3 phase/4 wire power for low voltage loads. Duplex 120V receptacles, fed from 20A circuits, will be spaced to provide a raw power density of 3.5W/GSF. The building spaces will be lit to an average 20 footcandle with a 3:1 avg:min ratio, using LED fixtures. Exit lights and battery-powered emergency lights will be provided to meet code egress requirements.

Site communication fibers will terminate in an IDF space. Switches will be provided for the voice telephone system, the conventional data (email, etc), building automation system, security access system, security video system, and fire alarm systems. Site research and control fibers, coming

from the Machine Control Center, will terminate in the same IDF. Machine communications fibers, between the support buildings, will terminate in the same IDF.

10.4.2.2 counting house - Building 3 Building dimension: 60' long x 60' wide x 14' high.

General The Detector Halls will be controlled from counting houses. counting houses will contain space for mechanical and computer equipment related to control and data acquisition for each detector. A raised floor will be provided to house data processing cables for ease of access and distribution.

Structural The counting house will be constructed using a steel braced frame building with square spread concrete footings at the column locations and continuous concrete wall footings. The roof will be constructed of steel joists with a metal deck roofing system. Lateral building stability is provided by cross bracing.

Mechanical Heating Ventilation and Air Conditioning (HVAC)

HVAC indoor design conditions are summarized in Table 10.3:

Table 10.3: HVAC Indoor Design Conditions: Occupied Space and Server Room

Room/Area	Occ'd Cooling (°F)	Unocc'd Cooling (°F)	Occ'd Heating (°F)	Unocc'd Heating (°F)	Relative Humidity (%)
Occupied Space	78	85	68	60	30–50
Server Room	75	75	68	68	40–50

Outdoor design conditions will be based on ASHRAE 2017 Fundamentals Handbook weather data for Norfolk, Virginia.

A variable volume air handling unit will provide heating, cooling and ventilation to the occupied spaces of the facility. Space temperature control will be provided by variable volume air terminal units with electric heating coils. The air handling unit will be equipped with a mixing box, filter section, preheat coil, cooling coil, reheat coil and supply fan. Primary supply air will be distributed to the variable volume air terminal units via a medium pressure galvanized sheet metal ductwork. Supply air will be distributed to the spaces via low pressure galvanized sheet metal ductwork using ceiling supply air diffusers and/or side wall supply air registers to introduce conditioned supply air to the space. Minimum outside ventilation air will be ducted from an outdoor air intake opening to the unit mixing box. Return air will be ducted from the area to the unit mixing box. The return air fan will recirculate space air back to the air handling unit mixing box and also relieve/exhaust the area.

The server room with raised floor will be provided with heating, cooling and humidity control by multiple computer room air conditioning units. The server room will be provided with N+1 computer room air conditioning units. The computer room air conditioning units will include a filter, cooling coil, reheat coil, humidifier and supply fan.

The HVAC system will be controlled by a direct digital control system which will be networked to a centrally located operator's interface.

Plumbing

The facility will be provided with domestic hot and cold water, sanitary and roof drainage systems. Domestic hot water will be provided by a storage type electrical water heater.

Fire Protection

The facility will be provided with an approved, automatic fire suppression system. The counting room access floor shall receive fire protection using individual clean agent systems. The clean agent

system shall provide up to two minutes of audio-visual alarm signal before releasing measured clean agent gas in case of fire. clean agent system shall use photocell type smoke detectors connected to the central alarm system.

A self-contained fire alarm and mass notification panel will be provided for the building. The fire alarm will be a standalone system for the JLEIC sub-campus, and will be monitored in the security office.

Electrical / Communication The counting house will be served by a 480V 75kVA to 500kVA transformer, size will be refined as loads in the building are refined. The transformer will serve a service entrance rated panelboard. Large mechanical loads and lighting will be served directly. Dry type transformers will be provided to provide 120V/3 phase/4 wire power for low voltage loads. Duplex 120V receptacles, fed from 20A circuits, will be spaced to provide a raw power density of 3.5W/GSF. The building spaces will be lit to an average 100 footcandle with a 3:1 avg:min ratio, using addressable, dimmable LED fixtures. Exit lights and battery-powered emergency lights will be provided to meet code egress requirements. An uninterruptable power supply (UPS) will be provided for each counting house.

Site communication fibers will terminate in an IDF space. Switches will be provided for the voice telephone system, the conventional data (email, etc), building automation system, security access system, security video system, and fire alarm systems. Site research and control fibers, coming from the Detector Halls, will terminate in the same IDF. Machine communications fibers, between the support buildings, will terminate in the same IDF.

Data processing equipment and general space in in counting room will be supplied by isolated ground receptacles whose grounding terminal is connected to the isolated ground bus in access floor space. The isolated ground bus shall be wired directly to service entrance neutral ground.

The counting room shall have a raised floor for data processing cables.

10.4.3 Support Facilities

The support facilities include the cryogenics plant, the access buildings, and the Ion Injector / LINAC.

10.4.3.1 Cryogenics Plant - Building 14 Building dimension: 165' long x 60' wide x 30' high

The Cryogenics Plant will house the Cold Box and Cryogenics Plant Control Facilities and the Compressor Room.

Cold Box Room: The Cold Box Room will have a high bay area with a mezzanine. The size of the cold box, which is 14 feet in diameter and 35 feet high, will require special considerations. This box must be set in a 15-foot pit and requires 12 feet clear space all around. The structure will contain a 5-ton bridge crane with a 32-foot hook height and have a removable roof hatch permit the entire box to be removed. Motor control centers, control room and offices will also be located in this facility.

Compressor Room: The Compressor Room will house the compressors, whose handling will require a 5-ton bridge crane. Because of the high noise generated by the compressors, special acoustical treatment will be provided to reduce impact to adjacent facilities. Truck access is also required for this area.

General The exterior metal panels will have a 30 db. sound attenuation from Compressor Room to exterior and 10 db. sound attenuation from Cold Box Room to exterior.

The facility will also have a mezzanine floor above the main floor, an equipment pit below the main floor containing vertical ladders and steel guard railings, storage and toilets. A loading area that has a truck access, entrance vestibule, control room, equipment mezzanine stair will be required.

A transfer line trench with removable grating that contains sub atmospheric cold box, helium supply and return transfer lines to LINACs and Detector Halls, bayonet cans, conduits and vertical ladders will be provided.

Structural Compressor Room: The foundation consists of a 3-foot-thick reinforced concrete mat, whose primary function is to provide sufficient mass to attenuate the vibration associated with heavy reciprocating equipment. Building columns will be supported directly on this mat. The superstructure for Compressor Room will consist of conventional steel framing. The roof deck is a steel structural diaphragm supported on bar joists.

Cold Box Room: This structure houses the cold box and the cryogenics plant control facilities. The cold box area is a high bay steel framed structure, the roof deck is not a diaphragm because of the large hatch provided for cold box removal. Lateral roof stability is accomplished with a cross bracing. Building columns are supported on spread footings.

The below grade portion of the cold box will be housed in a reinforced concrete pit. This pit will be waterproofed in the same manner as other grade concrete structures. The pit walls carry the weight of the cold box to the bottom slab, which acts as a mat foundation to support the cold box.

The control facilities area is a light steel framed structure with conventional spread footings and a concrete slab on grade.

Mechanical Heating Ventilation and Air Conditioning (HVAC)

HVAC indoor design conditions are summarized in Table 10.4:

Table 10.4: HVAC Indoor Design Conditions: Occupied Space and Server Room

Room/Area	Occ'd Cooling (°F)	Unocc'd Cooling (°F)	Occ'd Heating (°F)	Unocc'd Heating (°F)	Relative Humidity (%)
Compressor Rooms	TBD	TBD	55	55	TBD
Cold Box Rooms	TBD	TBD	55	55	TBD
Control Room	78	85	68	62	30–50
Toilet Room	78	85	68	62	30–50
Storage Room	78	85	68	62	30–50

Outdoor design conditions will be based on ASHRAE 2017 Fundamentals Handbook weather data for Norfolk, Virginia.

Overview: Two (2) liquid helium refrigeration plants will each generate 2 ° K and 4.5 ° K liquid nitrogen for electromagnet cooling. Each liquid helium refrigeration plan will consist of a Compressor Room, Cold Box Room, Control Room, Toilet Room and Storage Room.

Compressor Rooms: Each room will be provided with heating and ventilation only. No mechanical cooling will be provided. Oxygen levels in the room will be continuously monitored. A helium purge system will be provided to purge the room when oxygen levels falls below acceptable limits.

A condenser water system using a cooling tower for heat rejection, will be provided for compressor and turbo-expander cooling.

Cold Box Room: Each room will be provided with heating and ventilation only. No mechanical cooling will be provided. Oxygen levels in the room will be continuously monitored. A helium purge system will be provided to purge the room when oxygen levels falls below acceptable limits.

Control Room, Toilet Room and Storage Room: Each room will be provided with heating, cooling and ventilation by a fan coil unit which will include a mixing box, filter section, heating coil and cooling coil.

The HVAC system will be controlled by a direct digital control system which will be networked to a centrally located operator's interface.

Plumbing

The facility will be provided with domestic hot and cold water, sanitary and roof drainage systems. The Compressor Room and Cold Box Room floors will be provided with floor drains which will be connected to the sanitary piping system. The Cold Box Room pit will be provided with a sump pit and sewage ejector which will discharge to the sanitary drainage system. Domestic hot water will be provided by a storage type electrical water heater.

Fire Protection

The facility will be provided with an approved, supervised automatic sprinkler system.

A self-contained fire alarm and mass notification panel will be provided for the building. The fire alarm will be an extension of the existing site wide fire alarm system, a standalone system for the JLEIC sub-campus, and will be monitored in the security office.

Electrical / Communication Power from six 5MVA 4160 volt utility transformers will terminate in service entrance rated drawout vacuum breaker switchgear. Output breakers will serve the motor starters. The transformers will be divided between the two DVP sources serving the site to allow one service to maintain the helium system without a gas loss. Two 1500 kVA utility transformers will each terminate in a main-tie-main configured service entrance rated drawout switchgear, to allow either DVP service to provide power for the plant auxiliaries such as pumps, cooling towers, lighting, and dry type transformers to provide 120V/3 phase/4 wire power for low voltage loads. Air insulated power circuit breakers will serve 600A to 1200A distribution panels, which will in turn serve motor loads. Duplex 120V receptacles, fed from 20A circuits, will be spaced to provide a raw power density of 3.5W/GSF. The building spaces will be lit to an average 20 footcandle with a 3:1 avg:min ratio, using LED fixtures. Exit lights and battery-powered emergency lights will be provided to meet code egress requirements.

Site communication fibers will terminate in an IDF space. Switches will be provided for the voice telephone system, the conventional data (email, etc), building automation system, security access system, security video system, and fire alarm systems. Site research and control fibers, coming from the Machine Control Center, will terminate in the same IDF. Machine communications fibers, between the support buildings, will terminate on the plant floor in the same IDF.

10.4.3.2 Access Buildings The Access Buildings allow access to the Tunnel for equipment, personnel and mechanical systems. In addition, these buildings house the power supplies, heat exchangers and pumps, technicians' work area, instrumentation and control racks, toilet and access to the tunnels.

The Access Buildings include the following structures:

- Collider Access Buildings — Building 4 & 5
- Ion Source Access Building — Building 6
- Booster Access Building — Building 10
- He Cooling (ERL) Access Building — Building 15 - 100' long x 20' wide x 15' high

General The design of these buildings will conform to the architectural theme relating to light steel frame construction with deep rib insulated metal sandwich panels similar to those at the existing CEBAF. A typical Access Building program includes:

- Overhead doors for truck access to the interior space
- An access control vestibule for personnel access
- A large hatch with either an overhead bridge crane or monorail / hoist to move large equipment and material down to the tunnel level below
- An access stair from the grade level to the tunnel level that also serves as an emergency egress stair from the tunnel.
- Toilets / janitors closet

Some access buildings will also include a freight elevator, DC power room and/or LCW equipment / pumps.

Typically, equipment access to the beam tunnel level is by means of an opening in the floor which is covered by removable floor panels. A removable steel railing is provided around the opening in the floor for personnel safety while the floor panels are removed. An at-grade staging area, with a roll-up door to allow for truck access, is planned adjacent to the equipment access floor opening. A bridge crane, or monorail / hoist, is positioned in the bay above the removable floor panels permitting vertical access to another staging area below at the tunnel level. The below grade staging area is connected to the tunnel via a labyrinth connection.

Structural The substructure for the Access Buildings will be reinforced concrete and the superstructure will consist of conventional steel framing. The roof deck will be steel structural diaphragm supported on bar joists. The overhead crane will be supported from the building columns. Overall building stability will be provided by cross bracing. The horizontal spanning deep rib siding spans from column to column, hence girts will be required only to frame out doorways and other openings.

Mechanical Heating Ventilation and Air Conditioning (HVAC)

HVAC indoor design conditions are summarized in Table 10.5:

Table 10.5: HVAC Indoor Design Conditions: Access Buildings

Room/Area	Occ'd Cooling (°F)	Unocc'd Cooling (°F)	Occ'd Heating (°F)	Unocc'd Heating (°F)	Relative Humidity (%)
Access Buildings	TBD	TBD	55	55	TBD

Outdoor design conditions will be based on ASHRAE 2017 Fundamentals Handbook weather data for Norfolk, Virginia.

Collider Access Buildings 4 and 5 will house LCW system central equipment. Refer to Section 10.3.5 for a description of the LCW systems.

In general, Access Buildings will be provided with heating and ventilation only

The HVAC system will be controlled by a direct digital control system which will be networked to a centrally located operator's interface.

Plumbing

The facility will be provided with domestic cold water, sanitary and roof drainage systems. The wet mechanical spaces will be provided with floor drains which will be connected to the sanitary piping system. The facilities are assumed to be un-manned and will not require toilet rooms.

Fire Protection

The facility will be provided with an approved, supervised automatic sprinkler system.

A self-contained fire alarm and mass notification panel will be provided for the building. The fire alarm will be an extension of the existing site wide fire alarm system a standalone system for the JLEIC sub-campus, and will be monitored in the security office.

Electrical / Communication Power from the two 2500kVA utility transformers will each terminate in one or more vertical sections of service entrance rated drawout switchgear, with a maximum of six breakers. Air insulated power circuit breakers will serve 600A to 800A distribution panels, which will in turn serve LCW plant pump and cooling tower motor loads or dry type transformers to provide 120V/3 phase/4 wire power for low voltage loads. Duplex 120V receptacles, fed from 20A circuits, will be spaced to provide a raw power density of 3.5W/GSF. The building spaces will be lit to an average 20 footcandle with a 3:1 avg:min ratio, using LED fixtures. Exit lights and battery-powered emergency lights will be provided to meet code egress requirements.

Site communication fibers will terminate in an IDF space. Switches will be provided for the voice telephone system, the conventional data (email, etc), building automation system, security access system, security video system, and fire alarm systems. Site research and control fibers, coming from the Machine Control Center, will terminate in the same IDF on the machine floor. Machine communications fibers, between the support buildings, will terminate on the machine floor in the same IDF.

Unique Requirements by Building

Booster Access Building (10) Building Dimension: 60' long x 45' wide x 27' high

The Booster Access Building provides personnel and equipment access to the adjacent Ion Booster Tunnel (the small Figure-8), The Booster Access Building will house power supplies, a hatch with bridge crane above, a freight elevator, a stair, and toilets / janitor's closet.

Collider Access Building (4 & 5) Building Dimension: 100' long x 60' wide x 27' high In addition to the Detector Halls, the two Collider Access Buildings are the primary locations providing material and equipment access to the main collider tunnel (large Figure-8). These buildings house an equipment access hatch with 16-ton bridge crane above, a freight elevator, an access / egress stair, and toilets / janitor's closet. In addition, the Collider Access Buildings house the Low Conductivity Water (LCW) plants which include the following spaces:

- Deionizer Equipment Room,
- Low Conductivity Water (LCW) equipment room with exterior equipment and personnel doors
- DC Power Room

Ion Source Access Building (6) Building Dimension: 30' long x 30' wide x 14' high

The Ion Source Building provides personnel and equipment access to the adjacent Ion Injector / LINAC facility (Building 7) and these two structures could be combined into one facility above grade. This building will house an equipment hatch with mono-rail / hoist above, an access / egress stair and a toilet room.

He Cooling (ERL) Access Building (15) Building Dimension: 100' long x 20' wide x 15' high.

The He Cooling (ERL) Access Building provides personnel and equipment access to the He Cooling Tunnel below, The building will require a stairwell for personnel access down to the

tunnel. A 40 foot long by 8 foot wide access hatch with bridge crane is also need for movement of a cryomodule. The ERL access building will have LCW, power and water.

10.4.3.3 Ion Injector and LINAC — Building 7 Building dimension: 150' long x 15' wide x 14' high

The ion injector will be an extension of the LINAC structure.

General The design of this building will conform to the architectural theme relating to light steel frame construction with deep rib insulated metal sandwich panels similar to those at the existing CEBAF.

Ion Injector Room: Ion Injector area will contain an equipment room with equipment racks, klystrons, continuous cable trench, safety equipment lockers, and personnel and equipment exterior doors access control vestibule

LINAC area: Each LINAC will form a single long room containing equipment racks, klystrons, power supply units, control units, continuous cable trench, safety equipment lockers, and personnel and equipment exterior doors.

Structural Foundation: a minimum 5-inch floor slab including the required floor trench and footing elements will be contemplated as a monolithic concrete element, to take advantage of the relatively light column loads. The below grade stair enclosure will be a reinforced concrete structure designated to resist ground water pressure and lateral earth pressure.

Superstructure: the lateral resisting system and framing system for this building will be combined into a series of rigid frames. The identical rigid frames will be repeated until not required. The rigid frames will be constructed of standard hot rolled W shapes. The frames will be supported by a 1-foot continuous wall footing with grade beams spanning between the columns.

Mechanical / Fire Protection Heating Ventilation and Air Conditioning (HVAC)

HVAC indoor design conditions are summarized in Table 10.6:

Table 10.6: HVAC Indoor Design Conditions: Ion Injector and Linac

Room/Area	Occ'd Cooling (°F)	Unocc'd Cooling (°F)	Occ'd Heating (°F)	Unocc'd Heating (°F)	Relative Humidity (%)
Ion Injector / Linac Bldg. 7	78	85	68	55	30–50

Outdoor design conditions will be based on ASHRAE 2017 Fundamentals Handbook weather data for Norfolk, Virginia.

Fan coil units and/or constant volume air handling units will be used for heating, ventilation and cooling the spaces.

The HVAC system will be controlled by a direct digital control system which will be networked to a centrally located operator's interface.

Plumbing

The facility will be provided with domestic cold water, sanitary and roof drainage systems. The facilities are assumed to be un-manned and will not require toilet rooms.

Fire Protection

The facility will be provided with an approved, supervised automatic sprinkler system.

A self-contained fire alarm and mass notification panel will be provided for the building. The fire alarm will be an extension of the existing site wide fire alarm system a standalone system for the JLEIC sub-campus, and will be monitored in the security office.

Electrical / Communication Power from four 5000kVA utility transformers will each terminate in one or more vertical sections of service entrance rated drawout switchgear, with a maximum

of six breakers at Building 11, serving the magnets. Power from two 2500kVA utility transformers will each terminate in one or more vertical sections of service entrance rated drawout switchgear, with a maximum of six breakers at Building 12, serving the ion ring LINACs (RF). Power from four 5000kVA utility transformers will each terminate in one or more vertical sections of service entrance rated drawout switchgear, with a maximum of six breakers at Building 13, serving the electron ring LINACs (RF). Air insulated power circuit breakers will serve 600A to 800A distribution panels, which will in turn serve LCW plant pump and cooling tower motor loads or dry type transformers to provide 120V/3 phase/4 wire power for low voltage loads. Duplex 120V receptacles, fed from 20A circuits, will be spaced to provide a raw power density of 3.5W/GSF. The building spaces will be lit to an average 20 footcandles with a 3:1 avg:min ratio, using LED fixtures. The fixtures will be controlled to dim to 3 footcandles when the accelerator beams are on (space un-occupied) and at full illumination when the beams are off (potentially occupied). Exit lights and battery-powered emergency lights will be provided to meet code egress requirements.

Site communication fibers will terminate in an IDF space. Switches will be provided for the voice telephone system, the conventional data (email, etc), building automation system, security access system, security video system, and fire alarm systems. Site research and control fibers, coming from the Machine Control Center, will terminate in the same IDF. Machine communications fibers, between the support buildings, will terminate in the same IDF.

10.4.4 Service Buildings

The service buildings will provide access to the Beam Tunnel. The service buildings also contain DC power supply units for the and switchgear for the magnets.

The service buildings will include the following structures:

- Booster Service Building — Buildings 8 and 9
- Electron Transfer Building — Building ET1 thru ET4
- Service Building — Building 11
- Ion RF Service Building — Building 12
- Electron RF Service Building — Building 13
- DC Cooler Service Building

10.4.4.1 General The design of these buildings will conform to the architectural theme relating to light steel frame construction with deep rib insulated metal sandwich panels similar to those at the existing CEBAF.

The service buildings form a single room containing a cable trench equipment racks access to the buildings will be provided by personnel doors and equipment doors.

10.4.4.2 Structural **Foundation:** a minimum 5-inch floor slab including the required floor trench and footing elements will be contemplated as a monolithic concrete element, to take advantage of the relatively light column loads.

Superstructure: the lateral resisting system and framing system for this building will be combined into a series of rigid frames. The identical rigid frames will be repeated until not required. The rigid frames will be constructed of standard hot rolled W shapes. The frames will be supported by a 1-foot continuous wall footing with grade beams spanning between the columns.

10.4.4.3 Mechanical **Heating Ventilation and Air Conditioning (HVAC)**

Table 10.7: HVAC Indoor Design Conditions: service buildings

Room/Area	Occ'd Cooling (°F)	Unocc'd Cooling (°F)	Occ'd Heating (°F)	Unocc'd Heating (°F)	Relative Humidity (%)
Bldg 7, 11, 12, 13	78	85	68	55	30–50
All other service buildings	TBD	TBD	55	55	TBD

HVAC indoor design conditions are summarized in Table 10.7:

Outdoor design conditions will be based on ASHRAE 2017 Fundamentals Handbook weather data for Norfolk, Virginia.

All service buildings will be provided with heating and ventilation systems. Additionally, cooling will be provided in the following facilities:

- Bldg. 11 — Collider Service Building: Cooling above grade areas housing magnet power supplies and electronics.
- Bldg. 12 & 13 — Collider service buildings: Cooling above grade areas housing RF power supplies and electronics.

Where cooling is required, fan coil units and/or constant volume air handling units will be used for heating, ventilation and cooling.

The HVAC system will be controlled by a direct digital control system which will be networked to a centrally located operator's interface.

Plumbing

The facility will be provided with domestic cold water, sanitary and roof drainage systems. The facilities are assumed to be un-manned and will not require toilet rooms.

Fire Protection

The facility will be provided with an approved, supervised automatic sprinkler system.

A self-contained fire alarm and mass notification panel will be provided for the building. The fire alarm will be an extension of the existing site wide fire alarm system a standalone system for the JLEIC sub-campus, and will be monitored in the security office.

10.4.4.4 Electrical / Communication Each collider service building will be served by a 480V utility transformer serving a service entrance rated panelboard, which will in turn serve magnet power supplies or dry type transformers to provide 120V/3 phase/4 wire power for low voltage loads. Duplex 120V receptacles, fed from 20A circuits, will be spaced to provide a raw power density of 3.5W/GSF. The building spaces will be lit to an average 20 footcandles with a 3:1 avg:min ratio, using LED fixtures. The fixtures will be controlled to dim to 3 footcandles when the accelerator beams are on (space un-occupied) and at full illumination when the beams are off (potentially occupied). Exit lights and battery-powered emergency lights will be provided to meet code egress requirements.

Site communication fibers will terminate in an IDF space. Switches will be provided for the voice telephone system, the conventional data (email, etc), building automation system, security access system, security video system, and fire alarm systems. Site research and control fibers, coming from the Machine Control Center, will terminate in the same IDF. Machine communications fibers, between the support buildings, will terminate in the same IDF. Electrical panels and duplex outlets.

Lighting fixtures at entrances will be high-pressure sodium (HPS); interior lighting fixtures will be fluorescent.

10.4.4.5 Unique Requirements by Building

Collider service buildings (CS1 thru CS26) Building Dimensions: 30' long x 15' wide x 20' high

The Collider service buildings are located above, and along, the Collider Tunnel arcs on approximately 200 foot centers, based on cable lengths. They include racks and power supplies that support the equipment in the tunnel below. Personnel access is provided by a man-door and equipment access is provided by an 8'-0" wide overhead door.

Booster service buildings (Bldgs 8 & 9) Building Dimensions: 30' long x 15' wide x 14' high.

The Booster service buildings are located above, and along, the Booster Tunnel. They are very similar to the Collider service buildings relative to size, spacing and access.

Electron Transfer service buildings (ET1 thru ET4) Building Dimensions: 30' long x 15' wide x 14' high

The Electron Transfer service buildings are located above, and along, the Electron Transfer Tunnel. They are very similar to the Collider service buildings relative to size, spacing and access.

Service Building (Bldg 11) Building Dimensions: 45' long x 45' wide x 20' high

The Service Building (Bldg 11) is located above the central crossing of the main collider figure-eight. The building contains the electronic equipment and power supplies to support the magnets located at the tunnel crossing below. The character of the building is very similar to the Collider service buildings.

Electron RF Service Building (Bldg 13) Building Dimensions: 300' long x 40' wide x 16' high

The Electron RF Service Building is located above the Electron RF tunnel. The tunnel includes both warm and cold cavities. The Electron RF Service Building includes the electronics and power supplies that support the cavities in the tunnel below.

Ion RF Service Building (Bldg 12) Building Dimensions: 425' long x 20' wide x 20' high

The Ion RF Service Building is located above the Ion RF tunnel. The building is similar to the Electron RF Service Building but is smaller due to less radio frequency requirements.

DC Cooler Service Building Building Dimensions: 30' long x 15' wide x 14' high

The DC Cooler Building is located above the DC Cooler tunnel section and adjacent to the Electron RF Service Building. The building will house racks and power supplies that support the equipment in the tunnel below.

10.4.5 Miscellaneous Facilities

10.4.5.1 Egress Building - Building 16 Building dimension: 20' long x 15' wide x 14' high

There are several Egress Buildings that will house an emergency egress stair from the Beam Tunnel. Some Egress Buildings will be collocated with a Collider Service Building, especially along

the Tunnel arc segments. Each egress building will be provided with an access control vestibule, safety locker room and toilets.

General The Egress Buildings will have an exterior enclosure consisting of non-insulated, horizontal corrugated galvanized steel panels and paver blocks on rigid insulation on steel roof deck.

Interior spaces will be constructed out of concrete masonry units (CMU) partitions with exposed ceilings except for the toilet rooms which will have gypsum board ceilings. A stair that extends down to access labyrinth below and to exterior emergency exit door, an access control vestibule and a safety locker room with a door to the exterior will be provided.

Structural The superstructure for this facility will be steel framed supported on concrete substructure.

Mechanical Heating Ventilation and Air Conditioning (HVAC)

HVAC indoor design conditions are summarized in Table 10.8:

Table 10.8: HVAC Indoor Design Conditions: Egress Building 16

Room/Area	Occ'd Cooling (°F)	Unocc'd Cooling (°F)	Occ'd Heating (°F)	Unocc'd Heating (°F)	Relative Humidity (%)
Egress Stair	TBD	TBD	55	55	N/A
Toilet Room (where applicable)	TBD	TBD	68	68	N/A

Outdoor design conditions will be based on ASHRAE 2017 Fundamentals Handbook weather data for Norfolk, Virginia.

All egress structures will be provided with heating and ventilation systems only.

The HVAC system will be controlled by a direct digital control system which will be networked to a centrally located operator's interface.

Plumbing

Roof drainage systems will be provided. Toilet Rooms (where applicable) will be provided with domestic cold water, domestic hot water, and sanitary systems.

Fire Protection

The facility will be provided with an approved, supervised automatic sprinkler system. A standpipe system will be provided.

A self-contained fire alarm and mass notification panel will be provided for the building. The fire alarm will be a standalone system for the JLEIC sub-campus, and will be monitored in the security office.

10.4.5.2 Electrical / Communication The egress buildings will be supported by the adjacent collider service building for power and communications.

10.4.5.3 Gate house (Building 17) **General** A Gate House will provide shelter for personnel and equipment controlling access to the fenced-in EIC Tunnel and Facilities and it will be located at the entrance to perimeter road. The Gate House will have an exterior enclosure consisting of insulated, flat galvanized steel panels and paver blocks on rigid insulation on steel roof deck. The interior space will have exposed ceilings and vinyl composition tile flooring.

Structural

The superstructure for this facility will be steel framed supported on concrete substructure.

Mechanical Heating Ventilation and Air Conditioning (HVAC)

Table 10.9: HVAC Indoor Design Conditions: Gate House

Room/Area	Occ'd Cooling (°F)	Unocc'd Cooling (°F)	Occ'd Heating (°F)	Unocc'd Heating (°F)	Relative Humidity (%)
Gate House	78	85	68	62	30–50

HVAC indoor design conditions are summarized in Table 10.9:

Outdoor design conditions will be based on ASHRAE 2017 Fundamentals Handbook weather data for Norfolk, Virginia.

The Gate House will be provided with heating, cooling and ventilation by a fan coil unit which will include a mixing box, filter section, heating coil and cooling coil.

The HVAC system will be controlled by a direct digital control system which will be networked to a centrally located operator's interface.

Plumbing

The facility will be provided with a roof drainage system. The facilities are assumed to not require a toilet room.

Fire Protection The facility will be provided with an approved, supervised automatic sprinkler system.

A self-contained fire alarm and mass notification panel will be provided for the building. The fire alarm will be a standalone system for the JLEIC sub-campus, and will be monitored in the security office.

10.4.5.4 Electrical / Communication The gate house will be served from a 75kVA 208V transformer serving a service entrance rated panelboard. Duplex 120V receptacles, fed from 20A circuits, will be spaced to provide a raw power density of 3.5W/GSF. The building interior spaces will be lit to an average 20 footcandles with a 1.5:1 avg:min ratio, using LED fixtures. The building exterior spaces will be lit to an average 2 footcandles with a 2:1 avg:min ratio, using LED fixtures. Exit lights and battery-powered emergency lights will be provided to meet code egress requirements.

Site communication fibers will terminate in an IDF space. Switches will be provided for the voice telephone system, the conventional data (email, etc), building automation system, security access system, security video system, and fire alarm systems. Site research and control fibers, coming from the Machine Control Center, will terminate in the same IDF on the machine floor. Machine communications fibers, between the support buildings, will terminate [on the machine floor in the same IDF.

10.5 Codes, Standards, and Engineering Criteria

10.5.1 Codes

2012 Virginia Construction Code (Part I of the– effective July 14, 2014). References include the following major model codes:

- 2012 International Building Code with Virginia amendments
- 2012 International Energy Conservation Code with Virginia amendments
- 2012 Virginia Statewide Fire Prevention Code

- 2012 International Fuel Gas Code with Virginia amendments
- 2012 International Mechanical Code with Virginia amendments
- 2012 International Plumbing Code with Virginia amendments
- NFPA 101 Life Safety Code
- NFPA 92 Standard for Smoke Control Systems
- NFPA 204 Standard for Smoke and Heat Venting

10.5.2 Utilities Design Criteria

10.5.2.1 Water and Sanitary

1. The Hampton Roads Planning District Commission (HRPDC) Regional Construction Standards (RCS) with the Newport News, Special Provisions to the RCS
2. American Water Works Association (AWWA)
3. Virginia Department of Health (VDH)
4. City of Newport News, Design Criteria Manual
5. Newport News Waterworks Distribution Standards
6. DOD Standard 1066 (most recent edition)

10.5.2.2 Power

1. 2012 Blue Book: Dominion Virginia Power Information Requirements for Electric Service
2. International Electrical Code (IEC)
3. NFPA: National Electrical Code (NEC)

10.5.2.3 Communications

1. ANSI/TIA-758-B Customer-Owned Outside Plant Telecommunications Infrastructure Standard
2. ANSI/TIA 568 Commercial Building Telecommunications Cabling Standard
3. Building Industry Consulting Service International (BICSI) standards
4. NFPA: National Electrical Code (NEC)

10.5.2.4 Low conductivity water (LCW)

1. International Mechanical Code (IMC)
2. ASME B31.9 Building Services Piping
3. ASTM A 270/270M: Standard specification for 304 stainless steel welded pipe tube

10.5.2.5 Chilled water

1. International Mechanical Code (IMC)
2. ASME B31.9 Building Services Piping
3. ASTM A 53/53M: Standard specification for pipe, steel, black and hot-dipped, zinc-coated, welded
4. ASTM A 135/135M: Standard specification for electric resistance welded steel pipe

10.5.2.6 Cryogenic Casing System

1. The Hampton Roads Planning District Commission (HRPDC) Regional Construction Standards (RCS) with the Newport News, Special Provisions to the RCS

10.5.3 Buildings Design Criteria

10.5.3.1 Design Loads

1. Dead Loads: Dead loads include the weight of all permanent construction, all fixed equipment, and allowances for any additional loadings likely to be added at a later date.
2. Live Loads: Minimum distributed live loads, which are intended to account for occupancy loads, moveable equipment, maintenance loads, etc., will be in accordance with ASCE 7. Additional live loads not listed in the codes will be as follows:
   - Beam Enclosures: 100psf
   - End Stations: 300psf
   - Service Building/Vehicle AccessAASHTO Vehicle Loading
   - Electrical Equipment rooms: 250psf
   - Roofs (minimum): 20psf
   - Central Helium Liqifier: 250psf
3. Equipment Loads: These loads need to be coordinated with Jefferson Lab.
4. Wind Loads: Wind loads will be determined in accordance with ASCE 7. With ultimate wind speed design of 126 mph for a risk category III building structure.
5. Seismic Loads: Seismic loads will be determined in accordance with ASCE 7. Risk Category IV and site class of D.
6. Snow Loads: Ground snow load in the area is between 10-15psf for the Newport News area.

10.6 Survey and Alignment

This section describes the approach and methodology to be used in the survey and alignment of JLEIC collider. Whilst the instrumentation and methods described are considered "state of the art", they have been used extensively both at Jefferson Lab and at other labs, and have proved to be effective. The new green field site for the collider means that the existing survey network established for CEBAF and the 12 GeV upgrade will need to be extended considerably. At this stage the alignment tolerances have not been finalized, therefore, the alignment approach may need to be re-assessed and modified if necessary.

10.6.1 Tolerances

The positioning tolerances required by the various JLEIC elements will ultimately dictate the alignment methodology. Although these are still in development, we have made an assumption that they will be similar to other colliders, and in particular those of RHIC (Table 10.10) and PEP-II (Table 10.11). If indeed tolerances are similar to these, then they are within the capability of alignment techniques currently employed at Jefferson Lab. However, given the fact that these are super-conducting magnets, both the transfer of beamline alignment to outside fiducials and

repeatability during cooldown and warmup will have to be considered. It should be noted that in the CEBAF accelerator the beam based definition of BPM locations to adjacent quads has been widely used, and may reduce the tolerance needed for these elements.

Table 10.10: RHIC Alignment Tolerances [2]

Element	$D_{\mathbf{x}}$ **(mm)**	$D_{\mathbf{y}}$ **(mm)**	$D_{\mathbf{z}}$ **(mm)**	**Roll (mrad)**
Dipole to Reference Orbit	0.50	0.50	1.0	1.0
BPM to Reference Orbit	0.25	0.25	1.0	NA
Sextupole to BPM	0.13	0.13	1.0	NA
Quadrupole to BPM	0.25	0.25	1.0	1.0

Table 10.11: PEP-II Alignment Tolerances [3]

Element	$D_{\mathbf{x}}$ **(mm)**	$D_{\mathbf{y}}$ **(mm)**	$D_{\mathbf{z}}$ **(mm)**	**Roll (mrad)**
Quad to Quad HER	0.25	0.25	NA	0.5
Quad to Quad LER	0.15	0.15	NA	0.5
Dipole roll	NA	NA	NA	0.3

10.6.2 Reference Sysytems

The global coordinate system used for JLEIC alignment will be the same as that used for CEBAF. This is a Cartesian right-handed system with its origin at the center of the accelerator, $+Z$ running in the direction of the north linac, $+X$ perpendicular to the north, and Y =100 m defined by the beam elevation of the north and south linacs. Local coordinate systems will be used for the design of different sections of JLEIC (e.g. the collider ring, booster ring and transfer lines). Transformation parameters will be defined for each of these with respect to the global system as outlined in document [4].

Although geodetic corrections to horizontal observations will not be necessary, the effect of the earth's curvature will need to be taken into account, just as it is for the CEBAF accelerator. Survey measurements on the earth's surface are referenced to gravity. As such they follow a reference surface that is normal to the gravity vector, known as the geoid. Over small areas of the earth, such as the JLEIC site, it is reasonable to assume that the geoid approximates a sphere (Figure 10.2). The vertical differences between a tangential plane and a sphere grow rapidly with distance from the tangential point. For example, over the 81 m from the center of CEBAF to the north linac this difference is 0.5 mm; but for the possibly 400 m from the center of JLEIC to the furthest point on the collider it would be 9.6 mm.

10.6.3 Network Design

The network design for JLEIC is expected to incorporate a primary surface network and a secondary tunnel network. The surface network will form the principal tie to the CEBAF machine, whereas the much denser tunnel network will be used for aligning JLEIC components.

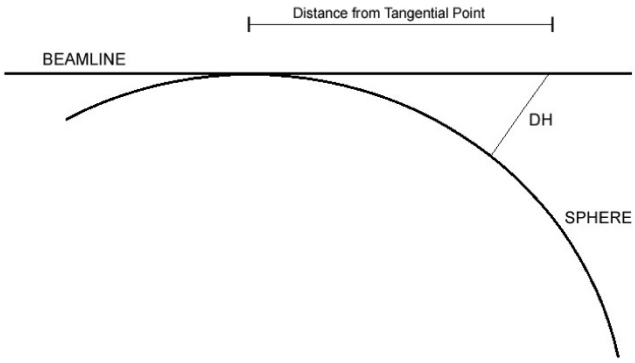

Figure 10.2: Earth's curvature.

Several monuments will need to be built spanning the JLEIC site. These should be stable and allow for clear lines of sight between monuments. Not only will these form the basis of the surface tie between accelerators, but they may also be used for quality control surveys during construction. Measurements could be made using total stations and precision EDM (Mekometer), as used successfully in the 12 GeV upgrade project. Network simulations will determine if a distance only scheme would improve the results. In either case, sub-millimeter accuracies should be achieved. There is also the possibility of using GPS measurements, the accuracy of which would have to be assessed to see if it is a viable alternative or possibly just a supplement to a terrestrial scheme. Elevation measurements would be made using digital levels.

Penetrations from the surface will tie this network to the tunnel (Figure 10.3). Optical plummets can be used to accurately center over tunnel monuments from the surface. The exact location of the penetrations may be guided by error propagation simulations. The design of the tunnel network will be dictated by the layout of the components. Monuments will be similar to those in the CEBAF tunnel, designed for a 1.5 inch retro-reflector (Figure 10.4, left). These should be located on the floors and walls to provide a robust three dimensional network (Figure 10.4, right).

Tunnel network measurements will be made primarily using a laser tracker, supplemented with digital levelling. Mekometer measurements may be made on long distances to strengthen the overall scheme. This method has successfully been used in the CEBAF accelerator, most recently on the arcs surveys. The surface network monuments will serve as the framework for the tunnel network. Direct links to the CEBAF accelerator will be possible through the transfer line tunnels, but these form a weak geometric connection, and may be susceptible to systematic reactional effects.

REFERENCES

1. K. Welch, E. Abkemeier, and B. May, "Technical Basis Document for Radioactivity Limits in Liquids as a Result of Activation or Contamination", Jefferson Lab Tech Note JLAB-TN-06-01, January 20, 2006.
2. RHIC Configuration Manual, 2006: `https://www.bnl.gov/cad/accelerator/docs/pdf/RHICConfManual.pdf`
3. M. Pietryka, M. Gaydosh, and R. Ruland, "PEP-II Alignment", SLAC-PUB-9825, Presented at the 5th International Workshop on Accelerator Alignment (IWAA'97), Oct 1997, `http://inspirehep.net/record/463371/files/slac-pub-9825.pdf`
4. Jefferson Lab internal survey document MEG0002017-S001, Rev. 3.

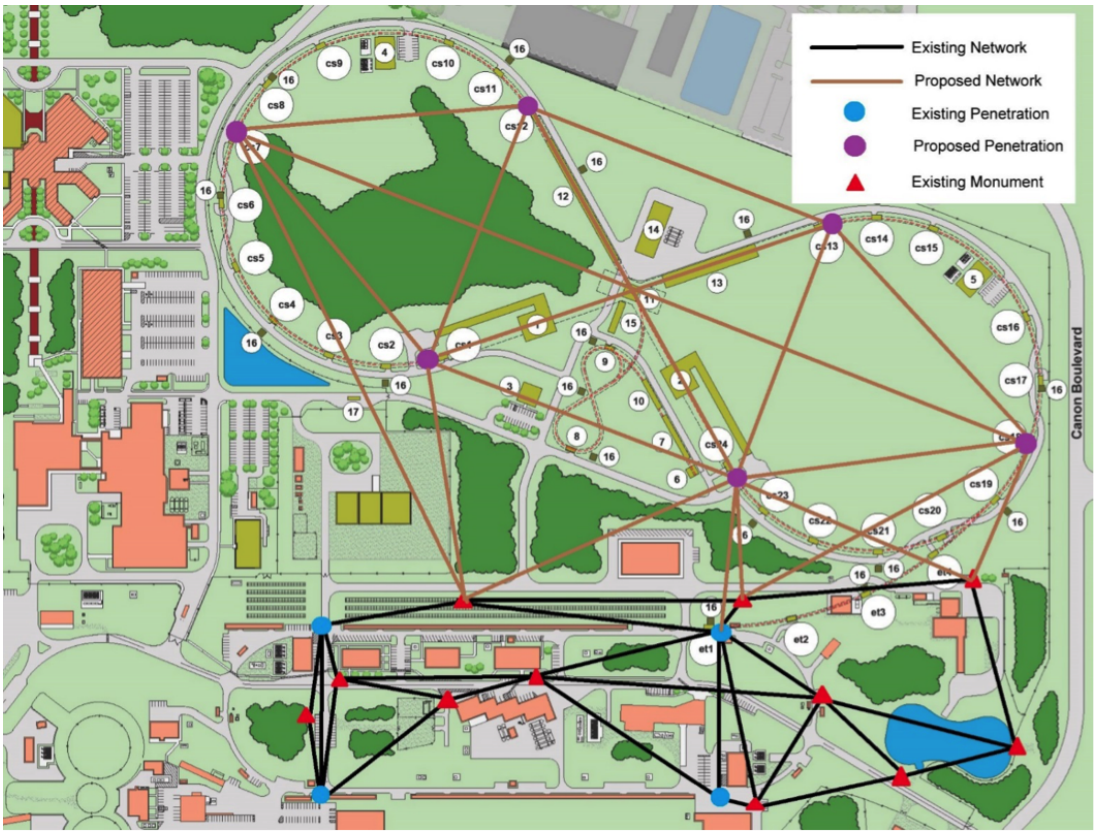

Figure 10.3: Possible surface network configuration.

Figure 10.4: Floor Monument and 1.5 inch sphere (left). Wall Monument (right).

CHAPTER 11

CRYOGENICS

11.1 Introduction

The JLEIC cryogenic system reflects the technical experience gained from the development of similar systems, such as Continuous Electron Beam Accelerating Facility (CEBAF) at Jefferson Lab (JLab) [1], the Facility for Rare Isotope Beams (FRIB) and National Superconducting Cyclotron Lab (NSCL) at MSU [2, 3, 4], the Spallation Neutron Source (SNS) at Oak Ridge National Lab [5], the Relativistic Heavy Ion Collider (RHIC) at Brookhaven National Lab (BNL) [6], NASA's Johnson Space Center (JSC) [7], and the Linear Coherent Light Source II (LCLS-II) at Stanford Linear Accelerator Center (SLAC) [7]. Jefferson Lab's Cryogenics Group has long been a center of technical excellence for cryogenics within the national lab system and will use this expertise towards the planning, design, fabrication and construction of the cryogenic plants and distribution systems for JLEIC. The operational experience of existing systems at JLab has resulted in standardized designs for the major sub-systems, such as the compressor skids, oil removal, and gas management. One example of a mature design is the compressor skid, initially developed for NASA-JSC, further advanced for JLab's 12 GeV upgrade, and upgraded again for FRIB and LCLS-II [9, 10]. The cryogenic plant design will take advantage of the 'Ganni Cycle — Floating Pressure Technology' [11], which enables a cryogenic system to efficiently, automatically, and stably adjust to different load capacities and changes in operating modes (i.e., mixed modes of liquefaction, refrigeration, and cold compressor, with varying shield loads). With a large number of installed and operating cryogenics plants at major accelerator facilities, the cryogenic system technology readiness is high and does not pose a technical risk for JLEIC.

There will be two cryogenic plants required to support all sections of the JLEIC machine. CEBAF, JLEIC's full energy injector, has an existing cryogenic plant which is operational. The

remainder of this section will address the cryogenic plant requirements for the loads in the electron collider ring, ion source and linac, booster ring, ion collider ring, interaction region, and ERL cooler.

The basic function of the JLEIC cryogenic plant is to maintain the superconducting magnets and SRF cryomodules at or below their design operating temperatures. It will also provide cooling for the electrical leads and superconducting bus. There are several key parameters which drive the design and performance of the plant.

- Superconducting magnet operating temperature of 4.7 K during steady-state operations,
- SRF cryomodule operating temperature of 2.1 K during steady-state operations,
- Superconducting portions of the Ion Linac operating with 4.5 K helium during steady-state operations,
- Appropriate lead flow of helium which maintain superconductivity of all electrical interfaces to superconducting elements, including a superconducting bus for DC power distribution,
- Appropriate segmentation of the distribution system to allow maintenance of individual or small groups of superconducting elements without having to warm up all elements and allowing flexibility in commissioning,
- Cold boxes, compressors, and distribution systems capable of handling the static heat load which can be cross connected to allow scheduled maintenance of sub components with the full system, magnets and cavities, storing most of the liquid helium. This will allow faster collider recovery and limit thermal cycling of components.

11.2 Basic Operational Overview

The liquefaction and refrigeration plant, or Central Helium Liquifier (CHL), for JLEIC will function on the refrigeration cycle. Further refinement has been made in the form of the Floating Pressure Process — Ganni Cycle [11, 12], leading to improvements in system efficiency.

The fundamental CHL system components are; cold compressors, warm compressors, cold box(es), compressor oil removal system, warm helium gas management, control system, liquid nitrogen storage, liquid helium storage, gaseous helium storage, instrument air system, guard vacuum system, helium gas purification, motor control centers, distribution (transfer) lines, and support systems such as electrical power and cooling water. Figure 11.1 shows the basic system for CHL operation.

The cryogenic plant will be centrally located on the JLEIC site, north of the crossing point of the collider tunnel. The cryogenic plant will supply 4.5 K helium to all the superconducting magnets, SRF cryomodules, and Ion Linac. The subatmospheric cold box will transition the 4.5 K helium to 2.1 K, within the cryomodule subcoolers, providing their requisite operational temperature. The cryogenic distribution system, referred to as cryogenic transfer lines, transports the helium to and from the cryogenic loads while minimizing thermal losses to the much warmer environment.

As previously mentioned, various components within the JLEIC complex operate at different temperatures to maintain their superconducting properties while providing the required performance. All SRF cryomodules, including the crab cavities, will operate at 2.1 K. All superconducting magnets and the latter half of the Ion Linac will operate at 4.5 K. Additionally, there is a cryogenically cooled thermal shield within each superconducting magnet and SRF cryomodule which serves to reduce conduction and radiation losses between the cold masses and the 300 K ambient environment. The helium will be distributed at 4.5 K to all elements. Subcoolers (4.5 K $\rightarrow$

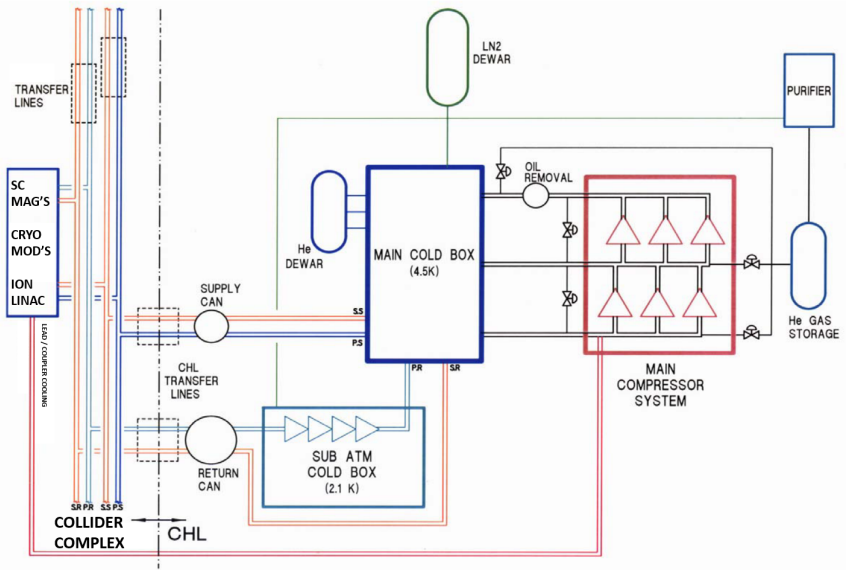

Figure 11.1: JLEIC CHL flow diagram.

2.1 K heat exchangers) will be installed in all SRF cryomodules to provide the requisite 2.1 K liquid helium [13], similar to what is employed in SNS (Figure 11.2) [14] and FRIB (Figure 11.3) [15] cryomodules. The superconducting magnets are convection cooled in a bath of supercritical helium which flows from one magnet to the next. This flow of helium is heated as it passes from magnet to magnet, therefore, it must be recooled periodically to assure the magnet coils remain below their maximum operating temperature. This is achieved by distributing recoolers along the magnet strings. The recooler, as shown in Figure 11.4, consists of the magnet coolant flowing through a heat exchanger suspended within a bath of liquid helium [6, 16]. Magnet leads use helium boiloff from recoolers to cool them and this is a liquefaction load on the refrigerator.

11.3 Cryogenic Plant Sub-Systems

11.3.1 Cold Compressors

The cold compressor system uses input electrical power to increase the availability of the helium gas being supplied to the cold box. They provide the required pressure differential within the refrigeration/liquefaction cycle. Cold compressors are turbomachines that pump off helium vapor at sub-atmospheric pressures and raise its pressure up to or close to atmospheric pressure while the gas is still at cryogenic temperatures. In addition, by boosting the return gas up to atmospheric pressure while still cold, cold compressors simplify the recovery of refrigeration on the low pressure side of the cryogenic plant cycle.

11.3.2 Cold Compressors

The cold box bridges the temperature difference from the load to ambient conditions, transferring the entropy increase at the load to the compressors. The cold box provides input power to the process stream and can only use the availability supplied to it by the compressors. Within the cold

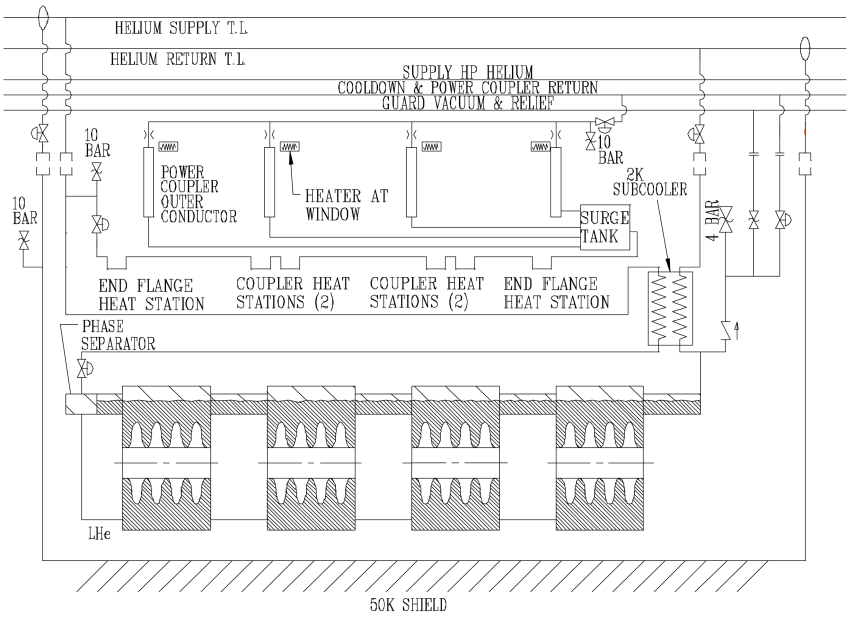

Figure 11.2: SNS cryomodule He flow schematic.

box are a series of heat exchangers and expanders (turbines), along with a series of instrumentation and valves to monitor and control process parameters.

11.3.3 Warm Helium Compressors

The compressor system uses input electrical energy to increase the availability of the helium gas being supplied to the cold box. They provide the required pressure differential within the refrigeration/liquefaction cycle. The warm compressors are oil flooded screw type compressors. The oil is added to provide cooling and a "seal" to compress the helium gas. The oil is removed later in the process.

11.3.4 Compressor Oil Removal System

This system removes the oil from the compressed helium gas. A series of coalescers and a final carbon bed reduce the oil carry over to less than 0.1 ppm. This process is critical, as any contaminants making their way into the cold section of the process will freeze and can clog the system components.

11.3.5 Warm Helium Gas Management System

To control the operating pressures of warm helium compressors and 4.5 K refrigerator, a helium control valve rack assembly is required to regulate helium gas into and out of refrigeration system as well as control the operating refrigeration operating pressures.

11.3.6 System Controls

Control and monitoring of the cryogenic liquefaction/refrigeration systems is critical to insuring safe and reliable operation. Each subsystem is equipped with PLC based control integrated to

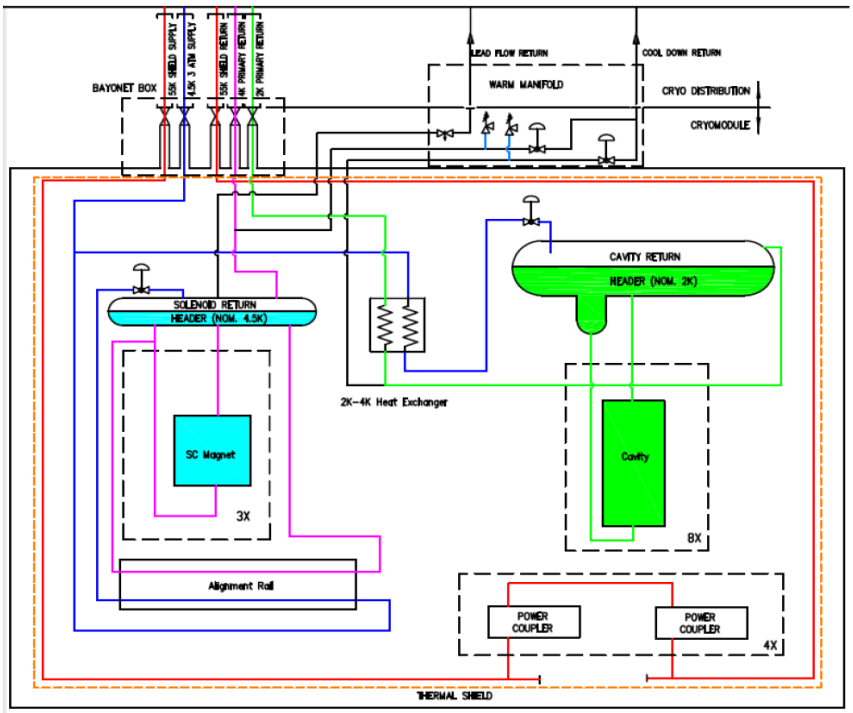

Figure 11.3: FRIB cryomodule He flow schematic.

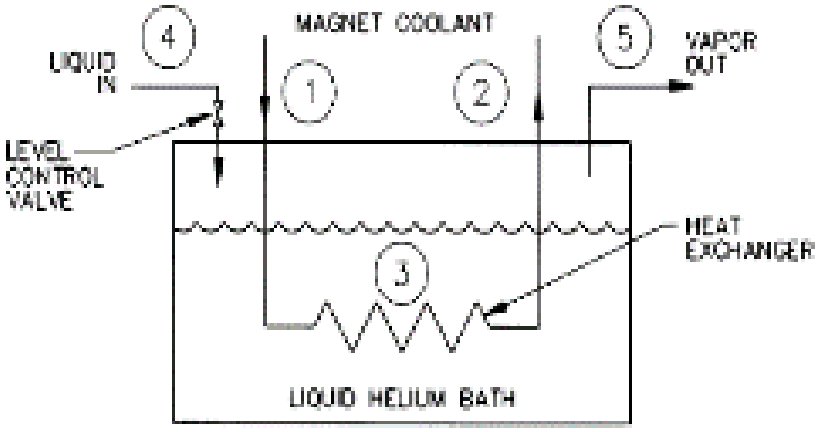

Figure 11.4: Magnet recooler process schematic.

the JLab EPICS control system. Instrumentation for temperatures, pressures, valve positions, and other operating conditions are located around the entire plant to provide input and feedback to the CHL control system.

Figure 11.5: Subatmospheric cold box (as operational (left), and internals (right).

Figure 11.6: 4.5 K cold box lower (left), and upper (right).

Figure 11.7: Warm compressor.

11.3.7 Liquid Nitrogen Dewar

Liquid nitrogen, stored in large dewars, is used to pre-cool the helium gas within the cold box and purify vendor supplied gas streams, received in tube trailers. Pre-cooling with LN2 saves up front

Figure 11.8: Oil removal system.

Figure 11.9: Gas management system with control valves.

capital costs of the refrigeration system, reduces its size, and also provides an anchor point at 80 K to help with contamination control.

11.3.8 Liquid Helium Storage

Liquid helium dewars are used to store liquid helium, aid in managing the stores of liquid helium within the loads, and as a means to boost capacity during high demands from the refrigerator.

11.3.9 Gaseous Helium Vessels

Gas helium storage is required to manage the helium gas on site.

11.3.10 Instrument Air System

Pneumatic control valves are used throughout the gas management system and the 4.5 K and sub-atmospheric cold boxes and these valves require instrument air. This system must be appropriately sized for flow rates and pressures to insure reliable control of all valves in the system.

11.3.11 Guard Vacuum System

A guard vacuum system is required for sub atmospheric process connections. The guard vacuum provides protection from air leaking into subatmospheric portions of the process piping. By having a double o-ring seal with guard vacuum between the two o-rings any leakage of air inward past the outer o-ring cannot make it into the helium space.

11.3.12 Helium Gas Purification

A helium gas purification system is required for processing and decontaminating the helium gas. This process is critical as any contaminants making their way into the cold section of the process will freeze and can clog the system components.

11.3.13 Cryogenic Distribution System

The cryogenic transfer lines are used to distribute the liquid and gaseous helium around the site. Insulated, cryogenic transfer lines will house the supply and return lines to the various connection points, see Figure 11.10 [17]. A series of valves is included as part of the distribution system to control the flow of cryogens throughout the system. Due to the size of the site and locations of cryogenic elements of different temperature, the transfer line system will be segmented.

Transfer line segmentation is favorable to accommodate site geometry as well as distribution to 2.1 K loads. The shape of the figure-8 collider tunnel is best suited for two distribution loops, one for each half of the collider rings. Separate branches to the Booster, Electron Cooler, and Ion Linac are also required. Superconducting elements operating at 2.1 K require an additional subatmospheric return line tied to their subcoolers. Locations of the 2.1 K loads are shown in Figure 11.11. To minimize the length of the cryogenic transfer lines, the Ion Collider Ring arc magnets will transfer the helium directly from magnet to magnet within their connected cryostats. The cryogenic transfer line will be connected to the magnet strings via hard connections. Cryogenic transfer line connections to cryomodules as well as the Interaction Region Magnet cryo-cans will be achieved via the combination of bayonets and u-tubes.

11.3.14 Civil Requirements and Utilities

Each cryogenic system is housed in a building or series of buildings. Additionally, storage tanks, filtering vessels, some cold boxes, and dewars are external to the buildings. Cooling towers and associated cooling water are required to remove heat from various points in the process. A significant amount of process piping interconnects all the sub systems. Electrical power is required throughout the cryogenic plants; multiple voltage and phase requirements must be satisfied to support all electrically powered motors, controls, pumps, etc.

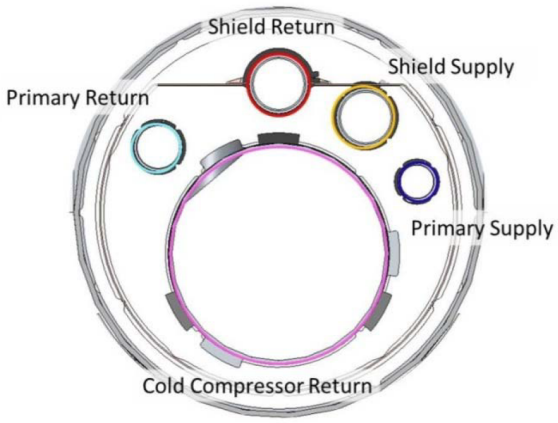

Figure 11.10: Cryogenic transfer line in FRIB tunnel.

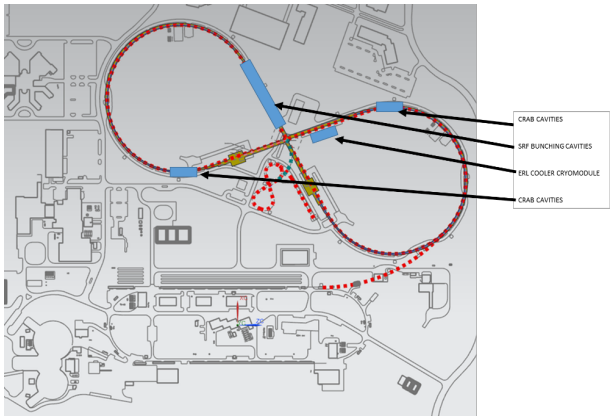

Figure 11.11: Location of JLEIC 2.1 K cryogenic loads.

11.4 Heat Loads

Table 11.1 presents the cryogenic loads for the various segments of the JLEIC machine. Primary 2.1 K loads are for the SRF Cryomodules, 4.5 K loads represent the superconducting magnets, and the shield load is present in both cryomodules and magnets. The final column, Flow, represents the lead flow required to maintain superconductivity in the cavity couplers and DC power leads. All cryogenic loads represent the maximum of the static and dynamic power dissipation which must be managed by the cryogenic plant. The interaction region magnet load is an estimate to include support for a second, potentially larger, interaction region and detector. Each segment of the machine is highlighted separately along with losses in the distribution system, electrical leads, and cavity couplers.

Table 11.1: JLEIC Cryogenic Loads

	Primary Load [W, 2.1K]	**Primary Load [W, 4.5K]**	**Primary Load [W, 55K]**	**Flow Rate [gal/sec]**
Ion source / linac	–	34	100	0.4
Ion booster magnets	–	2609	2801	–
Booster to collider transfer line	–	21	210	–
Ion collider ring magnets	–	814	8030	–
Ion collider ring SRF	439	–	2400	6.3
Electron collider ring magnets	–	200	–	–
Electron collider ring SRF	60	–	400	0.5
Interaction region magnets	–	400	250	12
ERL cooler SRF	112	–	400	0.8
Cryo distribution	–	4054	10779	9.0
Total	**611**	**7912**	**25221**	**22.7**

REFERENCES

1. V. Ganni *et al.*, "2014 Commissioning of Helium Refrigeration System at JLab for 12 GeV Upgrade", *AIP Conf. Proc.* **1573** (New York: American Institute of Physics) pp 944_8.
2. K. Dixon *et al.*, "2015 FRIB Cryogenic Plant Status", *IOP Conf. Ser.: Mater. Sci. Eng.* **101** 012071.
3. V. Ganni *et al.*"2015 FRIB Cryogenic Distribution System and Status", *IOP Conf. Ser.: Mater. Sci. Eng.* **101** 012034.
4. A. McCartney *et al.*, "2002 Cryogenic System Upgrade for the National Superconducting Cyclotron Laboratory", *Adv. Cryo. Eng.* **47** (New York: American Institute of Physics) pp 207_12.
5. F. Casagrande *et al.*, "2005 Status of the Cryogenic System Commissioning at SNS", *Proc. of 2005 Particle Accelerator Conf.* (Knoxville TN) pp 970_2
6. R. Than *et al.*, "2008 Relativistic Heavy Ion Collider (RHIC) Cryogenic System at Brookhaven National Laboratory: Review of Modifications and Upgrades since 2002 and Planned Improvements", *Adv. Cryo. Eng.* **53** (New York: American Institute of Physics) pp 578_87.
7. J. Homan *et al.*, "20 K Helium Refrigeration System for NASA-JSC Chamber", *Adv. Cryo. Eng.* **59A** (New York: American Institute of Physics) pp 307_14.
8. V. Ravindranath *et al.*, "Process Simulations for the LCLS-II Cryogenic Systems" *IOP Conf. Ser. : Mater. Sci. Eng.* **278** 012106.
9. P. Knudsen *et al.*, "2015 Performance Testing of Jefferson Lab 12 GeV Helium Screw Compressors", *IOP Conf. Ser.: Mater. Sci. Eng.* **90** 012072.
10. P. Knudsen *et al.*, "2016 Commissioning and Operational Results of the 12 GeV Compression System at JLab", *IOP Conf. Ser.: Mater. Sci. Eng.* **101** 012126.
11. V. Ganni *et al.*, "2010 Optimal Design and Operation of Helium Refrigeration Systems using the Ganni Cycle", *Adv. Cryo. Eng.* **55A** (New York: American Institute of Physics) pp 1057_71.
12. P. Knudsen *et al.*, "2017 Modifications to JLab 12 GeV Refrigerator and Wide Range Mix Mode Performance Testing Results", *IOP Conf. Ser.: Mater. Sci. Eng.* **171** 012015.

13. V. Ganni and P. Knudsen, "2014 Helium Refrigeration Considerations for Cryomodule Design", *Adv. Cryo. Eng.* **59B** (New York: American Institute of Physics) pp 1814_21.

14. W.J. Schneider *et al.*, "Design of the SNS Cryomodule", *Proc. PAC2001*, JACoW, pp. 1160-1162.

15. T. Xu *et al.*, "FRIB Cryomodule Design and Production", *Proc. LINAC2016,* JACoW-LINAC2016-WE2A02, pp. 673–679.

16. Brookhaven National Laboratory, Collider Division, Collider-Accelerator Department (2006). *Configuration Manual for RHIC* (Relativistic Heavy Ion Collider), Retrieved from: `https://www.bnl.gov/cad/accelerator/docs/pdf/RHICConfManual.pdf`

17. V. Ganni *et al.*, "FRIB Cryogenic Distribution System", *Adv. Cryo. Eng.* **59A** (New York: American Institute of Physics) pp. 880_6.

CHAPTER 12

ENVIRONMENT SAFETY AND HEALTH CONSIDERATIONS

Jefferson Lab considers no activity to be so urgent or important that we will compromise our standards for environmental protection, safety, or health. Among other ways, Jefferson Lab executes this policy by complying with all applicable Environment, Safety and Health (ES&H) laws, regulations, standards, and our contractual commitments to the Department of Energy.

Jefferson Lab's Integrated Safety Management System (ISMS) integrates the requirements of 10 CFR 851 and 10 CFR 835 and the ES&H requirements of the JSA contract with DOE into the mission and operation of Jefferson Lab. Jefferson Lab's ES&H program is made up of the necessary policies, documents, and implementing processes to provide a framework that allows employees, subcontractors, and visiting scientists to conduct their work in a safe manner.

All non-construction activities are managed according to a DOE approved Worker Health ans Safety Program (WHSP) that implements the requirements of 10 CFR 851, Worker Health and Safety. The WHSP is required by 10 CFR 851 and consists of two elements: the ISMS and a description of the ten functional programs required by 10 CFR 851, Appendix A, Section 1. The WHSP provides a description of the programs developed to meet the requirements of 10 CFR 851. Construction activities related to JLEIC will be managed according to a detailed Construction Project Safety and Health Plan derived from Preliminary and Final Hazard Analysis documents (PHAR and HAR) and developed according to the details of the proposed construction means and methods.

The WSHP does not include radiological hazards; they are not within the scope of 10 CFR 851. The Jefferson Lab Radiation Protection Program (RPP), which describes Jefferson Lab's

compliance with the requirements of 10 CFR 835, Occupational Radiation Protection, specifically incorporates elements necessary to satisfy those requirements. Detailed descriptions of the technical, operational and administrative aspects of the RPP are included in the Beam Containment and Access Control Policy [1], the Shielding Policy for Ionizing Radiation [2], the Jefferson Lab Radiological Control Manual (RadCon Manual or RCM), and technical basis documents and procedures that cover varying aspects of radiological work. All radiological operations and radiological work activities performed by JSA for the Department of Energy (DOE) at Jefferson Lab fall within the scope of the RPP.

Jefferson Lab employs an Environmental Management Program (EMS) to manage risk to the environment in a similar fashion as it manages risk to workers and the public. This is achieved through planning, operational controls, and continual improvement. The EMS applies to all Jefferson Lab facility operations and activities and to its entire population. The EMS considers support functions that allow research to occur including construction and management of site infrastructure, engineering and fabrication of equipment, and associated administrative support. Activities, products, and services that involve interaction with the environment are reviewed and prioritized annually, and measurable goals for improvement are set, tracked and communicated.

Chapter 10.2 Site Preparation and Development, Section 10.2.2 Environmental Site Assessment already addressed the environmental conditions in the Preliminary Environmental Evaluation and Environmental Checklist, dated June 15, 2017. This was prepared by SNC-Lavalin's Atkins Group (Atkins) in accordance with 10 CFR Part 1021 of the National Environmental Policy Act (NEPA) and DOE Quality Assurance Plan and Procedures for the proposed project.

The Environmental Compliance Checklist was prepared for submission to the DOE NEPA Compliance Officer. Atkins also prepared the federal information consistency package for Coastal Zone Consistency for submission by Jefferson Lab's DOE Site Office to Virginia Department of Environmental Quality (DEQ). This preliminary environmental document was prepared to present information and a preliminary analysis of the project that can be used as a foundation for a future environmental analysis if an Environmental Assessment (EA) is later deemed necessary. In addition, Environmental Specialties Group (ESG) prepared a Phase I Environmental Site Assessment prepared dated March 10, 2016 and a Phase I Supplemental Package and report of findings dated February 7, 2017. and was included in the discussion of the findings in the A Preliminary Environmental Evaluation and Environmental Checklist.

The Jefferson Lab WSHP, RPP, and EMS apply to all JSA employees and subcontractors performing DOE mission-related work activities in Jefferson Lab facilities located on JSA-controlled premises. The requirements of Jefferson Lab WSHP, RPP, and EMS have been flowed down to its subcontractors through the contract terms and conditions. Subcontractors are required to submit appropriate documentation that are reviewed for conformance. Visiting scientists from other institutions that may work at Jefferson Lab participate in the Jefferson Lab ES&H program just as employees are expected to participate and comply with the requirements of Jefferson Lab's programs; Jefferson Lab does not make this distinction within its ES&H programs. Taken together, these two elements describe a strong health and safety program that allows employees, subcontractors, and visiting scientists to work safely at Jefferson Lab.

12.1 Radiation Control

There are unique hazards associated with the operation of accelerators. These accelerator-specific hazards and their associated mitigations are addressed by the requirements of the Accelerator Safety Order (ASO), DOE 420.2C, which is one of the ES&H requirements of the JSA contract with DOE mentioned above. The ASO requires a detailed hazard analysis related to accelerator design and operation that is documented in a safety assessment document. Consequently, all safety aspects of the new facility design and operations will be covered by the updated JLab Final Safety Assessment Document (FSAD) [3], modified to address all new features of the new JLEIC project. The present FSAD Document identifies the hazards that are characteristic for Jefferson Lab accelerator complex, provides an analysis of postulated operational events that can lead to adverse consequences, and identifies the complete collection of specific controls necessary to minimize to acceptable levels the risks associated with these hazards. Safe and successful operation of the existing CEBAF accelerator and other facilities at JLab for more than two decades is confirmed by numerous internal and external reviews. The new FSAD document will contain detailed descriptions of various safety issues related to the design and operations of JLEIC facilities at JLab. Apart from the general and specific industrial hazards, such as electrical, oxygen deficiency, working in confined space, working with pressure vessels, and others, the most significant specific hazards arising from accelerator operations are the radiological hazards. Radiation Control Department at Jefferson Lab's Environmental, Safety, Health and Quality (ESH&Q) Division applies the DOE's mandated ALARA (As Low As Reasonably Achievable), also known as optimization [4]) policy when dealing with the radiation hazards to the environment, public, personnel, and equipment.

The design of the JLEIC machine and its operations plan must provide adequate radiation protection to JLab staff and users, and to the general population and environment. Radiation Control Department (RadCon) at JLab has accumulated extensive experience in planning and implementing the engineered and administrative radiation protection measures and procedures, and in providing continuous radiation monitoring both on-site, and around the site boundary. Current JLab accelerator-specific radiation protection measures and procedures are listed and discussed in detail in the "Radiation Protection Plan"(RPP) document, [5], and in the "JLab Shielding Policy" document [2], using guidelines of the Federal Law (10CFR835).

Jefferson Lab implements EH&S policy specific to radiation dose for workers and members of the public through the process of optimization [4] that maintains doses well below regulatory limits and ALARA, taking into account the state of technology, perceived benefit to workers and society, and the economics of dose reduction.

By design the internal JLab radiation limits and controls are set up lower than the already strict DOE limitations, allowing conservatism in the design and procedures. The practice virtually guarantees several layers of protection and the opportunity to address any arising issues before they become critical.

The Radiation Physics Group in RadCon has a long history of completed radiation protection projects, including the shielding designs for the CEBAF machine and for the Experimental Halls at JLab. We also provide measurements of the radiation fields, verifying our solutions, and giving the assurance of radiation safety.

The Radiation Control Department reviews any facility modification or new facility design for conformance with the JLab shielding policy. For large scale or new projects, such as JLEIC, this involves a detailed study of all significant radiation sources and the effectiveness of shielding associated with facility structure during the civil design process. This is typically an iterative evaluation with the facility designers, engineers, and physicists until an acceptable solution is found.The Radiation Physics Group, a group within RadCon, will collaborate with the System and Facility designers, Accelerator physicists, and staff and users in Physics Division to find and address radiation protection problems at early stages of the development to develop optimized solutions. This helps ensure that radiation doses to workers and members of the general public are ALARA.

This synergy, between the stakeholders to minimizing radiation impact by design, helps everyone, because it results in lower experimental equipment background counting rates, easier personnel access, less damage to beamline components, less radioactive waste, and less environmental impact during decommissioning.

Preliminary study [6] indicates that the proposed JLEIC complex can be installed at Jefferson Lab site in a tunnel similar to CEBAF tunnel. Solutions to the specific radiation protection problems will be optimized during the project's Conceptual Design stage when the operational parameters of the machine are finalized. All final solutions will be subject to independent external review.

12.1.1 Radiation impact and mitigation measures

Critical radiation protection issues at JLEIC include the evaluation and minimization of the radiation doses to personnel, radiation damage to equipment on site, and assuring that the environment and the general public outside the fence are not affected by JLEIC operations.

JLab Radiological Control Policy [7] sets the Facility Design Goals:

- maintaining individual worker dose less than 250 mrem per year for radiological workers
- maintaining individual dose less than 10 mrem per year for general employees and general population
- preventing degradation of groundwater quality
- controlling contamination by engineered means where possible
- minimizing the generation of radioactive material

12.1.1.1 Chronic beam losses Protons, heavy nuclei, and electrons of the colliding beams are lost at steady rates around the machine during the regular stable operations, due to beams interactions with residual gas in the beam line, beam optics effects leading to the beam particles escaping the stable apertures, energy losses due to the synchrotron radiation, losses during the bunch injection stages, beam cooling, and other mechanisms.

The main locations of such losses are the beamlines, limiting apertures (collimators), beam removal systems or dumps. The impact of such chronic losses includes high levels of prompt

radiation dose rates inside the tunnel during operations, and possible high level of activation of the beamline components, creating the areas of limited or delayed access, and producing radioactive waste. The locations and magnitude of expected beam losses strongly depend on the details of the machine design. The best way to mitigate effects of such inevitable radiation sources is to plan for them, and try to create the design in which such losses can be controlled. The planned dedicated beam loss locations in the machine will be better protected by design, and the rest of the machine will experience lower levels of prompt radiation. Detailed and iterative evaluation of these effects is part of the process of creating the final Conceptual Design Reports (CDR) for the machine.

The Interaction Points (IP) in the Experimental Halls will, by design, experience routine beam loss. This will result in high radiation levels around the IP, and some level of activation in the adjacent beamlines. The mitigation for these effects would include proper shielding of the walls, roof, and access ways to the Halls, and shielding protection of sensitive equipment. Detailed evaluation of such radiation source can be challenging, and will be required in the CDR.

12.1.1.2 Accidental beam losses All possible scenarios of the accidental beam losses will be considered and evaluated in terms of radiation safety and radiological controls.

12.1.1.3 Environmental radiation Direct emission and skyshine scattering of photons, neutrons, and muons emerging from the ground above the tunnel and from the roofs of the Experimental Halls during operations, will produce prompt radiation at the site fence. The design figure of merit is to limit the yearly radiation dose accumulation at the fence to 10 mrem per year, roughly below 10% of the natural radiation background in the area.

JLab has implemented a process of "Radiation Budgeting" in which the estimates of yearly dose accumulation at the boundary for each planned experiment are made prior to the period in which the experiment is scheduled to run. This is done early enough to allow extra time for additional controls – mitigation by experiment reconfiguration, adding more shielding, or adjusting the run schedule if necessary. The dose rates at the critical locations at the boundary are monitored, and the Radiation Budgets are "reconciled" yearly. Radiation Physics Group in the Radiation Control Department at JLab has a successful experience dealing with this radiation source in the high power beam operations at CEBAF's Hall A and Hall C end stations. Conditions at the JLEIC experimental Halls are very different from Halls A and C. There will be loss in the Halls associated with beam delivery and some equivalent loss at the interaction point. The latter will be asymmetric and very energetic, and can contribute significantly to skyshine.

Estimates will be done on the basis of anticipated luminosities for different energies and ion types, detailed civil engineering plans for the Halls, the expected power of the scattered beams coming into the Halls off-axis, and proposed typical run schedules at JLEIC.

The unique environmental radiation factor to consider at JLEIC will be the high energy muon flux produced in the tunnel, and then scattered and penetrated the soil above the tunnel, creating the long-range muon skyshine dose rate at the boundary. Preliminary estimates indicate that this source of radiation is small, but detailed evaluations will be incorporated into the CDR.

High-energy particles penetrating the tunnel walls interact in the surrounding soil and may produce radioactive isotopes in the ground water. The levels must satisfy the strict legal limitations preventing degradation of groundwater quality.

Radiation streaming along the ducts, access ways, and penetrations will be properly limited by their design and extra shielding if necessary to limit the dose rates outside.

12.1.2 Radiation Physics processes at JLEIC

We will evaluate the impact of the various sources of radiation at JLEIC by calculating Radiation Source Terms. Each Radiation Source Term will characterize all types of ionizing radiation produced at a given location under certain conditions. Such Source Terms will be developed for every possible location of beam loss, and will characterize intensity, type of radiation produced (such as photons, neutrons, protons, muons, nuclear fragments, etc.), angular and energy distributions for the secondary radiation, possibility and extent of material activation at the location. The Radiation Source Terms are required for successful modeling of the further radiological effects, and ALARA optimization of the design.

Different methods of Radiation Source Term evaluation are used. They include analytical evaluations in relatively simple cases, and more generally, detailed Monte Carlo (MC) simulations. The MC simulation packages GEANT3 [8], Geant4 [9], FLUKA [10], and MARS [11] are used both for Source Term evaluations and for particle transport and shielding evaluations.

Precision is achieved by multiple redundant cross-checks using different models and different methods by different people, and by using external reviewers in a structured External Review process. Tools and methods for such evaluations, and the expertise in their use are available within the RadCon, and have been tested in applications at JLab, as applied to high power 12 GeV electron beams. Compared to CEBAF accelerator, the new radiation source terms at JLEIC will include the high-energy proton and heavy ion beam interactions, new source terms for high-energy muon flux production. The new radiation source terms at the Interaction Points at JLEIC will require additional development and cross-checks between different electron nucleus interaction Physics simulation models.

12.1.2.1 Electromagnetic interactions of electrons and gammas The set of Physics processes and simulation tools that will be used for JLEIC Source Term calculations includes detailed knowledge of the basic electromagnetic processes of interactions of charged particles with matter, including the electromagnetic particle cascades and muon pair production by electrons. The level of confidence in the results of essentially all available models is quite high, at the level of accuracy better than 5-10 percent. These processes dominate in the conditions where the prompt dose rates are evaluated for electron beam losses.

12.1.2.2 Nuclear interactions of electrons and gammas These interactions are responsible for the source terms for the prompt neutron production and material activation in the electron beam losses. Corresponding photonuclear reactions caused by the real photons in the electromagnetic cascades are reasonably well known and implemented in different MC models. The reliability of the calculation results is generally considered to be 30-50%. Electrons can also interact with protons and nuclei directly, without the intermediate production of real photons. These processes are important in the electron beam interactions with thin targets, such as exit foils, interaction with the residual gas in the beamline, and interactions of the colliding beams. JLab pioneered in introducing the direct electro-production processes into the calculations of radiation environment at CEBAF accelerator. Presently it is available in different simulation tools.

12.1.2.3 Nuclear interactions of protons and nuclei Such interactions are the source of prompt hadrons in the tunnel, material activation, and the penetrating muon flux. Available simulation tools are capable of evaluating them quite reliably, and the codes and techniques at our disposal are ready to do the source term evaluations.

12.1.2.4 Combinations of the processes in real geometries, particle cascades Typical examples:

- Beam losses in the tunnel
- Electron-Ion collisions at the interaction point and consequent interaction of the products in the narrow beamline apertures
- Full beam absorption in a beam dump device
- Production of ^{3}H and ^{22}Na in the ground water

The radiation safety evaluations will require detailed geometrical model of the corresponding areas, and detailed assumptions for the beam losses.

12.1.3 Radiation monitoring

The radiation monitoring system presently operational at CEBAF consists of a network of Area Radiation Monitors covering all locations critical for the safe operation of the accelerator. Some of the monitors are connected to the Personnel Safety System network to protect personnel from accidental beam loss and have interlock capability to shut down operations in case of unexpected levels of radiation observed. Other detectors, situated at the site boundary, monitor radiation dose from Sky Shine.

The detectors at the site boundary are carefully constructed and calibrated neutron and gamma detectors that reliably monitor environmental-level dose rates correlated with accelerator operations. This ensures that JLab conforms to the strict limitations on the maximum radiation dose accumulation at JLab boundary.

For JLEIC the radiation monitoring system will be modernized and expanded to improve detector response and reliability.

12.1.3.1 Radiation monitors adjacent to accelerators The location of the new radiation monitors associated with JLEIC will be determined using the same principles that govern the system layout in the present CEBAF accelerator. This is illustrated in the following schematic plots. Groups of Area Radiation Monitors are placed strategically at the tunnel access points, critical penetrations, and essentially at all locations where detectable radiation associated with accelerator operation is expected. The accelerator EPICS control system continuously collects data from these Area Radiation Monitors.

Figure 12.1 shows the general layout of the Radiation Monitoring system at CEBAF.

Figure 12.2 shows the layout the monitors placed around the Experimental End Stations Hall A, B, and C. Access points to the Halls, both from the side of the Hall entrance ramps, and from

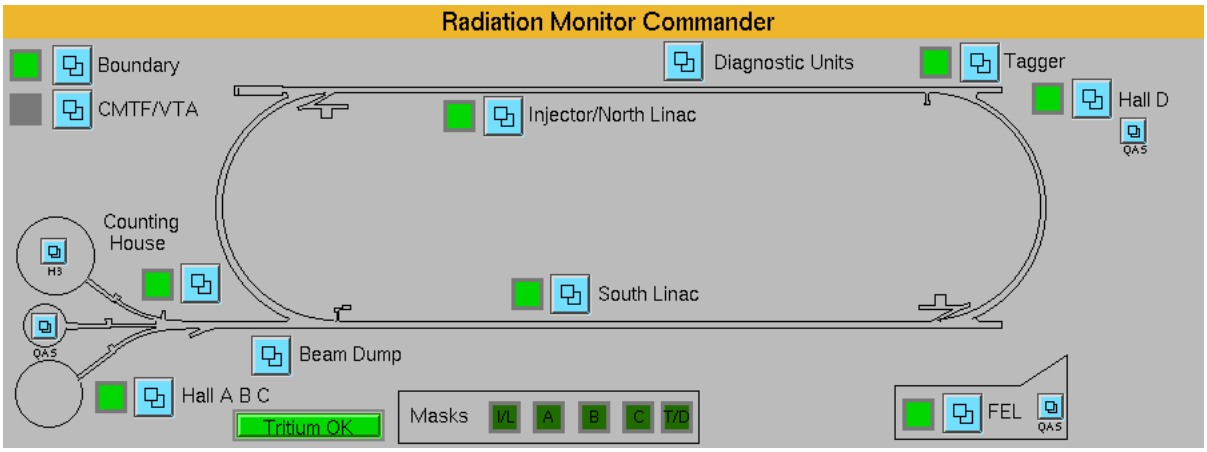

Figure 12.1: EPICS control screen showing different groups of radiation monitors around CEBAF.

the beamline tunnel, are equipped with the monitoring units capable of monitoring neutron and gamma dose rates. Some of the most critical units are interfaced with the Personal Safety System that would terminate beam delivery if the dose rates observed exceed the preset limits. High power Experimental Halls A and C are also monitored from the outside by the monitors installed on top of the roofs. These monitors serve as a part of the environmental radiation monitoring system, as the bulk of the radiation produced by CEBAF at the boundary is coming through the roofs.

12.1.3.2 Radiation monitors located at the site boundary Figure 12.3 shows the layout of the Radiation Boundary Monitors (RBMs) placed around the perimeter of JLab property. The RBMs serve an important role: to document that the low levels of the radiation produced by the CEBAF operations at the site boundary, remain below approximately 10% of the natural radiation levels in the area. At CEBAF, RBMs are clustered close to the area near Halls A and Hall C, two RBMs are located close to Hall D. Two RBMs are placed far from the expected radiation sources and are used to measure background levels.

The sensitivity of these monitors is sufficient to reliably detect and measure the radiation dose at the boundary from CEBAF operations, at the level of about one percent of the natural radiation background. This is illustrated in Figure 12.4.

Active radiation monitoring at CEBAF is supplemented by the extensive array of passive dosimeters of appropriate level of sensitivity and stability. While their accumulated results cannot be correlated with the machine operations and thus background-corrected, they provide extra layer of the radiation safety assurance around the site.

Similar sets of environmental radiation monitors will be placed around the boundary of the JLEIC site. At JLEIC we expect an additional source of environmental radiation, the energetic muons from the decays of charged pions produced in high energy proton and ion beam interactions. The source terms will be evaluated, appropriate shielding design measures taken, and proper monitoring systems installed. A good candidate for such monitoring systems will be the next generation of the presently deployed “Spectroscopic High Pressure Ion Chamber” environmental monitors. They are currently capable of distinguishing between photon and cosmic muon

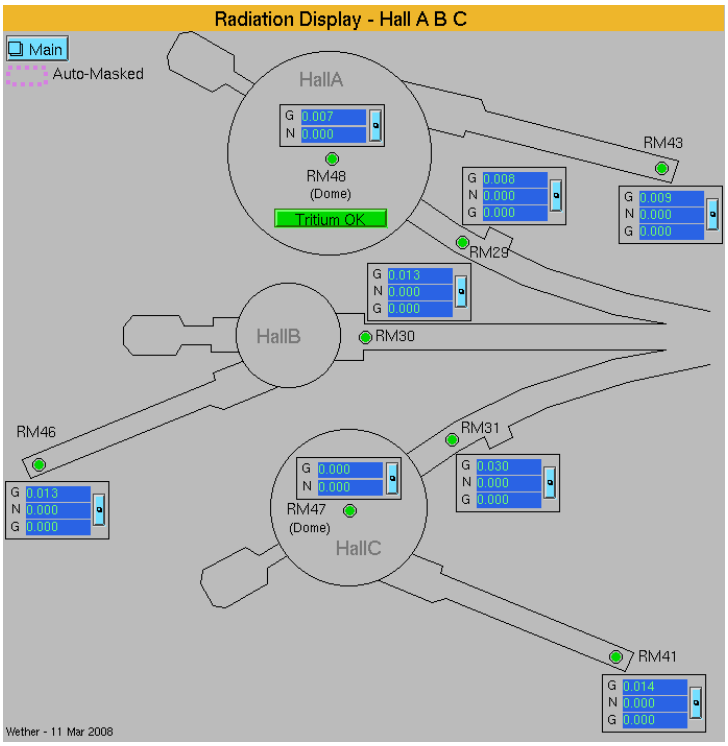

Figure 12.2: EPICS control screen showing the group of radiation monitors servicing the Experimental Halls A, B, C.

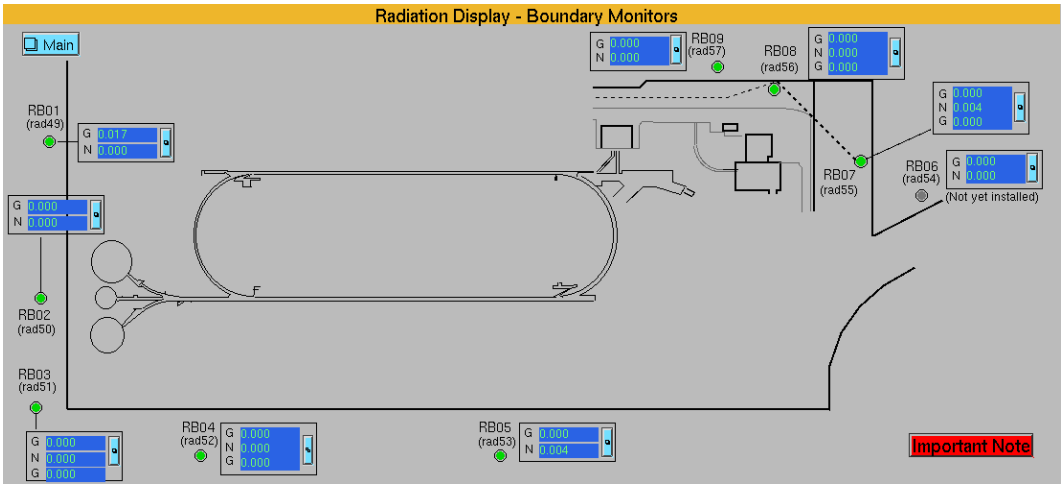

Figure 12.3: EPICS control screen showing environmental monitors around the CEBAF site at the property boundaries.

interactions and their capabilities may be expanded to measuring low level neutron fluxes, see Ref. [12].

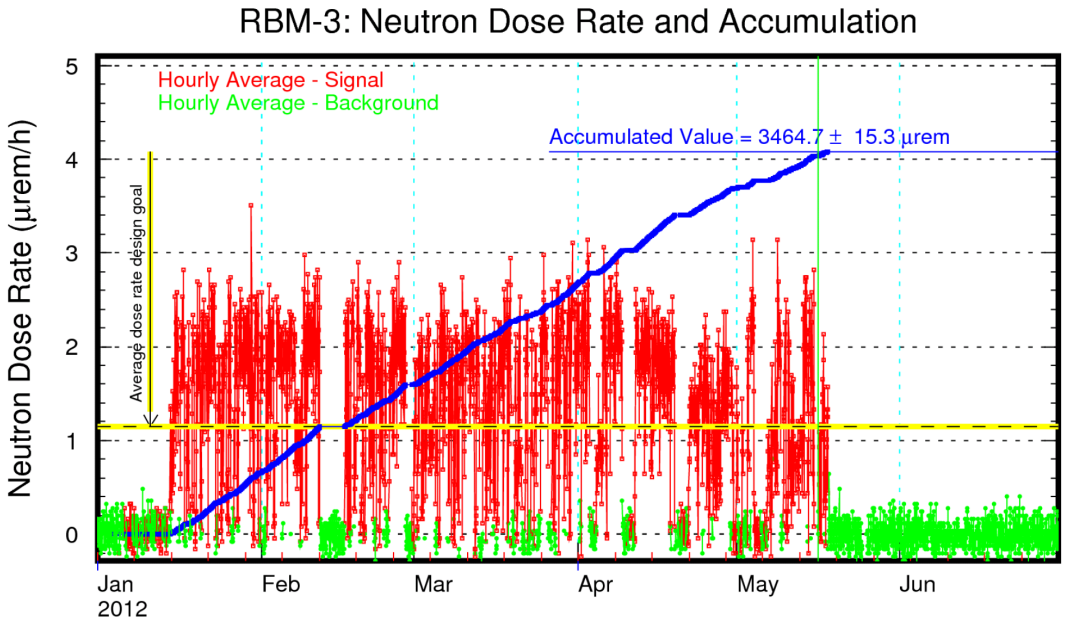

Figure 12.4: Measurements of the neutron environmental radiation at the boundary in the vicinity of Hall C in the six-month period from January to June 2012. All readings are hourly averages with background subtracted. Hours with no accelerator operations are shown by green points and used for the background calculation. Red points correspond to the hours with the beam present in the machine. The semi-annual dose accumulation history is shown by the violet line, and the result is shown on top. The so-called "Average dose rate design goal" value is indicated by the yellow dashed line; it corresponds to the average dose rate that would be required to achieve the administrative limit assuming continuous operation through the year.

12.1.3.3 Ground water monitoring The concentrations of radioactive pollutants and limits to the radiological effluent water discharges in the environment at Jefferson Lab are governed by the Virginia Pollutant Discharge Elimination System (VPDES) and the Hampton Roads Sanitation District (HRSD). VPDES permit #VA0089320 addresses groundwater quality, both in-situ (well monitoring) and related to discharges of groundwater to the surface (end station dewatering). The de-facto limit for the surface discharges is the EPA drinking water standard (at the point of dewatering sump discharge). HRSD permit #0117 addresses discharges to the sanitary sewer.

The primary limit is 5 Ci of ^{3}H and 1 Ci of all other gamma emitting nuclei. In addition, a monthly average ^{3}H concentration limit of 0.1 uCi/ml applies to these discharges, not to exceed 10 mCi/day. The details of the Jefferson Lab's infrastructure, and ground water monitoring procedures, including ALARA action limits may be found in Ref. [13].

For the new JLEIC facility the monitoring system will be extended to cover the new territory. New wells will be installed around the site to monitor tritium and ^{22}Na content in ground water and take appropriate actions if necessary, according to the established procedures.

12.1.3.4 Radiation monitoring of coolants and lubricants Water is the principal coolant used in the beam dumps, collimators, and other equipment. Oils and other lubricants are used in accelerator hardware to minimize wear and tear and corrosion. Both lubricants and coolants are subject

to high energy beams and can become activated. RadCon has a well developed the process for monitoring and safe disposal of such liquids in accordance with all applicable regulations. Details of the program may be found in Ref. [13]. The same well-developed principles will be implemented in the JLEIC design.

12.1.3.5 Radiation monitoring of exhaust air Consistent with the JLab's ALARA approach public doses associated with the operating history of Jefferson Lab are much less than 10 mrem/year (see Ref. [4]). Annual dose estimates associated with CEBAF operation are in the range of about 0.1 mrem up to 0.37 mrem; this dose is too low to measure and can only be estimated. Even under the conservative exposure scenarios required by the National Emission Standards for Hazardous Air Pollutants (NESHAP) that are used to estimate this dose, it is less than 4 percent of the Laboratory's administrative dose limit, and less than 0.4 percent of the public dose limit. Jefferson Lab's Annual Site Environmental Report ([14], [15]) documents the estimated contributions to the public doses from all air pathways. This dose is typically smaller than the radiation doses from the neutron and photon skyshine.

The ALARA approach to releasing potentially radioactive gases at JLab includes limiting air exchange with outside by design during operations, using HEPA air filters in all air exchanges, and radiation monitoring of all major pathways for air exchange. The same systematic approach will be used in JLEIC design and construction. The air activation source terms will be evaluated according to the planned beam loss source terms, and the air monitoring stations will be installed accordingly. The source terms are expected to be comparable or smaller than the present sources of activated air at CEBAF, mostly determined by the high power Experimental Halls operations.

12.1.4 Disposal of activated components

JLab RadCon has developed procedures for the disposal of the generated radioactive waste [16]. RadCon engineers expect that the amount and level of radioactive waste production at JLEIC will be comparable or lower than at present CEBAF.

12.1.5 Plan for JLEIC decommissioning

DOE requires accelerator facility decommissioning considerations to be included into the planning, construction and operation of accelerator facilities (see 10 CFR 835.1002). Disassembly and disposal of the activated materials and structures at the end of the facility lifetime must be planned and optimized with ALARA principle taken into account at the design stages of the project. Since the language in the Code of Federal Regulations and the corresponding DOE Guides [17] implies that the preliminary facility decommissioning plan needs to be prepared before accepting new projects, the preliminary decommissioning plans for the JLEIC facility will be a part of the design at CD-0 level.

The decommissioning plan will consider the long-term plans for operating JLEIC, design optimization, selection of material to limit activation, issues associated with the experimental program, and will anticipate engineered solutions to optimize decommissioning efforts.

12.1.6 RadCon Resources for JLEIC activities

Projected plan of the two-year RadCon efforts in support of JLEIC Conceptual Design Report has been developed, with approximate eight quarters of the work breakdown and estimated need in the additional expert FTE contributions.

The plan includes the following activities:

- Develop the list of potential radiation sources in and around the MEIC complex, including the description of corresponding radiological issues and critical machine parameter envelopes. Prioritize the time order in which the shielding of these should be optimized and designed.
- In discussions with the project management, iteratively develop the radiological models describing the potential radiation sources, evaluate the need for extra mitigation measures (shielding, labyrinths, geometry and material choices, etc). Estimate groundwater activation, assist ESH division in the choice of sampling wells. Estimate generation and release of radioactive and noxious gases.
- Perform activation calculations based on final preliminary design; prepare draft decommissioning plan based on the above, which includes assumptions about length of facility operation.
- Evaluate and plan deployment of radiation detection systems, associated communication infrastructure and DAQ as applicable for area, boundary and environmental monitoring. Establish system cost and procurement plans for early deployment to gather sufficient baseline data before start of facility operation. Evaluate needs and cost of operational aspects, such as posting, staging areas and rapid access system.
- Document the efforts and produce the radiation shielding design report ready for the external review

The approximate need in expert level Radiation Physicists will include approximately 3/4 FTE contribution during the first year, and about 2 FTE during the second year. The effort will be in addition to the current Radiation Physics workload in support of the JLab experimental program.

REFERENCES

1. Jefferson Lab, "Thomas Jefferson National Accelerator Facility Beam Containment and Access Control Policy", https://jlabdoc.jlab.org/docushare/dsweb/Get/Document-111187/Beam%20Containment%20and%20Access%20Control%20Policy%20Rev1.pdf, December 2015
2. Jefferson Lab, "JLab Shielding Policy", https://jlabdoc.jlab.org/docushare/dsweb/Get/Document-84801/Appendix3D.doc, March 2014.
3. Jefferson Lab, "Final Safety Assessment Document, Revision 7a", https://jlabdoc.jlab.org/docushare/dsweb/Get/Document-21395/FSAD%207a%20with%20signature.pdf, December 2014.
4. Tracy Ikenberry, Dade Moeller & Associates, and Gina Dixon Roemer, JLab RadCon, "Technical Basis for the Limitation and Optimization of Public Dose", JLAB-TN-13-022, March 4, 2013.
5. Jefferson Lab, "Radiation Protection Program, Revision 2", https://jlabdoc.jlab.org/docushare/dsweb/Get/Document-150505/2008%20%20Radiation%20Protection%20Program%20and%20Implementation%20Plan%20%20rev2.pdf, January 2008.

6. P. Degtiarenko, "Radiation Environment and Shielding Design Optimization at MEIC", https://www.jlab.org/conferences/meic-oct15/talks/degtiarenko.pdf, October 2015.
7. Jefferson Lab, "ES&H Manual, Radiation Control Supplement §111-06, §211-05"
8. Application Software Group, CERN Computing and Networks Division, "GEANT, Detector Description and Simulation Tool", CERN Program Library Long Writeup W5013, (1994).
9. S.Agostinelli *et al.*, "Geant4 – a simulation toolkit", Nuclear Instruments and Methods in Physics Research Section A: Accelerators, Spectrometers, Detectors and Associated Equipment Volume 506, Issue 3, 1 July 2003, Pages 250-303; https://doi.org/10.1016/S0168-9002(03)01368-8
10. T.T. Bohlen, F. Cerutti, M.P.W. Chin, A. Fassó, A. Ferrari, P.G. Ortega, A. Mairani, P.R. Sala, G. Smirnov and V. Vlachoudis, "The FLUKA Code: Developments and Challenges for High Energy and Medical Applications", Nuclear Data Sheets 120, 211-214 (2014); A. Ferrari, P.R. Sala, A. Fassó, and J. Ranft, "FLUKA: a multi-particle transport code", CERN-2005-10 (2005), INFN/TC_05/11, SLAC-R-773
11. N.V. Mokhov, "The Mars Code System User's Guide", Fermilab-FN-628 (1995); O.E. Krivosheev, N.V. Mokhov, "MARS Code Status", Proc. Monte Carlo 2000 Conf., p. 943, Lisbon, October 23-26, 2000; Fermilab-Conf-00/181 (2000); N.V. Mokhov, "Status of MARS Code", Fermilab-Conf-03/053 (2003); N.V. Mokhov, K.K. Gudima, C.C. James *et al.*, "Recent Enhancements to the MARS15 Code", Fermilab-Conf-04/053 (2004); https://mars.fnal.gov/
12. P. Degtiarenko and V. Vylet, "Method for detecting and distinguishing between specific types of environmental radiation using a high pressure ionization chamber with pulse-mode readout", US Patent No. 9,847,215 B2, December 2017.
13. Keith Welch, Erik Abkemeier, Bob May, "Technical Basis Document for Radioactivity Limits in Liquids as a Result of Activation or Contamination", Jlab Tech Note JLAB-TN-06-01, January 20, 2006.
14. Keith Welch, "CY2016 National Emissions Standards for Hazardous Air Pollutants (NESHAP) Report", in: Memorandum from Mary Logue, Associate Director, ESH&Q, to Joseph Arango, DOE Site Office Manager, June 22, 2017.
15. Vashek Vylet, "Technical Standard for Radiological Air Cleaning and Ventilation Systems at Jefferson Lab", JLAB-TN-07-004, Jefferson Lab, August, 2008
16. Keith Welch, Gina Dixon, Vashek Vylet, Mary Logue, "Jefferson Lab Process for Release of Material From Radiological Control", JLAB-TN-10-005, Jefferson Lab, March, 2010
17. DOE G 441.1-1C Chg 1, "DOE G 441.1-1C Chg 1, Radiation Protection Programs Guide for Use with Title 10, Code of Federal Regulations, Part 835, Occupational Radiation Protection"; "Accelerator Facility Safety Implementation Guide for DOE O 420.2C, SAFETY OF ACCELERATOR FACILITIES".

Appendix A: Higher Center-of-Mass Energy Alternative

The EIC design documented in this preCDR has a maximum CM energy of ∼70 GeV. This is achieved by collisions of 100 GeV protons and 12 GeV electrons. To expend the science reach, accelerator design concepts with various higher ranges of CM energy have been explored over the time, either as an alternate JLEIC baseline or as future energy upgrade options. The design study for a higher energy version of JLEIC described here focuses on reaching 100 GeV CM energy.

There are several ways to reach this high CM energy design goal. For example, collisions of 10 GeV electrons and 250 GeV protons could attain 100 GeV CM energy. One straightforward approach for realizing HE-JLEIC is doubling the maximum energy of the ion collider ring of the present JLEIC design, namely, 100 GeV to 200 GeV, while keeping the electron complex unchanged. The advantage of this approach is that, with a minimum change of the present JLEIC baseline design, the same advanced design concepts of JLEIC, namely the high luminosity concept and the figure-8 shape of collider rings, are preserved. This ensures that HE-JLEIC will be able to deliver similar ultra high performance in luminosity and beam polarization as the reference JLEIC design.

This design modification of JLEIC, even though apparently relatively minor, affects several other parts of the JLEIC design: design of the ion injector (particularly the ion booster), ion beam polarization, electron cooling, and interaction region design. Technologies of the ion collider ring superconducting magnets also must be evaluated and down-selected. These issues have been examined in the recent design studies, along with obtaining an assessment of luminosity performance of the HE-JLEIC. Here we provide a brief summary of this high CM energy option of JLEIC and discussed several associated accelerator issues.

A.1 Design Concept and Luminosity Performance

The present JLEIC design has an ion collider ring with proton energy up to 100 GeV. This ring is made of conventional SC magnets with up to 3 T maximum dipole field. A corresponding interaction region (IR) has also been designed, and many accelerator R&D projects have been carried out. A higher CM energy JLEIC design is derived from this design by increasing the ion collider ring dipole field from 3 T to 6 T, while keeping the electron collider ring the same.

The layout this JLEIC design is same as documented in this pre-CDR report. The footprint of the two collider rings remains unchanged. The field strength of the ion collider ring arc dipole is doubled; the maximum proton energy the ring can accommodate is 200 GeV and the proton energy at collision ranges from 30 GeV to 200 GeV. To balance energy ramp ranges in the ion booster and collider rings, the extraction energy of the ion booster ring is increased to 11 GeV, so the two rings have about 15 and 17 times the energy (and dipole field) ramp range respectively. This is consistent with what has been achieved in other superconducting hadron storage rings.

Table A.1 summarizes machine parameters at two design points. Figure A.1 shows the luminosity performance over the entire CM energy range.

As the proton beam energy increases, electron cooling efficiency decreases much faster than IBS growth rates. Under these conditions, the proton beam currents at higher energies (200 GeV for

Table A.1: High Energy JLEIC Design Parameters. Average luminosity was calculated assuming a one hour proton beam store time and 30 min nominal beam formation time (including detector turn-on), with 75% machine availability.

CM Energy	**[GeV]**	63.3		89.4	
		protons	**electrons**	**protons**	**electrons**
Beam energy	[GeV]	200	5	200	10
Collision frequency	[MHz]	476	476	59.5	59.5
Particles per bunch	10^{10}	0.56	5.2	7.9	7.2
Beam current	[A]	0.43	4	0.75	0.69
Polarization	[%]	80	80	80	75
RMS bunch length	[cm]	2	1	5.7	1
Normalize emittance, horizontal	[mm]	1.15	90	3.1	720
Normalized emittance, vertical	[mm]	0.23	18	1.5	360
Horizontal $\beta^\star$	[cm]	6.75	4	4	1.6
Vertical $\beta^\star$	[cm]	1.35	0.8	2.6	1
Vertical beam-beam parameter	[–]	0.009	0.023	0.004	0.03
Laslett tune-shift	[–]	0.002	negligible	0.002	negligible
Hour-glass (HG) reduction factor	[–]	0.74		0.48	
Peak Luminosity, with HG reduction	$10^{33}\,\mathrm{cm}^{-2}\,\mathrm{s}^{-1}$	11.3		3.9	
Average luminosity*	$10^{33}\,\mathrm{cm}^{-2}\,\mathrm{s}^{-1}$	7.9		1.9	

example) must be reduced to balance IBS and cooling rates. Peak luminosity is correspondingly lower, about $0.45 \times 10^{33}\,\mathrm{cm}^{-2}\,\mathrm{s}^{-1}$.

To optimize the JLEIC luminosity at high energy, we abandon the requirement that electron cooling and IBS balance each other, and instead purely optimize for higher integrated luminosity. As shown in Table A.1, at the design point of 200 GeV protons and 10 GeV electrons, we have restored the proton beam current to the full nominal current of 0.75 A, and the bunch repetition rate is reduced by a factor of 8. Average and integrated luminosity are raised by rapid replacement of the stored proton beam, since the proton emittance growth rate due to the unrestrained IBS is large. The luminosity decays rapidly, but integrated luminosity in the first several IBS growth times is significant. Table A.1 (right two columns) shows the average luminosity has a factor of 5 boost from the conventional approach (balanced IBS and cooling), assuming a 60 min proton beam store time and a 30 min nominal beam formation time (including detector overheads). It should be noted that, the average luminosities in Table A.1 also apply a 75% operational duty factor.

JLEIC can be further upgraded to reach even higher CM energy. When 6 T SC magnets in the ion collider ring arcs are replaced by 12 T SC magnets, the ring can reach up to 400 GeV proton energy, thus the CM energy can reach 140 GeV. At the mean time, a second ion booster ring with the extraction energy up to 25 GeV must be added to the ion injector to limit the energy ramping range below 20 in each booster or collider ring. This booster could have a same size as the ion collider ring so it could housed in the same tunnel and stacked above the ion collider ring. Figure A.1 shows the upgraded JLEIC average luminosity performance up to 140 GeV CM.

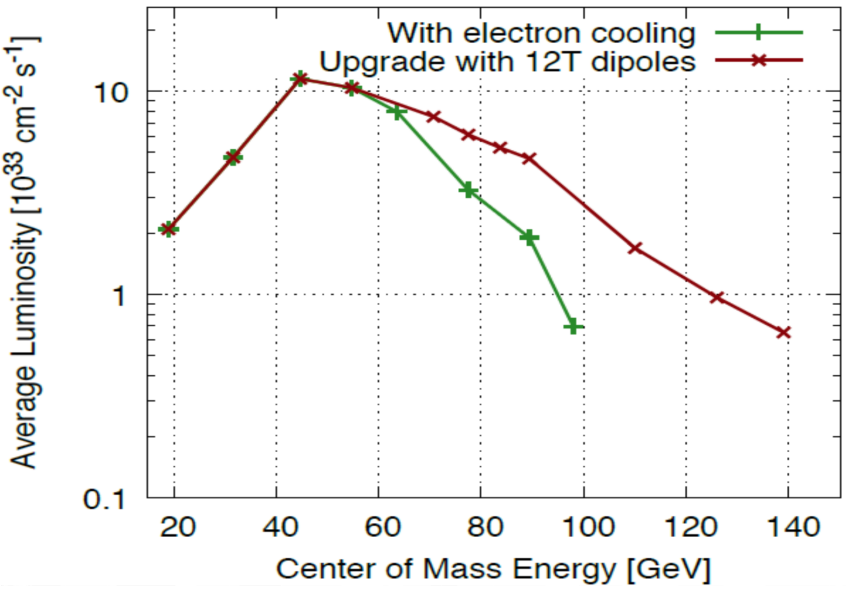

Figure A.1: JLEIC electron-proton collision average luminosity over the CM energy range from 20–140 GeV. Green and red curves show the two different design concepts, using 6 T and 12 T SC magnets respectively in the ion collider ring arcs.

A.2 Ion Ring Magnets

A.2.1 Superconducting Magnets

The superconducting (SC) magnet systems are in the Booster Ring and Ion Collider Ring. There are SC solenoids in the Electron Collider Ring. The Interaction Region contains final focusing quadrupoles, skew quads, correctors, and anti-solenoids. The details of all IR magnets can be found in Section 9.3. This section addresses changes to magnet designs required to attain 200 GeV ions in the Ion Collider Ring.

The magnets in the ion complex are primarily SC dipole, quadrupole, and sextupole magnets for guiding and focusing the ion beam into well-defined orbits in the machine lattices. These magnet systems are designed to allow operation in the energy range of 8–200 GeV in the Ion Collider Ring. The superconducting magnets must achieve the required field range as well as meet stringent requirements on field quality, reproducibility, and long-term reliability. To satisfy all these requirements without increasing technical risk, existing, proven superconducting magnet technology is used for the magnet design/analysis, construction, test measurement, cooling, quench protection, instrumentation, and quality control standards. All magnet designs for JLEIC are based on readily available superconductor materials. Functionality of all magnets is within state-of-the-art, as validated by production magnets in existing accelerators or in tested prototypes with published results [1, 2].

A.2.1.1 Ion Collider Ring Magnets Doubling the energy of ions in the JLEIC machine with the same figure-eight beam path length requires stronger magnets to guide and focus the ion beam along its

well-defined orbit. These dipole, quadrupole, and sextupole magnet systems are designed to allow operation in the energy range of 8 GeV/u to 200 GeV/u in the Ion Collider Ring. The superconducting magnets must achieve the required field range as well as meet stringent requirements on field quality, reproducibility, and long-term reliability. To satisfy all these requirements without increasing technical risk, existing, proven superconducting magnet technology is used for the magnet design/analysis, construction, test measurement, cooling, quench protection, instrumentation, and quality control standards. The dipole performance requirements, except ramp rate, are very similar to the magnet developed by IHEP for the SIS-300 program, therefore, the magnet design and fabrication are guided by this magnet. All magnet designs for JLEIC are based on readily available superconductor materials. Functionality of all magnets is within state-of-the-art, as validated by production magnets in existing accelerators or in tested prototypes with published results [1, 2].

A.2.2 Superconductor Cable

A.2.2.1 NbTi Rutherford Cable A 36-strand (or wire) superconductor cable (Figure A.2 is planned in the fabrication of all of the dipole magnets in the Ion Collider Ring. Due to similar magnet size and conductor requirements, this cable is expected to be very similar to what has been used in the RHIC dipole and quadrupole magnets. The wire and cable fabrication methods are well developed and can be acquired from various sources.

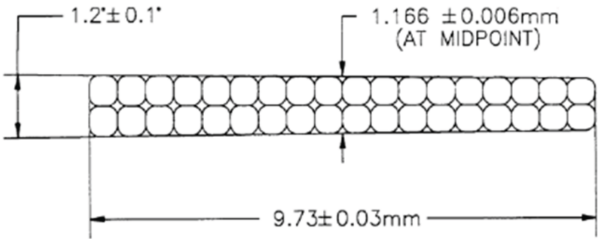

Figure A.2: 36 strand, keystoned NbTi Rutherford cable.

A.2.2.2 Sextupole Conductor The sextupoles have requirements which allow for using MRI style rectangular cross-section superconductor. This material is readily available from multiple sources and is very cost effective.

A.2.3 Dipole Design and Construction

Figure A.3 shows a cross-section of the dipole cold mass. The dipole design is based on a 100 m aperture diameter, two-layer cosine-theta coil, wound from a keystoned, NbTi superconducting Rutherford cable and mechanically supported by a laminated cold steel yoke. A stainless steel outer shell is welded around the yoke and acts as the helium vessel. The helium vessel is also a load bearing part of the yoke assembly. The nominal diameter of the cold mass is 670 mm. The nominal dipole operating temperature is between 4.5–4.7 K. The dipoles are built as straight magnets.

The dipole cold mass design incorporates a cold beam tube (80 mm diameter) to accommodate the beam dynamic aperture and associated sagitta. The Ion Collider Ring coil uses “standard”

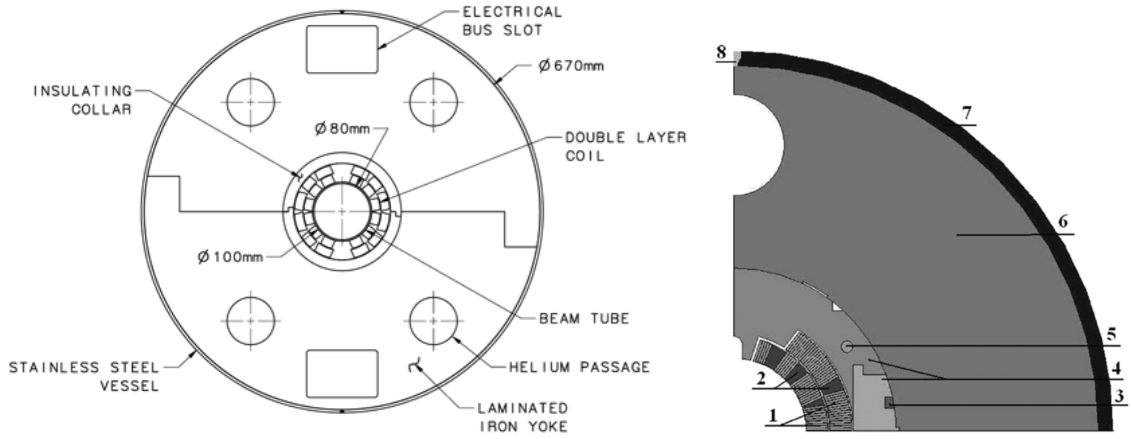

Figure A.3: Cross section view of an Ion Collider Ring dipole.

Rutherford cable and the Booster Ring coils are made using the Modified Rutherford cable for fast-ramping. Insulator material surrounds the coil assembly and interfaces with the yoke. The steel yoke serves as a magnetic return path and acts as a shield to reduce stray field. The yoke laminations contain holes for the necessary busses and for the flow of helium. The yoke and outer shell provide the structure to counteract the forces of the energized coils. End bells are added to complete the "helium vessel" .

A.2.4 Quadrupole Design and Construction

The quadrupole coil design is based on a single-layer or two-layer cosine two-theta coil, wound from a keystoned, NbTi superconducting cable and mechanically supported by a laminated cold steel yoke. Quadrupoles up to ∼90 T/m will be single-layer coil design. Quadrupoles up to 106 T/m will require two-layer coils. The highest field quadrupoles, 164.4 T/m, would require an adjustment to the lattice layout for longer magnets to avoid Nb_3Sn coils. A stainless steel outer shell is welded around the yoke and acts as the helium vessel for the magnet. The helium vessel is also a load bearing part of the yoke assembly. This cold mass assembly, along with that of the sextupole, is mounted within a common helium vessel. The nominal diameter of the cold mass is 670 mm. The nominal quadrupole operating temperature is 4.5–4.7 K. Figure A.4 shows a cross-section of the quadrupole magnet cold mass.

The quadrupole cold mass design incorporates a cold beam tube (80 mm diameter) to accommodate the beam dynamic aperture. Maintaining a common beam tube diameter also aids in minimizing impedance in the ion complex. The Ion Collider Ring coil uses "standard" Rutherford cable and the Booster Ring coils are made using the Modified Rutherford cable for fast-ramping. Insulator material surrounds the coil assembly and interfaces with the yoke. The steel yoke serves as a magnetic return path and acts as a shield to reduce stray field. The yoke laminations contain holes for the necessary busses and for the flow of helium. The yoke and outer shell provide the structure to counteract the forces of the energized coils. End bells are added to complete the common quadrupole-sextupole helium vessel.

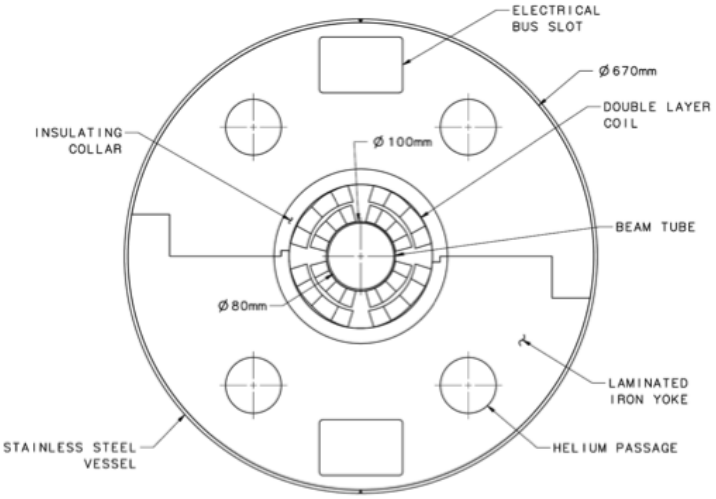

Figure A.4: Cross section view of an Ion Collider Ring quadrupole.

A.2.5 Sextupole Design and Construction

Sextupole magnets are required to compensate for chromaticity and correct for the sextupole field generated in the dipoles. The coils are wound from NbTi MRI type conductor. The laminated cold steel yoke incorporates the poles of the magnet as well. A stainless steel outer shell is welded around the yoke/poles and acts as the helium vessel for the magnet. This cold mass assembly, along with that of the quadrupole, is mounted within a common helium vessel assembly. The nominal diameter of the cold mass is 670 mm. The nominal sextupole operating temperature is 4.5–4.7 K. Figure A.5 shows a cross-section of the sextupole magnet cold mass.

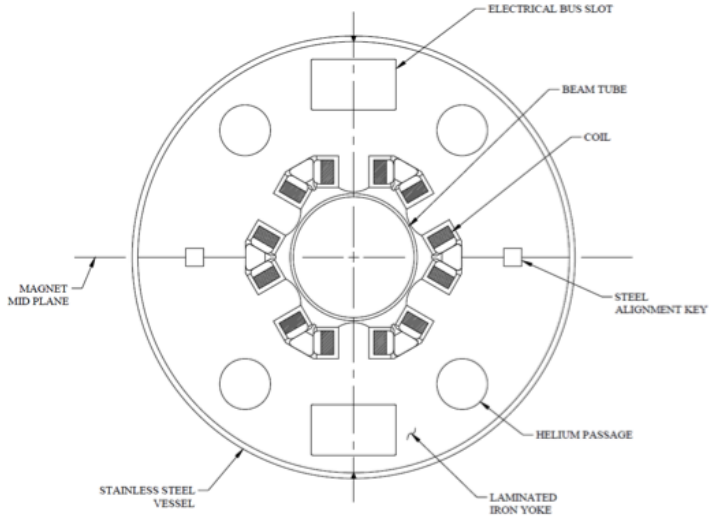

Figure A.5: Cross section view of an Ion Collider Ring sextupole.

The sextupole cold mass design incorporates a cold beam tube (80 mm diameter) to accommodate the beam dynamic aperture. The yoke laminations contain holes for the necessary busses and for the flow of helium. The yoke and outer shell provide the structure to counteract the forces of the energized coils. End bells are added to complete the common quadrupole-sextupole helium vessel.

A.2.6 Magnet Cryostat and Final Assembly

All magnets in an arc half-cell will be placed in a single cryostat. The 200 GeV Ion Collider Ring cryostat is 11.4 m long × 1.00 m diameter and contains 2 × 4 m dipole magnets, 1 quadrupole magnet, and 1 sextupole magnet. Magnets in the straight sections of the ion collider will be housed in individual cryostats. Due to the increased mass of the higher field magnets, three support points are required on the arc half-cell cryostat.

A.3 Electron Cooling

In general, electron cooling is less effective at higher ion beam energies due to the relatively higher momentum in the co-moving frame. We nevertheless want to maximize the luminosity of the system at the full center of mass energy. The questions then arises: how well can we cool the protons at an energy of 200 GeV?

The simplest upgrade to the cooling is a doubling of the maximum electron cooler energy from 55–110 MeV. The higher energy does reduce the relative energy spread of the electrons for a given normalized emittance but the effects of CSR are about the same as the energy is increased so the correlated energy limits should be similar at the higher energy.

The proton beam size will shrink due to the smaller geometric emittance at the higher energy and the electron beam size will remain the same unless we change the solenoid field. To keep the relative beam sizes the same we will double the solenoid field to 2 T. The radius of the electron beam beer can distribution will then be the same as the rms proton beam size.

The injector for the electron cooler will be exactly the same as for the lower energy cooler. The only difference will be that the merger system will have to kick the high energy beam twice as hard. The linac, on the other hand, will have to accelerate more than twice as much. This is more easily accomplished by doubling the number of linac cavities. The chirper and de-chirper cavities are already running at low gradient so they can just be doubled in gradient.

All the beam transport magnets must double in strength. This is not difficult since most magnets are rather weak at this low an energy. The vacuum chamber will be the same as at low energy.

We have carried out some cooling simulations with a 3.2 nC bunch at 110 MeV and a 2 T solenoid. The electron bunch length was increased to 3 cm full length. The proton bunch charge was lowered to 0.43×10^{10} particles. The results of the simulation are shown in Figure A.6.

We also assume that the electron beam size in the cooler is matched to the proton beam size, which is a flat beam. This requires a transformer that reduces the emittance in the vertical plane

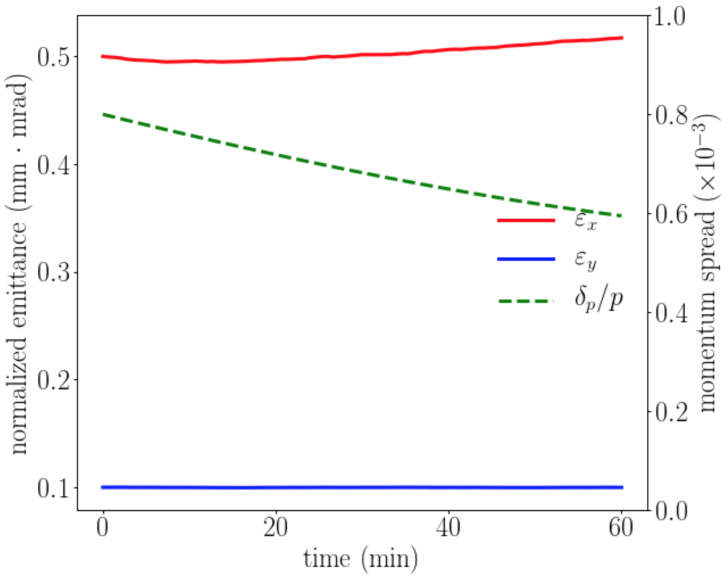

Figure A.6: The longitudinal emittance continues to cool over the first hour of storage. The transverse emittances are approximately constant. The dispersion in the proton beam is 1.8 m in this case and the x/y coupling in the proton beam is 24%.

and increases it in the horizontal plane. This increases the cooling while reducing the discrepancy between the horizontal and vertical cooling.

The equilibrium beam sizes are quite small so the luminosity will be good. It is assumed that the RF voltage is continuously varied to keep the proton bunch length constant. This reduces the tendency to overcool the proton bunches.

The cooler itself will look just like the one described in Chapter 6. The only noticeable difference will be that the linac will consist of two cryomodules instead of one. The specifications are listed in Table A.3. It is assumed here that we can achieve the higher charge of 3.2 nC for the electron cooler injector. The one technical challenge will be doubling the strength of the harmonic kickers. This might require the use of two cells instead of one.

A.4 Ion Polarization

A.4.1 Parameters of the spin rotators for polarization control

To preserve the ion polarization, the spin tune induced by the spin rotators must significantly exceed the incoherent part of the zero-integer spin resonance strength

$$\nu \gg \omega_{incoh} \tag{A.4.1}$$

Graphs of the incoherent parts of the proton and deuteron resonance strengths as functions of the beam momenta in the JLEIC ion collider ring are shown in Figure A.7. These calculations assume a normalized vertical beam emittance of 0.7 µm − rad. The graphs in Figure A.7 show that the

Table A.2: Ion Collider Ring Superconducting Magnet Inventory

Magnet Type	**Number of Magnets**	**Magnet Strength (T, T/m, T/m^2)**	**Magnetic length [m]**	**Coil Aperture radius [mm]**	**Beam Pipe Aperture Radius [mm]**	**Operating Current [A]**
Dipole	254	6.12 T	4.00	50	40	800
Dipole	5	9.34 T	4.00	50	40	1220
Quadrupole	41	40–60 T/m	0.80	50	40	312
Quadrupole	34	60–80 T/m	0.80	50	40	417
Quadrupole	28	80–100 T/m	0.80	50	40	520
Quadrupole	155	106 T/m	0.80	50	40	551
Quadrupole	44	164.4 T/m	0.80	50	40	558
Sextupole	56	1057 T/m^2	0.50	50	40	200

Table A.3: Electron beam specifications for the electron cooler. The repetition rate is for the case of highest proton luminosity.

Parameter	**Units**	**Value**
Energy	[MeV]	20–110
Charge	[nC]	3.2
CCR pulse frequency	[MHz]	476.3
Gun frequency	[MHz]	43.3
Bunch length (tophat)	[cm,○]	3 / 23
Thermal (Larmor) emittance	[mm-mrad]	<19
Cathode spot radius	[mm]	3.1
Cathode field	[T]	0.05
Normalized hor. drift emittance	[mm-mrad]	36
rms Energy spread (uncorr.)*		3×10^{-4}
Energy spread (p-p corr.)*		$<6\times10^{-4}$
Solenoid field	[T]	2
Electron beta in cooler	[cm]	37.6
Solenoid length	[m]	4× 15
Bunch shape		beer can

spin tune values of $\nu_p = 10^{-2}$ for protons and $\nu_d = 10^{-4}$ for deuterons are sufficient to preserve the polarization to 200 GeV/c.

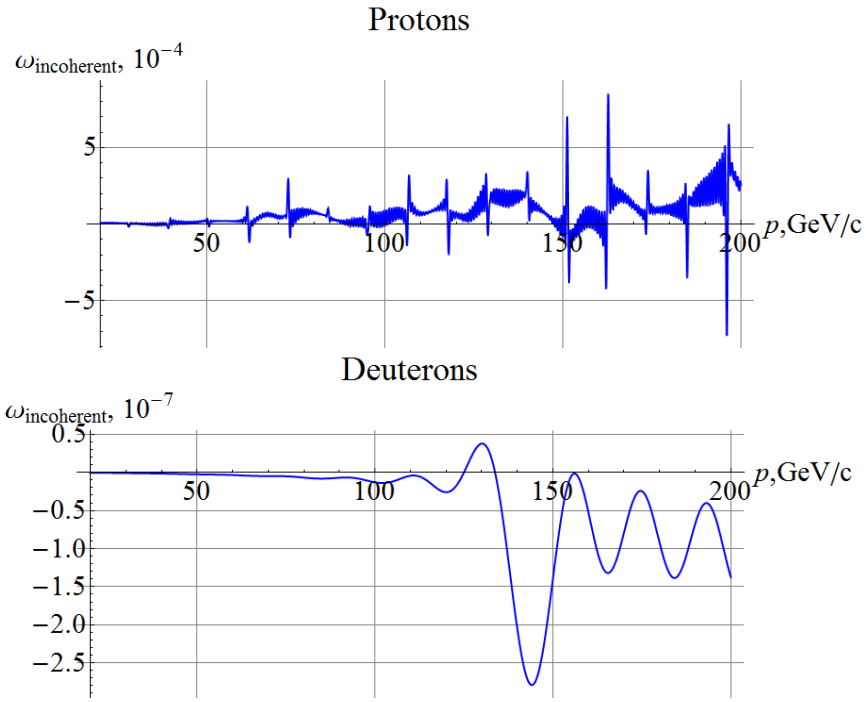

Figure A.7: Incoherent parts of the proton (top) and deuteron (bottom) zero-integer spin resonance strengths in the JLEIC ion collider ring as functions of the beam momenta.

When setting the polarization direction, one must account for the influence of the coherent part of the zero-integer spin resonance strength. The coherent part does not depolarize the beam. However, it produces a coherent rotation of all spins about a direction determined by lattice imperfections and alignment errors of the collider's magnetic elements. Therefore, when manipulating the polarization direction, the spin tune value induced by the spin rotators must be sufficient to "compensate" the coherent part of the resonance strength.

Graphs of the coherent parts of the proton and deuteron resonance strengths as functions of the beam momenta in the JLEIC collider ring are shown in Figure A.8. These calculations assume an rms vertical closed orbit distortion of 200 µm. The graphs in Figure A.8 show that compensation of the influence of the coherent part of the resonance strength on the polarization in the momentum range of up to 200 GeV/c requires spin tune values of $\nu_p = 7 \cdot 10^{-2}$ for protons and $\nu_d = 4 \cdot 10^{-4}$ for deuterons.

A.4.2 Universal spin rotator for protons and deuterons

The 100 GeV design for proton and deuteron polarization control uses a universal 3D spin rotator on the basis of weak solenoids, which allow one to induce spin tune values of 10^{-2} for protons and 10^{-4} for deuterons in the momentum range of up to 100 GeV/c. Schematic placement of the 3D rotator elements in the collider ring's experimental straight is shown in Figure A.9. The lattice

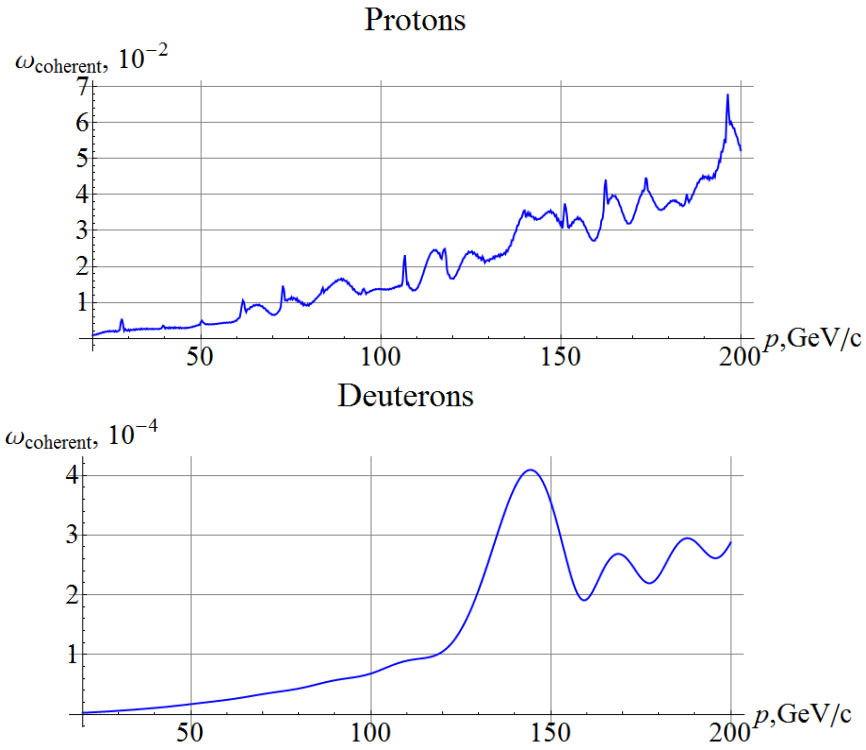

Figure A.8: Coherent parts of the proton and deuteron zero-integer spin resonance strengths in the JLEIC ion collider ring as functions of the beam momenta.

quadrupoles are shown in black, the vertical-field dipoles are green, the radial-field dipoles are blue, and the control solenoids are yellow. With each module's length of ∼8 m ($L_x = L_y$ =0.6 m, L_z = 2 m), the fixed orbit deviation in the bumps is ∼16 mm in the whole momentum range of the collider. Placement of each bump between lattice quadrupoles keeps the experimental straight dispersion-free.

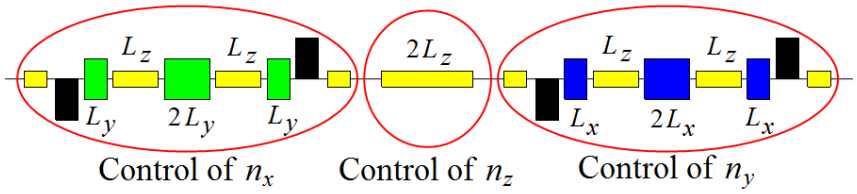

Figure A.9: Placement of the 3D spin rotator elements.

The 3D spin rotator can be used for deuterons of up to 200 GeV/c as well. For setting the spin tune of 10^{-4}, the maximum solenoid field is then 1.5 T. However, to set the spin tune of $4 \cdot 10^{-4}$, the maximum solenoid field is 6 T. In this case, spin reversal takes tens of seconds instead of a few seconds. For protons, the universal 3D spin rotator is no longer suitable. When operating in the momentum range of up to 200 GeV/c, it is most optimal to abandon the concept of rotator universality. While use of longitudinal fields is still optimal for deuterons at high momenta, it

becomes more optimal to use transverse fields for protons. Below we provide examples of such spin rotators for deuterons and protons.

A.4.3 Deuteron spin rotator using longitudinal fields

Figure A.10 shows a design of a deuteron spin rotator using two sections of the vertical-field arc magnets located symmetrically around the interaction point.

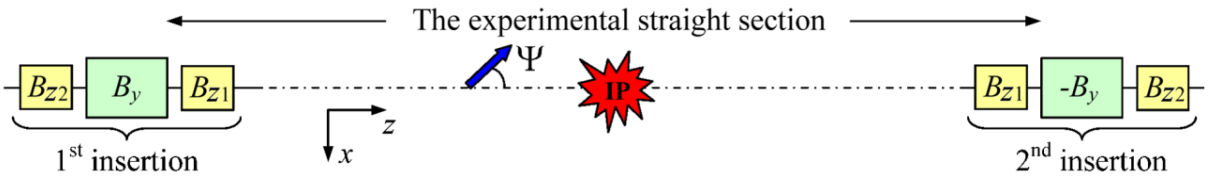

Figure A.10: Schematic of a spin rotator for deuterons.

Any horizontal angle Ψ between the polarization and the beam can be set in the experimental straight by introducing longitudinal fields around two sections of the arc magnets. The required spin rotations by the longitudinal fields in each insertion are given for small values of the spin tune ν by

$$\varphi_{z1} = \pi\nu\frac{\sin(\varphi_y - \Psi)}{\sin\varphi_y}, \qquad \varphi_{z2} = \pi\nu\frac{\sin\Psi}{\sin\varphi_y}, \tag{A.4.2}$$

where $\varphi_{z1} = (1+G)B_{z1}L/(B\rho)$ and $\varphi_{z2} = (1+G)B_{z2}L/(B\rho)$ are the spin rotation angles of the solenoids, $\varphi_y = \gamma G\alpha$ is the spin rotation angle of the dipole section between the solenoids, α is the orbit bending angle between the solenoids, Ψ is the angle between the polarization and the beam direction, and $B\rho$ is the magnetic rigidity.

To work in the whole deuteron energy range of the collider, the first longitudinal-field region is placed in the experimental straight while the second longitudinal-field region is located after one regular dipole with an orbital bending angle of 4.4°. The field integrals needed for setting the longitudinal ($\Psi = 0°$) and transverse ($\Psi = 90°$) polarizations are shown in Figure A.11 as functions of the beam momentum. The spin tune of the collider for the given field integrals has a value of $\nu = 10^{-3}$, which greatly exceeds the zeroth harmonic of the spin perturbations associated with imperfections of the collider's magnetic structure. The maximum field integral of a single solenoid at the maximum energy does not exceed $2.5\,\mathrm{T-m}$.

A.4.4 Proton spin rotator using transverse fields

Figure A.12 shows a design of a proton spin rotator using a constant orbit bump. The constant orbit bump is created in the collider's plane using alternating-direction vertical-field dipoles. The spin rotation angle in a dipole is proportional the beam energy $\varphi_y = \gamma G\alpha_{orb}$ where α_{orb} is the constant orbital angle of the dipole.

Control of the proton polarization is done using weak radial fields rotating the spin by small angles ϕ_{x1}, ϕ_{x2}, ϕ_{x3}, and ϕ_{x4}. These fields must satisfy the conditions of closed orbit restoration

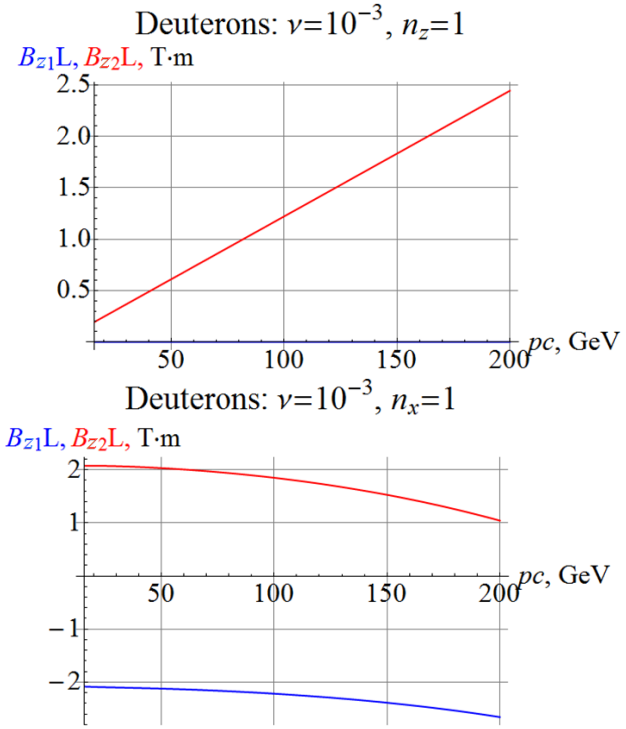

Figure A.11: Dependence of the insertion's longitudinal field integrals (T·m) on the beam momentum (GeV/c) for the longitudinal (left) and radial (right) polarization direction settings of the deuteron beam in the JLEIC collider ring.

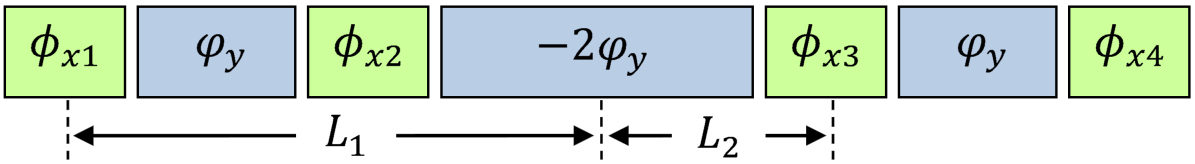

Figure A.12: Schematic of a proton spin rotator with a horizontal orbit bump.

at the entrance into and the exit from the rotator:

$$\phi_{x1} + \phi_{x2} + \phi_{x3} + \phi_{x4} = 0, \qquad L_1\phi_{x1} + L_2\phi_{x2} = L_2\phi_{x3} + L_1\phi_{x4}. \tag{A.4.3}$$

In the approximation of small angles $\phi_{xi} \ll 1$ and a small spin tune $\nu \ll 1$, this rotator rotates the spin about an axis in the collider's plane. To stabilize the spin in the direction $\vec{n} = (n_x, 0, n_z)$,

one must set the following spin rotation angles of the control (radial-field) dipoles:

$$\phi_{x1} = \frac{\pi\nu}{\sin(\varphi_y/2)}\left(\frac{n_x}{\sin(\varphi_y/2)} - \frac{L_2}{L_1}\frac{n_z}{\cos(\varphi_y/2)}\right), \tag{A.4.4}$$

$$\phi_{x2} = \frac{\pi\nu}{\sin(\varphi_y/2)}\left(-\frac{n_x}{\sin(\varphi_y/2)} + \frac{n_z}{\cos(\varphi_y/2)}\right), \tag{A.4.5}$$

$$\phi_{x3} = -\frac{\pi\nu}{\sin(\varphi_y/2)}\left(\frac{n_x}{\sin(\varphi_y/2)} + \frac{n_z}{\cos(\varphi_y/2)}\right), \tag{A.4.6}$$

$$\phi_{x4} = \frac{\pi\nu}{\sin(\varphi_y/2)}\left(\frac{n_x}{\sin(\varphi_y/2)} + \frac{L_2}{L_1}\frac{n_z}{\cos(\varphi_y/2)}\right). \tag{A.4.7}$$

The radial field integrals are related the spin rotation angles by:

$$B_{xi}L_x = \frac{\varphi_{xi}}{\gamma G}B\rho. \tag{A.4.8}$$

The formulae for the spin rotation angles give that the rotator's operation range is determined by

$$\varphi_{y\,max} = \gamma_{max}G\alpha_{orb} < \pi. \tag{A.4.9}$$

For optimal operation of the rotator in the energy range from 100–200 GeV, the spin rotation angle at 200 GeV should be chosen at $\varphi_{y\,max} = 2\pi/3$. This requires a vertical field integral of $\approx$3.6 T − m at 200 GeV. If the bump is created using 6 T magnets the length of each vertical-field dipole is L_y =0.6 m.

Let us select the length of the weak radial-field control dipoles at L_x =1 m. Then the total length of the spin rotator with gaps between the magnets of δL =0.2 m is

$$L_{tot} = 4L_y + 4L_x + 6\delta L = 2.4 + 4 + 1.2 = 7.6\,\text{m}. \tag{A.4.10}$$

The length L_1 and L_2 indicated in the scheme are 3.3 and 1.3 m, respectively.

Figure A.13 shows the integrals of the radial control fields as functions of the beam momentum when setting the longitudinal ($n_z = 1$, $\Psi = 0$) and radial ($n_x = 1$, $\Psi = 90^\circ$) polarization directions at the exit from the rotator.

The maximum vertical excursion of the closed orbit in the process of polarization control does not exceed 5 mm at 100 GeV. The size of the constant bump in the horizontal plane is about 11 mm. The maximum field of the control dipoles does not exceed 1.5 T.

To control the polarization in the vertical plane $\vec{n} = (0, n_y, n_z)$, it is sufficient to switch the radial- and vertical-field dipoles in the scheme shown in Figure A.12. The radial-field dipoles then create a constant vertical bump while polarization control is done using four weak vertical-field dipoles.

In addition, we note that, to compensate the coherent part of the proton zero-integer spin resonance strength, it is convenient to use several 3D rotators with reduced integrals of the control dipole fields. It is also efficient to use several pairs of symmetrically-located compact transverse-field Siberian snakes with longitudinal spin rotation axes.

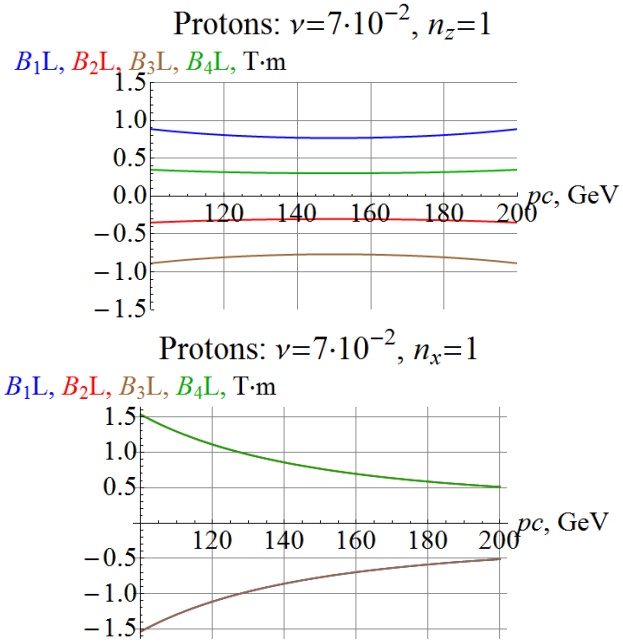

Figure A.13: Integrals of the radial control fields as functions of the beam momentum when setting the longitudinal (left) and radial (right) proton polarization directions. The spin tune is $\nu = 7{\cdot}10^{-2}$.

A.5 Interaction Region

The JLEIC interaction region (IR) design described above has been optimized for full acceptance detection at ion beam momenta of up to 100 GeV/c. Its operation at higher ion momenta is limited by the peak magnetic fields of the final focusing quadrupoles (FFQs), which reach their maxima of 6 T at 100 GeV/c. We consider a 6 T pole-tip field as a conservative limit of the conventional super-conducting magnet technology. Therefore, we modify the IR design to stay within this limit when increasing the top ion momentum to 200 GeV/c. There are also additional requirements to the 200 GeV/c IR design associated with its detection and beam dynamics performance. All of these requirements can be summarized as:

- Maximum pole-tip fields at 200 GeV/c of 6 T.
- Minimum impact on the forward hadron acceptance compared to the 100 GeV/c design.
- Minimum impact on the luminosity performance compared to the 100 GeV/c design.
- Minimum impact on the beam dynamics compared to the 100 GeV/c design.

Meeting these requirements is the most challenging in the forward ion direction with its forward hadron detection system. Therefore, we focus our discussion on the forward ion side of the IR. Note that no modifications are needed in the electron IR design. Sufficient acceptance to forward scattered products requires sufficiently large apertures of the FFQs forming an acceptance cone with a sufficiently large angle of about ±10 mrad as the 100 GeV/c design. Our solution to this problem is double the lengths of all FFQs. This drops their required field gradients by about a factor of two at a given momentum, thus, allowing operation at 200 GeV/c with a 6 T pole-tip

field. The optics of the modified IR design is shown in Figure A.14. The total length increase is 4.8 m. The associated change in the geometry of the IR is relatively small and is taken into account by adjustment of the downstream dipole section. The forward acceptance cone has an angle of ±9.1 mrad. Its reduction is not significant compared to the 100 GeV/c design and is caused by reduced solid angle of the back aperture of the first FFQ. The parameters of the modified FFQs are summarized in Table A.4.

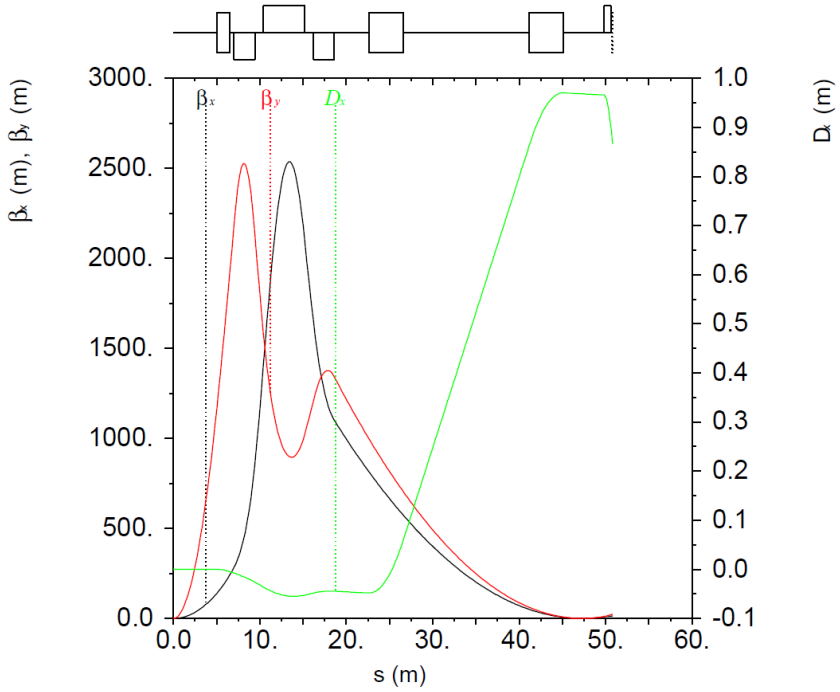

Figure A.14: Optics of the downstream side of the ion IR optimized for an ion momentum of 200 GeV/c.

Table A.4: Parameters of the downstream ion FFQs. ⋆ maximum values corresponding to 200 GeV/c protons. ⋆⋆ distance from the IP to the magnet side facing the IP

Magnet	$B_{pole-tip}$	$\partial B_y/\partial x$	Length	R_{inner}	R_{outer}	L to IP
	(T)⋆	(T/m)⋆	(m)	(cm)	(cm)	(m)⋆⋆
Quad 1d	6.0	-70.4	2×1.2	8.5	17	7
Quad 2d	5.5	39.4	4.8	13.8	26	10.4
Quad 3d	5.2	-30.7	2.4	16.9	29	16.2

In Figure A.14, we adjust the values of $\beta^{\star}_{x,y}$ from 10/2 cm to 18/2.15 cm to keep the maximum values of the β_{max} functions inside the FFQs at about 2500 m, the same as in the 100 GeV/c design. We impose this constraint to keep the contribution of the FFQs to the resonance driving terms approximately constant [3], since their normalized integrated strengths remain approximately constant. This should ensure a minimum impact on the beam dynamics. Keeping the β functions constant requires increase of $\beta^{\star}$ because doubling the lengths of the FFQs increases the effective

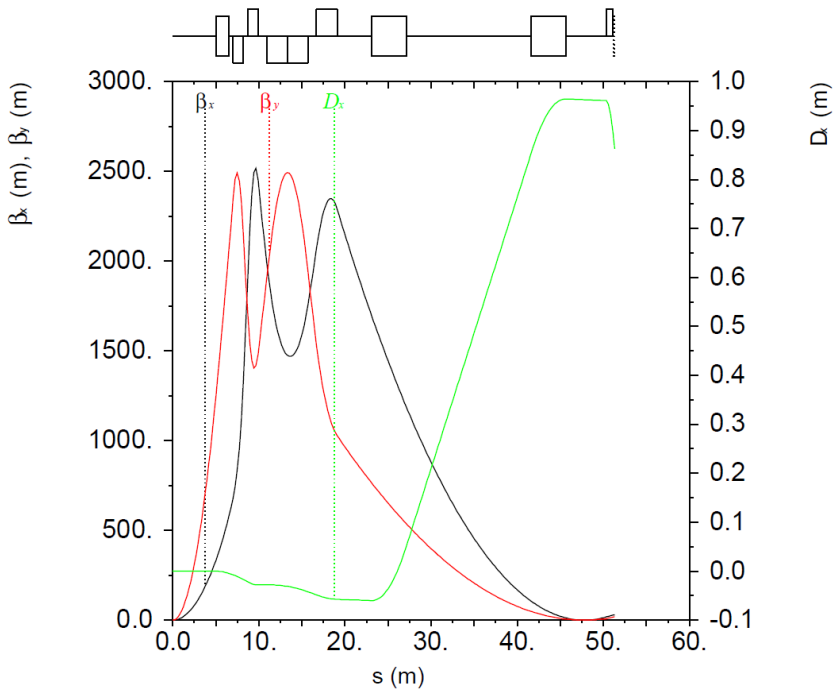

Figure A.15: Optics of the downstream side of the ion IR when operating below an ion momentum of 65 GeV/c.

focal length of the FFQ triplet. The $\beta^\star$ increase may lead to a luminosity loss. However, we mitigate this effect by replacing the first FFQ with a pair of half-length quadrupoles. At ion momenta below 65 GeV/c, the 6-T pole-tip limit allows one to run the half-length quadrupoles with opposite polarities as shown in Figure A.15. This reduces the effective focal length of the FFQs and allows one to reduce $\beta^\star$ to 7.5/2 cm with the same β_{max} of 2500 m. The $\beta^\star$ reduction below 65 GeV/c provides a luminosity boost of about 15%. Above 65 GeV/c, the two half-length quadrupoles are powered with the same polarities and operate as a single unit with a maximum pole-tip field of 6 T at 200 GeV/c. The luminosity loss associated with the reduction $\beta^\star$ is about 28% compared to the 100 GeV/c design. However, it allows for operation of the same IR design in the whole momentum range from 20–200 GeV/c. These luminosity factors are taken into account in the luminosity plot.

REFERENCES

1. S. Kozub *et al.*, "SIS 300 Dipole Model", IEEE Transactions on Applied Superconductivity, Vol. 20, No. 3, June 2010 (pp. 200–203).
2. J.E. Kaugerts *et al.*, "Design of a 6 T, 1 T/s Fast-Ramping Synchrotron Magnet for GSI's Planned SIS 300 Accelerator", IEEE Transactions on Applied Superconductivity, July 2005 (pp 1225–1227). Retrieved from: `https://www.researchgate.net/publication/3312818`
3. J. Bengtsson, "The Sextupole Scheme for the Swiss Light Source (SLS): An Analytic Approach" SLS Note 9/97, PSI, Switzerland (1997).

Appendix B: Reference Tables

Table B.1: JLEIC Booster Beam Kinematics Parameters

Parameter	**Symbol**	**Units**	**Protons**			^{208}**Pb**		
			Injection	**2 GeV**	**Extraction**	**Injection**	**2 GeV**	**Extraction**
Z	Z	[–]	1	1	1	67	67	67
A	A	[–]	1	1	1	208	208	208
Z/A	Z/A	[–]	1	1	1	0.322	0.322	0.322
Mass	m	[MeV/c^2]	938.272	938.272	938.272	193694	193694	193694
Mass	m/u	[MeV/c^2/u]	938.272	938.272	938.272	931.223	931.223	931.223
KE/u	E_k/u	[MeV/c^2/u]	280	2000	8000	100	361	2079
KE	$E_{k,tot}$	[MeV/c^2]	280	2000	8000	20800	75088	432432
Tot Energy	E_{tot}	[MeV/c^2]	1218.27	2938.27	8938.27	214494	268782	626126
Tot E/u	$E_{tot/u}$	[MeV/c^2/u]	1218.27	2938.27	8938.27	1031.22	1292.22	3010.22
Gamma	γ	[–]	1.29842	3.13158	9.52631	1.10739	1.38766	3.23255
Beta	β	[–]	0.637843	0.947644	0.994475	0.429582	0.693313	0.950947
Velocity	v	[10^8 m/s]	1.91221	2.84097	2.98136	1.28786	2.07850	2.85087
Momentum	p	[MeV/c]	777.066	2784.44	8888.89	92143.0	186350	595413
Momentum/u	p/u	[MeV/c/u]	777.066	2784.44	8888.89	442.995	895.915	2862.56
Rigidity	(Bρ)	[T-m]	2.592	9.288	29.650	4.587	9.278	29.643
Dipole field	B	[T]	0.262	0.940	3.001	0.464	0.939	3.000
Revolution frequency	f_{rev}	[kHz]	609.975	906.241	951.026	410.814	663.022	909.400
Revolution angular frequency	ω_{rev}	[kHz]	3832.59	5694.08	5975.47	2581.21	4165.89	5713.93
Revolution period	T_{rev}	[µs]	1.639	1.103	1.051	2.434	1.508	1.100
Phase slip factor	η_{tr}	[–]	-0.590	-0.099	-0.008	-0.813	-0.516	-0.093

Table B.3: Parameters During the JLEIC Ion Bunch Formation Process

	0.75 A **proton (26 booster cycles)**	0.4 A **Pb (27 booster cycles)**
Linac section 1 (RFQs, DTL, QWR1/QWR2)		
particle at entrance	H^-	Pb^{30+}
RFQ/DTL/QWR frequency (MHz)	100	100
exit E_k (MeV)	62	13
Linac section 2 (QWR3, 9 HWR modules)		
Particle	H^-	Pb^{67+}
$\Delta E/E$ (rms)	0.07%	0.05%
HWR RF frequency (MHz)	200	200
exit E_k (MeV)	285	100
Booster (322.19m circumference) capture		
Particle	H^+	Pb^{67+}
E_k (MeV)	285	100
$B\rho$ (T-m)	2.62	4.59

RF frequency Booster C_1 (MHz)	0.593	0.398
$\Delta E/E$ (rms)	0.10%	0.07%
σ_z (m, Gaussian)	56	56
# of bunches	1	1
Normalized emittance (μm)	2.65	1.5
$\sigma_{x,y}$ (mm)	6.7	6.7
Particles in booster	1.36×10^{12}	8.5×10^9
Laslett tuneshift (Gaussian)	0.131	0.065
booster ramp/compression		
RF frequency Booster C_1 (MHz)	0.925	0.883
E_k (GeV)	8	2.08
$B\rho$ (T-m)	29.65	29.65
Max RF voltage (kV)	23	23
booster 1:2 split		
RF frequency Booster C_2 (MHz)	7.402	7.070
$\Delta E/E$ (rms)	1.7×10^{-4} (2)	1.7×10^{-4}
σ_z (m, Gaussian)	6.7	6.7
# of bunches	2	2
harmonic number	8	8
Collider stacking/DC cooling (emittance maintenance) C =2255.34 m		
Particle	H^+	Pb^{82+}
Injected E_k (GeV/u)	8	2.08
$B\rho$ (T-m)	29.65	24.23
RF freq (MHz) I-Ring C_1	7.402	7.070
harmonic number	56	
rms Bunch length (m)	6.7	6.7
Normalized emittance (μm)	2.65	1.5
Laslett tuneshift (Gaussian)	0.046	0.152
# of bunches	52	54
rms $\Delta E/E$	$\sim 3 \times 10^{-3}$	$\sim 4 \times 10^{-4}$
RF voltage	1.9 kV	28 kV
Collider DC cooling (emittance reduction)		
E_k (GeV/u)	8	
RF freq (MHz) I-Ring C_1	7.402	
harmonic number	56	
$B\rho$ (T-m)	29.65	75.16
rms Bunch length (m)	6.7	6.7

# of bunches	52	54
rms $\Delta E/E$	3×10^{-4}	2×10^{-4}
Vertical normalized emittance ϵ_{ny} (µm)	0.75	0.164
Laslett tuneshift (Vertical, Gaussian)	0.152	0.150
RF voltage	1.1 kV	1.2 kV
Collider ramp, before splitting		
E_{k} (GeV/u)	20	
RF freq I-Ring C_1 (MHz)	7.436	
rms Bunch length (m)	5	5
# of bunches	52	54
rms $\Delta E/E$	1.6×10^{-4}	1.1×10^{-4}
Longitudinal emittance		
RF voltage I-Ring C_1	1.3 kV	1.47 kV
collider 2^6 splitting		
RF freq I-Ring C_2 (MHz)	14.873	
RF voltage I-Ring C_2	3.7 kV	4.3 kV
RF freq I-Ring C_3 (MHz)	29.746	
RF voltage I-Ring C_3	7.5 kV	8.5 kV
RF freq I-Ring C_4 (MHz)	59.492	
RF voltage I-Ring C_4	15 kV	17 kV
RF freq I-Ring C_5 (MHz)	118.983	
RF voltage I-Ring C_5	30 kV	34 kV
RF freq I-Ring C_6 (MHz)	237.967	
RF voltage I-Ring C_6	60 kV	68 kV
RF freq I-Ring C_7 (MHz)	475.934	
RF voltage I-Ring C_7	120 kV	136 kV
rms Bunch length (m)	0.079	0.079
rms $\Delta E/E$	1.9×10^{-4} (20% growth)	1.3×10^{-4} (20% growth)
Harmonic number	3584	
bucket insertion (for collision energy <36 GeV)		
RF freq (MHz) I-Ring C_7	475.934–476.066	475.934–476.066
compression for 952 MHz capture		
E_{k} (GeV/u)	20	
RF freq I-Ring C_8 (MHz)	475.9	
rms Bunch length (m)	0.063 (short enough to be captured by 952 MHz RF)	
# of bunches	3328	3456
rms $\Delta E/E$	4×10^{-4}	2.7×10^{-4}

RF voltage I-Ring C_8	812 kV	916 kV
beginning of collision		
E_k (GeV/u)	20	
RF freq (MHz)	9	52.65 ($h = 7174$)
rms Bunch length (mm)	14.2	14.5
# of bunches	3328	3456
rms $\Delta E/E$	1.07×10^{-3}	6.9×10^{-4}
RF voltage	56 MV	56 MV
E_k (GeV/u)	40	
RF freq (MHz)	952.56 ($h = 7168$)	
$B\rho$ (T-m)	136.5	346.2
rms Bunch length (mm)	12.8	13.1
# of bunches	3328	3456
rms $\Delta E/E$	5.9×10^{-4}	3.8×10^{-4}
RF voltage	56 MV	56 MV
E_k (GeV/u)	100	
$B\rho$ (T-m)	336.7	
RF freq (MHz)	952.77 ($h = 7168$)	
rms Bunch length (mm)	10.4	
# of bunches	3328	
rms $\Delta E/E$	2.9×10^{-4}	
RF voltage	45 MV	

Table B.2: JLEIC Ion Collider Ring Beam Kinematics Parameters

Parameter	**Symbol**	**Units**	**Protons**			^{208}**Pb**		
			Injection	**3T**	**6T**	**Injection**	**3T**	**6T**
Z	Z	[–]	1	1	1	82	82	82
A	A	[–]	1	1	1	208	208	208
Z/A	Z/A	[–]	1	1	1	0.394231	0.394231	0.394231
Mass	m	[MeV/c^2]	938.272	938.272	938.272	193687	193687	193687
Mass	m/u	[MeV/c^2/u]	938.272	938.272	938.272	931.185	931.185	931.185
KE/u	E_{k}/u	[MeV/c^2/u]	8000	97200	195300	2079	37760	76440
KE	$E_{\mathrm{k,tot}}$	[MeV/c^2]	8000	97200	195300	432432	7854080	15899520
Tot Energy	E_{tot}	[MeV/c^2]	8938.27	98138.27	196238.27	626119	8047767	16093200
Tot E/u	$E_{\mathrm{tot/u}}$	[MeV/c^2/u]	8938.27	98138.27	196238.27	3010.19	38691.2	77371.2
Gamma	γ	[–]	9.52631	104.595	209.149	3.23264	41.5505	83.0889
Beta	β	[–]	0.994475	0.999954	0.999989	0.950950	0.999710	0.999928
Velocity	v	[10^8 m/s]	2.98136	2.99779	2.99789	2.85088	2.99706	2.99771
Momentum	p	[MeV/c]	8888.89	98133.8	196236	595407	8045440	16092000
Momentum/u	p/u	[MeV/c/u]	8888.89	98133.8	196236	2862.54	38680.0	77365.6
Rigidity	(Bρ)	[T-m]	29.650	327.339	654.573	24.220	327.277	654.601
Dipole field	B	[T]	0.272	3.000	6.000	0.222	3.000	6.000
Revolution frequency	f_{rev}	[kHz]	138.417	139.180	139.185	132.359	139.146	139.176
Revolution angular frequency	ω_{rev}	[kHz]	869.702	874.493	874.523	831.637	874.280	874.470
Revolution period	T_{rev}	[µs]	7.225	7.185	7.185	7.555	7.187	7.185
Phase slip factor	η_{tr}	[–]	-0.005	0.006	0.006	-0.089	0.006	0.006